UNIVERSITÉ CATHOLIQUE DE LOUVAIN

EARTH AND LIFE INSTITUTE

ENVIRONMENTAL SCIENCES

Controls on weathering fluxes from hydrothermally-active volcanic regions

a Ge/Si ratio and Si isotopes perspective

François GASPARD

Thèse présentée en vue de l'obtention du grade de

Docteur en sciences agronomiques et ingénierie biologique

Membres du jury :

Président	Pr. Emmanuel Hanert (UCLouvain, Belgium)
Promotrice	Pr. Sophie Opfergelt (UCLouvain, Belgium)
Co-promoteur	Pr. Pierre Delmelle (UCLouvain, Belgium)
Lecteurs	Pr. Yannick Agnan (UCLouvain, Belgium)
	Pr. Alain Bernard (ULB, Belgium)
	Dr. Pascale Louvat (IPGP, France)
	Pr. Damien Cardinal (Sorbonne Université, France)

This PhD thesis was funded by

Foundation for Scientific Research (FNRS)

under Grant Agreement number 26043653

FluxHyd – Controls on weathering fluxes from hydrothermally-active volcanic regions

- *Rien n'est impossible, seules les limites de nos esprits définissent certaines choses comme inconcevables.* –
Marc Levy.

PS: Choisir, c'est profiter.

Remerciements

Chaque étape de la vie est une aventure où l'on apprend à mieux se connaître en tant que citoyen.ne, en tant que personne. Surtout une première expérience professionnelle. Sortir de ses routines en débarquant dans le monde inconnu de la communauté universitaire n'est pas une tâche aisée. Après quatre années passées au labo, l'heure est au bilan. Une thèse n'est pas seulement un travail de recherche pointilleux de longue haleine. C'est surtout une aventure humaine indescriptible. Avec ses joies, ses doutes, ses peines, ses remises en question permanentes. Cette aventure, qui peut paraître si solitaire, est avant doute une aventure humaine inenvisageable sans les formidables rencontres humaines côtoyées le long du périple. À travers ces quelques lignes, je voudrais adresser mes remerciements les plus sincères à celles.ceux qui ont contribué.e.s de loin ou de près à cette expérience.

Mes premiers remerciements s'adressent à mes deux co-promoteurs, *Pr.* Sophie Opfergelt et *Pr.* Pierre Delmelle, qui m'ont donné l'opportunité de me lancer dans l'aventure de la recherche scientifique lors de mon mémoire de fin d'étude en Guadeloupe. Sophie, je te suis sincèrement reconnaissant pour ton suivi au quotidien, ta structure exemplaire, ton professionnalisme et l'énergie que tu donnes pour que tou.te.s les collaborateur.e.s se sentent bien et à leur place. Je te remercie pour la confiance et la considération accordées tout au long de la thèse et ses nombreux défis (comme la rédaction ☺). Pierre, ta rigueur et ton intuition scientifique m'ont clairement inspiré. Votre complémentarité dans vos domaines respectifs d'expertise a contribué à la qualité du document final. Je vous remercie également pour les moments conviviaux passés ensemble lors de conférences (Paris, Toulouse, Boston) où lors de missions en Guadeloupe et Indonésie.

Je remercie cordialement le président *Pr.* Emmanuel Hanert ainsi que les membres de mon jury de thèse, *Pr.* Alain Bernard, *Pr.* Yannick Agnan, *Pr.* Damien Cardinal et *Dr.* Pascale Louvat pour l'intérêt et le temps consacré à mon travail ainsi que leurs conseils de grande valeur à la défense privée. Ceux-ci furent précieux dans l'amélioration du manuscrit. Je remercie cordialement *Pr.* Josh West et *Dr.* Pascale Louvat pour avoir accepté de faire partie de mon comité d'accompagnement.

Au cours des quatre dernières années, j'eus la chance de rencontrer des scientifiques passionnés et inspirants lors de missions, de conférences et/ou de workshops: *Pr.* Céline Dessert, *Pr.* Jens Hartmann, *Pr.* Takahiro Hosono, *Pr.* Shaul Hurwitz, *Pr.* Alain Bernard et *Dr.* Corentin Caudron. Votre passion pour la recherche et l'envie de contribuer à une meilleure compréhension des processus à la surface du globe m'ont stimulé. Je voudrais remercier Petra Zahajská pour les échanges fructueux sur le Yellowstone lors de son passage au laboratoire en janvier 2020 et Camille Delvigne pour son aide dans l'élaboration des différents protocoles analytiques.

Une thèse permet également de faire partie de l'éco-système UCLouvain et de prendre part à sa mission de pédagogie. Je voudrai remercier chaleureusement Charlotte Descamps avec qui je me suis formé à l'outil *Comcolors* et encadré durant trois années, les travaux pratiques de Dynamique de Groupes (LBIR1270) ainsi que les 600 étudiants qui y ont participés. Ce fut un plaisir incommensurable de collaborer avec une amie, d'apprendre à mieux se connaître en tant qu'individu et d'échanger avec les étudiants. Mes remerciements les plus sincères s'adressent à l'équipe enseignante (*Pr.* Anne-Laure Jacquemart, *Pr.* Pierre Delmelle, *Pr.* Muriel Quinet, *Pr.* Yannick Agnan, Aubry Vandeuren, Lola Leveaux) pour leur confiance, la liberté dans la création de support et surtout la bonne ambiance ☺. Une pensée toute particulière pour Julie Lecocq, du Louvain Learning Lab, pour l'incroyable relation professionnelle collaborative durant trois ans incluant une publication présentée lors de la conférence QPES 2019 à Brest. Je voudrais également remercier mes deux mémorants, Antoine de Wasseige et Julie Meunier, pour le travail effectué lors de leur travail de fin d'étude. Big up à Antoine pour la mission en Indonésie et à Julien Brack pour l'aide logistique sur place. Je remercie chaleureusement les copains de Louvain-la-Neige (Béné & J-C) et de TEDxUCLouvain pour m'avoir permis de penser à autre chose quelques nombreuses heures/an ;) Enfin, l'expérience « Ma Thèse en 180 secondes » me permettra de replonger dans les plaisirs de mon sujet de thèse et de la vulgarisation scientifique l'année prochaine, suite au report de l'édition 2019 dû à la crise de la COVID-19.

Ma thèse n'aurait pas eu la même couleur sans la présence des collègues…enfin de la famille SOLs. Je n'aurai pu espérer mieux comme premier contexte de travail et j'ai toujours été surpris par la bienveillance, le respect entre tous ses membres et l'ambiance professionnelle toute en convivialité. Je remercie chaleureusement Françoise pour son dévouement quotidien au labo, Anne pour son énergie débordante,

Claudine pour sa sagesse (et ses chaussettes), Hélène pour les discussions (parfois inspirantes) au MC-ICP-MS ainsi qu'à toute l'équipe MOCA (Matthieu, Elodie, Thomas,…). Merci à mes coéquipiers de recherche: Yolanda, Marie, Marie-Liesse, Mathilde, Carlos, Gabi, Jolan, Zimin, Marlon, Clairia, Michelle, Syldie, Elena, Maxime, Catherine, Charles, Noa, Fidèle, Benjamin & Inga (incroyable mariage à Moscou). Je voudrais plus particulièrement remercier Benoît, Aubry et Arthur, surnommés les « brows du bureau », pour tous les moments passés ensemble et la belle amitié créée, qui continuera en dehors du contexte ;) Arthur, nos petits lunchs à manger sainement (euh) me manqueront, je te suis sincèrement reconnaissant pour ton soutien lors de ces derniers mois de rédaction !

Les derniers moments de cette thèse ont été marqués par la pandémie de la COVID-19 et quelques mois de télé-travail, Je ne remercierai jamais suffisamment l'ensemble de mes collègues pour les échanges productifs, les notifications *Teams* de soutien et les pauses cafés virtuelles. Merci pour votre adaptation ! Merci à ma colloc Mo' pour les échanges et le soutien durant le confinement ;) Je remercie Catherine Hirst pour ses conseils linguistiques !

Finalement, cette thèse n'aurait pas eu la même couleur sans toutes les personnes qui m'ont accompagné au quotidien durant ces dernières années. Jona, merci d'avoir supporté les différentes phases de ma carapace émotionnelle lors de nos multiples escapades du Cocq/culturelles. Nos discussions/remises en question permanentes lors des runs hebdomadaires ont été source inépuisable de motivation. Je voudrais remercier mes amis, qui le temps d'un moment du quotidien/soirée/verre ont partagé mes ressentis: Jean-Baptiste, Maxime, Corentin, Thomas, Rémi, Stoefs, Gogo, Hélène, Adrien, Maude[2], Florian, Benoît, Alexis, Jean, Françoise, Guillaume, Mélanie, Romain, Victoria[2], Nelson, Linnea, Maëliss, Amandine, Claire, Juliane, Jonathan, Compote, JB, Pierre, Jordy, Chris, Kyng, Thib… La thèse m'aura permis de rencontrer une scientifique plutôt charmante dont la présence s'est révélée indispensable au fil du temps. Merci Elisabeth pour ton soutien infini. Je tenais à finir ces remerciements en les dédiant à ma famille en or qui me soutient depuis toujours et m'a offert la possibilité de mener une vie libre et heureuse: Papy, Mamy, Papa, Maman, Manon, Hélène, Bapt & Rose.

Journée de rédaction confinée à Fernand Cocq, Bruxelles, Mai 2020

François

CONTENTS

Part IV: **CONTRIBUTION OF THE STUDY**

LIST OF FIGURES

LIST OF TABLES

ACRONYMS

ANN	on annual basis
ASi	adsorbed silicon
atmCO_2	atmospheric CO_2
BF	base flow
BSi	biogenic silicon
CO_2m	magmatic CO_2
CO_{2c}	corrected atmospheric CO_2
CWR	chemical weathering rate
D	discharge
DEM	digital elevation model
DOC	dissolved organic carbon
DSi	dissolved silicon
E	enrichment factor
f	riverine dilution factor
HD	high discharge
HI	hydrothermally-impacted
HLGB	Heart Lake Geyser Basin
LD	low discharge
LGB	Lower Geyser Basin
LSi	lithogenic silicon
MHS	Mammoth Hot Springs

MV	Mud Volcano
NGB	Norris Geyser Basin
NI	non hydrothermally-impacted
PCA	principal component analysis
PFA	perfluoroalkoxy
PP	polypropylene
PSi	pedogenic silicon
SC	specific conductivity
SGB	Shoshone Geyser Basin
SI	saturation index
SM	snowmelt
TDS	total dissolved elements
UGB	Upper Geyser Basin
WR	water-rock interaction
YPVF	Yellowstone Plateau Volcanic Field

Part I

GENERAL OVERVIEW

General introduction

Volcanic rocks represent only 5% of the terrestrial surface but several studies of basaltic regions showed that, through weathering, these rocks contribute significantly to the global flux of solutes to the ocean and hence, consumption of atmospheric CO_2. However, recent data highlight the disproportionate contribution to weathering fluxes of volcanic island arc and continental hotspot regions where explosive eruptive activity dominates and is accompanied predominantly by pyroclast and tephra deposition. While these areas generally correspond to more silicic compositions, which tend to display lower dissolution rates compared to basalts, weathering is enhanced due to the fragmented nature of the volcanic deposits.

Potentially important uncertainties remain regarding the variables which control weathering fluxes in volcanic island arc and continental hotspot regions. For example, they are often associated with hydrothermal systems which act as a source of strong acids for weathering reactions. In addition, weathering of alteration deposits from extinct hydrothermal systems may also generate a source of acidity for weathering. There is evidence that the hydrothermally-derived flux of elements may be significant, i.e., contributing between 10 and 80% to the weathering fluxes. Thus, inclusion of the hydrothermal flux in the calculation of atmospheric CO_2 consumption by rock weathering may lead to overestimates.

The influence of runoff variability on weathering fluxes from volcanic regions is also overlooked. Runoff can change drastically in volcanic island as a function of orography and infiltration but also seasonally. Runoff is paramount to weathering processes as it dictates the amount of water available for mineral dissolution as well as the discharge of dissolved weathering fluxes to rivers. Seasonal runoff variability in volcanic island arc and continental hotspot regions may affect the contribution from meteoric weathering processes to weathering fluxes, which integrate hydrothermal and meteoric contributions. This highlights that the relative contributions from hydrothermal and meteoric sources and processes to weathering fluxes in these hydrothermally-active volcanic regions may therefore vary as a function of runoff. Importantly, these changes in contribution to weathering

fluxes may be amplified in the future given that runoff variability is predicted to increasingly affect dissolved riverine chemistry based on the projected changes in precipitation with ongoing climate change.

The uncertainties on the source of acidity for weathering reactions and the influence of runoff variability on weathering fluxes from volcanic island arc and continental hotspot regions prevent accurate estimates of atmospheric CO_2 consumption and production of solutes to the ocean in these regions. Better constraining these uncertainties requires to unravel the relative contributions of meteoric and hydrothermal sources and processes to the overall response of weathering fluxes to changing runoff. The germanium to silicon ratios (Ge/Si) and the stable silicon isotopes ($\delta^{30}Si$) are particularly well-suited geochemical tracers to assess the sources and processes controlling dissolved Si weathering fluxes in volcanic regions. However, there is a lack of constraint on the response of these tracers upon hydrothermal discharge given that the controls on the variability of Ge/Si ratio and $\delta^{30}Si$ in thermal waters are poorly understood.

The goal of the proposed research is to apply geochemical tracers (Ge/Si and $\delta^{30}Si$) used in combination to derive a detailed understanding of how hydrothermal input and runoff variability influence weathering fluxes from volcanic island arc and continental hotspot regions.

General Overview

1.1 Magma-related hydrothermal systems

1.1.1 Definition

In terms of nomenclature, many definitions exist in the literature to distinguish "geothermal" and "hydrothermal" systems. Generally, a "geothermal" system includes any system with a significant thermal gradient where heat transfers occur by conduction as well as by convection. On the other hand, a "hydrothermal system" is a geological system involving heat transfer by convection via water circulation. We refer to "hydrothermal system" throughout this PhD thesis.

A general description of hydrothermal systems is reported in numerous studies and review papers (e.g., Bogie et al, 2005; Rye, 2005; Arnórsson et al, 2007; Pirajno, 2009; German and Seyfrid, 2014; Hochstein and Brown, 2015; Stimac, 2015). A hydrothermal system is composed of three main components: (i) a fluid that transfers heat (e.g., water, generally meteoric-derivated and more rarely from marine origin, transporting heat by convection from the reservoir to the Earth's surface), (ii) a permeable rock including the geothermal reservoir (the host rock composition is a determining factor in the rock-fluid interaction and influence the final composition of the geothermal waters and gases) and (iii) a heat source that is dependent on the tectonic and geological setting (in volcanic islands, underlying magma chamber with molten lava).

The magma is supplied to the system by a high-temperature bedrock surrection process and is a mixture of molten or semi-molten rocks, volatiles and suspended crystals which pools beneath the Earth's surface (Rogers and Hawkesworth, 2015). The dissolved magmatic volatiles (H_2O, C, S, Cl and F) in magma may exsolve upon magma cooling,

decompression and crystallization and degas from the magma, depending on their solubility. H_2O and CO_2 are the major concentrated magmatic volatiles (~70-90% of the total volatile content) compared to S, Cl and F (~1-5%).

Once degassed from magma, volatiles can (i) directly reach the surface by conduits to form "fumaroles" (high temperature gas emissions), (ii) interact with groundwaters at depth and by creating a convective cell driven by temperature pressure gradients (hydrothermal system). A long lateral outlow zone may also develop if permitted by the topography and the pressure gradients (Goof and Janik, 2000; **Fig. 1.1**).

Boiling occurs once the confining pressure is too weak to keep upflowing fluids in the liquid form and the resulting rising hot gas follows different pathways: (i) directly rising buoyantly upward (the vapor phase includes non-condensable gases such as CO_2, H_2S, H_2, SO_2, CH_4) producing fumaroles bearing the initial magmatic gas composition, (ii) reacting, upon contact with shallow meteoric groundwater, producing fumaroles bearing a small remnant of the initial magmatic gas composition. The cooling fluids, in interaction with the volcanic rock, become enriched in dissolved cations. This may sometimes lead to precipitation of secondary minerals. The complex transition from rock dissolution to fluid-rock equilibrium results in highly variable water compositions within the hydrothermal system, controlled by gas composition, rock lithology, rock/water ratio, residence time, and thermal regime (Reed, 1982; Giggenbach, 1988; Symonds et al, 2001).

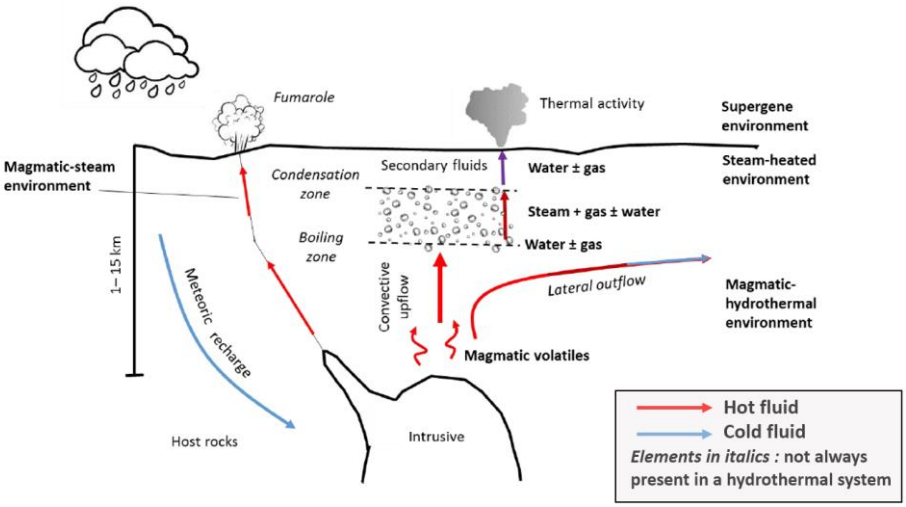

Fig. 1.1: Schematic figure of a sub-aerial magma-driven hydrothermal system (modified from Detienne, 2016).

1.1.2 Geological context

Hydrothermal systems arise preferentially in areas where significant thermal gradients and abundant fluid circulation are associated. Preferred areas for hydrothermal systems development worldwide therefore include zones of active volcanism located at the edge of spreading ridges, subduction zones or transform faults (**Fig. 1.2**). Moreover, hydrothermal systems occur in "hotspots" which are caused by plumes of hot material rising from the deep mantle within a continental plate (e.g., Yellowstone Plateau Volcanic Field) or oceanic plate (e.g., Hawaii). The geological context is one criterion for classifying hydrothermal systems. Three types of subdivisions can be established from this criterion (Goof and Janik, 2000):

- **Young magmatic systems**. Associated with quaternary volcanism and magmatic intrusions, about 95% of the volcanic activity is located on the plate boundaries. These thermal systems are generally the hottest (< 370 °C) with deep reservoirs (~1.5 km depth).

- **Tectonic systems**. They have a high heat flux but are essentially devoid of magmatic activity. They are located in back arc basins, regions of crustal extension, collision zones or along rifts zones. Tectonic systems are often associated with seismicity and heat flows resulting from Quaternary faults and thinning crust, respectively. In general, tectonic systems have reservoir temperatures ≤ 250 °C at depth of ~1.5 km.

- **Geopressurized systems**. Located in sedimentary basins where tectonic uplift and deep metamorphism of fluid-rich layers formed over-pressurized reservoirs. Depths and temperature reservoirs are typically range between 1.5-3.0 km, and 50-190 °C, respectively.

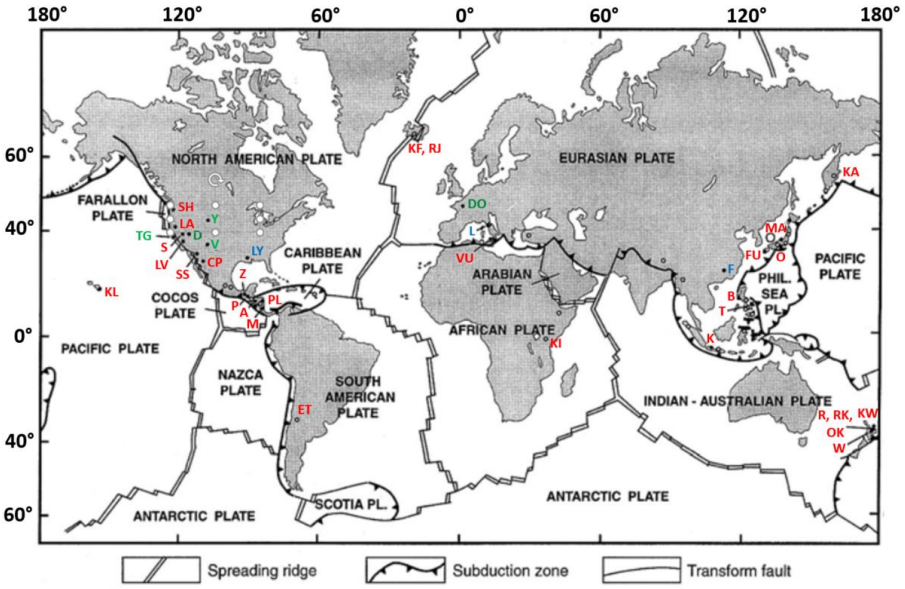

Fig. 1.2: Distribution of the world's main thermal resources. A (Ahuachapan, El Salvador), B (Bulako, Philippines), CP (Cerro Prieto, Mexico), D (Dixie Valley, USA), DO (Dogger, France), ET (ElTatio, Chile), F (Fuzhou, China), FU (Fushime, Japan), K (e.g., Kamojang, Darajat, Kawah Ijen, Indonesia), KA (Kamchatka, Russia), KI (e.g., Kilimanjaro, Tanzania), KF (Krafla, Iceland), KL (Kilauea, USA), KW (Kawarau, New Zealand), L (Larderello, Italy), LA (Lassen, USA), LV (Long Valley, USA), LY (Lafayette, USA), M (Miravalles, Costa Rica), MA (Matsukawa, Japan), O (Oku-aizu, Japan), OK (Ohaaki, New Zealand), P (Pacaya-Amatitlan, Guatemala), PL (Platanares, Honduras), R (Rotorua, New Zealand), RJ (Reykjanes, Iceland), RK (Rotokawa, New Zealand), S (Steamboat Hills, USA), SH (Mount St Helens, USA), SS (Salton Sea, USA), T (Tiwi, Philippines), TG (The Geysers, USA), W (Wairakei, New Zealand), V (Valles Caldera, USA), VU (Vulcano, Italy), Y (Yellowstone, USA), Z (Zunil, Guatemala). Other thermal fields are represented by circles (adapted from Rybach and Muffler, 1981). Red = young magmatic systems; blue = tectonic systems; green = geopressurized systems.

1.1.3 Description of subaerial magma-related hydrothermal systems

Due to the complexity of a tectonic classification, a classification by hydrology is generally applied, separating subaerial magma-related hydrothermal systems into two major groups: (i) hydrothermal systems associated with stratovolcanoes or volcanic domes and (ii) low-relief systems, which develop in topographic basins (**Fig. 1.3**; Bogie et al, 2005).

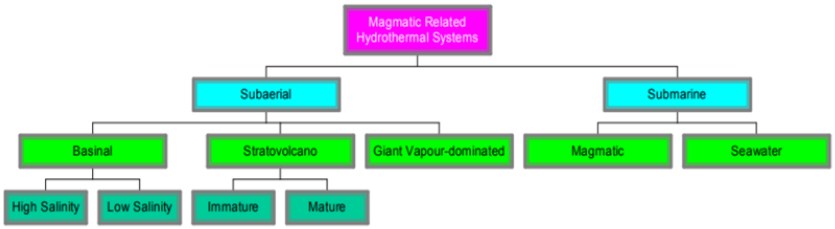

Fig. 1.3: Classification of magma-related hydrothermal systems (from Bogie et al, 2005).

1.1.3.1 Stratovolcano subaerial magmatic-related hydrothermal systems

Volcanic edifices-related hydrothermal systems are generally associated with magma intrusions at relatively shallow levels (sometimes at a depth < 1 km). The surrounding meteoric waters initiate a convective system forming an "immature" system and neutralize the water over the time forming a high temperature "mature" system.

In "**immature**" hydrothermal systems, the acid leaching of the host rock results in various stages of intermediate to advanced argillic alteration and deposition of native sulfur usually in the crater of the volcanic edifice (**Fig. 1.4a**). This system is characterized by the presence of thermal springs, boiling mud pools, and various secondary minerals kaolinite and alunite. At some volcanoes such as Kawah Ijen in Indonesia (**Fig 1.4b**), the summit crater contains a lake acting as a condenser for the hot magmatic gases released from the subsurface. These lakes typically display extremely low pH values and temperatures above that of ambient air because evaporation increases the concentration of acidic components and native S remobilization. Numerous hot springs (with SO_4-Cl-HCO_3 in various concentrations) may develop on the slopes of the volcano at moderate distances from its summit (**Fig. 1.4a**). This large range in anion concentrations in these hot spring waters at different elevations resuls from the mixing of thermal waters with perched secondary aquifers or groundwaters within the volcanic pile of the volcanic edifice: (i) perched acid SO_4 aquifers are found close to the system's upflow, (ii) HCO_3 enrichment are due to the flowing outward of these perched aquifers (neutralization of hosting rock converting dissolved gaseous CO_2) and (iii) the hydrothermal neutral Cl aquifers, found underlying the perched aquifers, boil in the upflow to form secondary aquifers (**Fig. 1.4a**).

a)

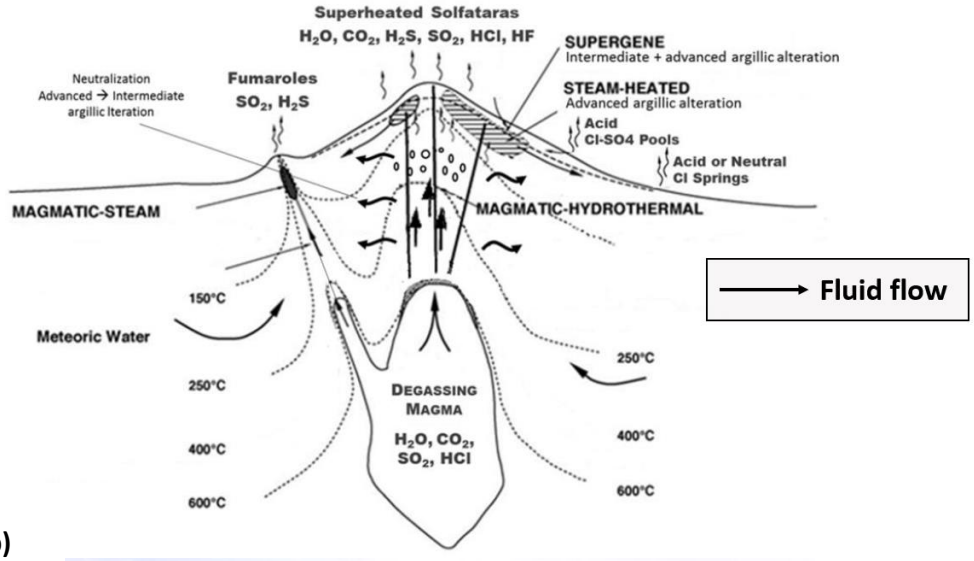

b)

Fig. 1.4: (a) Schematic model of an immature hydrothermal system associated with a stratovolcano (modified from Rye et al, 2005; Bogie et al, 2005) and (b) the summit hot hyper-acid crater lake (pH < 0.3, T > 35 °C, volume ~ 32 × 106 m^3; Delmelle and Bernard, 1994) of Kawah Ijen, Indonesia (photograph captured during the field mission in January 2017).

The "**mature**" hydrothermal systems are generally associated with eroded volcanic landforms within dome complexes and summit calderas **(Fig. 1.5**). Elevation determines whether surface exposure of hydrothermal features occurs over a wide area, or covers a very limited surface area: (i) acid SO_4-waters are observed at high elevation and (ii) neutral Cl-waters with increasing HCO_3/SO_4 as a function of decreasing elevation are found in lower altitude. The last observation that differentiates "mature" and "immature" systems, is that 'immature' systems can also display Cl-bearing water springs at high elevations. The circulating fluids are principally near-neutral pH fluids (**Fig. 1.5**).

Dome hydrothermal systems are also reported in the hydrological classification of hydrothermal systems. These can be spatially associated with lava domes and form on the upper flanks of stratovolcanoes, or occur as isolated domes. The rheology of these systems results from the high silica content of the source magma, typically dacitic, rhyolitic, or andesitic and is associated with subduction settings (Hale, 2008; Hicks et al, 2009; Stimac et al, 2015). Finally, **lithocarps** (sub-horizontal blankets of residual quartz and advanced argillic alteration overlying a shallow magmatic intrusion; Sillitoe, 1995; Hedenquist and Taran, 2013) are also classified in stratovolcano subaerial magmatic-related hydrothermal systems.

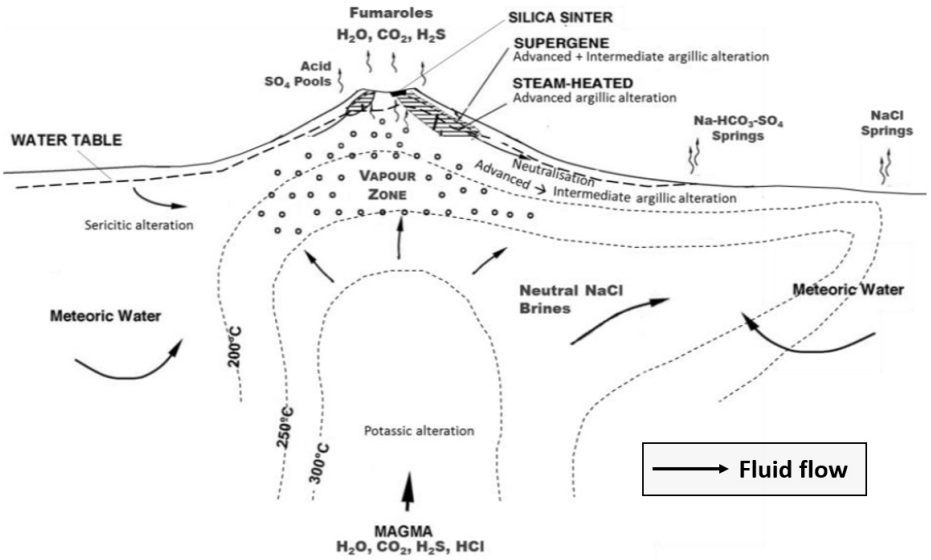

Fig. 1.5: Schematic model of a mature hydrothermal system associated with a stratovolcano (in eroded volcanic landform) (modified from Rye et al, 2005; Bogie et al, 2005).

1.1.3.2 Basinal subaerial magmatic-related hydrothermal systems

A low-relief hydrothermal system is a steam-heated environment overlying a boiling reservoir (deep-seated magma intrusion at 3-15 km depth) of near-neutral pH water situated in topographic low relief basins, mainly rifts, or calderas (**Fig. 1.6a**). The host rock neutralizes and reduces the magmatic volatiles released at great depth which are subsequently diluted by meteoric waters before reaching the surface. The release of CO_2-rich volatiles is favored under the high lithostatic pressure.

Low salinity systems are the most common low-relief type systems. Boiling neutral-Cl hot springs and geysers occur at the surface and significant areas of silica sinters generally form around the springs as is observed in the continental hotspot of Yellowstone Plateau Volcanic Field, Wyowing (**Fig. 1.6b**). Fumaroles and acid H_2S–rich steam-heated features such as mudpots can be found in these systems. Mudpots (or mud pools) are acidic hot springs, or fumaroles, with low water content and the presence of clay minerals formed by the interaction of acidic fluids with the host rock. The size of a typical low-relief system depends on the regional geology and topography.

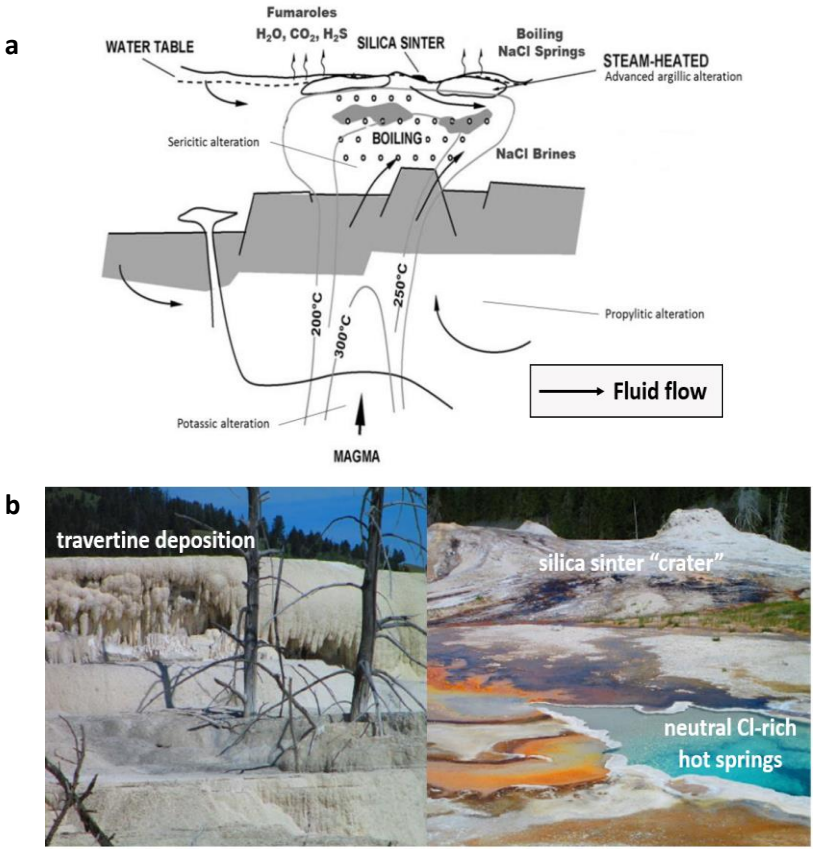

Fig. 1.6: (a) Schematic model of a low-relief hydrothermal system (modified from Rye et al, 2005; Bogie et al, 2005) and near-neutral fluid surface exposure (Yellowstone Plateau Volcanic Field, Wyoming) with (b) travertine deposition around neutral $CaCO_3$-rich hot springs (Mammoth hot springs, Yellowstone Plateau Volcanic Field, Wyoming) and boiling neutral Cl-rich hot springs with associated silica sinter "crater" associated to geyser and silica sinter (white deposits) (credit: U.S. Geological Survey).

1.1.4 Surface manifestation and classification of thermal waters

In general, hydrothermal systems can be identified by their surface manifestations in the form of fumaroles, hydrothermal deposits, weathering products and hot waters such as hot springs, geysers or acidic lakes (**Fig. 1.7**). The rise of fluids and formation of **fumaroles** is almost systematic in all active volcanoes, as is observed at the summit of the Soufrière volcano (Guadeloupe) (**Fig. 1.7**). These manifestations are mainly observed in areas located near heat sources in the active craters. At the closest point to the heat sources, there are higher fluid temperatures than the condensation temperature of the water vapor resulting in visible fumarole expulsion at the surface. When the distance from these heat sources increases, heat loss leads to the condensation of water vapor at soil depth. Once the temperatures are even lower and too weak to allow the vaporisation of water vapor, the hydrothermal system extends laterally resulting in thermal springs.

Solfataras are surface manifestations observed in the vicinity of active craters. These are sulfur deposits associated with the emission of water vapor, CO_2 and H_2S (more rarely SO_2). Considerable sulfur quantities can develop and are subsequently exploited, for example in Kawah Ijen (Indonesia). These sulfur deposits are also associated with sulfate minerals such as alunite, natroalunite, jarosite, gypsum, and a wide range of often ephemeral hydrated sulfates (e.g., gypsum ($CaSO_4.2H_2O$), anhydrite ($CaSO_4$), jarosite ($KFe_3(OH)_6(SO_4)_2$)). At depth, the geothermal fluids contain the reduced species of sulfur and their precipitation leads to sulfide minerals such as, e.g., pyrite (FeS_2), pyrrhotite (FeS), galena (PbS), sphalerite (ZnS), chalcopyrite ($CuFeS_2$), generally associated with metal-bearing deposits.

Fig. 1.7: Surface manifestations associated with magma-related hydrothermal systems such as, the summit fumaroles of La Soufrière volcano (left image) and Gallion hot spring (right image) in Basse-Terre Island, Guadeloupe (photographs during the field mission in January-February 2015).

The interaction of rising magmatic gas (mainly H_2O, CO_2, SO_2, H_2S and HCl) with meteoric water (e.g., shallow groundwaters, perched aquifers) results in different **thermal water** compositions. Most chemical waters found at high-temperature can be classified under the general headings that follow using their anionic concentrations (White; 1957; Ellis and Mahon, 1964):

- **Acid sulfate-chloride waters (acid SO_4-Cl waters).** Formed at higher magmatic gas contribution relative to meteoric water recharge ($4\ SO_2 + 4\ H_2O \rightleftarrows H_2S + 3\ H_2SO_4$). SO_4/Cl is function of absorption degree of magmatic gases in the system. These waters are generally acidic (pH 2-5) and the CO_2 is thus not converted into HCO_3^-. They are formed by several processes:

(i) at depth, oxidation of sulfide in Cl-water to bisulfate ions ($S^{2-} \rightarrow HSO_4^-$), perhaps resulting from association with oxidized lava. The resulting water has a near-neutral pH due to buffering action and the neutralization of water by weathering reactions with the host rock. With increasing elevation and cooler surface conditions, the dissociation constant of HSO_4^- increases ($HSO_4^- \rightleftarrows H^+ + SO_4^{2-}$) and solution may become acid.

(ii) at depth, interaction of high-temperature Cl-water with sulfur-containing rocks producing an acidic solution (resulting of $S^{2-} \rightleftarrows HS^- \rightleftarrows H_2S$ successive hydrolysis).

(iii) rising of high-temperature steam from molten rock at shallow depth to condense into surface or near-surface waters. The resulting fluid is concentrated into F^-, Cl^- and SO_4^{2-} derived from the volcanic steam. With decreasing steam temperature, F^-, Cl^- and sulfur gases decrease in abundance and the acid SO_4-Cl-F waters merge into SO_4-Cl waters and then, into acid SO_4-waters.

- **Acid sulfate waters (acid SO_4-waters).** Acidic waters with low chloride content, may be formed in volcanic areas when a fluid channel at temperatures below about 400 °C condenses into surface waters (e.g., perched aquifer). When the fluid rises to the surface, it boils and a fractionation takes place between the liquid and the vapor phase (composed of H_2O, CO_2 and H_2S). Morevover, mixing with perched aquifer results in acid SO_4-waters via $H_2S + 2\ O_2 \rightarrow 2\ H^+ + SO_4^{2-}$.
  The constituents present in the waters are mainly leached from the surrounding rocks. These waters are generally confined to the surface and their geochemical signifiance is usually minor in hydrothermal system survey work.

- **Alkaline bicarbonate waters (alkaline HCO_3-waters).** Formed at low magmatic gas contribution (mainly composed of CO_2 and H_2S) condensing into an aquifer. When the fluid rises

up to the surface, it boils and a fractionation takes place between Cl-waters and the vapor phase (composed of H_2O and CO_2). Morevover, the mixing of this fraction with perched aquifer results in HCO_3^- waters via
$CO_2 + H_2O \rightleftarrows H_2CO_3 \rightleftarrows HCO_3^- + H^+$ (~150-160 °C).
Sodium is often the main cation in the water, since $CaCO_3$ is not very soluble at high temperature and K and Mg are fixed in clays.

- **Neutral chloride waters (neutral Cl-waters).** Formed at low magmatic gas (mainly composed of CO_2 and H_2S) contribution. The high solubility of HCl gas in water makes it susceptible to condense in shallow low-temperature zones of the volcanic–hydrothermal system. At high depth, the CO_2 remains soluble. The dissolved salts in these waters are mainly NaCl and KCl, although in the more concentrated waters appreciable Ca concentration may occur. The waters are also highly-concentrated in silica. The Cl^-/SO_4^{2-} ratio is generally high and the pH ranges from neutral to slighty alkaline (pH 5-9). The waters often occur in areas with boiling springs and geyser activity is common in many developed hydrothermal areas (e.g., Yellowstone Plateau Volcanic Field).

The processes influencing the chemistry of these four thermal waters chemistry are summarized in **Fig. 1.8**.

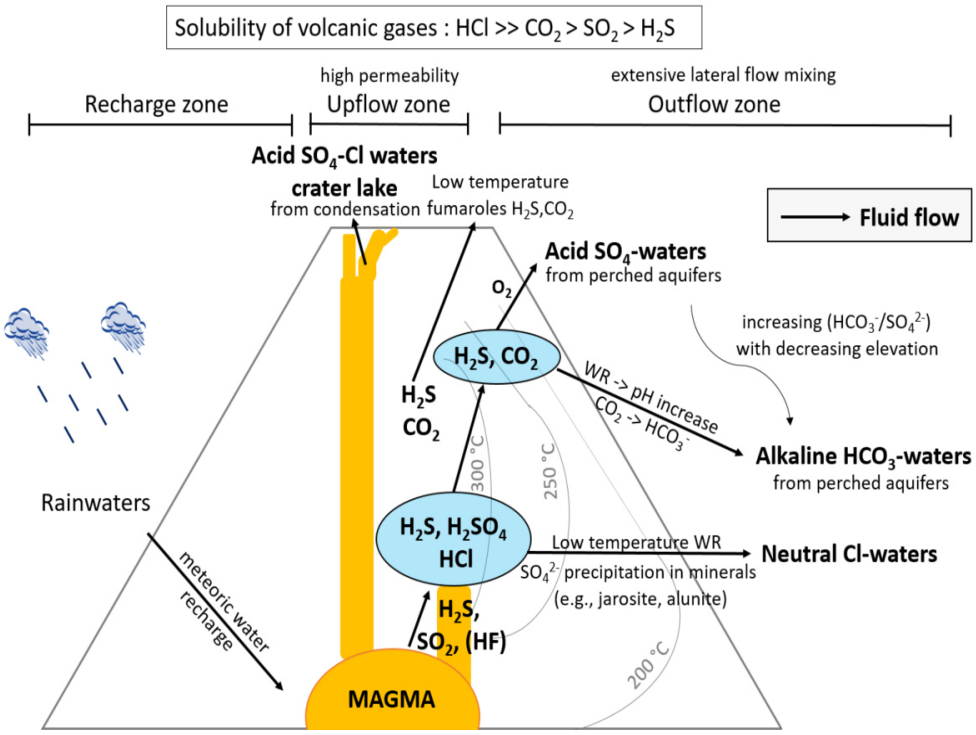

Fig. 1.8: Schematic model showing major processes influencing the four thermal waters classified by White (1957), Ellis and Mahon (1964). WR = water-rock interaction.

1.2 Chemical weathering

1.2.1 Definition

The **weathering of rock** is the physical disintegration and chemical decomposition of earthly and rocky materials on exposure to chemical, physical and biological agents on the Earth's surface, producing an in-place mantle of waste. This neutralization reaction of silicate and carbonate rocks by atmospheric CO_2 leads to (i) the promotion of soil formation via the accumulation of chemical constituents from the weathered material (**chemical weathering**) and to (ii) the mechanical mobilization and transport of the remaining fraction (ions, particles) via waters (groundwaters or surface waters) (**mechanical erosion**). In contrast with mechanical erosion implying the concept of transport, **physical weathering** corresponds to an in-place rock structure modification by climatic factors (e.g., temperature, freezing/thawing) without transport. **Denudation** is defined as the general wearing away of the land (laying bare of subjacent lands) and thus, is the collective name encompassing chemical weathering and mechanical erosion. In hydrothermal context, the term of **hydrothermal alteration** is used for chemical related to thermal fluids.

Many major chemical weathering processes had already been described in the 19th century (Belt, 1874; Merrill, 1897; Chamberlin, 1899). The study of Martin and Meybeck (1979) is one of the first studies to quantify **weathering** using waters of several large rivers. By studying the chemical composition of the dissolved phase, weathering quantification directly in terms of fluxes is possible but also to trace the sources of the material (rock weathering, atmospheric, anthropogenic), and even to distinguish the flows attributable to the different lithologies of the same basin slope (Negrel, 1992; Negrel et al, 1993). Studies on large river systems (Congo, Amazon) have thus made it possible to constrain the local chemical composition of the continental crust, and to quantify the coupling between mechanical erosion and chemical weathering via the erosion equilibrium model (Gaillardet et al, 1995, 1997, 1999).

Volcanic islands, characterized by rugged relief, specific flows, and small monolithic watersheds, have emerged as an object of study of choice to quantify weathering fluxes (Louvat, 1997). The islands occur in different geodynamic contexts (e.g., volcanic arcs, oceanic and continental hotspot) and are often isostatically unbalanced, leading to uneven relief and resulting in intense erosion and weathering. These islands span a range of latitudes and their climatic diversity provides them with a range of temperatures and an environmental diversity that can influence the effectiveness of weathering. The study of Louvat (1997) dealing with the alteration and erosion of the islands of the Réunion, Java, Sao Miguel (Azores) and Iceland is one of the first studies on the weathering of volcanic islands and estimates that chemical weathering and erosion in rivers of volcanic islands is 5 to 10 times higher than those of large rivers (**Fig. 1.9**; Louvat, 1997).

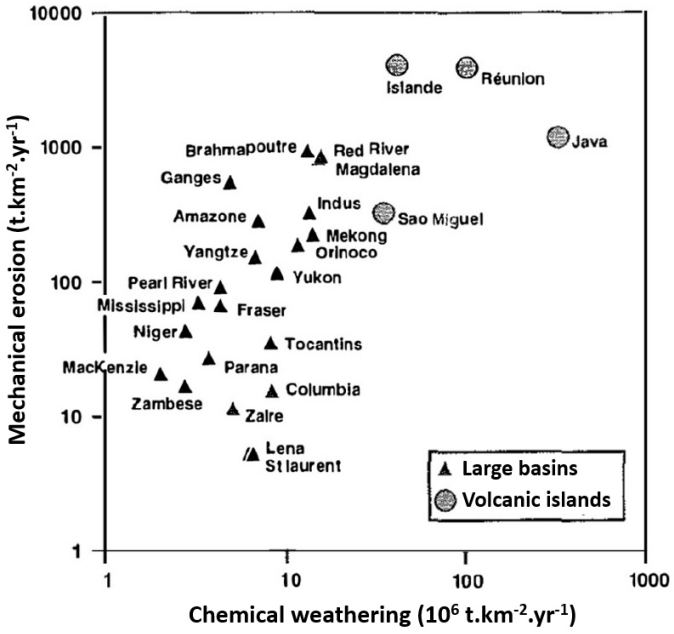

Fig. 1.9: Mechanical erosion ($t.km^{-2}.yr^{-1}$) as a function of chemical weathering (10^6 $t.km^{-2}.yr^{-1}$) in volcanic islands and watershed of large rivers corrected for carbonate inputs (from Louvat, 1997).

1.2.2 Water-rock interaction

Most weathering reactions occur within the soils and their development zone (regolith, or critical zone), at the interface between the atmosphere and the rock (**Fig. 1.10**). These weathering processes, studied by examining the interaction of solutions with solids through different types of reactions in the aqueous phase, can be classified into the following categories (White, 2013):

- **Acid-base reactions**: acid dissociation plays a major role in weathering by producing free protons. In the volcanic domain, the sources of acidity are atmospheric (e.g., atmospheric CO_2), magmatic origin (e.g., carbonic, sulfuric, hydrochloric acid) or CO_2 originated from organisms respiration. The CO_2 reacts with water to form carbonic acid H_2CO_3 whose dissociation reaction is:
  $H_2CO_3 \rightleftarrows H^+ + HCO_3^-$.
  The water in equilibrium with atmospheric CO_2 will thus become slightly acid (pH of rainwater ≈ 5-6). Many reactions are pH-dependent, e.g., hydroxides which can give or accept protons depending on the pH of the solution:
  $Al(OH)_2^+ + H^+ \rightleftarrows Al(OH)^{2+} + H_2O$ and
  $Al(OH)_2^+ + OH^- \rightleftarrows Al(OH)_3 + H_2O$.
  From their activity and dissociation constant, the concentration of each species in a solution can be calculated as a function of the pH and the temperature. Ions that remain in solution and do not transfer to the solid phase regardless of their chemical speciation are named "conservative". Under conditions of normal water pH, the main conservative ions totally dissociated from their natural acids and conjugates bases are: Na^+, K^+, Ca^{2+}, Mg^{2+}, Cl^-, SO_4^{2-} and NO_3^-.

- **Complexation**: ions in solution combine with other ions, forming “complexes”. The formation of complexes affects the solubility and reactivity of the ions, and may be intermediate step

in the precipitation process. The most common complex is that formed between metals and water or its dissociation products. In natural waters containing higher ion contents, various complexes are possible. For example, the reaction of hydrolysis involving magnesium:
$Mg^{2+} + H_2O \rightleftarrows Mg(OH)^{+} + H^{+}$.

- **Dissolution and precipitation**: dissolution is a process in which the solute (a mineral) is dissolved in a solvent (usually water) forming a homogeneous mixture. When the reaction is total, it is said to be "**congruent**". For example, the dissolution of silica:
$SiO_2 + 2H_2O \rightleftarrows H_4SiO_4$.
However, the majority of silicate minerals are at their minimum solubility and they react with water to release ions in solution, forming new minerals in place of the previous ones, in so-called "**incongruent**" dissolution reactions. For example, the transformation of kaolinite to gibbsite releases dissolved silicon (DSi) under the form of silicic acid (H_4SiO_4), while the aluminium will remain in the solid phase:
$0.5*Al_2Si_2O_5(OH)_4 + 2.5*H_2O \rightleftarrows Al(OH)_3 + H_4SiO_4$.

- **Adsorption and desorption**: the adsorption is the attachment of an ion in solution to a pre-existing solid surface. The adsorption capacity of a surface is pH dependent, depending on the number of protons already adsorbed. Clay and sedimentary particles, which are micrometric in size, have a very large surface/volume ratio, which give them a high capacity for ion exchange, adsorbed on their surface or bonded between their sheets. Thus, the concentration of many trace elements is less controlled by the reactions of precipitation/dissolution but only by adsorption on the surfaces of the minerals and/or organic matter.

In a theoretically closed system where the internal element cycle does not affect the outputs of the system, the chemical weathering reactions can be considered to conserve masses. The mass balance equation can therefore be written as follows: *Rock* + *Rainwater* = *Weathered rock* + *Solution*. However, in natural environments, dissolved species are transported from the site of weathering by water fluxes. Some studies on chemical weathering quantify this mass change using the composition of dissolved material carried by the rivers, the original rock and the various inputs (wet and dry atmospheric deposition), and thus determining the composition of the secondary phases remaining in the soil (White, 2013).

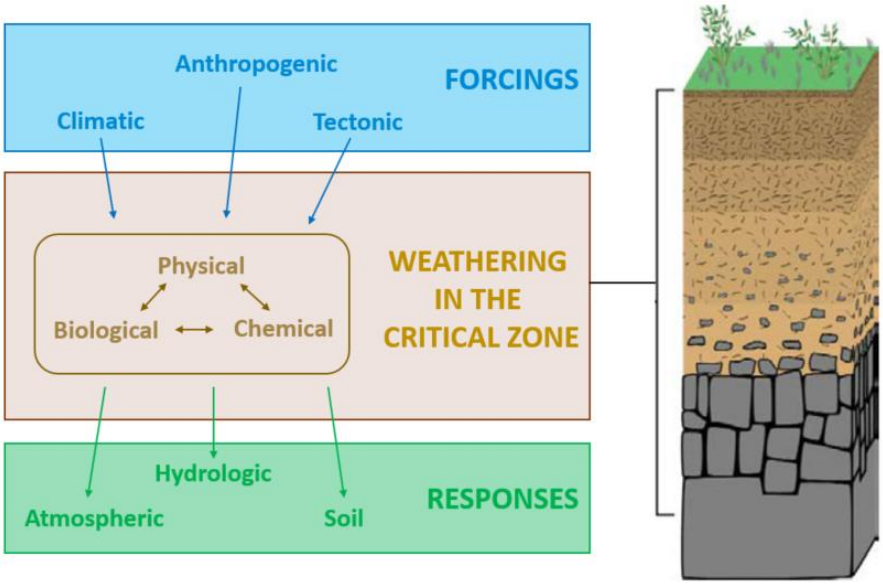

Fig. 1.10: Physical, chemical and biological processes controlling weathering in the regolith (adapted from Anderson et al (2004)).

1.2.3 Factors controlling chemical weathering

The chemical weathering intensity is influenced by several factors, including the lithology, mechanical erosion, relief, climate, runoff, biologic and anthropogenic impact.

The link between **lithology** and chemical weathering has been established by Garrels and Mackenzie (1971) and consolidated by Meybeck (1987) who report an order of rock solubility. The spatial variation in lithology is the main controlling factor of solute chemistry in rivers, which is particularly influenced by the weathering of carbonates and evaporites (Gaillardet et al, 1999). Lithology is now considered to be a dominant factor governing chemical weathering (Louvat and Allegre, 1997; Dupré et al, 2003; Hartmann and Moosdorf, 2011; Rad et al, 2013) and, Hartmann and Moosdorf (2011) order the susceptibility of different volcanic rocks to weathering from highest to the lowest rates: pyroclastic flows, deposits alluvial and basic to intermediate volcanic rocks, the metamorphic rocks, the acidic volcanic and plutonic rocks.

In a global study, Gaillardet et al (1999) suggest that runoff, temperature and **mechanical erosion** rates are the major factors influencing chemical weathering rates. This study shows the coupling between chemical and physical weathering processes arguing that only active physical erosion of the rocks can maintain high rates of chemical weathering. However, Rad et al (2013) assume that this relationship is different for the volcanic islands arcs where the chemical weathering is very intense such as in the Lesser Antilles. Indeed, the residence time of the upper part of the weathering profile is reduced because it is more rapidly eroded and exported, which limits its potential chemical weathering (Dixon et al, 2009).

Dixon et al (2012) focus on the impact of **relief** by considering the influence of catchment slope gradient on mechanical erosion and chemical weathering. For low slopes (< 25°), the rates of chemical weathering increase in conjunction with the rates of mechanical erosion, reflecting a balance between mineral surface exposure and mineral dissolution. However, when slopes are steep (> 25°), the intensity of

chemical weathering decreases with increasing rate of mechanical erosion and refinement of the regolith (Dixon et al, 2012). The proportion of material released by chemical weathering decreases with increasing altitude and air temperature decrease, reflecting the combination of climatic influence and potential dust inputs (Dixon et al, 2012). Volcanism is also a relief-creating phenomenon. The resulting steep topography favors precipitation and an effective infiltration through porous rocks, resulting in high chemical weathering fluxes. As a result, the chemical weathering fluxes of oceanic islands are strongly dependent on the relief (Gaillardet et al, 2011).

The **climate** controls the mechanical erosion and chemical weathering of landscapes through various processes that remain difficult to identify because of their complex interlinked pathways with other factors (Dixon et al, 2009). The **precipitations** effect on chemical weathering was studied in Hawaii by Chadwick et al (2003) and the results show a non-linear variation in the chemical weathering and properties of the regolith with the increasing rainfall resulting in lower pH and cationic exchange capacity of the regolith. The precipitations also influence the dissolved element concentrations in rivers and most of studies reports a **hysteresis pattern** (defined as the nonlinear relationship between discharge and concentration of nutrients or sediment) in rivers element chemistry following flood events (e.g., Bowes et al, 2003; Evans and Johnes, 2004; Burt et al, 2015). By comparing sites at varying **altitudes**, Dixon et al (2009) show that rates of soil production, mechanical erosion and chemical weathering are almost two time higher at low altitudes, where the temperature is higher. In Iceland, the **temperature** is the dominant variable controlling the weathering increase, and a robust linear relationship was found between the weathering index and the mean annual temperature (Oskarsson et al, 2012).

Finally, **vegetation** plays an important role in regulating the residence time of water in the vadose zone because evapotranspiration limits runoff and underground recharging. Changing vegetation patterns have contributed to long-term fluctuations in weathering fluxes (Riotte et al, 2014).

On a regional scale, the **runoff** (surface streams that appear after precipitation including accumulation, transpiration, meltage, seepage, evaporation and percolation) was identified as the most important predictive factor for rates of chemical weathering after the lithology (Hartmann and Moosdorf, 2011). At the global scale, the chemical weathering curve seems slightly disconnected from the runoff curve and these differences can be explained by climatic heterogeneities and variations in rock or regolith properties (Hartmann et al, 2014). Along a runoff gradient, the concentrations of solutes derived from rocks do not follow a law of pure dilution, and a buffer mechanism exists to stabilize the solute concentration in a process called "chemostatis" (Godsey et al, 2009; Gaillardet et al, 2011). As a result, concentrations vary less than the runoff, and chemical weathering rates are mainly controlled by the runoff (**Fig. 1.11**).

Few studies investigate the impact of **human activities** on the chemical weathering of volcanic islands. In the Lesser Antilles, regions highly impacted by agriculture induce significant changes in vegetation cover by replacing the native forest with banana and sugarcane plantations. There is a correlation between banana plantations and chemical weathering (Rad et al, 2011) but the age of these drained basins appears to be the controlling parameter and results show that human activity does not (or only slightly) disrupt the processes of regolith (Rad et al, 2011).

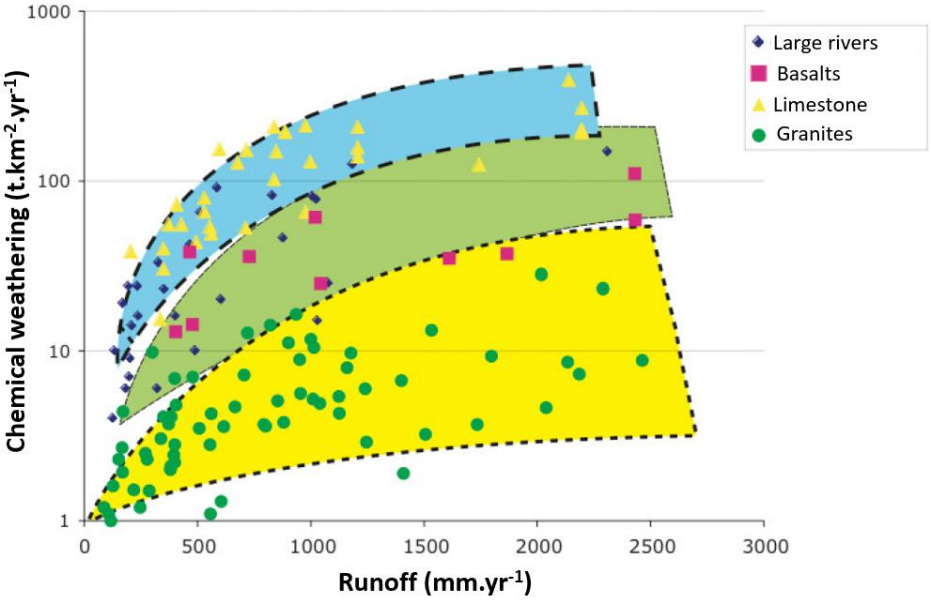

Fig. 1.11: Coupling between chemical weathering rates ($t.km^{-2}.yr^{-1}$) and runoff ($mm.yr^{-1}$) in large rivers, basaltic streams (rivers, lakes), limestone and granitic rivers (from Gaillardet et al, 2011; in Rad et al, 2007).

1.2.4 Chemical weathering reactions and carbon cycle

Numerical models and interpretations of the geological record reveal that chemical weathering has played a key role in maintaining climate stability over geological time (Walker et al, 1981; Berner et al, 1983, Holland, 1984; Raymo et al, 1988; Kump et al, 2000; Galvez and Gaillardet, 2012).

1.2.4.1 Carbon balance on reactions scale

During rock weathering, the dissolution reactions involve protons mainly derived from atmospheric CO_2 ($atmCO_2$) solubilization. The $atmCO_2$ is in turn mainly derived from the oxidation of soil organic matter (Boeglin and Probst, 1998). For example, the anorthite (calcium silicate) weathering is written:

$$CaAl_2Si_2O_8 + 3H_2O + 2CO_2 \rightleftarrows Al_2Si_2O_5(OH)_4 + Ca^{2+} + 2HCO_3^-.$$

This dissolving reaction releases free Ca^{2+} and HCO_3^-, which are transferred to the ocean via rivers. In the ocean, HCO_3^- are consumed by the precipitation of calcite ($CaCO_3$) depending on the reaction (Boeglin and Probst, 1998; Dupré et al, 2003):

$$Ca^{2+} + 2HCO_3^- \rightleftarrows CaCO3 + H_2O + CO_2.$$

Thus, on 2 moles of $atmCO_2$ consumed by weathering, only one mole of CO_2 returns to the atmosphere (Dupré et al, 2003), and the net budget for calcium silicate weathering can therefore be resumed by:

$$CaSiO_3 + CO_2 \rightleftarrows CaCO_3 + SiO_2.$$

The chemical weathering of silicates rocks can therefore be considered as a natural stabilization mechanism of $atmCO_2$ (Louvat, 1997).

However, the only weathering reactions with a significant effect on the carbon balance are those of the calcium and magnesium silicates (bivalent cations). The effect of the weathering of sodium and potassium silicates (monovalent cations) is much less obvious, since alkalis are subject to phenomena known as **"reverse"** weathering, which leads to the return of $atmCO_2$ during the formation of secondary minerals (Gaillardet et al, 1999).

This is also the case for pure limestone, whose dissolution reaction is written:
$CaCO_3 + H_2O + CO_2 \rightleftarrows Ca^{2+} + 2HCO_3^-$.

On a million-year scale, the carbon uptake by weathering of the continental carbonates is returned to the atmosphere by calcite precipitation in the oceans. Carbonate weathering is therefore commonly considered to have no effect on the $atmCO_2$ concentration in the long term (Gaillardet et al, 1999; Ludwig et al, 1999). In the volcanic domain and when there are no carbonates in the basins slopes, the total bicarbonate fluxes measured in the river can be directly associated on silicate weathering and $atmCO_2$ consumption (Louvat, 1997; Boeglin and Probst, 1998; Gaillardet et al, 1999; Dessert et al, 2001).

1.2.4.2 Carbon balance on geological time scale

The weathering of continental silicates represents a CO_2 consumption of 8.7×10^{12} $mol_{CO2}.yr^{-1}$ following studies of large rivers worldwide (Gaillardet et al, 1999). However, these values do not include the CO_2 consumed by the basalts weathering of volcanic islands and arcs. By extrapolating the results of Louvat and Allegre (1997), the CO_2 consumption specifically related to the weathering of volcanic islands is estimated to be 3×10^{12} $mol.yr^{-1}$, or about 30% of global CO_2 consumption derived from continental silicates (Gaillardet et al, 1999), although their surface area represents only 9% (Rad, 2007). Dessert et al (2003) re-evaluated this contribution to ~35% (4.08×10^{12} $mol_{CO2}.yr^{-1}$) of CO_2 consumption by continental silicates. The specific contribution of

calcium and magnesium silicates is estimated at 60% for the mainland and 70% for the islands (Meybeck, 1987).

1.2.4.3 Weathering reactions and associated CO_2 consumption quantification

The quantification of chemical weathering rates (CWR) is based on the sum of the total dissolved elements (TDS) in rivers generally expressed as follows: $TDS = cations + SiO_2$ with cations = Na^++Ca^{2+}+Mg^{2+}+K^+, the draining basin surface and the riverine discharge. However, there is no real consensus on the techniques used for the calculation of weathering rates (Rad et al, 2013). The elements used in the TDS definition differ between studies. The only elements commonly used are **silicon** and major cations. Moreover, silicon is not always considered in the same form: silicon (Si), silica (SiO_2) and silicic acid (H_4SiO_4) have been used. The most common units published are $mg.l^{-1}$ for TDS and $t.km^{-2}.yr^{-1}$ for weathering fluxes. In this PhD thesis, the weathering fluxes ($t.km^{-2}.year^{-1}$) will be assessed using TDS defined as: Ca^{2+}+Mg^{2+}+Na^++K^++SiO_2. The atmospheric CO_2 comsumption by silicate weathering can be calculated in different ways: (i) using alkalinity derived from silicate weathering (Schopka et al, 2011), (ii) using HCO_3^- fluxes measured at the outlet of the catchment (Gaillardet et al, 1999), (iii) using dissolved Si fluxes (assuming that silicate weathering consumes two moles of CO_2 and releases one mole of dissolved Si; C flux = 2 × Si flux; Edmont and Huh, 1997; Goldsmith et al, 2008; Freire et al, 2013) and (iv) using major cations flux (Ca^{2+} + Mg^{2+} + Na^+ + K^+) derived from silicate weathering in electrical equivalent (TZ^+).

1.3 Chemical weathering fluxes in hydrothermally-active volcanic regions

1.3.1 Overview

Due to the fragmented nature of the volcanic deposits, silicate weathering is enhanced in areas with volcanic rocks such as volcanic islands and continental hotspots. Indeed, volcanic rocks represent only 5% of the terrestrial land but contribute significantly to the global flux of solutes to the ocean and consumption of atmospheric CO_2 through silicate weathering (Louvat and Allègre, 1997; Gaillardet et al, 1999; Dupré et al, 2003; Dessert et al, 2003; Gislason and Oelkers, 2009).

Recent data highlight the disproportionate contribution to weathering fluxes of **volcanic island arcs** (Goldsmith, 2008; Jones et al, 2011). Volcanic island arcs environments are characterized by a recent geology, an active tectonic region of the circum-Pacific ring of fire, a high runoff and a high silicate weathering rate (Milliman and Meade, 1983; Milliman and Syvitski, 1992; Sommer et al, 2006). Globally, the silicate weathering fluxes reported for volcanic island arcs (Martinique and Guadeloupe: 100-120 $t.km^{-2}.yr^{-1}$; Rad et al, 2006; Kamchatka (21 $t.km^{-2}.yr^{-1}$; Dessert et al, 2009) compared with the CWR reported for basaltic hotspots (La Réunion: 63-170 $t.km^{-2}.yr^{-1}$; Louvat and Allègre, 1997; Iceland: 19-146 $t.km^{-2}.yr^{-1}$; Stefánsson and Gislason, 2001). Note that comparing the calculated fluxes of solutes obtained by various studies is complicated because of the different datasets representing a range of method providing estimates with highly variable temporal precision and accuracy (Hurwitz et al, 2010). All CWR reported worldwide were compiled by Rad et al (2013) and presented in **Fig. 1.12a**.

It follows that volcanic island arcs contribute disproportionately to the total dissolved Si mainly derived from surface waters (~66%, rivers and lake) to the ocean (Dürr et al, 2011; $t_{DSi}.km^{-2}.yr^{-1}$; **Fig. 1.12b**). Volcanic island arcs are called "**hyperactive areas**" contributing a DSi flux that is 5 to 10 times greater than the global mean in coastal catchments. For

example, the DSi yield in the Japanese Archipelago, a hyperactive region, is 6.6 times higher than the world average (Hartmann et al, 2010). This, in turn plays an important role in the global C cycle given that the global Si and C cycles are tightly coupled in diatoms, organisms that incorporate both Si and C in their tests (Smetacek, 1999). Note that part of the DSi is stationary in estuaries and lakes before reaching the ocean. According to Frings et al (2016), ~25% of DSi can re-precipitate as clay minerals ("**reverse weathering**") and a proportion of the DSi flux from river water, stagnating in estuaries, will not reach the ocean (1.5 $tmol.yr^{-1}$; Tréguer and De La Rocha, 2013). Rahman et al (2017) revisit the Si sink in different delta systems and point out a higher sedimentary Si storage flux of 3.5–3.9 $tmol.yr^{-1}$ as authigenic clay in tropical and subtropical deltas. However, this effect is **limited** in volcanic islands due to the strong connection between river waters and the ocean.

Many uncertainties exist concerning the factors influencing chemical weathering fluxes in hydrothermally-active volcanic regions such as in volcanic islands arcs and continental hotspots. Some spatial factors are reported in the literature including hydrothermal input and soil weathering intensity (discussed in **section 1.3.2.1**). Temporal factors depending on climate also influence riverine chemistry in hydrothermally-active volcanic regions and are discussed in **section 1.3.2.2**. Finally, the land use effect on Si riverine fluxes in volcanic islands is discussed in **section 1.3.2.3**.

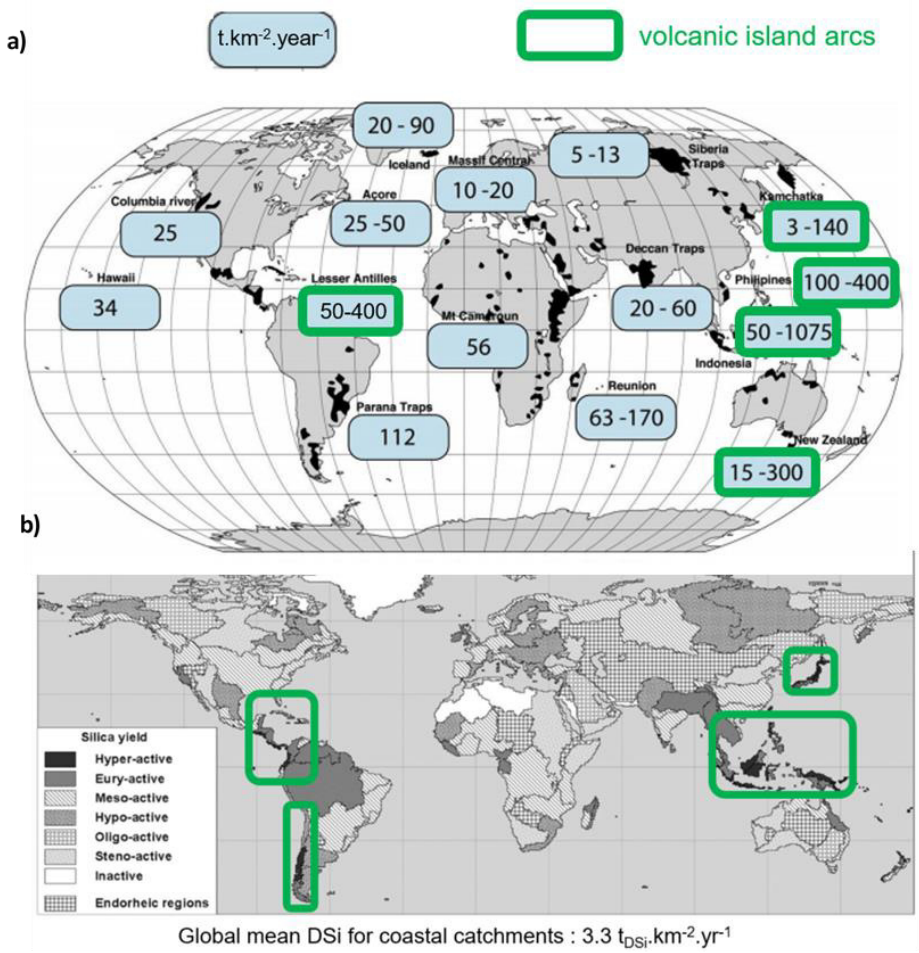

Fig. 1.12: (a) Chemical weathering rates (CWR; $t.km^{-2}.yr^{-1}$) reported worldwide. More specifically, volcanic islands arcs have the highest CWR on Earth (modified from compiled data by Rad et al, 2013) and (b) are hyperactive areas (contribute from 5 to 10 times relative to the global mean DSi for coastal catchment; $t_{DSi}.km^{-2}.yr^{-1}$) (modified from Dürr et al, 2011). The map legend is centered on the global mean dissolved Si for coastal catchments (3.3 $t_{DSi}.km^{-2}.yr^{-1}$). Inactive areas 0–0.01× global mean yield, steno-active 0.01–0.1x, oligo-active 0.1–0.2x, hypo-active 0.2–0.5x, mesoactive 0.5–2x, eury-active 2–5x, hyper-active 5–10x.

1.3.2 Factors influencing chemical weathering fluxes in hydrothermally-active volcanic regions

1.3.2.1 Spatial factors: weathering gradient and hydrothermalism

Once the atmospheric contribution to the river has been corrected, the riverine chemistry is usually attributed to the weathering of rock minerals (Gaillardet et al, 2011). Volcanic islands comprise **age gradients of volcanic rocks** influencing soil-weathering intensity and hence, weathering fluxes to rivers (e.g., Dessert et al, 2015).

Moreover, volcanic islands are often associated with **hydrothermal systems** which act as a source of strong acids for weathering reactions (due to the input of magmatic gas such as magmatic CO_2, SO_2, H_2SO_4 and HCl) thereby contributing to weathering fluxes (Louvat and Allègre, 1997; Dessert et al, 2009; Hurwitz et al, 2010; Schopka et al, 2011; Gaillardet et al, 2011; Rivé et al, 2013).

Hydrothermal systems also promote **hydrothermal alteration**. Secondary minerals resulting from hydrothermal alteration are formed in four hydrothermal environments: (i) magmatic-hydrothermal, (ii) magmatic-steam, (iii) steam-heated and (iv) supergene environments (**Fig. 1.4**; **1.5**; **1.6**). The magmatic-steam environment is the upper portion of a hydrothermal system dominated by a vapor phase of magmatic origin and is associated with high temperature fumarolic gases. The steam-heated environment represents the shallow level, at or above the water table, where secondary fluids are formed by oxidation of hydrothermal fluids. Supergene environments are found at the Earth surface where there is no influence of hydrothermal fluids. Many types of hydrothermal alteration exist. The nature and relative quantities of minerals that constitute various hydrothermal alteration assemblages depend on several factors such as temperature, pressure, host rock composition, primary fluid composition, and fluid/rock ratio (Reed, 1997). Generally, hydrothermal alteration is divided into:

- **Potassic alteration**: chemical alteration mainly found into low-relief system characterized by exchange of K^+ for Ca^{2+} and Na^+, leading to replacement of Ca-Na minerals and forming new K-feldspar and/or biotite (green colored and Fe-rich), e.g., muscovite, orthoclase and the mineral assemblage quartz ± albite ± chlorite ± anhydrite ± pyrite;

- **Prophylitic alteration**: from interaction between the host rocks and iron- and sulfur-bearing hydrothermal fluids and forming e.g., albite, chlorite, and epidote (Melling et al, 1990);

- **Phyllic/sericitic alteration**: hydrothermal alteration characterised by the assemblage of quartz + sericite + pyrite, and occurs at high temperatures and moderately acidic (low pH) conditions. Phyllic/sericitic alteration forms e.g., feldspar, kaolinite, calcite, biotite, rutile, anhydrite and apatite.

- **Argillic alteration:** clay mineral formation in response to intense rock leaching by acidic fluid forming e.g., plagioclase and mafic silicate;

- **Silicic alteration**. Silicic alteration is found in environments with dominant silica-rich fluids. Precipitation and re-distribution of silica is one of the most common features of hydrothermal activity. Generally, the solubility in water of various forms of silica (amorphous silica, opal, cristobalite, chalcedony and quartz) increases with temperature in the range of 10 to 100 $mg.l^{-1}$ for temperatures of < 50-100 °C, and up to 1000 $mg.l^{-1}$ above 300 °C; thereafter, solubility of silica decreases. Different types of silicic alteration include silica sinter, opaline, residual quartz, silicification, chalcedony horizon, chalcedony veins, colloform bands, cryptocrystalline veins and quartz veins (Hedenquist et al, 2000). Silica supersaturation promotes precipitation of amorphous silica at temperatures of approximately 140 °C, and near-neutral chloride-rich solutions generally deposit at the surface large quantities of amorphous silica, forming aprons of sinter material, as observed in Yellowstone Plateau Volcanic Field (Hurwitz et al, 2010). Residual quartz results from extreme leaching of volcanic rocks by magmatic acid-sulfate fluids at pH < 2 (Delmelle and Bernard, 1994; Hedenquist and Taran, 2013).

1.3.2.2 Temporal factors: climate-induced discharge variation and runoff

Temporal factors influence riverine chemistry in hydrothermally-active volcanic regions and mainly depend of climatic conditions. This is why, in the following part of the PhD thesis, the term "seasonal" will be used. The effect of climate on chemical weathering is generally evaluated by correlating variations in solute concentrations and fluxes with temperature, precipitation, runoff and evapotranspiration (White and Blum, 1995). The **tropical climate**, generally found in volcanic islands, drives high rates of precipitation that vary depending on the season. These seasonal variations result in distinct hydrological conditions including variations in catchment runoff and river discharge. In large rivers, a large portion of annual flux of materials from the continent to the ocean is carried by **extreme flood events**, and thus only in a short period (e.g., a few days) (Schafer et al, 2002; Blake et al, 2003; Antonelli et al, 2008). Recently, Fries et al (2019) show that storms are responsible for up to ~ 50% of total annual rainfall on tropical islands, result in rapid increases in river water discharge and have significant impact on weathering processes and therefore on the compositions of river waters delivered to the ocean. In addition to hydrology, Dessert et al (2020) highlight the important role of **atmospheric dust** in tropical rainforests on river chemistry from Basse-Terre Island and demonstrate that Saharan dust plays a significant role in maintaining ecosystem productivity in Guadeloupe over long-time scales.

Ultimately, climatic effects on chemical weathering cause fundamental differences in the thermodynamic and kinetic interactions between minerals and solutions. Quantifying such processes is difficult on a watershed scale. Therefore, most watershed weathering studies use simpler approaches, based on either solute concentrations or fluxes as surrogates for weathering intensity (White and Blum, 1995). White and Blum (1995) show, in 68 granitic watersheds worldwide, that the correlation between yearly variations in precipitation and solutes fluxes within individual watersheds is stronger than the correlation between precipitation and solute fluxes of watersheds with different climatic regimes. This underscores the significance of transport-induced

variability in controlling stream chemistry and the importance of distinguishing between short-term and long-term climatic trends. For example, Ingri et al (2005) use multi-elemental analyses and discharge normalization using Mg to estimate seasonal patterns in relative enrichment or depletion of dissolved Si in boreal rivers, demonstrating the effect of short-term climate variations on river water chemistry.

Runoff in volcanic islands can be strongly impacted by **seasonality,** as well as by orography and infiltration (Gaillardet et al, 2011). Runoff alters the residence time of water in soils and therefore influences the processes affecting weathering in soils (White and Blum, 1995). According to future climate predictions, runoff variability will affect the flux of dissolved elements in river waters, for example, increasing DSi fluxes in North America by up to 13% (Moosdorf et al, 2011). It is expected that runoff variability will particularly affect weathering fluxes in volcanic regions where seasonal variations in runoff during **intense rainfall** (flash flooding) produce ~ 21-31% of the annual chemical weathering fluxes (Dessert et al, 2015).

Beusen et al (2009) use modelling to indicate that DSi fluxes depend on the precipitation and the occurrence of volcanic rocks. Basic igneous rocks display the highest DSi yields with respect to a given runoff while the least DSi per runoff is mobilized from acidic plutonic rocks (Jansen et al, 2010; Hartmann et al, 2010). **Slope** constitutes another important controlling factor on DSi fluxes besides lithology and runoff (Hartmann et al, 2010). Uncertainties remain regarding runoff effect on processes influencing riverine chemistry and thus silicate weathering rates in hydrothermally-active volcanic regions.

1.3.2.3 Land use: Si-accumulating crops harvest

Land-use is another uncertainty that may influence CWR from hydrothermally-active volcanic regions.

Volcanic soils, mainly Andisols, cover less than 1% of the total land surface but support more than 10% of the total world population. They are fertile (defined as the soil ability to produce sustainably under current

growing conditions favored by adapted soil structure for anchoring plant roots, rich in carbon and nutrients (N, P, K) and high water retention) and suitable for crop cultivation (Delmelle et al, 2015). Indeed, young volcanic soils are light and fluffy, have a low bulk density and remarkable water-holding capacity, contain a clay fraction (solid material < 2 μm) dominated by poorly crystalline and noncrystalline minerals, and tend to accumulate organic matter (Delmelle et al, 2015). As a result, volcanic islands arcs are the most-cultivated areas worldwide (**Fig. 1.13**; Ramankutty et al, 2008) and the most cultivated crops worldwide, i.e., sugar cane, maize, rice, and wheat (FAOSTAT, 2015), are silicon-accumulating plants (Si-accumulating plants).

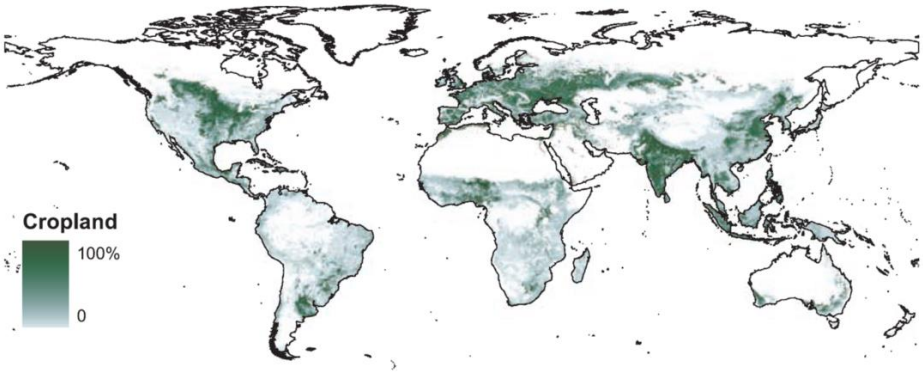

Fig. 1.13: Cropland percentage on the Earth surface in the year 2000 (from Ramankutty et al, 2008).

The silicon content in plant ranges from 0.1 to 10% Si dry weight (Ma and Takahashi, 2002; Hodson et al, 2005), which is significantly lower than the average Si content estimated for the global biosphere (0.03%). Plants species are classified into three categories according to their mode of Si-uptake (Sangster and Hodson, 1986; Epstein, 1999; Takahashi et al, 1990): (i) **Si-accumulating plants with an active uptake** (Si is taken up more than predicted by mass flow), (ii) **non Si-accumulating plants**

with a rejective uptake inducing a Si-accumulation in the soil solution and (iii) **intermediate plants** with passive diffusion by mass flow (Si is taken up in the same quantity as that predicted by mass flow). The mass flow is based on the pressure-flow hypothesis that posits a pressure gradient from the source plant area to the sink plant area that would allow solution flow without carrier.

The difference in Si-accumulation between plant species is attributed to a higher density of transporters for Si uptake in high Si accumulating plants (Mitani et al, 2005). In Si-accumulating plants, the Si taken up by the plant is precipitated as biogenic Si in the plant tissues (phytoliths; Jones and Handreck, 1965) leading to Si content of ~ 1% Si dry weight in the plant, and up to 5% in rice (Datnoff et al, 2001). In the literature, Si-accumulating plants are reported given their mean shoot content of Si (Hodson et al, 2005): bamboo (*Bambusa* sp., up to 7% Si), sugar cane (*Saccharum* sp., 1.5% Si), soybean (*Glycine* sp., 1.4% Si) and cereals (corn (*Zea* sp., 0.8% Si); rice (*Oryza* sp., 4.2% Si); wheat (*Triticum* sp., 2.4% Si); barley (*Hordeum* sp., 1.8% Si); sorghum (*Sorghum* sp., 1.5% Si); mil (*Pennisetum* sp., 0.9% Si) and oat (*Avena* sp., 1.5% Si)).

Rice (*Oryza* sp.) is a Si-accumulating plant where a significant portion of the Si taken up by the plant does not return to the soil. The rice plant is an annual grass with a round, hollow, flat-leaved stem and terminal panicle. Commonly, rice plants grow in flooded conditions. The different parts of the rice plant are: root (made up of secondary roots and absorbent hairs, serving as anchoring), stem, leaf, panicle and flower. The essentiality of silicon as plant nutrient has been debated, since Si nutrition has positive effect on crop yield (Takahashi et al, 1990; Epstein, 1999; Richmond and Sussman, 2003). Generally, studies report that Si increases plant tolerance to biotic and abiotic stresses by ensuring structural (keeping leaf blades erected improving light interception), physiological (decreasing transpiration) and protective functions (protection against insect attacks, fungal and mineral toxicity) (Sangster and Hodson, 1986; Marschner, 1995; Pilon-Smits et al, 2009; Guntzer et al, 2012). Some Si-containing fertilizers are routinely supplied to several crops in order to increase the crop yield and quality, e.g., rice (Ma et al, 2001) and sugar cane (Savant et al, 1999).

Cultivation and harvest of Si-accumulating crops, including plant biomass export, result in the loss of a non-accounted sink for Si released during weathering (e.g., Desplanques et al, 2006). Crop harvest may also influence the flux of dissolved Si exported to the ocean because the estimated global agricultural Si export (0.22×10^{12} $kg_{Si}.yr^{-1}$; Matichenkov and Bocharnikova, 2001) is on the same order of magnitude than the riverine Si discharged into the ocean as dissolved and biogenic Si (0.20×10^{12} $kg_{Si}.yr^{-1}$; Tréguer and De La Rocha, 2013). Taking into account the global increasing demand for agricultural soils (Godfray et al, 2010), the impact of crop harvest on global Si export to the ocean is likely to be emphasized in the future and needs to be better quantified given that Si is a key nutrient for diatoms, which are essential organisms for the oceanic C pump (Smetacek, 1999). The effect may be particularly pronounced in volcanic island arc regions contributing disproportionately to the dissolved Si delivery to the ocean (Dürr et al, 2011) and intensively cultivated.

1.4 Silicon as a tracer of chemical weathering

Silicon is included in the assessment of weathering fluxes ($t.km^{-2}.year^{-1}$) defined as $Ca^{2+}+Mg^{2+}+Na^{+}+K^{+}+SiO_2$ (**section 1.2.4.3**). Silicon (Si), the eighth-most-abundant chemical element in the universe (Ding et al, 1996), is also the second most abundant element (28%) after oxygen (49%) in the Earth crust (Epstein, 1999). Nevertheless, in the global biosphere, the Si average concentration (0.03%) is below H, O, C, N, S, Ca and K (Exley, 1998). Silicon constitutes, as tetrahedra (SiO_4), the skeletton of silica (SiO_2), and silicate minerals (pyroxenes, feldspars, amphiboles), the most important oxide on the Earth's surface that makes up more than 75% of the rocks exposed on the Earth's surface. Silicon is a key component of global biogeochemical cycles.

Studying the silicon cycle is directly relevant for the C cycle given the two following links between the Si and the C cyles. Firstly, DSi is a **nutrient** for many organisms. For some – notably photosynthetic marine diatoms – it is an essential nutrient (Yool and Tyrrell, 2003). Given that the availibility of DSi in aquatic ecosystem governs the amount of siliceous primary productivity (mainly diatoms, representing 40% of ocean primary productivity; Egge and Asknes, 1992), DSi indirectly plays a major role in controlling the oceanic CO_2 storage capacity (Smetacek, 1999). The siliceous production has a major influence on the ocean biological pump by determining the partitioning of carbon between the atmosphere and the deep ocean on centennial to millennial time scale (De La Rocha, 2006). Secondly, the **weathering of silicates** is key in the sequestration of atmCO_2 and hence is crucial in the long-term geological carbon cycle (Walker et al, 1981).

The global biogeochemical Si cycle includes the terrestrial Si cycle and the continental **dissolved silicon** transfer to the ocean (**Fig. 1.14**). Continental DSi comprises five reservoirs: rivers, vegetation, groundwater, soils and bedrock. In hydrothermally-active volcanic regions, hydrothermal fluids are considered as an additional reservoir due to the strong influence of hydrothermal water-rock interaction on chemical silicate weathering fluxes (Dessert et al, 2009; Jones et al, 2011;

Louvat et al, 2011). The beginning of the continental Si cycle is associated with the DSi release during weathering processes whose fractions follow different pathways: (i) direct transfer to the fluvial system via groundwaters and soil pore waters, (ii) incorportation into, or adsorbed onto, secondary phases of variable stability (weathering product) and (iii) precipitation as **biogenic silica** (BSi) in vascular plants (Piperno, 2001; Massey et al, 2006; Carey and Fulweiler, 2012).

The production of **BSi** by vegetation (60-200 $Tmol.yr^{-1}$; Conley, 2002) is on the same range as that coming from marine diatoms (240 $Tmol.yr^{-1}$; Tréguer et al, 1995). This is relevant compared to the annual riverine Si supply to the ocean (5 $Tmol.yr^{-1}$; Tréguer et al, 1995 ; **Fig. 1.14**) and suggests that the majority of DSi passes through this vegetation buffer before export into the river system (Derry et al, 2005; Struyf et al, 2009). Upon litterfall, the BSi is restitued to the soil by dissolution, storage or is structurally or chemically altered (Sommer et al, 2006; Barão et al, 2014; **Fig. 1.15**). In addition, Si will be lost to the fluvial system as both DSi and eroded particulate Si. Both biotic and abiotic processes can modify the Si flux into the river system. Low-turbidity environments such as lakes and reservoirs provide conditions favoring BSi production by diatoms (Lauerwald et al, 2013; Frings et al, 2014) and in-stream processes in floodplains, riparian and hyporheic zones may also be significant areas for BSi accumulation (Bouwman et al, 2013). Deltas and estuaries can also modify river Si fluxes (Milliman and Boyle, 1975; Conley and Malone, 1992; Weiss et al, 2015). In the ocean, hydrothermal input can contribute to oceanic DSi via axis and ridge flank hydrothermal systems (Tréguer and De La Rocha, 2013). Ultimately, shared understanding of the continental Si cycle and the continental DSi transfer to the ocean is essential because the chemical weathering of continental silicate rocks was responsible for 45% of the riverine dissolved load and rivers deliver 66% of the DSi supplied to the ocean (Tréguer and De La Rocha, 2013).

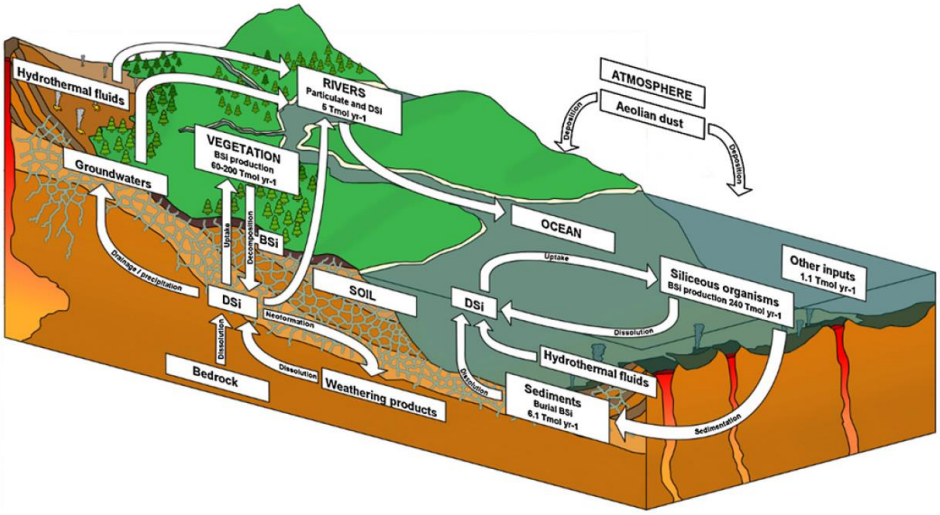

Fig. 1.14: Schematic diagram of the global biogeochemical Si cycle on Earth (from Opfergelt and Delmelle, 2012). The main reservoirs and processes involved in the continental Si transfer to the ocean were represented. Values of oceanic BSi and plant production are respectively from Tréguer et al (1995) and Conley (2002).

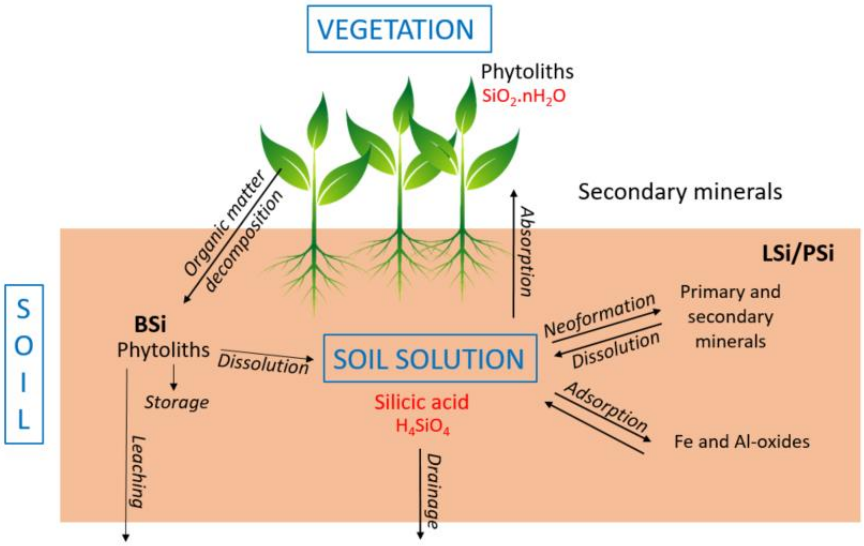

Fig. 1.15: Continental silicon cycle in the soil-plant system.

1.4.1 Silicon in soils

In derived soils, Si content ranges from 46% in silcretes to 7.9% in petrocalcic horizons, and even lower in highly-weathered Oxisols such as bauxites or ferricretes (Monger and Kelly, 2002). Soils mainly contain Si as silica minerals, primary silicates and secondary silicates, especially phyllosilicates (Iler, 1979). Silicon in soils can be distributed between adsorbed, solid and liquid phases (McKeague and Cline, 1693; Sommer et al, 2006; **Fig. 1.16**). The **adsorbed Si** species (ASi) is monosilicic acid ($H_4SiO_4^0$) and the pH-dependent sorption increases from pH 4 to pH 9 (McKeague and Cline, 1963). The Si sorption onto soil is mainly found on iron (Fe) and aluminium (Al) oxides, which are the major components of soils with a significant capacity of adsorption (Beckwith and Reeve, 1963). However, little adsorption is reported onto clay minerals (Siever and Woodford, 1973). The Si compounds in the solid phases of soils can be from litho- or pedo-genic origin originated from parental material and to secondary minerals formed during soil

formation. The Si pool occurs in crystalline, poorly crystalline or microcrystalline, or amorphous form (Dress et al, 1989).

The **lithogenic silicon** (LSi), originated from the parental material, is constituted of crystalline, poorly and micro-crystalline, and amorphous primary minerals concentrated in the sand (> 50 μm) and the silt (> 2-50 μm) fraction of the soil. Depending of the mafic or felsic nature of the parental magmatic rock, the major primary minerals from igneous rocks are feldspar, olivine, pyroxene, amphibole and mica (Schulze, 2002).

The **pedogenic silicon** (PSi) is mainly constitued of secondary minerals composed by clay-sized phyllosilicates and Al-Fe-oxides concentrated in the clay fraction (< 2 μm). The aqueous silicon can be adsorbed onto Al- and Fe-oxides and integrated into their crystalline structure (Carlson and Schwertmann, 1981). The drainage, the soil mineralogy and weathering stage are major factors influencing the silica activity in weathering solution and the nature of clay minerals (White, 1995).

The **liquid compound of Si** (DSi) is found in the soil solution as mainly uncharged monomeric monosilic acid ($H_4SiO_4^0$) (Dress et al, 1989) and can be transformed into polymeric form under strongly alkaline conditions (Dietzel, 2000). Monosilic acid is a very weak acid (dissociation constant at 25 °C: pK_1 = 9.51; pK_2 = 11.77). Usually, the silicon concentration in soil solutions ranges between 0.01 and 1.99 mMSi (below saturation limit of amorphous silica at 25 °C; Karathanasis, 2002). This concentration varies as a function of temperature, rainfall pattern, residence time of soil pore water, parent material, soil weathering stage and is also controlled by the dissolution of unstable minerals at given pH values, as predicted from a stability diagram (Karathanasis, 2002). Aqueous polymeric forms of Si occur at pH above 9 (Stumm and Morgan, 1996).

The **biogenic silicon** (BSi) is generally found as plant opal in soils (Smithson, 1956), ranging from 1 to 30 $g.kg^{-1}$ (Dress et al, 1989). Phytoliths ("plant stone") are opal-A particles (Bartoli and Wilding, 1980) and their solubilty strongly depends on their physical and chemical properties: specific surface area, Al content, hydradation state, age, rate of decomposition of organic residues (Bartoli and Wilding, 1980). The solubility product of soil phytoliths (pK_{sp}^0 = 2.74 à 25 °C) is on the same range as those of vitreous silica and is 17 times higher than that of quartz (Fraysse et al, 2006).

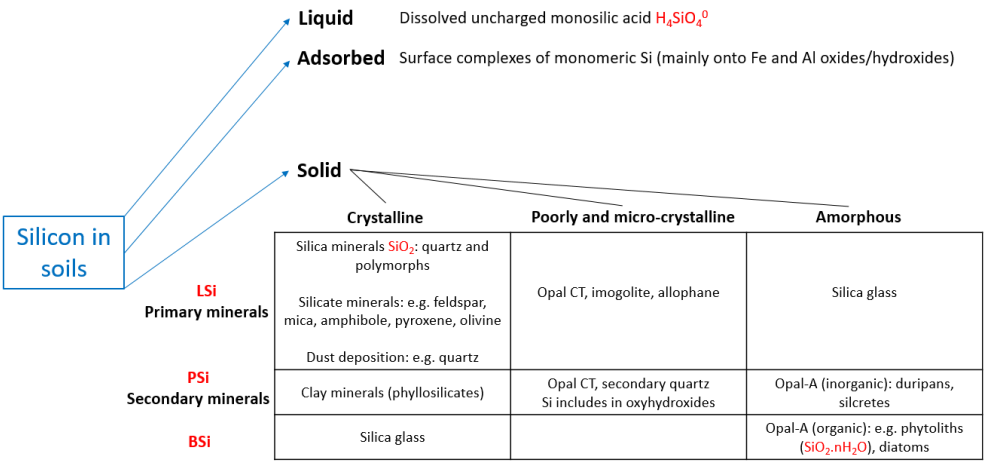

Fig. 1.16: Classification of silicon compounds classification in soils (modified from Matichenko and Bocharnikova 2001; Sauer et al, 2006).

1.4.2 Silicon in plants

Plants absorb the silicon as uncharged monosilic acid ($H_4SiO_4^0$) via water transpiration flux (Raven, 1983). Si is transported into the xylem as dissolved H_4SiO_4 (Mitani et al, 2005) and precipitates in aerial parts of the plant as hydrated amorphous silica $SiO_2.nH_2O$ called biogenic opaline phytolith (Jones and Handreck, 1965; illustrated in **Fig. 1.17** for rice Si-accumulating plants). The phytoliths are restored to the soil via the decomposition of organic debris from plant material. Generally, in most of plants, silica deposits are reported inside living cells, in cell walls, membranes and in intercellulare spaces (Lewing and Reimann, 1969; Sangster and Parry, 1981; Waterkeyn et al, 1982). Phytoliths have a broad range of morphologies varying with plant species and location of Si deposits.

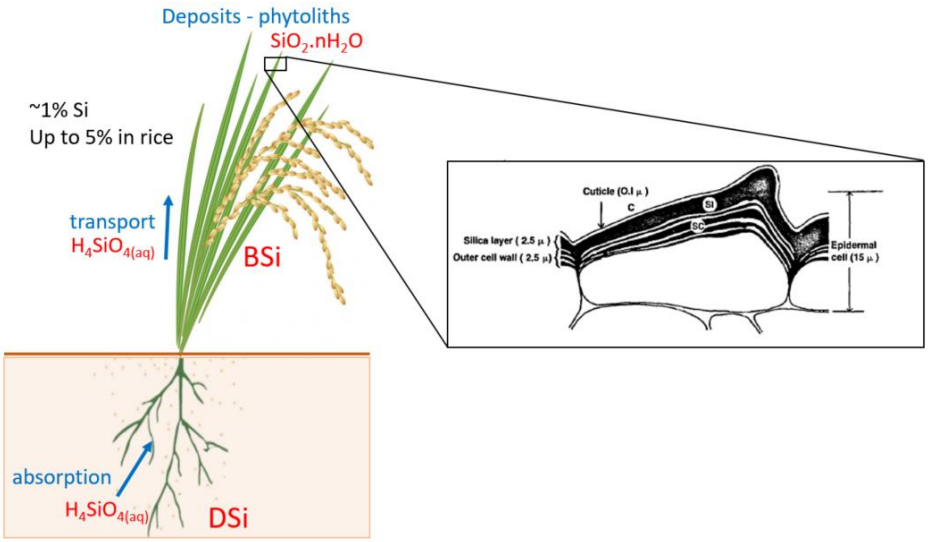

Fig. 1.17: Silicon transport in Si-accumulating plant (rice) and schematic representation of the rice leaf (Yoshida, 1975).

1.4.3 Silicon in natural and thermal waters

Silicon is supplied to **natural waters** as uncharged monomeric monosilic acid ($H_4SiO_4^0$) (DSi) and particulate forms. The solubility of amorphous Si in water to form monomeric $H_4SiO_4^0$ is pH-dependent and increases from pH above 8 (Alexander et al, 1953). Silicon in natural waters has a very low affinity for organic compounds (Pokrovsky and Schott, 1998). Diatoms and other siliceous organisms can directly take up DSi but many Si-containing solid phases, including quartz and silicate minerals, are unavailable for biological utilization (Iler, 1979; Cornelis et al, 2011; Dürr et al, 2011). A fraction of the Si in particles is nevertheless reactive solid and solid-bound forms and can potentially act as a soluble Si source in freshwater. Diatoms and riparian plants further contribute to the particulate reactive Si pool of a reservoir through the production of BSi (Sauer et al, 2006).

At the global scale, the mean DSi concentration of freshwaters displays a large range (65-389 $\mu mol.l^{-1}$ in Australia and Africa, respectively; Exley, 1998). Transport condition (runoff) and mineral weathering (physical denudation and temperature) are the main factor controlling processes driven the DSi input to rivers (Meybeck, 1979; Anderson et al, 1997; Gaillardet et al, 1999; Turner et al, 2003; Fulweiler and Nixon, 2005; Jennerjahn et al, 2006; Georg et al, 2006; Gislason et al, 2009). Today, the mean global DSi flux in tropical rivers is two to three time higher than in non-tropical rivers (Tréguer et al, 1995). This highlights the major contribution of tropical regions to the total annual DSi input by rivers into the oceans (74% of the total, $0.12 \times 10^{12} kg_{Si}.yr^{-1}$) (Hartmann et al, 2010). The soil-vegetation system type also influences the DSi fluxes in weathering-limited tropical watersheds (Sommer et al, 2006). Physical weathering and erosion in areas of high relief enhance weathering by continually exposing fresh mineral surfaces (Summerfield and Hulton, 1994; Street-Perrott and Barker, 2008).

In **thermal waters**, the different polymorphic forms of silica (quartz, chalcedony, cristobalite and amorphous silica $SiO_{2(a)}$) dissolve in equilibrium forming silicic acid (H_4SiO_4). The solubilization reaction is pH-independent (up to pH value > 9.5) and is mainly temperature-

dependent. The precipitation of polymorphic species depends on the temperature of the solution (Arnorsson, 1983). In Icelandic thermal waters, Àrnorsson (1975) estimates that the main polymorphic specis is quartz above 180 °C and chalcedony for temperatures < 110 °C. Between these two temperatures, quartz and chalcedony precipitate.

To conclude this section, driving variables controlling DSi fluxes from continental cycle to the ocean are: (i) runoff followed by temperature at large scale and at regional scale, (ii) the geomorphology, (iii) the catchment lithology, (iv) the discharge, (v) the soil development, (vi) the biological processes (Sommer et al, 2006; Beusen et al, 2009; Hartmann et al, 2010) and (vii) hydrothermalism.

1.5 Geochemical tracers of the silicon cycle

1.5.1 Germanium to silicon ratio

Germanium (Ge) is a trace metalloid element (atomic number: 32). The similarities in bond length between the tetrahedral GeO (1.75Å) and SiO (1.64Å) allow the isomorphic substitution of Ge in place of silicon in silicate minerals according to the "camouflage" principle (Martin, 1986). Germanium can thus be incorporated in place of silicon in the aluminosilicate network and follows the same behavior as silicon in most geological environments (Kurtz et al, 2002).

In dilute hydrothermal streams of near-neutral pH (pH<8) and in the temperature range of 20–350 °C, Ge is mainly transported as the neutral hydroxide $Ge(OH)_4^0$. The Ge solubility increases with temperature and salinity (Melcher, 2003). In addition to the hydroxide form $Ge(OH)_4^0$, Ge is also transported in hydrothermal fluids mainly in the form of chlorocomplexes (e.g., $GeCl_4$) in geological environments according to Pokrovski and Schott (1998).

The germanium/silicon ratio (Ge/Si ratio) has been employed as a tracer of weathering processes (e.g., Kurtz and Derry, 2004; Scribner et al, 2006; Lugolobi et al, 2010; Opfergelt et al, 2010), hydrothermal activity (e.g., Mortlock et al, 1993; Evans and Derry, 2002), biological processes (e.g., Derry et al, 2005; Sutton et al, 2010) and flow paths (e.g., Kurtz et al, 2011) in modern environments. Variations in the Ge/Si ratio (expressed in $\mu mol_{Ge}.mol_{Si}^{-1}$) in different reservoirs on the Earth's surface is well known (**Fig. 1.18**). The crustal rocks display uniform Ge/Si ratios (1-3 $\mu mol.mol^{-1}$; e.g., Mortlock and Froelich, 1987).

Soils have a higher Ge/Si ratio than the parent rock on which they formed (up to 36 $\mu mol.mol^{-1}$; Kurtz et al, 2002). This fractionation, caused by weathering, shows the preferential incorporation of Ge into secondary clay minerals (Kurtz et al, 2002), although Al oxy-hydroxides also play a role in their sequestration (Ge can be preferentially adsorbed at their surface; Scribner et al, 2006). The range of variation of the Ge/Si

ratio in river waters at the Earth's surface is from 0.16 µmol.mol^{-1} to 20 µmol.mol^{-1} (Mortlock and Froelich, 1987; Froelich et al, 1992; Kurtz et al, 2002; Kurtz and Derry, 2004; Derry et al, 2005; Scribner et al, 2006; Opfergelt et al, 2010; Han et al, 2015; Baronas et al, 2018, 2020). Several studies demonstrate that low-temperature chemical weathering (Bernstein, 1985; Murnane and Stallard, 1990; Froelich et al, 1992), biological processes from Si-accumulating plants (Derry et al, 2005; Delvigne et al, 2009; Seyfferth et al, 2013) and phytoliths dissolution (Derry et al, 2005; Blecker et al, 2007; Lugolobi et al, 2010) control the riverine Ge/Si ratio of rivers. Metamorphic (2 to 1000 µmol.mol^{-1}; Criaud and Fouillac, 1986; Evans and Derry, 2002; Han et al, 2015) and volcanic (0.72 to 185.23 µmol.mol^{-1}; Arnòrsson, 1983, 1987; Siebert et al, 2006; Wheat and McManus, 2008; Escoube et al, 2015) thermal waters display a higher range in Ge/Si compared to river waters (**Fig. 1.18**). In the ocean, Ge/Si ratios of diatoms reflect the Ge/Si ratio of the seawater (e.g., Froelich et al, 1992; Bareille et al, 1998). In plants, a recent study reveals that Si is mostly localized in phytoliths, while Ge is disorderly distributed within the leaf tissues. In fact, from the total amount of Ge accumulated in leaves, only 10% is present in phytoliths highlighting the necessity for using bulk plant Ge/Si instead of Ge/Si in phytoliths to trace biogeochemical cycling of Si in plants (Kaiser et al, 2020).

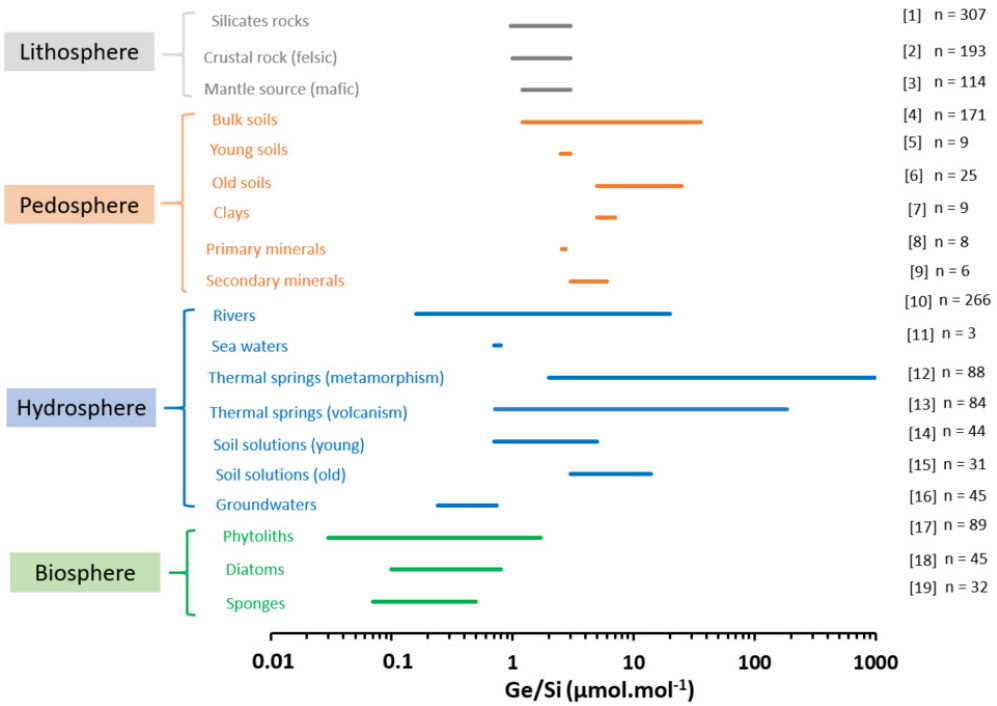

Fig. 1.18: Range of variations in germanium to silicon (Ge/Si) ratios (µmol.mol^{-1}) in different Earth reservoirs. [1] Bernstein, 1985 [2] Mortlock and Froelich, 1987; Kurtz and Derry, 2004 [3] Mortlock and Froelich, 1987; Kurtz et al, 2002 [4] Murnane and Stallard, 1990; Kurtz et al, 2002; Scribner et al, 2006; Delvigne et al, 2009; Opfergelt et al, 2010 [5] Kurtz et al, 2002 [6] Kurtz et al, 2002 [7] Kurtz et al, 2002; Lugolobi et al, 2010; Cornelis et al, 2010 [8] Kurtz et al, 2002 [9] Mortlock and Froelich, 1987; Murname and Stallard, 1990; Kurtz et al, 2002; Anders et al, 2003 [10] Mortlock and Froelich, 1987; Froelich et al, 1992; Kurtz et al, 2002; Kurtz and Derry, 2004; Derry et al, 2005; Scribner et al, 2006; Opfergelt et al, 2010; Han et al, 2015; Baronas et al, 2018, 2020 [11] Mortlock and Froelich, 1987 [12] Criaud and Fouillac, 1986; Evans and Derry, 2002; Han et al, 2015 [13] Arnòrsson, 1983, 1987; Siebert et al, 2006; Wheat and McManus, 2008; Escoube et al, 2015 [14] Derry et al, 2005 [15] Derry et al, 2005 [16] Lugolobi et al, 2010; Kurtz et al, 2011;

Ameijeras-Mariño et al, 2018; Baronas et al, 2020 [17] Kurtz et al, 2002; Kurtz and Derry, 2004; Derry et al, 2005; Delvigne et al, 2009 [18] Froelich et al, 1989; Filipelli et al, 2000 [19] Ellwood et al, 2006. n = total number of data.

1.5.2 Silicon isotopes

Silicon (Si, z = 14, atomic mass = 28.0855) has three stable isotopes: ^{28}Si (AMU (atomic mass unit) = 27.976927), ^{29}Si (AMU = 28.976495) and ^{30}Si (AMU = 29.973730) with abundance of 92.33, 4.67 and 3.10%, respectively (Faure and Mensing, 2005). Generally, the silicon isotope composition is expressed in the δ-notation (units: ‰) relative to NBS28, the accepted reference material for Si isotopes (Carignan et al, 2004): $\delta^{29}Si = [(^{29}Si/^{28}Si_{sample})/(^{29}Si/^{28}Si_{NBS28})-1] \times 1000$ and $\delta^{30}Si = [(^{30}Si/^{28}Si_{sample})/(^{30}Si/^{28}Si_{NBS28})-1] \times 1000$. The degree of isotope fractionation (‰) between two materials X and Y for a particular process is expressed as $\alpha_{X-Y} = R_X/R_Y$ with $R = ^{30}Si/^{28}Si$. It can also be defined as $\varepsilon_{X-Y} = 10^3 \times \ln(\alpha_{X-Y})$.

The Si isotopes offer advantages over other elements as a tracer of secondary mineral formation because of their element natural isotopic variation due to its geochemical behavior. Indeed, elements with several oxidation stages, multiple bonds of different energies with several atoms and a presence within different aggregates have a greater isotopic variation than elements with only a single oxidation state and always bound to the same atom. This is the case of Si, which is not active in redox reactions in nature and is always bound to oxygen in a tetrahedral coordination bond (Wiederhold, 2015).
The range of Si isotope variations at the Earth's surface is restricted compared to other elements such as C, H, O, N and is well documented (**Fig. 1.19**). The lightest Si isotopic composition on Earth is that of silcretes ($\delta^{30}Si$ = -5.7‰) and the heaviest is that of rice grains ($\delta^{30}Si$ = +6.1‰). The isotopic range in Si has thus a variation of 11.8‰ on the Earth's surface (Opfergelt and Delmelle, 2012). Globally, rivers display

δ^{30}Si values ranging between -0.1 and 3.4 ‰ (e.g., De La Rocha et al, 2000; Ding et al, 2004, 2016, 2017; Alleman et al, 2005; Georg et al, 2006, 2007; Cardinal et al, 2010; Engström et al, 2010; Hughes et al, 2011, 2013; Opfergelt and Delmelle, 2012; Pokrovsky et al, 2013; Frings et al, 2016; Baronas et al, 2020).

The natural variation in Si isotope compositions in natural reservoirs is attributed to three processes: rock forming processes, water-rock interaction, and biological processes (**Fig. 1.19**).

In **rock forming processes**, two types of reactions are responsible for isotopes fractionation: solid-solid (crystal-crystal) and solid-liquid. Magmatic differentiation can cause a small change in the isotopic signature (Savage et al, 2011). A heavier isotopic signature correlates with the silica content and the degree of silicates polymerization magma degassing does not appear to produce isotope fractionation (Savage et al, 2012).

The **interactions between rock and water** release H_4SiO_4, which, depending on the environmental conditions (e.g., temperature, concentrations, pH), can precipitate to form secondary minerals (clays, oxy-hydroxides and inorganic silica). During precipitation, the light isotopes of Si are preferentially incorporated in clay minerals (δ^{30}Si = -2.95 to -0.16‰, Douthitt, 1982; Bern et al, 2010; Cornelis et al, 2010; Opfergelt and Delmelle, 2012). As a result, soil solutions have generally heavier δ^{30}Si values than the silicate parent material (Ziegler et al, 2005). The complete dissolution of minerals takes place without isotopic fractionation of Si. The mineralogical composition of soils (proportion of primary and secondary silicate minerals) is therefore decisive for the value of δ^{30}Si of the soil. Soils with a low δ^{30}Si value are generally strongly weathered (Ziegler et al, 2005; Opfergelt et al, 2010). In heavily weathered environments, aerial dust input is significant and can influence the soil Si isotopic composition (Bern et al, 2010). In addition, light Si isotopes may be preferentially retained in soil secondary phases following the specific adsorption of monosilicic acid ($H_4SiO_4^0$) by Fe- (e.g., ferrihydrite and goethite) or Al-oxides, increasing the Si isotope signature of the corresponding fluid (Delstanche et al, 2009; Opfergelt et al, 2009;

Oelze et al, 2015). Few studies have been carried out to date on the Si isotope composition of thermal waters, but the reported Si isotope values range from -0.7 to 1.7‰ (Douthitt, 1982; Ding et al, 1996, 2017; Opfergelt et al, 2011, 2013; Geilert et al, 2014; Wang et al, 2019; Chen et al, 2020). Silicification associated with thermal waters (-0.1‰ to -0.4‰) leads to the preferential incorporation of light Si isotopes into the precipitates (Geilert et al, 2014; Li et al, 1995).

Biological processes involve the uptake of H_4SiO_4 by living organisms (plants, sponges or diatoms) and the transformation of DSi into BSi results in Si isotope fractionation. Si biomineralisation favors the absorption of light Si isotopes enriching the corresponding fluid in ^{30}Si as proved by diatoms (Cardinal et al, 2007). Furthermore, the dissolution of diatoms promotes the release of light Si isotopes (Demarest et al, 2009). Phytoliths show variable isotope signatures that depend on several factors: their location in the plant (signatures are higher in the upper parts of the plant), the nature and degree of soil alteration (Opfergelt et al, 2008). Plants also preferentially uptake the light isotope of Si as determined in wheat (Ziegler et al, 2005), bananas (Opfergelt et al, 2006), bamboos (Ding et al, 2008) or rice (Ding et al, 2008).

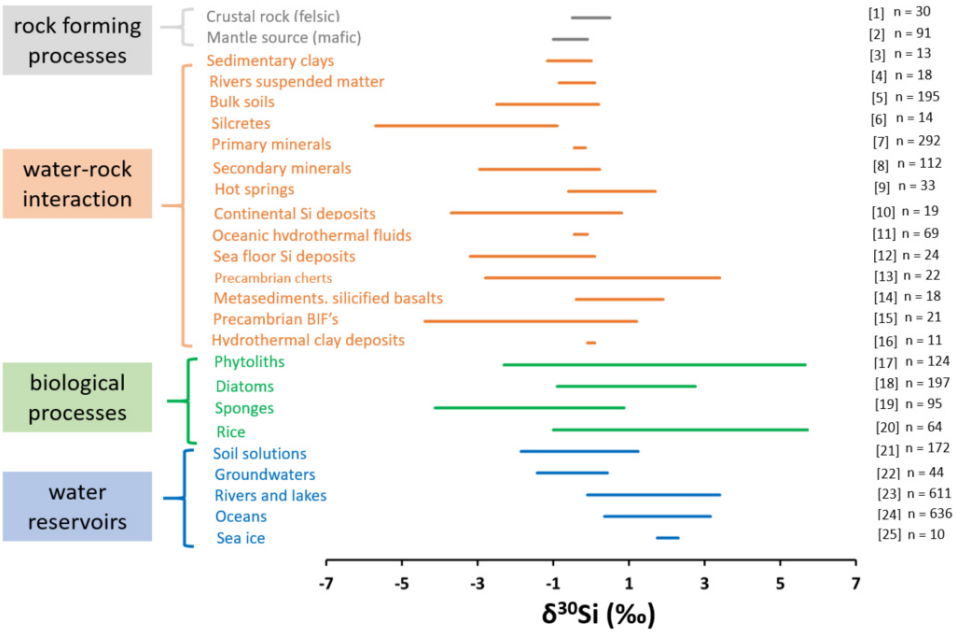

Fig. 1.19: Silicon (Si) isotope (δ^{30}Si; ‰) variations on Earth's surface separated according to affecting processes. [1] Douthitt, 1982; Ding et al, 1996 [2] Douthitt, 1982; Ding et al, 1996; Savage et al, 2011 [3] Ding et al, 1996 [4] Ding et al, 2004 [5] Ziegler et al, 2005; Opfergelt et al, 2012; Roerdink et al, 2015; Frings et al, 2016 [6] Basile-Doelsch et al, 2005 [7] Savage et al, 2011; Frings et al, 2016 [8] Douthitt, 1982; Ziegler et al, 2005; Georg et al, 2009; Bern et al, 2010; Cornelis et al, 2010; Opfergelt et al, 2010; Steinhoefel et al, 2011; Frings et al, 2016 [9] Douthitt, 1982; Ding et al, 1996, 2017; Opfergelt et al, 2011, 2013; Geilert, 2014; Wang et al, 2019; Chen et al, 2020 [10] Douthitt, 1982; Ding et al, 1996 [11] De La Rocha et al, 2000 [12] Douthitt, 1982; Ding et al, 1996 [13] André et al, 2006; van den Boorn et al, 2006; Robert and Chaussidon, 2006 [14] André et al, 2006; Abraham et al, 2011 [15] Ding et al, 1996; André et al, 2006 [16] Ding et al, 1996 [17] Douthitt, 1982; Ziegler et al, 2005; Ding et al, 2008; Engström et al, 2008; Hodson et al, 2008; Sun et al, 2008; Opfergelt et al, 2006, 2008, 2010; Bern et al, 2010; Cornelis et al, 2010;

Frings et al, 2016 [18] De La Rocha et al, 1997; Alleman et al, 2005; Cardinal et al, 2007; Fripiat et al, 2011 [19] Douthitt, 1982; De La Rocha, 2003; Ding et al, 2005; Wille et al, 2010; Hendry et al, 2010 [20] Ding et al, 2005 [21] Ziegler et al, 2005; Fring et al, 2016 [22] Georg et al, 2007, 2009; Frings et al, 2016 [23] De La Rocha et al, 2000; Ding et al, 2004, 2016, 2017; Allemand et al, 2005; Georg et al, 2006, 2007; Cardinal et al, 2010; Engström et al, 2010; Hughes et al, 2011, 2013; Opfergelt and Delmelle, 2012; Pokrovsky et al, 2013; Frings et al, 2016 ; Baronas et al, 2020 [24] Varela et al, 2004; Cardinal et al, 2005; Reynold et al, 2006; De la Rocha et al, 2011; Delvigne et al, 2014; Frings et al, 2016 [25] Fripiat et al, 2011. n = total number of data.

1.5.3 The growing interest for silicon geochemical tracers to study chemical weathering in a volcanic context

The interest of the scientific community for **chemical weathering in volcanic areas** increased at the end of the 1990's when it was demonstrated that volcanic rocks contribute significantly to the global flux of solutes to the ocean and to the atmospheric CO_2 consumption associated to silicate weathering (e.g., Louvat and Allègre, 1997; Gaillardet et al, 1999; Dessert et al, 2003; Dupré et al, 2003). The pioneering studies were based on the elemental concentrations in river waters. With the developments in mass spectrometry, the use of **isotopic tracers** to understand the processes involved in **chemical weathering fluxes** increases significantly after 2000 (**Fig. 1.20**). More specifically, the scientific community's interest to use silicon isotopes in the context of weathering in volcanic areas increased in the 2000s with MC-ICP-MS development allowing the detection of smaller Si isotope variations (precision ~ 0.18‰ in wet plasma; De La Rocha, 2002 and < 0.1‰ in dry plasma; Cardinal et al, 2003). The interest for the use of the Ge/Si ratio to study chemical weathering processes in volcanic regions increased at the same period, since the pioneer paper of Kurtz et al (2002).

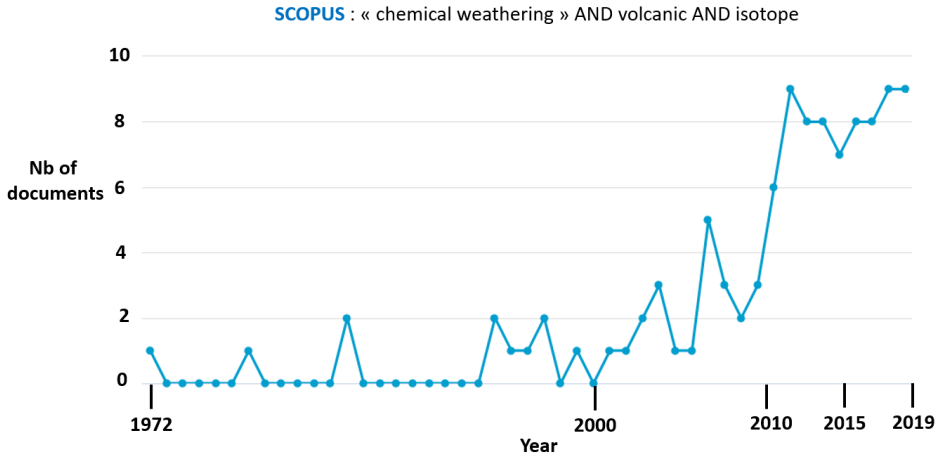

Fig. 1.20: Total number of scientific publications (Nb of documents) from 1972 to the present relative to the isotopes use on chemical weathering studies in volcanic context.

1.6 General objectives and thesis outline

The aim of this PhD thesis is to improve the understanding of the factors controlling weathering fluxes in rivers draining hydrothermally-active volcanic regions. We investigate the contributing sources and processes to rivers using a multi-proxy approach combining riverine element concentrations and geochemical compositions (Ge/Si ratio and Si isotopes). This PhD thesis involves the **analytical development** of a method to purify silicon from **anion-rich** waters (thermal springs and river waters affected by hydrothermal discharges) in order to determine their **Si isotope** composition (*Part II*).

Three specific **research questions** (Q) have been identified and define our research objectives:

Q1. What controls the variability of Ge/Si ratio and $\delta^{30}Si$ in thermal springs from the main generic types of thermal waters?

Q2. Can Ge/Si ratio and $\delta^{30}Si$ in rivers be used as good indicators of weathering processes in volcanic terranes featuring hydrothermal manifestations?

Q3. What is the influence of seasonal change in runoff on the relative hydrothermal and weathering contributions to rivers draining hydrothermally-active volcanic regions?

The overall structure of the PhD thesis is divided in four parts, and **Figure 1.21** schematically presents the outline of the PhD thesis.

Part I: *General overview*. This section provides a general background on the research topic, i.e., on magma-related hydrothermal systems, chemical weathering, the factors influencing chemical weathering fluxes in hydrothermally-active volcanic regions, the global biogeochemical silicon cycle, and the geochemical tracers Ge/Si ratios and Si isotopes.

Part II: *Materials and Methods*. This section presents the samples and the methodology used in the PhD thesis for water elemental analyses (liquid

chromatography, ICP-OES and ICP-MS) and Si isotope analysis (MC-ICP-MS), including the analytical developments performed for Ge concentration measurement by ICP-MS and the purification of Si for MC-ICP-MS measurement.

Part III: *Data chapters (Ch1, Ch2, Ch3, Ch4, Ch5)*[1]. This section discusses the results obtained. The data chapters successively investigate (**Q1**) the controls on the Ge/Si ratio and δ^{30}Si variability in **thermal springs** from the main generic types of thermal waters (*Ch1,* with thermal springs from six hydrothermally-active volcanic regions), (**Q2**) whether the Ge/Si ratio and δ^{30}Si in rivers can act as good indicators of **weathering processes** in volcanic terranes featuring **hydrothermal** manifestations, for a river draining a hyper acid hydrothermal environment (*Ch2*, Kawah Ijen volcano, Indonesia), and for rivers draining both extinct and active hydrothermal manifestations (*Ch3,* Basse-Terre Island, Guadeloupe), and (**Q3**) whether the Ge/Si ratio and δ^{30}Si in rivers can capture the **influence of seasonal change in runoff** on the relative hydrothermal and weathering contributions to rivers, upon snowmelt (*Ch4*, Yellowstone Plateau Volcanic Field, USA), and between the dry and the rain season (*Ch5,* Aso caldera, Japan).

Part IV: *Contribution of the study*. This section serves to conclude the thesis by summarizing the contribution of the study to our understanding of controls on weathering fluxes from hydrothermally-active volcanic regions.

Appendix 1. This section presents preliminary data obtained to contribute to assess the impact of Si-accumulating crops harvest on Si fluxes exported from volcanic islands at two spatial scales (Aso caldera, Japan and Asembagus plain, Indonesia).

[1] The data chapters are presented as a succession of manuscripts that can be read independently, involving some redundancies between the method section of the chapters.

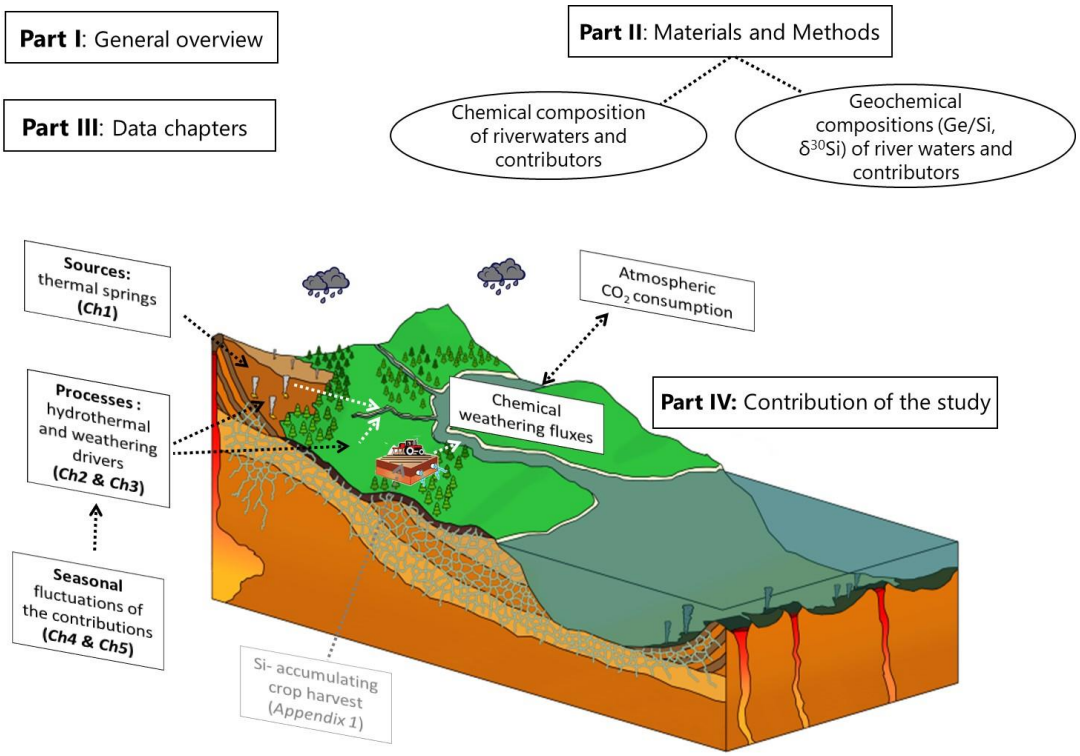

Fig. 1.21: Schematic presentation of the thesis outline. The data chapters are presented in **Part III** (*Ch1*, *Ch2*, *Ch3*, *Ch4*, *Ch5*).

1.7 References

Abraham, K., Opfergelt, S., Fripiat, F., Cavagna, A-J., de Jong, J., Foley, S.F., André, L., Cardinal, D., 2008. δ^{30}Si and δ^{29}Si determinations on USGS BHVO-1 and BHVO-2 reference materials with a new configuration on a Nu Plasma Multi-Collector ICP-MS. Geostand. Geoanal. Res. 32(2), 193-202.

Abraham, K., Hofmann, A., Foley, S.F., Cardinal, D., Harris, C., Barth, M., André, L., 2011. Coupled silicon-oxygen isotope fractionation traces Archaean silicification. Earth Planet. Sci. Lett. 301, 222-230.

Alexander, G.B., Heston, W.M., Iler, R.K., 1954. The solubility of amorphous silica in water. J. Phys. Chem. 58, 453–455.

Alleman, L.Y., Cardinal, D., Cocquyt, C., Plisnier, P.-D., Descy, J.P., Kimirei, I., Sinyinza, D., André, L., 2005. Silicon isotopic fractionation in Lake Tanganyika and its main tributaries. J. Great Lakes Res. 31, 509–519.

Ameijeiras-Mariño, Y., Opfergelt, S., Derry, L.A., Robinet, J., Govers, G., Minella, J.P., Delmelle, P., 2018. Ge/Si ratios point to increased contribution from deeper mineral weathering to streams after forest conversion to cropland. Appl. Geochem. 96, 24–34.

Anders, A.M., Sletten, R.S., Derry, L.A., Hallet, B., 2003. Germanium/silicon ratios in the Copper River Basin, Alaska: weathering and partitioning in periglacial versus glacial environments. J. Geophys. Res. 108, F1, 6005.

Anderson, S. P., Drever, J. I., Humphrey, N. F., 1997. Chemical weathering in glacial environments. Geology, 25, 399–402.

Anderson, S.P., Blum, J., Brantley, S.L., Chadwick, O., Chorover, J., Derry, L.A., Drever, J.I.,
Hering, J.G., Kirchner, J.W., Kump, L.R., Richter, D., White, A.E., 2004. Proposed initiative would study Earth's weathering engine. Eos, Transactions American Geophysical Union 85, 265-269.

André, L., Cardinal, D., Alleman, L.Y., Moorbath, S., 2006. Silicon isotopes in 3.8 Ga west Greenland rocks as clues to the Eoarchaen supracrustal Si cycle. Earth Planet. Sci. Lett. 245, 162-173.

Antonelli, C., Eyrolle, F., Rolland, B., Provansal, M., Sabatier, F., 2008. Suspended sediment and 137Cs fluxes during the exceptional December 2003 flood in the Rhone River, southeast France. Geomorphology 95, 350-360.

Arnórsson, S., 1975. Application of the Silica Geothermometer in Low-Temperature Hydrothermal Ares in Iceland. American Journal of Science edition. 275,7.

Arnórsson, S., 1983. Chemical Equilibrian in Icelandic Geothermal Systems. Geothermics 12, 119-128.

Arnòrsson, S., 1987. Germanium in Icelandic geothermal systems. Geochim. Cosmochim. Ac. 48, 2489-2502.

Arnórsson, S., Stefánsson, A., Bjarnason, J.Ö., 2007. Fluid-fluid interactions in geothermal systems. Reviews in Mineralogy and Geochemistry. 65, 259-312.

Barão, L., Clymans, W., Vandevenne, F., Meire, P., Conley, D.J., Struyf, E., 2014. Pedogenic and biogenic alkaline-extracted silicon distributions along a temperate land-use gradient. Eur. J. Soil Sci. 65, 693-705.

Bareille, G., Labracherie, M., Bertrand, P., Laberyie, L., Lavaux, G., Dignan, M., 1998. Glacial - interglacial changes in the accumulation rates of major biogenic components in Southern Indian Ocean sediments. J. Marine Syst. 17, 527-539.

Baronas, J.J., Torres, M.A., West, A.J., Rouxel, O., Georg, B., Bouchez, J., Gaillardet, J., Hammond, D.E., 2018. Earth Planet. Sci. 503, 194-215.

Baronas, J.J, West, A.J., Burton, K.W., Hammond, D.E., Opfergelt, S., Pogge von Strandmann, P.A.E., James, R.H., Rouxel, O.J., 2020. Ge and Si isotopes behaviour during intense tropical weathering. Global Biogeochem. Cy. doi:10.1029/2019gb006522.

Bartoli, F., Wilding, L. P, 1980. Dissolution of biogenic opal as a function of its physical and chemical properties. Soil. Sci. Soc. Am. J. 44, 873–878.

Basile-Doelsch, I. , Meunier, J.D. , Parron, C. , 2005. Another continental pool in the terrestrial sil icon cycle. Nature 433, 399-402.

Beckwith, R. S., Reeve, R., 1963. Studies on soluble silica in soils. I. The sorption of silicic acid by soils and minerals, Aust. J. Soil Res. 1, 157–168.

Belt, T., 1874. The naturalist in Nicaragua. University of Chicago Press. 326.

Bern, C., Brzezinski, M., Beucher, C., Ziegler, K., Chadwick, O., 2010. Weathering, dust, and biocycling effects on soil silicon isotope ratios. Geochim. Cosmochim. Acta 74, 876–889.

Berner, R.A., Lasaga, A.C., Garrels, R.M., 1983. The carbonate-silicate geochemical cycle and its effect on atmospheric carbon dioxide over the past 100 million years. Am. J. Sci. 283, 641-683.

Berner, R.A., 1995. Chemical weathering and its effect on the atmospheric CO_2 and climate. In White, A.F. and Branthley, S.L., editors. Chemical weathering rates of silicate minerals. Mineralogy society of America. Review of Mineralogy. 565-583.

Bernstein, L.R., 1985. Germanium geochemistry and mineralogy. Geochim. Cosmochim. Ac. 49, 2409–2422.

Beusen, A. H. W., Bouwman, A. F., Dürr, H. H., Dekkers, A. L. M., Hartmann, J., 2009. Global patterns of dissolved silica export to the coastal zone: results from a spatially explicit global model. Global Biogeochem. Cy. 23.

Blake, W.H., Walsh, R.P.D., Barnsley, M.J., Palmer, G., Dyrynda, P., James, J.G., 2003. Heavy metal concentrations during storm events in a rehabilitated catchment. Hydrol. Process. 17, 1923–1939.

Blecker, S.W., King, S.L., Derry, L.A., Chadwick, O.A., Ippolito, J.A., Kelly, E.F., 2007. The ratio of germanium to silicon in plant phytoliths: quantification of biological discrimination under controlled experimental conditions. Biogeochemistry 6, 189–199.

Boeglin, J.L., Probst, J.L., 1998. Physical and chemical weathering rates and CO_2 consumption in a tropical lateritic environment: the upper Niger basin. Chem. Geol. 148, 137-156.

Bogie, I., Lawless, J., Rychagov, S., Belousov, V., 2005. Magmatic-related hydrothermal systems: classification of the types of geothermal systems and their ore mineralization. Proceedings of Geoconference in Russia, Kuril.

Bouwman, A.F., Bierkens, M.F.P, Griffioen, J., Hefting, M.M., Middelburg, J.J., Middelkoop, H., Slomp, C.P., 2013. Nutrient dynamics, transfer and retention along the aquatic continuum from land to ocean: towards integration of ecological and biogeochemical models. Biogeosciences 10, 1-22.

Bowes, M. J., House, W. A., Hodgkinson, R. A. 2003. Phosphorus dynamics along a river continuum, Sci. Total Environ., 313, 199–212.

Burt, T. P., Worrall, F., Howden, N. J. K., Anderson, M. G., 2015. Shifts in discharge-concentration relationships as a small catchment recover from severe drought, Hydrol. Process., 29, 498– 507.

Cardinal, D., Alleman, L.Y., De Jong, J., Ziegler, K., André, L., 2003. Isotopic composition of silicon measured by multicollector plasma source mass spectrometry in dry plasma mode. J. Anal. Atom. Spectrom. 18, 213–218.

Cardinal, D., Alleman, L.Y., Dehairs, F., Savoye, N., Trull, T.W., André, L., 2005. Relevance of silicon isotopes to Si-nutrient utilization and Si-source assessment in Antartic waters. Glob. Biogeochem. Cycles 19, GB2007.

Cardinal, D., Savoye, N., Trull, T.W., Dehairs, F., Kopczynska, E.E., Fripiat, F., Tison, J.L., André, L., 2007. Silicon isotopes in spring Southern Ocean diatoms: large zonal changes despite homogeneity among size frations. Mar. Chem. 106, 46-52.

Cardinal, D., Gaillardet, J., Hugues, H., Opfergelt, S., André, L., 2010. Contrasting silicon isotope signatures in rivers from the Congo basin and the specific behaviour of organic-rich waters, Geophys. Res. Lett. 37, L12403.

Carey, J.C., Fulweiler, R.W., 2012. The terrestrial silica pump. pLoS One 7, e52932.

Carignan, J., Cardinal, D., Eisenhauer, A., Galy, A., Rehkamper, M., Wombacher, F., Vigier, N., 2004. A reflection on Mg, Cd, Ca, Li and Si isotopic measurements and related reference materials. Geostand. Geoanal. Res. 28, 139–148.

Carlson, L., Schwertmann, U., 1981. Natural ferrihydrites in surface deposits from Finland and their association with silica. Geochim. Cosmochim. Ac. 45, 421-429.

Chadwick, O.A., Gavenda, R.T., Kelly, E.F., Ziegler, K., Olson, C.G., Elliott, W.C., Hendricks, D.M., 2003. The impact of climate on the biogeochemical functioning of volcanic soils. Chem. Geol. 202, 195-223.

Chamberlin, TC., 1899. An attempt to frame a working hypothesis on the cause of glacial on an atmospheric basis. Geology 7, 545-584.

Chen, X-Y., Chafetz, H.S., Lapen, T.J., 2020. Silicon isotope variations in hydrothermal systems at Yellowstone National Park, Wyoming, USA. Geochim. Cosmochim. Ac. 283, 184-200.

Colmet-Daage, F., 1969. Cartes des sols des Antilles: Guadeloupe volcanique et Martinique au 1/20 000, ORSTOM Antilles.

Conley, D.J., 2002. Terrestrial ecosystems and the global biogeochemical silica cycle. Global Biogeochem. Cy. 16, 1–68.

Conley, D.J., Malone, T.C., 1992. The annual cycle of dissolved silicate in Chesapeake Bay: implications for the production and fat of phytoplankton biomass. Mar. Ecol. Prog. Ser. 81, 121-128.

Cornelis, J.-T., Delvaux, B., Cardinal, D., André, L., Ranger, J., Opfergelt, S., 2010. Tracing mechanisms controlling the release of dissolved silicon in forest soil solutions using Si isotopes and Ge/Si ratios. Geochim. Cosmochim. Ac. 74, 3913–3924.

Cornelis, J-T., Delvaux, B., Georg, R.B., Lucas, Y., Ranger, J., Opfergelt, S., 2011. Tracing the origin of dissolved silicon transferred from various soil-plant systems towards rivers: a review. Biogeosciences 8, 89-112.

Criaud, A., Fouillac, C., 1986. Study of CO_2-rich thermomineral waters from the Central French Massif: Behaviour of some trace-metals, arsenic, antimony and germanium. Geochim. Cosmochim. Ac. Ed.

Datnoff, L., Snyder, G.H., Korndöfer, G.H., 2001. Silicon in Agriculture, Studies in Plant science. 8, 393.

De La Rocha, C.L., Brzezinski, A., DeNiro, M.J., 1996. Purification, recovery and laser-driven fluorination of silicon from dissolved and particulate silica for the measurement of natural stable isotope abundances. Anal. Chem. 68, 3746-3750.

De La Rocha, C.L., Brzezinski, M.A., DeNiro, M.J., 1997. Fractionation of silicon isotopes by marine diatoms during biogenic silica formation. Geochim. Cosmochim. Acta 61, 5051-5056.

De La Rocha, C.L., Brzezinski, M.A., DeNiro, M.J., 2000. A first look at the distribution of the stable isotopes of silicon in natural waters. Geochim Cosmochim. Ac. 64, 2467–2477.

De La Rocha, C.L., 2002. Measurement of silicon stable isotope abundances via multicollector inductively coupled plasma mass spectrometry MC-ICP-MS. Geochem. Geophys. Geosyst. 3, 1–8.

De La Rocha, C.L., 2003. Silicon isotope fractionation by marine sponges and the reconstruction of the silicon isotope composition of ancient deep water. Geology 31, 423–426.

De La Rocha, C.L., 2006. The biological pump. Oceans Mar. Geochem. 6, 83-112.

De La Rocha, C.L., Bescont, P., Croguennoc, A., Ponzevera, E., 2011. The silicon isotopic composition of surface waters in the Atlantic

and Indian sectors of the Southern Ocean. Geochim. Cosmochim. Acta 75, 5283-5295.

Delmelle, P., Bernard, A., 1994. Geochemistry, mineralogy, and chemical modelling of the acid crater lake of Kawah Ijen volcano, Indonesia. Geochim. Cosmochim. Acta 58, 2445-2460.

Delmelle, P., Opfergelt, S., Cornelis, J.T., Ping, C.L, 2015. Volcanic soils, The Encyclopedia of Volcanoes, 2nd Edition, Academic Press, 1253-1264.

Delstanche, S., Opfergelt, S., Cardinal, D., Elsass, F., André, L., Delvaux, B., 2009. Silicon isotopic fractionation during adsorption of aqueous monosilic acid onto iron oxide. Geochim. Cosmochim. Ac. 73, 923–934.

Delvigne, C., Opfergelt, S., Cardinal, D., Delvaux, B., André, L. 2009. Distinct silicon and germanium pathways in the soil-plant system: Evidence from banana and horsetail. J. Geophys. Res. 114, G02013.

Delvigne, C., Opfergelt, S., Cardinal, D., Hofmann, A., Luc, A., 2014. Desilication in Archean weathering processes traced by silicon isotopes and Ge/Si ratios. Chem. Geol. 420, 139-147.

Demarest, M.S., Brzezinski, M.A., Beucher, C.P., 2009. Fractionation of silicon isotopes during biogenic silica dissolution. Geochim. Cosmochim. Acta 73, 5572–5583.

Derry, L.A., Kurtz, A.C., Ziegler, K., Chadwick, O.A., 2005. Biological control of terrestrial silica cycling and export fluxes to watersheds. Lett. Nature 433, 728–731.

Desplanques, V., Cary, L., Mouret, J.C., Trolard, F., Bourrie, G., Grauby, O., Meunier, J.C., 2006. Silicon transfers in a rice field in Camargue (France), J. Geochem. Explor. 88, 190-193.

Dessert, C., Dupré, B., Francois, L.M., Schott, J., Gaillardet, J., Chakrapani, G., Bajpai, S., 2001. Erosion of Deccan Traps determined by river geochemistry: impact on the global climate and the Sr-87/Sr-86 ratio of seawater. Earth. Planet. Sc. Lett. 188, 459-474.

Dessert, C., Dupré, B., Gaillardet, J., Francois, L.M., Allegre, C.J., 2003. Basalt weathering laws and the impact of basalt weathering on the global carbon cycle. Chem. Geol. 202, 257-273.

Dessert, C., Gaillardet, J., Dupré, B., Schott, J., Pokrovsky, O.S., 2009. Fluxes of high- versus low-temperature water-rock interactions in aerial volcanic areas: Example from the Kamchatka Peninsula, Russia. Geochim. Cosmochim. Ac. 73, 148–169.

Dessert, C., Lajeunesse, E., Lloret, E., Clergue, C., Crispi, O., Gorge, C., Quidelheur, X., 2015. Controls on chemical weathering on a mountainous volcanic tropical island : Guadeloupe (French West Indies). Geochim. Cosmochim. Ac. 171, 216-237.

Dessert, C., Clergue, C., Rousteau, A., Crispi, O., Benedetti, M.F., 2020. Atmospheric contribution to cations cycling in highly weathered catchment, Guadeloupe (Lesser Antilles). Chem. Geol. 531, 119354.

Detienne, M., 2016. Unravelling the role of hydrothermal alteration in volcanic flank and sector collapses using combined mineralogical, experimental, and numerical modelling studies. PhD thesis, UCLouvain.

Dietzel, M., 2000. Dissolution of silicates and the stability of polysilicic acid. Geochim. Cosmochim. Ac. 64, 3275–3281.

Ding, T. P., Jiang, S., Wan, D., Li, Y., Li, J., Song, H., Liu, Z., Yao, X., 1996. Silicon Isotope Geochemistry. Geological Publishing House edition.

Ding, T.P., 2004. Analytical methods for silicon isotope determinations. Handbook of Stable Isotope Analytical Techniques, Volume I, Elsevier B.V., 523–39.

Ding, T.P., Ma, G.R., Shui, M.X., Wan, D.F., Li, R.H., 2005. Silicon isotope study on rice plants from the Zhejiang province, China. Chem. Geol. 218, 41 -50.

Ding, T.P., Zhou, J.X., Wan, D.F., Chen, Z.Y., Wang, C.Y., Zhang, F., 2008. Silicon isotope fractionation in bamboo and its significance to the biogeochemical cycle of silicon. Geochim. Cosmochim. Ac. 72: 1381-1395.

Ding, T.P., Gao, J., Tian, S., Wang, H., Li, M., Wang, C., Luo, X., Han, D., 2016. Chemical and isotopic characteristics of the water and suspended particulate materials in the Yellow river and their geological and environmental implications. Acta Geol. Sin. (Engl. Ed.), 90(1), 285–351.

Ding, T.P., Jiang, S., Li, Y., Gao, J., Hu, B., 2017. Geochemistry of silicon isotopes. De Gruyter.

Dixon, J.L., Heimsath, A.M., Amundson, R., 2009. The critical role of climate and saprolite weathering in landscape evolution. Earth. Surf. Proc. Land. 34, 1507- 1521.

Dixon, J.L., Hartshorn, A.S., Heimsath, A.M., DiBiase, R.A., Whipple, K.X., 2012. Chemical weathering response to tectonic forcing: A

soils perspective from the San Gabriel Mountains, California. Earth. Planet. Sc. Lett. 323, 40-49.

Douthitt, C.B., 1982. The geochemistry of the stable isotopes of silicon. Geochim. Cosmochim. Acta 46, 1449–1458.

Dress, L.R., Wilding, L.P., Smeck, N.E., Senkayi, A.L., 1989. Silica in soils: quartz and disordered silica polymorphs. Soil Sci. Soc. Am. J. 913-974.

Dupré, B., Dessert, C., Oliva, P., Godderis, Y., Viers, J., Francois, L., Millot, R., Gaillardet, J., 2003. Rivers, chemical weathering and Earth's climate. Comptes Rendus Geoscience 335, 1141-1160.

Dürr, H.H., Meybeck, M., Hartmann, J., Laruelle, G.G., Roubeix, V., 2011. Global spatial distribution of natural riverine silica inputs to the coastal zone. Biogeosciences 8, 597-620.

Edmond, JM., Huh, Y., 1997. Chemical weathering yields from basement and organic terrains in hot and cold climates. In: Ruddiman WF, editor. Tectonic uplift and climate change. New York: Springer. 329-351.

Egge, J.K., Asknes, D.L., 1992. Silicate as regulating nutrient in phytoplankton competition. Mar. Ecol. Prog. Ser. 83, 281-289.

Ellis, A.J., Mahon, W.A.J., 1967. Natural hydrothermal systems and experimental hot water/rock interactions (Part II). Geochim. Cosmochim. Ac. 31, 519-538.

Ellwood, M.J., Kelly, M., Maher, W.A., De Deckker, P., 2006. Germanium incorporation into sponge spicules: development of a proxy for reconstructing inorganic germanium and silicon concentrations in seawater. Earth Planet. Sci. Lett. 243, 749-759.

Engström, E., Rodushkin, I., Öhlander, B., Ingri, J., Baxter, D.C., 2008. Silicon isotopic composition of boreal forest vegetation in Nothern Sweden. Chem. Geol. 257, 250-259.

Engström, E., Rodushkin, I., Ingri, J., Baxter, D., Ecke, F., Österlund, H., Öhlander, B., 2010. Temporal isotopic variations of dissolved silicon in a pristine boreal river. Chem. Geol. 271, 142–152.

Epstein, E., 1999. Silicon. Annu. Rev. Plant. Phys. 50, 641-664.

Escoube, R., Rouxel, O.J., Edwards, K., Glazer, B., Donard, O.F.X., 2015. Coupled Ge/Si and Ge isotope ratios as geochemical tracers of seafloor hydrothermal systems: Case studies at Loihi Seamount and East Pacific Rise 9°50'N. Geochim. Cosmochim. Ac. 167, 93-112.

Evans, M.J., Derry, L.A., 2002. Quartz control of high germanium/silicon ratios in geothermal waters. Geology 30, 1019–1022.

Evans, M.J., Johnes, P., 2004. Physico-chemical controls on phosphorus cycling in two lowland streams. Part 1 – the water column, Sci. Total Environ., 329, 145-163.

Exley, C., 1998. Silicon in life: a bioinorganic solution to bioorganic essentiality. J. Inorg. Biochem. 69, 139-144.

FAOSTAT, 2015. http://faostat3.fao.org/

Faure, F., Mensing, T.M., 2005. Isotopes: Principles and Applications. Wiley and sons, Inc., Hoboken, New Jersey.

Filippelli, G.M., Carnahan, J.W., Derry, L.A., Kurtz, A., 2000. Terrestrial paleorecords of Ge/Si cycling derived from lake diatoms. Chem. Geol. 168, 9-26.

Fraysse, F., Pokrovsky, O. S., Schott, J., Meunier, J.-D., 2006. Surface properties, solubility and dissolution kinetics of bamboo phytoliths. Geochim. Cosmochim. Ac. 70, 1939–1951.

Freire, P., Andrade C., Coutinho, R., Cruz, J., 2013. Fluvial geochemistry in Sao Miguel Island (Azores, Portugal): Source and fluxes of inorganic solutes in an active volcanic environment. The science of the total environment. 454-455, 154-169.

Fries, D.M., James, R.H., Dessert, C., Bouchez, J., Beaumais, A., Pearce, C.R., 2019. The response of Li and Mg isotopes to raine vents in a highly-weathered catchment. Chem. Geol. 519, 68-82.

Frings, P.J., De La Rocha, C.L., Struyf, E., van Pelt, D., Schoelynck, J., Hudson, M.M., Gondwe, M.J., Wolski, P., Mosimane, K., Gray, W., Schaller, J., Conley, D.J., 2014. Tracing silicon cycling in the Okavango Delta, a sub-tropical cycle of the Antartic zone in the Kerguelen area (KEOPS). Mar. Chem. 123, 11-22.

Frings, P.J., Clymans, W., Fontorbe, G., De La Rocha, C.L., Conley, D.J., 2016. The continental Si cycle and its impact on the ocean Si isotope budget. Chem. Geol. 425, 12-36.

Fripiat, F., Cavagna A-J., Savoye, N., Dehairs, F., Andre, L., Cardinal, D., 2011. Isotopic constraints on the Si-biogeochemical cycle of the Antarctic Zone in the Kerguelen area (KEOPS). Mar. Chem. 123, 11-22.

Froelich, P.N., Mortlock, R.A., Shemesh, A., 1989. Inorganic germanium and silica in the Indian Ocean: biological fractionation during $(Ge/Si)_{OPAL}$ formation. Global Biogeochemical Cycles 3, 1.

Froelich, P.N., Blanc, V., Mortlock, R.A., Chillrud, S.N., 1992. River fluxes of dissolved silica to the ocean were higher during glacials: Ge/Si in diatoms, rivers and oceans. Paleoceanography 7, 739-767.

Fulweiler, R. W., Nixon, S. W., 2005. Terrestrial vegetation and the seasonal cycle of dissolved silica in a Southern New England coastal river. Biogeochemistry 74, 115–130.

Gaillardet, J., Dupre, B., Allegre, C.J., 1995. A global geochemical mass budget applied to the Congo Basin – Erosion rates and continental-crust composition. Geochim. Cosmochim. Ac. 59, 3469-3485.

Gaillardet, J., Dupré, B., Allègre, C.J., Negrel, P., 1997. Chemical and physical denudation in the Amazon River basin. Chemical Geology 142, 141-173.

Gaillardet, J., Dupré, B., Louvat, P., Allègre, C.J., 1999. Global silicate weathering and CO_2 consumption rates deduced from the chemistry of large rivers. Chem. Geol. 159, 3-30.

Gaillardet, J., Dupré, B., Allègre, C.J., 1999. Geochemistry of large river suspended sediments:
Silicate weathering or recycling tracer. Geochim. Cosmochim. Ac. 63, 4037-4051.

Gaillardet, J., Rad, S., Rivé, K., Louvat, P., Gorge, C., Allègre, C-J., Lajeunesse, E., 2011. Orography-driven chemical denudation in the Lesser Antilles: Evidence for a new feed-back mechanism stabilizing atmospheric CO_2. Am. J. Sci. 311, 851-894.

Galvez, M.E., Gaillardet, J., 2012. Historical constraints on the origins of the carbon cycle concept. CR Geoscience 344, 11-12.

Garrels, R.M., Mackenzie, F.T., 1971. Evolution of sedimentary rocks. Norton, New York.

Geilert, S., Vroon, P.Z., Keller, N., Gudbrandsson, S., Stefànsson, A., Van Bergen, M.J., 2014. Silicon isotope fractionation during silica precipitation from hot springs waters, Geophys. Res. Abstract EGU 2014: EGU2014-7951.

Georg, R.B., Reynolds, B.C., Frank, M., Halliday, A.N., 2006. New sample preparation techniques for the determination of Si isotopic compositions using MC-ICP-MS. Chem. Geol. 235, 95–104.

Georg, R.B., Reynolds, B.C., Frank, M., Halliday, A.N., 2006. Mechanisms controlling the silicon isotopic compositions of river waters. Earth Planet. Sci. Lett. 249, 290–306.

Georg, R. B., Reynolds, B.C., West, A.J., Burton, K.W., Halliday, A.N., 2007. Silicon isotope variations accompanying basalt weathering in Iceland, Earth Planet. Sci. Lett. 261, 476-490.

Georg, R.B., West, A.J., Basu, A.R., Halliday, A.N., 2009. Silicon fluxes and isotope composition of direct groundwater discharge into the Bay of Bengal and the effect on the global ocean silicon isotope budget. Earth Planet. Sci. Lett. 283, 67–74.

Giggenbach, W.F., 1988. Geothermal solute equilibria. Derivation of Na-K-Mg-Ca geoindicators. Geochim. Cosmochim. Ac. 52, 2749-2765.

Gislason, S. R., Oelkers, E. H., Eiriksdottir, E. S., Kardjilov, M. I., Gisladottir, G., Sigfusson, B., Snorrason, A., Elefsen, S., Hardardottir, J., Torssander, P., Oskarsson, N., 2009. Direct evidence of the feedback between climate and weathering, Earth Planet. Sc. Lett. 277, 213–222.

Gislason, S. R., Oelkers, E. H., 2011. Silicate rock weathering and the global carbon cycle, in Harmon, R. S., and Parker, A., editors, Frontiers in Geochemistry: Contribution of Geochemistry to the Study of the Earth: Chichester, United Kingdom, Wiley-Blackwell, 84–103.

Godfray, H. C. J., Beddington, J. R., Crute, I. R., Haddad, L., Lawrence, D., Muir, J.F., Pretty, J., , Robinson, S., Thomas S.M., Toulmin, C., 2010. Food security: the challenge of feeding 9 billion people. Science 327, 812.

Godsey, S. E., Kirchner, J. W., Clow, D. W., 2009. Concentration-discharge relationships reflect chemostatic characteristics of US catchments. Hydrol. Process. 23, 1844–1864.

Goldsmith, S.T., Carey, A.E., Lyons, W.B., Hicks, D.M., 2008. Geochemical fluxes and weathering of volcanic terrains on high standing islands: Taranaki and Manawatu-Wanganui regions of New Zealand. Geochim. Cosmochim. Ac. 72, 2248-2267.

Goof, F., Janick, C.J., 2000. Geothermal systems. Encyclopedia of volcanoes. 817-834.

Guntzer, F., Keller, C., Meunier, J-D., 2012. Benefits of plant silicon for crops : a review. Agron. Sustain. Dev. 32, 201-213.

Hale, A., 2008. Lava dome growth and evolution with an independently deformable talus. Geophys. J. Int, 174, 391-417.

Han, Y., Huh, Y., Derry, L., 2015. Ge/Si ratios indicating hydrothermal and sulphide weathering input to rivers of the Eastern Tibetan Plateau and Mt. Baekdu. Chem. Geol. 410, 40-52.

Hartmann, J., Moosdorf, N., Dürr, H.H., Harashima, A., Okubo, K., Kempe, S., 2010. Predicting riverine dissolved silica fluxes to coastal zones from a hyperactive region and analysis of their first-order controls. Int. J. Earth. Sci. 99: 207-230.

Hartmann, J., Moosdorf, N., 2011. Chemical weathering rates of silicate-dominated lithological classes and associated liberation rates of phosphorus on the Japanese Archipelago-Implications for global scale analysis. Chem. Geol. 287, 125-157.

Hartmann, J., Moosdorf, N., Lauerwald, R., Hinderer, M., West, A.J., 2014. Global chemical weathering and associated P-release - The role of lithology, temperature and soil properties. Chem. Geol. 363, 145-163.

Hedenquist, J.W., Arribas, A., Gonzales-Urien, E., 2000. Exploration for Epithermal Gold Deposits. SEG Reviews. 13, 245-277.

Hedenquist, J.W., Taran, Y.A., 2013. Modeling the formation of advanced argillic lithocaps: Volcanic vapor condensation above porphyry intrusions. Econ. Geol. 108, 1523-1540.

Hendry, K.R., Leng, M.J, Robinson, L.F., Slone, H.J., Blusztjan, J., Rickaby, R.E.M., Georg, R.B., Halliday, A.N., 2010. Silicon isotopes in Antartic sponges: an interlaboratory comparison. Antartic Science 23, 34-42.

Henriet, C., De Jaeger, N., Dorel, M., Opfergelt, S., Delvaux, B., 2008. The reserve of weatherable primary silicates impacts the accumulation of biogenic silicon in volcanic ash soils. Biogeochemistry 90, 209-223.

Hicks, P.D., Matthews, A.J., Cooker, M.J., 2009. Thermal structure of a gas-permeable lava dome and timescale separation in its response to perturbation. J. Geophys. Res. 114, B7.

Hindshaw, R.S., Teisserenc, R., Le Dantec, T., Tananaev, N., 2019. Seasonal change of geochemical sources and processes in the Yenisei River: A Sr, Mg and Li isotope study. Geochim. Cosmochim. Ac. 255, 222-236.

Hochstein, M.P., Browne, P.R.L., 2015. Surface Manifestations of Geothermal Systems with Volcanic Heat Sources. Encyclopedia of volcanoes, 835-856.

Hodson, M.J., White, P.J., Mead, A., Broadley, M.R., 2005. Phylogenetic variation in the silicon compositions of plants. Ann. Bot-London. 96, 1027-1046.

Hodson, M.J., Parker, A.G., Leng, M.J., Sloane, H.J., 2008. Silicon, oxygen and carbon isotope composition of wheat (Triticum

aestivum L.) phytoliths: implications for palaecology and archaeology. J. Quaternary. Sci. 23, 331-339.
Holland, H.D., 1984. The chemical evolution of the atmosphere and oceans. Princeton series in geochemistry.
Hughes, H.J., Delvigne, C., Korntheuer, M., De Jong, J., André, L., Cardinal, D. 2011. Controlling the mass bias introduced by anionic and organic matrices in silicon isotopic measurements by MC-ICP-MS, J. Anal. Spectrom. 26, 1892-1896.
Hughes, H.J., Sondag, F., Santos, R.V., André, L., Cardinal, D., 2013. The riverine silicon isotopes composition of the Amazon Basin. Geochim. Cosmochim. Acta. 121, 637-651.
Hurwitz, S., Evans, W.C., Lowenstern, J.B., 2010. River solute fluxes reflecting active hydrothermal chemical weathering of the Yellowstone Plateau Volcanic Field, USA. Chem. Geol. 276, 331-343.
Iler, R. K., 1979. The Chemistry of Silica, Wiley-Interscience, New York.
Ingri, J., Widerlund, A., Land, M., 2005. Geochemistry of major elements in a pristine boreal river system; hydrological compartments and flow paths. Aquat. Geochem. 11, 57-88.
Jansen, N., Hartmann, J., Lauerwarld, R., Dürr, H.H., Kempe, S., Loos, S., Middelkoop, H., 2010. Dissolved silica mobilization in the conterminous USA. Chem. Geol. 270, 90-109.
Jennerjahn, T. C., Knoppers, B. A., de Souza, W. F. L., Brunskill, G. J., Ivan, E., Silva, L., Adi, S., 2006. Factors controlling dissolved silica in tropical rivers. Human perturbations and impacts on aquatic systems. SCOPE 66, 29–52.
Jones, L.H.P., Handreck, K.A., 1965. Studies of silica in the oat plant. Plant Soil. 23, 79-96.
Jones, M.T., Hembury, D.J., Palmer, M.R., Tonge, B., Darling, W.G., Loughlin, S.C., 2011. The weathering and element fluxes from active volcanoes to the oceans: a Montserrat case study. Bull. Volc. 73, 207–222.
Kaiser, S., Wagner, S., Moschner, C., Funke, C., Wiche, O., 2020. Accumulation of germanium (Ge) in plant tissues of grasses is not solely driven by its incorporation in phytoliths. Biogeochemistry. 148, 49-68.
Karathanasis, A. D., 2002. Mineral equilibria in environmental soil systems. Soil Sci. Soc. Am. J. 109–151.
Kump, L.R., Brantley, S.L., Arthur, M.A., 2000. Chemical, weathering, atmospheric CO_2, and

climate. Annu. Rev. Earth Planet. Sci. 28, 611-667.
Kurtz, A.C., Derry, L.A., Chadwick, O.A., 2002. Germanium-silicon fractionation in the weathering environment. Geochim. Cosmochim. Ac. 66, 1525–1537.
Kurtz, A. C., Derry, L. A., 2004. Tracing silicate weathering and terrestrial silica cycling with Ge/Si ratios, in: Proceedings of 11th International Symposium on Water Rock Interaction, Leiden, Netherlands. 833–836.
Kurtz, A.C., Lugolobi, F., Salvucci, G., 2011. Germanium-silicon as a flow path tracer: application to the Rio Icacos watershed. Water Resour. Res. 47.
Lauerwald, R., Hartmann, J., Moosdorf, N., Dürr, H.H., Keme, S., 2013. Retention of dissolved silica within the fluvial system of the conterminous USA. Biogeochemistry. 112, 637-659.
Lewing, J., Reimann, B.E.F., 1969. Silicon and plant growth. Annu. Rev. Plant. Phys. 20, 289-304.
Li, Y., Ding, T.P., Wan, D., 1995. Experimental study of silicon isotope dynamic fractionation and its application in geology. Chin. J. Geochem. 14, 212–219.
Lloret, E., Dessert, C., Gaillardet, J., Albéric, P., Crispi, O., Chaduteau, C., Benedetti, M., 2011. Comparison of dissolved inorganic and organic carbon yields and fluxes in the watersheds of tropical volcanic islands, examples from Guadeloupe (French West Indies). Chem. Geol. 280, 65–78.
Louvat, P., 1997. Étude géochimique de l'érosion fluviale d'îles volcaniques à l'aide des bilans
d'éléments majeurs et traces. Institut de Physique du Globe de Paris, p. 322.
Louvat, P., Allègre, C.J., 1997. Present denudation rates on the island of Reunion determined by river geochemistry: Basalt weathering and mass budget between chemical and mechanical erosions. Geochim. Cosmochim. Ac 61, 3645-3669.
Louvat, P., Gislason, S.R., Allègre, C.J., 2008. Chemical and mechanical erosion rates in Iceland as deduced from river dissolved and solid material. Am. J. Sci. 308, 679-726.
Louvat, P., Gaillardet, J., Paris, G., Dessert, C., 2011. Boron isotope ratios of surface waters in Guadeloupe, Lesser Antilles. Appl. Geochem. 26, S76–S79.

Ludwig, W., Amiotte-Suchet, P., Probst, J.L., 1999. Enhanced chemical weathering of rocks during the last glacial maximum: a sink for atmospheric CO_2. Chem. Geol. 159, 147-161.

Lugolobi, F., Kurtz, A.C., Derry, L.A., 2010. Germanium–Silicon fractionation in a tropical, granitic weathering environment. Geochim. Cosmochim. Ac. 74, 1294–1308.

Ma, J.F., Goto, S., […], Ichii, M., 2001. Role of root hairs and lateral roots in silicon uptake. American Society of Plant Biologists. 127, 1773-1780.

Ma, J.F., Takahashi, E., 2002. Soil, fertilizer and plant silicon research in Japan. Elsevier, Amsterdam.

Marschner, H., 1995. Mineral nutrition of higher plants. Annals of Botany. 4, 527-528.

Martin, J.M., Meybeck, M., 1979. Elemental Masse-balance of material carried by major world rivers. Mar. Chem. 7, 173-206.

Martin, H., 1986. Effect of steeper Archean geothermal gradient on geochemistry of subduction-zone magmas. Geology 14, 753– 756.

Massey, F.P., Ennos, A.R., Hartley, S.E., 2006. Silica in grasses as a defence against insect herbivores: contracting effects on folivores and a phloem feeder. J. Anim. Ecol. 75, 595-603.

Matichenkov, V.V., Bocharnikova, E.A., 2001. The relationship between silicon and soil physical and chemical properties. Studies in plant science. Elsevier. 209-219.

Milliman, J.D., Meade, R.H., 1983. World-Wide Delivery of River Sediment to the Oceans. J. Geol. 91, 1-21.

McKeague, J.A., Cline, M.G., 1963. Silica in soil solutions: II. The adsorption of monosilic acid by soil and by other substances. Can. J. Soil. Sci. 43, 83-86.

McKeague, J.A., Cline, M.G., 1963. Silica in soils. Advances in Agronomy 15, 339-396.

Melcher, F., 2003. The Otavi Mountain Land in Namibia: Tsumeb, Germanium and Snowball Earth. Mitteilungen Österreichischer Geologischer Gesellschaft. 148, 413-435.

Mellin, D.R., Watkinson, D.H., Fox, P.E., Cameron, R.S., 1990. Carbonatization and propylitic alteration of fragmental basaltic rocks, Quesnel River gold deposit, Central British Columbia. Mineralium Deposita. 25, 115-124.

Merrill, GP., 1906. A Treatise on Rocks, Rock weathering and Soil. New York, MacMillan.

Meybeck, M., 1979. Concentrations des eaux fluviales en elements majeurs et apports en solution aux oceans, Rev. Geol. Dyn. Geogr., 21, 215–246.

Meybeck, M., 1987. Global chemical-weathering of surficial rocks estimated from river dissolved loads. Am. J. Sci. 287, 401-428.

Milliman, J.D., Boyle, E., 1975. Biological uptake of dissolved silica in the Amazon River estuary. Science 189, 995-997.

Milliman, J.D., Syvitiski, P.M., 1991. Geomorphic Tectonic Control of Sediment Discharge to Ocean – The Importance of Small Mountainous Rivers. J. Geol. 100, 525-544.

Mitani, N., Ma, J. F., 2005. Uptake system of silicon in different plant species, J. Exp. Bot., 56, 1255–1261.

Monger, H. C., Kelly, E. F., 2002. Silica minerals, in: Soil Mineralogy with environmntal applications. Soil Sci. Soc. Am. J. 611-636.

Moosdorf, N., Hartmann, J., Lauerwald, R., 2011. Changes in dissolved silica mobilization into river systems draining North America until the period 2081-2100 J. Geochem. Explor. 110, 31-39.

Mortlock, R.A., Froelich, P.N., 1987. Continental weathering of germanium: Ge/Si in the global river discharge, Geochim. Cosmochim. Acta, 51, 2075-2082.

Mortlock, R.A., Froelich, P.N., Feely, R.A., Massoth, G.J., Butterfield, D.A., Lupton, J.E., 1993. Silica and Germanium in pacific ocean hydrothermal vents and plumes, Earth Planet. Sc. Lett. 119: 365-378.

Murnane, R.J., Stallard, R.F., 1990. Germanium and silicon in rivers of the Orinoco drainage basin. Nature 44, 749–752.

Negrel, P., 1992. Utilisation des isotopes du strontium, des alcalins et alcalino-terreux pour la
détermination des bilans des éléments chimiques dans les fleuves : apports atmosphériques, altération des roches. Université Paris VII.

Negrel, P., Allègre, C.J., Dupré, B., Lewin, E., 1993. Erosion sources determined by inversion of major and trace-element ratios and strontrium isotopic ratios in river waters – the Congo Basin case. Earth. Planet. Sc. Lett. 120, 59-76.

Oelze, M., von Blanckenburg , F., Bouchez, J., Vollprecht, D., Dietzel, M., 2015. The effect of Al on Si isotope fractionation investigated by silica precipitation. Chem. Geol. 397, 94-105.

Opfergelt, S., Cardinal, D., Henriet, C., Draye, X., André, L., Delvaux, B., 2006. Silicon isotopic fractionation by banana (Musa spp.)

grown in a continuous nutrient flow device. Plant Soil 285, 333–345.

Opfergelt, S., Delvaux, B., André, L., Cardinal, D., 2008. Plant silicon isotopic signature might reflect soil weathering degree. Biogeochemistry 91, 163–175.

Opfergelt, S., de Bournonville, G., Cardinal, D., André, L., Delstanche, S., Delvaux, B., 2009. Impact of soil weathering degree on silicon isotopic fractionation during adsorption onto iron oxides in basaltic ash soils, Cameroon. Geochim. Cosmochim. Acta 73, 7226–7240.

Opfergelt, S., Cardinal, D., André, L., Delvigne, C., Bremond, L., Delvaux, B., 2010. Variations of $d^{30}Si$ and Ge/Si with weathering and biogenic input in tropical basaltic ash soils under monoculture. Geochim. Cosmochim. Acta 74, 225–240.

Opfergelt, S., Eiriksdottir, E.S., Burton, K.W., Einarsson, A., Siebert, C., Gislason, S.R., Halliday, A.N., 2011. Quantifying the impact of freshwater diatom productivity on silicon isotopes and silicon fluxes: Lake Myvatn, Iceland. Earth Planet. Sci. Lett. 305, 73–82.

Opfergelt, S., Delmelle, P., 2012. Silicon isotopes and continental weathering processes: Assessing controls on Si transfer to the ocean. Comptes Rendus Geosci. 344, 723–738.

Opfergelt, S., Georg, R.B., Delvaux, B., Cabidoche, Y.M., Burton, K.W., Halliday, A.N., 2012. Silicon isotopes and the tracing of desilication in volcanic soil weathering sequences, Guadeloupe. Chem. Geol. 326-327, 113-122.

Opfergelt, S., Burton, K.W., Pogge von Strandmann, P.A.E., Gislason, S.R., Halliday, A.N., 2013. Riverine silicon isotope variations in glaciated basaltic terrains: implications for the Si delivery to the ocean over glacial-interglacial intervals. Earth. Planet. Sc. Lett. 369-370, 211-219.

Oskarsson, B.V., Riishuus, M.S., Arnalds, O., 2012. Climate-dependent chemical weathering of volcanic soils in Iceland. Geoderma 189, 635-651.

Pilon-Smits, E.A.H., Quinn, C.F., Tapken, W., Malagoli, M., Schiavon, M., 2009. Physiological functions of beneficial elements. Curr. Opin. Plant Biol. 12, 267-274.

Piperno, D.R., 2001. Phytoliths. In: Smol, J.P., Birks, H.J.B., Last, W.M. (Eds.). Tracking Environmental Change Using Lake Sediment Terrestrial, Algal and Siliceous Indicators. 3, 235-252.

Pirajno, F., 2009. Hydrothermal Processes and Mineral Systems. The Netherlands, Springer, 1249 p.

Pokrovsky, G.S., Schott, J., 1998. Experimental study of the complexation of silicon and germanium with aqueous organic species: implications for germanium and silicon transport and Ge/Si ratios in natural waters. Geochim. Cosmochim. Ac. 62, 3413-3428.

Pokrovsky, G. S., Schott, J., Garges, F., Hazemann, J. L., 2003. Iron (III)-silica interactions in aqueous solution: Insights from X-ray absorption fine structure spectroscopy. Geochim. Cosmochim. Ac. 67, 3559–3573.

Pokrovsky, O. S., Reynolds, B. C., Prokushkin, A. S., Schott, J., Viers, J., 2013. Silicon isotope variations in Central Siberian rivers during basalt weathering in permafrostdominated larch forests. Chem. Geol., 355, 103–116.

Rad, S., Louvat, P., Gorge, C., Gaillardet, J., Allègre, C.J., 2006. River dissolved and solid loads in the Lesser Antilles: new insight into basalt weathering processes. J. Geoch. Explor. 88, 308-312.

Rad, S., 2007. Mécanisme et temps d'érosion dans les îles volcaniques : apport des séries de l'uranium, des éléments majeurs et traces, exemple des Antilles et de la Réunion. Institut de Physique du Globe de Paris, p. 195.

Rad, S., Allègre, C.J., Louvat, P., 2007. Hidden erosion on volcanic islands. Earth. Planet. Sc. Lett. 262, 109-124.

Rad, S., Cerdan, O., Rive, K., Grandjean, G., 2011. Age of river basins in Guadeloupe impacting chemical weathering rates and land use. Appl. Geochem. 26, S123-S126.

Rad, S., Rive, K., Vittecoq, B., Cerdan, O., Allegre, C.J., 2013. Chemical weathering and erosion rates in the Lesser Antilles: An overview in Guadeloupe, Martinique and Dominica. J. S. Am. Earth. Sci. 45, 331-344.

Rahman, S., Aller, R.C., Cochran, J.K., 2017. The missing silica sink : revisiting the marine sedimentary Si cycle using cosmogenic ^{32}Si. Global biogeochem. Cycles. 31, 1559-1578.

Ramankutty, N., Evan, A.T., Monfreda, C., Foley, J.A., 2000. Farming the planet: 1. Geographic distribution of global agricultural lands in the year 2000. Global biogeochem. Cycles. 22, GB1003.

Raven, J. A., 1983. The transport and function of silicon in plants, Biol. Rev. 58, 179–207.

Raymo, M.E., Ruddiman, W.F., Froelich, P.N., 1988. Influence of late Cenozoic mountain building on ocean geochemical cycles. Geology 16, 649-653.

Reed, M. H., 1982. Calculation of multicomponent chemical equilibria and reaction processes in systems involving minerals, gases and an aqueous phase. Geochim. Cosmochim. Ac. 46, 513-528.

Reed, M.H., 1997. Hydrothermal alteration and its relationship to ore fluid composition. Geochemistry of Hydrothermal Ore Deposits. 3rd ed. John Wiley and Sons.

Reynolds, B.C., Frank, M., Halliday, A.N., 2006. Silicon isotope fractionation during nutrient utilization in the North Pacific. Earth. Planet. Sci. Lett. 244, 431-443.

Reynolds, B.C., Aggarwal, J., André, L., Baxter, D., Beucher, C., Brzezinski, M.A., Engström, E., Georg, B., Land, M., Leng, M.J., Opfergelt, S., Rodushkin, I., Sloane, H.J., Van den Boorn, S.H.J.M., Vroon, P.Z., Cardinal, D., 2007. An inter-laboratory comparison of Si isotope reference materials. J. Anal. Atom. Spectrom. 22, 561-568.

Richmond, K.E., Sussman, M., 2003. Got Silicon? The Non-Essential Beneficial Plant Nutrient. Current Opinion in Plant Biology. 6, 268-272.

Riotte, J., Ruiz, L., Audry, S., Sekhar, M., Mohan Kumar, M.S., Siva Soumya, B., Braun, J.J., 2014. Impact of Vegetation and Decennial Rainfall Fluctuations on the Weathering Fluxes Exported from a Dry Tropical Forest (Mule Hole). Procedia Earth and Planetary Science 10, 34-37.

Rivé, K., Gaillardet, J., Agrinier, P., Rad, S., 2013. Carbon isotopes in the rivers from the Lesser Antilles: origin of the carbonic acid consumed by weathering reactions in the Lesser Antilles. Earth Surf. Proc. Land. 38, 1020–1035.

Robert, F., Chaussidon, M., 2006. A palaeotemperature curve for the Precambrian oceans based on silicon isotopes in cherts. Nature, 443, 969-972.

Roerdink, D.L., van den Boorn, S.H., Geilert, S., Vroon, P.Z., van Bergen, M.J., 2015. Experimental constraints on kinetic and equilibrium silicon isotopes fractionation during the formation of non-biogenic chert deposits. Chem. Geol. 402, 40-51.

Rogers, N., Hawkesworth, C., 2015. Composition of Magmas. Encyclopedia of volcanoes. The Netherlands: Elsevier.

Rybach, L., Muffler, L.J.P., 1981. Geothermal systems: Principes and cases histories. Eds. Wiley, New York.

Rye, R. O., 2005. A review of the stable-isotope geochemistry of sulfate minerals in selected igneous environments and related hydrothermal systems. Chem. Geol. 215, 5-36.

Sangster, A., Parry, D., 1981. Ultrastructure of silica deposits in higher plants. Silicon and siliceous structures in biological systems. 383-407.

Sangster, A.G., Hodson, M.J., 1986. Silica in higher plants. Silicon Biogeohemistry, 90-107.

Sauer, D., Saccone, L., Conley, D. J., Herrmann, L., Sommer, M., 2006. Review of methodologies for extracting plant available and amorphous Si from soils and aquatic sediments. Biogeochemistry, 80, 89–108.

Savage, P.S., Georg, R.B., Williams, H.M., Burton, K.W., Halliday, A.N., 2011. Silicon isotope fractionation during magma differentiation. Geochim. Cosmochim. Ac. 75, 6124-6139.

Savage, P.S., Georg, R.B., Williams, H.M., Turner, S., Halliday, A.N., Chappell, B.W., 2012. The silicon isotope composition of granites. Geochim. Cosmochim. Acta 92, 184–202.

Savant, N.K., Korndörfer, G.H., Datnoff, L.E., Snyderc, G.H., 1999. Silicon nutrition and sugarcane production: A review. J. Plant. Nut. 22, 1853-1903.

Schafer, J., Blanc, G., Lapaquellerie, Y., Maillet, N., Maneux,E., Etcheber, H., 2002. A ten-year-observation of the Gironde tributary fluvial system: fluxes of suspended matter, particulate organic carbon and cadmium. Mar. Chem. 79, 229–242.

Schopka, H. H., Derry, L. A., Arcilla, C. A., 2011. Chemical weathering, river geochemistry and atmospheric carbon fluxes from volcanic and ultramafic regions on Luzon Island, the Philippines. Geochim. Cosmochim. Ac. 75, 978–1002.

Schulze, D.G., 2002. An introduction to soil mineralogy. Soil Sci. Soc. Am. J. 1-35.

Scribner, A.M., Kurtz, A.C., Chadwick, O.A., 2006. Germanium sequestration by soil: targeting the roles of secondary clays and Fe-oxyhydroxides, Earth and Plan. Sc. 243, 760-770.

Seyfferth, A.L., Kocar, B.D., Lee, J.A., Fendorf, S., 2013. Seasonal dynamics of dissolved silicon in a rice cropping system after straw incorporation. Geochim. Cosmochim. Ac. 123, 120–133.

Siebert, C., Ross, A., McManus, J., 2006. Germanium isotope measurements of high-temperature geothermal fluids using double-spike hydride generation MC-ICP-MS. Geochim. Cosmochim. Acta 70, 3986-3995.

Siever, R., Woodford, N., 1973. Sorption of silica by clay minerals. Geochim. Cosmochim. Ac. 37, 1851–1880.

Sillitoe, R.H., 1985. Ore-related breccias in volcanoplutonic arcs. Econ. Geol. 80, 1467-1514.

Smetacek, V., 1999. Diatoms and the ocean carbon cycle. Protist. 150, 25–32.

Smithson, F., 1956. Plant opal in soil. Nature 178, 107.

Sommer, M., Kaczorek, D., Kuzyakov, Y., Breuer, J., 2006. Silicon pools and fluxes in soils and landscapes – a review. J. Plant Nutr. Soil Sci. 169, 310-329.

Steinhoefel, G., Horn, I., von Blanckenburg, F., 2009. Micro-scale tracing of Fe and Si isotope signatures in banded iron formation using femtosecond laser ablation. Geochim. Cosmochim. Acta 73, 5343–5360.

Stefánsson, A., Gislason, S.R., 2001. Chemical weathering of basalts, southwest Iceland: effect of rock crystallinity and secondary minerals on chemical fluxes to ocean. J. Am. Sci. 301, 513-556.

Stimac, J., Goff, F., Goff, C., 2015. Intrusion-Related Geothermal Systems. The Encyclopedia of Volcanoes. Amsterdam, 799-822.

Street-Perrott, F. A., Barker, P., 2008. Biogenic silica: a neglected component of the coupled global continental biogeochemical cycles of carbon and silicon. Earth Surf. Proc. Land 33, 1436–1457.

Struyf, E., Smis, A., Van Damme, S., Meire, P., Conley, D., 2009. The global biogeochemical silicon cycle. SILICON. 1, 207-213.

Stumm, W., Morgan, J.J., 1996. Aquatic chemistry – chemical equilibria and rates in natural waters. John Winley and Sons.

Summerfield, M. A., Hulton, N. J., 1994. Natural controls of fluvial denudation rates in major world drainage basins. J. Geophys. Res. 99, 13871–13883.

Sun, L., Wu, L.H., Ding, T.P., Tian, S.H., 2008. Silicon isotope fractionation in rice plants, an experimental study on rice growth under hydroponic conditions. Plant and Soil 304, 291-300.

Sutton, J., Ellwood, M.J., Maher, W.A., Croot, P.L., 2010. Oceanic distribution of inorganic germanium relative to silicon:

Germanium discrimination by diatoms. Global Biochem. Cy. 24. GB2017.

Symonds, R., Gerlach, T., Reed, M., 2001. Magmatic gas scrubbing: implications for volcano monitoring. J. Volcan. Geoth. Res. 108, 303-341.

Takahashi, K., Ma, J.F., Miyake, Y., 1990. The possibility of silicon as an essential element for higher plants. Comment Agricultural and Food Chemistry. 2, 99-122.

Tréguer, P., Nelson, D.M., Van Bennekom, A.J., De Master, D.J., Leynaert, A., Quéguiner, B., 1995. The silica balance in the world ocean: a reestimate. Sciences. 268, 375-379.

Tréguer, P., De La Rocha, C.L., 2013. The world ocean silica cycle. Annu. Rev. Mater. Sci. 5, 477-501.

Turner, R. E., Rabalais, N. N., Justic, D., Dortch, Q., 2003. Global patterns of dissolved N, P and Si in large rivers. Biogeochemistry. 64, 297–317.

van den Boorn, S.H.J.M., Vroon, P.Z., van Belle, C.J., van der Wagt, B., Schwieters, J., van Bergen, M.J., 2006. Determination of the silicon isotope ratios in silicate materials by high resolution MC-ICP-MS using a sodium hydroxide sample digestion method. J. Anal. Atom. Spectrom. 21, 734–742.

van den Boorn, S.H.J.M., Vroon P.Z., van Bergen, M. J., 2009. Sulfur-induced offset in MC-ICP-MS silicon-isotope measurements. Anal. At. Spectrom. 24, 1111–1114.

Varela, D.E., Pride, C.J., Brzezinski, M.A., 2004. Biological fractionation of silicon isotopes in Southern Ocean surface waters. Global Biogeochem. Cycles 18: GB1047, doi.

Walker, J.C.G., Hays, P.B., Kasting, J.F., 1981. A negative feedback mechanism for the long-term stabilization of Earth's surface-temperature. J. Geophys. Res. Ocean Atmos. 86, 9776-9782.

Wang, W., Wei, H-Z., Jiang, S-Y., Tan, H-B., Eastoa, C.J., Williams-Jones, A.E., Hohl, S.V., Wu, H-P., 2019. The origin of rare alkali metals in geothermal fluids of southern Tibet, China: A silicon isotope perspective. Scientific reports 9, 7918.

Waterkeyn, L., Bienfait, A., Peeters, A., 1982. Callose et silice épidermiques : rapports avec la transpiration cuticulaire. Cellule 73, 267-287.

Weiss, A., De La Rocha, C.L., Amann, T., Hartmann, J., 2015. Silicon isotope composition of dissolved silica in surface waters of the Elbe Estuary and its tidal marshes. Biogeochemistry 1-19.

Wiederhold, J. G., 2015. Metal Stable Isotope Signatures as Tracers in Environmental Geochemistry. Env. Sci. Tec. 49, 2606–24.

Wille, M., Sutton, J., Ellwood, M.J., Sambridge, M., Maher, W., Eggins, S., Kelly, M., 2010. Silicon isotopic fractionation in marine sponges: a new model for understanding silicon isotopic variations in sponges. Earth Planet. Sci. Lett. 292, 281-289.

Wheat, C., McManus, J., 2008. Germanium in mid-ocean ridge flank hydrothermal fluids. Geochem. 9: Q03025.

White, D.E., 1957. Magmatic, connate, and metamorphic waters: Geol. Soc. America Bull. 68, 1659-1682.

White, A.F., Blum, A.E., 1995. Effects of climate on chemical weathering in watersheds. Geochim. Cosmochim. Ac. 59, 1729-1747.

White, W.M., 2013. Geochemistry. John Wiley & Sons.

Yoshida, T., 1975. Pesticides residues in upland rice soils. Major Research in Upland Rice. International Rice Research Institute.

Yool, A., Tyrrell, T., 2003. Role of diatoms in regulating the ocean's silicon cycle. Glob. Biogeochem. Cycles 17.

Ziegler, K., Chadwick, O.A., Brzezinski, M.A., Kelly, E.F., 2005. Natural variations of $d^{30}Si$ ratios during progressive basalt weathering, Hawaiian Islands. Geochim. Cosmochim. Acta 69, 4597–4610.

Part II

MATERIALS AND METHODS

Materials and Methods

The following section presents the study sites, the sampling and the methodology used in the PhD thesis for elemental analyses, Ge concentrations and Si isotope measurements in **water** (e.g., thermal springs, river waters, groundwater, soil solutions, surface runoff) and **rock** samples (e.g., hydrothermally-altered rock). This includes analytical protocols, instruments description, and methodological improvements of Ge concentrations by ICP-MS and Si isotope measurements by MC-ICP-MS.

Each method is described more specifically in the relevant chapters.

2.1. Study sites

The main study sites of the PhD thesis are four hydrothermally-active volcanic regions: three volcanic islands (the basaltic Java Island (Kawah Ijen volcano, Indonesia, *Ch1 and Ch2*), the andesitic Basse-Terre Island (La Soufrière volcano, Guadeloupe, *Ch1 and Ch3)* and the basaltic-rhyolitic Kyūshū Island (Aso volcano, Japan, *Ch1 and Ch5*)) and one continental hotspot (Yellowstone Plateau Volcanic Field (YPVF), United States, *Ch1 and Ch4*). Samples from two additional sites were also used in a smaller extent in *Ch1*: Negros Island (Kanlaon volcano, Philippines) and Kamchatcka (Mutnovsky volcano) (**Fig. 2.1**).

Study sites are described in details in *Ch1* (Negros Island and Kamchatka), *Ch2* (Java Island), *Ch3* (Basse-Terre Island), *Ch4* (YPVF) and *Ch5* (Kyūshū Island).

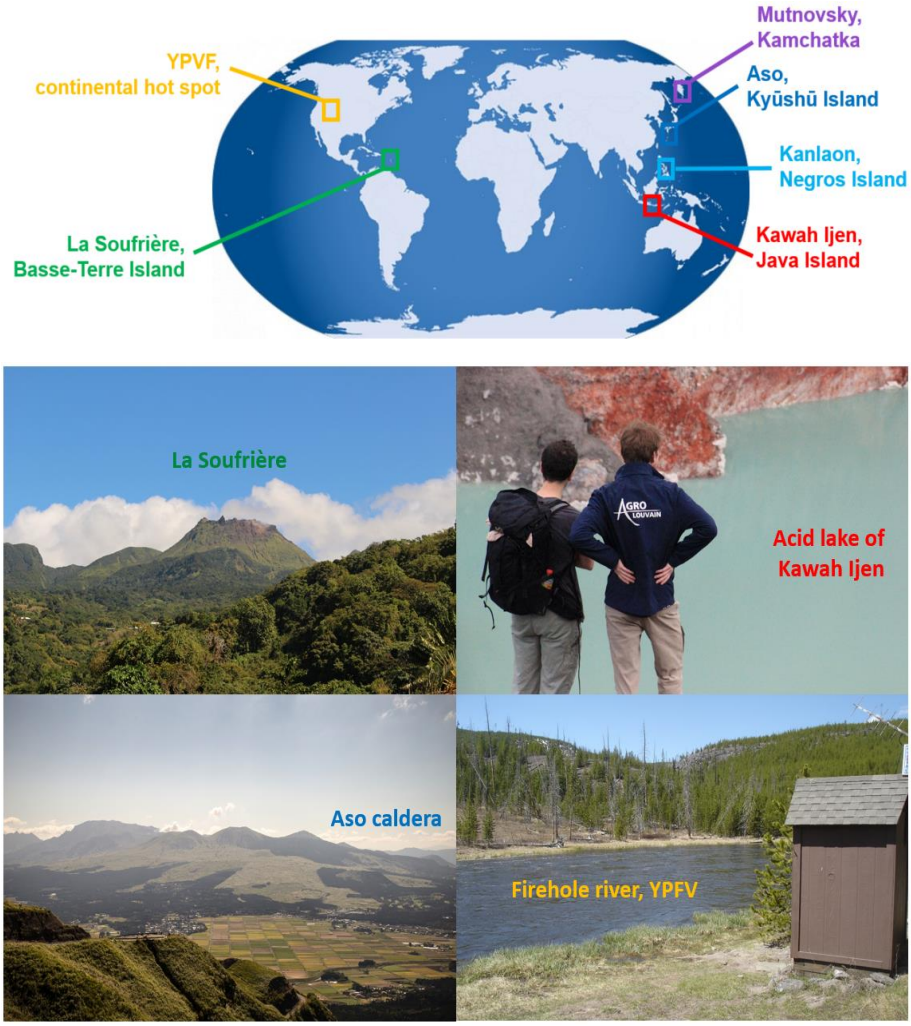

Fig. 2.1: Localisation of the study sites from this PhD thesis on a world map. Pictures on the four main study sites: La Soufrière volcano, Guadeloupe during field mission in January-February 2015 (*Ch3*). Kawah Ijen volcano's acid lake, Java during field mission in January 2017 (*Ch2*). The Aso caldera, Japan (credit: J. Hartmann) in Autumn 2014 (*Ch5*). The Firehole river (Yellowstone Plateau Volcanic Field, YPVF; credit: B. McCleskey) in the summer season (*Ch4*).

The number of samples (thermal springs, river waters, groundwater, soil solutions, surface runoff and hydrothermally-altered rock) studied in the different sites are summarized in **Table 2.1** with n correponding to the total number of samples (some locations were sampled multiple times for time series).

Table 2.1: Summary of the samples from the PhD thesis by study sites (YPVF = Yellowstone Plateau Volcanic Field). The color code refers to the location map in **Fig. 2.1**.

Samples	La Soufrière	Kawah Ijen	YPVF	Aso	Kanlaon	Mutnovsky
	Basse-Terre Island	Java Island	Continental hot spot	Kyūshū Island	Negros Island	Kamchatka
Thermal springs	15 (n=26)	13 (n=13)	8 (n=8)	17 (n=21)	1 (n=2)	2 (n=2)
River waters	22 (n=36)	4 (n=14)	15 (n=33)	30 (n=46)	-	-
Soil solutions	7 (n=7)	4 (n=4)	-	-	-	-
Groundwater	-	-	-	11 (n=28)	-	-
Surface runoff	-	-	-	3 (n=4)	-	-
Hydrothermally-altered rock	1 (n=1)	-	-	-	-	-
	Ch1 , Ch3	*Ch1 , Ch2*	*Ch1 , Ch4*	*Ch1 , Ch5*	*Ch1*	*Ch1*

2.2. Sampling

The samples analysed in this PhD thesis were either (i) collected on the field in January-February 2015 in Basse-Terre Island, Guadeloupe during my master thesis (*Ch1,Ch3*) and in January 2017 in Java Island, Indonesia during my PhD thesis (*Ch1,Ch2*), or (ii) obtained through collaborations as part of the FNRS project FluxHyd with S. Hurwitz from the USGS Yellowstone National Park for the samples from YPVF (*Ch1,Ch4*), with J. Hartmann from the University of Hamburg, Germany for the samples from Japan (*Ch1,Ch5*), with A. Bernard for the samples from the Philippines (*Ch1*), and with E. Maters for the samples from Kamchatka (*Ch1*). The details regarding sampling procedure and water filtration are given in the relevant chapters.

2.3 Water elemental analyses

2.3.1 Majors element concentrations by ICP-OES

The concentrations of major elements such as Ca, Na, Mg, K, Al, Fe and Si in the water samples were determined by inductively-coupled plasma-optical emission spectrometry (ICP-OES; iCAP 6500 Thermo Fisher Scientific) at the Earth and Life Institute – Environmental Sciences of the Université catholique de Louvain (*Ch1-Ch2-Ch3-Ch4-Ch5*).

This **optical emission spectrometry** method has different steps: (i) analyte transport by a peristaltic pump though a nebulizer into a spray chamber and aerosol production, (ii) aerosol production lead into an argon plasma (the forth state of matter, next to the solid, liquid and gaseous state, generated at the end of a quartz torch by a cooled induction coil through which a high frequency alternate current flows), (iii) collision between the argon atom and the electrons ionization, giving rise to a stable plasma (~6000-7000K) and inducing atomization and ionizations of the analyte sample in the desolvation torch, (iv) the analyte reaches a higher "excited" state due to the thermic energy taken up by the electrons and (v) releases light (photons) when the electrons drop back to ground level energy. Each element has its own characteristic emission spectrum that is measured with a spectrometer. The light intensity on the wavelength is measured and is converted into a concentration, via the calibration.

The accuracy on major elements (Ca, Na, Mg, K, Al, Fe, Si) analyses was assessed using the trueness on the river water reference material SLRS-5 (Yeghicheyan et al, 2013) and the analytical precision above the detection limit. The detection limit, the trueness and analytical precision for majors, Al, Fe and Si are given in **Table 2.2**. The blank level was below the detection limit of Ca, Na, Mg, K, Al, Fe and Si in ICP-OES.

Table 2.2: Detection limit (µmol.l^{-1}), trueness (%) and analytical precision (%) of major elements (Ca, Na, Mg, K, Al, Fe, Si) measured by ICP-OES (iCAP 6500).

ICP-OES iCAP 6500	Ca	Na	Mg	K	Al	Fe	Si
Detection limit (µmol.l^{-1})	0.05	0.43	0.21	0.26	0.37	0.18	0.36
Trueness (%)	± 3	± 4	± 1	± 7	± 4	± 2	± 4
Precision (%)	± 0.5	± 0.5	± 0.5	± 0.5	± 0.5	± 0.5	± 0.5

2.3.2 Anions concentrations by ionic chromatography

A subsample was taken for anion analyses *in situ* and measured by ionic chromatography (Dionex ICS2000, column: AG15/AS15) at the Earth and Life Institute – Environmental Sciences of the Université catholique de Louvain (*Ch1-Ch2-Ch3-Ch4-Ch5*). The ionic chromatography is a process that separates ions and polar molecules following their affinity to the ion exchanger. The analyte ions (SO_4^{2-}, Cl^-, NO_3^-, F^-) are retained depending of their ionic interactions with opposite charge of functional groups (R-X) of the stationary phase, such as quaternary aminoethyl.

In a few steps, **ionic chromatography** is summarized as (i) sample introduction with an auto sampler (~5 ml), (ii) sample transport via the mobile phase (buffered aqueous solution) from the loop onto a column that contains some form of stationary material (resin with covalently bonded charged functional groups), (iii) analytes retention on the stationary phase and analytes elution by increasing the concentration of a similarly charged species that will displace the analyte ions from the stationary phase and (iv) analytes detection and quantification.

The accuracy on SO_4^{2-}, Cl^- and NO_3 was assessed using the trueness on the river water certified reference material LGC6025 (UKAS, 2014) and the analytical precision above the detection limit. The detection limit, the trueness and analytical precision for SO_4^{2-}, Cl^-, NO_3^- and F^- are given in **Table 2.3**. The blank level was below the detection limit of SO_4^{2-}, Cl^-, NO_3^- and F^- in Dionex ICS2000.

Table 2.3: Detection limit (µmol.l^{-1}), trueness (%) and analytical precision (%) of species measured by ionic chromatography (Dionex ICS2000).

Dionex ICS2000	SO_4^{2-}	Cl^-	NO_3^-	F^-
Detection limit (µmol.l^{-1})	1.5	3.1	1.6	0.5
Trueness (%)	± 3	± 4	± 4	± 6
Precision (%)	± 2	± 2	± 2	± 2

2.4 Geochemical tracers

In this PhD thesis, we used two geochemical tracers: the Ge/Si ratios and the Si isotopes (*Ch1-Ch2-Ch3-Ch4-Ch5*).

2.4.1 Ge and Si analysis and Ge/Si calculation

2.4.1.1 Inventory of methods used for Ge concentrations measurements

Analytical difficulties to obtain reliable data of Ge is common because Ge concentrations in environmental samples are generally below the limit of detection of many modern analytical methods and suffer from various interferences ($^{56}Fe^{16}O$, $^{57}Fe^{16}O$, $^{58}Fe^{16}O$, ^{74}Se, $^{58}Ni^{16}O$) on its isotopes (^{70}Ge, ^{72}Ge, ^{73}Ge, ^{74}Ge, and ^{76}Ge) with ICP-MS techniques. Until now, the Ge concentration measurement in solution has been mainly performed using the isotope dilution hydride generation by high resolution ICP-MS (HR-ICP-MS) (Mortlock and Froelich, 1996; Hamade et al, 2003; McMahon et al, 2006; Frei and Polat, 2007; Delvigne et al, 2009; Cornelis et al, 2010; Tribovillard et al, 2011). This requires a hydride-generation system, which is not common in laboratories. Alternative techniques exist such as graphite furnace atomic absorption spectrometry (GF-AAS; McMahon et al, 2006), laser ablation ICP-MS (Hamade et al, 2003; Shen et al, 2011; Belissont et al, 2014; Dong et al, 2015) and X-ray fluorescence spectrometry (Frei and Polat, 2007). These techniques are currently close of the Ge detection limit for environmental samples. Preconcentration using a polysulfone membrane filter combined with spectrophotometric measurements are investigated (Soylak and Yigit, 2015) but requires specific materials (Delvigne et al, 2018).

2.4.1.2 Measurement of dissolved Ge concentrations and Ge/Si ratios

The **Ge concentrations** in the water samples and hydrothermally-altered rock were determined by ICP-mass spectrometry (ICP-MS, ICAPQ Thermo Fisher Scientific) using the ^{74}Ge isotope for the measurement (Delvigne et al, 2018). Prior to analysis, the hydrothermal-altered rock was dissolved by alkaline fusion with 99.99% pure NaOH at 720 °C in a silver crucible (Georg et al, 2006).

The Ge measurement by **ICP-mass spectrometry** has several steps: (i) sample dilution in acid matrix (0.5% HNO_3) to reach a TDS (total dissolved solids = total concentration of ionic species present in solution = Na+K+Mg+Ca+SiO_2) value below ~0.2% (2000 mg.l^{-1}), (ii) sample introduction as a liquid using a nebulizer (due to the supersonic expansion of gas to turn the liquid into a fine mist) and spray chamber (that remove any droplets too large to be processed in the plasma), (iii) ions (generated by the argon plasma) separation according their mass-to-charge (m/z), (iv) ions counting on the collector, (v) trace element quantification (counts per second) using a calibration curve from a reference standard (known concentrations of analyte).

Germanium has five different isotopes with variable abundances (**Table 2.4**). The measure is based on the most abundant Ge isotope (74) and Rh (^{103}Rh) is use as internal standard. The KED mode reduces spectral interferences from polyatomic ions due to argon gas but interference with Nd (^{148}Nd) were suspected. We finally use the STANDARD (STD) mode to avoid interference between ^{74}Ge and ^{128}Nd. Accuracy and long-term repeatability of the analyses were assessed by measuring two international riverine standards, namely SLRS-5 ([Ge] = 0.083 ± 0.014 nmol.l^{-1}; n=3) and SLRS-6 ([Ge] = 0.097 ± 0.0069 nmol.l^{-1}; n=3) (Yeghicheyan et al, 2013), and one in-house standard (i.e., the Gallion Blanc (GAB) thermal spring: [Ge] = 23.95 ± 0.096 nmol.l^{-1}; n=14) in each analytical session between July 2017 and June 2018. The detection limit for Ge is 0.04 nmol.l^{-1} and the analytical precision of the measurement is ± 8 % for Ge concentrations < 0.013 nmol.l^{-1} and ± 4 % for Ge concentrations > 0.013 nmol.l^{-1}.

Table 2.4: Germanium stable isotopes and their natural abundance (Yang and Meija, 2010).

Masse number	Nuclide mass	Natural abundance (%)
70	69.92	20.526
72	71.92	27.446
73	72.92	7.760
74	73.92	36.523
76	75.92	7.745

So far, dissolved Ge concentrations have been classically determined by High Resolution ICP-MS (HR-ICP-MS). Therefore, we compared the Ge concentrations in 12 thermal spring and 17 river water samples from Basse-Terre (see *Ch3*) measured by both HR-ICP-MS and ICP-MS (**Table 2.5**). The HR-ICP-MS analyses of Ge (noted Ge*) were performed at the Department of Earth and Atmospheric Sciences, Cornell University, USA, using a Thermo Fisher Scientific-Element2™ Series instrument equipped with a hydride generation system, and applying the isotope dilution technique (Mortlock and Froelich, 1996). The Si concentrations used for calculating the Ge*/Si (HR-ICP-MS) and Ge/Si (ICP-MS) ratios ($\mu mol.mol^{-1}$) were determined by ICP-OES (iCAP 6500 Thermo Fisher Scientific), and the standard deviation of our Ge/Si ratio determinations is 10%. **Figure 2.2** shows a strong correlation (R^2=0.99) between the Ge/Si ratio and Ge*/Si ratio measurements, indicating the validity of our ICP-MS analysis for determining the concentration of Ge in solution.

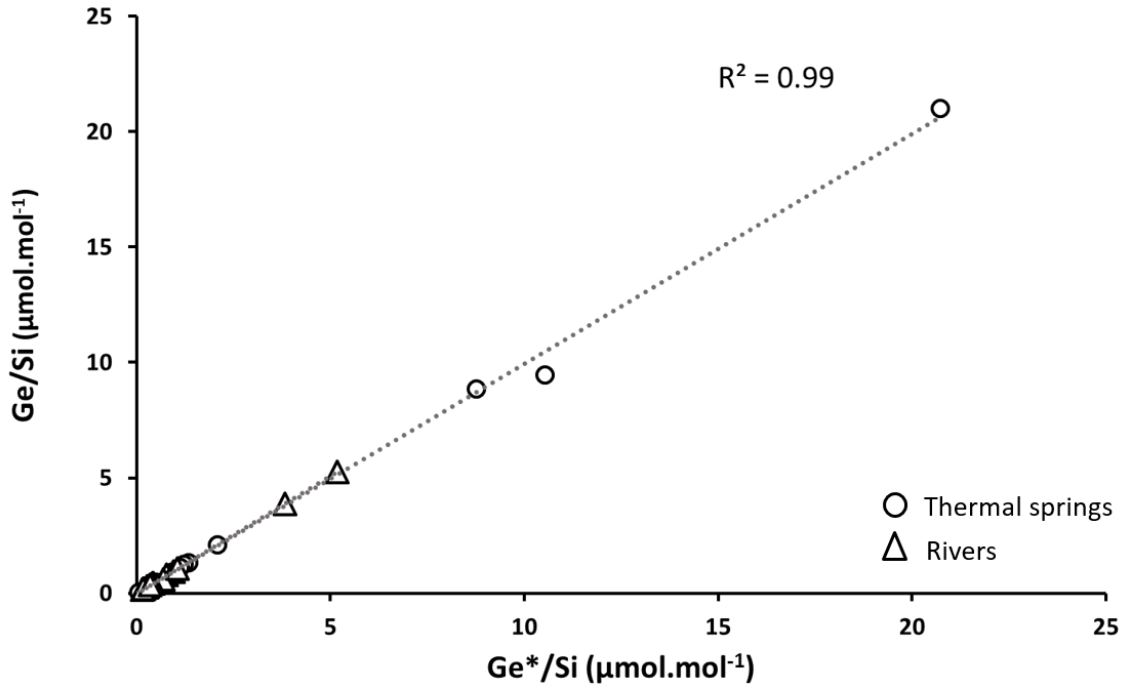

Fig. 2.2: Plot comparing the Ge/Si ratio (µmol.l^{-1}) of 12 thermal springs (n=12) and 17 river waters from Basse-Terre as measured by ICP-MS (Ge/Si) and HR-ICP-MS (Ge*/Si). See text for explanation.

Table 2.5: Germanium concentrations measured by HR-ICP-MS (Ge*), Ge concentrations measured by ICP-MS (Ge), and Ge*/Si and Ge/Si ratios calculated using Si concentrations measured by ICP-OES in 12 thermal springs and 17 river waters from Basse-Terre Island (samples from *Ch3*).

Label	Ge*	Ge*/Si	Ge	Ge/Si
	nmol.l^{-1}	µmol.mol^{-1}	nmol.l^{-1}	µmol.mol^{-1}
Thermal springs				
RM2(1)	1.83	1.33	1.85	1.35
RM3 (2)	3.11	1.21	3.60	1.25
GA(1)	25.25	8.76	25.55	8.86
GAB(1)	27.03	10.53	27.35	9.49
GAF	0.07	0.05	0.08	0.05
PR(1)	0.90	0.43	0.91	0.44
TA(1)	4.94	2.07	5.00	2.10
Sofaïa	0.52	0.92	0.53	0.94
BCM(1)	11.58	20.71	11.72	21.03
CC(1)	1.87	1.11	1.89	1.13
GC(1)	0.76	0.49	0.78	0.50
Dolé	0.53	0.38	0.55	0.39
River waters				
rMoustique Ste-Rose	0.09	0.29	0.09	0.30
rPP	0.10	0.19	0.10	0.19
rCorossol	0.14	0.34	0.14	0.34
rBD1	0.08	0.18	0.08	0.19
rCAE	0.16	0.41	0.16	0.42
rPBD1	0.05	0.14	0.06	0.15
rRM	1.38	0.96	1.39	0.93
rCap1	0.18	0.43	0.18	0.42
rRC1	0.38	0.78	0.39	0.80
rCC	0.22	0.34	0.23	0.35
rRN	0.83	0.68	0.84	0.61
rSt-Louis1	0.15	0.27	0.15	0.28
rRouge1	0.25	0.42	0.26	0.43
rGC	0.53	0.42	0.54	0.43
rGAam	6.72	3.83	6.80	3.88
rGAav	10.10	5.18	10.21	5.25
rGAbb	1.18	1.05	1.19	1.06

2.4.2 Si isotope measurements

2.4.2.1 Methods used for Si isotope measurements

Silicon isotope measurements on terrestrial samples require a high degree of accuracy to be able to detect limited natural Si isotope fractionations. In the 1950s, accuracies were so low that only significant differences in Si isotope signatures in meteorites were detected. In the last few decades, developments have allowed for small Si isotope variations in terrestrial samples to be detected. Silicon stable isotopes have been initially measured by gas source isotope ratio mass spectrometry (IRMS) and secondary ion microprobe mass spectrometry (SIMS) (Ding, 2004; Reynolds, 2011). Today, the inductively coupled plasma multicollector mass spectrometer (MC-ICP-MS) is commonly used for the Si isotope analyses in terrestrial samples given their high accuracy (~0.18‰ in wet plasma, De La Rocha, 2002; <0.1‰ in dry plasma, Cardinal et al, 2003). Since the 1980s, the Si isotope composition of the oceans, soils, rivers, and living organisms is well documented (**section 1.5.2**) but few studies have been carried out on the Si isotope composition of anion-rich thermal waters. A new method has been developed in this PhD thesis to purify Si from an anion matrix. The main steps for sample preparation throughout the different types of samples in the PhD thesis are presented here.

2.4.2.2 Sample preparation

Prior to Si isotope measurements, **samples preparation** includes **preliminary treatments** such as dissolution of solid samples (e.g., hydrothermally-altered rock specimen), and purification of Si from liquid samples (e.g., thermal springs, river waters, groundwater, soil solutions) in a dust clean environment. The Si isotopes analytical development for all sample matrix type (thermal springs, river waters, soil solutions, hydrothermally altered rock specimen) performed in this PhD thesis is shown at **Fig. 2.3**.

The rocks and silica standards and the hydrothermally-altered **rock** specimen were digested with NaOH following the alkaline fusion method developed by Georg et al (2006). A mass of 10 mg of finely crushed sample was weight in a silver crucible. A pellet of NaOH (~200 mg) was added inside the crucible directly in contact with the sample. The sample was next introduced in an oven preheated to 750 °C and left inside to react for 10 minutes. Then, the crucible was quickly dropped inside a Teflon vial containing ~10 ml of ultrapure water and left overnight. The solution was transferred into a previously acid-washed polypropylene bottle after short treatment with ultrasounds to remove the sample from the crucible. Bottles were prewashed with 5% HNO_3 left cold for two days then abundantly rinsed with ultrapure water and dried. The transferred solution was acidified to 1% HNO_3 with suprapure acid and left to equilibrate overnight.

For liquid sample, some pre-treatments were performed before the Si purification from anions and cations: removing dissolved organic matter (if necessary) and adapt the Si concentrations.

Soil solutions were pre-treated before column chemistry to remove **dissolved organic matter** (DOC). Indeed, the presence of DOC may produce mass bias on silicon isotope measurements by MC-ICP-MS due to matrix effect (treatment performed with DOC/Si at or > 0.69; Hughes et al, 2011). We put 5 ml of sample in Teflon vial and we added 200 µl of 0.1% v.v H_2O_2. The Teflon vial was put in a UV-box for one day. Then, the Teflon vial was removed at the end of the day for one hour, we added 0.1 % v.v H_2O_2 and the Teflon vial returned to the UV-box for the night. Finally, samples were acidified (0.2% v.v HNO_3). This was applied in *Ch2*.

The pre-treatment to remove DOC was not performed on thermal springs because of the low pH restricting the microbial activity development (Brock, 1970) and inhibiting complexation reactions by protonation of organics acids (Nordstrom et al, 1979; Herrmann and Baumgartner, 1992). In *Ch3*, the DOC pre-treatment step was not performed on rivers water samples and soil solution samples from Basse-Terre Island. In river waters, the DOC/Si ratio can be considered <0.17 (i.e., below the value for which a treatment is recommended; Hughes et

al, 2011) based on DOC concentrations in rivers sampled at the same location, at the same season and in a comparable flow regime (Lloret, 2010). In soil solutions, the DOC/Si ratio is <0.35 based on DOC concentrations on these samples (Lloret, 2010), i.e., below the value for which a treatment is recommended (Hughes et al, 2011).

For **low Si concentrations (< 10 µmol.l^{-1}) and anion-rich samples** (e.g., test of the feasibility on volcanic ash leachates), a pre-concentration step is applied using the so-called MAGIC method (Brzezinski et al, 2003).

For **high Si concentrations** (**> 1700-2300 µmol.l^{-1})** (e.g., thermal springs), a dry down and NaOH leaching is required to prevent from silica precipitation and obtain adapted Si concentrations. The water sample was dried down on a hotplate at 100 °C, followed by a leaching with 0.125M NaOH at 100 °C for four hours after sonication for 10 minutes (adapted from Ragueneau et al, 2005). Following leaching, the pH of sample solutions was adjusted using suprapure HNO_3 to reach pH 2 in a final volume at a Si concentration below the limit of amorphous silica solubility. This was applied in *Ch4* and *Ch5*.

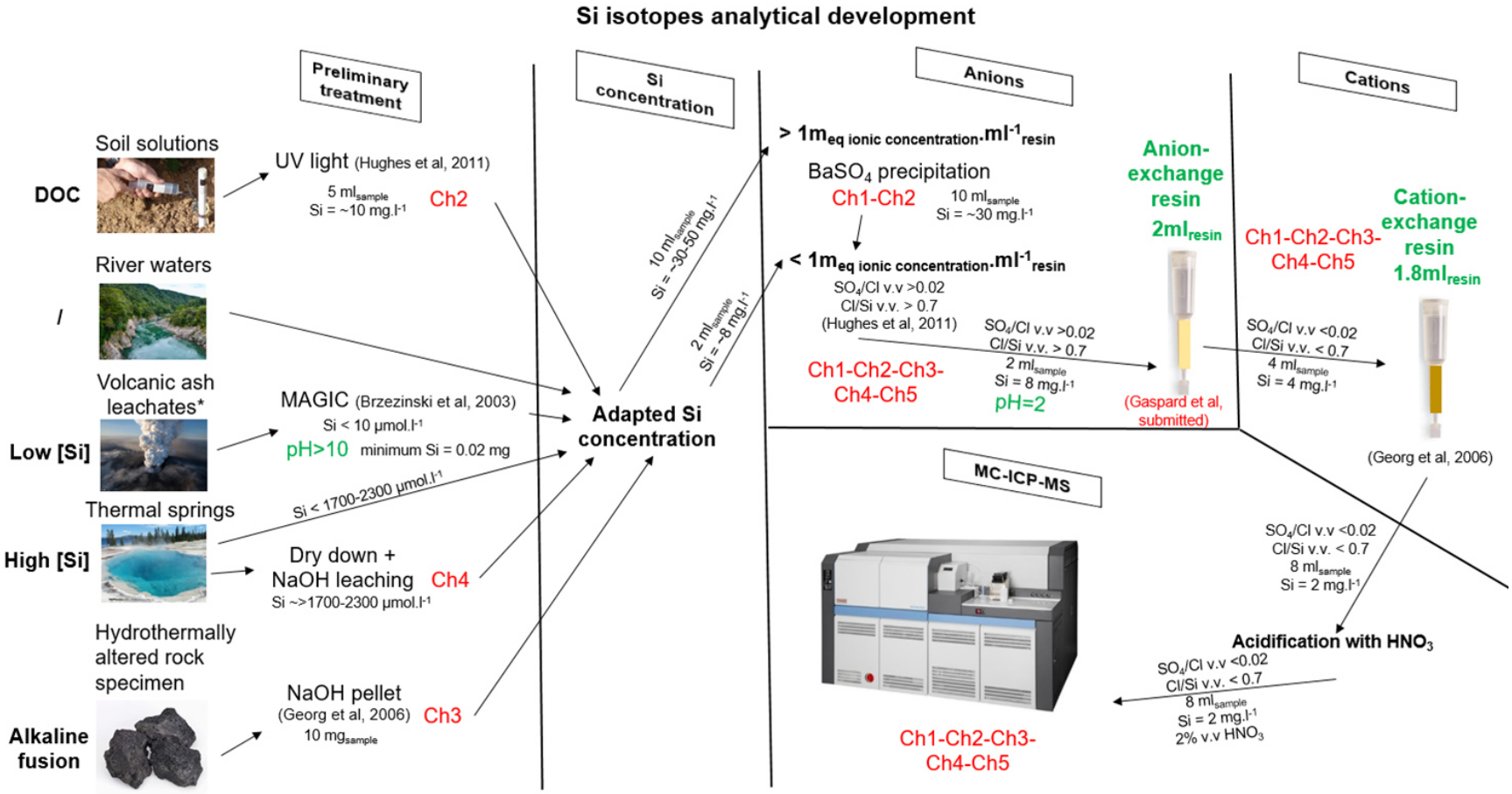
Si isotopes analytical development
Preliminary treatment
Si concentration
Anions
Cations
Soil solutions
DOC
UV light (Hughes et al, 2011)
5 ml sample
Si = ~10 mg.l-1
Ch2
River waters
I
Volcanic ash leachates*
Low [Si]
MAGIC (Brzezinski et al, 2003)
Si < 10 µmol.l-1
pH>10 minimum Si = 0.02 mg
Thermal springs
High [Si]
Si < 1700-2300 µmol.l-1
Dry down + NaOH leaching Ch4
Si ~>1700-2300 µmol.l-1
Hydrothermally altered rock specimen
Alkaline fusion
NaOH pellet
(Georg et al, 2006) Ch3
10 mg sample
Adapted Si concentration
10 ml sample Si = ~30-50 mg.l-1
2 ml sample Si = ~8 mg.l-1
> 1meq ionic concentration.ml-1resin
BaSO4 precipitation
Ch1-Ch2
10 ml sample Si = ~30 mg.l-1
< 1meq ionic concentration.ml-1resin
SO4/Cl v.v >0.02
Cl/Si v.v. > 0.7
(Hughes et al, 2011)
Ch1-Ch2-Ch3-Ch4-Ch5
SO4/Cl v.v >0.02
Cl/Si v.v. > 0.7
2 ml sample
Si = 8 mg.l-1
pH=2
Anion-exchange resin 2ml resin
(Gaspard et al, submitted)
Ch1-Ch2-Ch3-Ch4-Ch5
SO4/Cl v.v <0.02
Cl/Si v.v. < 0.7
4 ml sample
Si = 4 mg.l-1
Cation-exchange resin 1.8ml resin
(Georg et al, 2006)
MC-ICP-MS
Ch1-Ch2-Ch3-Ch4-Ch5
SO4/Cl v.v <0.02
Cl/Si v.v. < 0.7
8 ml sample
Si = 2 mg.l-1
Acidification with HNO3
SO4/Cl v.v <0.02
Cl/Si v.v. < 0.7
8 ml sample
Si = 2 mg.l-1
2% v.v HNO3

Fig. 2.3: Silicon isotopes analytical development performed on the different sample types in this PhD thesis. * = feasible application.
The PhD thesis chapters in which these steps have been applied are specified.

Once an **adapted Si concentration** was reached in all samples, a subsample of the solution (minimum 2 ml at 8 $mg.l^{-1}$ Si) was purified with an anion-exchange resin (Biorad AG MP-1) (fully described in **section 2.4.2.3**).

2.4.2.3 Purification of anion-rich samples

The method commonly applied to purify solutions prior to the determination of the isotope composition of dissolved Si involves the removal of cations from the matrix using a single step cation-exchange resin (Georg et al, 2006). However, this method does not remove anions from the aqueous solution, potentially leading to matrix effects and analytical mass bias during measurements by Multi-Collector Inductively Coupled Plasma Mass Spectrometry (MC-ICP-MS) and using the sample-standard bracketing technique (van den Boorn et al, 2009; Hughes et al, 2011). Anions in solution can be partly removed by co-precipitating Si with molybdate using the triethylamine (TEA) molybdate method, followed by dissolution of the silica precipitate in HF (De La Rocha et al, 1996). A pre-concentration step, the magnesium-induced coprecipitation (MAGIC) method, is usually applied prior to the analysis of low-Si solution (Si (< 10 µmol l^{-1}) (Brzezinski et al, 2003). The MAGIC method also removes some of the dissolved anions. When the anion-to-Si ratio of the sample to be analyzed is low (SO_4^{2-}/Si mass ratio < 0.7; Cl^-/Si mass ratio < 1.1), doping both the sample and the standard with anions is sufficient to correct for the mass bias during the isotopic analysis carried out via the sample-standard bracketing technique (Hughes et al, 2011). However, this condition is not fulfilled in thermal waters as these often contain high concentrations of dissolved SO_4^{2-}, and sometimes Cl^-. In this case, a purification step is necessary prior to the measurement (van den Boorn et al, 2009). The TEA and MAGIC methods are relatively labor-intensive and have drawbacks. The use of HF in the former may lead to the loss of volatile $SiF_4(g)$ during sample introduction, and thereby to unwanted Si isotope fractionation (Georg et al, 2006). Isotope fractionation may also be problematic when the recovery of Si at the end of the MAGIC pre-concentration step is incomplete. Moreover, MAGIC is performed at pH>10 and bringing acidic thermal waters to such basic pH values is often accompanied by the formation of various Fe- and Al-(oxy)hydroxide precipitates.

Here we describe a new purification method, comprised of two steps, which allows the Si isotopic analysis of anion-rich solutions, including thermal springs and river waters: a newly developed first step using an anion-exchange resin (Biorad AG MP-1) combined with the existing method using a cation-exchange resin (Biorad AG50WX12; Georg et al, 2006) as the second step. The anion-exchange resin (Biorad AG MP-1) is capable of exchanging anions of acidic, basic and neutral salts on the basic side of their isoelectric point (pI = pH at wich a molecule carries no net electrical charge or is electrically neutral in the statistical mean). The Biorad AG MP-1 resin is strongly basic anion exchangers with quaternary ammonium functional groups attached to the styrene divinylbenzene copolymer lattice. Usually, the resin is used in an ionic form with a lower selectivity for the functional group than the sample ions to be exchanged. Here, the resin is supplied in the Cl^- form and we convert the resin into NO_3^- form (given that Si isotope measurements by MC-ICP-MS are performed in 2% HNO_3). The relative selectivity of various counterions for HSO_4^-, NO_3^- and Cl^- are 85, 65 and 22, respectively. The anion-exchange resin has a defined exchange capacity (1 $m_{eq\ ionic\ concentration}.ml^{-1}_{resin}$ with $m_{eq\ ionic\ concentrations}$ (meq) = Si + SO_4^{2-} + Cl^- + F^-) (Biorad AG1, AG MP-1 and AG 2 Strong Anion Exchange Resin Instruction Manual). For each analysis, we ensured to be < 50% of the resin capacity.

In the first step, 2 ml of the sample to be analyzed, containing at least 8 $mg.l^{-1}$ of dissolved Si, are percolated through 2 ml of anion-exchange resin (Biorad AG MP-1) in order to remove SO_4^{2-} and Cl^- ions. Prior to purification, the anion-exchange resin is washed in batch with HNO_3 (3 x 5 ml) and milliQ water (3 x 5 ml), cleaned successively with 1 M HNO_3, 3 M HNO_3 and 1 M HNO_3, and rinsed with milli-Q water until a pH of 7 is reached (**Table 2.6**). The neutral pH is required to ensure that the sample is the unique acidity source to maintain an efficient cations purification in the second step of the method (the cation-exchange resin; Georg et al, 2006).

Table 2.6: First step of the separation scheme through anionic resin considering the preparation of a water sample with a Si concentration of 8 $mg.l^{-1}$ (minimum). This first step precedes the passage through cation-exchange resin (Georg et al, 2006).

2 ml resin bed of Biorad AG MP-1		
Separation stage	Solution matrix	Volume (ml)
Pre-cleaning	1M HNO_3	2
Pre-cleaning	3M HNO_3	2
Pre-cleaning	1M HNO_3	2
Pre-cleaning	milli-Q water	10 (pH should be neutral)
Sample load	Acidified water sample (pH=2)	2
Elution	milli-Q water	1
Elution	milli-Q water	1
Result		4 ml at 4 $mg.l^{-1}$ Si

Prior to the first step, to avoid overtaking the anion-exchange resin capacity (1 $m_{eq\ ionic\ concentration}.ml^{-1}_{resin}$ with $m_{eq\ ionic\ concentrations}$ (meq) = Si + SO_4^{2-} + Cl^- + F^-), **highly anion-rich thermal springs** (*Ch1, Ch2;* with SO_4^{2-} > 210 000 $\mu mol.l^{-1}$) are pre-treated to remove sulfates. Sulfates are purified by adding suprapure $Ba(NO_3)_2$ in a ratio of 3× $Ba(NO_3)_2$ $gram/SO_4$ ($gram_{sample}$) ratio considering $Ba(NO_3)_2$ in excess of 10%. This technique is commonly used for S isotopes measurements (e.g., Delmelle et al, 1998): sulfates are retained in the barytine precipitates ($BaSO_4$). The aliquot is filtered at 0.45 µm through polycarbonate membranes and the SO_4^{2-} removal (< 0.50 $\mu mol.l^{-1}$, i.e., below the detection limit values for S by ICP-OES) and Si recovery (>95%) in the dissolved phase are verified. Following this step, we add NaOH 10 $mol.l^{-1}$ to adjust the pH before anion-exchange column (pH=2).

In the second step (after passage through the anion-exchange resin), the anion-free solution is then percolated through 1.8 ml of a pre-cleaned cation-exchange resin (Biorad AG50WX12, 200-400 mesh; Georg et al, 2006; **Fig. 2.4**) with 4 ml of milli-Q water. The volume of the purified

sample for isotopic analysis is 8 ml and the concentration of dissolved Si is ≥ 2 $mg.l^{-1}$. The final purified solutions were with a minimum volume of 8 ml and Si concentration of 2 $mg.l^{-1}$ before Si isotope measurements. In each final purified solution, Si recovery of each preliminary step was >95% and SO_4^{2-} and Cl^- were below the detection limit of ICP-OES (1.5 and 3.1 $\mu mol.l^{-1}$, respectively) and ionic chromatography.

This method in two steps allows to obtain a purified Si solution (>95%) with anion removal close to ~ 100% for a anion-exchange resin capacity of <50% ($1 m_{eq\ ionic\ concentration}$).

Fig. 2.4: Samples purification via cation-exchange resin (Biorad AG50WX12) prior to Si isotope measurements.

2.4.2.4 MC-ICP-MS measurements

The purified Si solutions were analyzed for their Si isotope compositions by MC-ICP-MS (Neptune Plus™ High Resolution Multicollector ICP-MS, Thermo Fisher Scientific) at the Earth and Life Institute – Environmental Sciences of the Université catholique de Louvain.

The **MC-ICP-MS** has four parts (**Fig. 2.5**): a sample introduction system, a plasma source, a mass analyzer and a detection unit. The sample introduction system and plasma source are similar to ICP-MS and the detection unit is specific to MC. The principle is that the liquid sample (2% v/v HNO_3 matrix) is desolvated (introduction system) and then ionized in a hot argon plasma (a volume of partially ionized gas). More precisely, the ion source is inductively coupled argon plasma at 7500K. The argon flow meets an electro-magnetic field induced by a current within the coil. A high voltage ignition spark is applied to the argon gas and electrons are ripped off from argon atoms inducing a chain of collision. Ions are produced, accelerated and focused. More elements are ionized (ionization frequency close to 100%). As a result, analytes sample are desolvated, vaporized, atomized and finally ionized. The charged ions are accelerated by pressure differences inside the system (mass analyzer). In Neptune Plus™ High Resolution Multicollector ICP-MS, the mass analyzer consists of two parts called double-focusing: the electrostatic analyzer (ESA) dispersing ions with respect to ion energy (kinetic energy = $0.5 \times m \times v^2$) and the magnetic sector dispersing ions with respect to ion energy and mass (momentum: $m \times v$). The ions are deviated and detected on different collectors (Faraday cups) of the mass spectrometer depending on their kinetic energy and mass (based on their m/z ratios) (detection unit). The MC arrays allow for detection of multiple ion beams of adjacent isotope masses simultaneously which cancel out beam fluctuations. This improves precision on isotope ratios. When ion beam enters the cup, the positively charge ions are neutralized by inducing a current through the resistor recorded as a change in voltage. Isotope ratios are calculated by comparing voltages from the different collectors.

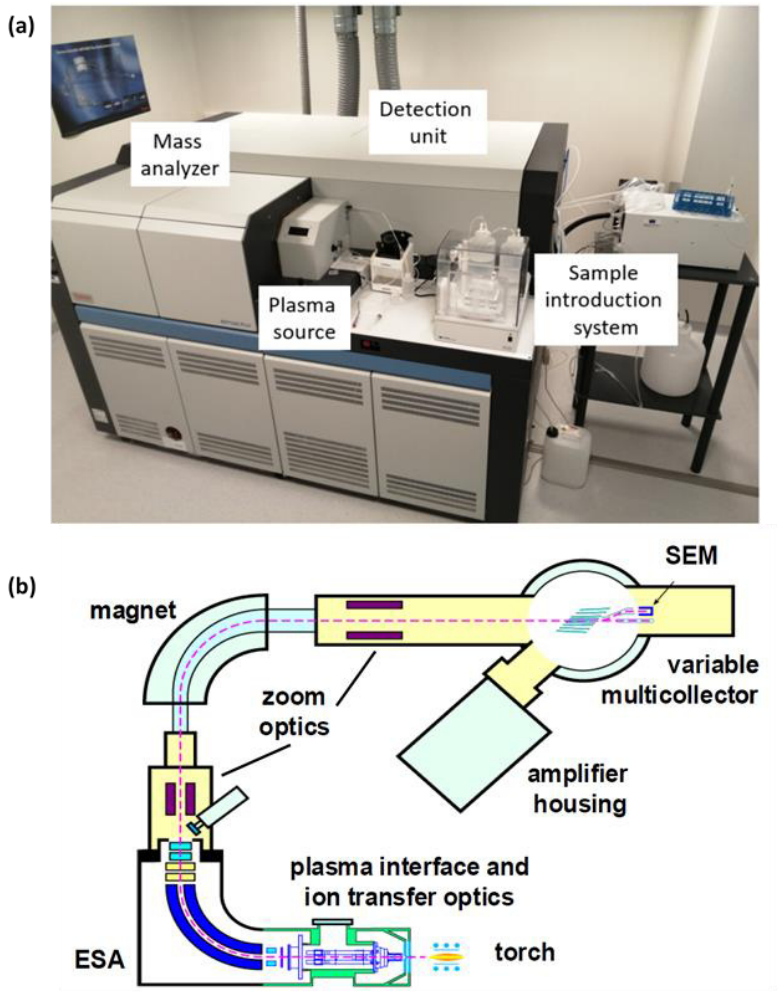

Fig. 2.5: (a) Four parts (picture taken in UCLouvain) and (b) schematic overview of Neptune Plus™ High Resolution Multicollector ICP-MS.

Silicon isotope compositions are expressed in relative deviations of $^{30}Si/^{28}Si$ ratio from the NBS-28 reference standard using the common δ-notation (‰): $\delta^{30}Si=[(^{30}Si/^{28}Si)_{sample}/(^{30}Si/^{28}Si)_{NBS-28} -1]\times1000$. One measurement comprises 30 cycles with 4.2 s integration time corrected by blank in a 2% v/v HNO_3 matrix. Each single δ-value (n) represents one sample run and two bracketing standards (intensity ratio within ±

10% for Si between sample and bracketing standards). δ^{30}Si-values are reported as the mean of replicate isotope analyses ± standard deviation (SD). When n=1, SD is the standard deviation of the two δ^{30}Si obtained for a sample relative to the two bracketing standards. When n>1, SD is the pooled deviation standard corresponding to $[(SD_1^2+SD_2^2+\ldots+SD_n^n)/n]^{0.5}$. If SD < 0.005, the SD value reported is 0.01. Measurements were performed in wet plasma mode (with a spray chamber) using a PFA nebulizer of 100 µl.min^{-1} uptake rate. Si isotopes (^{28}Si, ^{29}Si and ^{30}Si) have several interferences (**Table 2.7**), such as $^{X}C^{X}O$ and $^{X}N^{X}O$ on ^{30}Si.

Table 2.7: Interferences on Si isotopes (^{28}Si, ^{29}Si and ^{30}Si).

	Interferences
^{28}Si	$^{14}N_2^+$, $^{12}C^{16}O^+$,
^{29}Si	$^{14}N^{15}N+$, $^{14}N_2{}^1H^+$, $^{13}C^{16}O^+$, $^{12}C^{17}O^+$, $^{12}C^{16}O^1H^+$
^{30}Si	$^{15}N_2$, $^{14}N^{15}N^1H^+$, $^{14}N^{16}O^+$, $^{12}C^{18}O^+$, $^{13}C^{17}O^+$, $^{13}C^{16}O^1H^+$, $^{12}C^{17}O^1H^+$, $^{14}N_2{}^1H_2{}^+$, $^{12}C^{16}O^1H_2{}^+$

To overcome this issue, we run in medium resolution (Δm/m~6000) and we set the magnet on the flat part of the ^{30}Si peak as shown in **Fig. 2.6**.

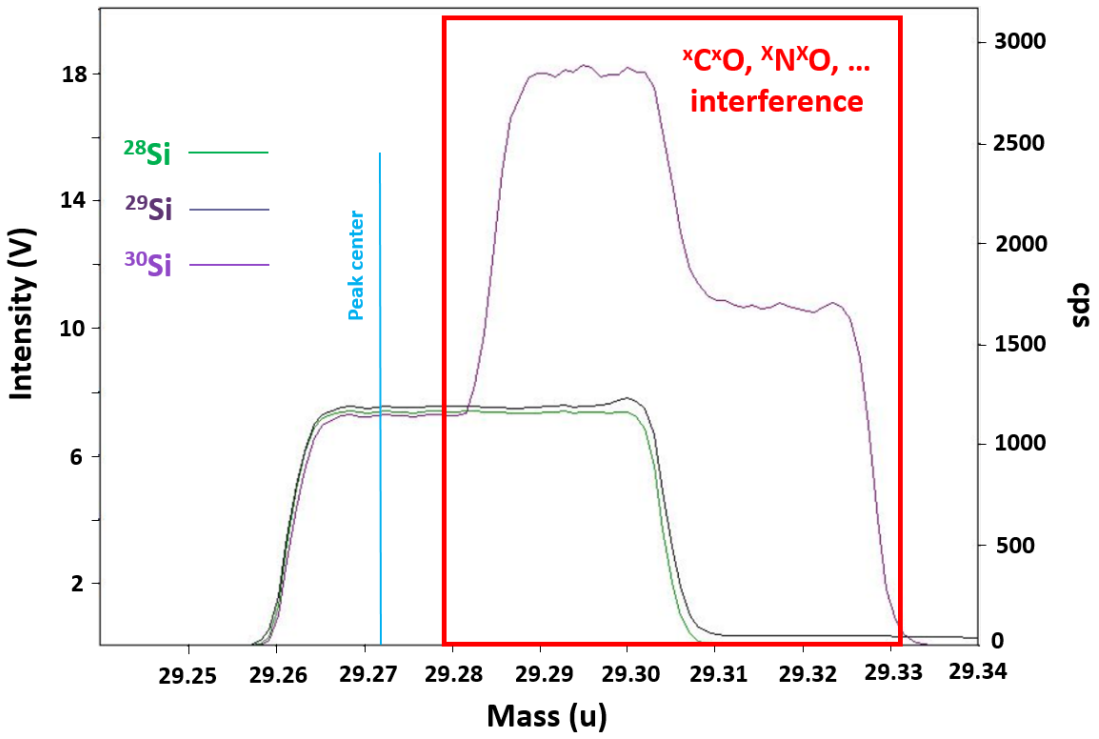

Fig. 2.6: Interferences on Si isotopes during measurements on Neptune Plus™ High Resolution Multicollector ICP-MS.

The instrumental mass bias was corrected using the standard-sample bracketing technique and an external Mg doping (Cardinal et al, 2003) with a intensity ratio Si:Mg within ± 10%. The analyses were performed with a typical sensitivity of 7 V for 2 mg.l^{-1} Si and an instrumental blank <30 mV. Quality control of data was performed by ensuring that: (i) during one analytical session, the long-term plot of the measured Mg isotope ratios for samples and bracketing standards (ln(^{25}Mg/^{24}Mg) vs. ln (^{26}Mg/^{24}Mg)) should display a slope around ±0.51 (Galy et al, 2001), (ii) the long-term plot of the measured Si isotope ratios vs. measured Mg isotope ratios for bracketing standards during one analytical session should display a constant slope of ± 0.86 (between 0.81 and 1.08; Cardinal et al, 2003), (iii) the long-term plot of δ^{30}Si vs. δ^{29}Si

measurements fit to a mass-dependent fractionation array, supporting the interference-free determination of all three Si isotopes by MC-ICP-MS (Young et al, 2002).

2.4.2.5 Precision and accuracy of Si isotope measurements on anion-rich samples

The long-term precision and accuracy of the MC-ICP-MS $\delta^{30}Si$ analyses were assessed from multiple measurements of three reference materials prepared using the single step cation-exchange resin method after alkaline fusion with NaOH (Georg et al, 2006). The Si isotopes values of reference materials are given in **Table 2.8**. These checks were performed within each analytical session. The values obtained for diatomite ($\delta^{30}Si$ = 1.29 ± 0.09 ‰, SD, n=19), USGS basalt BHVO-2 ($\delta^{30}Si$ = -0.27 ± 0.06 ‰, SD, n=10) and quartz Merck ($\delta^{30}Si$ of 0.04 ± 0.09 ‰, SD, n=6) (**Fig. 2.7**; **Table 2.9**) are consistent with those reported earlier (Reynolds et al, 2007; Abraham et al, 2008).

Table 2.8: Si isotope compositions of reference materials (Diatomite, BHVO-2 and Quartz Merck).

	$\delta^{29}Si$	SD	$\delta^{30}Si$	SD	Reference
Diatomite	0.64	0.07	1.26	0.10	Reynolds et al, 2007
BHVO-2	-0.17	0.04	-0.29	0.11	Abraham et al, 2008
Quartz Merck	0.00	0.07	-0.01	0.12	Abraham et al, 2008

The absence of Si isotope fractionation during the two-step purification method was verified by running the solutions obtained after digestion by alkaline fusion of the diatomite, BHVO-2 and quartz Merck reference materials. One set of diatomite and BHVO-2 solutions was spiked with SO_4^{2-} and Cl^- to mimic an anion-rich matrix containing 100 and 400 mg $SO_4^{2-}.l^{-1}$ and 50 and 100 mg $Cl^-.l^{-1}$ (**Suppl. Mat. 5.4**). The repeatability of the two-step purification method was assessed by performing replicate measurements of the reference materials. The replicates are either full replicates, i.e. each measurement corresponds to the reference material

subjected to digestion by alkaline fusion and two-step purification (noted as F in **Table 2.9**), or to partial replicates, i.e. each measurement corresponds to the same sample of reference material obtained after alkaline fusion but the two-step purification method was repeated (noted as C in **Table 2.9**). The Si isotope compositions of diatomite (δ^{30}Si of 1.34 ± 0.07 ‰, n=7), BHVO-2 (δ^{30}Si of -0.37 ± 0.07 ‰, n=3) and quartz Merck (δ^{30}Si of 0.04 ± 0.05 ‰, n=9) subjected to the newly-developed two-step purification method are in good agreement with those obtained using the single step cation-exchange resin. The results also match previously published values (**Fig. 2.7**; **Table 2.9**).

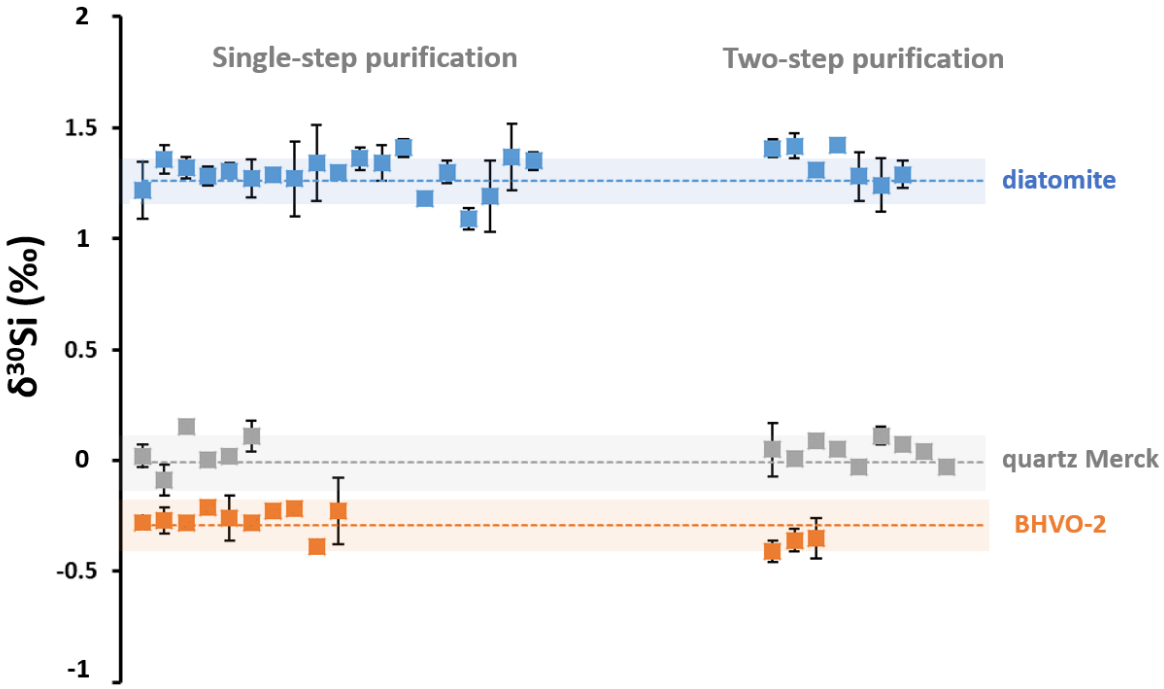

Fig. 2.7: Plot of the δ^{30}Si values (± SD) of the three reference materials (diatomite, quartz Merck and BHVO-2) as obtained using a single purification (cation-exchange resin) and the two-step purification method (cation-exchange resin + anion-exchange resin) developed in this study. The data are reported in **Table 2.9**. Our δ^{30}Si values agree well (within error) with the Si isotope compositions (dashed line ± SD

shown as a colored box) reported for the diatomite, quartz Merck and BHVO-2 reference materials (Reynolds et al, 2007; Abraham et al, 2008).

Table 2.9: Silicon isotope compositions ($\delta^{29}Si$ and $\delta^{30}Si$) of the reference materials diatomite, BHVO-2, and quartz Merck measured after one-step purification, or with the new two-step purification method (An = anion). F1, F2, F3 stand for solutions from separate alkaline fusions. C1, C2, C3, C4, C5, C6 stand for solutions from separate purification onto different columns of exchange resin. The average Si isotope values obtained after one-step or two-step purification are compared with existing Si isotope values reported in the literature for these reference materials.

Meas. date[1]	Sample	$\delta^{29}Si$ (‰)	SD	$\delta^{30}Si$ (‰)	SD	n
14.06.18	DiatomiteF1	0.66	0.10	1.22	0.13	
14.06.18	DiatomiteF1	0.72	0.01	1.36	0.06	
15.06.18	DiatomiteF1	0.62	0.06	1.32	0.05	
10.07.18	DiatomiteF1	0.63	0.02	1.28	0.04	
11.10.18	DiatomiteF1	0.64	0.05	1.31	0.03	
12.10.18	DiatomiteF1	0.66	0.06	1.27	0.09	
12.10.18	DiatomiteF1	0.66	0.03	1.29	0.01	
07.02.19	DiatomiteF3C1	0.74	0.02	1.27	0.17	
07.02.19	DiatomiteF3C1	0.67	0.10	1.34	0.17	
08.02.19	DiatomiteF3C1	0.65	0.02	1.30	0.01	
22.02.19	DiatomiteF3C1	0.63	0.06	1.36	0.05	
22.02.19	DiatomiteF3C1	0.61	0.04	1.34	0.08	
22.02.19	DiatomiteF3C1	0.66	0.05	1.41	0.04	
22.02.19	DiatomiteF3C1	0.79	0.05	1.18	0.03	
04.03.19	DiatomiteF3C1	0.74	0.05	1.30	0.05	
04.03.19	DiatomiteF3C1	0.58	0.01	1.09	0.05	
22.02.19	Diatomite F3C2	0.69	0.07	1.19	0.16	
26.02.19	Diatomite F3C2	0.72	0.06	1.37	0.15	
08.02.19	Diatomite F3C3	0.76	0.02	1.35	0.04	
14.06.18	AnDiatomiteF2C1	0.65	0.08	1.41	0.04	
15.06.18	AnDiatomiteF2C1	0.68	0.02	1.42	0.06	
08.02.19	AnDiatomiteF3C2	0.69	0.01	1.31	0.02	
08.02.19	AnDiatomiteF3C3	0.60	0.01	1.42	0.03	
22.02.19	AnDiatomiteF3C4 100 50[2]	0.76	0.01	1.28	0.11	
22.02.19	AnDiatomiteF3C5 400 300[2]	0.67	0.10	1.24	0.12	
22.02.19	AnDiatomiteF3C6	0.57	0.06	1.29	0.06	
	Average diatomite (one-step purification)	**0.67**	**0.06**	**1.29**	**0.09**	**19**
	Average diatomite (two-step purification)	**0.66**	**0.05**	**1.34**	**0.07**	**7**
	Diatomite reference value[3]	**0.64**	**0.07**	**1.26**	**0.10**	

14.06.18	BHVO-2F1	-0.13	0.02	-0.28	0.02	
15.06.18	BHVO-2F1	-0.14	0.01	-0.27	0.06	
06.11.18	BHVO-2F1	-0.16	0.03	-0.28	0.02	
07.11.18	BHVO-2F1	-0.16	0.01	-0.21	0.01	
08.11.18	BHVO-2F1	-0.18	0.02	-0.26	0.10	
19.11.18	BHVO-2F1	-0.14	0.03	-0.28	0.03	
07.11.18	BHVO2F2C1	-0.14	0.03	-0.23	0.03	
10.07.18	BHVO2F2C2	-0.15	0.01	-0.22	0.02	
05.02.19	BHVO2F3C1	-0.15	0.01	-0.39	0.03	
08.02.19	BHVO2F3C1	-0.15	0.05	-0.23	0.15	
04.03.19	AnBHVO-2F3C1 400 300[2]	-0.20	0.09	-0.41	0.05	
04.03.19	AnBHVO-2F3C2	-0.19	0.00	-0.36	0.05	
04.03.19	AnBHVO-2F3C3	-0.18	0.03	-0.35	0.09	
	Average BHVO-2 (one-step purification)	**-0.15**	**0.03**	**-0.27**	**0.06**	**10**
	Average BHVO-2 (two-step purification)	**-0.19**	**0.05**	**-0.37**	**0.07**	**3**
	BHVO-2 reference value[4]	**-0.17**	**0.04**	**-0.29**	**0.11**	
09.07.18	QuartzF2C1	-0.01	0.05	0.02	0.05	
06.11.18	QuartzF1	-0.07	0.09	-0.09	0.07	
24.02.19	QuartzF1	0.03	0.05	0.15	0.03	
05.02.19	QuartzF3C1	-0.02	0.04	0.00	0.01	
07.02.19	QuartzF3C1	0.01	0.01	0.02	0.03	
08.02.19	QuartzF3C2	0.00	0.01	0.11	0.07	
15.06.18	AnQuartzF2C1	0.04	0.04	0.05	0.12	
15.06.18	AnQuartzF2C1	0.00	0.01	0.01	0.01	
11.10.18	AnQuartzF2C2	0.02	0.03	0.09	0.01	
09.07.18	AnQuartzF2C3	-0.04	0.04	0.05	0.03	
08.02.19	AnQuartzF3C1	-0.01	0.01	-0.03	0.01	
08.02.19	AnQuartzF3C2	0.00	0.01	0.11	0.04	
22.02.19	AnQuartzF3C4	0.13	0.01	0.07	0.02	
08.02.19	AnQuartzF3C3	0.01	0.01	0.04	0.01	
08.02.19	AnQuartzF3C5	0.08	0.01	-0.03	0.03	
	Average quartz Merck (one-step purification)	**-0.01**	**0.05**	**0.04**	**0.09**	**6**
	Average quartz Merck (two-step purification)	**0.03**	**0.02**	**0.04**	**0.05**	**9**
	Quartz Merck reference value[4]	**0.00**	**0.07**	**-0.01**	**0.12**	

[1]Date of measurement: day of analysis by MC-ICP-MS.
[2]Spiked diatomite or BHVO-2 with X mg.l^{-1} SO_4^{2-} and X mg.l^{-1} Cl^-.
[3]Reynolds et al, 2007.
[4]Abraham et al, 2008.

The $\delta^{30}Si$ data measured by MC-ICP-MS in this PhD thesis after a silicon purification by the newly developped method to remove anions on thermal waters from Midway Geyser Basin in the Yellowstone Plateau Volcanic Field ($\delta^{30}Si$ = from -0.14 to -0.04 ‰, n=6, *Ch4*) were directly comparable with the value measured 38 years ago by a gas source mass

spectrometer by the fluorination technique producing SiF_4 for Ear spring located also in Midway Geyser Basin ($\delta^{30}Si$ = -0.1‰; Douthitt, 1982).

The **advantages** of our method are that: (i) the low amount of Si needed for one analysis by MC-ICP-MS (~2 µg Si), (ii) there is no hazardous fluorine technique, and (iii) the precision by MC-ICP-MS is higher (0.01-0.08‰, SD) than by IRMS (0.25‰, SD; Douthitt, 1982).

We tested the limit of our method to measure the Si isotope composition of samples with **low Si amount available and an anion-rich matrix** on volcanic ash leachates. We performed a Si pre-concentration with the MAGIC protocol on volcanic ash leachates from Eyjafjallajökull eruption of 2010. The protocol of Brzezinski et al (2003) requires a minimum quantity of Si (~0.02 mg) in volcanic ash leached and a pH>10 (by adding NH_4OH) to initiate the brucite precipitation. The Si recovery after MAGIC method was >90%. Samples were then passed through the anion and cation-exchange column and analyzed by MC-ICP-MS. The limited amount of samples available did not allow to repeat this test but it was successful for two samples.

2.5 References

Abraham, K., Opfergelt, S., Fripiat, F., Cavagna, A-J., de Jong, J., Foley, S.F., André, L., Cardinal, D., 2008. δ^{30}Si and δ^{29}Si determinations on USGS BHVO-1 and BHVO-2 reference materials with a new configuration on a Nu Plasma Multi-Collector ICP-MS. Geostand. Geoanal. Res. 32(2), 193-202.

Belissont, R., Boiron, M-C., Luais, B., Cathelineau, M., 2014. LA-ICP-MS analyses of minor and trace elements and bulk Ge isotopes in zoned Ge-rich sphalerites from the Noailhac–Saint-Salvy deposit (France): Insights into incorporation mechanisms and ore deposition processes. Geochim. Cosmochim. Ac. 126, 518–540.

Brock, T.D., 1970. Limits of microbial existence: temperature and pH. Science 169, 1316–1318.

Brzezinski, M. A., Jones, J. L., Bidle, K. D., Azam, F., 2003. The balance between silica production and silica dissolution in the sea: insights from Monterey Bay, California, applied to the global data set. Limnol. Oceanogr. 48, 1846-1854.

Cardinal, D., Alleman, L.Y., De Jong, J., Ziegler, K., André, L., 2003. Isotopic composition of silicon measured by multicollector plasma source mass spectrometry in dry plasma mode. J. Anal. Atom. Spectrom. 18, 213–218.

Cornelis, J.-T., Delvaux, B., Cardinal, D., André, L., Ranger, J., Opfergelt, S., 2010. Tracing mechanisms controlling the release of dissolved silicon in forest soil solutions using Si isotopes and Ge/Si ratios. Geochim. Cosmochim. Ac. 74, 3913–3924.

De La Rocha, C.L., Brzezinski, A., DeNiro, M.J., 1996. Purification, recovery and laser-driven fluorination of silicon from dissolved and particulate silica for the measurement of natural stable isotope abundances. Anal. Chem. 68, 3746-3750.

De La Rocha, C.L., 2002. Measurement of silicon stable isotope abundances via multicollector inductively coupled plasma mass spectrometry MC-ICP-MS. Geochem. Geophys. Geosyst. 3, 1–8.

Delmelle, P., Fischer, T., Kusakae, M., 1998. Geochemical and isotopic evidence for seawater contamination of the hydrothermal system of Taal Volcano, Luzon, the Philippines. Bull. Volcanol. 59, 562-576.

Delvigne, C., Opfergelt, S., Cardinal, D., Delvaux, B., André, L. 2009. Distinct silicon and germanium pathways in the soil-plant system: Evidence from banana and horsetail. J. Geophys. Res. 114, G02013.

Delvigne, C., Angeletti, B., Guihou, A., Basile-Doelsch, I., Meunier, J-D., 2018. Reliable Determination of Ge in Solid Environmental Samples Using a Chemical Preparation Procedure Developed for Si Isotopes and ICP-MS Analysis. Geostand. Geoanal. Res. 42, 139-149.

Ding, T.P., 2004. Analytical methods for silicon isotope determinations. Handbook of Stable Isotope Analytical Techniques, Volume I, Elsevier B.V., 523–39.

Dong, L., Shen, B., Lee, C.T.A., Shu, X.-J., Peng, Y., Sun, Y., Tang, Z., Rong, H., Lang, X., Ma, H., Yang, F., Guo, W., 2015. Germanium/silicon of the Ediacaran-Cambrian Laobao cherts: Implications for the bedded chert formation and paleoenvironment interpretations. Geochemistry 16, 751–763.

Douthitt, C.B., 1982. The geochemistry of the stable isotopes of silicon. Geochim. Cosmochim. Acta 46, 1449–1458.

Frei, R., Polat, A., 2007. Source heterogeneity for the major components of 3.7 Ga Banded Iron Formations (Isua Greenstone Belt, Western Greenland): Tracing the nature of interacting water masses in BIF formation. Earth Planet. Sc. Lett. 253, 266–281.

Galy, A., Belshaw, N.S., Halicz, L., O'Nions, R.K., 2001. High-precision measurement of magnesium isotopes by multiple-collector inductively coupled plasma mass spectrometry. Int J Mass Spectrom 208, 89-98.

Georg, R.B., Reynolds, B.C., Frank, M., Halliday, A.N., 2006. Mechanisms controlling the silicon isotopic compositions of river waters. Earth Planet. Sci. Lett. 249, 290–306.

Hamade, T., Konhauser, K., Raiswell, R., Goldsmith, S., Morris, R., 2003. Using Ge/Si ratios to decouple iron and silica fluxes in Precambrian banded iron formations. Geology 31, 35–38.

Herrmann, R., Baumgartner, B., 1992. Aluminum species distribution during mixing of acid coal and slate mine drainage with neutral stream waters. Geol. Rundsch. 81, 759–767.

Hughes, H.J., Delvigne, C., Korntheuer, M., De Jong, J., André, L., Cardinal, D. 2011. Controlling the mass bias introduced by anionic and organic matrices in silicon isotopic measurements by MC-ICP-MS, J. Anal. Spectrom. 26, 1892-1896.

Lloret, E., 2010. Dynamique du carbone organique dans des petits bassins versants tropicaux. PhD.

McMahon, M., Regan, F., Hughes, H. 2006. The determination of total germanium in real food samples including Chinese herbal remedies using graphite furnace atomic absorption spectroscopy. Food Chem. 97, 411– 417.

Mortlock, R.A., Froelich, P.N., 1996. Determination of germanium by isotope dilution-hybride generation inductively coupled plasma mass spectrometry. Anal. Chem. Ac. 332, 277- 284.

Nordstrom, D.K., Jenne, E.A., Ball, J.W., 1979. Redox equilibria of iron in acid mine waters. In: Jenne E.A. (Ed.), Chemical Modelling in Aqueous Systems-Speciation. Am. Chem. Soc. Symp Ser 93, 51–79.

Ragueneau, O., Savoye, N., Del Amo, Y., Cotten, J., Tardiveau, B., Leynaert, A., 2005. A new method for the measurement of biogenic silica in suspended matter of coastal waters: using Si:Al ratios to correct for the mineral interference. Cont. Shelf Res. 25, 697–710.

Reynolds, B.C., Aggarwal, J., André, L., Baxter, D., Beucher, C., Brzezinski, M.A., Engström, E., Georg, B., Land, M., Leng, M.J., Opfergelt, S., Rodushkin, I., Sloane, H.J., Van den Boorn, S.H.J.M., Vroon, P.Z., Cardinal, D., 2007. An inter-laboratory comparison of Si isotope reference materials. J. Anal. Atom. Spectrom. 22, 561-568.

Reynolds, B.C., 2011. Silicon Isotopes as Tracers of Terrestrial Processes. Handbook of Environmental Isotope Geochemistry, Advances in Isotope Geochemistry. Part 2, 87–104.

Shen, B., Lee, C.T.A., Xiao, S., 2011. Germanium/silica ratios in diagenetic chert nodules from the Ediacaran Doushantuo Formation, south China. Chem. Geol. 280, 323–335.

Soylak, M., Yigit, S., 2015. Preconcentration-separation of germanium at ultra trace levels on polysulfone membrane filter and its determination by spectrophotometry. Journal of Industrial and Engineering Chemistry 24, 322–325.

Tribovillard, N., Bout-Roumazeilles, V., Riboulleau, A., Baudin, F., Danelian, T., Riquier, L., 2011. Transfer of germanium to marine sediments: Insights from its accumulation in radiolarites and authigenic capture under reducing conditions. Some examples through geological ages. Chem. Geol. 282, 120–130.

United Kingdom Accreditation Body (UKAS)., 2014. Certificate of measurement, river water-anion, certified reference material LGC6025. 4005.

van den Boorn, S.H.J.M., Vroon P.Z., van Bergen, M. J., 2009. Sulfur-induced offset in MC-ICP-MS silicon-isotope measurements. Anal. At. Spectrom. 24, 1111–1114.

Yang, L., Meija, J., 2010. Resolving the germanium atomic weight disparity using multicollector ICP-MS. Anal. Chem. 82, 4188–4193.

Young, E.D., Galy, A., Nagahara, H., 2002. Kinetic and equilibrium mass-dependent isotope fractionation laws in nature and their geochemical and cosmochemical significance. Geochim. Cosmochim. Ac. 66, 1095-1104.

Yeghicheyan, D., Bossy, C., Bouhnik Le Coz, M., Douchet, C., Granier, G., Heimburger, A., Lacan, F., Lanzanova, A., Rousseau, T.C.C., Seidel, J-L., Tharaud, M., Candaudap, F., Chmeleff, J., Cloquet, C., Delpoux, S., Labatut, M., Losno, R., Pradoux, C., Sivry, Y., Sonke, J.E., 2013. A Compilation of Silicon, Rare Earth Element and Twenty-One other Trace Element Concentrations in the Natural River Water Reference Material SLRS-5 (NRC-CNRC). Geostand. Geoanal. Res. 37(4), 449-467.

Part III

DATA CHAPTERS

Chapter 1:
Influence of volcanic gases and water-rock interaction on the Ge/Si ratio and Si isotopes of volcanic thermal springs

3.1 Abstract

The Ge/Si ratios and Si isotopes ($\delta^{30}Si$) are applied in rivers draining volcanic regions to trace weathering processes. However, the applicability of these tracers in rivers draining hydrothermally-active volcanic regions is still limited given the input from thermal springs to rivers. Thermal waters present a range of compositions, from immature to mature waters. The lack of knowledge on the variability and on the controls on Ge/Si ratio and $\delta^{30}Si$ in thermal waters prevent from the identification of their influence on the riverine Ge/Si ratio and $\delta^{30}Si$ values. Here, we measure the Ge/Si ratios and $\delta^{30}Si$ values in 56 thermal springs from six hydrothermally-active volcanic regions worldwide, covering the main thermal waters types, from immature to mature waters, and we investigate the influence of volcanic gases and water-rock interaction on these geochemical tracers.

The thermal springs display a large range of Ge/Si ratios (0.05-507.89 $\mu mol.mol^{-1}$) and Si isotope compositions (from -0.44 to 1.57 ‰). The higher Ge/Si ratios (46.99-507.89 $\mu mol.mol^{-1}$) are found in immature hyper acid SO_4-Cl waters, considered as the "magmatic end-member", and likely result from Ge enrichment in the thermal waters due to Ge volatility transported by volcanic gases (via GeF_4, $GeCl_4$ and GeS). These hyper acid SO_4-Cl waters waters also present low $\delta^{30}Si$ values (-0.14 to 0.21 ‰), which can result from pervasive acid alteration of volcanic rock followed by amorphous silica precipitation. Relative to this magmatic end-member, lower Ge/Si ratios and heavier $\delta^{30}Si$ values are found in acid SO_4-waters, alkaline HCO_3-waters and immature neutral-Cl waters (overlapping values between these thermal water types for Ge/Si = 0.20-21.03, 0.25-19.47 and 0.50-0.56 $\mu mol.mol^{-1}$, and $\delta^{30}Si$ = 0.27 to 1.35, -0.05 to 1.57 and 1.13 ‰, respectively). This range of values can be explained by different intensities of water-rock interaction. Only mature neutral Cl-thermal waters, considered as the "mature end-member", present higher Ge/Si ratio

(110.98-188.92 μmol.mol^{-1}) and lower δ^{30}Si (-0.44 to -0.05 ‰), suggesting that extensive water-rock interaction erases the imprint of intermediate levels of water-rock interaction on Ge/Si ratios and δ^{30}Si values in thermal waters and leads to similar Ge/Si values and lower δ^{30}Si values in thermal waters than the in waters from the original magmatic end-member (hyper acid SO_4-Cl waters). These data highlights the major role of magmatic gases and water-rock interaction on the variability of Ge/Si ratios and δ^{30}Si values in thermal waters, and thereby providing a better knowledge to expand the applicability of these geochemical tracers in rivers influenced by thermal inputs.

3.2 Introduction

In a hydrothermal system, the interaction of rising magmatic gases (mainly H_2O, CO_2, SO_2, H_2S and HCl) with meteoric water (e.g., shallow groundwater, perched aquifer) is a direct source of acidity for weathering reactions. This leads to different thermal water types in surface. Thermal waters are classified (White, 1957; Ellis and Mahon, 1964, 1977; Giggenbach, 1988) depending on the proportion of magmatic gas contribution relative to meteoric water recharge as (i) acid sulfate-chloride waters formed at higher magmatic gas contribution relative to meteoric water recharge with SO_4/Cl being function of absorption degree of magmatic gases in the system, (ii) acid sulfate-waters formed when steam below about 400 °C condenses into surface waters (e.g., perched aquifer), (iii) alkaline bicarbonate waters formed at low magmatic gases contribution condensing into an aquifer (mainly CO_2 and H_2S) and (iv) alkali/neutral chloride waters formed at low magmatic gas contribution (mainly CO_2 and H_2S). This source of strong acids for weathering reactions contributes to weathering fluxes in hydrothermally-active volcanic regions (Louvat and Allègre, 1997; Dessert et al, 2009; Hurwitz et al, 2010; Schopka et al, 2011; Gaillardet et al, 2011; Rivé et al, 2013).

Identifying the contribution of the different types of thermal waters to weathering fluxes in hydrothermally-active volcanic regions is needed to retrieve their contribution from weathering fluxes measured in volcanic regions. This is part of the challenge to improve the estimates of the net atmospheric CO_2 consumption associated to weathering fluxes not derived from a volcanic source of acidity (e.g., Hurwitz et al, 2007; Dessert et al, 2009; Gaillardet et al, 2011).

The germanium to silicon (Ge/Si) ratio and the stable silicon isotopes ($\delta^{30}Si$) have been used in rivers draining volcanic regions to trace the intensity of weathering processes (e.g., Derry et al, 2005; Ziegler et al, 2005; Opfergelt et al, 2010; 2013; Baronas et al, 2018; 2020). The application of these tracers in rivers influenced by thermal input has been limited given that the variability in Ge/Si ratios (Arnórsson, 1987; Siebert et al, 2006; Escoubé et al, 2015) and $\delta^{30}Si$ (Douthitt, 1982; Opfergelt et al, 2011; Geilert et al, 2015; Ding et al, 2017; Chen et al, 2020) in thermal springs is poorly constrained, and the processes controlling this variability have not been investigated so far.

This study was carried out with the objectives to (i) document the $\delta^{30}Si$ and Ge/Si ratio variability in thermal springs from the different water types (i.e., hyper acid SO_4-Cl waters, acid SO_4-waters, alkaline HCO_3- and neutral Cl-waters, and in mixed thermal waters; as defined by White, 1957; Ellis and Mahon, 1964, 1977; Giggenbach, 1988), and (ii) investigate the role of volcanic gases and water-rock interaction in the volcanic edifice on this variability. More specifically, this study is based on a total of 56 volcanic thermal springs from six hydrothermally-active volcanic regions (La Soufrière volcano, Basse-Terre Island; Kawah Ijen volcano, Java Island; Aso volcano, Kyūshū Island; Yellowstone Plateau Volcanic Field, United States; Kanlaon volcano, Negros Island; Mutnovsky volcano, Kamchatka).

3.3 Environmental setting

La Soufrière volcano, Basse-Terre Island, Guadeloupe

Formed by the subduction of the Atlantic Plate beneath the Caribbean Plate, the Lesser Antilles volcanic arc is formed of several islands whose largest is Guadeloupe (16°N, 61°W; 1630 km^2). Basse-Terre island (950 km^2), the western island of Guadeloupe consists of different volcanic-structural unit of basaltic-andesitic composition. The most recent is Madeleine-Soufrière unit and contains the presently active dome of La Soufrière volcano. The hydrothermal system of La Soufrière is composed of a main aquifer delimited by the Amic caldera borders (Barat, 1986). The main aquifer is subjected to a gas flux consequent from an underlying magma chamber (Villemant et al, 2005) and fed by meteoric water percolating through recent pyroclastic deposits (Brombach et al, 2000). Located under the dome summit at a depth of 500m, the roof of main aquifer has temperatures ranging from 190 °C and 260 °C (Brombach et al, 2000). The hydrothermal system of La Soufrière is very active with numerous hot springs and fumaroles. Thermal springs distribution is restrained by the internal volcanic structure and important hydrothermal clays formation in the upper layer (Brombach et al, 2000). Thermal springs of Basse-Terre Island have relatively constant flow rates ranging from 3 to 140 $l.min^{-1}$ (annual report of the Volcanological and Seismological Observatory of Guadeloupe OVSG-IPGP, 2010-2015). La Soufrière volcanism is younger than 200 ky (Gailler et al, 2014). Thermal manifestations are mainly concentrated around La Soufrière dome. Each of the Basse-Terre springs is monitored by the OVSG-IPGP, producing a continuous data record over the past ~40 years.

Thermal springs of Basse-Terre Island are well-studied and generally classified based on their cation and anion concentrations into Ca-SO_4, Ca-Na-HCO_3 and Ca-Na-Cl waters (Brombach et al, 2000; Villemant et al, 2005; 2014; Dessert et al, 2015). These three types of thermal waters correspond to acid SO_4-waters, alkaline HCO_3-waters and neutral Cl-waters, respectively, in the classification used in this study (Giggenbach, 1988).

Fifteen thermal springs were collected: ten were sampled twice (in January-February 2015, and in October-November 2017 and April 2018; n=26) on both sides of Basse-Terre Island.

Kawah Ijen volcano, Java Island, Indonesia

Formed by the subduction of the Indian-Australian plate beneath the Eurasian plate, the Sunda arc arbours the Indonesian archipelago. Located in East Java (7°S, 110°E), within the Ijen caldera, Kawah Ijen is an active stratovolcano of basalt-andesitic to andesitic composition (Whitford et al, 1979; Delmelle and Bernard, 1994). The hydrothermal system of Kawah Ijen shows as visible surface manifestations a hot acidic crater lake (pH < 0.3; T > 35 °C, volume ~ 32×10^6 m^3; Delmelle and Bernard, 1994), crater fumaroles and few thermal springs. The Ijen lake is acid sulfate-chloride type crater-lake waters carrying a high load of dissolved elements. The lake chemistry is determined by dissolution of magmatic volatiles, fluid-rock interaction, evaporation of the lake water, dilution by meteoric water and recycling of lake water through seepage into the subsurface hydrothermal system (Bernard and Delmelle, 1994). The acidic waters dissolve the rock isochemically to produce "immature waters". Three sets of hyper acid SO_4-Cl thermal springs are reported on the flanks of Kawah Ijen. When the first set of thermal springs (2090 m asl) emerges, this water rapidly saturates in gypsum due to evaporation, which has led to the development of a large gypsum plateau covered terraced slope 50 m wide 100 m long (van Hinsberg et al, 2010). The second set of acid springs is observed at 2075 m asl and the third set of acid springs is located at 1975 m asl, characterized by bright, yellow-green colored water (Palmer, 2009). Finally, hot springs occur at several locations near Blawan village (located about 17 km below the volcano) and are classified as neutral HCO_3-SO_4 waters. The springs are associated with deposits of travertine and based on SO_4-Cl relations. Delmelle et al (2000) suggest they represent a mixture of acidic brines, similar to that of the summit hydrothermal system, with HCO_3 steam-heated waters produced in the shallow part of the system.

The crater lake, the lake seepage and eleven thermal springs located on the flanks of Kawah Ijen volcano and near Blawan village (~17 km below the volcano) were collected in January 2017.

Aso volcano, Kyūshū Island, Japan

Formed by the subduction of the Philippine Sea plate beneath the Eurasian plate, Kyūshū Island houses the Aso caldera, one of the largest caldera in the world (24 km NS by 18 km EW). The Aso volcano (32°N, 131°E), situated within the caldera, is a cluster of central volcanoes

consisting of various types of rocks ranging from basalt to rhyolite reflecting different magmatic activities (Ono and Watanabe, 1985). The north (Aso Valley) and south (Nango Valley) part of the caldera are respectively discharged by Kurokawa river and Shirakawa river. Geothermal surface manifestations of Aso volcano are only observed on the central cones with volcanic gas discharge from a hot, highly acidic crater lake at the first crater of Mt. Naka-dake (Saito et al, 2008) and fumarolic gas. Thermal springs are recognized as steam-heated hot springs in this area but formation processes of the hot spring waters, including their relation to magmatic emanation, have not been investigated at Aso volcano (Yamada et al, 2011). Recently, Hosono et al (2018) presented a deep fluid discharge model showing that thermal springs located in the northwestern plain have highly-concentrated dissolved concentrations.

Seventeen thermal springs were collected at Aso by J. Hartmann (University of Hamburg): four of them were sampled twice on both sides of the Aso caldera in three periods: fall 2014, spring 2015 and summer 2016 (n=21).

Yellowstone Plateau Volcanic Field, Wyoming, United States

The continental hotspot of the Yellowstone Plateau Volcanic Field (YPVF) hosts Earth's largest "restless" caldera (Newhall and Dzurisin, 1988). The YPVF (44°N, 110°W) hydrothermal system invokes a single "parent" fluid rich in dissolved CO_2 and H_2S with Cl^- ~ 400 $mg.l^{-1}$ and little HCO_3^- and SO_4^{2-} with temperature of about 340 to 370 °C (Fournier, 1989) and estimated depth between 2 and 5 km. The YPVF is predominantly underlain by two volcanic rock types, the Tertiary andesitic rocks and the Quaternary rhyolitic rocks (Trettin and Bartelli, 1980). Thermal springs, mainly found in Midway Geyser Basin along the Firehole and Gibbon rivers and in Shoshone and Heart Lake Geyser Basin in the Snake river drainage, show neutral to slightly alkaline water and relatively high concentrations of Cl^-, SiO_2 and siliceous sinter deposition (Hurwitz et al, 2007). The range in Cl^- and HCO_3^- in thermal springs are associated with varying degrees of conductive cooling, decompressional boiling and with mixing of different thermal waters (Fournier, 1989). In thermal fluids that do not boil, CO_2 remains in solution forming H_2CO_3 which, as temperature declines, reacts with the wall rock, causing higher HCO_3^- concentrations (Fournier, 1989).

Eight thermal springs from Midway Geyser Basin were collected in April 2015 by S. Hurwitz (USGS).

Kanlaon volcano, Negros Island, Philippines

Formed by the subduction of the Sulu Sea plate along the Negros Trench, the Negros volcanic belt is composed of six volcanoes whose Kanlaon complex stratovolcano (2435 m asl) in the Philippine microplate (~260 km in NS direction) (Cardwell et al, 1980). Located in Negros Island, Kanlaon volcano's (10°N, 123°E) of andesite and basaltic andesite bulk rocks composition (von Bidersee and Pichler, 1995) has extensive hydrothermal system comprised of two independent distinct hydrothermal systems. A mature hydrothermal system represented by Pataan thermal area is characterized by neutral Cl-HCO_3 waters and an immature system represented by Hagdan is characterized by the presence of acid SO_4-waters (e.g., Mambu thermal springs). Within the mature hydrothermal system, the origin of sulfur is linked to the superficial oxidation of H_2S and in contrast within the immature hydrothermal system, sulfur has originated from the disproportionation of magmatic SO_2 or from the fractionation between hydrothermal sulfate and sulfide (SO_4^{2-}/H_2S) pairs (Maximo, 2019).

In this site, one thermal spring was sampled twice by A. Bernard (ULB) in July 2014 (n=2) from Philippian Kanlaon volcano.

Mutnovsky volcano, Kamchatka volcanic belt, Russia

Formed by the subduction of the Pacific Plate beneath the Okhotsk Plate, the Eastern Kamchatka volcanic belt consists of more than 160 volcanoes whose 29 are active (Shapiro et al, 1987). The Mutnovsky volcano (52°N, 158°E; 2322m asl) is a complex of four stratovolcanoes volumetrically dominated by basalt and basaltic andesite, and discrete eruptions of intermediate to felsic magmas have erupted over the approximately 80 ky life of the volcano (Robertson et al, 2013). The geothermal area shows different thermal manifestations: fumaroles within the crater itself, thermal waters of the North Mutnovskaya volcanic zone (North Mutnovsky and Dachny hot springs) and volcano peripheral thermal fields (Vluchinsky hot springs). Eastern Kamchatka is not been well studied, only few publications are available about chemistry in acidic hot springs

of Kamchatka (Karpov et al, 2013). Ca-SO_4 acid hot springs were reported for the crater of the Mutnovsky volcano and the composition of hot springs water changes at the periphery of the volcano, becoming neutral with Na-HCO_3 composition (e.g., K1 and K3) (Chudaev et al, 2017).

Two thermal springs were collected in August 2015 by E. Maters (UCLouvain) on the flanks of Mutnovsky volcano.

3.4 Materials and methods

3.4.1 Sampling

All sampling sites are located in **Fig. 3.1**. Thermal springs were sampled at their outlets from the riverbed. Temperature (°C) and pH were measured *in situ*. Redox potential (Eh; mV) was measured in thermal springs of Kawah Ijen *in situ*. Thermal springs samples were filtered within 24 h after collection at 0.45 μm through polycarbonate membranes, and stored at 4 °C in the dark in pre-washed polypropylene (PP) bottles. One aliquot was acidified at 0.5% suprapure HNO_3 "to determine major and trace element concentrations, Ge/Si ratios, and Si isotope signatures, and one aliquot was non-acidified to determine anions.

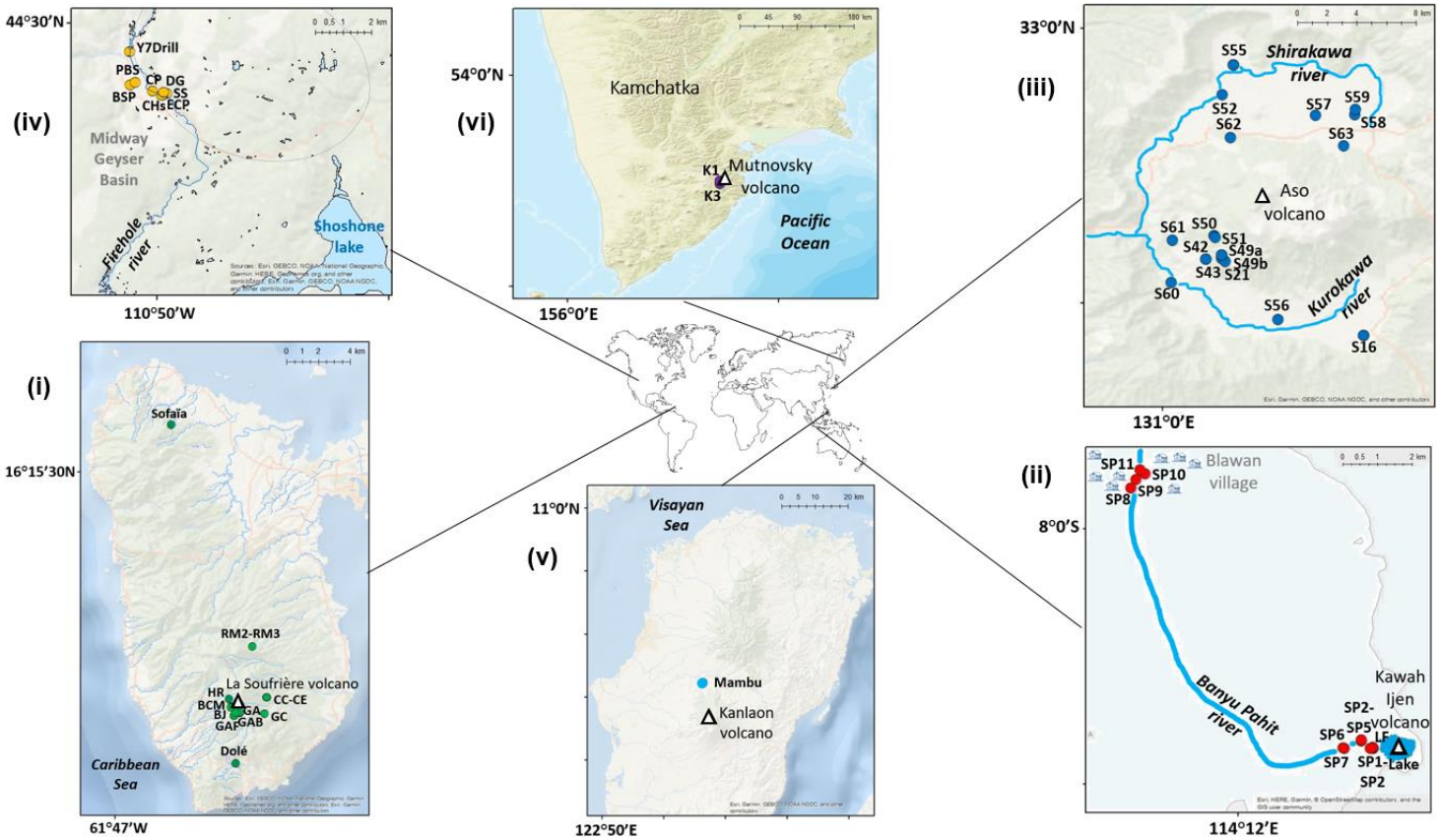
(iv)
44°30'N
110°50'W
Y7Drill
PBS
CP
DG
BSP
SS
CHs
ECP
Midway Geyser Basin
Firehole river
Shoshone lake
(vi)
54°0'N
156°0'E
Kamchatka
K1
K3
Mutnovsky volcano
Pacific Ocean
(iii)
33°0'N
131°0'E
S55
Shirakawa river
S52
S62
S57
S59
S58
S63
Aso volcano
S61
S50
S51
S42
S49a
S49b
S43
S21
S60
S56
Kurokawa river
S16
(i)
16°15'30N
61°47'W
Sofaïa
RM2-RM3
La Soufrière volcano
HR
BCM
BJ
GA
CC-CE
GAB
GC
GAF
Dolé
Caribbean Sea
(v)
11°0'N
122°50'E
Visayan Sea
Mambu
Kanlaon volcano
(ii)
8°0'S
114°12'E
SP11
SP10
SP9
SP8
Blawan village
Banyu Pahit river
Kawah Ijen volcano
SP2-
SP5
SP6
LF
SP7
SP1-Lake
SP2

Fig. 3.1: Location of thermal springs collected in (i) Basse-Terre Island (green), (ii) Java Island (red), (iii) Kyūshū Island (dark blue), (iv) YPVF (yellow), (v) Negros Island (light blue) and (vi) Kamchatka (purple). This color code will be used in figures comparing multiple sites. La Soufrière volcano, Kawah Ijen volcano, Aso volcano, Kanlaon volcano and Mutnovsky volcano are represented in the appropriated maps (white triangle).

3.4.2 Water elemental analyses

The concentrations of Ca, Na, Mg, K, Al, Fe and Si in the water samples were determined by inductively-coupled plasma-optical emission spectrometry (ICP-OES; iCAP 6500 Thermo Fisher Scientific). The accuracy on majors elements (Ca, Na, Mg, K, Al, Fe and Si) analyses was assessed using the trueness (± 3%, ± 4%, ± 1%, ± 7%, ± 4%, ± 2% and ± 4%; respectively) on the river water reference material SLRS-5 (Yeghicheyan et al, 2013) and the analytical precision (± 0.5%) for each element. The detection limit are 0.05, 0.43, 0.21, 0.26, 0.37, 0.18 and 0.36 $\mu mol.l^{-1}$ for Ca, Na, Mg, K, Al, Fe and Si, respectively. Anions (SO_4^{2-}, Cl^-, NO_3^-) were measured by ion chromatography (Dionex ICS2000, column: AG15/AS15). The accuracy on SO_4^{2-}, Cl^- and NO_3^- was assessed by using the trueness (± 3%, ± 4% and ± 4%; respectively) on river water certified reference material LGC6025 (UKAS, 2014) and the analytical precision (± 2%) for each anion. The detection limit are 1.5, 3.1 and 1.6 $\mu mol.l^{-1}$ for SO_4^{2-}, Cl^- and NO_3^-, respectively. Alkalinity ($\mu mol.l^{-1}$) for thermal springs from Basse-Terre Island was determined on the same day the samples were collected by performing three replicates and using an automatic titrator (Metrohm 916 Ti-Touch titrator). Total dissolved solids (TDS; $\mu mol.l^{-1}$) were obtained by summing major elements (Ca, Na, Mg, K) and SiO_2 concentrations in thermal waters.

3.4.3 Ge concentration measurements by ICP-MS

The germanium concentration was measured on samples from 15 thermal waters of La Soufrière volcano (n=26), 13 thermal waters of Kawah Ijen volcano (n=13), 17 thermal waters of Aso volcano (n=21), 8 thermal waters of YPVF (n=8), one thermal water of Kanlaon volcano (n=2) and 2 thermal waters of Mutnovsky volcano by inductively coupled plasma mass spectrometry (ICP-MS, ICAPQ Thermo Fisher Scientific) using ^{74}Ge isotope (detection limit = 0.04 $nmol.l^{-1}$). Accuracy and long-term

repeatability were assessed by running international riverine standards SLRS-5 (0.083 ± 0.014 nmol.l^{-1}; n=3) and SLRS-6 (0.097 ± 0.0069 nmol.l^{-1}; n=3) (Yeghicheyan et al, 2013), and one in-house standard within each analytical session between July 2017 and June 2018 (GAB, one thermal spring of La Soufrière volcano: 23.95 ± 0.096 nmol.l^{-1}; n=14). The analytical precision is ± 8% for Ge concentrations < 0.001 µg.l^{-1} and 4% for Ge concentrations > 0.001 µg.l^{-1}. The limit of detection for Ge is 0.04 nmol.l^{-1}. Ge/Si ratios (expressed in µmol.mol^{-1}) were calculated using Si concentrations measured by ICP-OES (**section 3.4.2**), and Ge concentrations measured by ICP-MS. The precision on the Ge/Si ratio is 10% (SD).

3.4.4 Silicon isotope analysis

Sample purification

Silicon isotope measurements in thermal waters are scarce given the complexity of the sample matrices involving high concentrations in anions such as SO_4^{2-} and Cl^-. To prevent from matrix effects in mass spectrometry, silicon has been purified using a two-step column chemistry: anion-exchange resin (Biorad AG MP-1) and cation-exchange resin (Biorad AG50W-X12) following the method developed by Gaspard et al, submitted.

For the hyper acid thermal waters from Kawah Ijen volcano, a pre-treatment was needed before the two-step column chemistry for samples with SO_4^{2-} > 20 000 mg.l^{-1} to avoid overtaking the anion-exchange resin capacity. Sulfates were purified by adding suprapure $Ba(NO_3)_2$ in a ratio of 3 × 1g $Ba(NO_3)_2$ /g SO_4 in the sample considering $Ba(NO_3)_2$ in excess of 10%. This technique is commonly used for S isotopes measurements (e.g., Delmelle et al, 1998): sulfates are retained in the barytine precipitates ($BaSO_4$). The aliquot was filtered at 0.45 µm through polycarbonate membranes. The SO_4^{2-} removal (< 0.50 µmol.l^{-1}, i.e., below the detection limit values for S by ICP-OES) and Si recovery (>95%) in the dissolved phase were verified. Following this step, NaOH 10 mol.l^{-1} was used to raise the pH in solution at 2 before the anion-exchange column step from Gaspard et al, submitted.

For thermal waters with high Si concentrations (i.e., the thermal springs from YPVF) in the range of saturation for amorphous silica (~1700-2300 µmol.l^{-1} at 25 °C), a different pre-treatment was needed before the two-

step column chemistry to prevent from Si loss by precipitation. The water samples were dried down at 100 °C and dissolved with a 0.125N NaOH leaching then neutralized with suprapure HNO_3. The Si recovery was verified (>95%).

After the two-step column chemistry, the Si recovery was always > 98% and the concentrations of Na, SO_4^{2-} and Cl^- in the purified solution were < 0.43, 1.5 and 3.1 μmol.l^{-1}, respectively (i.e., below the detection limit values). The blank level was < 0.36 μmol Si.l^{-1}, i.e., the detection limit for Si by ICP-OES.

Mass spectrometry

Silicon isotope compositions were measured in 9 thermal waters of La Soufrière volcano (n=12), 13 thermal waters of Kawah Ijen volcano (n=13), 9 thermal waters of Aso volcano (n=11), 7 thermal waters of YPVF (n=7), one thermal water of Kanlaon volcano (n=2) and 2 thermal waters of Mutnovsky volcano (n =2). Silicon isotope compositions were analyzed by MC-ICP-MS (Neptune Plus™ High Resolution Multicollector ICP-MS, Thermo Fisher Scientific, Earth & Life Institute, UCLouvain, Belgium) in wet plasma mode in medium resolution (Δm/m~6000) using a PFA nebulizer of 100 μl.min^{-1} uptake rate. The instrumental mass bias was corrected using the standard-sample bracketing technique and an external Mg doping (Cardinal et al, 2003). The analyses were performed in 2% HNO_3 matrix, with a typical sensitivity of 7V for 2 mg.l^{-1} Si and an instrumental blank <30 mV. Silicon isotope compositions are expressed in relative deviations of $^{30}Si/^{28}Si$ ratio from the NBS-28 reference standard using the common δ-notation (‰) as follow: $\delta^{30}Si=[(^{30}Si/^{28}Si)_{sample}/(^{30}Si/^{28}Si)_{NBS\text{-}28} -1]\times1000$. One measurement comprises 30 cycles with 4.2 s integration time corrected by blank in a 2% HNO_3 matrix. Each single δ-value (n) represents one sample run and two bracketing standards. $\delta^{30}Si$-values are reported as the mean of replicate isotopic analyses ± standard deviation (SD). Quality control of mass bias was performed by ensuring that $\delta^{30}Si$ and $\delta^{29}Si$ measurements fit onto a mass-dependent fractionation array, supporting the interference-free determination of all three Si isotopes via MC-ICP-MS (**Suppl. Mat. 3.1**). The long-term precision and accuracy of the MC-ICP-MS $\delta^{30}Si$ analyses were assessed from multiple measurements of reference materials prepared using two-step column chemistry performed within each analytical session over a period of nine months. The values obtained for diatomite ($\delta^{30}Si$ of 1.34 ± 0.07 ‰, SD, n=7), BHVO-2 ($\delta^{30}Si$ of -0.37 ±

0.07 ‰, SD, n=3) and quartz Merck (δ^{30}Si of 0.04 ± 0.05 ‰, SD, n=9) are consistent with those reported earlier (Reynolds et al, 2007; Abraham et al, 2008).

3.4.5 Statistical data analysis

To test for multivariate similarity (i.e., geochemical likeness) between thermal springs from the six hydrothermally-active volcanic regions studied, we performed a principal component analysis (PCA; **Suppl. Mat. 3.2** for definitions) on the element concentrations measured in all thermal waters including H^+ concentrations calculated from pH values, after centered logratio transformation of the data using rgr package (clr function). The R software packages FactoMineR (Le et al, 2008) was used.

3.5 Results

The temperature, pH, TDS, alkalinity and major element concentrations of the thermal springs collected in La Soufrière volcano, Kawah Ijen volcano, Aso volcano, YPVF, Kanlaon volcano and Mutnovsky volcano are shown in **Table 3.1**. The abbreviations used below for referring to the thermal spring are explained in **Table 3.1**. The ion balance of the water samples never exceeds 10%.

Table 3.1: General parameters (temperature, pH, TDS) and major element concentrations of thermal springs collected on Basse-Terre Island (La Soufrière, Guadeloupe), Java Island (Kawah Ijen, Indonesia), Kyūshū Island (Aso, Japan), Yellowstone Plateau Volcanic Field (YPVF, USA), Negros Island (Kanlaon, Philippines) and Kamchatka (Mutnovsky, Russia). Some locations have been sampled more than once at different sampling dates.

	Sampling date	Sample	Label	Type	Temperature	pH	TDS	Ca	Na	Mg	K	Al	Fe	Si	SO_4	Cl	HCO_3	NO_3	F
	dd.mm.yy				°C		µmol.l^{-1}												
La Soufrière	27.01.15	Ravine Marchand 2	RM2(1)	acid SO_4-waters	21.5	3.3	5307	1268	589	442	68	226	54	1375	2291	813	0	n.d	7
	12.10.17	Ravine Marchand 2	RM2(2)	acid SO_4-waters	21.6	3.6	6334	1863	696	602	75	167	54	1449	2697	1336	0	n.d	n.d
	27.01.15	Ravine Marchand 3	RM3(1)	acid SO_4-waters	41.1	5.5	13492	4029	1948	1605	384	n.d	208	2585	4281	3960	0	n.d	16
	12.10.17	Ravine Marchand 3	RM3(2)	acid SO_4-waters	43.3	5.3	14995	4416	2221	1765	431	n.d	253	2882	4788	5141	0	n.d	n.d
	17.11.17	Chute du Carbet	CE(1)	acid SO_4-waters	21.0	5.3	11788	5115	1170	1646	148	16	1200	1735	8136	301	114	n.d	10
	15.03.18	Chute du Carbet	CE(2)	acid SO_4-waters	20.9	5.3	11945	5217	1196	1655	148	17	1170	1744	8752	315	130	n.d	n.d
	29.01.15	Bain Jaune	BJ(1)	acid SO_4-waters	29.2	4.9	8151	1935	1334	786	133	3	n.d	1853	2734	1132	7	n.d	18
	14.11.17	Bain Jaune	BJ(2)	acid SO_4-waters	29.6	5.2	7849	1819	1290	710	128	4	n.d	1825	2497	958	12	n.d	17
	29.01.15	Pas du Roy	PR(1)	acid SO_4-waters	34.1	5.4	10767	2706	2008	1306	267	n.d	42	2095	3898	1641	73	n.d	31
	14.11.17	Pas du Roy	PR(2)	acid SO_4-waters	33.9	5.7	10569	2622	1997	1272	230	n.d	42	2080	3559	1537	116	26508	32
	29.01.15	Tarade	TA(1)	acid SO_4-waters	42.0	5.5	15865	4276	3796	2210	485	n.d	n.d	2384	6076	3393	160	3	23
	14.11.17	Tarade	TA(2)	acid SO_4-waters	43.5	5.8	16859	4693	3941	2294	515	n.d	n.d	2533	6155	3841	320	102	22
	20.10.17	Habitation Revel	HR	acid SO_4 waters	32.6	6.5	4549	484	1020	209	91	n.d	n.d	1284	175	241	1070	7	3
	30.01.15	Bain Chaud de Matouba	BCM(1)	acid SO_4 waters	58.5	5.9	10100	6629	1551	521	208	n.d	n.d	557	7491	573	93	n.d	104
	20.10.17	Bain Chaud de Matouba	BCM(2)	acid SO_4 waters	58.3	5.6	10159	6595	1610	537	208	1	n.d	566	7759	577	96	n.d	104
	28.01.15	Chute du Carbet	CC(1)	alkaline HCO_3-waters	43.0	6.7	9891	1698	2949	1218	438	n.d	n.d	1678	847	278	1667	n.d	n.d
	07.11.17	Chute du Carbet	CC(2)	alkaline HCO_3-waters	42.0	6.7	9283	1608	2636	1117	393	n.d	n.d	1651	847	214	1743	n.d	n.d
	04.02.15	Dolé	Dolé	alkaline HCO3-waters	30.8	8.3	7085	1293	1690	903	174	n.d	n.d	1415	843	870	3209	38	7
	28.01.15	Grosse corde	GC(1)	neutral Cl-waters	38.3	6.3	12528	2801	4047	1790	522	n.d	n.d	1576	2272	4749	1158	9	n.d
	07.11.17	Grosse corde	GC(2)	neutral Cl-waters	37.5	6.5	11620	2590	3727	1651	495	n.d	n.d	1477	2489	4468	1463	n.d	n.d
	29.01.15	Gallion	GA(1)	mixed Cl-SO_4 waters	48.0	4.6	18457	6635	2545	2623	492	1	287	2882	6638	7930	11	n.d	54
	14.11.17	Gallion	GA(2)	mixed Cl-SO_4 waters	48.6	4.8	16130	5649	2184	2136	454	3	275	2669	6281	7194	17	78	57
	29.01.15	Gallion Blanc	GAB(1)	mixed Cl-SO_4 waters	42.8	4.6	16710	5692	2455	2546	444	7	111	2607	5842	7295	9	n.d	34
	14.11.17	Gallion Blanc	GAB(2)	mixed Cl-SO_4 waters	44.1	4.8	16382	5414	2364	2369	416	5	159	2721	5568	7793	13	n.d	36
	29.01.15	Gallion froid	GAF	mixed Cl-SO_4 waters	21.7	4.5	4915	905	485	281	55	26	4	1491	1211	517	3	n.d	3
	02.02.15	Sofaïa	Sofaïa	mixed Cl-SO_4 waters	29.3	3.8	1834	97	435	69	25	34	5	565	358	422	0	n.d	2
Kawah Ijen	31.01.17	Lake	Lake	hyper acid Cl-SO_4 waters	22.8	0.6	51787	11602	16964	10142	10486	72642	14683	1212	247223	215182	-	-	26617
	31.01.17	Lake seepage	LF	hyper acid Cl-SO_4 waters	19.2	1.3	32308	14734	6490	3870	3443	26314	5499	1764	89248	57915	-	-	7927
	31.01.17	Spring 1	SP1	hyper acid Cl-SO_4 waters	35.2	0.7	131661	19478	49239	28924	30820	215110	44189	1497	669232	594475	-	-	74710
	31.01.17	Spring 2	SP2	hyper acid Cl-SO_4 waters	32.0	0.2	134452	21109	49239	29574	31331	218112	44767	1496	651188	578096	-	-	72830
	29.01.17	Spring 3	SP3	hyper acid Cl-SO_4 waters	33.7	0.1	140669	24798	50718	29928	32099	223468	45434	1462	675769	600347	-	-	74709
	29.01.17	Spring 4	SP4	hyper acid Cl-SO_4 waters	29.3	0.2	105420	22285	35799	21835	21975	156088	33195	1649	457034	400627	-	-	52923
	29.01.17	Spring 5	SP5	hyper acid Cl-SO_4 waters	27.2	0.3	111551	22408	38178	23464	24055	167355	37304	1612	497100	425090	-	-	56217
	29.01.17	Spring 6	SP6	hyper acid Cl-SO_4 waters	24.9	0.8	57673	11757	18791	11825	11609	81815	18833	1726	240011	198636	-	-	30982
	29.01.17	Spring 7	SP7	hyper acid Cl-SO_4 waters	25.1	0.7	102359	19620	35242	21300	22888	156681	36189	1547	457095	393386	-	-	47586
	30.01.17	Spring 8	SP8	mixed neutral HCO_3-SO_4 waters	43.6	6.6	20768	2430	8652	3148	1152	n.d	40	2519	2456	2334	-	-	22
	30.01.17	Spring 9	SP9	mixed neutral HCO_3-SO_4 waters	45.1	6.6	23551	2899	9382	4258	1293	2	35	2674	3092	3006	-	-	24
	30.01.17	Spring 10	SP10	mixed neutral HCO_3-SO_4 waters	41.1	6.8	23250	3262	8425	4707	1039	3	45	2720	3505	3833	-	-	31
	31.01.17	Spring 11	SP11	mixed neutral HCO_3-SO_4 waters	32.6	6.8	14741	1537	5829	2395	859	2	18	1928	1463	1323	-	-	17

- : not measured; n.d : not detected

	Season/Sampling date	Sample	Label	Type	Temperature	pH	TDS	Ca	Na	Mg	K	Al	Fe	Si	SO_4	Cl	HCO_3	NO_3	F
	dd.mm.yy				°C		$\mu mol.l^{-1}$												
Aso	spring 15	hot spring	S21	acid SO_4-waters	42.3	2.1	7169	897	784	492	269	-	-	2211	9499	145	0	5	31
	spring 15	hot spring	S43	acid SO_4-waters	66.2	2.4	6150	659	439	453	176	1411	204	2069	8014	78	0	n.d	36
	spring 15	hot spring	S49a	acid SO_4-waters	41.0	3.4	7930	662	927	491	284	259	24	2603	2590	149	0	n.d	25
	spring 15	hot spring	S49b	acid SO_4-waters	45.9	5.8	8671	916	1268	805	436	0.06	0.05	2453	1302	191	0	333	22
	fall 16	hot spring	S52	acid SO_4-waters	23.5	6.7	19049	4148	6037	3477	538	n.d	0.80	2268	5853	3225	500	3	274
	fall 16	cold spring	S56	acid SO_4-waters	16.2	6.0	4825	844	577	411	108	0.34	0.02	1349	1119	243	153	24	21
	fall 16	cold spring	S57	acid SO_4-waters	15.7	6.8	4899	874	897	651	147	0.05	0.02	1090	1265	610	617	14	80
	spring 15	cold spring	S16	alkaline HCO3-waters	15.6	8.0	3133	331	298	231	89	0.20	0.13	1022	58	86	1235	6	6
	fall 16	cold spring	S16	alkaline HCO_3-waters	16.2	7.8	2904	334	257	222	81	0.05	0.01	940	47	65	1241	5	4
	fall 14	hot spring	S42	alkaline HCO_3-waters	46.0	6.0	11234	2387	2642	1263	404	0.48	13.91	2122	1779	162	1459	1	8
	spring 15	hot spring	S42	alkaline HCO_3-waters	46.0	6.1	11785	2340	2494	1216	505	0.04	0.95	2446	1688	152	2486	1	8
	fall 16	hot spring	S50	alkaline HCO_3-waters	39.8	6.5	8229	2019	446	931	158	n.d	0.05	2186	570	69	3354	7	2
	sum 16	hot spring	S55	alkaline HCO_3-waters	42.9	7.1	12857	793	6372	1052	575	0.15	2.24	1901	2972	1267	2566	2	65
	fall 16	cold spring	S58	alkaline HCO_3-waters	15.9	7.0	3974	631	497	376	125	0.02	0.01	1097	552	253	958	36	27
	fall 16	cold spring	S59	alkaline HCO_3-waters	15.7	6.9	4253	737	590	442	155	0.01	0.01	1090	646	306	941	43	35
	fall 16	hot spring	S60	alkaline HCO_3-waters	26.5	7.0	7317	570	2670	719	304	0.03	0.02	1428	494	229	3270	3	28
	fall 16	hot spring	S61	alkaline HCO_3-waters	43.4	7.3	15063	672	8387	949	959	0.13	6.13	1916	1836	906	6631	0.4	24
	fall 16	hot spring	S62	alkaline HCO_3-waters	52.6	6.9	13343	623	7133	824	819	n.d	0.11	1844	1606	762	4266	0.4	20
	fall 16	hot spring	S51	mixed neutral HCO_3-SO_4 waters	25.7	7.6	5510	461	738	362	272	0.12	0.01	1720	1149	75	762	185	25
	fall 16	hot spring	S55	mixed neutral HCO_3-SO_4 waters	40.8	7.2	12079	723	5823	953	523	0.07	2.60	1898	2606	1187	2397	0.2	53
	fall 16	hot spring	S63	mixed neutral HCO_3-SO_4 waters	19.8	7.2	7885	932	2824	1195	224	0.00	0.03	1268	2060	846	1645	5	48
YPVF	12.04.15	Y7 Drillhole (70 m depth)	Y7Drill	neutral Cl-waters	135.6	6.9	31805	14	18236	n.d	2136	12	0.29	5341	111	7528	-	n.d	-
	13.04.15	Black Sand Pool (6 m depth)	BSP	neutral Cl-waters	94.2	8.7	30066	8	19583	n.d	541	13	0.17	4647	183	10172	-	n.d	-
	14.04.15	Punch Bowl Spring (4.4 m depth)	PBS	neutral Cl-waters	93.0	7.6	30963	9	19243	n.d	482	7	n.d	5252	179	8787	-	n.d	-
	15.04.15	Crested Pool (11.33 m depth)	CP	neutral Cl-waters	111.4	9.2	29119	10	17501	n.d	493	13	n.d	5198	219	11040	-	n.d	-
	16.04.15	East Chinaman Pool (5 m depth)	ECP	neutral Cl-waters	95.2	7.6	25987	18	14326	n.d	464	6	n.d	5229	217	11955	-	n.d	-
	16.04.15	Chinese Springs (4.6 m depth)	CHs	neutral Cl-waters	97.2	7.8	24082	16	13921	n.d	438	6	n.d	4540	237	11454	-	n.d	-
	16.04.15	Sulfide Spring	SS	neutral Cl-waters	90.1	6.6	10485	70	4833	12	394	2	0.54	2421	319	3144	-	n.d	-
	16.04.15	Dome Geyser	DG	neutral Cl-waters	88.5	7.1	27474	13	14554	0.4	536	4	n.d	5786	451	11489	-	n.d	-
Kanlaon	30.07.14	Mambu 6 dilué 1	Mambu1	acid SO_4-waters	-	-	1929	92	444	33	73	n.d	n.d	602	766	94	-	35	-
	30.07.14	Mambu 6 non dilué 2	Mambu2	acid SO_4-waters	-	-	4918	249	641	98	170	1	0	1759	2025	197	-	n.d	-
Mutnovsky	08.15	Kamchatka1	K1	alkaline HCO_3-waters	-	-	22446	9506	2392	2551	307	6115	1128	3596	16477	94482	-	n.d	-
	08.15	Kamchatka3	K3	alkaline HCO_3-waters	-	-	3608	61	200	45	28	n.d	0	1531	489	155	-	n.d	-

- : not measured; n.d : not detected.

3.5.1 Field parameters and elemental composition of the thermal springs

Based on **Fig. 3.2b**, the thermal waters from the six sites were grouped into four thermal waters types as defined in previous studies (White, 1957; Ellis and Mahon, 1964, 1977; Giggenbach, 1988): acid SO_4-Cl, acid SO_4-, alkaline HCO_3- and neutral Cl-waters. Acid SO_4-Cl waters with pH<2 are referred as hyper acid SO_4-Cl waters in the classification, a criteria met for acid SO_4-Cl waters from Kawah Ijen (pH<0.8; **Table 3.1**). We identified two additional thermal waters as "mixed" waters: mixed acid SO_4-Cl in La Soufrière volcano originated from mixing between acid SO_4-waters and alkali/neutral Cl-waters (Brombach et al, 2000) and mixed neutral HCO_3-SO_4 in Kawah Ijen volcano representing a mixture of hyper acid SO_4-Cl waters with HCO_3 steam-heated waters produced in the shallow part of the system (Delmelle et al, 2000).

The hyper acid SO_4-Cl waters include seven thermal springs, the acid lake and lake seepage from Kawah Ijen volcano, the acid SO_4-waters include fifteen thermal springs from La Soufrière volcano, seven thermal springs from Aso volcano and one thermal spring from Kanlaon volcano. The alkaline HCO_3-waters include three thermal springs from La Soufrière volcano, eleven thermal springs from Aso volcano and two thermal spring from Mutnovsky volcano. The neutral Cl-waters include two thermal springs from La Soufrière volcano and eight thermal springs from YPVF. The mixed acid SO_4-Cl waters include six thermal springs from La Soufrière volcano, whereas the mixed neutral HCO_3-SO_4 waters include four thermal springs from Kawah Ijen volcano and three thermal springs from Aso volcano.

The thermal springs grouping is in agreement with the thermal waters chemistry reported in the literature for these sites, i.e., La Soufrière volcano (Brombach et al, 2000; Villemant et al, 2014; Dessert et al, 2015), Kawah Ijen volcano (Bernard and Delmelle, 1994; Delmelle et al, 2000), Aso volcano (Hosono et al, 2018), YPVF (Hurwitz et al, 2007; Hurwitz and Lowenstern, 2014), Kanlaon volcano (Maximo, 2019) and Mutnovsky volcano (Chudaev et al, 2017).

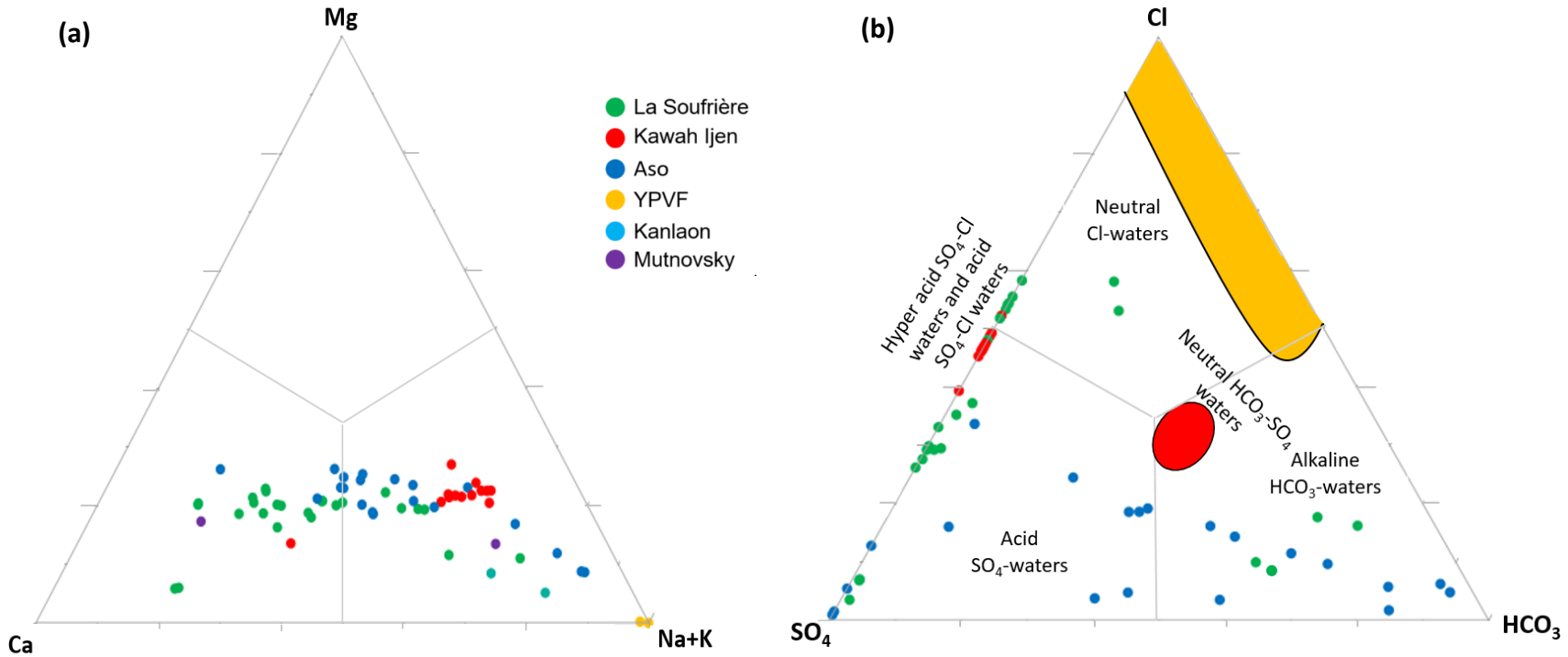

Fig. 3.2: Ternary diagrams of the major cation (a) and anion (b) composition of the thermal springs (circle) studied (following Giggenbach, 1988). The HCO_3 concentration is calculated based on the charge balance and is not available for waters from Kanlaon and Mutnovsky volcano. Literature data: thermal springs from YPVF (colored in yellow; Hurwitz and Louvenstern, 2014); thermal springs from Blawan in Kawah Ijen volcano (colored in red; Delmelle et al, 2000).

The highest temperatures are measured for the neutral Cl-waters (up to 135.6 °C, 70 m depth) (**Fig. 3.3a**). The hyper acid SO_4-Cl, acid SO_4- and alkaline HCO_3-waters display the same range in temperature (19.2-48.0 °C, 15.7-66.2 °C and 15.6-52.6 °C, respectively) than the mixed acid SO_4-Cl and mixed neutral HCO_3-SO_4 waters (21.7-48.6 °C and 19.8-45.1 °C, respectively) (**Fig. 3.3a**).

The hyper acid SO_4-Cl and acid SO_4-waters display pH ranging from 0.1 to 4.6 and 2.1 to 6.8, respectively (**Fig. 3.3b**). The alkaline HCO_3- and neutral Cl-waters have pH values in the range 6.0-8.3 and 6.3-9.2, respectively (**Fig. 3.3b**). The mixed acid SO_4-Cl waters have lower pH values (3.8-4.8) than the mixed neutral HCO_3-SO_4 waters (6.6-7.6). Regarding the TDS, the highest values (32308-140669 $\mu mol.l^{-1}$) are measured in the hyper acid SO_4-Cl waters relative to the other thermal springs water types (**Fig. 3.3c**).

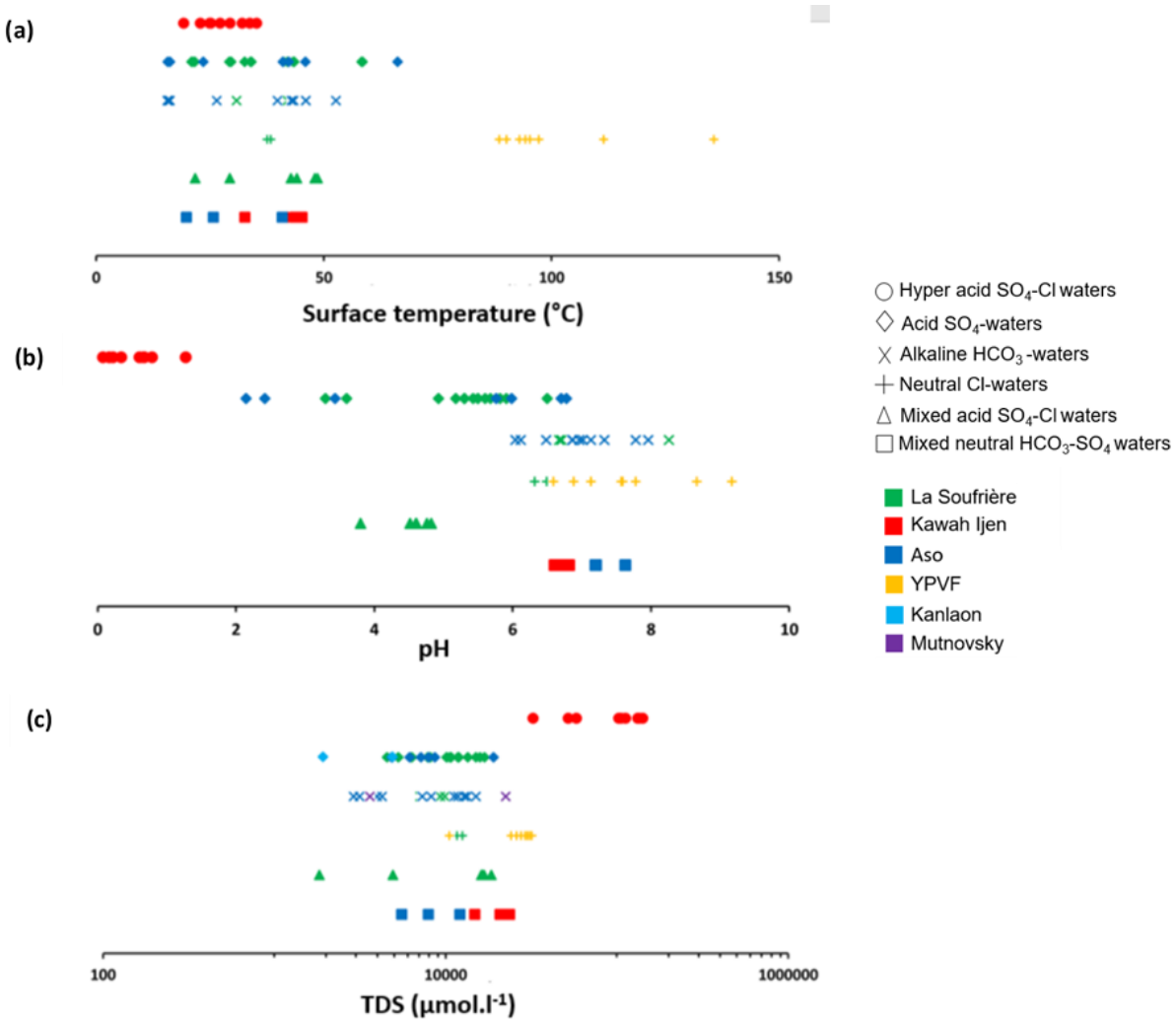

Fig. 3.3: (a) Surface temperature (°C), (b) pH and (c) TDS (µmol.l^{-1}) in the different water types (represented by symbols; hyper acid SO_4-Cl, acid SO_4-, alkaline HCO_3-, neutral Cl-waters and mixed thermal springs, i.e., acid SO_4-Cl, neutral HCO_3-SO_4 waters) collected in the different sites (color-coded; La Soufrière volcano, Kawah Ijen volcano, Aso volcano, YPVF, Kanlaon volcano and Mutnovsky volcano). The surface temperature and pH are not available for thermal springs from Kanlaon and Mutnovsky volcanoes.

The thermal springs display a large range of Si concentrations with the lowest values found in the acid SO_4-waters (557 µmol.l^{-1}; BCM(1)) and the highest values in the neutral Cl-waters (5786 µmol.l^{-1}; DG) (**Table 3.1**). The mixed acid SO_4-Cl waters are characterized by Si concentrations ranging from 565 to 2882 µmol.l^{-1} and the mixed neutral HCO_3-SO_4 waters are characterized by Si concentrations (1268-2720 µmol.l^{-1}) in the same range as the alkaline HCO_3-waters from which they were mixed (940-2446 µmol.l^{-1}).

The highest SO_4^{2-} and Cl^- concentrations correspond to the hyper acid SO_4-Cl waters from Kawah Ijen volcano (89248-675769 µmol.l^{-1} and 57915-600347 µmol.l^{-1}, respectively). The hyper acid SO_4-Cl and mixed acid SO_4-Cl waters have lower SO_4^{2-}/Cl^- ratio (1.1-1.5 and 0.8-2.3, respectively) than those reported in acid SO_4-waters and mixed neutral HCO_3-SO_4 waters (0.7-103.3 and 0.9-15.3, respectively) (**Fig. 3.2b**). Bicarbonates are the major anions in alkaline HCO_3-waters (941-6631 µmol.l^{-1}) also generally associated with Na as major cation (3727-19583 µmol.l^{-1}).

The hyper acid SO_4-Cl, acid SO_4- and mixed acid SO_4-Cl waters display generally higher values for the Ca/Mg ratio (0.7-3.8, 1.4-3.2 and 1.3-12.7, respectively) than for the Na/Mg ratio (**Fig. 3.2a**). The opposite is observed for the alkaline HCO_3-, the neutral Cl- and mixed neutral HCO_3-SO_4 waters (**Fig. 3.2a**).

The hyper acid SO_4-Cl, the acid SO_4- and the alkaline HCO_3-waters fall within the "immature group" in a $K.100^{-1} - Na.1000^{-1} - Mg^{0.5}$ and are far from equilibrium with K- ($KAlSi_3O_8$) and Na- ($NaAlSi_3O_8$) feldspars (**Fig. 3.4**; Giggenbach, 1988). Immature waters are generally acidic waters due to the continuous feeding by magmatic sources exceeding protons consumption by chemical weathering. This is also the case for the mixed waters acid SO_4-Cl and neutral HCO_3-SO_4 waters. On the opposite, the neutral Cl-waters (with high pH (6.6-8.7) and TDS (10485-31805 µmol.l^{-1}) values) fall mainly within "mature waters" (the protons consumption by chemical weathering exceeds their supply by magmatic sources). Two exceptions among neutral Cl-waters are the GC(1), GC(2) thermal springs from La Soufrière volcano falling into the "immature group".

A PCA was performed on the 72 thermal spring samples to test geochemical likeness between element concentrations (**Fig. 3.5**). The two principal components explained 78% of the data variance (**Fig. 3.5c**). The principal component 1 (46% of the data variance) allowed the grouping of

Si, K, Na concentrations with positive scores and H^+ and Fe concentrations with negatives scores (**Fig. 3.5a**). The principal component 2 (32% of the data variance) associated Mg, SO_4 and Ca concentrations with positives scores and Cl and Ge concentrations with negative scores (**Fig. 3.5a**). Two types of thermal waters are separated from the others (**Fig. 3.5d**): the hyper acid SO_4-Cl waters from Kawah Ijen volcano (**Fig. 3.5b**; negatively correlated with the first principal component) mainly driven by dissolved concentration in H^+ and Fe, supporting the solubilization of Fe in low pH, and the mature neutral Cl-waters from YPVF (**Fig. 3.5b**; negatively correlated with the second principal component) mainly driven by Cl and Ge concentrations.

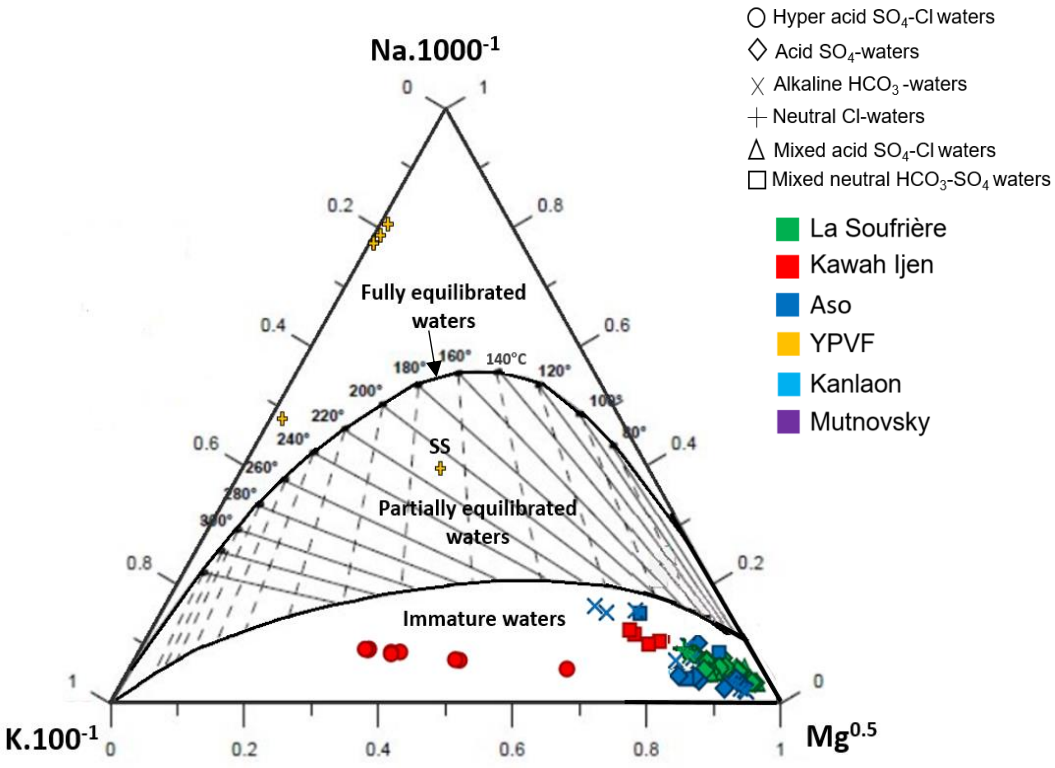

Fig. 3.4: Ternary diagram of the relative Na, K , Mg content (Giggenbach, 1988) in the different types of thermal waters (represented by symbols; hyper acid SO_4-Cl, acid SO_4-, alkaline HCO_3-, neutral Cl-waters and mixed thermal springs, i.e., acid SO_4-Cl, neutral HCO_3-SO_4 waters) collected in the different sites (color-coded; La Soufrière volcano, Kawah Ijen volcano, Aso volcano, YPVF, Kanlaon volcano and Mutnovsky volcano). SS = Sulfide Spring.

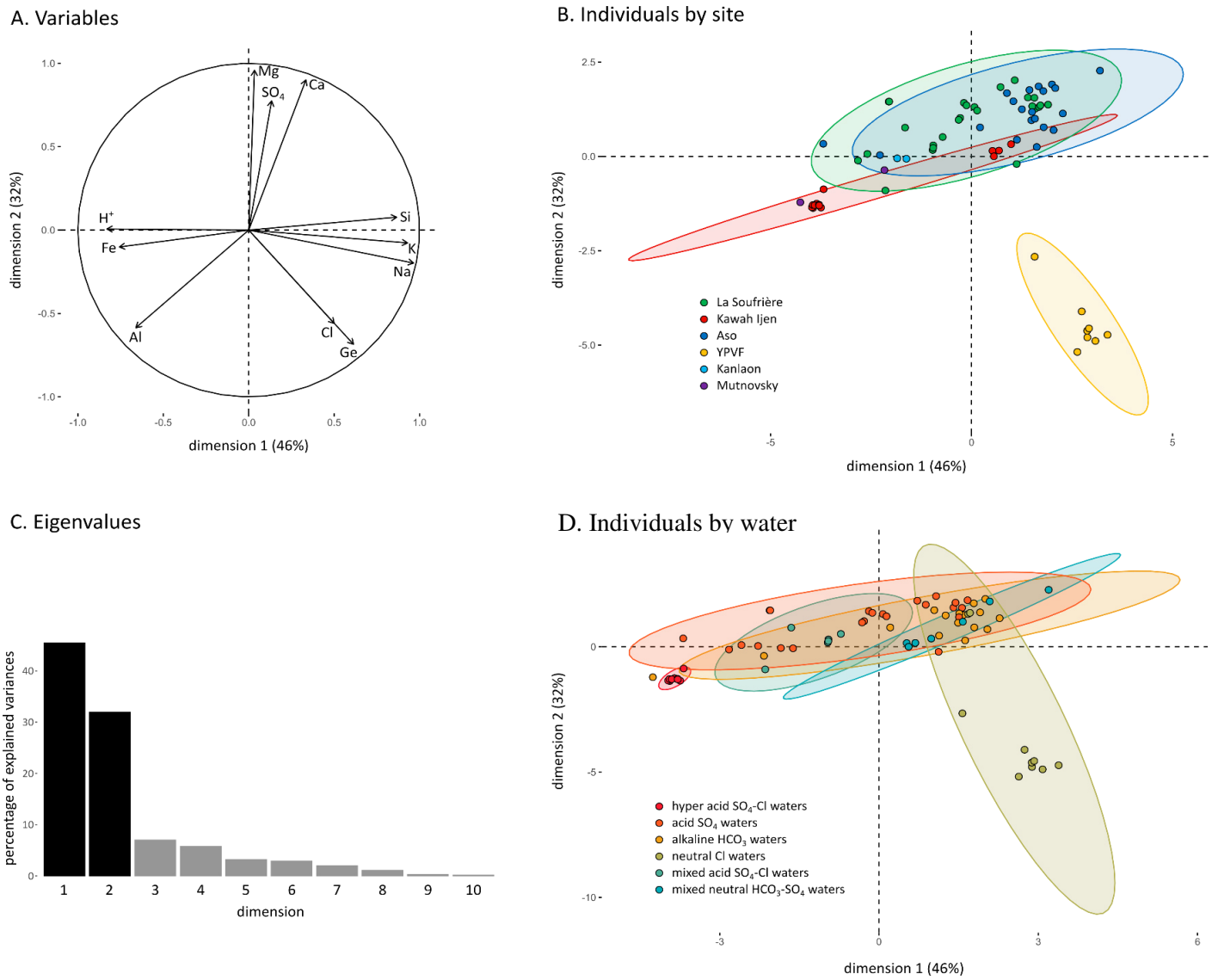

Fig. 3.5: Plots of the principal component analysis (PCA) with (a) variables (concentrations in H, Ca, Na, Mg, K, Al, Fe, Si, SO_4, Cl, Ge), (b) individuals of the 56 thermal springs (total of 72 samples) from the six hydrothermally-active volcanic regions studied (La Soufrière volcano (green), Kawah Ijen volcano (red), Aso volcano (dark blue), YPVF (yellow), Kanlaon volcano (light blue) and Mutnovsky volcano (purple)), (c) eigenvalues and (d) individuals by the six thermal waters types.

3.5.2 Ge/Si ratio and Si isotope composition of the thermal springs

The Ge/Si ratio and Si isotope compositions of the thermal springs collected on La Soufrière volcano, Kawah Ijen volcano, Aso volcano, YPVF, Kanlaon volcano and Mutnovsky volcano are reported in **Table 3.2** and shown in **Fig. 3.6**.

Table 3.2: Germanium concentrations, Ge/Si ratios and silicon isotope compositions ($\delta^{29}Si$ and $\delta^{30}Si$) in thermal springs of Basse-Terre Island (La Soufrière), Java Island (Kawah Ijen), Kyūshū Island (Aso), Yellowstone Plateau Volcanic Field (YPVF), Negros Island (Kanlaon) and Kamchatka (Mutnovsky). Note that some locations have been sampled at different sampling dates. n = number of measurements.

	Label	Sampling date	Type	Ge	Ge/Si	$\delta^{29}Si$	SD	$\delta^{30}Si$	SD	n
		dd.mm.yy		nmol.l^{-1}	µmol.mol^{-1}	‰		‰		
La Soufrière	RM2(1)	27.01.15	acid SO_4-waters	1.85	1.35	0.54	0.04	1.04	0.02	2
	RM2(2)	12.10.17	acid SO_4-waters	1.51	1.05	0.57	0.02	1.07	0.08	1
	RM3(1)	27.01.15	acid SO_4-waters	3.15	1.22	-	-	-	-	-
	RM3(2)	12.10.17	acid SO_4-waters	3.60	1.25	-	-	-	-	-
	CE(1)	17.11.17	acid SO_4-waters	2.34	1.36	-	-	-	-	-
	CE(2)	15.03.18	acid SO_4-waters	2.62	1.50	0.63	0.01	1.35	0.05	1
	BJ(1)	29.01.15	acid SO_4-waters	0.48	0.26	-	-	-	-	-
	BJ(2)	14.11.17	acid SO_4-waters	0.69	0.38	-	-	-	-	-
	PR(1)	29.01.15	acid SO_4-waters	0.91	0.44	-	-	-	-	-
	PR(2)	14.11.17	acid SO_4-waters	1.25	0.60	-	-	-	-	-
	TA(1)	29.01.15	acid SO_4-waters	5.00	2.10	0.67	0.08	1.28	0.12	2
	TA(2)	14.11.17	acid SO_4-waters	5.81	2.30	-	-	-	-	-
	HR	20.10.17	acid SO_4 waters	14.44	11.28	-	-	-	-	-
	BCM(1)	30.01.15	acid SO_4 waters	11.72	21.03	0.64	0.01	1.14	0.02	1
	BCM(2)	20.10.17	acid SO_4 waters	10.67	18.92	-	-	-	-	-
	CC(1)	28.01.15	alkaline HCO_3-waters	1.89	1.13	0.65	0.04	1.22	0.07	2
	CC(2)	07.11.17	alkaline HCO_3-waters	1.80	1.09	0.48	0.02	0.99	0.03	1
	Dolé	04.02.15	alkaline HCO_3-waters	0.55	0.39	-	-	-	-	-
	GC(1)	28.01.15	neutral Cl-waters	0.78	0.50	-	-	-	-	-
	GC(2)	07.11.17	neutral Cl-waters	0.83	0.56	0.57	0.01	1.13	0.01	1
	GA(1)	29.01.15	mixed Cl-SO_4 waters	25.55	8.86	0.49	0.02	1.00	0.02	2
	GA(2)	14.11.17	mixed Cl-SO_4 waters	22.15	8.33	-	-	-	-	-
	GAB(1)	29.01.15	mixed Cl-SO_4 waters	27.35	9.49	0.50	0.02	1.06	0.05	1
	GAB(2)	14.11.17	mixed Cl-SO_4 waters	18.13	6.69	0.77	0.07	1.50	0.13	3
	GAF	29.01.15	mixed Cl-SO_4 waters	0.08	0.05	-	-	-	-	-
	Sofaïa	02.02.15	mixed Cl-SO_4 waters	0.53	0.94	0.37	0.04	0.71	0.05	1
Kawah Ijen	Lake	31.01.17	hyper acid Cl-SO_4 waters	248.21	205.52	0.42	0.05	0.85	0.08	3
	LF	31.01.17	hyper acid Cl-SO_4 waters	82.60	46.99	0.28	0.04	0.49	0.03	2
	SP1	31.01.17	hyper acid Cl-SO_4 waters	757.16	507.89	0.04	0.02	0.03	0.11	2
	SP2	31.01.17	hyper acid Cl-SO_4 waters	688.33	461.94	0.02	0.08	-0.14	0.03	2
	SP3	29.01.17	hyper acid Cl-SO_4 waters	729.63	500.86	0.05	0.04	0.03	0.01	3
	SP4	29.01.17	hyper acid Cl-SO_4 waters	481.83	293.33	0.06	0.01	0.02	0.03	2
	SP5	29.01.17	hyper acid Cl-SO_4 waters	550.66	342.94	0.07	0.02	0.04	0.06	2
	SP6	29.01.17	hyper acid Cl-SO_4 waters	275.33	160.12	0.26	0.01	0.47	0.01	2
	SP7	29.01.17	hyper acid Cl-SO_4 waters	523.13	339.36	0.16	0.05	0.21	0.03	3
	SP8	30.01.17	mixed neutral HCO_3-SO_4 waters	45.45	18.11	-0.10	0.01	-0.18	0.03	1
	SP9	30.01.17	mixed neutral HCO_3-SO_4 waters	44.14	16.57	0.00	0.06	-0.05	0.02	1
	SP10	30.01.17	mixed neutral HCO_3-SO_4 waters	41.92	15.47	-0.17	0.06	-0.35	0.05	2
	SP11	31.01.17	mixed neutral HCO_3-SO_4 waters	19.39	10.10	0.11	0.02	0.19	0.02	1

- : not measured.

	Label	Season/Sampling date	Type	Ge	Ge/Si	$\delta^{29}Si$	SD	$\delta^{30}Si$	SD	n
		dd.mm.yy		$nmol.l^{-1}$	$\mu mol.mol^{-1}$	‰		‰		
Aso	S21	spring 15	acid SO_4-waters	6.88	3.12	0.24	0.07	0.47	0.01	2
	S43	spring 15	acid SO_4-waters	3.44	1.67	-	-	-	-	-
	S49a	spring 15	acid SO_4-waters	2.75	1.06	-	-	-	-	-
	S49b	spring 15	acid SO_4-waters	12.39	5.07	0.14	0.03	0.27	0.01	1
	S52	fall 16	acid SO_4-waters	1.65	0.73	-	-	-	-	-
	S56	fall 16	acid SO_4-waters	0.28	0.20	-	-	-	-	-
	S57	fall 16	acid SO_4-waters	0.28	0.25	-	-	-	-	-
	S16	spring 15	alkaline HCO_3-waters	0.28	0.27	0.43	0.02	0.86	0.07	1
	S16	fall 16	alkaline HCO_3-waters	0.28	0.29	0.43	0.07	0.77	0.06	1
	S42	fall 14	alkaline HCO_3-waters	41.16	19.47	0.20	0.06	0.38	0.08	1
	S42	spring 15	alkaline HCO_3-waters	37.72	15.48	0.10	0.01	0.22	0.01	1
	S50	fall 16	alkaline HCO_3-waters	5.92	2.72	-	-	-	-	-
	S55	sum 16	alkaline HCO_3-waters	3.44	1.82	-	-	-	-	-
	S58	fall 16	alkaline HCO_3-waters	0.28	0.25	0.59	0.01	1.05	0.03	1
	S59	fall 16	alkaline HCO_3-waters	0.28	0.25	-	-	-	-	-
	S60	fall 16	alkaline HCO_3-waters	1.93	1.36	0.30	0.01	0.59	0.06	1
	S61	fall 16	alkaline HCO_3-waters	30.56	16.02	-	-	-	-	-
	S62	fall 16	alkaline HCO_3-waters	5.23	2.85	0.03	0.01	-0.05	0.06	2
	S51	fall 16	mixed neutral HCO_3-SO_4 waters	0.96	0.56	0.72	0.06	1.39	0.02	1
	S55	fall 16	mixed neutral HCO_3-SO_4 waters	3.30	1.75	0.17	0.00	0.51	0.03	1
	S63	fall 16	mixed neutral HCO_3-SO_4 waters	4.82	3.82	-	-	-	-	-
YPVF	Y7Drill	12.04.15	neutral Cl-waters	744.77	140.36	-0.21	0.02	-0.44	0.04	2
	BSP	13.04.15	neutral Cl-waters	828.74	159.71	-0.04	0.04	-0.04	0.03	2
	PBS	14.04.15	neutral Cl-waters	775.06	143.85	-0.12	0.01	-0.13	0.07	1
	CP	15.04.15	neutral Cl-waters	1011.84	188.92	-0.09	0.05	-0.09	0.08	2
	ECP	16.04.15	neutral Cl-waters	991.19	182.29	-0.09	0.02	-0.14	0.03	2
	CHs	16.04.15	neutral Cl-waters	960.90	181.70	-0.07	0.04	-0.05	0.05	2
	SS	16.04.15	neutral Cl-waters	235.41	110.98	-	-	-	-	-
	DG	16.04.15	neutral Cl-waters	1010.46	170.69	-0.04	0.05	-0.08	0.01	2
Kanlaon	Mambu1	30.07.14	acid SO_4-waters	2.62	4.37	0.17	0.07	0.31	0.02	1
	Mambu2	30.07.14	acid SO_4-waters	8.26	4.71	0.21	0.02	0.34	0.03	1
Mutnovsky	K1	08.15	alkaline HCO_3-waters	17.62	4.92	0.36	0.03	0.68	0.03	1
	K3	08.15	alkaline HCO_3-waters	2.20	1.44	0.78	0.09	1.57	0.03	1

- : not measured.

The highest Ge/Si ratios are measured in the hyper acid SO_4-Cl (46.99-507.89 µmol.mol^{-1}) and neutral Cl-waters (0.50-188.92 µmol.mol^{-1}) (**Fig. 3.6a**). Among YPVF's thermal springs, the neutral Cl-waters display the highest Ge/Si ratios (110.98-188.92 µmol.mol^{-1}). The other thermal water types show various Ge/Si ratios ranging, but the range of values are roughly comparable: acid SO_4-waters (0.20-21.03 µmol.mol^{-1}), alkaline HCO_3-waters (0.25-19.47 µmol.mol^{-1}), mixed acid SO_4-Cl waters (0.05-9.49 µmol.mol^{-1}) and mixed neutral HCO_3-SO_4 waters (0.56-18.11 µmol.mol^{-1}) (**Fig. 3.6a**). The lower value of Ge/Si is measured in the GAB mixed acid SO_4-Cl water of La Soufrière volcano (Ge/Si = 0.05 µmol.mol^{-1}).

The δ^{30}Si of all thermal springs display a large range of values (from -0.44 to 1.57 ‰). The lowest values are reported for the hyper acid SO_4-Cl waters (δ^{30}Si = -0.14 to 0.85 ‰), the neutral Cl-waters (δ^{30}Si = -0.44 to 1.13 ‰) and the mixed neutral HCO_3-SO_4 waters (δ^{30}Si = -0.35 to 1.39 ‰). The thermal springs located close to the acidic lake (SP1-SP5) of Kawah Ijen (SP1-SP5) display the lowest values in the hyper acid SO_4-Cl waters (δ^{30}Si = -0.14 to 0.04 ‰). The thermal springs located near the Blawan village display the lower values in the mixed neutral HCO_3-SO_4 waters (δ^{30}Si = -0.35 to 0.19 ‰) and thermal springs from YPVF display the lower values in the neutral Cl-waters (δ^{30}Si = -0.44 to -0.08 ‰) (**Fig. 3.6b**). The higher range of Si isotope composition is reported for alkaline HCO_3-waters (δ^{30}Si = -0.05 to 1.57 ‰) following by the acid SO_4-waters (δ^{30}Si = 0.27 to 1.35 ‰). The highest δ^{30}Si value is reported for the alkaline HCO_3-waters from Kamchatka (K3) with δ^{30}Si = 1.57 ± 0.03 ‰ (**Fig. 3.6b**). The mixed acid SO_4-Cl waters display Si isotope composition ranging from 0.71 to 1.50 ‰.

Based on the PCA graphs of variables (**Fig. 3.5a**) and individuals (**Fig. 3.5b**), the Ge/Si ratio contributes mainly to the first principal component and is positively correlated with the hyper acid SO_4-Cl waters, and the δ^{30}Si value contributes mainly to the second principal component and is negatively correlated with the neutral Cl-waters (from YPVF).

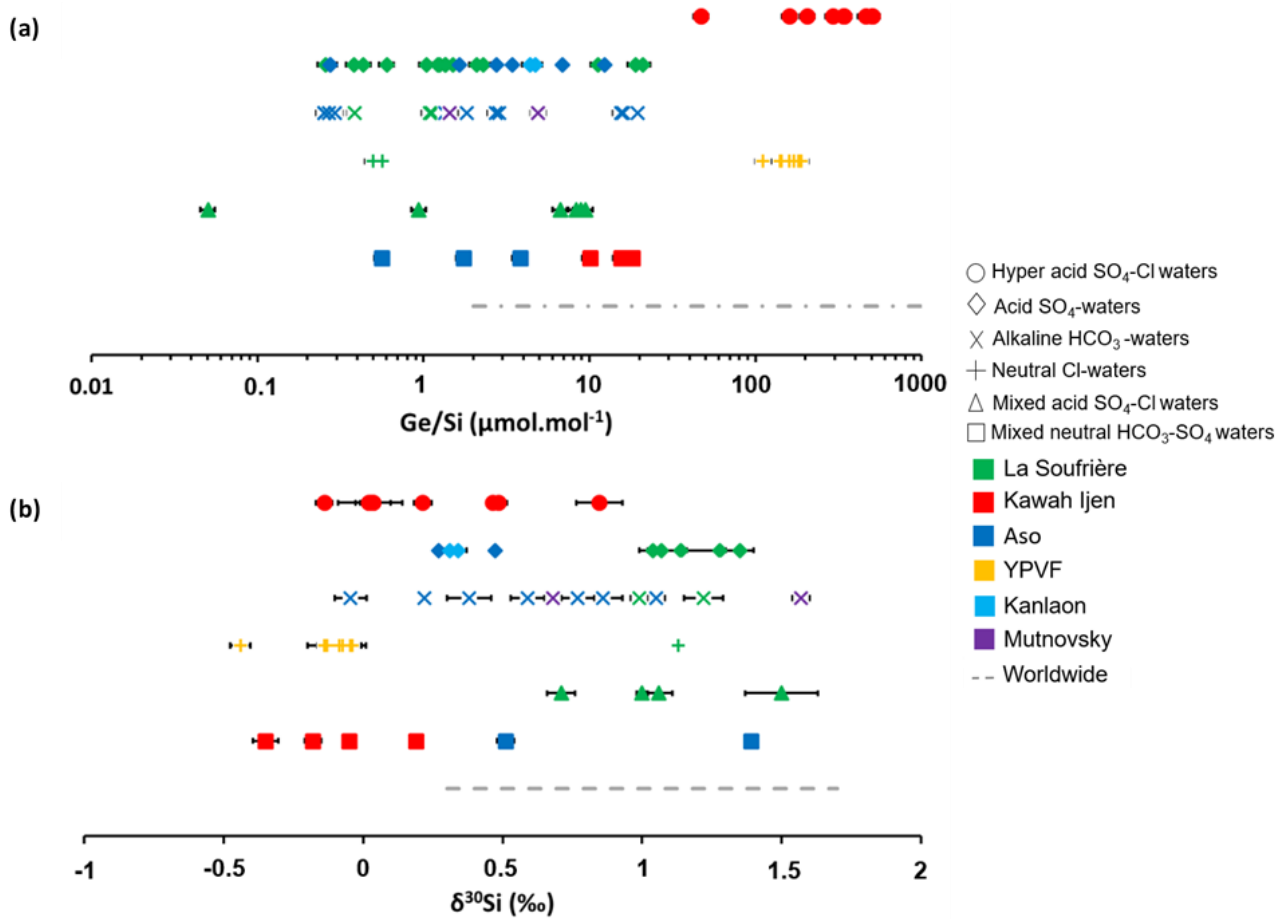

Fig. 3.6: Plots of the (a) Ge/Si ratios (± SD) and (b) Si isotope composition (δ^{30}Si ± SD) in the different types of thermal waters (represented by symbols; hyper acid SO_4-Cl, acid SO_4-, alkaline HCO_3-, neutral Cl-waters and mixed thermal springs, i.e., acid SO_4-Cl, neutral HCO_3-SO_4 waters) collected in the different sites (color-coded; La Soufrière, Kawah Ijen, Aso, YPVF, Kanlaon, Mutnovsky).

3.6 Discussion

3.6.1 Influence of magmatic gas condensation on the Ge/Si ratio and Si isotope compositions of hyper acid SO_4-Cl thermal waters

3.6.1.1 The influence of Si and Ge transport by magmatic gases on the Ge/Si ratio in hyper acid SO_4-Cl thermal waters

We first focus on processes influencing the Si and Ge chemistry of hyper acid SO_4-Cl waters. These waters are generally formed from a high magmatic gases contribution relative to meteoric water recharge, which explains their high concentrations in SO_4^{2-} and Cl^- resulting from magmatic gases condensation (**Table 3.1**). Their SO_4^{2-}/Cl^- ratio is function of absorption degree of magmatic gases in the system (White, 1957; Ellis and Mahon, 1964).

The Si concentration (1212-1764 $\mu mol.l^{-1}$) shows only slight variations in hyper acid SO_4-Cl with increasing $SO_4^{2-}+Cl^-$ concentrations, whereas Ge (82.60-757.16 $nmol.l^{-1}$) increases with increasing $SO_4^{2-}+Cl^-$ concentrations (**Fig. 3.7a**). This suggests that the Ge concentration controls the variation of Ge/Si ratios in hyper acid SO_4-Cl thermal springs (**Fig. 3.7a**). The positive relationship between the Ge and $SO_4^{2-}+Cl^-$ concentrations (R^2=0.99) suggests that a fraction of the Ge in solution relates to magmatic gas condensation.

Our hypothesis is that the higher Ge/Si ratios found in hyper acid SO_4-Cl thermal waters waters reflect a higher Ge volatility in magmatic gas than Si.

Only few studies focused on Ge volatility in high-temperature gases. The Ge volatility behavior is used for Ge isotope measurements via gas isotope mass spectrometry after Ge fluorination (Rouxel and Luais, 2017). In this application, the temperature used to evaporate Ge ranges from 60-120 °C (Luais, 2012; Meng et al, 2015; Escoubé et al, 2015), which is a low temperature relative to the conditions in a magmatic hydrothermal system. There is evidence for the formation of volatile $GeCl_4$ species (Kaya and Volkan, 2011), and this is a reason to avoid the use of HCl or $HClO_4$ for Ge isotope measurements which may lead to up to 100% Ge loss even at medium temperature (80° C) (Luais, 2012). There is also evidence for the formation of volatile GeF_4 (Kwasnik, 1963), and this is a complication for

the dissolution of silicate rocks for Ge isotopic measurements involving higher temperature (i.e., up to 300 °C) (Rouxel and Luais, 2017). Moreover, Ge can be transported in magmatic gas as GeS (Sossi and Fegley, 2018). Recently, Renggli and Klemme (2020) show that above 900 °C, Ge is predominantly in the gas phase as GeS, whereas at lower temperatures the predicted solids are GeO_2 and GeS_2. At lower temperature (500 °C), the volatility of Ge increases again as $GeCl_4$ becomes stable. The study of Zelenski et al (2014) details the volatility of Ge in the Tolbachik gases (Kamchatka) sampled at 1060-1070 °C using the enrichment factor (EF). The EF, used to ascertain the contribution of the volatile and particulate fractions to the total amount of an element in a volcanic gas, is calculated via the following equation:

$$EF(x) = (C_X/C_R)_{gas}/(C_X/C_R)_{rock}$$

where R is a reference material (a low volatile and abundant element), X is the element of interest and rock is the substance that is supposed to contribute to the aerosol particles. The Ge volatility in the Tolbachik condensates (relative to Mg content in Tolbachik lavas) is confirmed (log (EF)=2.29) and is higher than the Si volatility (log (EF)=0.93) but is limited compared to highly volatile elements such as S (log (EF)=7.13) and Cl (log (EF)=5.98) (Zelenski et al, 2014).

Regarding Si volatility in high-temperature gases, F is likely to play a role in these hyper acid SO_4-Cl waters containing high F concentrations (from 7927 to 74710 µmol.l^{-1}; **Table 3.1**). Indeed, Si may be transported by HF-rich gas as SiF_4, a highly volatile compound at ambient temperature and atmospheric pressure (sublimation point = -86 °C at atmospheric pressures) which at elevated temperature reacts with water vapor to form HF and silica through the following reaction: $SiF_{4(g)} + 2H_2O_{(g)} <-> SiO_{2(s)} + 4HF_{(g)}$. The reaction is very sensitive to temperature and is shifted in favor of SiF_4 at low temperature (<400 °C; Rosenberg, 1973), whereas in high-temperature fumaroles HF is the dominant fluorine-bearing species. The reaction is also sensitive to pressure and is shifted in favor or silica phase formation when decompression of HF-rich gas during ascent of vapor-satured magma occurs (de Hoog et al, 2015). We assume that the F may play a role on the Ge/Si in the hyper acid SO_4-Cl waters (**Fig. 3.7b**) given (i) the surface temperatures (169-244 °C) <400 °C of F-bearing fumaroles (HF=3-9 µmol.l^{-1}; Delmelle et al, 2000) linked to the same magmatic reservoir than the hyper acid SO_4-Cl waters favor the formation of SiF_4 (de Hoog et al, 2015). However, this hypothesis remains to be further tested since higher temperatures have also been reported for

fumaroles sampled deeper in this area (600-700 °C; van Hinsberg et al, 2009, 2017).

This section suggests that Ge is more volatile than Si in volcanic gases and may be transported by magmatic gases as GeF_4, $GeCl_4$ and GeS, and Si as SiF_4. Further investigations on fumaroles or magmatic gas should be carried out in the future to validate this hypothesis, as it is out of the scope of this study on thermal springs. This transport of Ge and Si by magmatic gases could therefore potentially influence the Ge/Si ratios of hyper acid SO_4-Cl thermal springs.

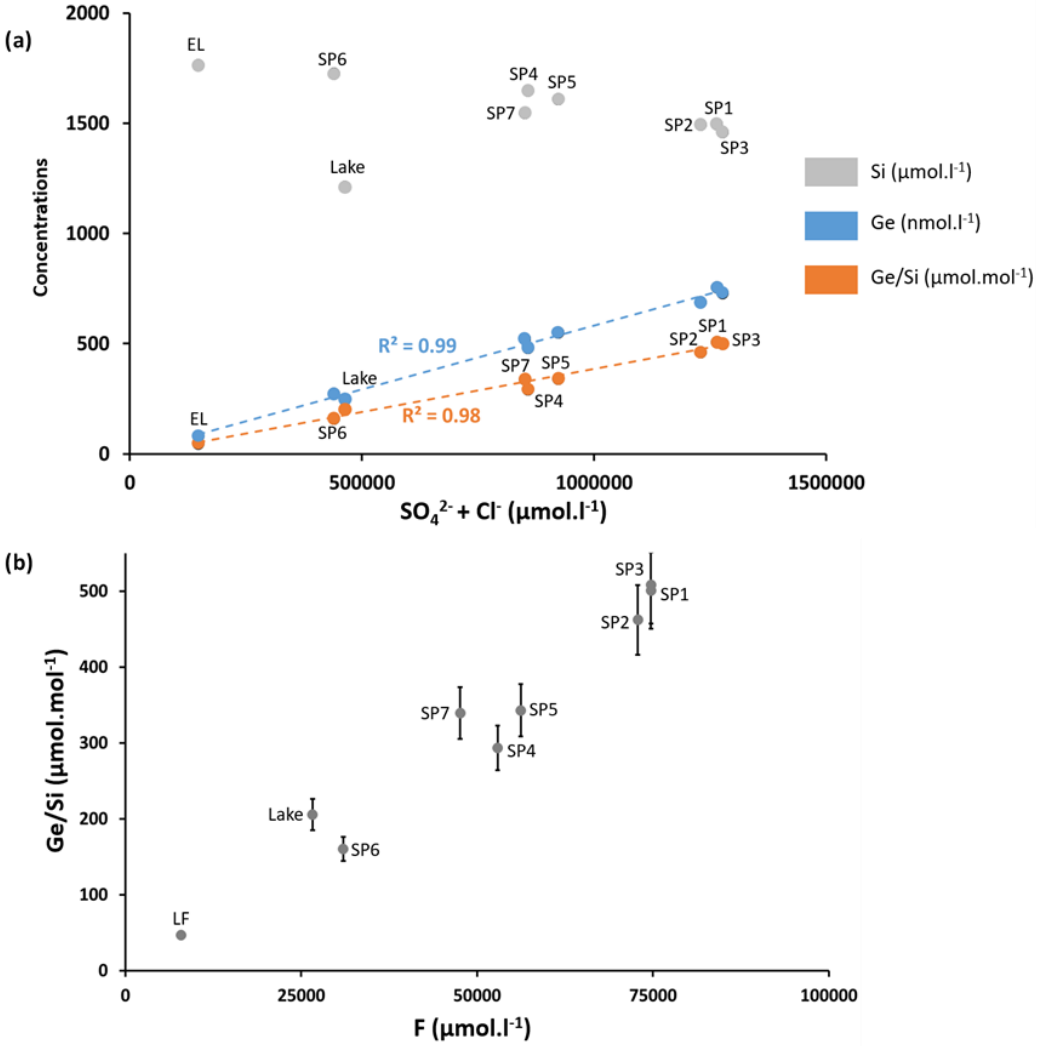

Fig. 3.7: Plots of variations in the hyper acid SO_4-Cl thermal springs (all from Kawah Ijen volcano; sample codes as in **Table 3.1**): (a) Si concentration (µmol.l^{-1}), Ge concentration (nmol.l^{-1}) and Ge/Si ratios (µmol.mol^{-1}) as a function of SO_4^{2-} + Cl^- concentrations (µmol.l^{-1}); (b) Ge/Si ratios (µmol.mol^{-1}) as a function of F concentration (µmol.l^{-1}).

3.6.1.2 The influence of magmatic fluoride on silicon isotope compositions in hyper acid SO_4-Cl thermal waters

The hyper acid SO_4-Cl waters display the highest F concentrations (7927-600347 µmol.l^{-1}) associated with the lowest Si isotope composition (δ^{30}Si = -0.14 to 0.85 ‰; **Fig. 3.8a**). The effect of F mainly derived from magma degassing on Si isotope compositions in thermal waters is investigated here. The volatility of SiF_4 had been used for Si isotope measurements via the gas source isotope ratio mass spectrometer (IRMS) via three different method: the $BaSiF_6$ decomposition method (Reynolds and Verhoogen, 1953), the direct fluorination method using F_2 + HF (Epstein and Taylor, 1970) or BrF_5 (Clayton et al, 1978) as fluorination reagents and the laser probe extraction method (De La Rocha et al, 1996). The loss of volatile SiF_4 during the sample introduction into the MC-ICP-MS (Georg et al, 2007) induced the development of other methods.

So far, magma degassing has not been shown to produce fractionation of Si isotopes (Opfergelt and Delmelle, 2012). A possible cause of the observed ^{30}Si-depleted fluid compositions is Si isotope fractionation between multiple coexisting Si-bearing aqueous species as reported by Chemtob et al (2015). The dominant species at high F concentrations are SiF_6^{2-} (hexafluorosilicate) and $Si(OH)_2F_2$ (Busey et al, 1980). Si-bearing precipitates likely formed from aqueous silicic acid and not from Si-hydroxyfluoride complexes. Thus, the observed bulk isotopic fractionations could be imparted by fractionations between aqueous species and the preferential removal of $Si(OH)_{4(aq)}$ from solution. The octahedral coordination of Si in SiF_6^{2-} would favor the lighter isotopes relative to the tetrahedrally coordinated $Si(OH)_4$. Thus, the fractionation between SiF_6^2 and $Si(OH)_{4(aq)}$, approximated +5 ‰ by Chemtob et al (2015) implies that Si speciation has drastic effect on the isotopic signature of chemical weathering in high-fluorine environments. The Si isotope compositions of F highly-concentrated thermal springs, with SiF_6^{2-} as the dominant F (confirmed with PHREEQC geochemical modeling program; Parkhurst and Appelo, 2013) may therefore be lighter as observed for hyper acid SO_4-Cl waters from Kawah Ijen (**Fig. 3.8a**).

Given that there is no direct evidence for Si transport with Cl or S in the magmatic gas phase, the Si isotope composition in thermal springs is poorly related to the SO_4^{2-} + Cl^- concentrations (R^2=0.1; **Fig. 3.8b**).

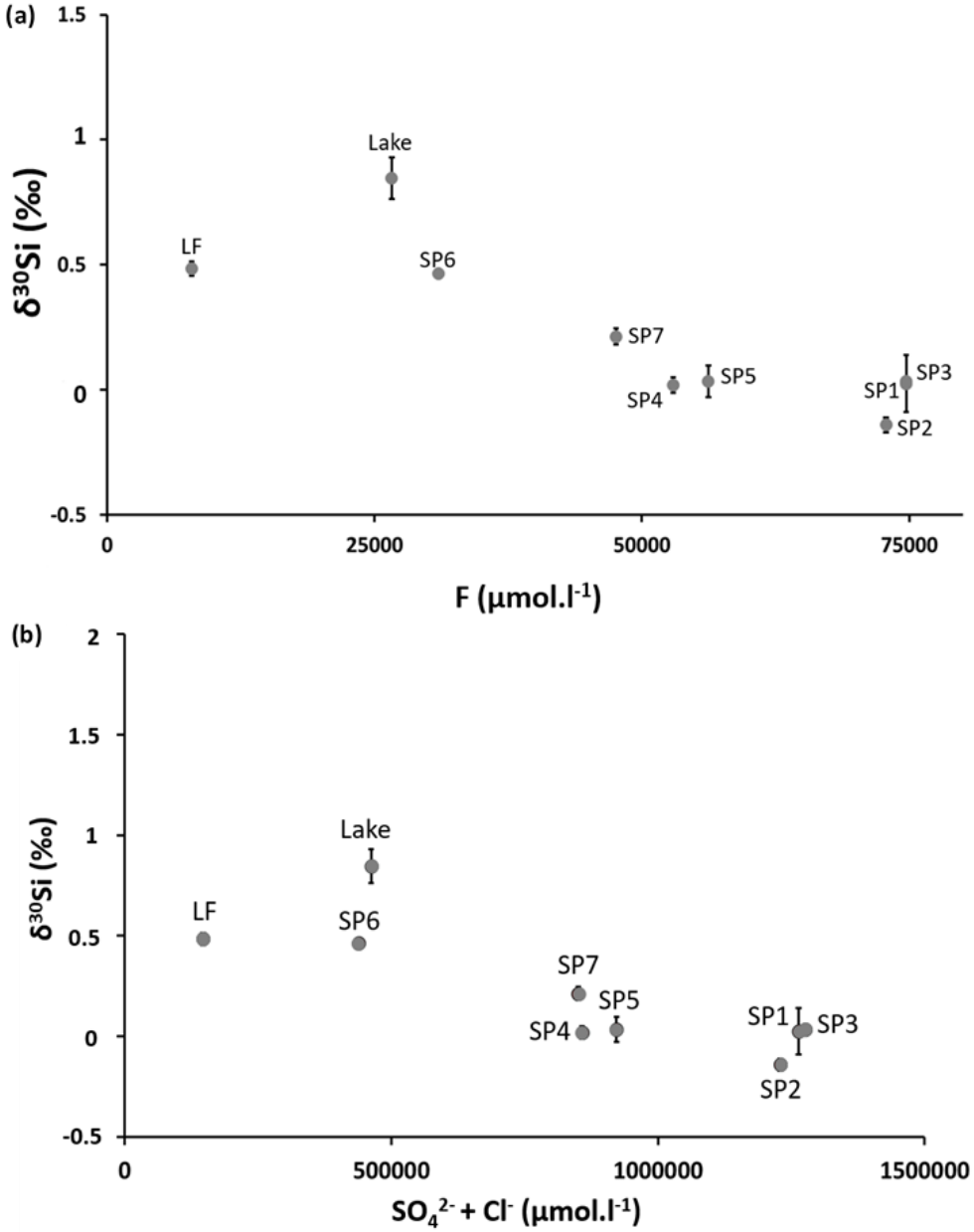

Fig. 3.8: Plots of variations in the hyper acid SO_4-Cl thermal springs (all from Kawah Ijen volcano; sample codes as in **Table 3.1**): (a) $\delta^{30}Si$ (‰) as a function of F concentration (µmol.l^{-1}) and (b) $\delta^{30}Si$ (‰) as a function of SO_4^{2-} + Cl^- concentrations (µmol.l^{-1}).

3.6.2 The release of proton flux from volcanic gases condensation favors weathering reactions: influence on Ge/Si and $\delta^{30}Si$ in hyper acid SO_4-Cl thermal waters

Magmatic gases condensation releases proton flux explaining the acidic pH values of the hyper acid SO_4-Cl thermal springs (0.1-1.3). This proton flux leads to high TDS values in hyper acid SO_4-Cl thermal springs (32308-140669 $\mu mol.l^{-1}$) increasing with weathering intensity. Relative to other thermal waters and based on their SO_4^{2-} (89248-675769 $\mu mol.l^{-1}$), Cl^- (57915-600347 $\mu mol.l^{-1}$), pH (0.1-1.3) and TDS (32308-140669 $\mu mol.l^{-1}$) values, the hyper acid SO_4-Cl thermal springs of Kawah Ijen can be considered as a "magmatic end-member" of acid weathering reactions. We investigate the role of volcanic rock and acid water-rock interaction on Ge and Si concentrations, Ge/Si ratios and Si isotope compositions of these thermal springs.

The hyper acid SO_4-Cl thermal springs (SP1-SP7) of Kawah Ijen with a chemical composition corresponding to the dissolution of an average crustal rock (Giggenbach, 1988; Delmelle and Bernard, 1994) display a large range of Ge concentrations (275.13-757.16 $nmol.l^{-1}$) (**Fig. 3.7a**). The composition of rocks at Kawah Ijen is basalt-andesitic to andesitic (Whitford et al, 1979). Considering congruent dissolution of andesite (Ge = 1.4 $mg.l^{-1}$, Arnòrsson, 1987) and basalt (Ge = 1.52-1.64 $mg.l^{-1}$ in BHVO-2, Escoubé et al, 2012; Ge = 1.3 $mg.l^{-1}$ in Icelandic fresh basalt, Arnòrsson, 1987), the quantity (g) of volcanic rock required to obtain the Ge concentration of the most-concentrated hyper acid SO_4-Cl thermal spring (SP1: Ge = 757.16 $nmol.l^{-1}$) in one liter is 105.3-113.6 g for BHVO-2, 132.8 g for Icelandic fresh basalt and 123.4 g for andesite (**Table 3.3**).

Table 3.3: Germanium (Ge) concentrations in basalt (USGS reference material BHVO-2 and Icelandic fresh basalt) and in andesite volcanic rocks and calculated volcanic rock quantity (g) to dissolve in order to obtain 1 liter (1L) of Ge most-concentrated thermal spring (SP1 with Ge = 757.16 nmol.l^{-1}).

Volcanic rock	Label	Ge	Reference	Bulk density	volcanic rock to dissolve (g) to obtain 1L of SP1 (Ge = 757.16 nmol.l^{-1})
		mg.kg^{-1}		g.cm^{-3}	
Basalt	BHVO-2	1.52	Escoubé et al, 2012	3.1	113.6
Basalt	BHVO-2	1.63	Lalonde and Rouxel, unpublished	3.1	106.0
Basalt	BHVO-2	1.61	Lalonde and Rouxel, unpublished	3.1	107.3
Basalt	BHVO-2	1.64	Lalonde and Rouxel, unpublished	3.1	105.3
Basalt	Icelandic fresh basalt	1.30	Arnòrsson, 87	3.1	132.8
Andesite	Andesite	1.40	Arnòrsson, 87	2.6	123.4

Conversely to Ge concentrations, the Si concentrations in the hyper acid SO_4-Cl thermal springs are relatively constant (1212-1764 µmol.l^{-1}) (**Fig. 3.7a**). This may be explained by amorphous silica precipitation. This hypothesis is supported by a saturation index (SI) (SI = log IAP/K_{sp} with IAP the ion activity product of the chemical species in the fluids and K_{sp} their solubility product; calculated with the PHREEQC geochemical modeling program) of amorphous silica > 0, demonstrating that these waters are supersaturated with respect to amorphous silica. The high Ge/Si values obtained for these thermal springs (46.99-507.89 µmol.mol^{-1}) is therefore likely influenced by the precipitation of amorphous silica, i.e., a Ge poor phase (Evans and Derry, 2002).

Moreover, van Hinsberg et al (2020) recently investigated the interaction between andesite and hyper acid volcanic lake water of Kawah Ijen, affected by the same processes than the hyper acid SO_4-Cl thermal springs (Delmelle et al, 2000). The results show that the chemical composition of the andesite in contact with Kawah Ijen lake water is modified with a Si enrichment (enrichment factor=10000) and no modification for Ge concentrations (enrichment factor=1). The silicification induced by pervasive acid alteration may decrease the Ge/Si ratios of the volcanic rock thereby increasing the Ge/Si ratio of the residual fluid part of thermal springs.

The range of Si isotope composition of the hyper acid SO_4-Cl thermal springs (-0.14 to 0.47 ‰; **Table 3.2**) is in the lower end of Si isotope signatures for thermal springs reported worldwide (from -0.6 to 1.7‰, Douthitt, 1982; Ding et al, 1996; Opfergelt et al, 2011, 2013; Geilert et al, 2014). If the Si isotopes of the hyper acid SO_4-Cl thermal springs was only controlled by silica precipitation, the Si isotope values of the hyper acid SO_4-Cl thermal springs should be higher given that light Si isotopes are incorporated in silica precipitate (δ^{30}Si = -0.1‰ to -0.4‰, e.g., Douthitt, 1982; Geilert et al, 2014; Ding et al, 2016). We therefore assume a process releasing light Si isotopes. Altered rocks are isotopically heavier (δ^{30}Si for the most altered/silicified rock = 1.5 ‰) relative to non-altered rocks (δ^{30}Si of unaltered basalt < -0.2‰ and δ^{30}Si of unaltered andesite = -0.2 ‰; Van den Boorn et al, 2007). This suggests a preferential leaching of light Si isotopes during rock weathering by hyper acid weathering, which can explain the low Si isotopes values reported in the hyper acid SO_4-Cl thermal springs.

The Si isotope value of acidic lake ($\delta^{30}Si$ = 0.85 ‰) should be even higher if only controlled by inorganic silica precipitation renowned for discriminate against the heavy isotope (e.g., Basile-Doelsch et al, 2006). One possible explanation is that this value reflects the lake chemistry collected during wet season. Indeed, dilution effect occurs in wet season (annual average precipitation are 4.5 higher in wet than dry season; Ijen Monthly Climate Averages, 2020) on the superficial layer of acid lake from Kawah Ijen (Caudron et al, 2015) as proved by lower dissolved element compositions in wet season than from average crater lake water reported by Delmelle et al (2000). The dilution effect can modify silicon concentration and therefore decrease the saturation index for amorphous silica controlling the Si isotope fractionation. If verified, the Si isotope composition of the lake in the wet season should be lower than in the dry season due to a more limited precipitation of amorphous silica, which preferentially incorporate light Si isotopes (Li et al, 1995). We do not know the Si isotope composition of the lake in the dry season to validate this suggestion. The Si isotope composition of the lake water is lower compared to what would be expected based on the $\delta^{30}Si$ values reported for the layered opaline lake sediments (1.2 ±0.2 ‰; Van den Boorn et al, 2007). Indeed, these opaline lake sediments are believed to represent precipitates from the silica-saturated water and should preferentially incorporate the light Si isotopes relative to the dissolved Si. This is however beyond the scope of this study to investigate the implications for solid silica precipitates.

3.6.3 Influence of water-rock interaction on the Ge/Si ratio and Si isotope compositions of acid SO_4 -, alkaline HCO_3- and neutral Cl-thermal waters

3.6.3.1 The dissolved Ge concentration in acid SO_4-, alkaline HCO_3- and neutral Cl-thermal waters results from water-rock interaction

In the "immature waters", the hyper acid SO_4-Cl thermal springs located on the flank of Kawah Ijen volcano (lake, SP1-7) were identified in **section 3.6.2** as the "magmatic end-member" of acid weathering reactions with a composition corresponding to the dissolution of an average crustal rock (Giggenbach, 1988; Delmelle and Bernard, 1994). On the opposite, **Figure 3.4** suggests that neutral Cl-waters of YPVF fall within "mature waters". These mature waters are partially in equilibrium with Na- and K-

feldspars (Giggenbach, 1988). **Figure 3.4** suggests that the Sulfide Spring (SS) neutral Cl-waters of YPVF is within "partially equilibrated water" with estimated T(Na/K) (hydrothermal reservoir temperature assuming feldspar equilibrium between a potassium feldspar and plagioclase; Ellis and Mahon, 1977) comprised between 200 and 220 °C. This agrees with the commonly accepted view that thermal springs composition, firstly originated by magmatic processes, may then be influenced by distinct water-rock interaction intensity in deep reservoir (White, 1957; Ellis and Mahon, 1964, 1977). The two neutral-Cl waters from La Soufrière volcano (GC(1), GC(2); **Table 3.1**) are immature, and this is why they are distinct from the mature neutral Cl-waters from YPVF based on the PCA diagram (**Fig. 3.5**).

The Ge concentrations vary in thermal waters between lower concentrations in acid SO_4-waters (0.28-14.44 nmol.l^{-1}), intermediate concentrations in alkaline HCO_3-waters (0.28-41.16 nmol.l^{-1}), and higher in neutral Cl-waters (0.78-1011.84 nmol.l^{-1}) (**Fig. 3.9**). The mixed acid SO_4-Cl waters are characterized by Ge concentrations in the large range of 0.08-27.35 nmol.l^{-1} and the neutral HCO_3-SO_4 waters are characterized by Ge concentrations in the same range as the alkaline HCO_3-waters from which they were mixed (0.96-45.45 nmol.l^{-1}).

It is not expected that the range of Ge concentrations in thermal waters, exhibiting a range of variability between the lowest values in acid SO_4-waters and the highest values in neutral Cl-waters (**Table 3.2**), is influenced by the hosting igneous rock. Indeed, no significant variation is observed in the total Ge content of different types of igneous rocks (e.g., Burton et al, 1959), despite a slight increase in the Ge content of minerals from basic to acid rocks (Hörmann, 1970).

If not controlled by the host rock, the Ge behavior in the aqueous phase of thermal waters resulting from water-rock interaction is investigated in more details. Higher concentrations of Ge (nmol.l^{-1}) are observed in thermal springs characterized by higher TDS concentrations (**Fig. 3.9a**) and surface temperature (**Fig. 3.9b**). This could be explained by an increase in Ge solubility with temperature and salinity (Melcher, 2003). In dilute hydrothermal streams of near-neutral pH (pH<8) and in the temperature range of 20–350 °C, Ge is mainly transported as the neutral hydroxide $Ge(OH)_4^0$. Pokrovski and Schott (1998) show that the $Ge(OH)_4^0/Si(OH)_4^0$ ratio increases by more than an order of magnitude when the temperature is raised from 25 to 500 °C. This contributes to increase in the same order of magnitude the Ge/Si ratio in natural thermal

springs. To a lesser extent, Cl^- may also contribute to Ge transport in thermal water, as illustrated by high Cl^- concentration associated with high Ge concentrations in thermal springs (**Fig. 3.9c**). Indeed, in addition to the hydroxide form $Ge(OH)_4^0$, Ge is also transported in hydrothermal fluids mainly in the form of chlorocomplexes (e.g., $GeCl_4$) in geological environments according to Pokrovski and Schott (1998). Germanium concentrations in thermal springs may therefore result from one or more than these factors and this is supported by the large range of Ge concentrations found in our data. This agrees with Kraynqv (1965) arguing that highest Ge concentrations occurred in thermal waters with one or more of the following characteristics: (i) high temperature, (ii) high dissolved solids content and (iii) high Cl^- concentrations.

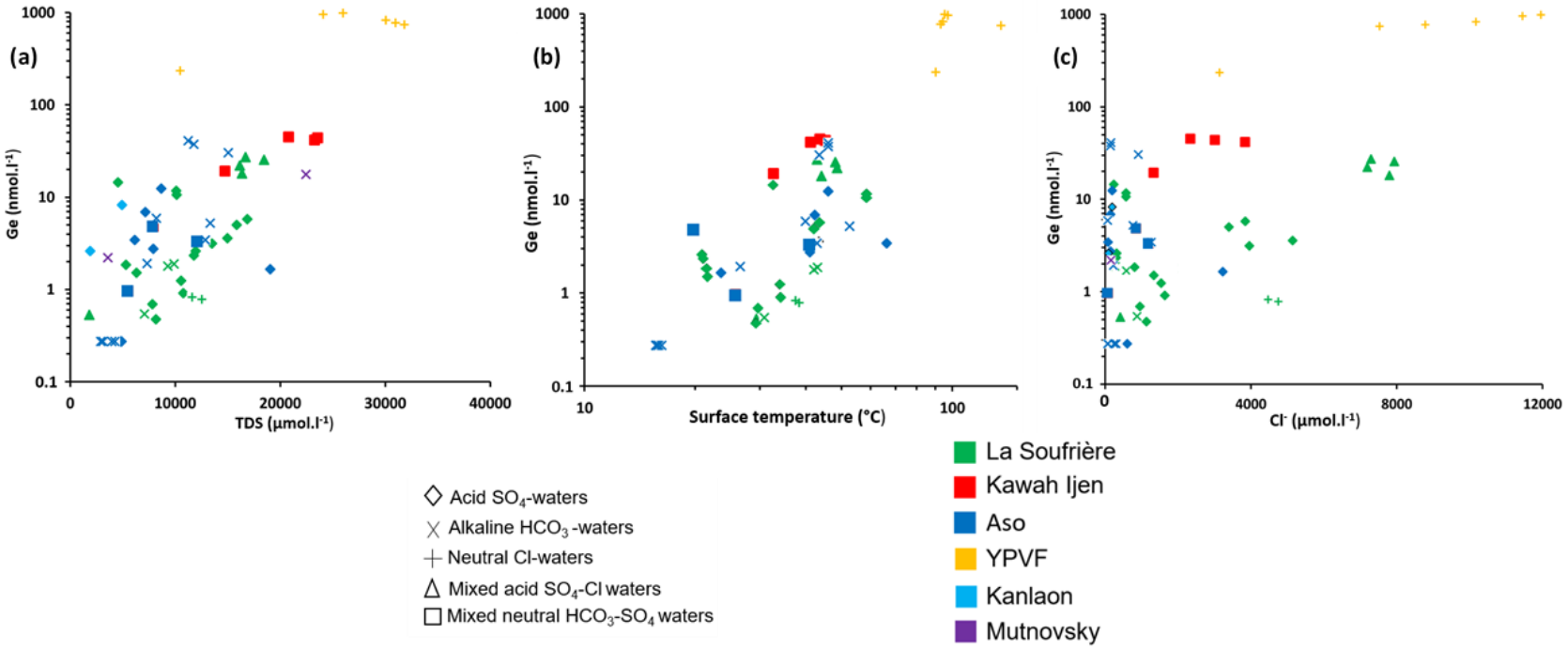

Fig. 3.9: Plot of the Ge concentration (nmol.l^{-1}) as a function of (a) Total Dissolved Solid (TDS), (b) surface temperature and (c) Cl^- concentration in the different types of thermal waters (represented by symbols; hyper acid SO_4-Cl, acid SO_4-, alkaline HCO_3-, neutral Cl-waters and mixed thermal springs, i.e., acid SO_4-Cl, neutral HCO_3-SO_4 waters) collected in the different sites (color-coded; La Soufrière, Kawah Ijen, Aso, YPVF, Kanlaon, Mutnovsky). Surface temperature are not available for thermal waters of Kanlaon volcano and from Mutnovsky volcano.

3.6.3.2 Silica precipitation controls the Si concentration in acid SO_4-, alkaline HCO_3- and neutral Cl-thermal waters

The Si concentrations in thermal springs are correlated with surface temperature (°C) (R^2=0.78; **Fig. 3.10**; except Sofaïa and BCM). This is likely controlled by amorphous silica precipitation. The solubility of amorphous silica (2300 µmol.l^{-1} at 25 °C; Fournier and Rowe, 1977) increases with temperature. As the thermal springs rise to the surface, cooling causes a decrease in solubility and results in the precipitation of amorphous silica (Arnòrsson, 1987). All of the thermal waters are indeed supersaturated with respect to amorphous silica (SI>0 as calculated with PHREEQC; Parkhurst and Appelo, 2013).

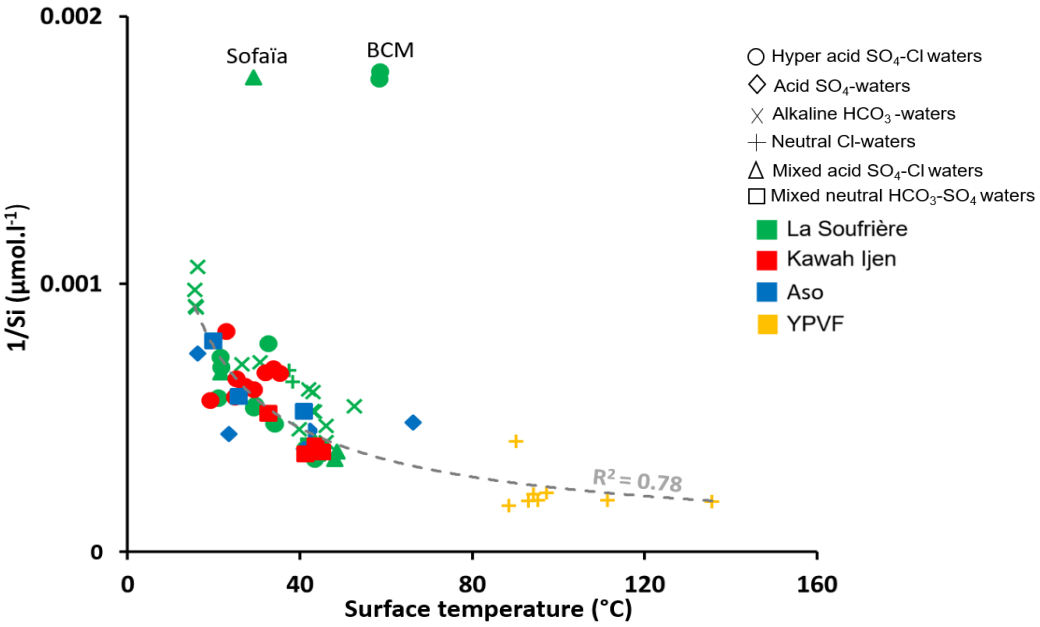

Fig. 3.10: Plot of the Si concentration (µmol.l^{-1}) (expressed as 1/Si) as a function of surface temperature in the different types of thermal waters (represented by symbols; hyper acid SO_4-Cl, acid SO_4-, alkaline HCO_3-, neutral Cl-waters and mixed thermal springs, i.e., acid SO_4-Cl, neutral HCO_3-SO_4 waters) collected in the different sites (color-coded; La Soufrière, Kawah Ijen, Aso and YPVF). Surface temperature are not available for thermal waters of Kanlaon volcano and from Mutnovsky volcano.

3.6.3.3 Impact of water-rock interaction on the Ge/Si ratio in acid SO_4-, alkaline HCO_3- and neutral Cl-thermal waters

The Ge/Si ratios measured in thermal waters resulting from water-rock interaction (i.e., acid SO_4, alkaline HCO_3 and neutral Cl-thermal waters, and the mixed waters derived from these waters (0.05 to 188.92 µmol.mol^{-1}) are in the same range than Ge/Si values reported in a context of regional metamorphism (Massif Central: from 2 to 1000 µmol.mol^{-1}, Criaud and Fouillac, 1986; Himalaya: 4 to 1000 µmol.mol^{-1}, Evans and Derry, 2002; Tibetan Plateau and North Korea: 78 to 125 µmol.mol^{-1}; Han et al, 2015) and volcanism (3-185 µmol.mol^{-1}; Arnòrsson, 1983).

The Ge/Si ratios in thermal waters resulting from water-rock interaction (i.e., acid SO_4, alkaline HCO_3, neutral Cl-, mixed acid SO_4-Cl and mixed neutral HCO_3-SO_4 thermal waters) are significantly lower than in the "magmatic end-member" of hyper acid SO_4-Cl thermal waters (e.g., SP1 = 507.89 µmol.mol^{-1}; **section 3.6.1**). These lower values can partly result from a reduced fraction from the hydrothermal contribution (**Fig. 3.7a**).

Among acid SO_4-, alkaline HCO_3-, neutral Cl-, mixed acid SO_4-Cl and mixed neutral HCO_3-SO_4 thermal waters, the highest Ge/Si ratios are found in the "mature end-member" (resulting from prolonged water-rock interaction leading to conditions approaching equilibrium between the Na- and K- feldspar and the aqueous solution), i.e., the mature neutral Cl-waters of YPVF (110.98-188.92 µmol.mol^{-1}). Such high Ge/Si ratios (110.98-188.92 µmol.mol^{-1}) may be the result of several factors: Ge enrichment in the thermal waters due to high TDS, high temperature and high Cl^- concentrations (**Fig. 3.9a**, **3.9b** and **3.9c**) and precipitation of amorphous silica in the thermal water originally enriched in both Ge and Si (**Fig. 3.10**). Indeed, these thermal springs have high surface temperature (> 88.5 °C; **Table 3.1**). The Ge/Si enrichment is supported by Evans and Derry (2002) showing a significant increase of Ge/Si ratios (>50 µmol.mol^{-1}) in waters in equilibrium with Ge-bearing quartz (Ge = 1.2 mg.l^{-1}) when the temperature are below 200 °C. This is due to the fact that in thermal springs, the main dominant Ge-bearing species is $Ge(OH)_4^0$ over a wide range of pH (0-8) and temperatures (20-350 °C) (Pokrovski and Schott, 1998) and the main Si species in these conditions is $Si(OH)_4^0$ (Ding et al, 2017). The distribution of Ge hydroxide species as a function of pH and temperature is similar to that of silicon hydroxide complexes (Pokrovski and Schott, 1998). However, significant differences between the thermodynamic properties of $Ge(OH)_4^\circ(aq)$ and $Si(OH)_4^\circ(aq)$ such as

enthalpies of formation and heat capacities can lead to an increase of the Ge/Si ratio with temperature in aqueous solutions in equilibrium with Ge-bearing silicates (Pokrovski and Schott, 1998).

In summary, the range of Ge/Si ratios in thermal waters resulting from water-rock interaction likely results from (i) different water-rock interaction intensity, i.e., being associated with large range of Cl^- concentrations and TDS values in these waters (mainly for immature waters such as acid SO_4- and alkaline HCO_3-waters), and (ii) combined with various surface temperature affecting amorphous silica precipitation (for immature waters such as acid SO_4- and alkaline HCO_3-waters, but also affecting mature waters, i.e., neutral Cl-thermal waters).

3.6.3.4 Impact of water-rock interaction on the $\delta^{30}Si$ value in acid SO_4-, alkaline HCO_3- and neutral Cl-thermal waters

The range of Si isotope compositions in the acid SO_4-, alkaline HCO_3- and neutral Cl-waters and the mixed waters derived from these waters (from -0.44 to 1.57 ‰) is higher than the $\delta^{30}Si$ values reported for thermal waters in a context of regional metamorphism (Tibet: from -0.67 to 0.25 ‰; Wang et al, 2019) and in thermal waters of Iceland ($\delta^{30}Si$ = 0.3-1.7 ‰; e.g., Opfergelt et al, 2011; Geilert et al, 2014).

The large range of Si isotope values in these thermal springs likely reflects different water-rock interaction intensity, combined with various surface temperatures affecting amorphous silica precipitation (**Fig. 3.10**; **section 3.6.3.2**).

All of these thermal waters types are supersaturated with amorphous silica (**section 3.6.3.2**) and the temperature surface and dissolved Si concentrations variation induce differences in conditions for the precipitation of silica remove. The Si concentrations and the surface temperatures are lower in acid SO_4-, and alkaline HCO_3- thermal springs than in the neutral Cl-waters of YPVF (**Fig. 3.10**). According to **section 3.6.3.2**, lower temperatures can lead to more extensive silica precipitation. Silica precipitates incorporate the lighter Si isotopes and enrich surrounding waters in the heavy Si isotopes, and the soil-fluid isotope fractionation factor decreases when the temperature increases (Geilert et al, 2014). This has been confirmed by field measured in Iceland (Geilert et

al, 2015) and in YPVF (Chen et al, 2020). This likely explains the higher Si isotope compositions in acid SO_4-, and alkaline HCO_3- thermal springs than in the neutral Cl-waters of YPVF.

The mature neutral Cl-waters are characterized by lower Si isotope composition ($\delta^{30}Si$ = -0.44 to -0.04 ‰) than immature thermal springs. These mature waters reflect more intensive water-rock interaction. The Si isotopic composition of igneous material range from -0.14 to -0.33 ‰ (Savage et al, 2011). This would lead to low $\delta^{30}Si$ into the aqueous phase upon dissolution of this material.

3.6.4 Evolution of Ge/Si ratios and Si isotope compositions in thermal springs from immature to mature waters

The immature hyper acid SO_4-Cl waters (i.e., from Kawah Ijen volcano) and the mature neutral-Cl waters influenced by intensive water-rock interaction (i.e., from YPVF) exhibit higher Ge/Si ratios and lower $\delta^{30}Si$ values relative to intermediate waters (acid SO_4-, alkaline HCO_3-, immature neutral-Cl waters (i.e., from Basse-Terre), and mixed thermal waters) (**Fig. 3.11**). This observation is well in agreement with these two types of waters (hyper acid SO_4-Cl waters and mature neutral-Cl waters from YPVF) being distinct from the other types of thermal waters in the PCA (**Fig. 3.5**).

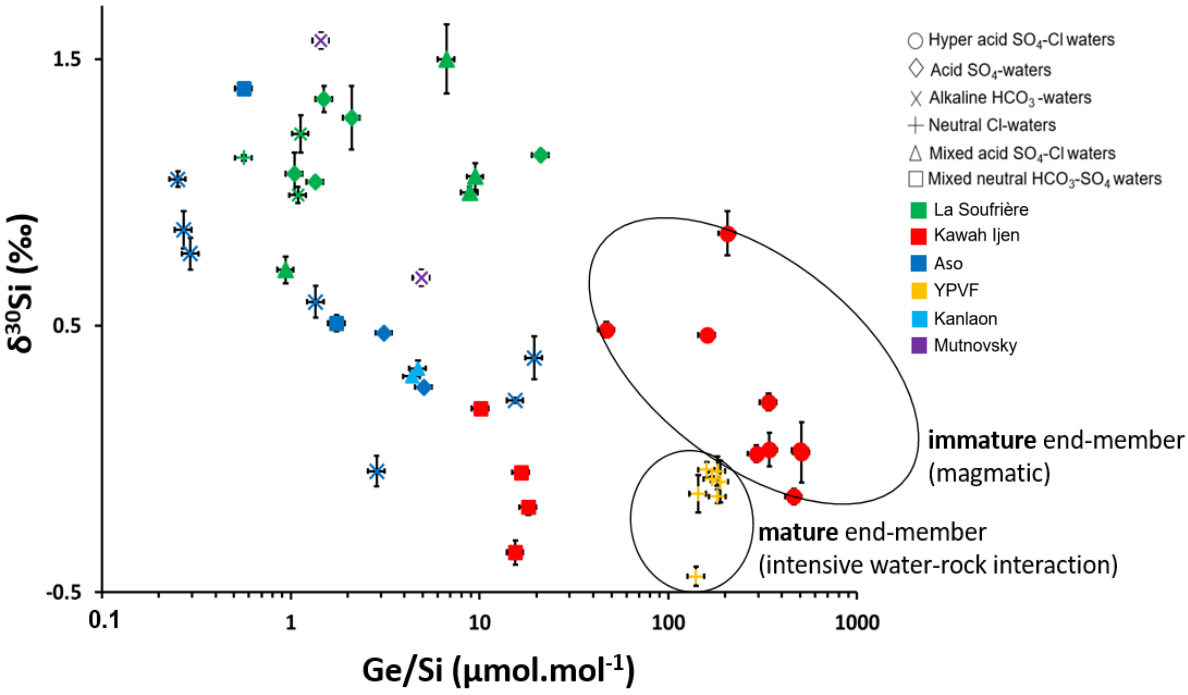

Fig. 3.11: Plot of the $\delta^{30}Si$ (± SD) as a function of the Ge/Si ratios (± SD) in the different types of thermal waters (represented by symbols; hyper acid SO_4-Cl, acid SO_4-, alkaline HCO_3-, neutral Cl-waters and mixed thermal springs, i.e., acid SO_4-Cl, neutral HCO_3-SO_4 waters) collected in the different sites (color-coded; La Soufrière, Kawah Ijen, Aso, YPVF, Kanlaon and Mutnovsky).

This can be regarded as an evolution trend from (i) high Ge/Si ratios and low $\delta^{30}Si$ values (Ge/Si > 50 µmol.mol^{-1}; $\delta^{30}Si$ < 0.5 ‰) in the "magmatic endmember" represented by immature hyper acid SO_4-Cl waters, formed by volcanic gases condensation and influenced by silica precipitation (as well shown by the PCA analysis where the dissolved Si concentration is well-correlated with the principal component 1 for this water type; **Fig. 3.5b**) to (ii) lower Ge/Si ratios and heavier $\delta^{30}Si$ values (Ge/Si < 20 µmol.mol^{-1}; $\delta^{30}Si$ -0.5 to 1.5 ‰) with increasing water-rock interaction in acid SO_4 -waters, alkaline HCO_3-waters, and immature neutral-Cl waters, (iii) then back to high Ge/Si ratios and low $\delta^{30}Si$ values (Ge/Si > 100 µmol.mol^{-1}; $\delta^{30}Si$ < 0 ‰) in the "mature endmember" represented by mature neutral-Cl waters dominated by the influence of water-rock interaction and the solubility of Ge in Cl-rich waters (as well shown by the

PCA analysis where the dissolved Ge concentration is well-correlated with Cl concentration for this water type; **Fig. 3.5b)** (**Fig. 3.12**).

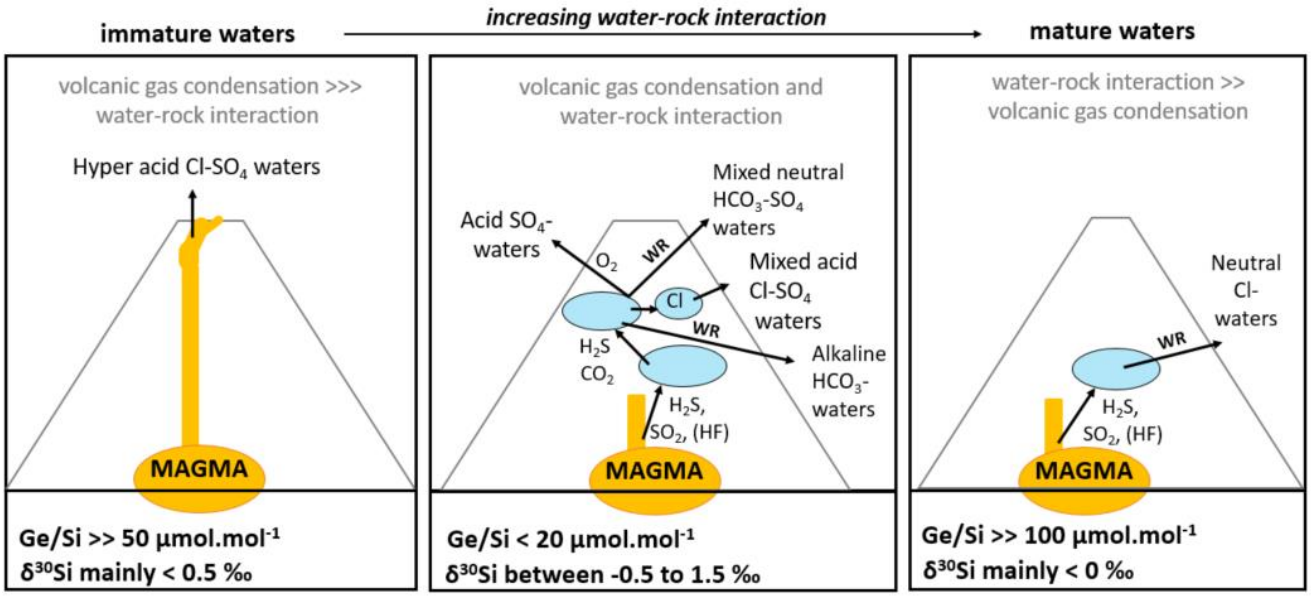

Fig. 3.12: Schematic illustrating the evolution of Ge/Si ratio and $\delta^{30}Si$ value in thermal springs from immature to mature waters, involving the processes influencing the thermal waters chemistry, i.e., magmatic processes and water-rock interaction (WR).

3.7 Conclusion

This study provides for the first time analyses of the Ge/Si ratios and Si isotope compositions of a range of waters representative of the main generic types of thermal springs, based on measurements on 56 different thermal springs (database on 72 water samples) from six hydrothermally-active volcanic regions. The study reveals that a broad range of Ge/Si ratios and Si isotope compositions characterizes thermal waters, and some key processes that likely control their Ge/Si ratios and Si isotope compositions have been identified. The following conclusions can be drawn from this study:

(i) Overall, the Ge/Si ratios and the $\delta^{30}Si$ values in thermal springs evolve from high Ge/Si ratios and low $\delta^{30}Si$ values in immature hyper acid SO_4-Cl waters ("magmatic end-member") to lower Ge/Si ratios and heavier $\delta^{30}Si$ values in acid SO_4 -, alkaline HCO_3-waters and immature neutral-Cl waters, then back to high Ge/Si ratios and low $\delta^{30}Si$ values in the mature neutral-Cl waters, i.e., similar Ge/Si values and lower $\delta^{30}Si$ values than in waters from the magmatic end-member.

(ii) The data support that in immature hyper acid SO_4-Cl waters ("magmatic end-member"), the high Ge/Si ratios likely result from Ge enrichment in thermal waters due to the Ge volatility and transport by volcanic gases (via GeF_4, $GeCl_4$ and GeS) and silica precipitation in thermal fluids.

(iii) The large range of values of Ge/Si ratios and $\delta^{30}Si$ values measured in acid SO_4 -, alkaline HCO_3- and neutral Cl-thermal waters can be explained by an increasing intensity of water-rock interaction involving silica precipitation, and Ge transport with salinity and Cl^-.

This study demonstrates that generating new knowledge on the influence of volcanic gas and water-rock interaction on the variations of Ge/Si ratios and $\delta^{30}Si$ values in thermal springs requires including thermal springs from multiple locations in order to cover the four main types of thermal waters (hyper acid SO_4-Cl waters, acid SO_4 -, alkaline HCO_3- and neutral Cl-thermal waters). Indeed, a first investigation based on thermal springs from one site mislead to no apparent relationship between Ge/Si ratios and $\delta^{30}Si$ values and the water composition type (Gaspard et al, submitted).

3.8 References

Abraham, K., Opfergelt, S., Fripiat, F., Cavagna, A-J., de Jong, J., Foley, S.F., André, L., Cardinal, D., 2008. δ^{30}Si and δ^{29}Si determinations on USGS BHVO-1 and BHVO-2 reference materials with a new configuration on a Nu Plasma Multi-Collector ICP-MS. Geostand. Geoanal. Res. 32(2), 193-202.

Arnòrsson, S., 1983. Chemical equilibria in Icelandic geothermal systems, Geothermics 12, 119-128.

Arnòrsson, S., 1987. Germanium in Icelandic geothermal systems. Geochim. Cosmochim. Ac. 48, 2489-2502.

Barat, A., 1986. Etude du rôle des eaux souterraines dans le mécanisme des éruptions phréatiques. Application à la Montagne Pelée de Martinique et à la Soufrière de Guadeloupe, Document du BRGM. 115.

Baronas, J.J., Torres, M.A., West, A.J., Rouxel, O., Georg, B., Bouchez, J., Gaillardet, J., Hammond, D.E., 2018. Earth Planet. Sci. 503, 194-215.

Baronas, J.J, West, A.J., Burton, K.W., Hammond, D.E., Opfergelt, S., Pogge von Strandmann, P.A.E., James, R.H., Rouxel, O.J., 2020. Ge and Si isotopes behaviour during intense tropical weathering. Global Biogeochem. Cy. doi:10.1029/2019gb006522.

Basile-Doelsch, I., 2006. Si stable isotopes in the Earth's surface: a review. J. Geochem. Explor. 88, 252–256.

Brombach, T., Marini, L., Hunziker, J.C., 2000. Geochemistry of the thermal springs and fumaroles of Basse-Terre Island, Guadeloupe, Lesser Antilles. B. Volcanol. 61(7), 477-490.

Burton, J.D., Culiun, F., Riley, J.P., 1959. The abundance of gallium and germanium in terrestrial materials. Geochim. Cosmochim. Acta 16, 151-180.

Busey, R. H., Schwartz, E., Mesmer, R. E., 1980. Fluorosilicate equilibria in sodium-chloride solutions from 0 to 60°C. Inorg. Chem. 19, 758–761.

Cardinal, D., Alleman, L.Y., De Jong, J., Ziegler, K., André, L., 2003. Isotopic composition of silicon measured by multicollector plasma source mass spectrometry in dry plasma mode. J. Anal. Atom. Spectrom. 18, 213–218.

Cardwell, R.K., Isaacks, B.L., Karig, D.E., 1980. The spatial distribution of earthquakes, focal mechanism solutions, and subducted lithosphere in the Philippine and Northeastern Indonesian Islands. The Tectonic and Geologic Evolution of Southeast Asian Seas and Islands. 1–35.

Caudron, C., Syahbana, D.K., Lecocq, T., van Hinsberg, V., McCausland, W., Triantafyllou, A., Camelbeek, T., Bernard, A., Surono, 2015. Kawah Ijen volcanic activity: a review. Bull. Volcanol. 77, 16.

Chemtob, S.M., Rossman, G.R., Young, E.D., Ziegler, K., Moynier, F., Eiler, J.M., Hurowitz, J.A., 2015. Silicon isotopes systematics of acidic weathering of fresh basalts, Kilauea Volcano, Hawai'i. Geochim. Cosmochim. Ac. 169. 63, 81.

Chen, X-Y., Chafetz, H.S., Lapen, T.J., 2020. Silicon isotope variations in hydrothermal systems at Yellowstone National Park, Wyoming, USA. Geochim. Cosmochim. Ac. 283, 184-200.

Chudaev, O.V., Chelnokov, G.A., Bragin, I.V., Kharitonova, N.A., Rychagov, S.N., Nuzhdaev A.A., Nuzhdaev, I.A., 2017. Rare earth and major elements geochemistry of geothermal waters from Mutnovsky volcano, Kamchatka. Procedia Earth. Planet. Sc. 17, 92-95.

Clayton, R. N., Mayeda, T. K., Epstein, S., 1978. Isotopic fractionation of silicon in Allende inclusions. In Lunar and planetary science conference proceedings.

Criaud, A., Fouillac, C., 1986. Study of CO_2-rich thermomineral waters from the Central French Massif: Behaviour of some trace-metals, arsenic, antimony and germanium. Geochim. Cosmochim. Ac. Ed.

de Hoog, J.C.M, van Bergen, M.J., Jacobs, M.H.G., 2015. Vapour-phase crystallisation of silica from SiF4-bearing volcanic gases. Annals of Geophysics. 48, 4/5.

De La Rocha, C.L., Brzezinski, A., DeNiro, M.J., 1996. Purification, recovery and laser-driven fluorination of silicon from dissolved and particulate silica for the measurement of natural stable isotope abundances. Anal. Chem. 68, 3746-3750.

Delmelle, P., Bernard, A., 1994. Geochemistry, mineralogy, and chemical modelling of the acid crater lake of Kawah Ijen volcano, Indonesia. Geochim. Cosmochim. Acta 58, 2445-2460.

Delmelle, P., Fischer, T., Kusakae, M., 1998. Geochemical and isotopic evidence for seawater contamination of the hydrothermal system of Taal Volcano, Luzon, the Philippines. Bull. Volcanol. 59, 562-576.

Delmelle, P., Bernard, A., Kusakabe, M., Fisher, T.P., Takano, B., 2000. Geochemistry of the magmatic-hydrothermal system of Kawah Ijen volcano, East Java, Indonesia. J. Volcanol. Geoth. Res. 97, 31-53.

Derry, L.A., Kurtz, A.C., Ziegler, K., Chadwick, O.A., 2005. Biological control of terrestrial silica cycling and export fluxes to watersheds. Lett. Nature 433, 728–731.

Dessert, C., Gaillardet, J., Dupré, B., Schott, J., Pokrovsky, O.S., 2009. Fluxes of high- versus low-temperature water-rock interactions in aerial volcanic areas: Example from the Kamchatka Peninsula, Russia. Geochim. Cosmochim. Ac. 73, 148–169.

Dessert, C., Lajeunesse, E., Lloret, E., Clergue, C., Crispi, O., Gorge, C., Quidelleur, X., 2015.

Controls on chemical weathering on a mountainous volcanic tropical island: Guadeloupe (French West Indies). Geochim. Cosmochim. Ac. 171, 216–237.

Ding, T. P., Jiang, S., Wan, D., Li, Y., Li, J., Song, H., Liu, Z., Yao, X., 1996. Silicon Isotope Geochemistry. Geological Publishing House edition.

Ding, T.P., Gao, J., Tian, S., Wang, H., Li, M., Wang, C., Luo, X., Han, D., 2016. Chemical and isotopic characteristics of the water and suspended particulate materials in the Yellow river and their geological and environmental implications. Acta Geol. Sin. (Engl. Ed.), 90(1), 285–351.

Ding, T.P., Jiang, S., Li, Y., Gao, J., Hu, B., 2017. Geochemistry of silicon isotopes. De Gruyter.

Douthitt, C.B., 1982. The geochemistry of the stable isotopes of silicon. Geochim. Cosmochim. Acta 46, 1449–1458.

Ellis, A.J., Mahon, W.A.J., 1964. Natural hydrothermal systems and experimental hot water/rock interactions (Part II). Geochim. Cosmochim. Ac. 31, 519-538.

Ellis, A.J., Mahon, W. A. J., 1977. Chemistry and Geothermal Systems. Academic Press, New York.

Epstein, S., Taylor, H. P. Jr., 1973. The isotopic composition and concentration of water, hydrogen, and carbon in some Apollo 15 and 16 soils and in the Apollo 17 orange soil. Opt. Lett. 27, 45–46.

Escoubé, R., Rouxel, O. J., Luais, B., Ponzevera, E., Donard, O.F., 2012. An intercomparison study of the Germanium isotope composition of geological reference materials. Geostand. Geoanal. Res. 36, 149–159.

Escoubé, R., Rouxel, O., Edwards, K., Glazer, B., Donard, O., 2015. Coupled Ge/Si and Ge isotope ratios as geochemical tracers of seafloor hydrothermal systems: case studies at Loihi Seamount and East Pacific Rise 9°50'N. Geochim. Cosmochim. Ac. 167, 93−112.

Evans, M.J., Derry, L.A., 2002. Quartz control of high germanium/silicon ratios in geothermal waters. Geology 30, 1019–1022.

Fournier, R.O., Rowe, J.J., 1977. The solubility of amorphous silica in water at high temperatures and high pressures. Am. Mineral. 62, 1052-1056.

Fournier, R.O., 1989. Geochemistry and dynamics of the Yellowstone National Park hydrothermal system. Annu. Rev. Earth Planet. Sci. 17, 13–53.

Gaillardet, J., Rad, S., Rivé, K., Louvat, P., Gorge, C., Allègre, C-J., Lajeunesse, E., 2011. Orography-driven chemical denudation in the Lesser Antilles : Evidence for a new feed-back mechanism stabilizing atmospheric CO_2. Am. J. Sci. 311, 851-894.

Gailler, L-S., Bouchot, V., Martelet, G., Thinon, I., Coppo, N., Baltassat, J-M., Bourgeois, B., 2014. Contribution of multi-method

geophysics to the understanding of a high-temperature geothermal province: The Bouillante area (Guadeloupe, Lesser Antilles). J. Volcanol. Geoth. Res. 275, 34-50.

Gaspard, F., Opfergelt, S., Dessert, C., Robert, V., Ameijeras-Marino, Y., Delmelle, P. Imprint of chemical weathering and hydrothermalism on the Ge/Si ratio and Si isotopic composition of rivers in a volcanic tropical island, Basse-Terre, Guadeloupe (French West Indies). Submitted to Chem. Geol.

Geilert, S., Vroon, P.Z., Keller, N., Gudbrandsson, S., Stefànsson, A., Van Bergen, M.J., 2014. Silicon isotope fractionation during silica precipitation from hot springs waters, Geophys. Res. Abstract EGU 2014: EGU2014-7951.

Geilert, S., Vroon, P.Z., Keller, N., Gudbrandsson, S., Stefànsson, A., Van Bergen, M.J., 2015. Silicon isotope fractionation during silica precipitation from hot-springs waters: evidence from the Geysir geothermal field, Iceland. Geoch. Cosmochim. Acta 164, 403-427.

Georg, R.B., Reynolds, B.C., West, A.J., Burton, K.W., Halliday, A.N., 2007. Silicon isotope variations accompanying basalt weathering in Iceland. Earth Planet. Sci. Lett. 261, 476–490.

Giggenbach, W.F., 1988. Geothermal solute equilibria. Derivation of Na-K-Mg-Ca geoindicators. Geochim. Cosmochim. Ac. 52, 2749-2765.

Han, Y., Huh, Y., Derry, L., 2015. Ge/Si ratios indicating hydrothermal and sulphide weathering input to rivers of the Eastern Tibetan Plateau and Mt. Baekdu. Chem. Geol. 410, 40-52.

Hörmann, P.K., 1970. Germanium. In Handbook of Geochemistry vol. 3. (ed. WEDEPOHL K. H.). Springer Verlag.

Hosono, T., Hartmann, J., Louvat, P., Amann, T., Washington, K.E., West, A.J., Okamura, K., Böttcher, M.E., Gaillardet, J., 2018. Earthquake-induced structural deformations enhance long-term solute fluxes from active volcanic systems. Scientific reports.

Hurwitz, S., Lowenstern, J.B., Heasler, H., 2007. Spatial and temporal geochemical trends in the hydrothermal system of Yellowstone National Park: Inferences from river solute fluxes. J. Volcanol. Geoth. Res. 162, 149-171.

Hurwitz, S., Evans, W.C., Lowenstern, J.B., 2010. River solute fluxes reflecting active hydrothermal chemical weathering of the Yellowstone Plateau Volcanic Field, USA. Chem. Geol. 276, 331-343.

Hurwitz, S., Lowenstern, J.B., 2014. Dynamics of the Yellowstone hydrothermal system. Rev. Geophys. 51.

Ijen Monthly Climate Average, consulted on April 2020. https://www.worldweatheronline/ijen-weather/east-java/id.aspx.

Karpov, G.A., Nikolaeva, A.G., Alekhin, Y.V., 2013. Contents and sources of rear earth elements in modern hydrothermal systems of Kamchatka. J. Petrol. 21, 163-176.

Kaya, M., Volkan, M., 2011. Germanium determination by flame atomic absorption spectrometry: An increased vapour pressure-chloride generation system. Talanta. 84, 122−126.

Kraynov, S.R., 1965. Geochemistry of fluorine, tungsten and germanium in nitrogenous thermal waters of crystalline rocks. Geochem. Int. 2, 1001-101.

Kwasnik, W., 1963. Section 4. Fluorine compounds. In: Handbook of Preparative Inorganic Chemistry. Brauer G, (ed) Academic Press Inc., New York, 150.

Le, S., Josse, J., Husson, F., 2008. FactoMineR: An R Package for Multivariate Analysis. Journal of Statistical Software. 25, 1-18.

Li, Y., Ding, T.P., Wan, D., 1995. Experimental study of silicon isotope dynamic fractionation and its application in geology. Chin. J. Geochem. 14, 212–219.

Louvat, P., Allègre, C.J., 1997. Present denudation rates on the island of Reunion determined by river geochemistry: Basalt weathering and mass budget between chemical and mechanical erosions. Geochim. Cosmochim. Ac 61, 3645-3669.

Luais, B., 2012. Germanium chemistry and MC-ICPMS isotopic measurements of Fe–Ni, Zn alloys and silicate matrices: Insights into deep Earth processes. Chem Geol. 334, 295−311.

Maximo, R.P.R., 2019. Geochemical and isotopic characterization of hydrothermal systems of active volcanoes in the Philippines. PhD. Université Libre de Bruxelles (ULB), Belgium.

Melcher, F., 2003. The Otavi Mountain Land in Namibia: Tsumeb, Germanium and Snowball Earth. Mitteilungen Österreichischer Geologischer Gesellschaft. 148, 413-435.

Meng, Y.M., Qi, H.W., Hu, R.Z., 2015. Determination of germanium isotopic compositions of sulphides by hydride generation MC-ICP-MS and its application to the Pb–Zn deposits in SW China. Ore Geol Rev. 65,1095−1109.

Newhall, C.G., Dzurisin, D., 1988. Historical unrest at large calderas of the world. U.S. Geol. Surv. Bull. 1855 (1108 pp.).

Ono, K., Watanabe, K., 1985. Geological Map of Aso Volcano. Geological Map of volcanoes, vol. 4. Geological Survey of Japan.

Opfergelt, S., Cardinal, D., André, L., Delvigne, C., Bremond, L., Delvaux, B., 2010. Variations of $d^{30}Si$ and Ge/Si with weathering and biogenic input in tropical basaltic ash soils under monoculture. Geochim. Cosmochim. Acta 74, 225–240.

Opfergelt, S., Eiriksdottir, E.S., Burton, K.W., Einarsson, A., Siebert, C., Gislason, S.R., Halliday, A.N., 2011. Quantifying the impact of freshwater diatom productivity on silicon isotopes and silicon fluxes: Lake Myvatn, Iceland. Earth. Planet. Sc. Lett. 305, 73-82.

Opfergelt, S., Delmelle, P., 2012. Silicon isotopes and continental weathering processes: Assessing controls on Si transfer to the ocean. Comptes Rendus Geosci. 344, 723–738.

Opfergelt, S., Burton, K.W., Pogge von Strandmann, P.A.E., Gislason, S.R., Halliday, A.N., 2013. Riverine silicon isotope variations in glaciated basaltic terrains: implications for the Si delivery to the ocean over glacial-interglacial intervals. Earth. Planet. Sc. Lett. 369-370, 211-219.

OVSG-IPGP Data Base & Field Monthly Reports. 2010-2015. nd. Volcanological and Seismological Observatory of Guadeloupe, OVSG-IPGP. <http://www.ipgp.fr/>.

Palmer, 2009. Hydrogeochemical insights into the nature of magmatic-hydrothermal fluid at Kawah Ijen volcano, Indonesia. PhD. McGill University, Canada.

Parkhurst, D.L., Appelo, C.A.J., 2013. Description of input and examples for PHREEQC version 3-a computer program for speciation, batch-reaction, one-dimensional transport, and inverse geochemical calculations. In: U.S. Geological Survey Techniques and Method book 6, chap. A43, 497p., available only at http://pubs.usgs.gov/tm/06/a43.

Pokrovski, G.S., Schott, J., 1998. Thermodynamic properties of aqueous Ge(IV) hydroxide complexes from 25 to 350°C: implications for the behavior of germanium and the Ge/Si ratio in hydrothermal fluids. Geochim. Cosmochim. Ac. 62, 1631-1642.

Renggli, C.J., Klemme, S., 2020. Experimental constraints on metal transport in fumarolic gases. J. Volcanol. Geoth. Res. 400, 106929.

Reynolds, J. H., Verhoogen, J., 1953. Natural variations in the isotopic constitution of silicon. Geochim. Cosmochim. Acta, 3, 224–234.

Reynolds, B.C., Aggarwal, J., André, L., Baxter, D., Beucher, C., Brzezinski, M.A., Engström, E., Georg, B., Land, M., Leng, M.J., Opfergelt, S., Rodushkin, I., Sloane, H.J., Van den Boorn, S.H.J.M., Vroon, P.Z., Cardinal, D., 2007. An inter-laboratory comparison of Si isotope reference materials. J. Anal. Atom. Spectrom. 22, 561-568.

Rivé, K., Gaillardet, J., Agrinier, P., Rad, S., 2013. Carbon isotopes in the rivers from the Lesser Antilles: origin of the carbonic acid consumed by weathering reactions in the Lesser Antilles. Earth Surf. Proc. Land. 38, 1020–1035.

Robertson, K., Simon, A., Pettke, T., Smith, E., Selyangin, O., Kiryukhin, A., Mulcahy, S.R., Walker, J.D., 2013. Melt inclusion evidence for magma evolution at Mutnovsky volcano, Kamchatka. Geofluids. 13, 4.

Rosenberg, P.E., 1973. HF/SiF4 ratios in volcanic and magmatic gases. Geochim. Cosmochim. Acta, 37, 109-112.

Rouxel, O.J., Luais, B., 2017. Germanium isotope Geochemistry. Reviews in Mineralogy & Geochemistry. 82, 601-656.

Saito, T., Ohsawa, S., Hashimoto, T., Terada, A., Yoshikawa, S., Ohkura, T., 2008. Water, heat and chloride balances of the crater lake at Aso

volcano, Japan. J. Geotherm Res. Soc. Jpn. 30, 107–120 (in Japanese).

Savage, P.S., Georg, R.B., Williams, H.M., Burton, K.W., Halliday, A.N., 2011. Silicon isotope fractionation during magmatic differentiation. Geochim. Cosmochim. Ac. 75, 6124-6139.

Schopka, H. H., Derry, L. A., Arcilla, C. A., 2011. Chemical weathering, river geochemistry and atmospheric carbon fluxes from volcanic and ultramafic regions on Luzon Island, the Philippines. Geochim. Cosmochim. Ac. 75, 978–1002.

Shapiro, M. N., Ermakov, V.A., Shantser, A. E., Shuldiner, V. I., Khanchuk, A. I., Visotski, S. V., 1987. Description of the Tectonic Evolution of Kamchatka, Nauka, Moscow. (Russian).

Siebert, C., Ross, A., McManus, J., 2006. Germanium isotope measurements of high-temperature geothermal fluids using double-spike hydride generation MC-ICP-MS. Geochim. Cosmochim. Acta 70, 3986-3995.

Sossi, P.A., Fegley, B., 2018. Thermodynamics of Element Volatility and its Application to Planetary Processes. Rev. Mineral. Geochem. 84, 393–459.

Trettin, C.C., Bartelli, L.J., 1980. Characterization of Soils in Yellowstone National Park. Annual Reports of Wyoming University. 4, 22.

United Kingdom Accreditation Body (UKAS)., 2014. Certificate of measurement, river water-anion, certified reference material LGC6025. 4005.

Ustunisik, G., DiFrancesco, N., Yang, S., Humayun, M., Rogaski, A., 2018. Role of Cl and S on the volatility of Ge, Zn, and Li in martian basaltic magmas: implications for volatile contribution to martian surface lithologies. 49th Lunar and Planetary Sciences Conference 2018 (LPI Contrib. No. 2083).

Van den Boorn, S.H., van Bergen, M.J., Vroon, P.Z., 2007. Silicon isotope fractionation during acid water-igneous rock interaction. American Geophysical Union. Abstract AGU, V11E-08.

Van Hinsberg, V., Palmer, S., King, J., Williams-Jones, G,. Susanto, G,. Nasution, A., 2009. Visual, geochemical, and geophysical observations during mid-2008. Vol 34.

van Hinsberg, V., Berlo, K., Sumarti, S., van Bergen M., Williams-Jones, A., 2010. Extreme alteration by hyperacidic brines at Kawah Ijen volcano, East Java, Indonesia: II. J. Volcanol. Geoth. Res. 196(3-4): 169-184

van Hinsberg, V., Vigouroux, N., Palmer, S., Berlo, K., Mauri, G., Williams-Jones, A., McKenzie, J., Williams-Jones, G., Fischer, T., 2017. Element fluxe to the environment of the passively degassing crater lake-hosting Kawah Ijen volcano, Indonesia, and implications for estimates of the global volcanic flux. The Geological Society of London.

van Hinsberg, V., Berlo, K., Lowenstern, J., 2020. An experimental investigation of interaction between andesite and hyperacidic volcanic lake water. Minerals. 10, 96.

Villemant, B., Hammouya, G., Michel, A., Semet, M.P., Komorowski, J-C., Boudon, G., Cheminée, J-L., 2005. The memory of volcanic waters: shallow magma degassing revealed by halogen monitoring in thermal springs of La Soufrière volcano (Guadeloupe, Lesser Antilles). Earth Planet. Sc. Lett. 237, 710-728.

Villemant, B., Komorowski, J-C., Dessert, C., Michel, A., Crispi, O., Hammouya, G., Beauducel, F., De Chabalier, J-B., 2014. Evidence for a new shallow magma intrusion at La Soufrière of Guadeloupe (Lesser Antilles), Insights from long-term geochemical monitoring of halogen-rich hydrothermal fluids. J. Volcanol. Geotherm. Res. 285, 247–277.

von Bidersee, H., Pichler, H., 1995. The Canlaon and its neighbouring volcanoes in the Negros Belt/Philippines. Journal of Southeast Asian Earth Sciences. 11, 113-123.

Wang, W., Wei, H-Z., Jiang S-Y., Tan, H-B., Eastoe C.J., Williams-Jones, A.E., Hohl, S.V., Wu, H-P., 2019. The origin of rare alkali metals in geothermal fluids of southern Tibet, China: a silicon isotope perspective. Sci. Rep. 9, 7918.

White, D.E., 1957. Magmatic, connate, and metamorphic waters: Geol. Soc. America Bull. 68, 1659-1682.

Whitford, D.J., Nicholls, I.A., Taylor, S.R., 1979. Spatial variations in the geochemistry of quaternary lavas across the Sunda Arc in Java and Bali. Contrib. Mineral. Petrol. 70, 341–356.

Yamada, M., Ohsawa, S., Kazahaya, K., Yasuhara, M., Takahashi, H., Amita, K., Mawatari, H., Yoshikawa S., 2011. Mixing of magmatic CO_2 into volcano groundwater flow at Aso volcano assessed combining carbon and water stable isotopes. J. Geochem. Explor. 108, 81-87.

Yeghicheyan, D., Bossy, C., Bouhnik Le Coz, M., Douchet, C., Granier, G., Heimburger, A., Lacan, F., Lanzanova, A., Rousseau, T.C.C., Seidel, J-L., Tharaud, M., Candaudap, F., Chmeleff, J., Cloquet, C., Delpoux, S., Labatut, M., Losno, R., Pradoux, C., Sivry, Y., Sonke, J.E., 2013. A Compilation of Silicon, Rare Earth Element and Twenty-One other Trace Element Concentrations in the Natural River Water Reference Material SLRS-5 (NRC-CNRC). Geostand. Geoanal. Res. 37(4), 449-467.

Young, E.D., Galy, A., Nagahara, H., 2002. Kinetic and equilibrium mass-dependent isotope fractionation laws in nature and their geochemical and cosmochemical significance. Geochim. Cosmochim. Ac. 66, 1095-1104.

Zelenski, M., Malik, N., Taran, Yu., 2014. Emissions of trace elements during the 2012-2013 effusive eruption of Tolbachik volcano,

Kamchatka: enrichment factors, partition coefficients and aerosol contribution. J. Volcanol. Geotherm. Res. 285, 247–277.

Ziegler, K., Chadwick, O.A., Brzezinski, M.A., Kelly, E.F., 2005. Natural variations of $d^{30}Si$ ratios during progressive basalt weathering, Hawaiian Islands. Geochim. Cosmochim. Acta 69, 4597–4610.

3.9 Supplementary Materials

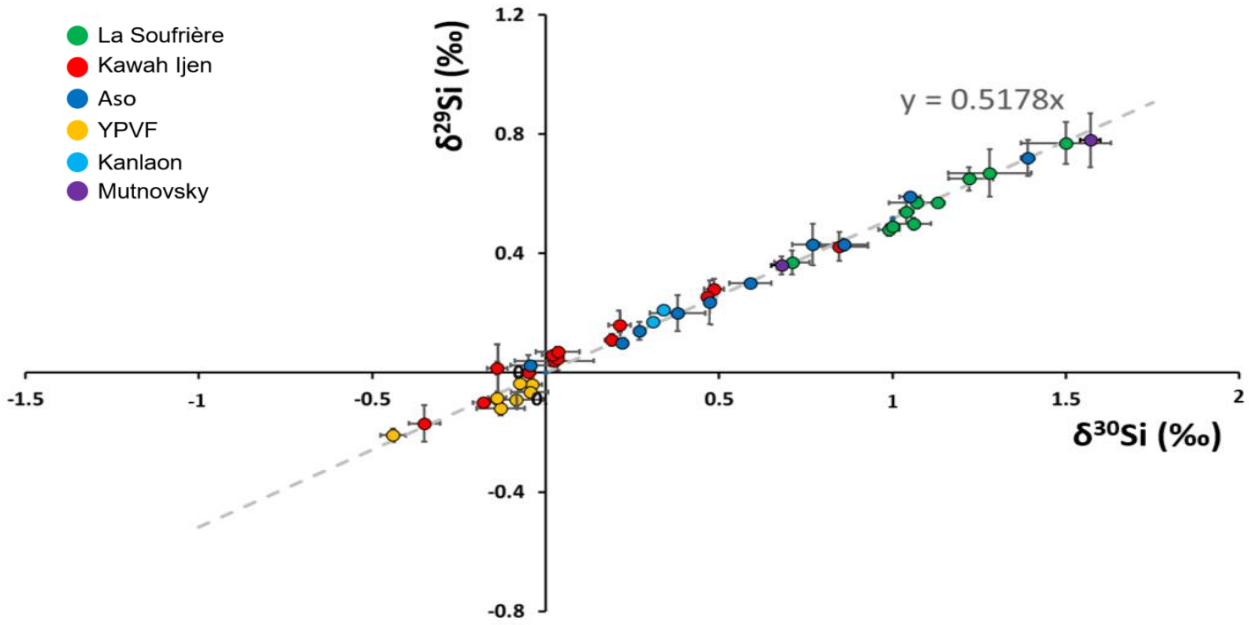

Suppl. Mat. 3.1: Silicon isotopes measurements of all thermal springs fit onto a mass-dependent fractionation array $\delta^{30}Si$ and $\delta^{29}Si$ (theorical 0.5178 slope for equilibrium mass-dependent fractionation; Young et al, 2002).

Suppl. Mat. 3.2: Principles and definitions for the Principal Component Analysis (PCA).

A PCA is useful to (i) visualize the data and identify key information by projecting them in a reduced dimension space, (ii) identify relationship between variables and between variables and individuals (definitions are given in Table here below). For n individuals (n=thermal springs from six hydrothermally-active volcanic regions) and k variables (k=cationic and anionic compositions, Si and Ge), a PCA creates a new set of variables q<k (q=principal components, the linear combinations of the k variables), containing most of the data information. For k variables in a multiple dimensions space, an algorithm calculates the projection on an axis maximizing the dispersion (variance). This is the first principal component. Each principal component is defined by a eigenvector, showing the axes direction on which the data is projected and by a eigenvalue giving the total variance's percentage explained by the principal component. The PCA supplies the graphs of variables and individuals plotting variables and individuals as a function of the two principal components, respectively. The graph of variables is useful to (i) see which variables are positively or negatively correlated with the principal components and (ii) to visualize potential correlations between the original variables. The graph of individuals allows to (i) visualize how individuals behave as a function of the two principal components and (ii) detect proximity between individuals and outliers. Used together, these two graphs are needed to link variables and individuals together.

Individuals (n)	Thermal springs from La Soufrière volcano, Kawah Ijen volcano, Aso volcano, YPVF, Kanlaon volcano and Mutnovsky volcano (n=6)
Variables (k)	H, Ca, Na, Mg, K, Al, Fe, Si, SO_4, Cl and Ge (k=11)
Principal components (q)	Linear combinaisons of the variables that maximise the variance of the dataset
Eigenvector	Direction of the axes on which the data is projected
Eigenvalue	Percentage of the total variance that is explained by the principal component
Graph of variables	Plot of the variables as a function of two principal components
Graph of individuals	Plot of the individuals as a function of two principal components

Chapter 2:

Influence of hyper acid thermal waters on the Ge/Si ratio and Si isotopic composition of the Banyu Pahit/Banyu Putih river, Kawah Ijen volcano, East Java, Indonesia

4.1 Abstract

Hyper acid hydrothermal system sustained by magmatic gases as a source of acidity likely provide the uppermost contribution from magmatic CO_2, a source of CO_2 generally overlooked in the estimates of the atmospheric CO_2 consumption associated to volcanic rock weathering. Precise estimations of the thermal input to rivers is particularly difficult due to the variability of the chemical composition of thermal springs, and the influence of seasonal change in discharge affecting the relative contribution of thermal inputs to river weathering fluxes. Here, in a well-known hyper acid hydrothermal context, the variability of the germanium to silicon ratio (Ge/Si ratio) and the stable silicon isotopes ($\delta^{30}Si$) in the Banyu Pahit/Banyu Putih river waters draining from Kawah Ijen volcano (Java Island, Indonesia) and in their contributors (thermal springs, tributaries, soil solutions) is used to quantify thermal contributions to the river and assess the associated magmatic CO_2 input. Original data of the discharge and chemical composition of the river in wet season are compared with existing data in dry season to calculate annual weathering fluxes.

The upstream section of the Banyu Pahit/Banyu Putih river influenced by hyper acid SO_4-Cl thermal water discharges exhibit the highest Ge/Si ratios reported in river waters (220.68-513.90 μmol.mol^{-1}) and low δ^{30}Si values (-0.08 to 0.48 ‰). In this hyper acid hydrothermal context, the Ge/Si ratio is a powerful tracer of the thermal input to rivers due to high Ge/Si ratios values in thermal waters (160.12-507.89 μmol.mol^{-1}). The lower Ge/Si ratios (4.47-17.47 μmol.mol^{-1}) and higher δ^{30}Si values (1.06 to 1.73 ‰) of the downstream section relative to the upstream section of the river confirms the contribution from mixed neutral HCO_3-SO_4 thermal waters and alkaline tributaries, but importantly also from soil weathering processes in the Asembagus plain. A well constrained discharge-based model combined with the riverine Ge/Si ratios is successfully used to (i) nail down all contributions to the Banyu Pahit/Banyu Putih river, including low discharge thermal contributors to rivers (hyper acid SO_4-Cl thermal waters and mixed neutral HCO_3-SO_4 thermal waters) not detected in the field and to (ii) estimate the magmatic CO_2 input associated to thermal input. Depending if the sampling location used for the calculation is closer or further from the acid crater lake, the hydrothermal contribution to the riverine CO_2 consumption by chemical weathering decreases from 54.54 to 2.36%, highlighting the importance of carefully considering hyper acid hydrothermal context in the estimation of the atmospheric CO_2 consumption by volcanic rock weathering.

4.2. Introduction

Volcanic rocks represent only 5% of the terrestrial land but contribute significantly to the global flux of solutes to the ocean and consumption of atmospheric CO_2 trough silicate weathering (Louvat and Allègre, 1997; Gaillardet et al, 1999; Dessert et al, 2003; Dupré et al, 2003; Gislason and Oelkers, 2011). Rock alteration is intensified in volcanic regions characterized by the presence of a highly acidic crater lake testifying for the presence of a hyper acid hydrothermal system sustained by magmatic gases as a source of acidity such as at Rincón de la Vieja volcano, Póas volcano, and Irazú in Costa Rica, Copahue volcano in Argentina, and Kawah Ijen volcano in Indonesia (Delmelle et al, 2015). Hydrothermally-derived flux of elements may contribute to the weathering fluxes from volcanic regions (Louvat and Allègre, 1997; Dessert et al, 2009; Hurwitz et al, 2010; Schopka et al, 2011; Gaillardet et al, 2011; Rivé et al, 2013), leading to overestimations of the atmospheric CO_2 consumption by volcanic rock weathering. Precise estimations of the thermal input to rivers is particularly difficult based on element ratios (Louvat and Allègre, 1997; Gaillardet et al, 2011; Louvat et al, 2011) due to (i) the variability of the chemical composition of thermal springs, and (ii) the influence of seasonal change in discharge affecting the relative contribution of thermal inputs to river weathering fluxes (*Ch4* on YPVF).

Quantifying the thermal input to rivers in a hyper acid hydrothermal context would likely provide the uppermost contribution from magmatic CO_2, i.e., a necessary boundary to more precisely estimating the atmospheric CO_2 consumption by volcanic rock weathering. Specific germanium to silicon ratio (Ge/Si ratio) and Si isotope compositions ($\delta^{30}Si$) were found in hyper acid SO_4-Cl thermal waters (*Ch1* on thermal springs) suggesting that the contribution from this type of thermal input to river weathering fluxes could be traced using these geochemical tracers.

The Banyu Pahit-Banyu Putih river (Java Island, Indonesia) is particularly well-suited to trace the influence of hyper acid thermal input on riverine chemistry given that (i) the river drains the hyper acid crater lake of Kawah Ijen volcano, (ii) the upstream section of river is mainly influenced by hydrothermal input whereas the downstream riverine section receives additional input from tributaries, (iii) the river catchment is well constrained and the chemical composition of the thermal springs and river is well-studied (e.g., Delmelle et al, 2000; Heikens et al, 2005; Löhr et al, 2005; van Rotterdam-Los et al, 2008). However, the chemical composition of the river was only determined in the dry season so far. Therefore, the influence of seasonal change in discharge on the relative thermal contribution and on the riverine chemistry is not known.

With the aim to quantify thermal contributions to the river and to assess the associated annual magmatic CO_2 input, (i) we lead a sampling campaign of the Banyu Pahit-Banyu Putih river from the Kawah Ijen volcano acid lake down to the Asembagus plain 40 km downstream during the wet season to compare the chemical composition of the river in wet season with the available data in dry season, and hence estimate the annual weathering fluxes from a river draining a hyper acid hydrothermal system, (ii) we determined the Ge/Si ratio and the $\delta^{30}Si$ values in the Banyu Pahit-Banyu Putih river waters and in the contributors (thermal springs, tributaries, soil solutions), (iii) we quantified all contributions to the Banyu Pahit/Banyu Putih river using a discharge-based model combined with the riverine Ge/Si ratios, and (iv) we calculated the hydrothermal contribution of magmatic CO_2 input and the implication on atmospheric CO_2 consumption by weathering in this river draining a hyper acid hydrothermal system.

4.3. Environmental setting

Indonesia has tropical climate with mean annual temperature ranging from 22 to 29 °C. Two seasons are reported: the dry season (from May to October with mean precipitation ranging from 10 to 300 mm) and the wet season (from November to April with mean precipitation ranging from 230 to 1100 mm; Ijen Monthly Climate Averages, 2020).

The Banyu Pahit river water originates on the western flank of Kawah Ijen volcano that is part of the large Ijen Caldera Complex in eastern-most Java Island, Indonesia. Located within the Ijen caldera, Kawah Ijen (7°S, 110°E) is an active stratovolcano of basalt-andesitic to andesitic composition (Whitford et al, 1979; Delmelle and Bernard, 1994) renowned for its hot acidic crater lake (pH < 0.3; T > 35 °C, volume ~ 32 × 10^6 m^3; Delmelle and Bernard, 1994), which represents the world's largest naturally body of hot hyper acid brine (Kemmerling, 1921; Delmelle and Bernard, 1994; Delmelle et al, 2000; Takano et al, 2004; van Hinsberg et al, 2010). The lake chemistry is determined by dissolution of magmatic volatiles, fluid-rock interaction, evaporation of the lake water, dilution by meteoric water and recycling of lake water through seepage into the subsurface hydrothermal system (Delmelle and Bernard, 1994). Water from acidic crater lake leaks through the rock basement of the crater emerging on the western flank and is regarded as the major source of the Banyu Pahit river water (Delmelle et al, 2000). Recent studies argue that the primary source of Banyu Pahit river is a set of springs located approximately 375 m below crater lake elevation considered as outflow from the hydrothermal system and distinctly lack a crater lake contribution (Palmer, 2009). Three set of hyper acid SO_4-Cl thermal springs are reported on the upper (uspstream) section of Banyu Pahit river on the flanks of Kawah Ijen where the acid waters remain essentially undiluted and conservative element behavior dominates (Delmelle et al, 2000).

Downstream of these springs up to Blawan village, water-rock interaction and dilution control the river water composition of Banyu Pahit (Delmelle and Bernard, 1994; Delmelle et al, 2000; Palmer, 2009; van Hinsberg et al, 2010). Emerging from the canyon to the south of Blawan village located about 17 km below the volcano, the Banyu Pahit river receives input of several neutral HCO_3-SO_4 hot springs, associated with deposits of travertine and as a mixture of acidic brines, similar to that of the summit hydrothermal system, with HCO_3 steam-heated waters produced in the shallow part of the system (Delmelle et al, 2000). In the Blawan village, Banyu Pahit river also merges with the alkaline tributaries Kali Sat (KST) and Kali Senggon (KS) rivers, which drain respectively the western and eastern parts of the Ijen caldera, resulting in increasing pH. In this lower section of Banyu Pahit, it was shown that elements are also added to the acid waters due to aggressive water-rock interaction (van Hinsberg et al, 2010).

Finally, owing to its milky-white color resulting from the formation of a white precipitate upon mixing of the Banyu Pahit with the various inflows of alkaline water, the river is now named Banyu Putih ('White river") and flows on the outer slopes of the Ijen Caldera Complex towards the Strait of Madura (Palmer et al, 2011). Most of the Banyu Putih river is regulated at an irrigation dam near Lewung village and used to irrigation on the coastal Asembagus plain (15x13 km) situated in the north-easthern part of Java. The large part of arable land (~36 km^2) with rice, sugar cane, maize, cassava and mixed vegetables is irrigated with Banyu Putih resulting in a strong toxicological impact on soil and crops, and health issue for the local population (Heikens et al, 2005; Löhr et al, 2005; van Rotterdam-Los et al, 2008).

4.4. Materials and methods

4.4.1 Sampling campaign

All sampling sites are presented in **Fig. 4.1**. Acid lake, lake seepage, eleven thermal springs (n=11) and four river waters (Banyu Pahit/Banyu Putih, Kali Sat, Kali Senggon and Bangoran) were collected during wet season (January-February 2017) on eastern part of Java Island.

Acid lake, lake seepage, seven thermal springs (SP1-SP7) and six samples of Banyu Pahit water (BP1-BP5) were taken on the flanks of Kawah Ijen volcano. Four thermal springs (SP8-SP9), three samples of Banyu Pahit water (BP6-BP8) and two alkaline rivers (Kali Sat (KST) and Kali Senggon (KS)) were collected near Blawan village (~17 km below the volcano). In addition, two samples of Banyu Putih (BP9-BP10) water were collected at an irrigation dam near Lewung village (~40 km below the volcano) and one alkaline river (Bangoran, BA) was sampled in the northeast of Java Island. Soil solutions (A, B, C1, C2) were collected in the Asembagus Plain irrigating by the Banyu Putih river.

Acid lake water was sampled at the surface, thermal springs were sampled at their outlets from the riverbed and river waters were collected in fields with minimum anthropogenic impact.

Temperature (°C), pH and conductivity ($\mu S.cm^{-1}$, referenced to 25 °C) were measured *in situ* with a Hanna HI 991300 electrod. Redox potential (Eh; mV) was measured *in situ* with a Thermo Scientific Orian Star electrod. Water samples were filtered within 24 h at 0.45 µm through polycarbonate membranes, and stored at 4 °C in the dark in acid-washed polypropylene (PP) bottles. One aliquot was acidified at 0.5% suprapure HNO_3 for majors, trace elements, Ge/Si and silicon isotope analysis, and one aliquot was non-acidified to determine anions.

Existing data in this area are reported in dry season for the same locations of thermal springs (e.g., Delmelle and Bernard, 1994; Delmelle et al, 2000; Palmer, 2009) and nearby locations of river waters (e.g., Delmelle et al, 2000; Delmelle and Bernard, 2000; Heikens et al, 2005; van Hinsberg et al, 2010; Palmer et al, 2011).

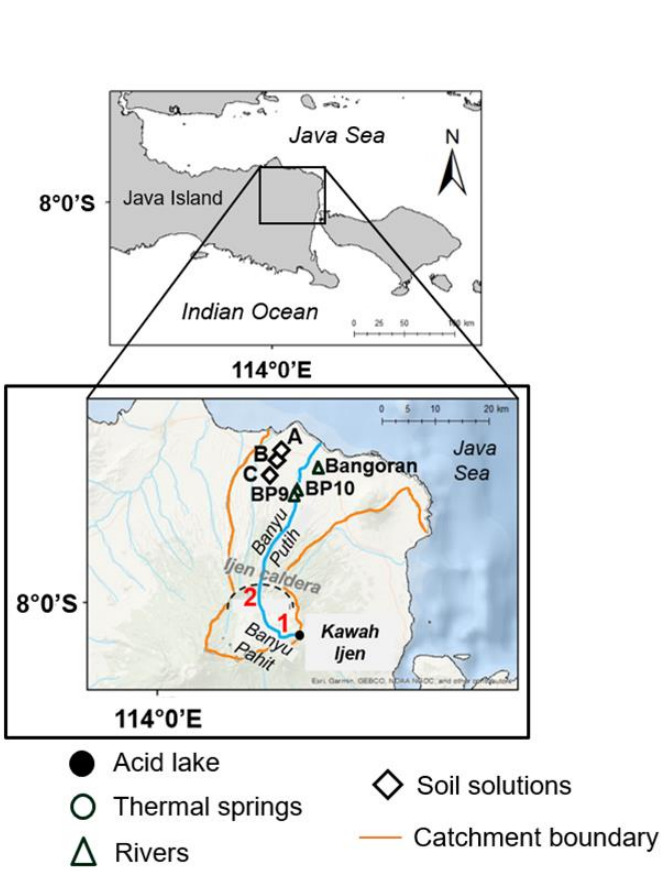
Java Sea
N
8°0'S
Java Island
Indian Ocean
114°0'E
Java Sea
A
B
C
Bangoran
BP9
BP10
Banyu Putih
Ijen caldera
2
1
Kawah Ijen
Banyu Pahit
8°0'S
114°0'E
Acid lake
Thermal springs
Rivers
Soil solutions
Catchment boundary

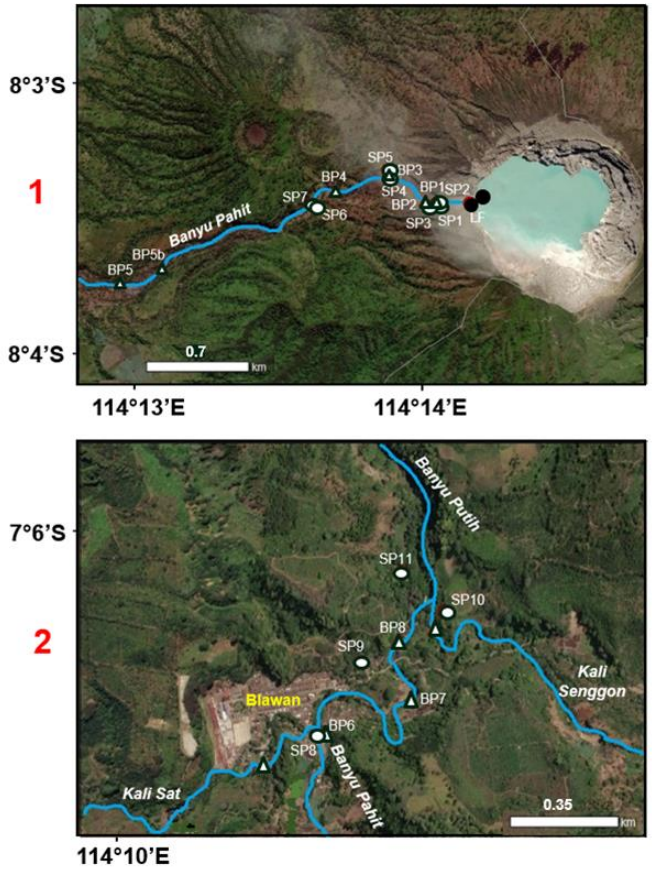
8°3'S
1
8°4'S
SP5
BP3
BP4
SP4
BP1
SP2
SP7
BP2
SP6
SP3
SP1
Banyu Pahit
BP5b
BP5
0.7
km
114°13'E
114°14'E
Banyu Putih
7°6'S
SP11
SP10
2
BP8
SP9
Kali Senggon
Blawan
BP7
BP6
SP8
Banyu Pahit
Kali Sat
0.35
km
114°10'E

Fig. 4.1: Sampling locations on Java Island, Indonesia for the acid lake from Kawah Ijen volcano (plain circle), the thermal springs (open circle), the river waters (triangle; including the Banyu Pahit/Banyu Putih rivers sampled at eleven different locations 40 km downstream and the three alkaline rivers Kali Sat, Kali Senggon and Bangoran), and the soil solutions (diamond; A, B, C, including C1 and C2, collected in the Asembagus Plain irrigated by the Banyu Putih river). The sample names refer to **Table 4.1**.

4.4.2 Water discharges measurement

Water discharges ($m^3.s^{-1}$) in thermal springs and river waters were measured *in situ* using flow meter (Flo-Mate Model FH950) based on the Faraday law of electromagnetic induction. Discharges ($m^3.s^{-1}$) were calculated from the average steam velocity ($\bar{U}$; $m.s^{-1}$) and cross-sectional area (m^2). On field, we divided the width of the riverine channel into 3 equal segments, doing a velocity profile and calculating the flow for each segment, and finally summing the segment flow for the total flow. The average steam velocity ($\bar{U}$) is based on velocity obtained by Fixed Point Averaging (FPA, average of velocities over a fixed period of time, time = 45 seconds) taken at a number of positions in the flow.

For thermal springs with low discharges, we took five points velocity measurements throughout the entire flow and we calculated discharges using $\bar{U}_{thermal\ spring} = 0.9 \times V_{max}$ with V_{max} = the fastest measured velocity.

For river waters, developed method for circular conduit was used and discharges were calculated using $\bar{U}_{river\ water} = (V_{0.2} + V_{0.8} + 2 \times V_{0.4}).4^{-1}$ with $V_{0.2}$, $V_{0.8}$ and $V_{0.4}$ = measured velocity at 0.2, 0.8 and 0.4 × depth, respectively.

Note that the sensor of Flo-Mate was positioned in stationary water for 10 minutes to practise zero check before each water discharges measurement sessions. Zero stability is 0.001 $m.s^{-1}$. The inaccuracies of water discharges measurement associated with low discharges and assessment of $\bar{U}$ using circular conduit for river waters were corrected by the discharge-based mixing model (**section 4.5.1**).

4.4.3 Water elemental analyses

The concentrations of Ca, Na, Mg, K, Al, Fe and Si in the water samples were determined by inductively-coupled plasma-optical emission spectrometry (ICP-OES; iCAP 6500 Thermo Fisher Scientific). The accuracy on majors elements (Ca, Na, Mg, K, Al, Fe and Si) analyses was assessed using the trueness (± 3%, ± 4%, ± 1%, ± 7%, ± 4%, ± 2% and ± 4%; respectively) on the river water reference material SLRS-5 (Yeghicheyan et al, 2013) and the analytical precision (± 0.5%) for each element. The detection limit are 0.05, 0.43, 0.21, 0.26, 0.37, 0.18 and 0.36 $\mu mol.l^{-1}$ for Ca, Na, Mg, K, Al, Fe and Si, respectively. Anions (SO_4^{2-}, Cl^-, NO_3^-, F^-) were measured by ion chromatography (Dionex ICS2000, column: AG15/AS15). The accuracy on SO_4^{2-}, Cl^-, NO_3^- and F^- was assessed by using the trueness (± 3%, ± 4%, ± 4% and ± 6%; respectively) on river water certified reference material LGC6025 (UKAS, 2014) and the analytical precision (± 2%) for each anion. The detection limit are 1.5, 3.1, 1.6 and 0.5 $\mu mol.l^{-1}$ for SO_4^{2-}, Cl^-, NO_3^-,- and F^- respectively. Total dissolved solids (TDS; $\mu mol.l^{-1}$) were obtained by summing major elements (Ca, Na, Mg, K) and SiO_2 concentrations in thermal waters. The ion balance of the water samples never exceeds 10%. The saturation index SI (SI = log IAP/K_{sp} with IAP the ion activity product of the chemical species in the fluids and K_{sp} their solubility product) for specific solid phases has been calculated with the PHREEQC geochemical modeling program (Parkhurst and Appelo, 2013).

4.4.4 Ge concentration measurements by ICP-MS

The germanium concentration was measured on samples from acid lake, lake seepage, 11 thermal springs, 4 river waters (n=14) and 4 soil solutions by inductively coupled plasma mass spectrometry (ICP-MS, ICAPQ Thermo Fisher Scientific) using ^{74}Ge isotope (detection limit = 0.04 $nmol.l^{-1}$) at the Earth & Life Institute, UCLouvain, Belgium. Accuracy and long-term repeatability were assessed by running international riverine standards SLRS-5 (0.083 ± 0.014 $nmol.l^{-1}$; n=3) and SLRS-6 (0.097 ±

0.0069 nmol.l^{-1}; n=3) (Yeghicheyan et al, 2013), and one in-house standard within each analytical session between July 2017 and June 2018 (GAB, one thermal spring of La Soufrière volcano: 23.95 ± 0.096 nmol.l^{-1}; n=14). The analytical precision (n= 3) is ± 8% for Ge concentrations < 0.001 µg.l^{-1} and 4% for Ge concentrations > 0.001 µg.l^{-1}. The limit of detection for Ge is 0.04 nmol.l^{-1}. Ge/Si ratios (expressed in µmol.mol^{-1}) were calculated using Si concentrations measured by ICP-OES (**section 4.4.3**), and Ge concentrations measured by ICP-MS. The precision on the Ge/Si ratio is 10% (SD).

4.4.5 Silicon isotopes analysis

Sample purification for anion-rich samples

To prevent from matrix effects in mass spectrometry from anions such as SO_4^{2-} and Cl^- in thermal waters, Si has been purified by performing a two steps column chemistry: anion-exchange resin (Biorad AG MP-1) and cation-exchange resin (Biorad AG50W-X12) following the method developed by Gaspard et al, submitted.

In the context of hyper acid conditions of Kawah Ijen volcano, a preliminary sample purification was performed on samples with SO_4^{2-} > 210 000 µmol.l^{-1} to avoid overtaking anion-exchange resin capacity (1 $meq_{ionic\ concentration}.ml_{resin}^{-1}$ with ionic concentration = sum of dissolved anions in samples in meq). Sulfates were purified by adding suprapure $Ba(NO_3)_2$ in a ratio of 3 × 1g $Ba(NO_3)_2$ /g SO_4^{2-} in the sample considering $Ba(NO_3)_2$ in excess of 10%. This technique is commonly used for S isotopes measurements (e.g., Delmelle et al, 1998): sulfates are retained in the barytine precipitates ($BaSO_4$). The aliquot was filtered at 0.45 µm through polycarbonate membranes and the SO_4^{2-} removal (< 0.50 µmol.l^{-1}, i.e., below the detection limit values for S by ICP-OES) and Si recovery (>95%) in the dissolved phase were verified. Following this step, NaOH 10 mol.l^{-1} was used to raise the pH in solution at 2 before the anion-exchange column step from Gaspard et al, submitted.

Soil solutions were also pre-treated before column chemistry to remove dissolved organic matter (Hughes et al, 2011). Briefly, 5 ml of sample was mixed in a Teflon vial with 200 µl 0.1% v.v H_2O_2 and set in a UV-box for

7h. After cooling down, the UV-box step was repeated for one night with another addition of 0.1 % v.v H_2O_2. Finally, samples were acidified (0.2% v.v HNO_3).

After column chemistry, the Si recovery was always > 98% and the concentrations of Na, SO_4^{2-} and Cl^- in the purified solution were < 0.43, 0.50 and 3.10 µmol.l^{-1}, respectively (i.e., below the detection limit values for Na, S and Cl^- respectively), and the blank level was < 0.36 µmol Si.l^{-1}, i.e., the detection limit for Si by ICP-OES.

Mass spectrometry

Silicon isotope compositions were measured in acid lake, lake seepage, 11 thermal springs, 4 river waters (n=11) and 2 soil solutions. Silicon isotope compositions were analyzed by MC-ICP-MS (Neptune Plus™ High Resolution Multicollector ICP-MS, Thermo Fisher Scientific, Earth & Life Institute, UCLouvain, Belgium) in wet plasma mode in medium resolution ($\Delta m/m \sim 6000$) using a PFA nebulizer of 100 µl.min^{-1} uptake rate. The instrumental mass bias was corrected using the standard-sample bracketing technique and an external Mg doping (Cardinal et al, 2003). The analyses were performed in 2% HNO_3 matrix, with a typical sensitivity of 7V for 2 mg.l^{-1} Si and an instrumental blank <30 mV. Silicon isotope compositions are expressed in relative deviations of $^{30}Si/^{28}Si$ ratio from the NBS-28 reference standard using the common δ-notation (‰) as follow: $\delta^{30}Si=[(^{30}Si/^{28}Si)_{sample}/(^{30}Si/^{28}Si)_{NBS-28} -1]\times1000$. One measurement comprises 30 cycles with 4.2s integration time corrected by blank in a 2% HNO_3 matrix. Each single δ-value (n) represents one sample run and two bracketing standards. $\delta^{30}Si$-values are reported as the mean of replicate isotopic analyses ± standard deviation (SD). Quality control of mass bias was performed by ensuring that $\delta^{30}Si$ and $\delta^{29}Si$ measurements fit onto a mass-dependent fractionation array, supporting the interference-free determination of all three Si isotopes via MC-ICP-MS (**Suppl. Mat. 4.1**). The protocol was tested on reference material (diatomite) and Si isotope values obtained for diatomite ($\delta^{30}Si$ = 1.20 ± 0.05 ‰, SD, n=2) are consistent with the reference value ($\delta^{30}Si$ = 1.26 ± 0.10 ‰, SD, Reynolds et al, 2007).

4.5 Results

4.5.1 Field parameters and water discharges of the thermal springs and the rivers from the Kawah Ijen area

General field water parameters (temperature, pH, Eh) and measured water discharges of the acid lake, thermal springs and four river waters collected are shown in **Table 4.1**. The abbreviations used below for referring to the thermal spring and river water samples are explained in **Table 4.1**.

Table 4.1: General parameters (temperature, pH, Eh, TDS), measured discharges and major element concentrations in acid lake, thermal springs, Banyu Pahit/Banyu Putih river water draining from Kawah Ijen volcano (sampled at eleven different location 40 km downstream), three alkaline rivers (Kali Sat, Kali Senggon and Bangoran) of Java Island, Indonesia, and soil solutions (A, B, C1, C2) from the Asembagus Plain irrigated by the Banyu Putih river.

	Sampling date	Sample	Label	Altitude	Lake distance	Measured discharge	Temperature	pH	Eh	TDS	Ca	Na	Mg	K	Al	Fe	Si	SO_4	Cl	F
	dd.mm.yy			m	km	$m^3.s^{-1}$	°C		mV											
															$\mu mol.l^{-1}$					
Thermal springs	31.01.17	Lake	Lake	2181	0	-	22.8	0.6	349	51787	11602	16964	10142	10486	72642	14683	1212	247223	215182	26617
	31.01.17	Lake seepage	LF	2343	0.11	0.001	19.2	1.3	479	32308	14734	6490	3870	3443	26314	5499	1764	89248	57915	7927
	31.01.17	Spring 1	SP1	2108	0.10	0.001	35.2	0.7	375	131661	19478	49239	28924	30820	215110	44189	1497	669232	594475	74710
	31.01.17	Spring 2	SP2	2100	0.10	0.004	32.0	0.2	366	134452	21109	49239	29574	31331	218112	44767	1496	651188	578096	72830
	29.01.17	Spring 3	SP3	2115	0.15	0.003	33.7	0.1	380	140669	24798	50718	29928	32099	223468	45434	1462	675769	600347	74709
	29.01.17	Spring 4	SP4	2184	0.22	-	29.3	0.2	455	105420	22285	35799	21835	21975	156088	33195	1649	457034	400627	52923
	29.01.17	Spring 5	SP5	2063	0.49	0.003	27.2	0.3	458	111551	22408	38178	23464	24055	167355	37304	1612	497100	425090	56217
	29.01.17	Spring 6	SP6	1980	1.14	0.005	24.9	0.8	496	57673	11757	18791	11825	11609	81815	18833	1726	240011	198636	30982
	29.01.17	Spring 7	SP7	1980	1.16	0.018	25.1	0.7	462	102359	19620	35242	21300	22888	156681	36189	1547	457095	393386	47586
	30.01.17	Spring 8	SP8	951	15.46	>0.004	43.6	6.6	-57	20768	2430	8652	3148	1152	n.d	40	2519	2456	2334	22
	30.01.17	Spring 9	SP9	939	16.00	0.033	45.1	6.6	-36	23551	2899	9382	4258	1293	2	35	2674	3092	3006	24
	30.01.17	Spring 10	SP10	1507	16.36	0.002	41.1	6.8	-65	23250	3262	8425	4707	1039	3	45	2720	3505	3833	31
	31.01.17	Spring 11	SP11	962	16.57	0.041	32.6	6.8	-64	14741	1537	5829	2395	859	2	18	1928	1463	1323	17
Rivers	31.01.17	Banyu Pahit 1	BP1	2087	0.13	0.002	28.2	0.2	382	132989	21759	48674	28842	30666	213906	43688	1426	642389	569163	71088
	29.01.17	Banyu Pahit 2	BP2	2075	0.19	0.033	22.0	0.1	370	133022	22995	47934	28607	30436	211941	43173	1426	632319	565586	70606
	29.01.17	Banyu Pahit 3	BP3	2070	0.31	0.040	20.8	0.1	408	124493	23479	43846	26373	27699	193910	39820	1448	597794	524364	66833
	29.01.17	Banyu Pahit 4	BP4	1987	1.02	0.003	21.1	0.3	429	117064	22535	41023	24662	25461	179122	37689	1582	525736	461410	60086
	07.02.17	Banyu Pahit 5 before	BP5b	1829	2.34	-	18.1	1.0	460	86717	16726	28782	17737	20034	131349	32196	1608	362791	309658	40000
	30.01.17	Banyu Pahit 5	BP5	1719	2.89	0.172	20.1	1.2	470	84569	16293	28134	17297	19364	127643	31404	1628	344950	300426	36643
	30.01.17	Banyu Pahit 6	BP6	962	15.48	3.413	26.8	2.7	494	26858	7655	7234	5464	1940	13537	2136	2135	35589	33996	4087
	30.01.17	Kali Sat	KST	951	15.00	1.237	21.7	8.3	346	7171	1792	1287	1157	251	2	1	1255	1602	1684	45
	30.01.17	Banyu Pahit 7	BP7	908	15.84	4.842	22.9	3.1	501	10417	2637	2294	1862	583	2968	454	1422	8186	7694	816
	30.01.17	Banyu Pahit 8	BP8	934	16.10	4.842	18.9	3.0	499	10600	2650	2375	1913	595	2994	463	1435	8295	7768	818
	30.01.17	Kali Senggon	KS	918	15.74	2.062	23.9	8.0	108	9272	2436	1798	1832	321	8	1	1349	2358	2313	76
	03.02.17	Banyu Putih 9	BP9	129	39.34	4.558	22.8	3.7	519	9823	2268	2144	1733	511	1847	149	1481	5668	5352	498
	03.02.17	Banyu Putih 10	BP10	128	39.64	5.288	24.1	3.8	532	9839	2333	2146	1710	500	1822	144	1473	5667	5405	547
	06.02.17	Bangoran	BA	46	40.50	0.249	21.1	8.1	115	9646	1900	3361	1047	391	n.d	0	1378	1100	1194	32
Soil solutions	05.02.17	soil solution A	A	46	-	-	25.4	4.7	-	10586	2558	2216	1834	563	1683	2	1597	5614	5571	692
	05.02.17	soil solution B	B	70	-	-	24.9	4.7	-	8684	2119	1603	1454	394	1151	4	1456	3579	4417	567
	04.02.17	soil solution C1	C1	106	-	-	28.2	4.3	-	10078	2513	2147	1830	462	1086	404	1462	5267	4895	543
	04.02.17	soil solution C2	C2	99	-	-	28.2	4.4	-	8336	2810	2082	1649	275	89	2310	711	5496	5061	59

- : not measured; n.d : not detected.

Thermal springs (SP1-SP7) located on the flank of Kawah Ijen volcano display very low pH values ranging from 0.1 to 0.7 similar than the hyper acidic crater lake (pH = 0.6) and the upper section of Banyu Pahit river (BP1-BP5; pH = 0.1-1.2), in contrast with the thermal springs (SP8-SP11) located near Blawan village (pH = 6.6-6.8). The lower section of Banyu Pahit/Banyu Putih river has higher pH values (2.7-3.8) probably due to mixing with more-alkaline meteoric water and with alkaline KST and KS river waters (pH = 8.3 and 8.0, respectively). The surface temperatures of SP1-SP7 show values ranging from 25.1 to 35.2 °C lower than those of SP8-SP11 (32.6-45.1 °C) and those of Banyu Pahit river water sampled at eleven different location 40 km downstream (18.1-28.2 °C). Thermal springs located on the flank of Kawah Ijen volcano (SP1-SP7) have Eh > 0 (ranging from 375 to 496 mV) and thermal springs near Blawan village (SP8-SP11) have Eh < 0 (ranging from -65 to -36 mV) (**Table 4.1**). All river waters display Eh (mV) > 0 with lowest values reported for BA river (Eh = 115 mV) (**Table 4.1**).

All thermal springs display low water discharges < 0.033 $m^3.s^{-1}$. Banyu Pahit river water has discharges of 0.172 $m^3.s^{-1}$ in the basement of Kawah Ijen volcano and 3.413 $m^3.s^{-1}$ before reaching the Blawan village at 17 km of the Kawah Ijen volcano. The two alkaline river waters of KST and KS show discharge of, respectively, 1.237 and 2.062 $m^3.s^{-1}$ and contribute to increase the Banyu Putih discharge before irrigating Asembagus Plain (BP10; discharge = 5.288 $m^3.s^{-1}$; **Table 4.1**). This discharge value for BP10 in wet season (February 2017) is 1.2 to 1.3 times higher than the discharge measured in dry season (August 1996 = 4 $m^3.s^{-1}$, Delmelle et al, 2000; June 2016 = 3.6 $m^3.s^{-1}$ and October 2016 = 4.3 $m^3.s^{-1}$, Asembagus Irrigation Office) and 1.5 times higher than the average discharge over 18 years (1981-1999: 3.5 $m^3.s^{-1}$; Löhr et al, 2005; **Suppl. Mat. 4.2**).

Using the discharge measurements and the equations for discharge presented in **Fig. 4.2**, we can calculate the proportion of each contributor (thermal springs and alkaline river waters) to Banyu Pahit/Banyu Putih river and obtain "calculated discharge" (**Fig. 4.2**). The Banyu Pahit river (BP1) originated from hydrothermally-impacted waters (mixing of 11% of LF, 21% of SP1 and 68% of SP2) and the river discharge in the upper section is mainly influenced by hydrothermal input (SP3, SP4, SP5, SP6 and SP7) (**Fig. 4.2**). Discharging at the Blawan village inlet and located at ~12.6 km downstream BP5 (discharge = 0.065 $m^3.s^{-1}$), BP6 (discharge = 3.413 $m^3.s^{-1}$) is mainly influenced by dilution with meteoric water such as

runoff (97.97%). The estimated contribution of alkaline river waters is significant in the lower section of Banyu Pahit river water with 26.61% and 29.84% for KST and KS in BP7 and BP9 location, respectively. The contribution of KS fits with the value of 23% reported by Palmer et al (2011). In contrast, the contribution of KST to BP7 (in wet season in this study) is lower than the value reported in dry season (79%; Palmer et al, 2011). This could be explained by higher Banyu Pahit discharge water flowing through Kawah Ijen flank during wet season.

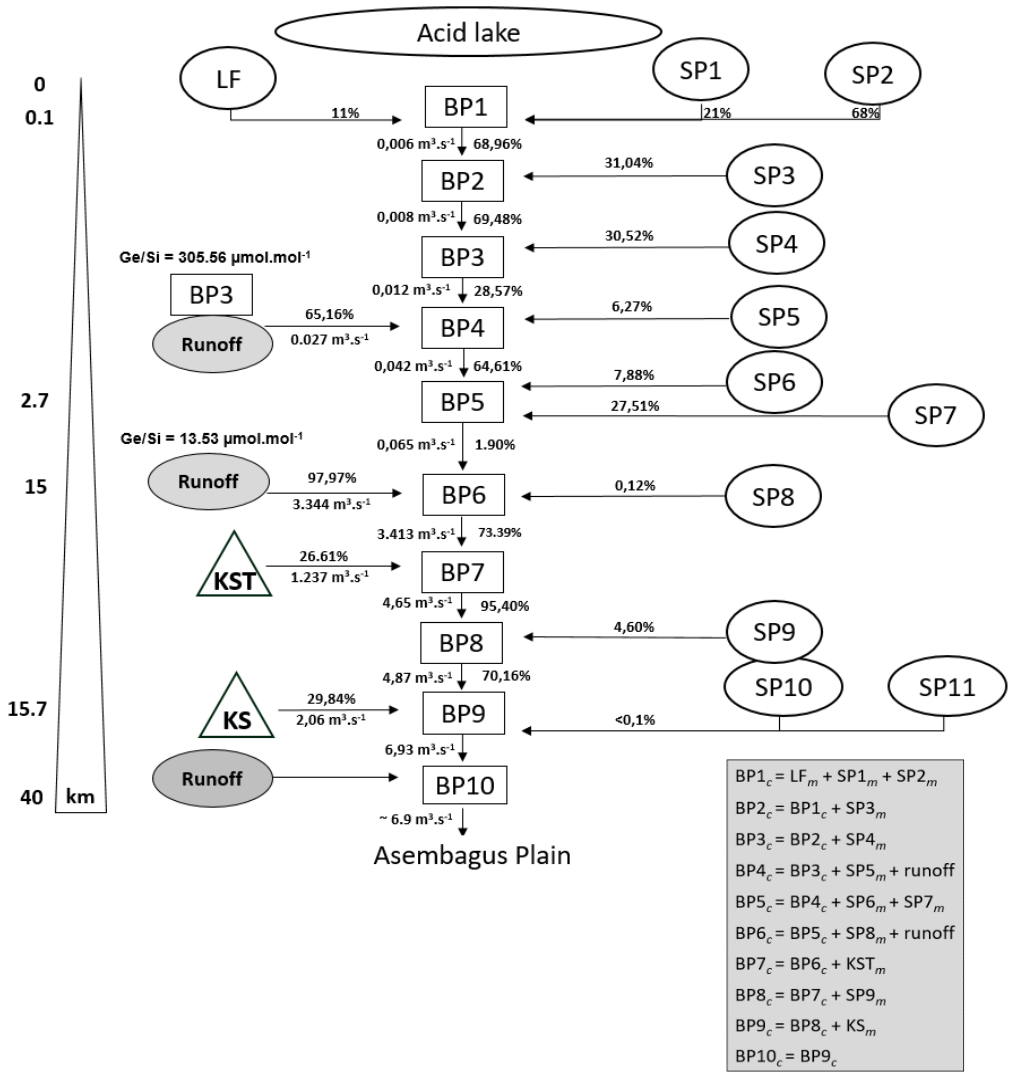

Fig. 4.2: Calculated water discharges ($m^3.s^{-1}$) of Banyu Pahit/Banyu Putih rivers (BP) from the acid lake at the summit of Kawah Ijen volcano to the Lewung irrigation dam located 40 km downstream (from BP1 to BP10, respectively), including the measured discharge contribution from thermal springs (SP), surface runoff (Runoff) and alkaline river waters (KST, KS). In the grey box: the calculated water discharge of each location (symbolised by *c* in subscript, e.g., $BP2_c$) has been obtained from the sum of the *in situ* measured water discharge of each contributor (symbolised by

m in subscript, e.g., SP3$_m$) and the calculated discharge of the upstream main river location (e.g., BP1$_c$ for BP2$_c$). The discharge for SP4 (not available) has been considered as equal to the nearby SP3. The Ge/Si ratio mentioned for the contributors to BP4 and BP6 derive from the combination of the discharge based-model and the Ge/Si ratio measured (see **section 4.6.3** for details). The sample names refer to **Table 4.1**.

4.5.2 Elemental composition of the lake and the thermal springs from the Kawah Ijen area

Major element concentrations and calculated TDS of the acid lake and thermal springs collected are shown in **Table 4.1**.

The chemical compositions of the acid lake and the thermal springs near the lake (SP1-SP7) are closely related, whereas the element concentrations are lower in the lake seepage (LF) (**Fig. 4.3**). The acidic lake concentrations reported here in wet season differs from the chemical composition reported for the average crater lake water in dry season (**Fig. 4.3**; Delmelle et al, 2000) probably due to dilution by meteoric input decreasing element concentrations at the lake surface (Caudron et al, 2015). A seasonal fluctuation in element concentrations in Kawah Ijen lake is also reported by Sumarti (1998) with elemental dilution during the wet season.

The thermal springs collected near the lake of Kawah Ijen (SP1-SP7) exhibit high total dissolved elements (TDS: 32308-134452 $\mu mol.l^{-1}$). The most concentrated thermal springs are directly located on the flanks of Kawah Ijen volcano (SP1-SP7) and display Si concentrations ranging from 1497 to 1726 $\mu mol.l^{-1}$. Sulfates (89248-675769 $\mu mol.l^{-1}$) and Cl^- (57915-600347 $\mu mol.l^{-1}$) are the dominant anions following by high F^- concentrations (7927-74709 $\mu mol.l^{-1}$) (**Table 4.1**). The thermal springs exhibit a wide range of Al (26314-223468 $\mu mol.l^{-1}$) and Na (6490-50718 $\mu mol.l^{-1}$) followed by Fe (5499-45434 $\mu mol.l^{-1}$), K (3443-32099 $\mu mol.l^{-1}$), Mg (3870-29928 $\mu mol.l^{-1}$) and Ca (11602-24798 $\mu mol.l^{-1}$). The acid (pH = 0.1-0.8) highly-SO_4-Cl concentrated thermal springs located on the flank of Kawah Ijen volcano (SP1-SP7) correspond to the thermal springs classified as hyper acid SO_4-Cl by Delmelle and Bernard (1994), Delmelle et al (2000), Palmer (2009). The high SO_4^{2-} and Cl^- concentrations are

caused by volcanic gases condensation and oxidation at the bottom of the lake (Delmelle and Bernard, 1994).

The thermal springs collected near Blawan village (SP8-SP11; ~17 km below the volcano) present lower elements concentration relative to thermal springs in the flank of Kawah Ijen volcano (SP1-SP7) (**Table 4.1; Fig. 4.3**). The alkalinity has been not measured *in situ* for neutral (pH = 6.6-6.8) thermal springs near Blawan village (SP8-SP11) but these sources were classified as neutral HCO_3-SO_4 waters by Delmelle et al (2000) and are associated with HCO_3 steam-heated waters produced in the shallow part of the system.

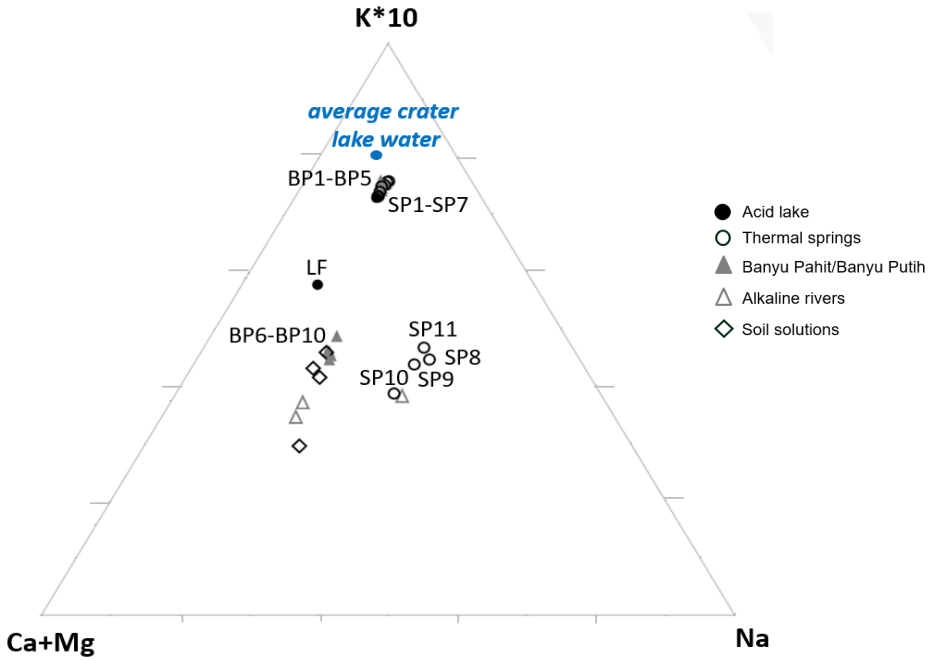

Fig. 4.3: Ternary diagram of the cation concentrations of waters sampled on Java Island, Indonesia (wet season, February 2017): acid lake (plain circle), thermal springs (open circle), rivers (triangles; including Banyu Pahit/Banyu Putih river waters (plain grey triangle), and three neutral river waters (open grey triangle; KST, KS and BA)), and soil solutions (diamond). The sample names refer to **Table 4.1**. The chemical

composition of the average crater lake water in dry season is given for comparison (plain blue circle; data from Delmelle et al, 2000).

4.5.3 Elemental composition of the river waters and the soil solutions from the Kawah Ijen area

Major element concentrations and calculated TDS of the rivers and the soil solutions sampled are shown in **Table 4.1** and **Fig. 4.3**.

The upper section of Banyu Pahit river (BP1-BP5) displays decreasing values of TDS (84569-132989 $\mu mol.l^{-1}$) with increasing lake distance (0.13-2.89 km) and decreasing elevation (2087-1719 m asl). This range is similar than the TDS values of thermal springs (SP1-SP7; TDS = 32308-134452 $\mu mol.l^{-1}$), showing that the upper section of Banyu Pahit river is mainly influenced by hydrothermalism as previously well-established by Delmelle et al (2000), Heikens et al (2005), van Hinsberg et al (2010), Palmer et al (2011). This is also supported by the cation concentrations (Na, K, Mg, Ca) in the upper section of Banyu Pahit river plotting in the same area than thermal springs at the same elevation in a triangular diagram (**Fig. 4.3**). This hydrothermal contribution is progressively diluted as concentrations in anions decreases downstream (from BP1 to BP5) with SO_4^{2-} as the major anion (344950 to 642389 $\mu mol.l^{-1}$) followed by Cl^- (300426-569163 $\mu mol.l^{-1}$) and F^- (36643-71088 $\mu mol.l^{-1}$) (**Table 4.1**). In this upper section of Banyu Pahit river, the silicon concentration varies in the narrow range of 1426 to 1628 $\mu mol.l^{-1}$ (**Table 4.1**).

The lower section of Banyu Pahit near Blawan village (BP6-BP8) is characterized by lower dissolved element concentrations than the upper section (BP1-BP5; **Fig. 4.3**), with SO_4^{2-} (8295-35589 $\mu mol.l^{-1}$), Cl^- (7768-33996 $\mu mol.l^{-1}$), F^- (818-4087 $\mu mol.l^{-1}$), Al (2994-13537 $\mu mol.l^{-1}$), Na (2375-7234 $\mu mol.l^{-1}$) and Fe (463-2136 $\mu mol.l^{-1}$) decreasing with lake distance (**Table 4.1**). In this lower section of Banyu Pahit river, Si concentration varies between 1435 and 2135 $\mu mol.l^{-1}$ (**Table 4.1**). The alkaline KST and KS river waters, which do not drain the Kawah Ijen volcano, exhibit lower calculated TDS values (7171 and 9272 $\mu mol.l^{-1}$, respectively) relative to Banyu Pahit/Putih river, as illustrated for cation concentrations (**Fig. 4.3**). These alkaline rivers are also Al and Fe-depleted compared to Banyu

Pahit/Putih river (**Table 4.1**) in agreement with chemical compositions previously reported (Palmer et al, 2011). Banyu Putih has Si concentration of 1473 μmol.l^{-1} and display F^- concentration of 547 μmol.l^{-1} at the irrigation dam near Lewung village (BP10) before reaching the coastal Asembagus plain (**Table 4.1**). The lower section of Banyu Putih chemistry (BP6-BP10) has lower TDS values (10417-26858 μmol.l^{-1}) than the upper section (BP1-BP5), reflecting input of less-concentrated neutral tributaries KST and KS (TDS= 7171 and 9272 μmol.l^{-1}, respectively) in agreement with Delmelle et al (2000), Heikens et al (2005), van Hinsberg et al (2010), Palmer et al (2011). The soil solutions collected in the coastal Asembagus Plain have Si concentrations ranging from 711 to 1597 μmol.l^{-1} (**Table 4.1**), and cation concentrations in the same range than the closest river water samples (BP9-BP10; **Fig. 4.3**).

The comparison of riverine element concentrations in the wet season (this study) with available data in dry season (August 1993-1996; data from Delmelle and Bernard, 2000; **Fig. 4.4**) confirms a conservative behavior for SO_4^{2-} and Cl^- (**Fig. 4.4a and 4.4b**), as previously established (Delmelle and Bernard, 1994, 2000; Sumarti, 1998; van Hinsberg, 2001; van Hinsberg et al, 2010). This is driven by the dilution with rainwater input (more than 4.5 times higher in wet season relative to dry season based on annual average of 1100 mm and 230 mm in wet and dry season, respectively; Ijen Monthly Climate Averages, 2020) characterized by low SO_4^{2-} and Cl^- concentrations (25-65 and 4-28 μmol.l^{-1}, respectively, in rainwaters from Indonesia; Hasan et al, 2017). The cations (Ca, K, Al, Fe) and Si display a lower concentration in wet than in dry season (illustrated for Ca and Si; **Fig. 4.4c and 4.4d**) regulated by equilibrium with mineral phases (non-conservative behavior) as previously established (Delmelle and Bernard, 1994, 2000). The Ca solubility is regulated by the calcium sulfate precipitation ($CaSO_4.2H_2O$; Delmelle et al (2000), and this is supported by gypsum deposit found in SP1 and SP2 (SI > 0 with PHREEQC). The K concentrations are controlled by jarosite ($KFe_3(OH)_6(SO_4)_2$) precipitation (SI > 0 with PHREEQC) (Delmelle et al, 2000). The concentrations of dissolved Al and Fe are driven by increasing pH values (1.2-3.0) induced by dilution with meteoric-derivated waters and mixing with alkaline rivers (KST, KS) affecting Al and Fe-containing mineral precipitation (SI of $Al(OH)_3$ and FeOOH > 0 from BP7). The dissolved riverine Si concentrations along Banyu Pahit/Banyu Putih river waters (BP1-BP10) show only slight variation between wet and

dry seasons, e.g., overlapping average values within error with 1789 ± 400 µmol.l^{-1} in dry season and 1503 ± 208 µmol.l^{-1} in wet season (**Fig. 4.5**). This can be explained by the fact that Si concentrations are controlled by silica precipitation (SI > 0 for BP1-BP10 for chalcedony and quartz, and close to 0 for amorphous silica; **Fig. 4.6**) in agreement with Delmelle et al (2000).

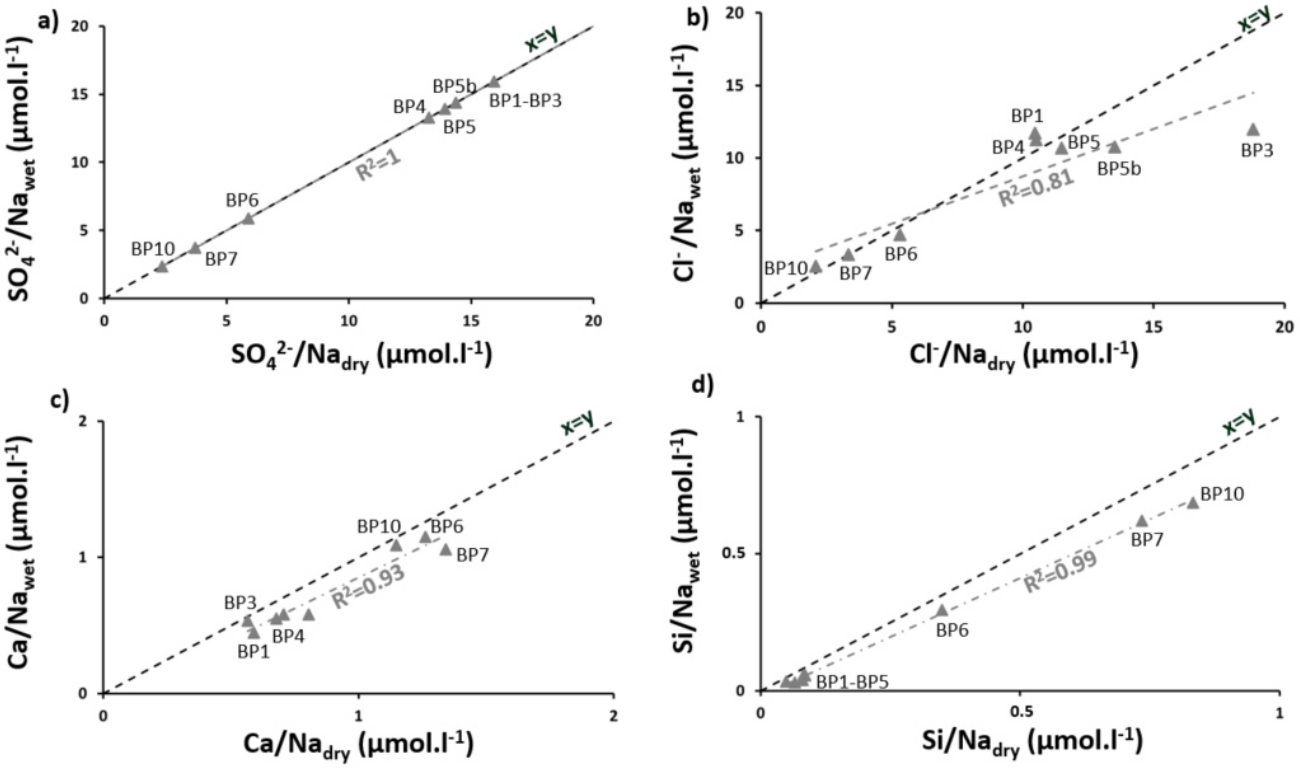

Fig. 4.4: Plots of the dilution-corrected element concentrations in the wet season (February 2017, this study) as a function of the dilution-corrected element concentrations in the dry season (August 1993-1996; data from Delmelle and Bernard, 2000) for SO_4^{2-} (a), Cl^- (b), Ca (c), and Si (d). Data are presented for locations were measurements at both seasons were available, i.e., in Banyu Pahit/Banyu Putih river waters (BP1, BP3, BP4, BP5b, BP5, BP6, BP7, BP10). The sample names refer to **Table 4.1**. The Na has been chosen for dilution-correction based on the strong positive

correlation between Na concentration and TDS (R^2 = 0.99, **Suppl. Mat. 4.3**), indicating that riverine Na concentrations are governed by dilution.

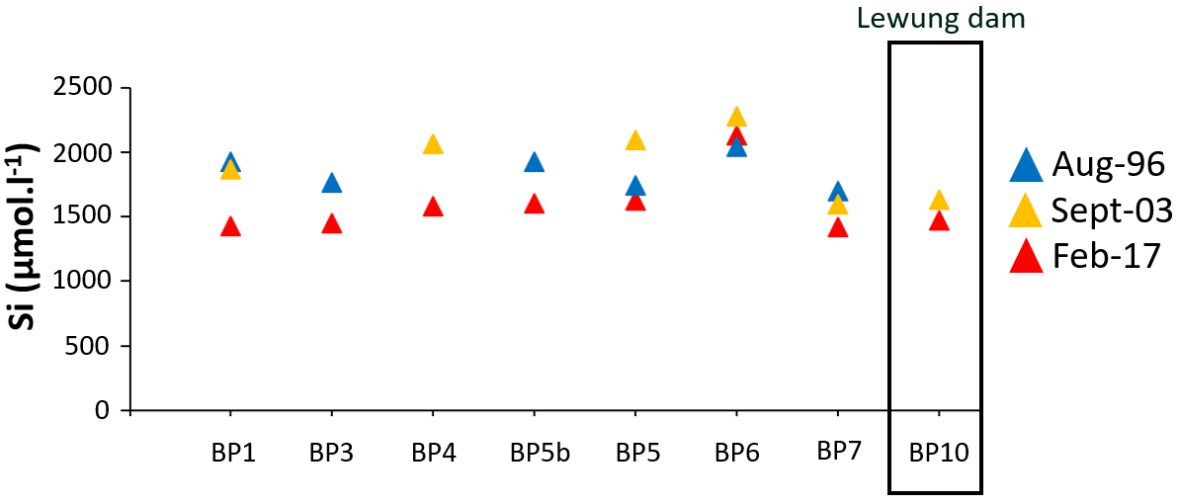

Fig. 4.5: Plot of the Si concentrations in Banyu Pahit/Banyu Putih rivers in wet (February 2017; this study) and dry (August 1996: Delmelle and Bernard, 2000 - September 2003: Asembagus Irrigation Office) seasons from from BP1 (close to acid lake) to BP10 (40 km downstream). The sample names refer to **Table 4.1**.

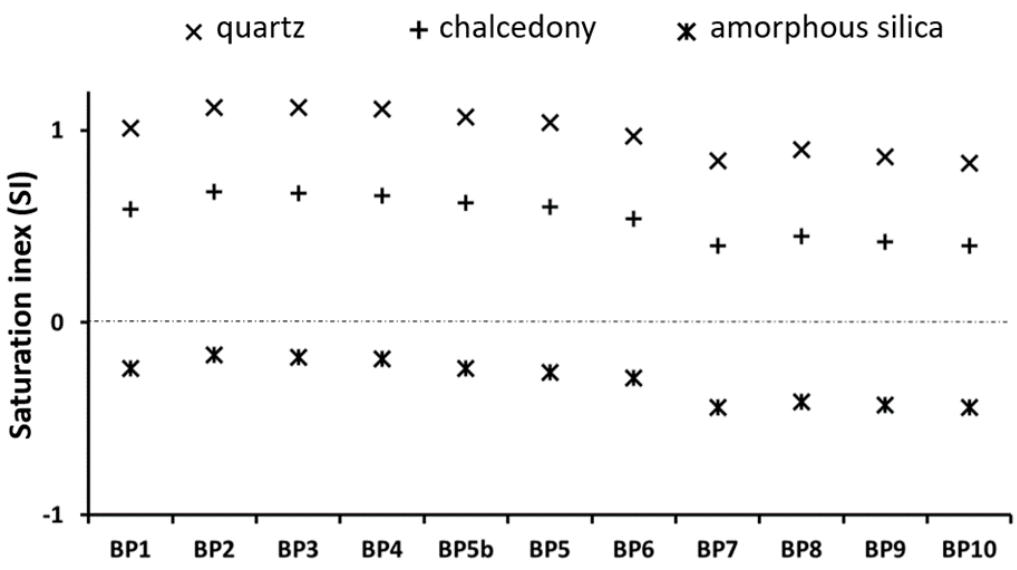

Fig. 4.6: Plot of the evolution of the saturation index (SI) of silica (SiO_2: chalcedony, quartz and amorphous silica) in Banyu Pahit/Banyu Putih river waters from BP1 (close to acid lake) to BP10 (40 km downstream). The sample names refer to **Table 4.1**.

4.5.4 Ge/Si ratio of the waters from the Kawah Ijen area

The Ge/Si ratio of the acid lake, thermal springs, the four river waters and the four soil solutions collected on Java Island are reported in **Table 4.2** and shown in **Fig. 4.7a.**

Table 4.2: Germanium concentrations, Ge/Si ratios and silicon isotope compositions ($\delta^{29}Si$ and $\delta^{30}Si$) in acid lake, thermal springs, Banyu Pahit/ Banyu Putih river water draining from Kawah Ijen volcano (sampled at eleven different location 40 km downstream), three alkaline rivers (Kali Sat, Kali Senggon and Bangoran) of Java Island, Indonesia, and soil solutions (A, B, C1, C2) from the Asembagus Plain irrigated by the Banyu Putih river. n = number of measurements.

	Label	Sampling date	Ge	Ge/Si	n	$\delta^{29}Si$	SD	$\delta^{30}Si$	SD	n
		dd.mm.yy	nmol.l^{-1}	µmol.mol^{-1}		‰		‰		
Thermal springs	Lake	31.01.17	248.21	205.52	1	0.42	0.05	0.85	0.08	3
	LF	31.01.17	82.60	46.99	1	0.28	0.04	0.49	0.03	2
	SP1	31.01.17	757.16	507.89	1	0.04	0.02	0.03	0.11	2
	SP2	31.01.17	688.33	461.94	1	0.02	0.08	-0.14	0.03	2
	SP3	29.01.17	729.63	500.86	1	0.05	0.04	0.03	0.01	3
	SP4	29.01.17	481.83	293.33	1	0.06	0.01	0.02	0.03	2
	SP5	29.01.17	550.66	342.94	1	0.07	0.02	0.04	0.06	2
	SP6	29.01.17	275.33	160.12	1	0.26	0.01	0.47	0.01	2
	SP7	29.01.17	523.13	339.36	1	0.16	0.05	0.21	0.03	3
	SP8	30.01.17	45.45	18.11	1	-0.10	0.01	-0.18	0.03	1
	SP9	30.01.17	44.14	16.57	1	0.00	0.06	-0.05	0.02	1
	SP10	30.01.17	41.92	15.47	1	-0.17	0.06	-0.35	0.05	2
	SP11	31.01.17	19.39	10.10	1	0.11	0.02	0.19	0.02	1
River waters	BP1	31.01.17	729.63	513.90	1	-0.05	0.02	-0.08	0.04	1
	BP2	29.01.17	743.39	504.20	1	-	-	-	-	-
	BP3	29.01.17	605.73	419.97	1	0.06	0.05	0.04	0.06	2
	BP4	29.01.17	536.89	340.59	1	-	-	-	-	-
	BP5b	07.02.17	413.00	257.85	1	0.25	0.05	0.39	0.03	1
	BP5	30.01.17	357.93	220.68	1	0.33	0.09	0.48	0.09	1
	BP6	30.01.17	37.15	17.47	1	0.85	0.04	1.73	0.01	1
	KST	30.01.17	1.69	1.35	1	0.51	0.01	0.99	0.10	1
	BP7	30.01.17	8.59	6.06	1	-	-	-	-	-
	BP8	30.01.17	9.85	6.49	1	0.60	0.02	1.16	0.01	1
	KS	30.01.17	2.51	1.87	1	0.59	0.01	1.22	0.05	1
	BP9	03.02.17	6.73	4.56	1	0.48	0.07	1.06	0.01	1
	BP10	03.02.17	6.56	4.47	1	0.57	0.13	1.07	0.01	1
	BA	06.02.17	0.81	0.59	1	0.46	0.06	0.87	0.01	1
Soil solutions	A	05.02.17	4.82	3.02	1	-	-	-	-	-
	B	05.02.17	2.75	1.90	1	0.80	0.06	1.56	0.04	1
	C1	04.02.17	4.96	3.40	1	0.68	0.04	1.24	0.03	1
	C2	04.02.17	3.58	5.05	1	-	-	-	-	-

- : not measured.

The acidic springs located on the flank of Kawah Ijen volcano (SP1-SP7) display higher values of Ge/Si ratios (160.12-507.89 μmol.mol^{-1}) than the neutral springs collected near Blawan village (SP8-SP11; 10.10-18.11 μmol.mol^{-1}) (**Fig. 4.7a**). The acidic lake has Ge/Si ratio in the same range (205.52 μmol.mol^{-1}) than SP1-SP7 and higher than Ge/Si ratio of the lake seepage (46.99 μmol.mol^{-1}). The upper section of Banyu Pahit is characterized by the same range of Ge/Si ratios (220.68-513.90 μmol.mol^{-1}) than acidic thermal springs, decreasing with increasing lake distance and resulting in lower Ge/Si ratios in Banyu Pahit collected near Blawan village (6.49-17.47 μmol.mol^{-1}) and before irrigating Asembagus Plain (BP10; 4.47 μmol.mol^{-1}). The three alkaline river waters (KST, KS and BA) display lowest values of Ge/Si ratios with 1.35, 1.87 and 0.59 μmol.mol^{-1}, respectively (**Fig. 4.7a).** The soil solutions collected in the coastal Asembagus Plain have Ge/Si ratios ranging from 1.90 to 5.05 μmol.mol^{-1} (**Fig. 4.7a**).

4.5.5 Si isotope composition of the waters from the Kawah Ijen area

The Si isotope compositions of the acid lake, thermal springs, the four river waters and two soil solutions collected on Java Island are reported in **Table 4.2** and shown in **Fig. 4.7b**.

Acidic springs located on the flank of Kawah Ijen volcano are characterized by higher δ^{30}Si values (from -0.14 ± 0.03 ‰ to 0.47 ± 0.01 ‰) than those of the neutral springs of Blawan (from -0.35 ± 0.05 ‰ to 0.19 ± 0.02 ‰). Acid lake of Kawah Ijen and lake seepage are enriched in ^{30}Si and display values of δ^{30}Si of 0.85 ± 0.08 ‰ and 0.49 ± 0.03 ‰, respectively. The Banyu Pahit river water is characterized by increasing δ^{30}Si values from acid lake (BP1; -0.08 ± 0.04 ‰) to the inlet of Blawan village (BP6; 1.73 ± 0.01 ‰). BA river water is enriched in ^{29}Si (0.87 ± 0.00 ‰) relative to KST (0.99 ± 0.10 ‰) and KS (1.22 ± 0.05 ‰). The Banyu Putih (BP10) displays δ^{30}Si value of 1.07 ± 0.01 ‰ before irrigating Asembagus Plain (**Fig. 4.7b**). The soil solutions collected in the coastal Asembagus Plain have Si isotope compositions ranging from 1.24 ± 0.03 ‰ to 1.56 ± 0.04 ‰ (**Fig. 4.7b**).

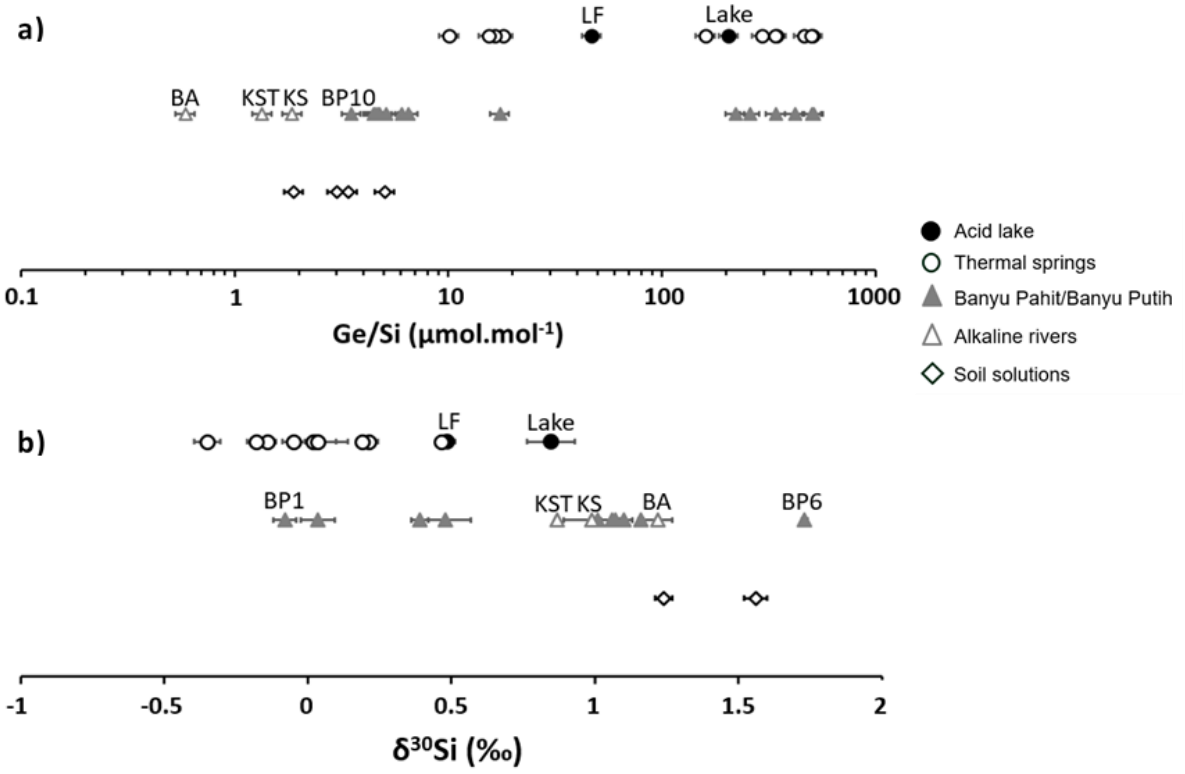

Fig. 4.7: Plots of the (a) Ge/Si ratios (± SD) and (b) Si isotope composition (δ^{30}Si ± SD) of waters sampled on Java Island, Indonesia: the acid lake (plain circle), the thermal springs (open circle), the rivers (triangles; including Banyu Pahit/Banyu Putih river waters (plain grey triangle), and the three neutral river waters (open grey triangle; KST, KS and BA)), and the soil solutions (diamond). The sample names refer to **Table 4.1**.

4.6. Discussion

4.6.1. Ge/Si tracing hydrothermal contribution in Banyu Pahit/Banyu Putih river waters

As discussed in *Ch1*, in hyper acid SO_4-Cl thermal waters (SP1-SP7) representing the "magmatic end-member" of thermal springs, the high Ge/Si ratios (160.12-507.89 μmol.mol^{-1}) likely result from Ge enrichment in thermal waters due to Ge volatility and transport by volcanic gases (via GeF_4, $GeCl_4$ and GeS), and from amorphous silica precipitation. In all these thermal waters, silica is oversaturated (SI > 0 with PHREEQC) (silica solubility = ~ 2300 μmol.l^{-1} at 25 °C; Fournier and Rowe, 1977). Also consistently with *Ch1*, in the mixed neutral HCO_3-SO_4 thermal waters near Blawan (SP8-SP11), the lower values of Ge/Si ratios (18.11-10.10 μmol.mol^{-1}) are likely explained by an increasing intensity of water-rock interaction involving silica precipitation, and Ge transport with salinity and Cl^-.

The upper section of Banyu Pahit (BP1-BP5) is known to be mainly influenced by hydrothermal discharges (Delmelle et al, 2000; Delmelle and Bernard, 2000; Heikens et al, 2005; van Hinsberg et al, 2010; Palmer et al, 2011) whereas the lower section of Banyu Putih (BP6-BP10) reflects input of less-concentrated neutral tributaries KST and KS (Delmelle et al, 2000; Delmelle and Bernard, 2000; Heikens et al, 2005; van Hinsberg et al, 2010; Palmer et al, 2011) and aggressive water-rock interaction (van Hinsberg et al, 2010).

The Ge/Si ratios measured in the hyper acidic-weathered catchment of Banyu Pahit/Banyu Putih river water strongly support the hydrothermal contribution. Indeed, the Banyu Pahit/Banyu Putih river waters display a range of Ge/Si ratios (4.47-513.90 μmol.mol^{-1}; **Table 4.2**; **Fig. 4.7a**) much larger than the range of values reported for rivers draining volcanic areas worldwide (Ge/Si = 0.16-20 μmol.mol^{-1}; e.g., Derry et al, 2005; Scribner et al, 2006; Baronas et al, 2020). More precisely, in the upper section of Banyu Pahit river water (BP1-BP5), the riverine Ge/Si ratios show values (220.68-513.90 μmol.mol^{-1}) in the same range than those of hyper acid SO_4-Cl thermal springs located on the flank of Kawah Ijen volcano (SP1-

SP7; 160.12-507.89 μmol.mol^{-1}), supporting Ge/Si ratio as a tracer for hydrothermal input to rivers in regions affected by hyper acid thermal discharges.

The Ge concentrations of Banyu Pahit (BP1-BP5) decrease downstream (729.63 to 6.56 nmol.l^{-1}; **Table 4.1**) and the riverine Ge/Si ratio is correlated with the riverine Cl^- concentration (**Fig. 4.8**). This can be explained by (i) the dilution downstream of the hydrothermal signal from a common SO_4-Cl reservoir controlling Ge concentration, which is consistent with the view of Delmelle et al (2000), and by (ii) a control by amorphous silica precipitation for Si concentrations remaining stable (1422-2135 μmol.l^{-1}; **section 4.5.3**; **Fig. 4.6**). In the lower section of Banyu Pahit river near Blawan village (BP6-BP8), the lower Ge/Si ratios and Cl^- concentrations (**Fig. 4.8**) suggest further dilution from the same hydrothermal reservoir. The even lower Ge/Si ratios in Banyu Putih after the Blawan village (BP9-BP10; **Fig. 4.8**) likely result from the mixing with alkaline rivers KST and KS characterized by low Ge/Si values (**Fig. 4.8**).

The alkaline river tributaries (KST and KS) are non-impacted by hydrothermalism and display Ge/Si values in agreement with values reported for non hydrothermally-impacted rivers systems (Ge/Si: 0.16-2.72 μmol.mol^{-1}; Scribner et al, 2006). However, comparatively to Bangoran river located in the north of Java island (Ge/Si = 0.59 μmol.mol^{-1}), higher Ge/Si values of KST and KS associated with high solute contents (TDS = 7171 and 9272 μmol.l^{-1}, respectively) possibly suggest thermal water inputs somewhere along their flow in the Ijen caldera as reported by Delmelle et al (2000).

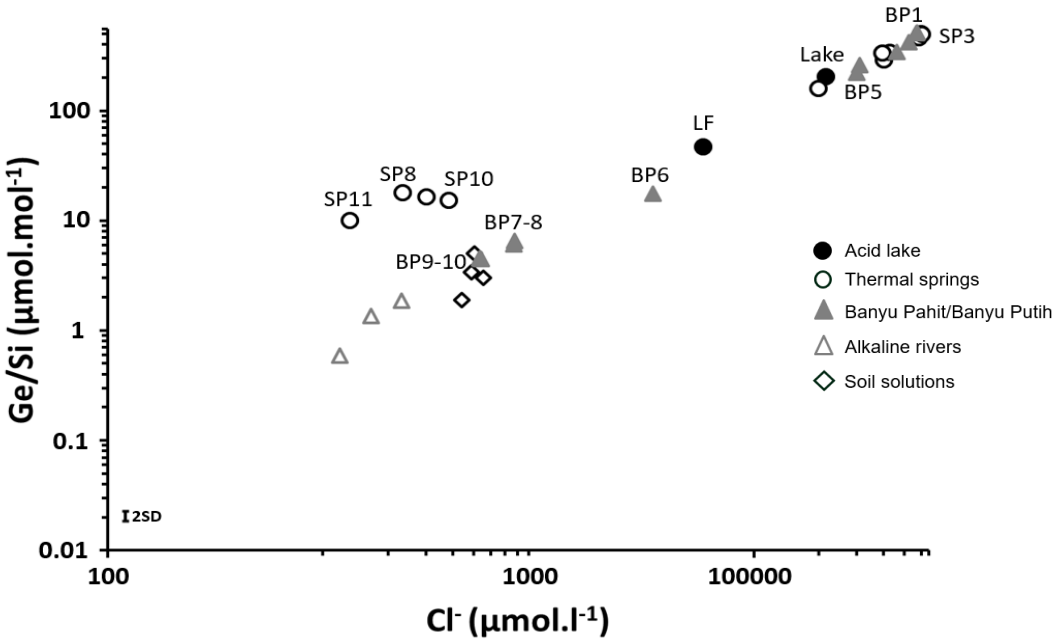

Fig. 4.8: Plot of the Ge/Si ratio as a function of the Cl concentration in waters sampled on Java Island, Indonesia: acid lake (plain circle), thermal springs (open circle), rivers (triangles; including Banyu Pahit/Banyu Putih river waters (plain grey triangle), and the three neutral river waters (open grey triangle; KST, KS and BA)), and soil solutions (diamond). The sample names refer to **Table 4.1**.

4.6.2. Si isotopes tracing surface water contribution to Banyu Pahit/Banyu Putih river waters

The Banyu Pahit/Banyu Putih river displays a large range of $\delta^{30}Si$ values (-0.08 to 1.73 ‰; **Table 4.2**; **Fig. 4.7b**) in the range of values reported for rivers worldwide ($\delta^{30}Si$ = -0.1 to 3.4 ± 0.01 ‰; e.g., De La Rocha et al, 2000; Alleman et al, 2005; Cardinal et al, 2010; Opfergelt and Delmelle, 2012; Frings et al, 2016; Baronas et al, 2020).

The upper section of the river (BP1-BP5; $\delta^{30}Si$ = -0.08 to 0.48 ‰) displays lower Si isotope compositions than the rivers from the lower section (BP6-BP10; $\delta^{30}Si$= 1.06 to 1.73 ‰). As supported by the riverine chemical composition and Ge/Si ratio (**section 4.6.1**), the upper section of the river (BP1-BP5) is mainly controlled by hydrothermal input. The hyper acid SO_4-Cl thermal waters (SP1-SP7) representing the "magmatic end-member" can contribute with low Si isotope values (from -0.14 to 0.21 ‰) to river waters (**Fig. 4.9**).

As shown in **section 4.6.1**, the lower section of the river (BP6-BP10) is controlled by hydrothermal dilution and by the contribution from alkaline river waters KST and KS. The higher $\delta^{30}Si$ values of BP8-BP10 (1.06 to 1.16 ‰) than in BP1-BP5 likely result from the contribution from alkaline tributaries KST and KS ($\delta^{30}Si$= 0.99 and 1.22 ‰, respectively; **Fig. 4.9**). But this cannot explain the higher riverine $\delta^{30}Si$ value measured in BP6 (1.73‰). According to the discharge-based model (**Fig. 4.2**), BP6 is associated with 97.97% of surface runoff water. Our hypothesis is that the high $\delta^{30}Si$ value of BP6 can be explained by a significant contribution of meteoric-originated surface water that percolated into the soil represented here by soil pore waters ($\delta^{30}Si$ = 1.24-1.56 ‰) (**Fig. 4.9**). The $\delta^{30}Si$ of soil solutions reflect secondary formation and plant uptake, i.e., processes which incorporate light Si isotopes leaving heavier Si isotopes in the soil solutions (Ziegler et al, 2005; Georg et al, 2009; Opfergelt and Delmelle, 2012). Relative to these contributions, biological processes within the river likely have a negligible influence on the chemical composition of rivers because of the low pH restricting the microbial activity development (Brock, 1970) and inhibiting complexation reactions by protonation of organics acids (Nordstrom et al, 1979; Herrmann and Baumgartner, 1992).

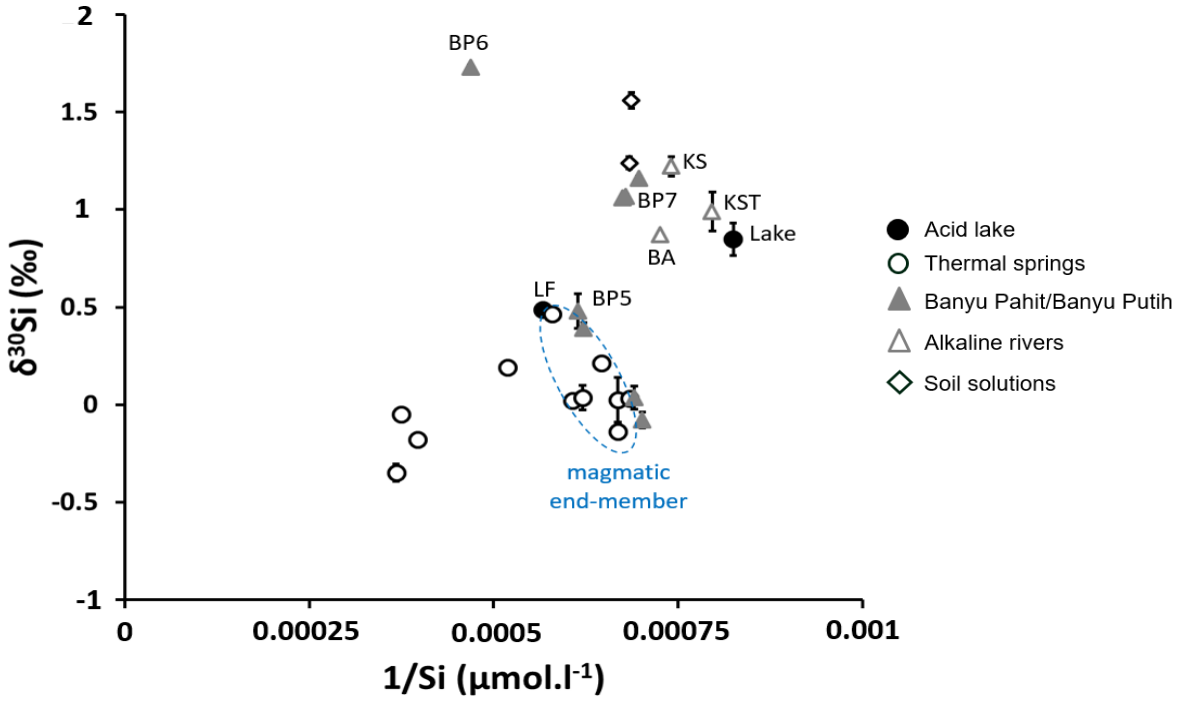

Fig. 4.9: Plot of the Si isotope compositions ($\delta^{30}Si \pm SD$) as a function of the Si concentration (1/Si) in the acid lake (plain circle), the thermal springs (open circle), the rivers (triangles; including Banyu Pahit/Banyu Putih river waters (plain grey triangle), and the three neutral river waters (open grey triangle; KST, KS and BA)), and the soil solutions (diamond). The sample names refer to **Table 4.1**.

4.6.3. Using the Ge/Si ratio in a discharge-based model to quantify contribution from thermal springs, runoff and alkaline tributaries to the Banyu Pahit/Banyu Putih river

The Ge concentrations show conservative behavior along Banuyu Pahit flow and the riverine Ge/Si ratios are correlated with the dilution of the hydrothermal reservoir (**Fig. 4.8**). Using the discharge-based model (**Fig. 4.2**), we evaluate to what extent the Ge concentration and the Ge/Si ratios may be used to assess quantitatively to contribution from thermal springs, runoff and alkaline tributaries in a well-constrained catchment influenced by acid weathering. By mass balance, we calculate the Ge concentration and Ge/Si ratio of the acidic river via the following equations (Eq. 1 and Eq. 2):

$$Ge_{BPX}.D_{BPX} = Ge_{BP(X-1)}.D_{BP(X-1)} + Ge_{contributors}.D_{contributors} \text{ (Eq. 1)}$$

$$Ge/Si_{BPX}.D_{BPX} = Ge/Si_{BP(X-1)}.D_{BP(X-1)} + Ge/Si_{contributors}.D_{contributors} \text{ (Eq. 2)}$$

with D = discharge, contributors = thermal springs, runoff or alkaline rivers. We compared the calculated values with the measured values of Ge concentration and Ge/Si ratios (**Table 4.3**). There is overall a good agreement between measured and calculated values, supporting the conservative behavior of Ge, except for BP4, BP6 and BP7.

The calculated Ge/Si ratio of BP4 (considering the two contributors for BP4 collected on the field, i.e., BP3 and SP5) is too low as compared to the measured value for BP4 (**Table 4.3**). We hypothesize an additional contribution to BP4, likely from runoff. We estimate the Ge/Si ratio of this additional contributor to BP4 via the following equation (Eq. 3):

$$Ge/Si_{contributors} = [Ge/Si_{BP4}.D_{BP4} - Ge/Si_{SP5}.D_{SP5}]/D_{contributors} \text{ (Eq. 3)}$$

We obtain a Ge/Si ratio of 305.56 μmol.mol^{-1} for this additional contributor to BP4 (**Fig. 4.2**), which strongly support a missed contribution from hyper acid SO_4-Cl thermal waters characterized by high Ge/Si ratios (similar to SP1-SP7; **Fig. 4.8**).

The calculated Ge/Si ratio of BP6 is also too low as compared to the measured value for BP6 (**Table 4.3**). Using the same approach as for BP4, it is hypothesized that the Ge/Si measured in BP6 results from the mixing of BP5 (1.90%), SP8 (0.12%) and a major runoff contribution (97.97%). We assess the Ge/Si ratio of the contributor to BP6 via the following equation (Eq. 4):

$$Ge/Si_{contributors} = [Ge/Si_{BP5}.D_{BP5} - Ge/Si_{SP8}.D_{SP8}]/D_{contributors} \text{ (Eq. 4)}$$

We obtain a Ge/Si ratio of 13.53 μmol.mol^{-1} for this additional contributor to BP6 (**Fig. 4.2**), which strongly support a missed contribution from mixed neutral HCO_3-SO_4 thermal waters (similar to SP8-SP11; **Fig. 4.8**).

For BP7, the calculated Ge/Si value is higher than the measured value (**Table 4.3**). We hypothesize that an additional process influencing the Ge/Si ratios of BP7 may be the precipitation of secondary Al-oxyhydroxide minerals affecting the catchment of KST, a contributor to BP7. Precipitation of $Al(OH)_3$ is expected based on PHREEQC simulations for KST (SI > 0 for $Al(OH)_3$). Their precipitation may be the result of higher pH values (>8; **Table 4.1**). Germanium can be sequestered by secondary Al-oxyhydroxides contributing to deplete solutions in Ge (Scribner et al, 2006), which may lead to lower Ge/Si values measured than calculated, as the impact of the precipitation of $Al(OH)_3$ was not included in the calculation.

Table 4.3: Comparison between the "measured" Ge concentrations and Ge/Si ratios (**Table 4.2**) and "calculated" Ge concentrations and Ge/Si ratios (using discharge-based mixing model) from acid lake located in the Kawah Ijen summit (BP1) to the Lewung irrigation dam located 40 km downstream at the coastal Asembagus Plain inlet (BP10). "Measured" discharge = water discharge *in situ* and "calculated" discharge = water discharge corrected by equations in **Fig. 4.2**. Matching for Ge (%) = [(Measured Ge-Calculated Ge)/Measured Ge]*100 and matching for Ge/Si (%) = [(Measured Ge/Si-Calculated Ge/Si)/Measured Ge/Si]*100.

Label	Measured discharge	Calculated discharge	Measured Ge	Calculated Ge	Matching for Ge	Measured Ge/Si	Calculated Ge/Si	Matching for Ge/Si
	$m^3.s^{-1}$	$m^3.s^{-1}$	$nmol.l^{-1}$	$nmol.l^{-1}$	%	$\mu mol.mol^{-1}$	$\mu mol.mol^{-1}$	%
BP1	0.002	0.006	729.63	636.15	13	513.90	425.95	17
BP2	0.033	0.008	743.39	726.12	2	504.20	509.85	-1
BP3	0.040	0.012	605.73	663.56	-10	419.97	439.84	-5
BP4	0.003	0.042	536.89	602.27	-12	340.59	141.49	58
BP5	0.172	0.065	357.93	512.50	-43	220.68	326.03	-48
BP6	3.413	3.413	37.15	6.86	82	17.47	4.21	76
KST	1.237	1.237	1.69	-	-	1.35	-	-
BP7	4.842	4.650	8.59	27.71	-223	6.06	13.18	-117
BP8	4.842	4.870	9.85	10.22	-4	6.49	6.55	-1
KS	2.062	2.062	2.51	-	-	1.87	-	-
BP9	4.558	6.932	6.73	7.22	-7	4.56	5.11	-12
BP10	5.288	6.932	6.56	6.73	-3	4.47	-	-2

4.6.4 Implications for atmospheric CO_2 consumption by chemical weathering in a hyper acid hydrothermal context

The chemical weathering rates (CWR, $t.km^{-2}.yr^{-1}$) of the Banyu Pahit/Banyu Putih catchment can be estimated using the Si (expressed as SiO_2), Na, K, Mg and Ca concentrations of the river collected at Lewung dam (BP10) before irrigating the coastal Asembagus Plain. We performed three scenarios: (i) dry season (DS) using element concentrations and discharge of BP10 in dry season (Delmelle and Bernard, 2000), (ii) wet season (WS) using element concentrations and calculated discharge of BP10 in wet season (**Table 4.1**; **Fig. 4.2**), and (ii) on an annual basis (ANN) using the discharge-weighted mean element concentrations in BP10 in dry and wet seasons (Delmelle and Bernard, 2000 and **Table 4.1**, respectively) and the mean water discharge over 18 years at BP10 (Löhr et al, 2005).

The CWR of BP10 in WS (141 $t.km^{-2}.yr^{-1}$) is higher than the one in DS (84 $t.km^{-2}.yr^{-1}$) which is in the same range than the CWR in the ANN scenario (73 $t.km^{-2}.yr^{-1}$) (**Table 4.1**). This suggests that in volcanic regions where the riverine Si concentration is controlled by silica precipitation due the input from hyper acid thermal waters (as confirmed by the Ge/Si ratio; **section 4.6.1 and 4.6.3**), the higher riverine discharge in wet season do not substantially influence the annual Si riverine fluxes. These CWR values are in the range of CWR values reported for basaltic volcanic islands (East Java: 65-277 $t.km^{-2}.yr^{-1}$, Louvat, 1997; La Réunion: 63-170 $t.km^{-2}.yr^{-1}$, Louvat and Allègre, 1997; Sao Miguel: 26-50 $t.km^{-2}.yr^{-1}$, Louvat and Allègre, 1997; Iceland: 19-146 $t.km^{-2}.yr^{-1}$, Stefánsson and Gislason, 2001).

We estimated the associated atmospheric CO_2 consumption by chemical weathering of Banyu Pahit/Banyu Putih river ($atmCO_2$ consumption; $t_{atmCO2}.km^{-2}.yr^{-1}$) using the Si mass from BP10 ($t_{Si}.yr^{-1}$) for the three scenarios (DS, WS, ANN) based on the method developed by Edmond and Huh (1997); Goldsmith et al (2008); Freire et al (2013). The results are 40, 62 and 33 $t_{atmCO2}.km^{-2}.yr^{-1}$ in DS, WS and ANN, respectively (**Table 4.4**; details in **Suppl. Mat. 4.4**). These values are (i) higher than values of

atmospheric CO_2 consumption by chemical weathering (in $t_{atmCO2}.km^{-2}.yr^{-1}$) reported in active orogenic region (Andes : 8-21, Himalaya: 4-14; Edmond and Huh, 1997) or in one of the largest tropical basin (Amazon: 5-15; Moquet et al, 2011) or in cold volcanic regions (Kamchatka: 15-20, Dessert et al, 2009), (ii) lower than values reported for some tropical volcanic regions, mainly basaltic (Réunion: 48-180, Louvat and Allègre, 1997; Deccan trapp: 26-110, Dessert et al, 2001; Philippines: 162-180; Schopka et al, 2001), and (iii) in the range of values reported for some tropical volcanic island arcs such as Java (Dominique: 8-69, Goldschmidt et al, 2010; Martinique/Guadeloupe: 48-62, Rad et al, 2006) or for a mid-ridge volcanic island (Iceland: 6-78, Stefánsson and Gislason, 2001).

However, the values calculated for the Banyu Pahit/Banyu Putih river catchment overestimate the atmospheric CO_2 consumption by chemical weathering given that CO_2 originated from magmatic sources also contributed to chemical weathering in the river catchment (**section 4.6.1**). According to the discharge-based model combined with the Ge/Si ratio (**section 4.6.3**), most of the thermal springs contributions to the Banyu Pahit/Banyu Putih catchment have been sampled and analyzed for their Si concentration and discharge (**Table 4.1**; except a missed contribution for BP4 and for BP6, see **section 4.6.3** and **Fig. 4.2**). Therefore, the amount of CO_2 originated from magmatic sources ($t_{CO2m}.km^{-2}.yr^{-1}$; considered as a magmatic source of acidity including all volatiles degassing from magma such as CO_2, HF, HCl, H_2SO_4) in the Banyu Pahit/Banyu Putih river catchment can be calculated based on the total thermal springs Si mass ($t_{Si}.yr^{-1}$) and the same method developed by Edmond and Huh (1997); Goldsmith et al (2008); Freire et al (2013) (**Table 4.4**; details in **Suppl. Mat. 4.4**). By subtracting this amount of CO_2 originated from magmatic sources to the first value obtained for the atmospheric CO_2 consumption by chemical weathering in the catchment, we provide a value for the atmospheric CO_2 consumption by chemical weathering the Banyu Pahit/Banyu Putih catchment corrected for magmatic CO_2 ($t_{CO2c}.km^{-2}.yr^{-1}$; **Table 4.4**). This calculation supports that the hydrothermal contribution to the riverine CO_2 consumption by chemical weathering in the Banyu Pahit/Banyu Putih river catchment ranges from 2.36 % in wet season to 4.44 % on an annual basis (**Table 4.4**; details in **Suppl. Mat. 4.4**). This highlights that a hyper acid hydrothermal environment contributes substantially to provide CO_2 from magmatic sources and

should be accounted for in global estimates of atmospheric CO_2 consumption by silicate weathering from volcanic regions.

A similar calculation of the hydrothermal contribution to the riverine CO_2 consumption by chemical weathering can be done before reaching the Asembagus plain for the river water of Banyu Pahit on the flank of Kawah Ijen volcano (at BP5). This calculation shows that in wet season, instead of a hydrothermal contribution of 2.36 % at BP10, there is a 54.54 % hydrothermal contribution at BP5 (**Table 4.4**). Even if not on annual basis (based on available discharge data for BP5 and BP10), this comparison importantly highlights the importance of the sampling location used for the estimation of the hydrothermal contribution to the overall input of CO_2 from magmatic sources, and hence for the correction on the atmospheric CO_2 consumption by silicate weathering from volcanic regions.

Table 4.4: Chemical weathering rates (CWR, $t.km^{-2}.yr^{-1}$) and atmospheric CO_2 consumption by chemical weathering for Banyu Putih river at Lewung dam (BP10; draining area estimated at 450 km^2) and for Banyu Pahit on the flank of Kawah Ijen volcano (BP5; draining area estimated at 15 km^2). The atmospheric CO_2 consumption by chemical weathering ($t_{atmCO2}.km^{-2}.yr^{-1}$) is corrected for the amount of CO_2 originated from magmatic sources ($t_{CO2m}.km^{-2}.yr^{-1}$) to obtain a corrected value for atmospheric CO_2 consumption by chemical weathering ($t_{CO2c}.km^{-2}.yr^{-1}$). Si concentrations and riverine discharge: in dry season (DS) (data from Delmelle and Bernard, 2000), wet season (WS) (data from this study) and on an annual basis (ANN) (based on mean BP10 Si concentrations in dry and wet season, and on mean discharge on 18 years reported by Löhr et al (2005)). Calculations for atmospheric CO_2 consumption by chemical weathering are detailed in **Suppl. Mat 4.4**.

		CWR	Si	atmCO_2 consumption	magmatic sources	hydrothermal contribution	Corrected atmCO_2 consumption
		$t.km^{-2}.yr^{-1}$	$t_{Si}.yr^{-1}$	$t_{atmCO2}.km^{-2}.yr^{-1}$	$t_{CO2m}.km^{-2}.yr^{-1}$	%	$t_{CO2c}.km^{-2}.yr^{-1}$
Thermal springs between BP1 and BP10		-	211	-	1.5	-	-
BP10	DS	84	5777	40	1.5	3.66	38.5
	WS	141	8943	62	1.5	2.36	60.5
	ANN	73	4768	33	1.5	4.44	31.5
Thermal springs between BP1 and BP5		-	51	-	0.36	-	-
BP5	WS	265	94	0.65	0.36	54.54	0.29

4.7 Conclusion

This study investigated the influence of hyper acid thermal waters on the Ge/Si ratio and $\delta^{30}Si$ value of the Banyu Pahit/Banyu Putih river draining from the Kawah Ijen volcano to the Asembagus plain located 40 km downstream. The main following conclusions can be drawn from the data:

(i) The Banyu Pahit/Banyu Putih river exhibit the highest Ge/Si ratios reported in river waters (4.47-513.90 $\mu mol.mol^{-1}$), with the highest values in the upstream section reflecting hyper acid SO_4-Cl thermal water discharges characterized by high Ge/Si ratios (160.12-507.89 $\mu mol.mol^{-1}$).

(ii) In this hyper acid hydrothermal environment, the Si concentration in rivers is controlled by the saturation of silica, and the Ge concentration reflect hydrothermal input to rivers decreasing with hydrothermal dilution. In this context, the Ge/Si ratio is a powerful tracer of the thermal input to rivers.

(iii) The low $\delta^{30}Si$ values of the hyper acid SO_4-Cl thermal water discharges (-0.14 to 0.47‰) explain the lower $\delta^{30}Si$ values in the upstream section of the Banyu Pahit/Banyu Putih river (-0.08 to 0.48 ‰) relative to the downstream section of the river (1.06 to 1.73 ‰). The higher $\delta^{30}Si$ values in the downstream riverine section reflect a contribution from mixed neutral HCO_3-SO_4 thermal waters (-0.35 to 0.19‰) and alkaline tributaries (0.99-1.22 ‰) combined with an influence from soil weathering processes (i.e., soil pore water input = 1.24-1.56‰).

(iv) This study provides the first quantitative assessment of all contributions to the Banyu Pahit/Banyu Putih river by combining a discharge-based model with the riverine Ge/Si ratio, including low discharge thermal contributors to rivers (either hyper acid SO_4-Cl thermal waters or mixed neutral HCO_3-SO_4 thermal waters) which are not detected on the field.

(v) This study highlights the importance to account for the contribution from CO_2 from magmatic sources from hyper acid hydrothermal environments to global estimates of atmospheric CO_2 consumption by silicate weathering from volcanic regions.

4.8. References

Alleman, L.Y., Cardinal, D., Cocquyt, C., Plisnier, P.-D., Descy, J.P., Kimirei, I., Sinyinza, D., André, L., 2005. Silicon isotopic fractionation in Lake Tanganyika and its main tributaries. J. Great Lakes Res. 31, 509–519.

Baronas, J.J, West, A.J., Burton, K.W., Hammond, D.E., Opfergelt, S., Pogge von Strandmann, P.A.E., James, R.H., Rouxel, O.J., 2020. Ge and Si isotopes behaviour during intense tropical weathering. Global Biogeochem. Cy. doi:10.1029/2019gb006522

Brock, T.D., 1970. Limits of microbial existence: temperature and pH. Science 169, 1316–1318.

Cardinal, D., Alleman, L.Y., De Jong, J., Ziegler, K., André, L., 2003. Isotopic composition of silicon measured by multicollector plasma source mass spectrometry in dry plasma mode. J. Anal. Atom. Spectrom. 18, 213–218.

Cardinal, D., Gaillardet, J., Hugues, H., Opfergelt, S., André, L., 2010. Contrasting silicon isotope signatures in rivers from the Congo basin and the specific behavior of organic-rich waters, Geophys. Res. Lett. 37, L12403.

Caudron, C., Syahbana, D.K., Lecocq, T., Van Hinsberg, V., McCausland, W., Triantafyllou, A., Camelbeek, T., Bernard, A., Surono, 2015. Kawah Ijen volcanic activity: a review. Bull. Volcanol. 77, 16.

De La Rocha, C.L., Brzezinski, M.A., DeNiro, M.J., 2000. A first look at the distribution of the stable isotopes of silicon in natural waters. Geochim Cosmochim. Ac. 64, 2467–2477.

Delmelle, P., Bernard, A., 1994. Geochemistry, mineralogy, and chemical modelling of the acid crater lake of Kawah Ijen volcano, Indonesia. Geochim. Cosmochim. Acta 58, 2445-2460.

Delmelle, P., Fischer, T., Kusakae, M., 1998. Geochemical and isotopic evidence for seawater contamination of the hydrothermal system of Taal Volcano, Luzon, the Philippines. Bull. Volcanol. 59, 562-576.

Delmelle, P., Bernard, A., 2000. Dowstream composition changes of acidic volcanic waters discharged into the Banyupahit stream, Ijen caldera, Indonesia. J. Volcanol. Geotherm. Res. 97, 55-75.

Delmelle, P., Bernard, A., Kusakabe, M., Fisher, T.P., Takano, B., 2000. Geochemistry of the magmatic-hydrothermal system of Kawah Ijen volcano, East Java, Indonesia. J. Volcanol. Geoth. Res. 97, 31-53.

Delmelle P., Henley R.W., Opfergelt S., Detienne M. Summit acid crater lakes and flank instability in composite volcanoes. In: Volcanic

Lakes, Advances in Volcanology, Eds: D. Rouwet, B. Christenson, F. Tassi, J. Vandemeulebrouck, Springer-Heidelberg, 2015, pp 289-305, ISBN 978-3-642-36832-5.

Derry, L.A., Kurtz, A.C., Ziegler, K., Chadwick, O.A., 2005. Biological control of terrestrial silica cycling and export fluxes to watersheds. Lett. Nature 433, 728–731.

Dessert, C., Dupré, B., Francois, L.M., Schott, J., Gaillardet, J., Chakrapani, G., Bajpai, S., 2001. Erosion of Deccan Traps determined by river geochemistry: impact on the global climate and the Sr-87/Sr-86 ratio of seawater. Earth. Planet. Sc. Lett. 188, 459-474.

Dessert, C., Dupré, B., Gaillardet, J., Francois, L.M., Allegre, C.J., 2003. Basalt weathering laws and the impact of basalt weathering on the global carbon cycle. Chem. Geol. 202, 257-273.

Dessert, C., Gaillardet, J., Dupré, B., Schott, J., Pokrovsky, O.S., 2009. Fluxes of high- versus low-temperature water-rock interactions in aerial volcanic areas: Example from the Kamchatka Peninsula, Russia. Geochim. Cosmochim. Ac. 73, 148–169.

Dupré, B., Dessert, C., Oliva, P., Godderis, Y., Viers, J., Francois, L., Millot, R., Gaillardet, J., 2003. Rivers, chemical weathering and Earth's climate. Comptes Rendus Geoscience 335, 1141-1160.

Edmond, J.M., Huh, Y., 1997. Chemical weathering yields from basement and organic terrains in hot and cold climates. In: Ruddiman WF, editor. Tectonic uplift and climate change. New York: Springer. 329-351.

Fournier, R.O., Rowe, J.J., 1977. The solubility of amorphous silica in water at high temperatures and high pressures. Am. Mineral. 62, 1052-1056.

Freire, P., Andrade C., Coutinho, R., Cruz, J., 2013. Fluvial geochemistry in Sao Miguel Island (Azores, Portugal): Source and fluxes of inorganic solutes in an active volcanic environment. The science of the total environment. 454-455, 154-169.

Frings, P.J., Clymans, W., Fontorbe, G., De La Rocha, C.L., Conley, D.J., 2016. The continental Si cycle and its impact on the ocean Si isotope budget. Chem. Geol. 425, 12-36.

Gaillardet, J., Dupré, B., Louvat, P., Allègre, C.J., 1999. Global silicate weathering and CO_2 consumption rates deduced from the chemistry of large rivers. Chem. Geol. 159, 3-30.

Gaillardet, J., Rad, S., Rivé, K., Louvat, P., Gorge, C., Allègre C-J., Lajeunesse E., 2011. Orography-driven chemical denudation in the Lesser Antilles: evidence for a new feed-back mechanism stabilizing atmospheric CO_2. Am. J. Sci. 311, 851 894.

Gaspard, F., Opfergelt, S., Dessert, C., Robert, V., Ameijeras-Marino, Y., Delmelle, P. Imprint of chemical weathering and hydrothermalism on the Ge/Si ratio and Si isotopic composition of rivers in a volcanic tropical island, Basse-Terre, Guadeloupe (French West Indies). Submitted to Chem. Geol. Georg, R.B., West, A.J., Basu, A.R., Halliday, A.N., 2009. Silicon fluxes and isotope composition of direct groundwater discharge into the Bay of Bengal and the effect on the global ocean silicon isotope budget. Earth Planet. Sci. Lett. 283, 67–74.

Gislason, S. R., Oelkers, E. H., 2011. Silicate rock weathering and the global carbon cycle, in Harmon, R. S., and Parker, A., editors, Frontiers in Geochemistry: Contribution of Geochemistry to the Study of the Earth: Chichester, United Kingdom, Wiley-Blackwell, 84–103.

Goldsmith, S.T., Carey, A.E., Lyons, W.B., Hicks, D.M., 2008. Geochemical fluxes and weathering of volcanic terrains on high standing islands: Taranaki and Manawatu-Wanganui regions of New Zealand. Geochim. Cosmochim. Ac. 72, 2248-2267.

Goldsmith, S.T., Carey, A.E., Johnson, B.M., Welch, S.A., Lyons, W.B., McDowell, W.H., Pigott, J.S., 2010. Stream geochemistry, chemical weathering and CO_2 consumption potential of andesitic terrains, Dominica, Lesser Antilles. Geochim. Cosmochim. Ac. 74, 85-103.

Hasan, N.Y., Driejana, Sulaeman, A., 2017. Composition of ions and trace metals in rainwaters in Bandung City, Indonesia. The Third International Conference on Civil Engineering Research (ICCER).

Heikens, A., Sumarti, S., van Bergen, M., Widianarko, B., Fokkert, L., van Leeuwen, K., Seinen, W., 2005. The impact of the hyperacid Ijen Crater Lake: risks of excess fluoride to human health. Sci. Total Envir. 346, 56-69.

Herrmann, R., Baumgartner, B., 1992. Aluminum species distribution during mixing of acid coal and slate mine drainage with neutral stream waters. Geol. Rundsch. 81, 759–767.

Hughes, H., Delvigne, C., Korntheuer, M., De Jong, J., André, L., Cardinal, D., 2011. Controlling the mass bias introduced by anionic and organic matrices in silicon isotopic measurements by MC-ICP-MS, J. Anal. Spectrom. 26, 1892-1896.

Hurwitz, S., Evans, W.C., Lowenstern, J.B., 2010. River solute fluxes reflecting active hydrothermal chemical weathering of the Yellowstone Plateau Volcanic Field, USA. Chem. Geol. 276, 331-343.

Ijen Monthly Climate Average, consulted on April 2020. https://www.worldweatheronline/ijen-weather/east-java/id.aspx.

Kemmerling, G.L.L., 1921. Het Idjen Hoogland. De geologie en geomorphologie van den Idjen. Koninklijke Natuurkundige Vereeniging Monografie II, G. Kolff & Co. Weltevreden-Batavia.

Löhr, A.J., Bogaard, T.A., Heikens, A., Hendriks, M.R., Sumarti, S., Van Bergen, M.J., Van Gestel, C.A.M., Van Straalen, N.M., Vroon, P.Z., Widianarko, B., 2005. Natural pollution caused by the extremely acidic crater Lake Kawah Ijen, East Java, Indonesia. Environ. Sci. Pollut. Res. 12, 89–95.

Louvat, P., 1997. Étude géochimique de l'érosion fluviale d'îles volcaniques à l'aide des bilans d'éléments majeurs et traces. Institut de Physique du Globe de Paris, PhD thesis.

Louvat, P., Allègre, C.J., 1997. Present denudation rates on the island of Réunion determinated by river geochemistry: Basalt weathering and mass budget between chemical and mechanical erosions. Geochim. Cosmochim. Ac. 61, 3645-3669.

Louvat, P., Gaillardet, J., Paris, G., Dessert, C., 2011. Boron isotope ratios of surface waters in Guadeloupe, Lesser Antilles. Appl. Geochem. 26, S76–S79.

Moquet, J.S., Crave, A., Viers, J., Seyler, P., Armijos, E., Bourrel, L., Chavarri, E., Lagane, C., Laraque, A., Casimoro, W.S.L., Pombosa, R., Noriega, L., Vera, A., Guyot, J.L., 2011. Chemical weathering and atmospheric/soil CO_2 uptake in the Andean and Foreland Amazon basins. Chem. Geol. 287, 1-26.

Nordstrom, D.K., Jenne, E.A., Ball, J.W., 1979. Redox equilibria of iron in acid mine waters. In: Jenne E.A. (Ed.), Chemical Modelling in Aqueous Systems-Speciation. Am. Chem. Soc. Symp Ser 93, 51–79.

Opfergelt, S., Delmelle, P., 2012. Silicon isotopes and continental weathering processes: Assessing controls on Si transfer to the ocean. Comptes Rendus Geosci. 344, 723–738.

Palmer, C.J.S., 2009. Hydrogeochemical insights into the nature of magmatic-hydrothermal fluid at Kawah Ijen volcano, Indonesia. PhD. McGill University, Canada.

Palmer, C.J.S., van Hinsberg, V.J., Mc Kenzie, J.M., Yee, S., 2011. Characterization of acid river dilution and associated trace element behavior through hydrogeochemical modelling: a case study of the Banyu Pahit river in East Java, Indonesia. Appl. Geochem. 26, 1802-1810.

Parkhurst, D.L., Appelo, C.A.J., 2013. Description of input and examples for PHREEQC version 3-a computer program for speciation,

batch-reaction, one-dimensional transport, and inverse geochemical calculations. In: U.S. Geological Survey Techniques and Method book 6, chap. A43, 497p, available only at http://pubs.usgs.gov/tm/06/a43.

Rad, S., Louvat, P., Gorge, C., Gaillardet, J., Allègre, C.J., 2006. River dissolved and solid loads in the Lesser Antilles: new insight into basalt weathering processes. J. Geoch. Explor. 88, 308-312.

Reynolds, B.C., Aggarwal, J., André, L., Baxter, D., Beucher, C., Brzezinski, M.A., Engström, E., Georg, B., Land, M., Leng, M.J., Opfergelt, S., Rodushkin, I., Sloane, H.J., Van den Boorn, S.H.J.M., Vroon, P.Z., Cardinal, D., 2007. An inter-laboratory comparison of Si isotope reference materials. J. Anal. Atom. Spectrom. 22, 561-568.

Rivé, K., Gaillardet, J., Agrinier, P., Rad, S., 2013. Carbon isotopes in the rivers from the Lesser Antilles: origin of the carbonic acid consumed by weathering reactions in the Lesser Antilles. Earth Surf. Proc. Land. 38, 1020–1035.

Schopka, H. H., Derry, L. A., Arcilla, C. A., 2011. Chemical weathering, river geochemistry and atmospheric carbon fluxes from volcanic and ultramafic regions on Luzon Island, the Philippines. Geochim. Cosmochim. Ac. 75, 978–1002.

Scribner, A.M., Kurtz, A.C., Chadwick, O.A. 2006. Germanium sequestration by soil: targeting the roles of secondary clays and Fe-oxyhydroxides, Earth and Plan. Sc. 243, 760-770.

Stefánsson, A., Gislason, S.R., 2001. Chemical weathering of basalts, southwest Iceland: effect of rock crystallinity and secondary minerals on chemical fluxes to ocean. J. Am. Sci. 301, 513-556.

Sumarti, S., 1998. Volcanic Pollutants in Hyperacid River Water Discharged from Ijen Caldera Lake, East Java, Indonesia, Unpubl. MSc Thesis Utrecht Univ., Netherlands.

Takano, B., Suzuki, K., Sugimori, K., Ohba, T., Fazlullin, S.M., Bernard, A., Sumarti, S., Sukhyar, R., Hirabayashi, M., 2004. Bathymetric and geochemical investigation of Kawah Ijen crater lake, east Java, Indonesia. J. Volcanol. Geotherm. Res. 135, 299–329.

United Kingdom Accreditation Body (UKAS)., 2014. Certificate of measurement, river water-anion, certified reference material LGC6025. 4005.

van Hinsberg, V.J., 2001. Water-Rock Interaction and Element Fluxes in the Kawah Ijen Hyperacid Crater Lake and the Banyu Pahit River, East-Java, Indonesia. Unpubl. MSc Thesis Utrecht Univ., Netherlands.

van Hinsberg, V.J., Berlo, K., Sumarti, S., van Bergen M., Williams-Jones, A., 2010. Extreme alteration by hyperacidic brines at Kawah Ijen

volcano, East Java, Indonesia: II. J. Volcanol. Geoth. Res. 196(3-4): 169-184.

van Rotterdam-Los, A.M.D., Vriend, S.P., van Bergen, M.J., van Gaans, R.F.M., 2008. The effect of naturally acidified irrigation water on agricultural volcanic soils: the case of Asembagus, Java, Indonesia. J. Geochem. Explor. 96, 53–68.

Whitford, D.J., Nicholls, I.A., Taylor, S.R., 1979. Spatial variations in the geochemistry of quaternary lavas across the Sunda Arc in Java and Bali. Contrib. Mineral. Petrol. 70, 341–356.

Yeghicheyan, D., Bossy, C., Bouhnik Le Coz, M., Douchet, C., Granier, G., Heimburger, A., Lacan, F., Lanzanova, A., Rousseau, T.C.C., Seidel, J-L., Tharaud, M., Candaudap, F., Chmeleff, J., Cloquet, C., Delpoux, S., Labatut, M., Losno, R., Pradoux, C., Sivry, Y., Sonke, J.E., 2013. A Compilation of Silicon, Rare Earth Element and Twenty-One other Trace Element Concentrations in the Natural River Water Reference Material SLRS-5 (NRC-CNRC). Geostand. Geoanal. Res. 37(4), 449-467.Young, E.D., Galy, A., Nagahara, H., 2002. Kinetic and equilibrium mass-dependent isotope fractionation laws in nature and their geochemical and cosmochemical significance. Geochim. Cosmochim. Ac. 66, 1095-1104.

Ziegler, K., Chadwick, O.A., Brzezinski, M.A., Kelly, E.F., 2005. Natural variations of $d^{30}Si$ ratios during progressive basalt weathering, Hawaiian Islands. Geochim. Cosmochim. Acta 69, 4597–4610.

4.9. Supplementary Materials

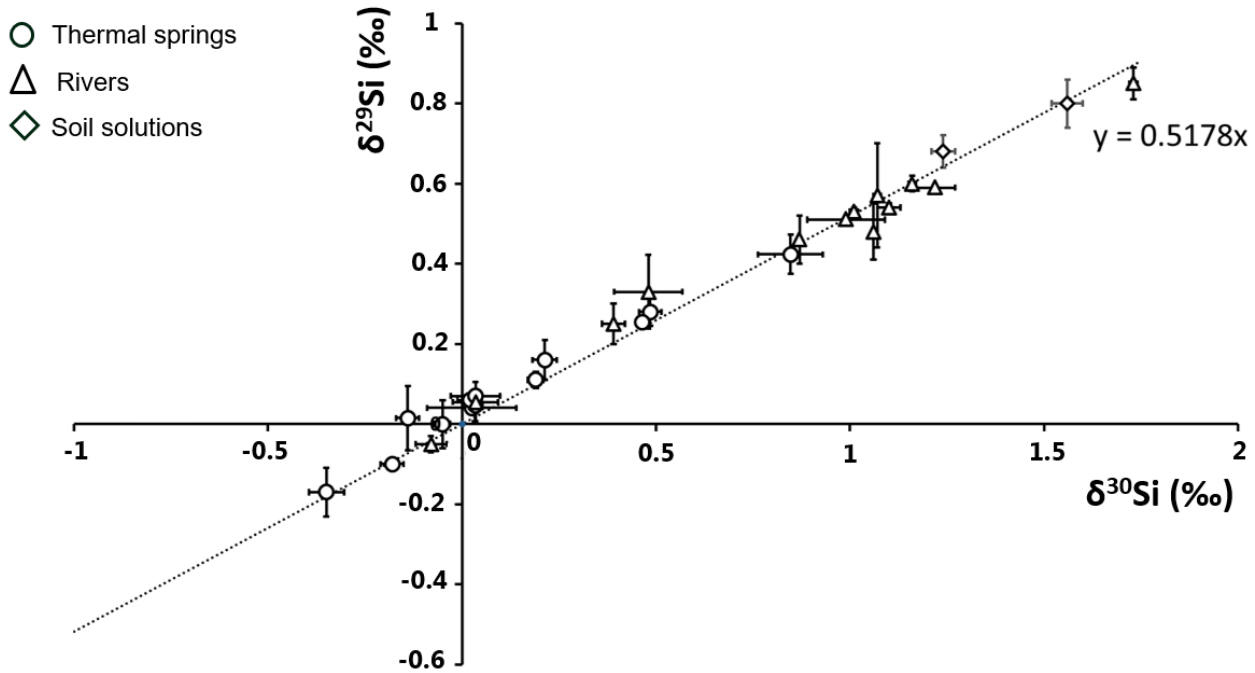

Suppl. Mat. 4.1: Silicon isotopes measurements of all water samples plotted onto a mass-dependent fractionation array $\delta^{30}Si$ and $\delta^{29}Si$ (theorical 0.5178 slope for equilibrium mass-dependent fractionation; Young et al, 2002).

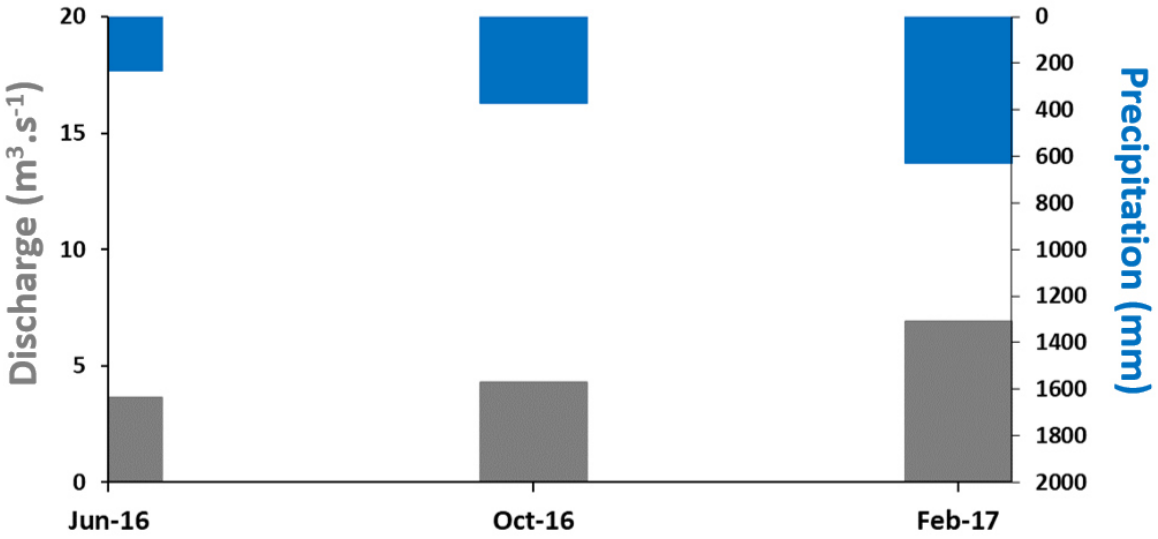

Suppl. Mat. 4.2: Discharge at the Lewung dam (BP10) in wet (February 2017; this study) and dry (June 2016 and October 2016; data from Asembagus Irrigation Office) seasons as a function of the precipitation (data from Asembagus Irrigation Office).

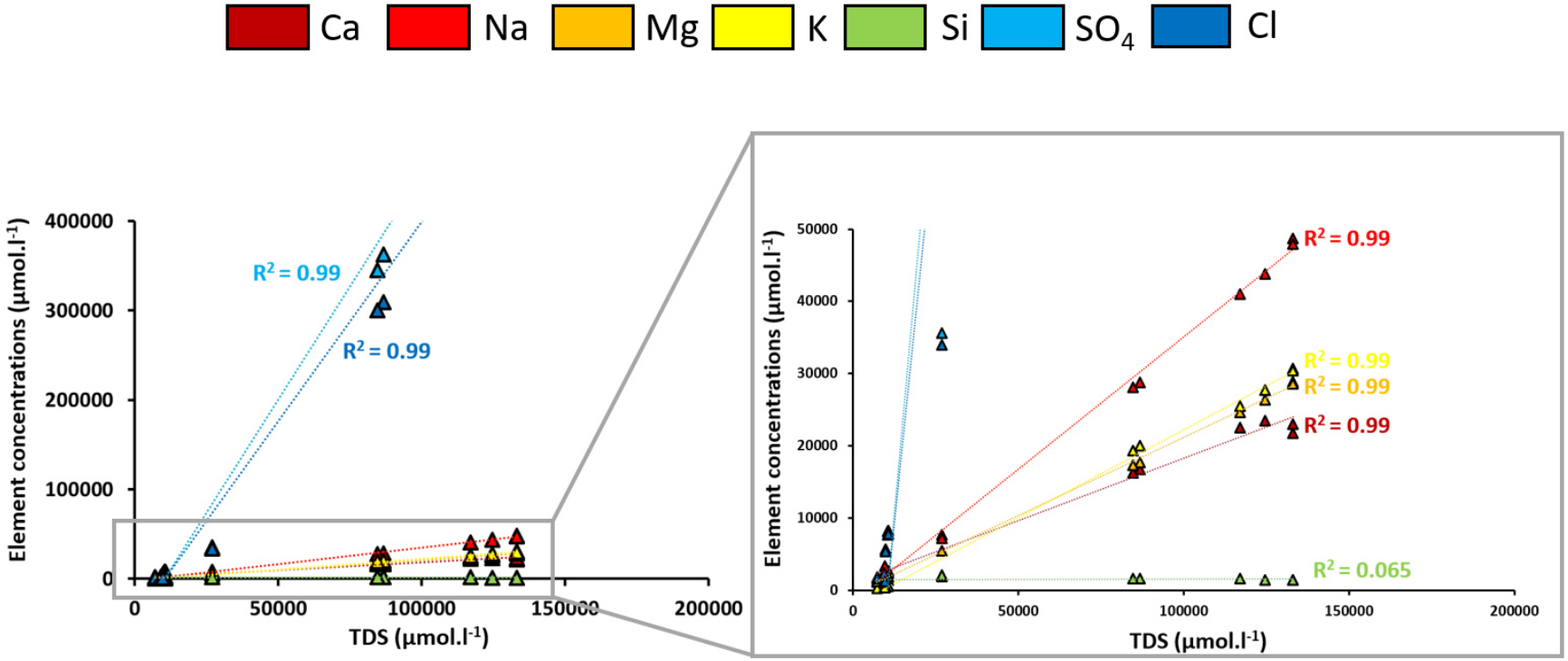

Suppl. Mat. 4.3: Major element concentrations (µmol.l^{-1}) as a function of total dissolved solids (TDS; µmol.l^{-1}) in Banyu Pahit/Banyu Putih river water draining from Kawah Ijen volcano (sampled at eleven different location 40 km downstream) and the three alkaline river waters (KST, KS and BA).

Suppl. Mat. 4.4: Assessment of the magmatic CO_2 consumed by silicate chemical weathering (using the method developed by Edmond and Huh (1997); Goldsmith et al (2008); Freire et al (2013)).

First, we calculate the Si mass ($t_{Si}.yr^{-1}$) exported by thermal springs (LF, SP1-SP11) yearly considering that thermals springs discharge and Si concentrations are constant throughout the year (Eq. 1):

$$Si_{thermal\ springs} = [\ (D_{LF}.Si_{LF}) + (D_{SP1}.Si_{SP1}) + \ldots + (D_{SP11}.Si_{SP11})\ ] * 1000\ (l.m^{-3}) * 3600 * 24 * 365\ (s.yr^{-1}) \quad \text{(Eq. 1)}$$

with D_{LF} = LF discharge ($m^3.s^{-1}$) and Si_{LF} = LF Si concentrations ($mg.l^{-1}$),…

Second, we calculate the Si mass ($t_{Si}.yr^{-1}$) exported by BP10 for the three scenarios (DS, WS, ANN) (Eq. 2):

$$Si_{BP10} = (D_{BP10}.Si_{BP10}) * 1000\ (l.m^{-3}) * 3600 * 24 * 365\ (s.yr^{-1}) \quad \text{(Eq. 2)}$$

Edmond and Huh (1997), Goldsmith et al (2008) and Freire et al (2013) argue that silicate chemical weathering need 2 mol of CO_2 to release 1 mol of Si.

For **thermal springs**, we assume that 1 mol of Si is responsible of the consumption of 2 mol of magmatic CO_2 (magmatic sources including all volatiles degassing from magma such as HF, HCl, H_2SO_4; CO_2m) (Eq. 4) and we convert the mol of magmatic CO_2 into fluxes ($t_{CO2m}.km^{-2}.yr^{-1}$) (Eq. 3, 5-7):

$$Si_{thermal\ springs} = mol_{Si}\ \text{in thermal springs}\ .\ M_{Si}^{-1} \quad \text{(Eq. 3)}$$

$$2x\ mol_{Si}\ \text{in thermal springs} = x\ mol_{CO2m} \quad \text{(Eq. 4)}$$

$$x\ mol_{CO2m}\ .\ M_{CO2m} = mg_{CO2m}.yr^{-1} \quad \text{(Eq. 5)}$$

$$mg_{CO2m}.yr^{-1} . 10^{-9} = t_{CO2m}.yr^{-1}$$
(Eq. 6)

$$t_{CO2m}.yr^{-1} . (\text{Banyu Pahit/Banyu Putih catchment size})^{-1} = t_{CO2m}.km^{-2}.yr^{-1}$$
(Eq. 7)

with M_{CO2m} = 44.01 $g.mol^{-1}$; Banyu Pahit/Banyu Putih catchment size = 450 km^2.

For **the three scenario of BP10** (DS, WS, ANN), we assume that 1 mol of Si is responsible of the consumption of 2 mol of $atmCO_2$ (Eq. 9) and we convert the mol of $atmCO_2$ into $atmCO_2$ fluxes ($t_{atmCO2}.km^{-2}.yr^{-1}$) (Eq. 8, 10-12):

$$Si_{BP10} = mol_{Si} \text{ in BP10} . M_{Si}^{-1}$$
(Eq. 8)

$$2x\ mol_{Si} \text{ in BP10} = x\ mol_{atmCO2}$$
(Eq. 9)

$$x\ mol_{atmCO2} . M_{atmCO2} = mg_{atmCO2}.yr^{-1}$$
(Eq. 10)

$$mg_{atmCO2}.yr^{-1} . 10^{-9} = t_{atmCO2}.yr^{-1}$$
(Eq. 11)

$$t_{atmCO2}.yr^{-1} . (\text{Banyu Pahit/Banyu Putih catchment size})^{-1} = t_{atmCO2}.km^{-2}.yr^{-1}$$
(Eq. 12)

with M_{atmCO2} = 44.01 $g.mol^{-1}$; D_{BP10} = BP10 discharge; Banyu Pahit/Banyu Putih catchment size = 450 km^2.

Values of BP10 Si concentrations and discharge for each scenario (DS, WS, ANN) are given in **Table 4.4**.

Finally, we calculated hydrothermal contribution (Eq. 13) and we obtained the corrected $atmCO_2$ consumption by silicate chemical weathering (CO_{2c}) (Eq. 14):

hydrothermal contribution (%) = [(magmatic sources/atmCO_2 consumption)]*100
(Eq. 13)

$$t_{atmCO2}.km^{-2}.yr^{-1} - t_{CO2m}.km^{-2}.yr^{-1} = t_{CO2c}.km^{-2}.yr^{-1}$$
(Eq. 14)

Chapter 3:

Imprint of chemical weathering and hydrothermalism on the Ge/Si ratio and Si isotope composition of rivers in a volcanic tropical island, Basse-Terre, Guadeloupe (French West Indies)[1]

5.1 Abstract

A significant portion of the disproportionally high weathering flux in volcanic island arcs may originate from hydrothermal activity, thereby compromising the accurate estimate of atmospheric CO_2 consumption rates. The objective of this study is to evaluate how the riverine Ge/Si ratio and Si isotopes, two well-established tracers of weathering, respond to hydrothermal inputs. The work took place in Basse-Terre, Guadeloupe, a tropical volcanic arc island with a dense river network, high weathering fluxes and various hydrothermal surface manifestations. We characterized the Ge/Si ratio and $\delta^{30}Si$ of 15 thermal springs, 9 non-impacted (NI) rivers and 13 hydrothermally-impacted (HI) rivers. The soil solution from a highly weathered soil profile (Ferralsol) and a clayey-rock corresponding to the material exposed in an extinct hydrothermal system were also measured. Basse-Terre's thermal springs display variable Ge/Si ratios (0.05-21.03 $\mu mol.mol^{-1}$) and $\delta^{30}Si$ (0.71-1.50 ‰), but with no apparent relationship to the water compositional type. The Ge/Si ratio (0.15-2.57

[1] Adapted from Gaspard, F., Opfergelt, S., Dessert, C., Robert, V., Ameijeiras-Marino, Y., Delmelle, P.,. Imprint of chemical weathering and hydrothermalism on the Ge/Si ratio and Si isotope composition of rivers in a volcanic tropical island, Basse-Terre, Guadeloupe (French West Indies). Submitted in **Chemical Geology**.

μmol.mol^{-1}) and Si isotope composition (δ^{30}Si = 0.26-1.21 ‰) values of the NI rivers reveal differences in the watersheds' weathering degree. Redissolution of Ge- and ^{28}Si-rich clay minerals and Ge-bearing aluminum oxides explains the high Ge/Si and isotopically light composition of the northern NI rivers draining strongly weathered terranes. The Ge/Si ratio and δ^{30}Si values measured for the NI and HI rivers overlap, implying that they cannot be used to diagnose hydrothermal contributions to river basins unambiguously. However, when combined with the Cl^- and SO_4^{2-} concentrations, the analysis of Ge and Si in the HI rivers suggests that water seeping through an extinct hydrothermal system produces SO_4-rich drainages with distinctively lower Ge/Si ratios than those inferred for watersheds receiving thermal spring discharges associated with an active hydrothermal system. Overall, our results provide new constraints on the applicability and meaning of Ge/Si and Si isotope measurements to study weathering in volcanic environments.

5.2 Introduction

Recent studies highlight that weathering in volcanic island arcs with intermediate and felsic rock compositions is responsible for a disproportionately large contribution to global weathering budgets (e.g., Goldsmith et al, 2008, 2010; Jones et al, 2011; Schopka et al, 2011; Gaillardet et al, 2011; Blazina et al, 2013). This is due in part to the high abundances of Ca and Mg silicates in arc terranes, the weathering of which results in high CO_2 consumption rates (e.g., Berner et al, 1983; François and Walker, 1992; Louvat and Allègre, 1997; Gaillardet et al, 1999; Dessert et al, 2003), but also to the mineralogy (olivine, pyroxene, amphibole, glass) and texture (tephra) of volcanic arc-derived rocks which enhance dissolution reactions. Moreover, many of the active island arcs are located in the wet tropics where high runoff rates prevail (e.g., Vörösmarty et al, 2000; Gaillardet et al, 2011).

Chemical weathering rates are controlled by bedrock age, temperature, runoff, uplift/erosion rate and relief, among other variables (e.g., Lerman and Meybeck, 1988; White and Brantley, 1995; Gaillardet et al, 1999; Dixon et al, 2009). Volcanic arc islands usually display rock substrata that vary little in composition, but which can span a range of ages, depending on the eruptive history of the volcanic center(s). On Basse-Terre Island, Guadeloupe, previous studies (Gaillardet et al, 2011; Lloret et al, 2011; Dessert et al, 2015) demonstrated that highly weathered watersheds are characterized by much lower weathering rates than rivers draining soils developed on younger bedrock. This reflects mainly the combined effect of bedrock ages and runoff. Additional studies focused on the most reactive terranes should contribute to improve our understanding of weathering in volcanic arc islands.

Another characteristic of active volcanic arc islands is that they usually host various hydrothermal manifestations, including fumaroles, thermal springs and hot grounds, which are sustained by the cooling and degassing of a magma intrusion at depth. Importantly, there is evidence that a significant portion of the chemical weathering fluxes generated in volcanic terranes is driven by water-rock interaction involving hydrothermal

waters. For example, Rivé et al (2013) concluded for the Lesser Antilles that up to 40% of the weathering flux is hydrothermal in origin. In the Philippines, Schopka et al (2011) argued that on average approximately 10% of the dissolved cation load in rivers relates to hydrothermal activity. Similarly, but in different volcanic settings, other studies have demonstrated a substantial influence of hydrothermalism on weathering rates in La Réunion (Louvat and Allègre, 1997), Kamchatka, Russia (Dessert et al, 2009), Iceland (Louvat et al, 2008) and Yellowstone, USA (Hurwitz et al, 2010). The acidity responsible for such weathering reactions originates from the degassing and dissolution of magmatic volatiles, mainly CO_2, SO_2, H_2S and sometimes HCl, in the subsurface hydrothermal system. Preferentially generated in active hydrothermal systems, this additional source of acidity can also derive from the weathering of alteration deposits in extinct hydrothermal systems (Gaillardet et al, 2011; Rivé et al, 2013; Dessert et al, 2015). Ignoring the volcanic contribution to the chemical weathering fluxes produces overestimates of atmospheric CO_2 consumption rates.

Thus, concomitant to the recognition that bedrock age exerts a strong control on weathering in volcanic island arcs, it appears that a better knowledge of the hydrothermal influence on weathering fluxes is required in order to test further the idea that these tectonic settings represent a quantitatively significant contribution to global CO_2 consumption. Among the various geochemical tools that have been used to track weathering in volcanic terranes, the combination of Si isotopes and Ge/Si ratio measurements has proven to be particularly powerful for identifying the processes underpinning the dissolved chemical fluxes (e.g., Derry et al, 2005; Ziegler et al, 2005; Opfergelt et al, 2010; 2013; Baronas et al, 2018; 2020). However, the few Si isotope (Douthitt, 1982; Opfergelt et al, 2011; Geilert et al, 2015; Ding et al, 2017; Chen et al, 2020) and Ge/Si ratio (Arnórsson, 1987; Siebert et al, 2006; Escoube et al, 2015) compositions available in the scientific literature for volcanic thermal springs suggest that hydrothermalism may alter the original isotopic and chemical signatures recorded during low-temperature weathering reactions. On the other hand, the tracers (e.g., concentration ratios and isotopes, including C, Sr, U-Th, B) used to decipher a hydrothermal contribution to rivers in

volcanic terranes (Louvat and Allègre, 1997; Gaillardet et al, 2011; Rad et al, 2011; Louvat et al, 2011; Rivé et al, 2013) have not been designed to identify catchments with contrasted weathering degrees.

This study was carried out with the objective of characterizing the Si isotope composition and Ge/Si ratio of thermal springs and rivers in Basse-Terre, Guadeloupe. More specifically, our goals are to (i) document the $\delta^{30}Si$ and Ge/Si ratio variability in thermal springs that vary in composition, (ii) assess if the riverine $\delta^{30}Si$ and Ge/Si ratio record an influence from hydrothermal inputs, and (iii) confirm the suitability of $\delta^{30}Si$ and Ge/Si ratio determinations for tracing low-temperature weathering processes in volcanic terranes with hydrothermal surface manifestations.

Basse-Terre is a prime location to address the above objectives because (i) the lithology is largely invariant across the island (Westercamp, 1988; Boudon et al, 2008; Samper et al, 2007; 2009), (ii) there is a clear south to north weathering gradient (Colmet-Daage and Lagache, 1965; Colmet-Daage, 1969; Cabidoche et al, 2009; Gaillardet et al, 2011; Lloret et al, 2011; Dessert et al, 2015), (iii) the island hosts both extinct and active hydrothermal systems (Verati et al, 2014, 2018; Favier et al, 2019; Salaün et al, 2011), and (iv) the geochemistry of the thermal springs and rivers are well-described (e.g., Brombach et al, 2000; Villemant et al, 2005; Gaillardet et al, 2011; Lloret et al, 2011; Villemant et al, 2014; Dessert et al, 2015).

5.3 Geological, pedological and climatic setting

The study took place on Basse-Terre Island (950 km^2; 16°N, 61°W) in Guadeloupe, Lesser Antilles, Caribbean Sea (**Fig. 5.1**). Basse-Terre consists of four main volcanic massifs varying in composition from basaltic-andesite to andesite (e.g., Samper et al, 2007, 2009; Boudon et al, 2008; Ricci et al, 2017; Favier et al, 2019). The oldest massifs are found in north Basse-Terre and include the Basal Complex (4.30–2.68 Ma) and the Septentrional Chain (1.81–1.15 Ma). Younger volcanism in the southern part of the island formed the Axial Chain (1.02–0.44 Ma) and the La Grande Découverte-La Soufrière composite volcano (445-205 ka to present). The Amic crater, which lies within the La Grande Découverte Caldeira, hosts the andesitic dome of La Soufrière (1464 m above sea level; **Fig. 5.1**). The lava dome was emplaced at the end of the last magmatic eruptive activity in 1530 AD (Boudon et al, 2008). Extinct hydrothermal systems, such as those found at Deshaies Dome, Les Mamelles Complex, Bouillante, and Carmichaël, are associated to old volcanic centers occurring in the main volcanic massifs (Basal Complex, Septentrional Chain, Axial Chain, La Grande Découverte complex, respectively; Verati et al, 2014, 2018; Favier et al, 2019; Salaün et al, 2011; **Fig. 5.1**).

Numerous fumaroles, thermal springs and temperature anomalies at the summit and periphery of the lava dome reveal the presence of an active hydrothermal system centered on La Soufrière (Brombach et al, 2000). This shallow aquifer (~500 m below the surface), delimited by the Amic caldera border, has an estimated temperature of 190-260 °C. It is fed by meteoric water percolating through pyroclastic deposits and by hot magmatic fluids (Brombach et al, 2000). The distribution of thermal springs on La Soufrière is controlled by several fracture systems, where intense hydrothermal alteration of the andesitic rocks takes place (Nicollin et al, 2006; Zlotnicki et al, 2006). Thermal springs are also found around extinct hydrothermal systems, for example in the Bouillante geothermal area. Several studies have described the geochemistry of Basse-Terre's thermal springs (e.g., Bigot and Hammouya, 1982; Brombach et al, 2000;

Louvat et al, 2011; Ruzié et al, 2013; Villemant et al, 2014; Dessert et al, 2015).

Basse-Terre Island has a dry-winter tropical climate, with annual temperature and relative humidity averaging to ~23 °C and 75 %, respectively (Météo-France, 2019). The dry and rainy seasons run from January to April and from June to November, respectively. The average annual precipitation (between 1981 and 2010; Météo-France, 2019) fluctuates between 1050 and 8500 $mm.yr^{-1}$, depending on relief. This large variation reflects an orographic effect; the east coast receives high rainfall due to the strong influence of the Easterly and conversely, the west coast, protected by the orographic barrier, receives less rainfall (Chaperon et al, 1985). Combined with the rugged and steep relief of Basse-Terre, the abundant rainfall feeds a dense river network. There are 30 and 25 independent river systems on the west and east coasts of Basse-Terre, respectively, all with a watershed area greater than 1 km^2 (DIREN; French Water Survey agency). Gaillardet et al (2011), Lloret et al (2011) and Dessert et al (2015) provide a detailed description of the river geochemistry. Depending on location, the river systems drain terrains with contrasted soil properties. Highly-weathered soils, which include clay mineral-rich Ferralsols and Vertisols are found in the northern and central parts of Basse-Terre (**Fig. 5.1**), where Pliocene volcanic deposits dominate the landscape (Colmet-Daage, 1969). In contrast, young and less weathered Andosols derived from Quaternary volcanic deposits occur in the south of the island.

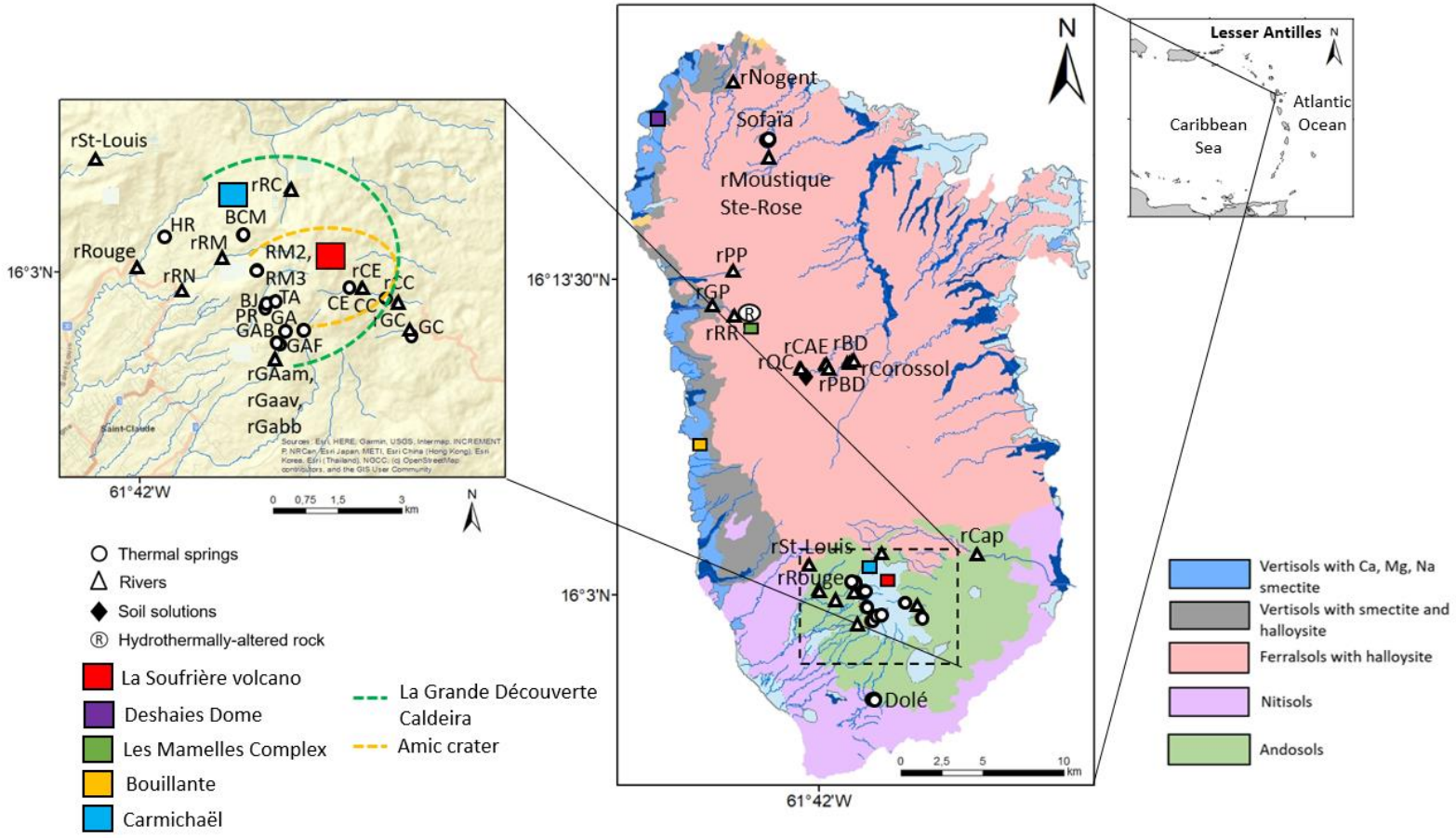
rSt-Louis
rRC
BCM
HR
rRM
rRouge
RM2,
RM3
rRN
rCE
rCC
BJ
TA
PR
GA
GAB
GAF
CE
CC
GC
GC
rGAam,
rGaav,
rGabb
16°3'N
61°42'W
0 0.75 1.5 3 km
N
rNogent
Sofaïa
rMoustique
Ste-Rose
rPP
rGP
R
rRR
rCAE
rBD
rQC
rCorossol
rPBD
16°13'30"N
16°3'N
rCap
rSt-Louis
rRouge
Dolé
61°42'W
0 2.5 5 10 km
Lesser Antilles
Caribbean Sea
Atlantic Ocean
Thermal springs
Rivers
Soil solutions
Hydrothermally-altered rock
La Soufrière volcano
Deshaies Dome
Les Mamelles Complex
Bouillante
Carmichaël
La Grande Découverte Caldeira
Amic crater
Vertisols with Ca, Mg, Na smectite
Vertisols with smectite and halloysite
Ferralsols with halloysite
Nitisols
Andosols

Fig. 5.1: Sampling locations on Basse-Terre Island, Guadeloupe, Lesser-Antilles. The thermal springs (black circle), rivers (black triangle), soil solutions (black diamond) and hydrothermally-altered rock (®) are depicted on a simplified soil map (modified from Cabidoche, 2011). Also shown are La Soufrière volcano, Deshaies Dome, Les Mamelles Complex, Bouillante geothermal area and Carmichaël. The approximate boundaries of the La Grande Découverte caldeira and Amic crater are represented by dotted lines (Barat, 1986; Komorowski et al, 2005). All the sample codes are described in **Table 5.1**.

5.4 Materials and methods

5.4.1 Sampling

Fifteen thermal springs were sampled on Basse-Terre Island between 2015 and 2018 (**Fig. 5.1**; **Table 5.1).** Most of these springs have been monitored routinely by the Observatoire Volcanologique et Sismologique de la Guadeloupe-Institut de Physique du Globe de Paris (OVSG-IPGP) since 1978. The springs Ravine Marchand (RM2 and RM3), Galion (GA), Galion Blanc (GAB), Galion Froid (GAF), Carbet-Echelle (CE), Bains Jaunes (BJ), Pas du Roy (PR) and Tarade (TA) sit inside the Amic Crater at elevations ranging from ~980 to 1150 m. Grosse Corde (GC) and Chute du Carbet (CC) lie farther away from the lava dome on the eastern side of the volcano, whereas Bains Chauds du Matouba (BCM) and Habitation Revel (HR) are located on its western flank. Dolé is a thermal spring located ~5.8 km to the south of La Soufrière. We also sampled a thermal spring (Sofaïa) in the northern part of the island. We did not include thermal springs from the Bouillante geothermal area in our study as these are contaminated by seawater (Brombach et al, 2000).

Water samples from 22 rivers were obtained in January-February 2015, October-November 2017 and April 2018 (**Table 5.1**). The river samples were collected as much as possible from areas with minimum anthropogenic disturbances. The rivers drain watersheds in the north (n=5; rivière Nogent (rNogent), Moustique Ste-Rose (rMoustique Ste-Rose), Petite Plaine (rPP), Grande Plaine (rGP) and Ravine Rouge (rRR)), the center (n=5; Corossol (rCorossol), Bras David (rBD), Quiock Creek (rQC), Cascade aux écrevisses (rCAE), Petit Bras David (rPBD)), and the south of Basse-Terre (n=3; Ravine Marchand (rRM), Ravine Chaude (rRC) and Galion (rGA). Water samples from rGA were obtained from

three locations: "amont" (rGAam), "aval" (rGAav) and "bassin bleu" (rGAbb). Three rivers were sampled on the west coast (Noire (rRN), St-Louis (rSt-Louis) and Rouge (rRouge)) and fours rivers on the east coast (n=4; Capesterre (rCap), Chute du Carbet (rCC), Carbet (rCE), Grosse Corde (rGC)) of South Basse-Terre (**Fig. 5.1**). The rPP, rGP, and rRR rivers drain the extinct hydrothermal system associated with Les Mamelles, and the rRouge river drains the extinct hydrothermal system of Carmichaël. Several of these rivers (rBD, rQC, rPBD, rSt-Louis, rRouge and rCap) have been monitored routinely by the Observatoire de l'Eau et de l'Erosion-Institut de Physique du Globe de Paris (OBSERA-IPGP) since 2006.

The temperature, pH and conductivity ($\mu S.cm^{-1}$, referenced to 25 °C) of the thermal springs and rivers were measured *in situ* with a Hanna HI 991300 electrode. The water samples were filtered within 24 hours after collection using 0.45 µm polycarbonate membranes, and then stored at 4 °C in the dark in pre-washed polypropylene bottles. An aliquot filtered and acidified to 0.5% v/v with suprapure HNO_3 was used for major, trace element and Si isotope analysis. The anions were measured on a separate unacidified sample aliquot.

Soil solutions were collected from a soil profile (GBD2 in **Table 5.1**) from the Quiock Creek catchment, which is monitored regularly by OBSERA. The soil is a Ferralsol, a soil group commonly encountered in the north and center of Basse-Terre and which is characterized by an advanced stage of weathering (**Fig. 5.1**). The soil solutions were retrieved at depths of 61, 91, 152, 274, 344, 457 and 823 cm using no-suction 5-cm diameter nested lysimeters equipped with porous ceramic cups (Buss et al, 2010; Clergue et al, 2015). The solutions were filtered with 0.45 µm polycarbonate filters prior to storage at 4 °C.

Finally, a sample of clayey, hydrothermally-altered rock collected from the Grande Plaine watershed which drains the extinct hydrothermal system of Les Mamelles (**Fig. 5.1**) was determined by X-ray powder diffraction (XRD, Bruker D8 Advance, Cu Kα, I = 0.15418 nm, 40 kV, 30 mA, 2θ = 1°/min). The analysis revealed the presence of pyrite, pyrophyllite and dickite, with minor smectite and residual feldspar in this sample (**Suppl. Mat 5.1**).

5.4.2 Water composition analysis

The concentrations of Ca, Na, Mg, K, Al, Fe and Si in the water samples were determined by inductively-coupled plasma-optical emission spectrometry (ICP-OES; iCAP 6500 Thermo Fisher Scientific). The accuracy on majors elements (Ca, Na, Mg, K, Al, Fe and Si) analyses was assessed using the trueness (± 3%, ± 4%, ± 1%, ± 7%, ± 4%, ± 2% and ± 4%; respectively) on the river water reference material SLRS-5 (Yeghicheyan et al, 2013) and the analytical precision (± 0.5%) for each element. The detection limit are 0.05, 0.43, 0.21, 0.26, 0.37, 0.18 and 0.36 µmol.l^{-1} for Ca, Na, Mg, K, Al, Fe and Si, respectively. Anions (SO_4^{2-}, Cl^-) were measured by ion chromatography (Dionex ICS2000, column: AG15/AS15). The accuracy on SO_4^{2-} and Cl^- was assessed by using the trueness (± 3% and ± 4%; respectively) on river water certified reference material LGC6025 (UKAS, 2014) and the analytical precision (± 2%) for each anion. The detection limit are 1.5 and 3.1 for SO_4^{2-} and Cl^-, respectively. Alkalinity (µmol.l^{-1}) was determined on the same day as sampling using an automatic titrator (Metrohm 916 Ti-Touch titrator). In all cases, the charge balance of the water analyses never exceeds 10%.

5.4.3 Ge concentration measurements by ICP-MS

The Ge concentration in all thermal springs, river waters, soil solutions and hydrothermally-altered rock was determined by ICP-mass spectrometry (ICP-MS, ICAPQ Thermo Fisher Scientific) using the ^{74}Ge isotope for the measurement (Delvigne et al, 2018). Prior to analysis, the hydrothermal-altered rock was dissolved by alkaline fusion with 99.99% pure NaOH at 720 °C in a silver crucible (Georg et al, 2006). Accuracy and long-term repeatability of the analysis were assessed by measuring two international riverine standards, namely SLRS-5 ([Ge] = 0.083 ± 0.014 nmol.l^{-1}, SD; n=3) and SLRS-6 ([Ge] = 0.097 ± 0.0069 nmol.l^{-1}, SD; n=3) (Yeghicheyan et al, 2013). The GAB thermal spring ([Ge] = 23.95 ± 0.096 nmol.l^{-1}, SD; n=14) was used as an in-house standard. SLRS-5, SLRS-6 and GAB were measured in each of the analytical sessions that took place between July 2017 and June 2018. The detection limit for Ge is 0.04 nmol.l^{-1} and the analytical precision of the measurement is ± 8 % for Ge concentrations < 0.013 nmol.l^{-1} and ± 4 % for Ge concentrations > 0.013 nmol.l^{-1}. The standard deviation of our Ge/Si ratio determinations is 10%.

5.4.4 Silicon isotope measurements

5.4.4.1 Purification of anion-rich samples

To prevent from matrix effects in mass spectrometry from anions such as SO_4^{2-} and Cl^-, Si in waters influenced by thermal manifestations has been purified by performing a two-step column chemistry, anion-exchange resin (Biorad AG MP-1) and cation-exchange resin (Biorad AG50W-X12; Georg et al, 2006) following the method developed by Gaspard et al, submitted.

The Si isotope compositions of 9 thermal springs (RM2, CC, CE, GC, GA, GAB, TA, Sofaïa, BCM), 15 river waters (rNogent, rMoustique Ste-Rose, rPP, rGP, rRR, rCorossol, rBD, rQC, rPBD, rCap, rRC, rCC, rRouge, rGC, rGAam), 7 soil solutions (GBD2) and the hydrothermally-altered rock from Les Mamelles were determined after sample treatment using the two-step purification method. The hydrothermally-altered rock was first digested by alkaline fusion with NaOH (Georg et al, 2006) prior to purification; the Na concentration in the resulting solution was below the detection limit (< 0.43 µmol.l^{-1}). The SO_4^{2-} and Cl^- concentrations in all the purified solutions were < 1.5 and < 3.1 µmol.l^{-1}, respectively, i.e., below the detection limits for these anions. The Si recovery in all the solutions was always > 98% and the blank level was below the ICP-OES detection limit for Si (i.e., < 0.36 µmol.l^{-1}).

5.4.4.2 Mass spectrometry

The Si isotope composition of the thermal spring, river water, soil solution and hydrothermally-altered rock samples were determined by MC-ICP-MS (Neptune Plus™ High Resolution Multicollector ICP-MS, Thermo Fisher Scientific) in wet plasma mode and medium resolution ($\Delta m/m \sim 6000$), using a PFA nebulizer of 100 µl.min^{-1} uptake rate. The instrumental mass bias was corrected using the standard-sample bracketing technique and an external Mg doping (Cardinal et al, 2003). The analyses were performed in a 2% v/v HNO_3 matrix, with a typical sensitivity of 7 V for 2 mg.l^{-1} Si and an instrumental blank < 30 mV. Silicon isotope compositions are expressed in relative deviations of $^{30}Si/^{28}Si$ ratio from the NBS-28 reference standard using the common δ-notation (‰): $\delta^{30}Si = [(^{30}Si/^{28}Si)_{sample}/(^{30}Si/^{28}Si)_{NBS\text{-}28} - 1] \times 1000$. One measurement comprises 30 cycles with 4.2 s integration time corrected by blank in a 2%

v/v HNO_3 matrix. Each single δ-value represents one sample run and two bracketing standards. $\delta^{30}Si$-values are reported as the mean of replicate isotopic analyses ± SD. Quality control of mass bias was performed by ensuring that $\delta^{30}Si$ and $\delta^{29}Si$ measurements fit to a mass-dependent fractionation array, supporting the interference-free determination of all three Si isotopes via MC-ICP-MS (**Suppl. Mat. 5.2**). The long-term precision and accuracy of the MC-ICP-MS $\delta^{30}Si$ analyses were assessed from multiple measurements of three reference materials prepared using the single step cation-exchange resin method. The values obtained for diatomite ($\delta^{30}Si$ = 1.29 ± 0.09 ‰, SD, n=19), USGS basalt BHVO-2 ($\delta^{30}Si$ = -0.27 ± 0.06 ‰, SD, n=10) and quartz Merck ($\delta^{30}Si$ of 0.04 ± 0.09 ‰, SD, n=6) are consistent with those reported earlier (Reynolds et al, 2007; Abraham et al, 2008).

5.5 Results

5.5.1 Major element compositions

The chemical compositions of the thermal spring, river water and soil solution samples are presented in **Table 5.1**.

Table 5.1: Description and compositions of the thermal springs, river waters and soil solutions as sampled in 2015, 2017 and 2018. Eleven springs and seven rivers were collected several times on different dates. The thermal springs are sorted by type, following Brombach et al (2000)'s classification (see text). The river water samples are sorted by their positioning on Basse-Terre from North to South. Rivers affected by hydrothermal inputs are denoted by "HI".

Sample	Code	Sampling date	Type	Temperature	pH	Conductivity	Alkalinity	Ca	Na	Mg	K	Al	Fe	Si	SO_4	Cl
		dd.mm.yy		°C		$\mu s.cm^{-1}$	$\mu mol.l^{-1}$									
Thermal springs																
Ravine Marchand 2	RM2(1)	27.01.15	Ca-SO_4 water	21.5	3.3	549	0	1268	589	442	68	226	54	1375	2291	813
Ravine Marchand 2	RM2(2)	12.10.17	Ca-SO_4 water	21.6	3.6	711	0	1863	696	602	75	167	54	1449	2697	1336
Ravine Marchand 3	RM3(1)	27.01.15	Ca-SO_4 water	41.1	5.5	1360	1900	4029	1948	1605	384	n.d	208	2585	4281	3960
Ravine Marchand 3	RM3(2)	12.10.17	Ca-SO_4 water	43.3	5.3	1581	2043	4416	2221	1765	431	n.d	253	2882	4788	5141
Carbet-Echelle	CE(1)	17.11.17	Ca-SO_4 water	21.0	5.3	1442	883	5115	1170	1646	148	16	1200	1735	8136	301
Carbet-Echelle	CE(2)	15.03.18	Ca-SO_4 water	20.9	5.3	1469	1001	5217	1196	1655	148	17	1170	1744	8752	315
Galion	GA(1)	29.01.15	Ca-SO_4 water	48.0	4.6	2040	603	6635	2545	2623	492	1	287	2882	6638	7930
Galion	GA(2)	14.11.17	Ca-SO_4 water	48.6	4.8	1909	599	5649	2184	2136	454	3	275	2669	6281	7194
Galion Blanc	GAB(1)	29.01.15	Ca-SO_4 water	42.8	4.6	1844	499	5692	2455	2546	444	7	111	2607	5842	7295
Galion Blanc	GAB(2)	14.11.17	Ca-SO_4 water	44.1	4.8	1795	502	5414	2364	2369	416	5	159	2721	5568	7793
Galion Froid	GAF	29.01.15	Ca-SO_4 water	21.7	4.5	304	194	905	485	281	55	26	4	1491	1211	517
Bains Jaunes	BJ(1)	29.01.15	Ca-SO_4 water	29.2	4.9	706	181	1935	1334	786	133	3	n.d	1853	2734	1132
Bains Jaunes	BJ(2)	14.11.17	Ca-SO_4 water	29.6	5.2	673	194	1819	1290	710	128	4	n.d	1825	2497	958
Pas du Roy	PR(1)	29.01.15	Ca-SO_4 water	34.1	5.4	994	677	2706	2008	1306	267	n.d	42	2095	3898	1641
Pas du Roy	PR(2)	14.11.17	Ca-SO_4 water	33.9	5.7	980	661	2622	1997	1272	230	n.d	42	2080	3559	1537
Tarade	TA(1)	29.01.15	Ca-SO_4 water	42.0	5.5	1574	1292	4276	3796	2210	485	n.d	n.d	2384	6076	3393
Tarade	TA(2)	14.11.17	Ca-SO_4 water	43.5	5.8	1693	1405	4693	3941	2294	515	n.d	n.d	2533	6155	3841
Sofaïa	Sofaïa	02.02.15	Ca-SO_4 water	29.3	3.8	165	0	97	435	69	25	34	5	565	358	422
Bain Chaud du Matouba	BCM(1)	30.01.15	Ca-SO_4 water	58.5	5.9	1183	348	6629	1551	521	208	n.d	n.d	557	7491	573
Bain Chaud du Matouba	BCM(2)	20.10.17	Ca-SO_4 water	58.3	5.6	1362	391	6595	1610	537	208	1	n.d	566	7759	577
Chute du Carbet	CC(1)	28.01.15	Ca-Na-Cl water	43.0	6.7	935	2395	1698	2949	1218	438	n.d	n.d	1678	847	278
Chute du Carbet	CC(2)	07.11.17	Ca-Na-Cl water	42.0	6.7	852	2577	1608	2636	1117	393	n.d	n.d	1651	847	214
Grosse corde	GC(1)	28.01.15	Ca-Na-Cl water	38.3	6.3	1383	2399	2801	4047	1790	522	n.d	n.d	1576	2272	4749
Grosse corde	GC(2)	07.11.17	Ca-Na-Cl water	37.5	6.5	1640	2522	2590	3727	1651	495	n.d	n.d	1477	2489	4468
Habitation Revel	HR	20.10.17	Ca-Na-HCO_3 water	32.6	6.5	254	2098	484	1020	209	91	n.d	n.d	1284	175	241
Dolé	Dolé	04.02.15	Ca-Na-HCO_3 water	30.8	8.3	555	3248	1293	1690	903	174	n.d	n.d	1415	843	870

Sample	Code	Sampling date	Type	Temperature	pH	Conductivity	Alkalinity	Ca	Na	Mg	K	Al	Fe	Si	SO_4	Cl
		dd.mm.yy		°C		$\mu s.cm^{-1}$	$\mu mol.l^{-1}$									
River waters																
North Basse-Terre																
Nogent	rNogent	02.02.15		23.8	7.6	144	540	162	668	127	47	5	1	538	64	561
Moustique Sainte-Rose	rMoustique Ste-Rose	02.02.15		23.3	6.5	85	233	100	387	78	20	4	2	287	39	414
Petite Plaine	rPP	03.02.15	HI	23.4	7.5	169	893	302	541	182	31	2	0	546	95	410
Grande Plaine	rGP	27.04.18	HI	23.3	6.1	-	-	761	1044	546	50	4	2	560	741	401
Ravine Rouge	rRR	27.04.18	HI	23.4	4.2	-	0	435	482	237	29	3	4	560	1441	346
Central Basse-Terre																
Corossol	rCorossol	05.02.15		22.9	7.7	69	416	125	322	64	16	1	n.d	408	12	221
Bras David	rBD1	05.02.15		22.7	7.2	83	443	132	362	82	20	1	n.d	429	42	308
Bras David	rBD2	03.10.17		25.7	7.6	77	410	107	311	73	24	1	0	391	17	278
Bras David	rBD3	19.10.17		23.7	7.5	83	412	102	299	69	25	1	0	370	15	263
Bras David	rBD4	10.11.17		23.5	7.5	71	381	106	295	69	22	1	1	360	20	260
Quiock Creek	rQC1	05.02.15		23.1	4.8	46	-	11	274	31	4	2	n.d	89	13	318
Quiock Creek	rQC2	03.10.17		25.1	5.7	46	56	11	246	31	12	2	1	71	9	330
Quiock Creek	rQC3	19.10.17		24.6	5.5	48	43	12	241	29	15	2	1	69	21	323
Quiock Creek	rQC4	10.11.17		23.9	5.4	42	68	13	242	30	13	5	2	76	11	290
Cascade aux Ecrevisses	rCAE	04.02.15		24.9	8.2	137	433	122	450	75	20	1	n.d	373	23	409
Petit Bras David	rPBD1	05.02.15		22.8	7.2	80	291	106	362	74	21	1	n.d	388	21	278
Petit Bras David	rPBD2	03.10.17		24.5	7.2	75	276	86	318	68	29	1	1	360	35	317
Petit Bras David	rPBD3	10.11.17		23.2	7.1	70	297	89	305	66	25	2	1	331	35	295
South Basse-Terre																
Ravine Marchand	rRM	27.01.15	HI	22.8	4.0	585	1370	1813	780	607	107	139	45	1451	2452	1347
Capesterre	rCap1	29.01.15		21.7	7.8	62	408	134	247	56	15	n.d	n.d	428	23	150
Capesterre	rCap2	27.10.17		22.5	7.3	41	489	68	157	33	20	1	0	211	17	139
Ravine Chaude	rRC1	30.01.15	HI	18.8	6.9	197	267	570	361	117	38	n.d	n.d	491	645	178
Ravine Chaude	rRC2	20.10.17	HI	20.5	7.2	128	295	327	265	84	29	1	n.d	445	373	168
Ravine Chaude	rRC3	24.01.18	HI	18.9	7.0	126	285	277	252	72	21	0	0	444	307	157
Chute du Carbet	rCC	28.01.15	HI	22.1	7.6	221	358	620	488	275	61	1	1	657	2018	2434
Rivière Carbet	rCE	17.11.17	HI	20.9	5.5	750	-	2620	674	735	86	1	808	1442	4573	211
Rivière Noire	rRN	27.01.15	HI	21.2	7.5	429	352	1290	944	556	138	1	n.d	1239	1649	1055

Saint-Louis	rSt-Louis1	30.01.15		22.9	7.1	106	690	222	340	113	27	n.d	n.d	543	51	193
Saint-Louis	rSt-Louis2	20.10.17		22.6	7.4	82	639	164	272	89	29	0	n.d	474	35	189
Rivière Rouge	rRouge1	30.01.15	HI	19.1	4.0	176	67	347	278	95	22	70	1	608	643	132
Rivière Rouge	rRouge2	20.10.17	HI	20.8	4.7	133	43	267	243	83	27	37	1	538	495	145
Rivière Rouge	rRouge3	26.01.18	HI	19.2	4.6	133	27	269	247	81	19	47	1	556	519	141
Grosse Corde	rGC	28.01.15	HI	31.5	7.3	983	1937	2305	3417	1494	443	1	n.d	1245	2720	5643
Rivière Galion amont	rGAam	29.01.15	HI	26.6	4.8	645	-	2218	1054	854	156	78	30	1755	2598	2365
Rivière Galion aval	rGAav	29.01.15	HI	28.2	5.1	848	110	3084	1370	1180	223	42	72	1947	3403	3483
Rivière Galion Bassin Bleu	rGAbb	30.01.15	HI	20.9	6.5	478	173	1576	883	623	94	2	n.d	1124	1551	2051
Soil solutions	Soil depth	Sampling date		Temperature	pH	Conductivity	Alkalinity	Ca	Na	Mg	K	Al	Fe	Si	SO_4	Cl
	cm	dd.mm.yy		°C		$\mu s.cm^{-1}$	$\mu mol.l^{-1}$									
GBD2-61	61	10.11.17		-	5.0	-	-	8	170	30	4	10	n.d	83	19	230
GBD2-91	91	10.11.17		-	5.6	-	-	6	241	31	4	4	n.d	96	14	278
GBD2-152	152	10.11.17		-	5.1	-	-	2	199	30	2	7	n.d	63	13	239
GBD2-274	274	10.11.17		-	4.8	-	-	1	208	29	3	10	n.d	70	14	289
GBD2-344	344	10.11.17		-	4.2	-	-	2	195	26	9	8	n.d	62	20	254
GBD2-457	457	10.11.17		-	5.0	-	-	10	198	19	6	6	n.d	116	14	217
GBD2-823	823	10.11.17		-	4.8	-	-	1	232	15	12	1	n.d	106	18	268

-: not measured; n.d: not detected.

5.5.1.1 Thermal springs

The spring BCM has the highest temperature (~58 °C), whereas RM2 and CE correspond to cold spring waters (~21 °C), in accordance with Brombach et al (2000) and Villemant et al (2005; 2014). Except Dolé (pH 8.3), all the thermal discharges are slightly (pH 6.3-6.7; CC, GC, HR), moderately (pH 4.5-5.9; RM3, CE, GA, GAB, GAF, BJ, PR, TA, BM) and strongly (pH 3.3-3.8; RM2, Sofaïa) acidic. In accordance with previous studies (Brombach et al, 2000; Villemant et al, 2005; Villemant et al, 2014; Dessert et al, 2015), the thermal springs are classified in three groups based on their major anion (SO_4^{2-}, Cl^- and HCO_3^-) and cation (Ca, Mg and Na) contents (**Fig. 5.2**): Ca-SO_4 waters (RM2, RM3, CE, GA, GAB, GAF, BJ, PR, TA, Sofaïa, BCM), Ca-Na-Cl waters (GC, CC) and Ca-Na-HCO_3 waters (Dolé, HR).

The Ca-SO_4 thermal springs are acidic (pH: 3.3-5.9) and except BCM and Sofaïa, they are all located in the Amic crater (**Fig. 5.1**). They exhibit SO_4^{2-} and Cl^- concentrations ranging from 358 (Sofaïa) to 8752 (CE) $\mu mol.l^{-1}$ and from 301 (CE) to 7930 (GA) $\mu mol.l^{-1}$, respectively. According to Brombach et al (2000), the acidity and SO_4^{2-} content of these springs originate from the oxidation of hydrogen sulfide at shallow levels in the hydrothermal system. The presence of Cl^- in significant concentrations in GA, GAB, GAF is due to mixing with neutral pH and Cl-rich waters. The Ca-Na-Cl thermal springs are slightly acidic (pH: 6.3-6.7) and are located on the eastern side of the Amic crater (**Fig. 5.1**). They exhibit Ca and Na concentrations ranging from 1608 (CC) to 2801 $\mu mol.l^{-1}$ (GC) and from 2636 (CC) to 4047 (GC) $\mu mol.l^{-1}$, respectively. The Ca-Na-HCO_3 thermal springs display near-neutral to alkaline pH values (6.5-8.3) and are located outside the Amic crater (**Fig. 5.1**). Sodium is their major cation, with concentrations ranging from 1020 (HR) to 1690 $\mu mol.l^{-1}$ (Dolé) $\mu mol.l^{-1}$, followed by Ca (484-1293 $\mu mol.l^{-1}$).

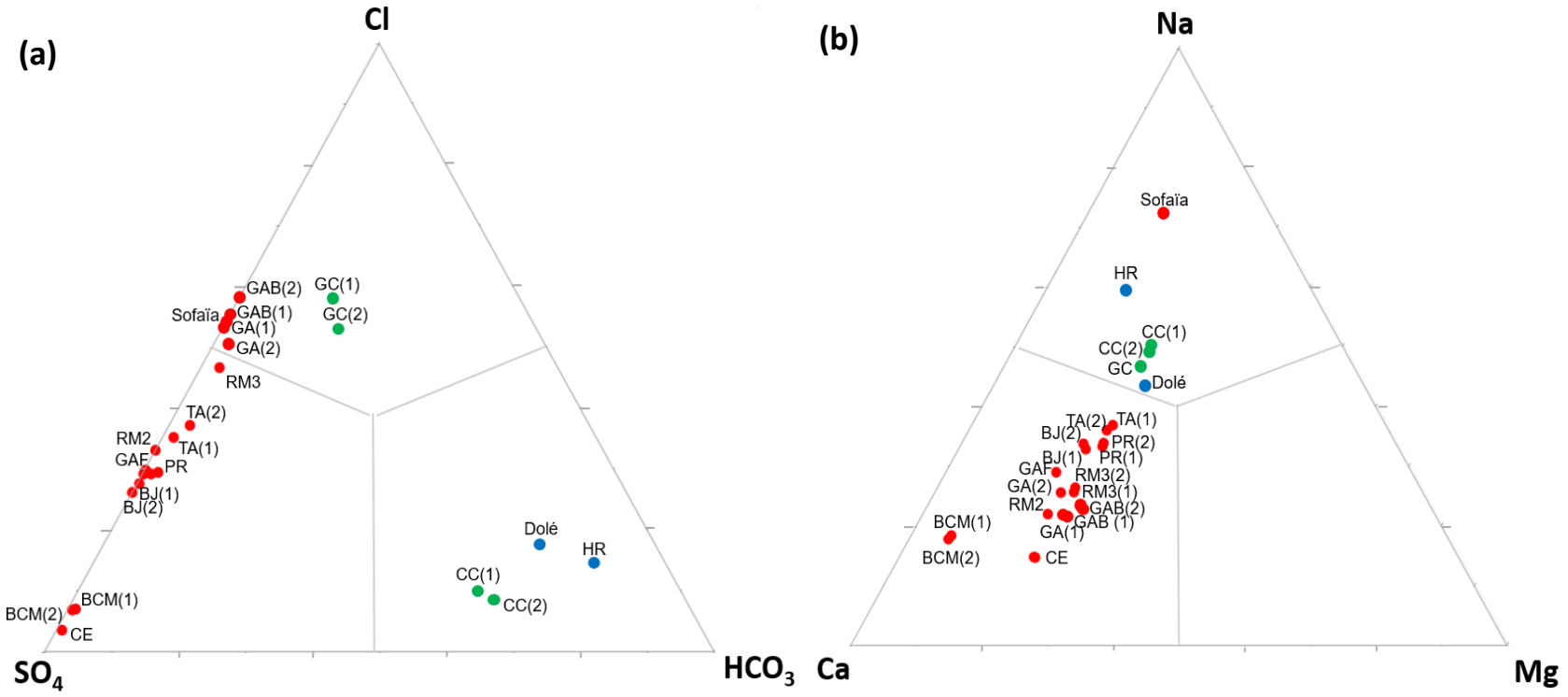

Fig. 5.2: Ternary diagrams of the major anion (a) and cation (b) composition of the thermal springs studied. The HCO_3 concentration is calculated based on the measured alkalinity and the charge balance. The samples are grouped as Ca-SO_4 (red), Ca-Na-Cl (green) and Ca-Na-HCO_3 (blue) waters.

5.5.1.2 River waters

Sulfate and Cl^- are the major anions in the river waters. The concentrations range from 95 (rPP) to 3403 (rGAav) $\mu mol.l^{-1}$ and from 132 (rRouge) to 5643 (rGC) $\mu mol.l^{-1}$, respectively. Following Gaillardet et al (2011), we assume that rivers with a Cl^-/SO_4^{2-} molar ratio < 8-10 and a SO_4^{2-} concentration > 25-50 $\mu mol.mol^{-1}$ are impacted by hydrothermal activity. The river compositions were first corrected for atmospheric salt contribution using Cl^- as a conservative element. The concentration of atmospheric Cl^- in rivers is obtained by multiplying the Cl^- concentration in rainfall (92 $\mu mol.l^{-1}$; Dessert, unpublished data) by the evapotranspiration factor (~1.5; Lloret et al, 2011). According to this calculation, the concentration of atmosphere-derived Cl^- in the rivers is 138 $\mu mol.l^{-1}$. This estimate is in good agreement with the Cl^- concentration of rRouge (140 $\mu mol.l^{-1}$; **Table 5.1**) which is believed to derive solely from atmospheric inputs (Dessert et al, 2015).

Table 5.1 indicates that thirteen (rPP, rGP, rRR, rRM, rRC, rCC, rCE, rRN, rRouge, rGC, rGAam, rGAav, rGAb) out of the 22 rivers collected on Basse-Terre display a molar Cl^-/SO_4^{2-} ratio < 8-10 and a SO_4^{2-} concentration > 25-50 $\mu mol.mol^{-1}$, likely pointing to hydrothermal inputs (**Fig. 5.3**). These rivers will be referred in the following sections as "HI" rivers. The river waters displaying a molar Cl^-/SO_4^{2-} ratio > 8-10 and/or a SO_4^{2-} < 25-50 $\mu mol.mol^{-1}$ (rNogent, rMoustique Ste-Rose, rCorossol, rBD, rQC, rCAE, rPBD, rCap, rSaint-Louis) and which presumably are not influenced by hydrothermal contributions will be called NI rivers.

The temperature (18.8-31.5 °C) and pH (4.0-7.6) values of the HI rivers compare with the values measured for the NI rivers (21.7-25.7 °C and 4.8-8.2, respectively). However, conductivity (and hence the dissolved solid load) are three to six times higher in the HI samples than in the NI samples. Among the HI river waters, rRouge, rRM and rGAam, rGAav, rGAbb display the lowest pH values (pH: 4.0-4.8), whereas rPP and rGP are slightly alkaline (pH: 7.5). The pH of rQC fluctuates (pH: 4.8-5.6) depending on the time of sampling, an observation already made in previous studies (Clergue et al, 2015; Fries et al, 2019). The alkalinity of the NI rivers ranges from 43 (rQC3) to 690 (rSt-Louis) $\mu mol.l^{-1}$. The riverine concentration of dissolved Si varies between 444 (rRC) and 1947 (rGAav) $\mu mol.l^{-1}$. Our results are in generally good agreement with the river compositions reported by other authors (Rad et al, 2007; Gaillardet

et al, 2011; Lloret et al, 2011; Rivé et al, 2013; Clergue et al, 2015; Dessert et al, 2015).

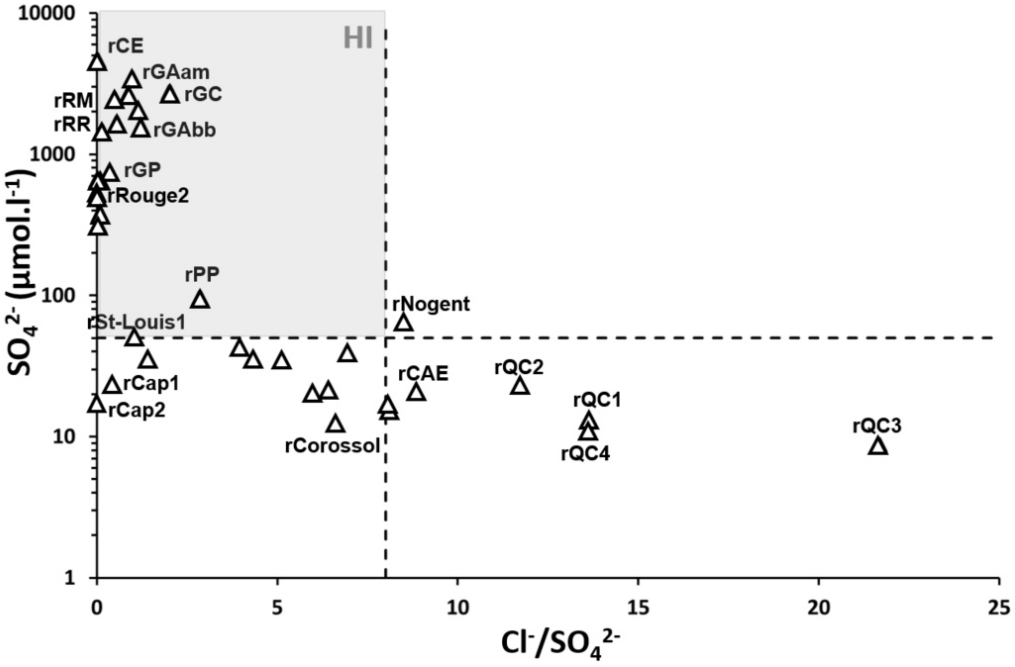

Fig. 5.3: Plot showing the SO_4^{2-} concentration ($\mu mol.l^{-1}$) as a function of the Cl^-/SO_4^{2-} molar ratio measured in the river water samples. Following Gaillardet et al (2011), the river compositions which fall in the grey-shaded area of the graph (SO_4^{2-} > 25-50 $\mu mol.l^{-1}$ and Cl^-/SO_4^{2-} < 8-10) are affected by volcanic hydrothermal inputs; these river waters are denoted by "HI". Sample codes as in **Table 5.1**.

5.5.1.3. Soil solutions

The Ferralsol soil solutions are acidic (pH: 4.9-5.5). Sulfate and Cl^- concentrations are in the ranges 13-20 and 217-278 $\mu mol.l^{-1}$, respectively. Sodium (170-241 $\mu mol.l^{-1}$) is the major cation for all soil depths. The concentration of dissolved Si varies between 63 (at a depth of 152 cm) and 116 (at a depth of 457 cm) $\mu mol.l^{-1}$. Clergue et al (2015) and Fries et al (2019) have reported similar soil solution compositions at Quiock Creek.

5.5.2 Ge/Si ratios and Si isotope compositions

The Ge/Si ratio values and Si isotope compositions of the thermal spring, river water, soil solution and hydrothermally-altered rock samples are compiled in **Table 5.2** and also plotted in **Fig. 5.4**.

Table 5.2: Concentration of Ge, Ge/Si ratio, and Si isotope compositions ($\delta^{29}Si$ and $\delta^{30}Si$) of the thermal springs, river waters, soil solutions and hydrothermally-altered rock sampled at Basse-Terre. Eleven springs and seven rivers were collected several times on different dates between 2015 and 2018. The thermal springs are sorted by type, following Brombach et al (2000)'s classification (see text). Rivers affected by hydrothermal inputs are denoted by "HI".

Label	Type	Ge	Ge/Si	SD	n	$\delta^{29}Si$	SD	$\delta^{30}Si$	SD	n
		$nmol.l^{-1}$	$\mu mol.mol^{-1}$			‰		‰		
Thermal springs										
RM2(1)	Ca-SO_4 water	1.85	1.35	-	1	0.54	0.04	1.04	0.02	2
RM2(2)	Ca-SO_4 water	1.51	1.05	-	1	0.57	0.02	1.07	0.08	1
RM3(1)	Ca-SO_4 water	3.15	1.22	-	1	-	-	-	-	-
RM3 (2)	Ca-SO_4 water	3.60	1.25	-	1	-	-	-	-	-
CE(1)	Ca-SO_4 water	2.34	1.36	-	1	-	-	-	-	-
CE(2)	Ca-SO_4 water	2.62	1.50	-	1	0.63	0.01	1.35	0.05	1
GA(1)	Ca-SO_4 water	25.55	8.86	-	1	0.49	0.02	1.00	0.02	2
GA(2)	Ca-SO_4 water	22.15	8.33	-	1	-	-	-	-	-
GAB(1)	Ca-SO_4 water	27.35	9.49	0.96	14	0.5	0.02	1.06	0.05	1
GAB(2)	Ca-SO_4 water	18.13	6.69	-	1	0.77	0.07	1.50	0.13	3
GAF	Ca-SO_4 water	0.08	0.05	-	1	-	-	-	-	-
BJ(1)	Ca-SO_4 water	0.48	0.26	-	1	-	-	-	-	-
BJ(2)	Ca-SO_4 water	0.69	0.38	-	1	-	-	-	-	-
PR(1)	Ca-SO_4 water	0.91	0.44	-	1	-	-	-	-	-
PR(2)	Ca-SO_4 water	1.25	0.60	-	1	-	-	-	-	-

TA(1)	Ca-SO_4 water	5.00	2.10	-	1	0.67	0.08	1.28	0.12	2
TA(2)	Ca-SO_4 water	5.81	2.30	-	1	-	-	-	-	-
Sofaïa	Ca-SO_4 water	0.53	0.94	-	1	0.37	0.04	0.71	0.05	1
BCM(1)	Ca-SO_4 water	11.72	21.03	-	1	0.64	0.01	1.14	0.02	1
BCM(2)	Ca-SO_4 water	10.67	18.92	-	1	-	-	-	-	-
CC(1)	Ca-Na-Cl water	1.89	1.13	-	1	0.65	0.04	1.22	0.07	2
CC(2)	Ca-Na-Cl water	1.80	1.09	-	1	0.48	0.02	0.99	0.03	1
GC(1)	Ca-Na-Cl water	0.78	0.50	-	1	-	-	-	-	-
GC(2)	Ca-Na-Cl water	0.83	0.56	-	1	0.57	0.01	1.13	0.01	1
HR	Ca-Na-HCO_3 water	14.44	11.28	-	1	-	-	-	-	-
Dolé	Ca-Na-HCO_3 water	0.55	0.39	-	1	-	-	-	-	-
River waters										
rNogent		0.08	0.15	-	1	0.44	0.04	0.83	0.03	1
rMoustique Ste-Rose		0.09	0.30	-	1	0.25	0.04	0.55	0.13	2
rPP	HI	0.10	0.19	-	1	0.53	0.03	1.17	0.06	4
rGP	HI	0.11	0.20	-	1	0.75	0.01	1.50	0.02	2
rRR	HI	0.22	0.39	-	1	0.72	0.01	1.39	0.09	1
rCorossol		0.14	0.34	-	1	0.51	0.04	0.97	0.03	1
rBD1		0.08	0.19	-	1	-	-	-	-	-
rBD2		0.11	0.28	-	1	-	-	-	-	-
rBD3		0.11	0.30	-	1	-	-	-	-	-
rBD4		0.09	0.24	-	1	0.15	0.01	0.33	0.01	1
rQC1		0.09	0.96	-	1	0.20	0.05	0.47	0.01	1
rQC2		0.11	1.56	-	1	-	-	-	-	-
rQC3		0.14	2.00	-	1	-	-	-	-	-
rQC4		0.19	2.57	-	1	0.09	0.01	0.26	0.05	2
rCAE		0.16	0.42	-	1	-	-	-	-	-
rPBD1		0.06	0.15	-	1	0.53	0.02	0.95	0.04	1
rPBD2		0.11	0.31	-	1	-	-	-	-	-
rPBD3		0.08	0.25	-	1	-	-	-	-	-
rRM	HI	1.39	0.93	0.01	2	-	-	-	-	-
rCap1		0.18	0.42	0.02	2	0.58	0.01	1.21	0.02	1
rCap2		0.14	0.65	-	1	-	-	-	-	-
rRC1	HI	0.39	0.80	-	1	0.59	0.02	1.12	0.08	3
rRC2	HI	0.28	0.62	-	1	-	-	-	-	-
rRC3	HI	0.28	0.62	-	1	-	-	-	-	-
rCC	HI	0.23	0.35	-	1	0.60	0.01	1.15	0.01	1
rCE	HI	0.28	1.48	-	1	-	-	-	-	-
rRN	HI	0.84	0.61	-	1	-	-	-	-	-
rSt-Louis1		0.15	0.28	-	1	-	-	-	-	-
rSt-Louis2		0.14	0.29	-	1	-	-	-	-	-
rRouge1	HI	0.26	0.43	-	1	0.78	0.07	1.47	0.11	3
rRouge2	HI	0.21	0.39	-	1	0.64	0.01	1.28	0.03	1
rRouge3	HI	0.22	0.40	-	1	-	-	-	-	-
rGC	HI	0.54	0.43	-	1	0.70	0.04	1.54	0.07	1
rGAam	HI	6.80	3.88	-	1	0.68	0.01	1.33	0.09	1
rGAav	HI	10.21	5.25	-	1	-	-	-	-	-
rGAbb	HI	1.19	1.06	-	1	-	-	-	-	-
Soil solutions										
GBD2-61		0.25	2.99	-	1	-0.60	0.04	-1.09	0.04	1
GBD2-91		0.25	2.59	-	1	-0.37	0.01	-0.66	0.04	1
GBD2-152		0.28	4.40	-	1	-0.40	0.01	-0.79	0.04	1
GBD2-274		0.52	7.46	-	1	-0.41	0.08	-0.69	0.01	1
GBD2-344		0.17	2.67	-	1	-0.26	0.01	-0.54	0.01	2
GBD2-457		0.22	1.90	-	1	-0.19	0.05	-0.38	0.05	1

GBD2-823	0.19	1.82	-	1	-0.29	0.01	-0.52	0.04	1
Hydrothermally altered rock									
	5524.86	0.68	-	1	-0.19	0.04	-0.35	0.02	1

- : not measured

5.5.2.1 Thermal springs

As shown in **Fig. 5.4a**, the Ge/Si ratio of the thermal springs of Basse-Terre Island spans a large range of values (0.05-21.03 µmol.mol^{-1}). The two BCM spring samples display the highest ratios. High Ge/Si ratios are also measured in Galion's thermal waters (GA, Ge/Si = 8.33 and 8.66 µmol.mol^{-1} and GAB, Ge/Si = 9.49 and 6.49 µmol.mol^{-1}). All the other springs have much lower Ge/Si ratios, i.e., ≤ 2.30 µmol.mol^{-1}. The δ^{30}Si values of the thermal springs range from 0.71 ± 0.05 ‰ (Sofaïa) to 1.50 ± 0.13 ‰ (GAB in 2017) (**Fig. 5.4b**). The RM2 spring collected in October 2017 and February 2015 display similar Si isotope compositions (1.07 ± 0.08 ‰ and 1.04 ± 0.02 ‰, respectively). In contrast, GAB has a lighter Si isotope value in January 2015 (1.06 ± 0.05 ‰) compared to November 2017 (1.50 ± 0.13 ‰).

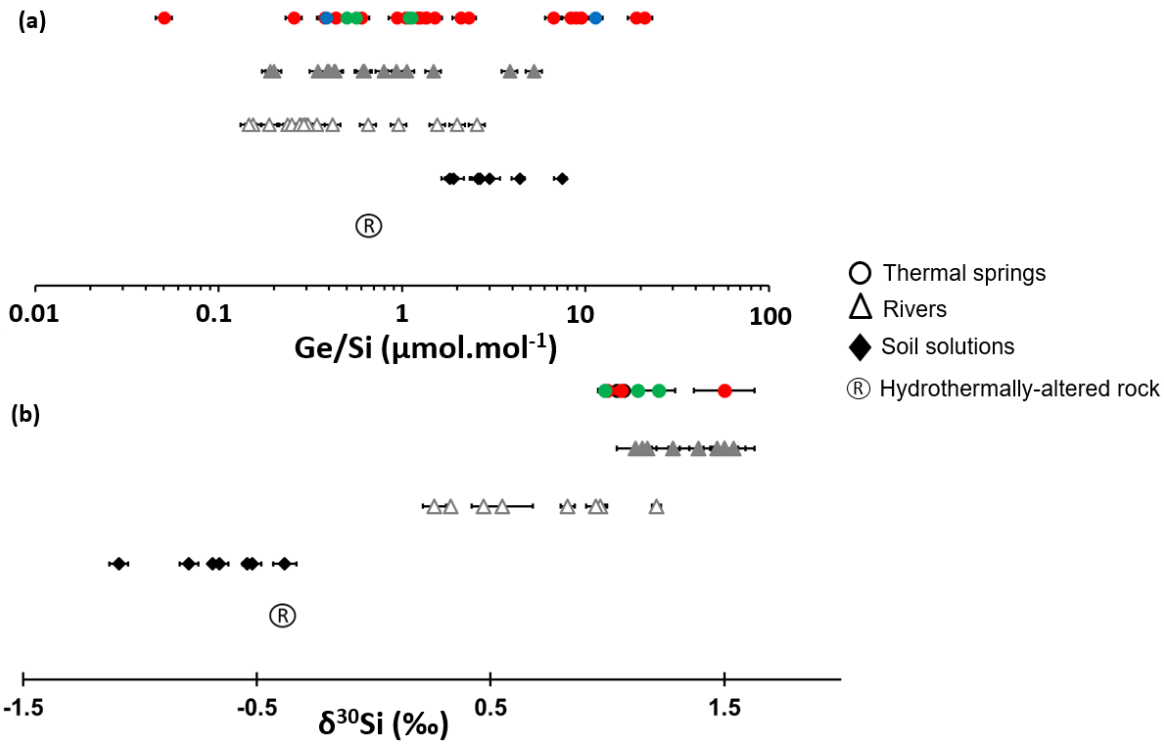

Fig. 5.4: Plots showing the Ge/Si ratio (± SD) (a) and Si isotope composition (δ^{30}Si ± SD) (b) of the thermal spring (circle), river water (triangle), soil solution (diamond) and hydrothermally-altered rock (®) samples. The Ca-SO_4, Ca-Na-Cl and Ca-Na-HCO_3 thermal springs are shown with red, green and blue-filled symbols, respectively. The hydrothermally-impacted rivers (plain grey triangle) are distinguished from the non-impacted rivers (open grey triangle) following Gaillardet et al (2011) (see **Fig. 5.3**).

5.5.2.2 River waters

Thirty out of the 36 riverine samples analyzed display Ge/Si values ~ ≤ 1.1 µmol.mol^{-1} (**Fig. 5.4a**). Higher Ge/Si ratios are measured in rQC (2017 sample; 1.56-2.57 µmol.mol^{-1}), rCE (1.48 µmol.mol^{-1}), rGAam (3.88 µmol.mol^{-1}), rGAav (5.25 µmol.mol^{-1}) and rGAbb (1.06 µmol.mol^{-1}). Except rQC, these rivers receive hydrothermal inputs (**Fig. 5.3**). The

Ge/Si ratio of rPP, rGP and rRR, which drain the extinct hydrothermal system of Les Mamelles, varies in the range 0.19-0.39 μmol.mol^{-1}. The Ge/Si ratio of rRouge, which drains the extinct hydrothermal system of Carmichaël, shows little fluctuations (0.39-0.43 μmol.mol^{-1}) between January 2015, October 2016 and January 2017. In contrast, rQC collected in February 2015 has a lower Ge/Si ratio (0.96 μmol.mol^{-1}) than the samples collected in October and November 2017.

The δ^{30}Si values of the HI river waters tend to be heavier (1.12-1.54 ‰) than those measured for the NI river waters (0.26-1.21 ‰; **Fig. 5.4b**). The lowest δ^{30}Si values correspond to the NI rivers rQC (0.26 ± 0.05 ‰) and rBD (0.33 ± 0.01 ‰). Except these two samples, the Si isotope compositions of the rivers do not differ markedly from those of the thermal springs.

5.5.2.3 Soil solutions

The Ge/Si ratio of the soil solutions varies between 1.82 and 7.46 μmol.mol^{-1}, but no trend with depth in the soil profile can be inferred (**Fig. 5.4a**; **Table 5.2**). The highest value (7.46 μmol.mol^{-1}) corresponds to a soil depth of 274 cm. The Si isotope composition of the soil solutions varies between -0.38 ± 0.05 ‰ (at a depth of 427 cm) and -1.09 ± 0.04 ‰ (at a depth of 61 cm) (**Fig. 5.4b**).

5.5.2.4 Hydrothermally-altered rock

The bulk Ge/Si ratio and δ^{30}Si values of the hydrothermally-altered rock are 0.68 μmol.mol^{-1} and -0.35 ± 0.02 ‰, respectively (**Fig. 5.4a and b**).

5.6 Discussion

5.6.1 Ge/Si ratio and Si isotope composition of the thermal springs

The Ge/Si ratio in the thermal spring waters do not reflect their compositional type. For example, the Ge/Si ratio values of the Ca-SO_4 waters and Ca-Na-HCO_3 waters overlap (0.05-21.03 and 0.39-11.28 $\mu mol.mol^{-1}$, respectively). The Ge/Si ratios in the Ca-Na-Cl springs also compare with those found for several Ca-SO_4 springs (**Table 5.2**).

We note that the two Ca-SO_4 springs (GA and GAB) sampled in 2015 and 2017 exhibit consistently high Ge/Si ratio values (6.69-9.49 $\mu mol.mol^{-1}$). Many factors can influence the Si and Ge contents of thermal discharges. The composition of the primary rock reacting with the hydrothermal fluid is one of them, but other processes control the Ge/Si ratio in solution. In an experimental study, Pokrovski and Schott (1998) determined the thermodynamic properties of aqueous Ge(IV) hydroxide complexes from 25 to 350 °C and predicted a strong dependence of the Ge/Si ratio on temperature in aqueous solutions in equilibrium with Ge-bearing silicates. Evans and Derry (2002) investigated Himalayan hot springs and concluded that the wide range of Ge/Si ratios resulted from the progressive precipitation of Ge-poor quartz. These authors also highlighted that mixing of hydrothermal fluids with surface waters influence the Ge/Si ratio in the thermal discharges. Arnórsson (1987) indicates that the Ge/Si ratio in silica sinters from Iceland and New Zealand is always lower than in the thermal waters from which the deposits originate, pointing again to the non-conservative behavior of Ge during silica precipitation. In contrast, the formation of sulfide minerals, such as pyrite, in the hydrothermal system incorporates Ge, producing lower Ge/Si ratios in the liquid phase (Bernstein, 1985). The rate of dissolution and the abundance of hydrothermal alteration minerals that can take up Ge to a variable extent will also govern the relative proportions of Ge and Si in thermal springs. Finally, in shallow hydrothermal systems associated with active volcanoes, high-temperature magmatic gases may contribute Ge and Si to the thermal waters sampled at the surface (de Hoog et al, 2005; Rouxel and Luais, 2017). The broad range of Ge/Si ratio values measured in the thermal springs from Basse-Terre likely results from various and complex interactions, some being more significant than others, perhaps depending on the extent of water-rock interaction prior to resurgence at the surface. A full understanding of the thermal spring's

geochemistry requires additional data, including stable isotope measurements, and is out of the scope of this study.

The thermal springs' Si isotope compositions (0.7-1.5 ‰, **Fig. 5.4b**) compare well with the range of values reported for thermal springs worldwide, i.e., -0.6-1.7 ‰ (Douthitt, 1982; Opfergelt et al, 2011; Geilert et al, 2015; Ding et al, 2017; Chen et al, 2020). Similar to the Ge/Si ratio, the δ^{30}Si values do not discriminate different spring types (**Fig. 5.4b**). Geilert et al (2015) report the δ^{30}Si of dissolved Si and silica sinter from the Geysir geothermal area, Iceland, and show that the deposit becomes progressively isotopically lighter downstream from the resurgence. While the isotope fractionation correlates inversely with temperature, the authors highlight that the dominant control is the rate at which silica precipitates from the flowing spring waters. A similar observation was made at Yellowstone National Park, USA (Chen et al, 2020). These results corroborate previous experimental observations (Geilert et al, 2014). Akin weathering reactions in soils (Opfergelt and Delmelle, 2012; Frings et al, 2016), the formation of clay minerals (e.g., kaolinite and smectite) during water-rock interaction in the subsurface hydrothermal system may also fractionate Si isotopes by depleting the source solution in ^{28}Si. The light Si isotope composition of the clayey hydrothermally-altered rock (δ^{30}Si = -0.35 ‰) supports this idea. Thus, both silica deposition and alteration reactions in different parts of the hydrothermal system(s), extinct and active, are likely responsible for the variations in the Si isotope composition of the thermal springs across Basse-Terre Island.

5.6.2 Ge/Si ratio and Si isotope compositions of rivers

The Ge/Si ratio in the river samples (0.15-5.25 μmol.mol^{-1}) do not differ significantly from the values measured for the thermal waters, although a few springs (GA, GAB, HR and BCM) are characterized by much higher values (**Fig. 5.3**). The riverine Ge/Si ratios are within the range of values reported for other river systems in the world (0.16-20 μmol.mol^{-1}; e.g., Derry et al, 2005; Han et al, 2015; Baronas et al, 2018). They are also in good agreement with the few analyses reported for rivers draining volcanic terrains elsewhere (0.18-3.16 μmol.mol^{-1}; Derry et al, 2005; Baronas et al, 2018; Ameijeiras-Mariño et al, 2018).

Using chemical and Mg isotope compositions, Dessert et al (2015) showed that the river chemistry on Basse-Terre Island is the result of mixing in

various proportions of rainwater, water that has reacted with andesitic rocks, water draining through highly-weathered soils, water leaching extinct hydrothermal areas and thermal water associated with La Soufrière volcano. The authors also emphasize that the contributions of these end-members vary from north to south and from east to west, reflecting the influence of bedrock age and rainfall gradient.

The wet atmospheric contribution to the Ge and Si concentrations in Basse-Terre's river is not known. According to Heartsill-Scalley et al (2007), the Si concentration in rainwater collected in Puerto Rico, also a subtropical island, is less than 1.1 $mg.l^{-1}$ and does not vary seasonally. The Ge concentration in rainwater can be assumed to be negligible according to the low Ge concentrations reported in rainwater from Tallahassee, USA (Ge=1.7-7.3 $ng.l^{-1}$; Hambrick et al, 1984). As mentioned above, our river water samples were collected upstream of croplands and we dismiss an indirect influence of Si-accumulating plants on the riverine Ge/Si ratios.

Since the Ge/Si ratio values of the HI rivers (0.19-5.25 $\mu mol.mol^{-1}$) largely overlap with those of the NI rivers (0.15-2.57 $\mu mol.mol^{-1}$) (**Fig. 5.4a**), the Ge/Si ratio cannot be used to trace a potential hydrothermal contribution. The majority of the HI rivers display a heavier Si isotope composition than that measured for the NI rivers. However, the $\delta^{30}Si$ of the former also tend to be higher than the values obtained for the thermal springs (**Fig. 5.4b**), already suggesting an additional control on the isotope composition of the riverine Si. In the next sections, we discuss the Ge/Si ratio and Si isotope compositions of the NI and HI rivers taken separately.

5.6.2.1 NI rivers

Although the Ge/Si ratios of the NI rivers in the north and in the south of the island overlap, the southern river waters exhibit lower values (0.28-0.65 µmol.mol^{-1}) compared to those typical of the magmatic rock that is being weathered (Ge/Si: 1-3 µmol.mol^{-1} for igneous rocks; Bernstein, 1985; DeArgollo and Schilling, 1978). This is consistent with the preferential incorporation of Ge into the solid phase during chemical weathering and associated clay mineral formation and adsorption processes on aluminum oxides (Kurtz et al, 2002; Derry et al, 2005; Scribner et al, 2006). As a result, with the advance of weathering, the Ge/Si ratio in the soil solution can evolve towards higher values when the Ge-rich clay minerals (e.g., kaolinite, biotite) and aluminum oxide phases become unstable and redissolve progressively, thereby producing a broad range of compositions (Derry et al, 2005). This probably explains the comparatively more variable Ge/Si ratio found for the NI rivers in North Basse-Terre (0.15-2.57 µmol.mol^{-1}; **Fig. 5.5a**) as these drain highly weathered terranes dominated by the presence of Vertisols and Ferralsols (**Fig. 5.1**).

By the same token, the formation of clay minerals during chemical weathering typically depletes the soil solution in ^{28}Si, leaving behind heavier dissolved Si (Ziegler et al, 2005; Opfergelt and Delmelle, 2012). In agreement with this view, rCap (1.21 ± 0.02 ‰), which drain Andosols in South Basse-Terre, display higher δ^{30}Si values than rNogent (0.83 ± 0.03 ‰) and rMoustique Ste-Rose (0.55 ± 0.13 ‰,), which both flow through older terrains in North Basse-Terre. According to Dessert et al (2015), the Ca/Mg ratio in Basse-Terre's rivers decreases with increasing chemical weathering, i.e., along a south to north age gradient. **Figure 5.5** shows that, except rQC, the NI rivers exhibit a large range in Ca/Mg with higher Ca/Mg values mainly found in the southern rivers draining less-weathered soils (associated with higher Ge/Si ratios and δ^{30}Si compositions) than Ca/Mg values found in the northern rivers draining more weathered soil (associated with lower Ge/Si ratios and δ^{30}Si compositions).

In contrast to the NI rivers characterized by Ge/Si ratio values < 1 µmol.mol^{-1}, the rQC samples display Ge/Si ratio close to or > 1 µmol.mol^{-1} (**Table 5.2**). The Quiock creek catchment is underlain by Pleistocene andesitic pyroclasts covered by >15 m of a deeply weathered and cation-depleted regolith (Buss et al, 2010). Clergue et al (2015) consider that the Li isotope composition of Quiock Creek's drainage waters represents an endmember of such weathering conditions. The regolith contains ~95

wt.% of secondary minerals, of which ~70% are almost entirely made of halloysite and kaolinite, the rest being comprised of iron and aluminum (oxy)hydroxides (Buss et al, 2010). Accordingly, the soil solution of the Ferralsol from Quiock creek is acidic (pH: 4.2-5.5). It also exhibits a high Ge/Si ratio, i.e., 1.82-7.46 μmol.mol^{-1} (**Table 5.2**). Kurtz et al (2002) found that strongly desilicated (weathered) volcanic soils in Hawaii exhibit high Ge/Si ratios, ranging from 6 to 20 μmol.mol^{-1}. The Ge enrichment of the Hawaiian soils results from preferential fractionation of Ge into the solid phase as clay minerals precipitate out of the soil solution (Kurtz et al, 2002). Moreover, adsorption on aluminum oxides favors Ge over Si (Scribner et al, 2006). Derry et al (2005) explain the high Ge/Si ratios (2-14 μmol.mol^{-1}) measured in the soil solutions from the same strongly weathered volcanic soils in Hawaii by the dissolution of Ge-enriched secondary minerals. Thus, the high Ge/Si ratios measured in our Ferralsol soil solutions likely reflect the dissolution of Ge-rich clay minerals and aluminum oxides. We attribute the Ge/Si ratio > 1 μmol.mol^{-1} of rQC as a result of the dissolution under acidic conditions of Ge-rich secondary minerals that accumulated in the Ferralsols due to intense weathering.

The δ^{30}Si compositions of the rQC samples, which represent the most depleted values measured in any of the rivers (**Fig. 5.5b**, **Table 5.2**), support the idea that clay mineral dissolution exerts a major control on the riverine Ge/Si ratio. Since weathering of primary minerals enriches the neo-formed clay minerals in ^{28}Si (Ziegler et al, 2005; Opfergelt and Delmelle, 2012), soils that are strongly weathered, and for which the primary mineral reservoir is exhausted, tend to display low δ^{30}Si values (Bern et al, 2010; Opfergelt et al, 2010, 2012a; Baronas et al, 2020). With the advance of weathering under increasingly acidic conditions, the clay minerals are no longer stable and their dissolution releases isotopically light Si in solution.

We further propose that a similar dissolution process influences the Si isotope composition of some of the rivers draining the old lithologies of northern Basse-Terre. A good candidate is rMoustique Ste-Rose, which displays a light δ^{30}Si (0.55 ‰). The low riverine δ^{30}Si value lend credence to Dessert et al (2015)'s hypothesis that the δ^{26}Mg isotope composition measured for this river (-0.09 ‰, i.e., heavier than andesitic rocks, whereas other rivers are generally lighter) reflects a chemical weathering situation where dissolution of ^{26}Mg-rich secondary minerals contributes significantly to the Mg release. However, despite the agreement between the riverine Si and Mg isotopic signatures, we advocate caution in using δ^{26}Mg alone as a proxy for weathering degree since Mg release from

secondary minerals in highly weathered soils may be controlled largely by ion exchange reactions rather than by dissolution of Mg-containing secondary minerals (Teng et al, 2010; Huang et al, 2012; Opfergelt et al, 2012b, 2014; Trostle et al, 2014).

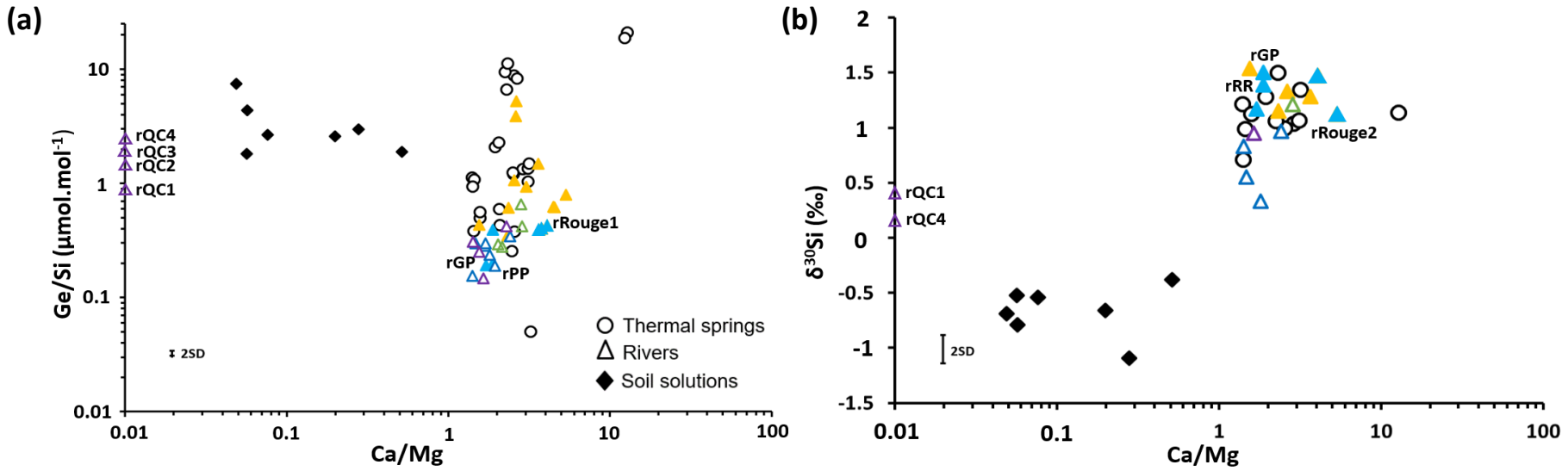

Fig. 5.5: Plots showing the Ge/Si ratio (log scale) (a) and the Si isotope composition ($\delta^{30}Si$) (b) as a function of the Ca/Mg molar ratio (log scale) in the thermal spring (circle), river water (triangle) and soil solution (diamond) samples. The HI rivers that receive discharges from thermal springs (plain orange triangle) are distinguished from those receiving drainages from an extinct hydrothermal system (plain blue triangle). The NI rivers are displayed according to their locations in Basse-Terre Island: north (open blue triangle), center (open purple triangle), and south (open green triangle). The 2SD error bar reported correspond to ±10% for Ge/Si, and to the largest 2SD value measured on a sample for $\delta^{30}Si$ (**Table 5.2**). The river codes are explained in **Table 5.1**.

5.6.2.2 HI rivers

Some of the HI rivers (rGAam, rGAav, rGAbb and rCE) display high Ge/Si ratios > 1 μmol.mol^{-1}. In contrast, rPP, rGP, rRR, rRM, rRC, rCC, rRN, rRouge and rGC show ratios < 1 μmol.mol^{-1} (the lowest values correspond to rPP and rGP) (**Table 5.2**), on par with the values measured for the NI rivers (except rQC). Most of the HI rivers are located in southern Basse-Terre and flow through relatively young lithologies (except rPP, rGP and rRR). Some HI rivers are characterized by Ge/Si values (rCC, rRouge, rGC: 0.35 to 0.43 μmol.mol^{-1}) in the same range than the value measured for rRR in Central Basse-Terre (0.39 μmol.mol^{-1}). Therefore, unlike the NI rivers, the disparity in the Ge/Si ratio values is unlikely to be imparted by different soil weathering degrees. We surmise that the SO_4-rich hydrothermal inputs to the HI rivers have a distinct Ge/Si composition. This is suggested based on a plot of Ge/Si vs. Cl^-/SO_4^{2-} (**Fig. 5.6a**). The highest Ge/Si ratio values in the HI river samples (rGAam, rGAav, rGAbb and rCE) probably reflect the admixing of Ca-SO_4 thermal waters with high Ge/Si ratios. For example, River Galion drains terrains where the thermal discharges are characterized by Ge/Si values > 6 μmol.mol^{-1} (i.e., GA and GAB thermal springs: 6.69-9.49 μmol.mol^{-1}, **Table 5.2**), low pH and elevated SO_4^{2-} concentrations (**Table 5.1**). Similarly, River Carbet probably collects Ca-SO_4 waters with relatively elevated Ge/Si ratios; the CE thermal spring (Ge/Si ratio: 1.36-1.50 μmol.mol^{-1}, **Table 5.2**) being a potential candidate representative of such inputs. Lower Ge/Si values in the HI rivers rRM, rRC, rCC, rRN and rGC likely reflect contributions from thermal waters that are less enriched in Ge compared to hydrothermal discharges affecting River Galion and River Carbet. For example, rCC and rGC receive discharges from Ca-Na-Cl thermal springs, which exhibit relatively low Ge/Si ratios (CC and GC: 0.50-1.13 μmol.mol^{-1}, **Table 5.2**).

We argue that the lowest Ge/Si ratios in rPP, rGP, rRR and rRouge (0.19, 0.20, 0.39, 0.40 μmol.mol^{-1}, respectively, **Table 5.2**) reflect the Ge and Si concentrations acquired by the rivers' tributaries as they drain through extinct hydrothermal systems, i.e., Les Mamelles for rPP, rGP, rRR, and Carmichaël for rRouge (**Fig. 5.1**). The hydrothermally-altered rock collected from the area of Les Mamelles is comprised of pyrophyllite, dickite and pyrite (FeS_2), with minor smectite and residual feldspar (**Suppl. Mat. 5.1**). This mineral assemblage is typically encountered when acid-sulfate fluids interact with volcanic rocks in the subsurface hydrothermal system (Reed, 1997). According to Gaillardet et al (2011), the source of

the high SO_4^{2-} concentration measured in rGP is the oxidative dissolution of pyrite present in the extinct hydrothermal system. Our clay-rich, hydrothermally-altered rock specimen has a low Ge/Si value (0.68 $\mu mol.mol^{-1}$), which contrasts with the Ge-enrichment usually noticed in secondary clay minerals formed during the meteoric weathering of rocks (Kurtz et al, 2002). The reason for this apparently low accumulation of Ge in the hydrothermal material is not known. Since pyrite tends to incorporate Ge during precipitation from a hydrothermal solution (Bernstein, 1985), its subsequent oxidative dissolution at shallow levels may lead to a progressive loss of Ge in the altered rock, whereas Si would not be modified. Thus, extinct hydrothermal systems such as Les Mamelles release low-pH and SO_4-rich drainages that probably exhibit a low Ge/Si ratio inherited from the clayey, hydrothermally-altered rocks found in these areas.

Our riverine $\delta^{30}Si$ measurements suggest that all the NI rivers (0.26-0.97‰) except one are isotopically lighter than the HI rivers (1.12-1.54‰), the NI river rCap1 (1.21‰) being the exception (**Table 5.2**). The Si isotope compositions of the HI rivers partly reflect contributions from thermal spring waters with relatively high $\delta^{30}Si$ values (**Fig. 5.6b**). However, the high $\delta^{30}Si$ of rCap1 indicates that ^{30}Si-enriched riverine compositions are not necessarily linked to hydrothermalism. As discussed earlier, the isotope composition of dissolved Si in NI rivers is strongly dictated by soil weathering degree; rivers (such as rCap1) which drain younger soils typically display heavier values than rivers flowing through older terrains. Since the HI rivers which receive thermal spring discharges exhibit similar $\delta^{30}Si$ values as those collecting drainages from extinct hydrothermal systems (**Fig. 5.6b**), Si isotopes cannot be used to differentiate between the two types of hydrothermal contributions.

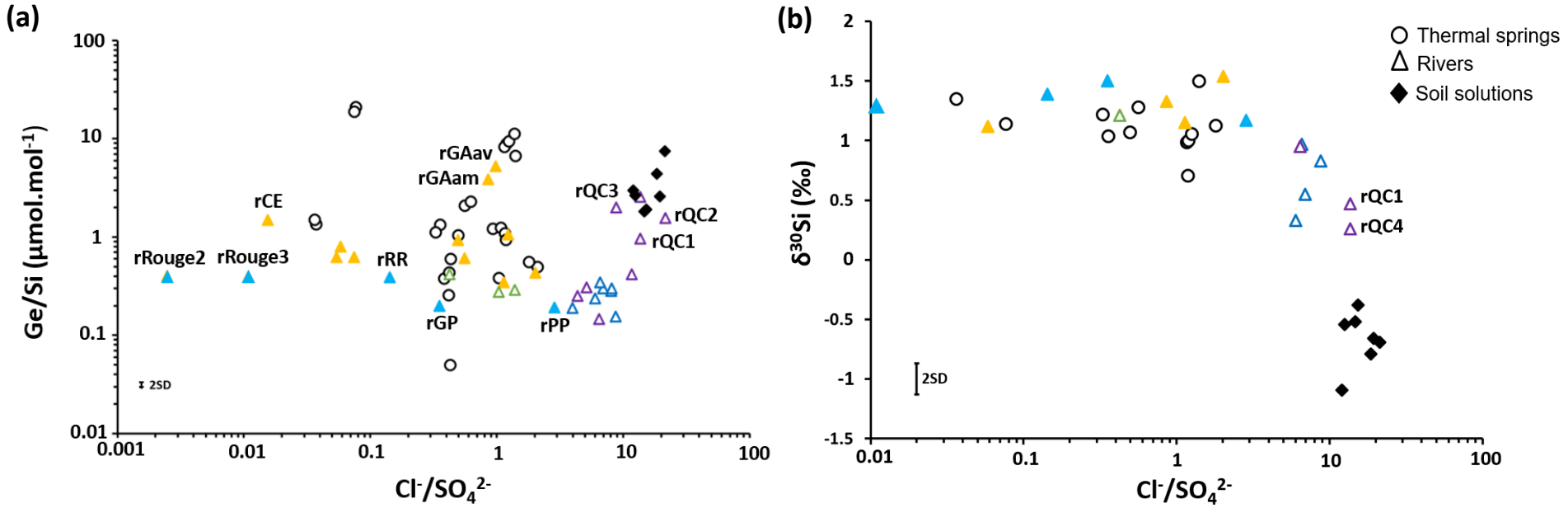

Fig. 5.6: Plots showing the Ge/Si ratio (a) and the Si isotope composition ($\delta^{30}Si$) (b) as a function of the Cl^-/SO_4^{2-} molar ratio in the thermal spring (circle), river water (triangle) and soil solution (diamond) samples. The HI rivers that receive discharges from thermal springs (plain orange triangle) are distinguished from those receiving drainages from an extinct hydrothermal system (plain blue triangle). The NI rivers are displayed according to their locations in Basse-Terre Island: north (open blue triangle), center (open purple triangle), and south (open green triangle). The 2SD error bar reported correspond to ± 10% for Ge/Si, and to the largest 2SD value measured on a sample for $\delta^{30}Si$ (**Table 5.2**). The river codes are explained in **Table 5.1**.

5.7 Conclusions

We carried out an extensive sampling campaign of volcanic thermal springs and river waters in Basse-Terre Island with the objective to gain insight into the influence of hydrothermalism on the riverine Ge/Si ratio and Si isotope compositions, and to assess if the Ge/Si ratio and $\delta^{30}Si$ can act as good indicators of weathering in volcanic terranes featuring both extinct and active hydrothermal manifestations.

The following principal conclusions can be drawn using our data:

(i) The thermal springs display a broad range of Ge/Si ratio and $\delta^{30}Si$ values with no apparent relationship to their compositional types. The Ge/Si ratio and Si isotope composition of the thermal springs are probably the result of various processes, including wall-rock alteration and precipitation reactions occurring along the hydrothermal flow paths and at different temperatures.

(ii) The Ge/Si ratio and $\delta^{30}Si$ measured for the NI rivers record different degrees of soil weathering. The rivers which drain the south (younger lithologies) of Basse-Terre display a narrow range of Ge/Si ratios and heavier $\delta^{30}Si$ than the river waters sampled in the north (older lithologies). When the watershed drains highly weathered terrains where the soil mineral reserve has been almost or completely exhausted, redissolution of Ge- and ^{28}Si-rich clay minerals and Ge-bearing aluminum oxides under acidic conditions enriches the soil solution in Ge and ^{28}Si, thereby increasing and lowering the riverine Ge/Si ratio and $\delta^{30}Si$ values, respectively.

(iii) The Ge/Si ratio imparted to rivers due to weathering is largely concealed when thermal spring discharges mix with river waters. Although the Si isotope composition of such rivers is also affected, the isotopically light signature inherited from highly weathered terranes may still persist.

(iv) Watersheds draining areas where hydrothermal activity took place in the past collect SO_4-rich tributaries that appear to be depleted in Ge relative to Si. We tentatively attribute this characteristic to the redissolution of clay-rich, hydrothermally-altered rocks, which also display low Ge/Si ratio values. The use of the Cl^-/SO_4^{2-} ratio and SO_4^{2-} concentration cannot discriminate rivers impacted by such hydrothermal contributions from those receiving thermal spring discharges. We propose

that the determination of the Ge and Si concentrations can circumvent this difficulty.

Overall, our results provide new evidence that Ge/Si ratio and Si isotopes determinations in river waters are powerful tracers of weathering sources. However, in volcanic terranes, they are poor indicators of hydrothermal contributions, except perhaps when these are represented by acid SO_4-rich thermal spring discharges, which seem to exhibit high Ge/Si ratios. When used in combination with Cl^- and SO_4^{2-} measurements, the Ge/Si ratio separates rivers impacted by active hydrothermalism from those affected by tributaries draining through clayey rocks formed in the past during hydrothermal circulation.

5.8 References

Abraham, K., Opfergelt, S., Fripiat, F., Cavagna, A-J., de Jong, J., Foley, S.F., André, L., Cardinal, D., 2008. δ^{30}Si and δ^{29}Si determinations on USGS BHVO-1 and BHVO-2 reference materials with a new configuration on a Nu Plasma Multi-Collector ICP-MS. Geostand. Geoanal. Res. 32(2), 193-202.

Ameijeiras-Mariño, Y., Opfergelt, S., Derry, L.A., Robinet, J., Govers, G., Minella, J.P., Delmelle, P., 2018. Ge/Si ratios point to increased contribution from deeper mineral weathering to streams after forest conversion to cropland. Appl. Geochem. 96, 24–34.

Arnòrsson, S., 1987. Germanium in Icelandic geothermal systems. Geochim. Cosmochim. Ac. 48, 2489-2502.

Barat, A., 1986. Etude du rôle des eaux souterraines dans le mécanisme des éruptions phréatiques. Application à la Montagne Pelée de Martinique et à la Soufrière de Guadeloupe. BRGM, 115.

Baronas, J.J, West, A.J., Burton, K.W., Hammond, D.E., Opfergelt, S., Pogge von Strandmann, P.A.E., James, R.H., Rouxel, O.J., 2020. Ge and Si isotopes behaviour during intense tropical weathering. Global Biogeochem. Cy. doi:10.1029/2019gb006522.

Baronas, J.J., Torres, M.A., West, A.J., Rouxel, O., Georg, B., Bouchez, J., Gaillardet, J., Hammond, D.E., 2018. Earth Planet. Sci. 503, 194-215.

Bern, C., Brzezinski, M., Beucher, C., Ziegler, K., Chadwick, O., 2010. Weathering, dust, and biocycling effects on soil silicon isotope ratios. Geochim. Cosmochim. Acta 74, 876–889.

Berner, R.A., Lasaga, A.C., Garrels, R.M., 1983. The carbonate–silicate geochemical cycle and its effect on atmospheric carbon-dioxide over the past 100 million years. Am. J. Sci. 283, 641-683.

Bernstein, L.R., 1985. Germanium geochemistry and mineralogy. Geochim. Cosmochim. Ac. 49, 2409–2422.

Bigot, S., Hammouya, G., 1982. Chemistry of the Soufrière of Guadeloupe hot springs. S.E.A.N. Bull. 7, 2.

Blazina, T., Sharma, M., 2013. Chemical weathering on the North Island of New Zealand: CO_2 consumption and fluxes of Sr and Os. Geochem. Geophys. Geosyst. 14, 3600-3615.

Boudon, G., Komorowski, J.-C., Villemant, B., Semet, M. P., 2008. A new scenario for the last magmatic eruption of La Soufrière de Guadeloupe (Lesser Antilles) in 1530 A.D.: evidence from stratigraphy, radiocarbon dating and magmatic evolution of erupted products. J. Volcanol. Geotherm. Res. 178, 474–490.

Brombach, T., Marini, L., Hunziker, J.C., 2000. Geochemistry of the thermal springs and fumaroles of Basse-Terre Island, Guadeloupe, Lesser Antilles. B. Volcanol. 61(7), 477-490.

Buss, H., White, A., Dessert, C., Gaillardet, J., Blum, A., Sak, P., 2010. Depth profiles in a tropical volcanic critical zone observatory: Basse-Terre, Guadeloupe. In: Torres-Alvarado, I.S., Birkkle, P. (Eds.), Proceedings of the 13th International Conference on Water–Rock Interaction. Taylor & Francis Group, London, UK.

Cabidoche, Y.-M., Achard, R., Cattan, P., Clermont-Dauphin, C., Massat, F., Sansoulet, J., 2009. Long-term pollution by chlordecone of tropical volcanic soils in the French West Indies: a simple leaching model accounts for current residue. Environ. Pollut. 157, 1697–1705.

Cardinal, D., Alleman, L.Y., De Jong, J., Ziegler, K., André, L., 2003. Isotopic composition of silicon measured by multicollector plasma source mass spectrometry in dry plasma mode. J. Anal. Atom. Spectrom. 18, 213-218.

Chaperon, P., L'Hote, Y., Vuillaume, G., 1985. Les ressources en eau de surface de la Guadeloupe. Editions de l'ORSTOM, Collection Monographies Hydrologiques 7, France.

Chen, X-Y., Chafetz, H.S., Lapen, T.J., 2020. Silicon isotope variations in hydrothermal systems at Yellowstone National Park, Wyoming, USA. Geochim. Cosmochim. Ac. 283, 184-200.

Clergue, C., Dellinger, M., Buss, H.L., Gaillardet, J., Benedetti, M.F., Dessert, C., 2015. Influence of atmospherics deposits and secondary minerals on Li isotopes budget in a highly weathered catchment, Guadeloupe (Lesser Antilles). Chem. Geol. 414, 28-41.

Colmet-Daage, F., 1969. Cartes des sols des Antilles: Guadeloupe volcanique et Martinique au 1/20 000, ORSTOM Antilles.

Colmet-Daage, F., Lagache, P., 1965. Caractéristiques de quelques groupes de sols dérivés de roches volcaniques aux Antilles françaises. Cah. L'ORSTOM Ser. Pédologie 8, 91–121.

de Hoog, J.C.M, van Bergen, M.J., Jacobs, M.H.G., 2005. Vapour-phase crystallisation of silica from SiF4-bearing volcanic gases. Annals of Geophysics. 48, 4/5.

DeArgollo, R., Schilling, J.G., 1978. Ge-Si and Ga-Al fractionation in Hawaiian volcanic rocks. Geochim. Cosmochim. Acta 42, 623–630.

Delvigne, C., Angeletti, B., Guihou, A., Basile-Doelsch, I., Meunier, J.D., 2018. Reliable determination of Ge in solid environmental samples using a chemical preparation procedure developed for Si isotopes and ICP-MS Analysis. Geostand. Geoanal. Res. 42, 139-149.

Derry, L.A., Kurtz, A.C., Ziegler, K., Chadwick, O.A., 2005. Biological control of terrestrial silica cycling and export fluxes to watersheds. Lett. Nature 433, 728–731.

Dessert, C., Dupré, B., Gaillardet, J., François, L. M., Allègre, C.J., 2003. Basalt weathering laws and the impact of basalt weathering on the global carbon cycle. Chem. Geol. 202, 257-273.

Dessert, C., Gaillardet, J., Dupré, B., Schott, J., Pokrovsky, O.S., 2009. Fluxes of high- versus low-temperature water-rock interactions in

aerial volcanic areas: Example from the Kamchatka Peninsula, Russia. Geochim. Cosmochim. Ac. 73, 148–169.

Dessert, C., Lajeunesse, E., Lloret, E., Clergue, C., Crispi, O., Gorge, C., Quidelleur, X., 2015. Controls on chemical weathering on a mountainous volcanic tropical island: Guadeloupe (French West Indies). Geochim. Cosmochim. Ac. 171, 216–237.

Ding, T.P., Jiang, S., Li, Y., Gao, J., Hu, B., 2017. Geochemistry of silicon isotopes. De Gruyter.

Dixon, J.L., Heimsath, A.M., Amundson, R., 2009. The critical role of climate and saprolite weathering in landscape evolution. Earth. Surf. Proc. Land. 34, 1507-1521.

Douthitt, C.B., 1982. The geochemistry of the stable isotopes of silicon. Geochim. Cosmochim. Acta 46, 1449–1458.

Escoube, R., Rouxel, O.J., Edwards, K., Glazer, B., Donard, O.F.X., 2015. Coupled Ge/Si and Ge isotope ratios as geochemical tracers of seafloor hydrothermal systems: Case studies at Loihi Seamount and East Pacific Rise 9°50'N. Geochim. Cosmochim. Ac. 167, 93-112.

Evans, M.J., Derry, L.A., 2002. Quartz control of high germanium/silicon ratios in geothermal waters. Geology 30, 1019–1022.

Favier, A., Lardeaux, J-M., Legendre, L., Verati, C., Philippon, M., Corsini, M., Münch, P., Ventalon, S., 2019. Tectono-metamorphic evolution of shallow crustal levels within active volcanic arcs. Insights from the exhumed Basal Complex of Basse-Terre (Guadeloupe, French West Indies). Earth Sciences Bulletin 190, 10.

François, L.M., Walker, J.C.G., 1992. Modelling the Phanerozoic carbon cycle and climate: constraints from the $^{87}Sr/^{86}Sr$ isotopic ratio of seawater. Am. J. Sci. 292, 81-135.

Fries, D.M., James, R.H., Dessert, C., Bouchez, J., Beaumais, A., Pearce, C.R., 2019. The response of Li and Mg isotopes to rain events in a highly-weathered catchment. Chem. Geol. 519, 68–82.

Frings, P.J., Clymans, W., Fontorbe, G., De La Rocha, C.L., Conley, D.J., 2016. The continental Si cycle and its impact on the ocean Si isotope budget. Chem. Geol. 425, 12-36.

Gaillardet, J., Dupré, B., Louvat, P., Allègre, C. J., 1999. Global silicate weathering and CO_2 consumption rates deduced from the chemistry of the large rivers. Chem. Geol. 159, 3-30.

Gaillardet, J., Rad, S., Rivé, K., Louvat, P., Gorge, C., Allègre C-J., Lajeunesse E., 2011. Orography-driven chemical denudation in the Lesser Antilles: evidence for a new feed-back mechanism stabilizing atmospheric CO_2. Am. J. Sci. 311, 851 894.

Gaspard, F., Opfergelt, S., Dessert, C., Robert, V., Ameijeras-Marino, Y., Delmelle, P. Imprint of chemical weathering and hydrothermalism on the Ge/Si ratio and Si isotopic composition

of rivers in a volcanic tropical island, Basse-Terre, Guadeloupe (French West Indies). Submitted to Chem. Geol.

Geilert, S., Vroon, P.Z., Keller, N., Gudbrandsson, S., Stefànsson, A., Van Bergen, M.J., 2014. Silicon isotope fractionation during silica precipitation from hot springs waters, Geophys. Res. Abstract EGU 2014: EGU2014-7951.

Geilert, S., Vroon, P.Z., Keller, N., Gudbrandsson, S., Stefànsson, A., Van Bergen, M.J., 2015. Silicon isotope fractionation during silica precipitation from hot-springs waters: evidence from the Geysir geothermal field, Iceland. Geoch. Cosmochim. Acta 164, 403-427.

Georg, R.B., Reynolds, B.C., Frank, M., Halliday, A.N., 2006. New sample preparation techniques for the determination of Si isotopic compositions using MC-ICP-MS. Chem. Geol. 235, 95–104.

Goldsmith, S.T., Carey, A.E., Johnson, B.M., Welch, S.A., Lyons, W.B., McDowell, W.H., Pigott, J.S., 2010. Stream geochemistry, chemical weathering and CO_2 consumption potential of andesitic terrains, Dominica, Lesser Antilles. Geochim. Cosmochim. Ac. 74, 85-103.

Goldsmith, S.T., Carey, A.E., Lyons, W.B., Hicks, D.M., 2008. Geochemical fluxes and weathering of volcanic terrains on high standing islands: Taranaki and Manawatu-Wanganui regions of New Zealand. Geochim. Cosmochim. Ac. 72, 2248-2267.

Hambrick, G.A., Froelich, P.N., Meinrat, O.A., Lewis, B.L., 1984. Determination of methylgermanium species in natural waters by graphite furnace atomic absorption spectrometry with hydride generation. Anal. Chem. 56, 421-424.

Han, Y., Huh, Y., Derry, L., 2015. Ge/Si ratios indicating hydrothermal and sulphide weathering input to rivers of the Eastern Tibetan Plateau and Mt. Baekdu. Chem. Geol. 410, 40-52.

Heartsill-Scalley, T., Scatena, F.N., Estrada, C., McDowell, W.H., Lugo, A.E., 2007. Disturbance and long-term patterns of rainfall and throughfall nutrient fluxes in a subtropical wet forest in Puerto Rico. J. Hydrol. 333, 472-485.

Huang, K.J., Teng, F.Z., Wei, G.J., Ma, J.L., Bao, Z.Y., 2012. Adsorption- and desorption-controlled magnesium isotope fractionation during extreme weathering of basalt in Hainan Island, China. Earth. Planet. Sci. Lett. 359-360, 73-83.

Hurwitz, S., Evans, W.C., Lowenstern, J.B., 2010. River solute fluxes reflecting active hydrothermal chemical weathering of the Yellowstone Plateau Volcanic Field, USA. Chem. Geol. 276, 331-343.

Jones, M.T., Hembury, D.J., Palmer, M.R., Tonge, B., Darling, W.G., Loughlin, S.C., 2011. The weathering and element fluxes from active volcanoes to the oceans: a Montserrat case study. Bull. Volc. 73, 207-222.

Komorowski, J.-C., Boudon, G., Semet, M., Beauducel, F., Antenor-Habazac, C., Bazin, S., Hammouya, G., 2005. Guadeloupe. In Volcanic Atlas of the Lesser Antilles; Lindsay, J.M., Robertson, R.E.A., Shepherd, J.B., Ali, S., Eds.; Seismic Research Unit, The University of the West Indies: Kingston, Jamaica, 65-102.

Kurtz, A.C., Derry, L.A., Chadwick, O.A., 2002. Germanium-silicon fractionation in the weathering environment. Geochim. Cosmochim. Ac. 66, 1525–1537.

Lerman, A., Meybeck, M., 1988. Physical and Chemical Weathering in Geochemical Cycles. Nato Science Series C. 251, Springer, 394.

Lloret, E., Dessert, C., Gaillardet, J., Albéric, P., Crispi, O., Chaduteau, C., Benedetti, M., 2011. Comparison of dissolved inorganic and organic carbon yields and fluxes in the watersheds of tropical volcanic islands, examples from Guadeloupe (French West Indies). Chem. Geol. 280, 65–78.

Louvat, P., Allègre, C.J., 1997. Present day denudation rates of the island of Reunion determined by river geochemistry: basalt weathering and mass budgets between chemical and mechanical erosions. Geochim. Cosmochim. Ac. 61, 3645–3669.

Louvat, P., Gaillardet, J., Paris, G., Dessert, C., 2011. Boron isotope ratios of surface waters in Guadeloupe, Lesser Antilles. Appl. Geochem. 26, S76–S79.

Louvat, P., Gislason, S.R., Allègre, C.J., 2008. Chemical and mechanical erosion rates in Iceland as deduced from river dissolved and solid material. Am. J. Sci. 308, 679-726.

Météo-France, 2019. Bulletin Climatique, Guadeloupe.

Nicollin, F., Gibert, D., Beauducel, F., Boudon, G., Komoroswski, J-C., 2006. Electrical tomography of La Soufrière of Guadeloupe volcano: Field experiments, 1D inversion and qualitative interpretation. Earth. Planet. Sc. Lett. 244, 709-724.

Opfergelt, S., Burton, K.W., Georg, R.B., West, A.J., Guicharnaud, R.A., Sigfusson, B., Siebert, C., Gislason, S.R., Halliday, A.N., 2014. Magnesium retention on the soil exchange complex controlling Mg isotope variations in soils, soil solutions and vegetation in volcanic soils, Iceland. Geochim. Cosmochim. Ac. 125, 110-130.

Opfergelt, S., Burton, K.W., Pogge von Strandmann, P.A.E., Gislason, S.R., Halliday, A.N., 2013. Riverine silicon isotope variations in glaciated basaltic terrains: implications for the Si delivery to the ocean over glacial-interglacial intervals. Earth. Planet. Sc. Lett. 369-370, 211-219.

Opfergelt, S., Cardinal, D., André, L., Delvigne, C., Bremont, L., Delvaux, B., 2010. Variations of δ^{30}Si and Ge/Si with weathering and biogenic input in tropical basaltic ash soils under monoculture. Geochim. Cosmochim. Ac. 74, 225-240.

Opfergelt, S., Delmelle, P., 2012. Silicon isotopes and continental weathering processes: Assessing controls on Si transfer to the ocean. Comptes Rendus Geosci. 344, 723–738.

Opfergelt, S., Eiriksdottir, E.S., Burton, K.W., Einarsson, A., Siebert, C., Gislason, S.R., Halliday, A.N., 2011. Quantifying the impact of freshwater diatom productivity on silicon isotopes and silicon fluxes: Lake Myvatn, Iceland. Earth Planet. Sc. Lett. 305, 73-82.

Opfergelt, S., Georg, R.B., Delvaux, B., Cabidoche, Y.M., Burton, K.W., Halliday, A.N., 2012a. Silicon isotopes and the tracing of desilication in volcanic soil weathering sequences, Guadeloupe. Chem. Geol. 326-327, 113-122.

Opfergelt, S., Georg, R.B., Delvaux, B., Cabidoche, Y.M., Burton, K.W., Halliday, A.N., 2012b. Mechanisms of magnesium isotope fractionation in volcanic soil weathering sequences, Guadeloupe. Earth. Planet. Sc. Lett. 311-344, 176-185.

Pokrovski, G.S., Schott, J., 1998. Experimental study of the complexation of silicon and germanium with aqueous organic species: implications for germanium and silicon transport and Ge/Si ratios in natural waters. Geochim. Cosmochim. Ac. 62, 3413-3428.

Rad, S., Allègre, C.J., Louvat, P., 2007. Hidden erosion on volcanic islands. Earth. Planet. Sc. Lett. 262, 109-124.

Rad, S., Rivé, K., Allègre, C.J., 2011. Weathering regime associated with subsurface circulation on volcanic islands. Aquat. Geochem. 17, 221-241.

Reed, M.H., 1997. Hydrothermal alteration and its relationship to ore fluid composition. Geochemistry of Hydrothermal Ore Deposits. 3rd ed. John Wiley and Sons.

Reynolds, B.C., Aggarwal, J., André, L., Baxter, D., Beucher, C., Brzezinski, M.A., Engström, E., Georg, B., Land, M., Leng, M.J., Opfergelt, S., Rodushkin, I., Sloane, H.J., Van den Boorn, S.H.J.M., Vroon, P.Z., Cardinal, D., 2007. An inter-laboratory comparison of Si isotope reference materials. J. Anal. Atom. Spectrom. 22, 561-568.

Ricci, J., Quidelleur, X., Pallares, C., Lahitte, P., 2017. High-resolution K-Ar dating of a complex magmatic system: The example of Basse-Terre Island (French West Indies). J. Volcanol. Geotherm. Res. 345,142-160.

Rivé, K., Gaillardet, J., Agrinier, P., Rad, S., 2013. Carbon isotopes in the rivers from the Lesser Antilles: origin of the carbonic acid consumed by weathering reactions in the Lesser Antilles. Earth Surf. Proc. Land. 38, 1020–1035.

Rouxel, O.J., Luais, B., 2017. Germanium isotope Geochemistry. Reviews in Mineralogy & Geochemistry. 82, 601-656.

Ruzié, L., Auband, C., Moreira, M., Agrinier, P., Dessert, C., Gréau, C., Cripsi, O., 2013. Carbon and helium isotopes in thermal springs of

La Soufrière volcano (Guadeloupe, Lesser Antilles): Implications for volcanological monitoring. Chem. Geol. 359, 70-80.

Salaün, A., Villemant, B., Gérard, M., Komorowski, J-C., Agnès, M., 2011. Hydrothermal alteration in andesitic volcanoes: Trace element redistribution in active and ancient hydrothermal systems of Guadeloupe (Lesser Antilles). Fuel and Energy Abstracts 111, 59-83.

Samper, A., Quidelleur, X., Komorowski, J.C., Lahitte, P., Boudon, G. 2009. Effusive history of the Grande Découverte Volcanic Complex, southern Basse-Terre (Guadeloupe, French West Indies) from new K–Ar Cassignol-Gillot ages. J. Volcanol. Geotherm. Res. 187, 117–130.

Samper, A., Quidelleur, X., Lahitte, P., Mollex, D., 2007. Timing of effusive volcanism and collapse events within an oceanic arc island: Basse-Terre, Guadeloupe archipelago (Lesser Antilles Arc). Earth. Planet. Sc. Lett. 258, 175-191.

Schopka, H. H., Derry, L. A., Arcilla, C. A., 2011. Chemical weathering, river geochemistry and atmospheric carbon fluxes from volcanic and ultramafic regions on Luzon Island, the Philippines. Geochim. Cosmochim. Ac. 75, 978–1002.

Scribner, A.M., Kurtz, A.C., Chadwick, O.A., 2006. Germanium sequestration by soil: targeting the roles of secondary clays and Fe-oxyhydroxides, Earth and Plan. Sc. 243, 760-770.

Sieber, C., Ross, A., McManus, J., 2006. Germanium isotope measurements of high-temperature geothermal fluids using double-spike hydride generation MC-ICP-MS. Geochim. Cosmochim. Acta 70, 3986-3995.

Teng, F.Z., Li, W.Y., Rudnick, R.L., Gardner, L.R., 2010. Contrasting lithium and magnesium isotope fractionation during continental weathering. Earth. Planet. Sci. Lett. 300, 63-71.

Trostle, K., Derry, L., Vigier, N., Chadwick, O., 2014. Magnesium isotope fractionation during arid pedogenesis on the Island of Hawaii (USA). Procedia Earth Planet. Sci. 10, 243-248.

United Kingdom Accreditation Body (UKAS)., 2014. Certificate of measurement, river water-anion, certified reference material LGC6025. 4005.

Verati, C,. Patrier-Mas, P,. Lardeaux, J-M,. Bouchot, V., 2014. Timing of geothermal activity in an active island-arc volcanic setting: First 40Ar/39Ar dating from Bouillante geothermal field (Guadeloupe, French West Indies). Geological Society, London, Special Publications 378, 285–295.

Verati, C., Lardeaux, J-M., Favier, A., Corsini, M., Philippon, M., Legendre, L., 2018. Arc-related metamorphism in the Guadeloupe archipelago (Lesser Antilles active island arc): First report and consequences. Lithos 320-321: 592–598.

Villemant, B., Hammouya, G., Michel, A., Semet, M.P., Komorowski, J-C., Boudon, G., Cheminée, J-L., 2005. The memory of volcanic waters : Shallow magma degassing revealed by halogen monitoring in thermal springs of La Soufrière volcano (Guadeloupe, Lesser Antilles). Earth. Planet. Sc. Lett. 237, 710-728.

Villemant, B., Komorowski, J-C., Dessert, C., Michel, A., Crispi, O., Hammouya, G., Beauducel, F., De Chabalier J-B., 2014. Evidence for a new shallow magma intrusion at La Soufrière of Guadeloupe (Lesser Antilles), Insights from long-term geochemical monitoring of halogen-rich hydrothermal fluids. J. Volcanol. Geotherm. Res. 285, 247–277.

Vörösmarty, C.J., Fekete, B.M., Meybeck, M., Lammers, R.B., 2000. Global system of rivers: Its role in organizing continental land mass and defining land-to-ocean linkages. Global Biocheochem. Cy. 14, 599-621.

Westercamp, D., 1988. Magma generation in the Lesser Antilles: geological constraints. Tectonophysics 149, 145–163.

White, A.F., Brantley, S.L., 1995. Chemical weathering rates of silicate minerals: an overview. In Chemical Weathering Rates of Silicate Minerals, ed. AF White, SL Brantley. Rev. Miner. 31, 1-22.

Yeghicheyan, D., Bossy, C., Bouhnik Le Coz, M., Douchet, C., Granier, G., Heimburger, A., Lacan, F., Lanzanova, A., Rousseau, T.C.C., Seidel, J-L., Tharaud, M., Candaudap, F., Chmeleff, J., Cloquet, C., Delpoux, S., Labatut, M., Losno, R., Pradoux, C., Sivry, Y., Sonke, J.E., 2013. A Compilation of Silicon, Rare Earth Element and Twenty-One other Trace Element Concentrations in the Natural River Water Reference Material SLRS-5 (NRC-CNRC). Geostand. Geoanal. Res. 37(4), 449-467.

Young, E.D., Galy, A., Nagahara, H., 2002. Kinetic and equilibrium mass-dependent isotope fractionation laws in nature and their geochemical and cosmochemical significance. Geochim. Cosmochim. Ac. 66, 1095-1104.

Ziegler, K., Chadwick, O.A., Brzezinski, M.A., Kelly, E.F., 2005. Natural variations of $d^{30}Si$ ratios during progressive basalt weathering, Hawaiian Islands. Geochim. Cosmochim. Acta 69, 4597–4610.

Zlotnicki, J., Vargemezis, G., Mille, A., Bruère, F., Hammouya, G., 2006. State of the hydrothermal activity of Soufrière of Guadeloupe volcano inferred by VLF surveys. J. Appl. Geophys. 58, 265-249.

5.9 Supplementary Materials

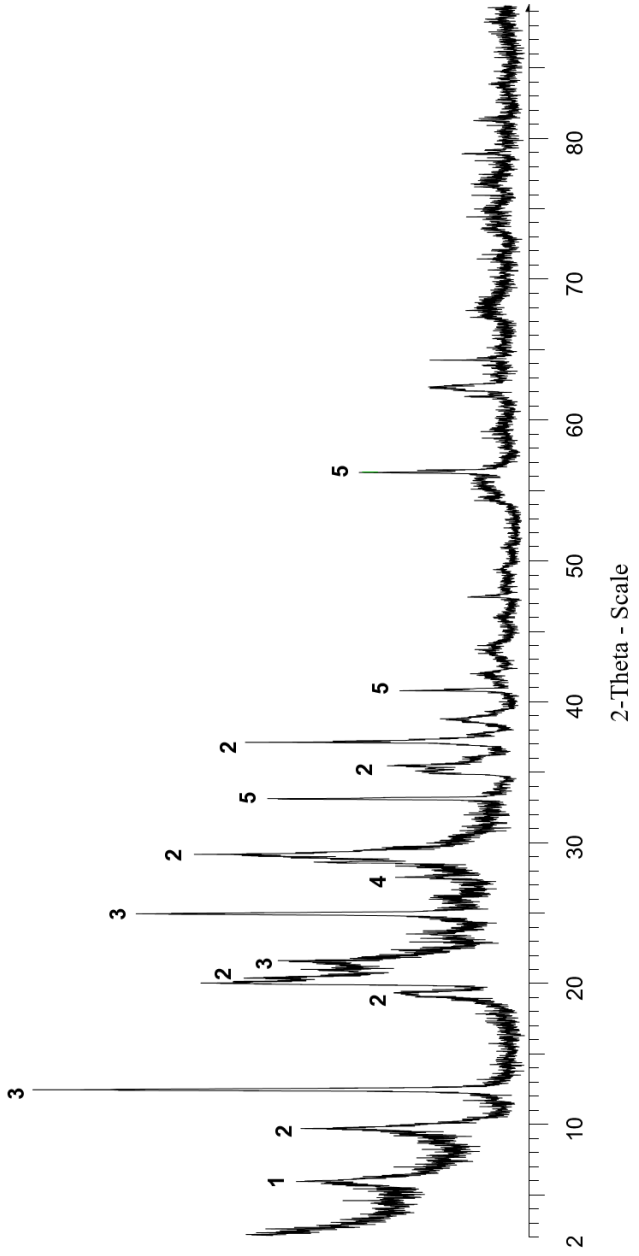

Suppl. Mat 5.1: Diffractogram of the hydrothermally-altered rock located on the flanks of Grande Plaine river water obtained by X-ray diffraction (XRD). The hydrothermally-altered rock sample is composed of (1) smectite, (2) pyrophyllite, (3) dickite, (4) feldspar and (5) pyrite.

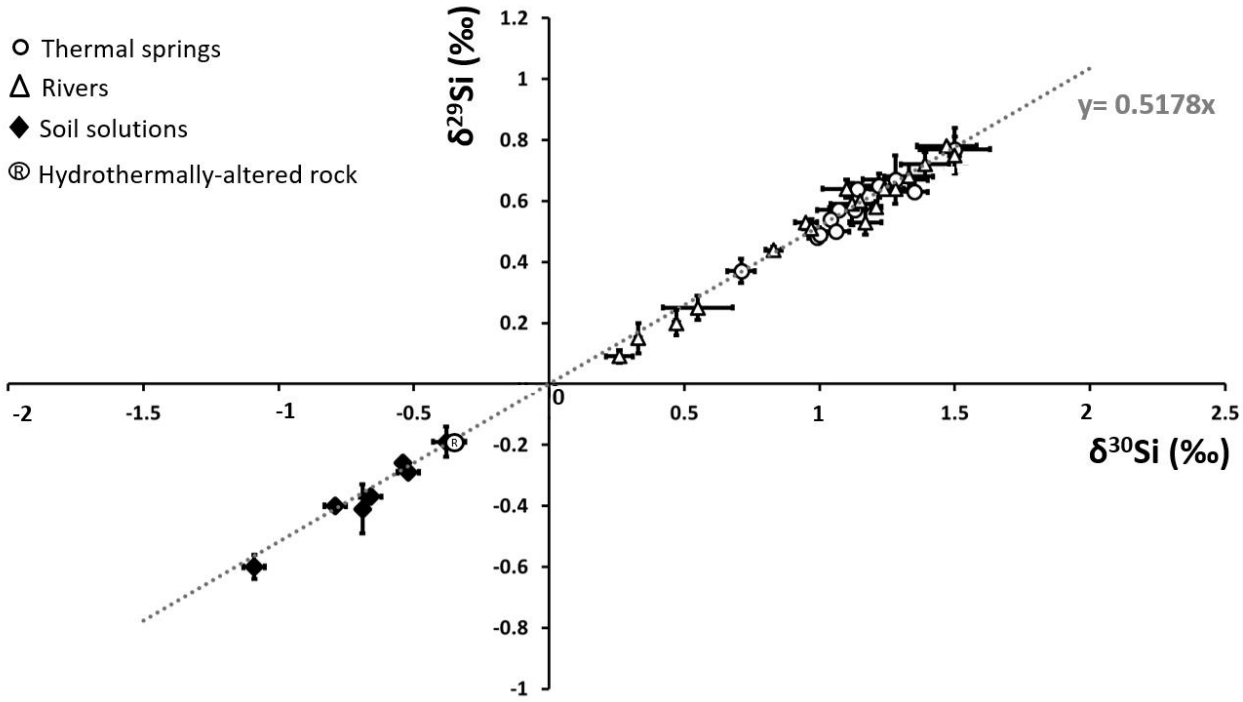

Suppl. Mat. 5.2: Plot showing that the $\delta^{29}Si$ and $\delta^{30}Si$ compositions (± SD) of the thermal spring, river water, soil solution and hydrothermally-altered rock samples fall within error of the mass dependent fractionation array. The slope of the regression line (0.5178) supports an interference-free determination of all three Si isotopes via MC-ICP-MS (Young et al, 2002).

Chapter 4:

Enhanced chemical weathering during snowmelt: inferences from Ge/Si and $\delta^{30}Si$ in rivers draining the Yellowstone Plateau Volcanic Field, USA

6.1 Abstract

Hydrothermally-active volcanic regions are characterized by the highest silicate weathering rates on Earth. The source of acidity for weathering reactions in these areas includes protons derived from magmatic activity in addition to the protons derived from the dissolution of atmospheric CO_2 in surface water generally driving meteoric weathering processes. However, the seasonal variability on the processes controlling weathering fluxes in these regions remain poorly constrained, preveting from accurate estimates of the atmospheric CO_2 consumption in these key weathering loci. Here we use the germanium to silicon ratio (Ge/Si ratio) and the stable silicon isotopes ($\delta^{30}Si$) as geochemical tracers to assess the sources and processes controlling seasonal dissolved Si weathering fluxes in rivers from the Yellowstone Plateau Volcanic Field, USA.

We determined the Ge/Si ratios and $\delta^{30}Si$ of 7 thermal springs and 14 rivers samples collected in September (at base flow) and June (Spring, at high discharge, during snowmelt). Elevated riverine Ge/Si ratios (29 ± 3 $\mu mol.mol^{-1}$) at base flow can be explained by a dominant contribution from thermal springs (160 ± 27 $\mu mol.mol^{-1}$). At snowmelt, decreasing riverine Ge/Si ratios and increasing dilution-corrected dissolved riverine Si concentrations ($Si/Na_{snowmelt} > Si/Na_{base\ flow}$) suggest an additional process controlling Si contribution to rivers in Spring. Higher surface

runoff at snowmelt may release surface water influenced by (i) dissolution of primary minerals from rhyolite (reflected by riverine $\delta^{30}Si_{snowmelt} < \delta^{30}Si_{base\ flow}$) in large drainage basins, or by (ii) dissolution of primary minerals and clay mineral formation (reflected by riverine $\delta^{30}Si_{snowmelt} > \delta^{30}Si_{base\ flow}$) in smaller basins. Using a Ge/Si mass balance calculation, and boundary conditions fixed using Si isotopes, we calculate that rivers with a large increase in discharge at snowmelt receive between 57 and 84% of Si contribution from surface waters influenced by rhyolite weathering, and to some extent by the dissolution of cryogenic opal, whereas rivers with little or no change in discharge receive between 29 and 63% of Si contribution from surface waters influenced not only by primary minerals weathering but also by clay mineral formation. Our results demonstrate that seasonal variability in runoff during snowmelt adds pulses of Si derived from meteoric weathering processes to riverine Si fluxes generally dominated by hydrothermal contribution. This seasonal meteoric weathering signal, previously unaccounted for in hydrothermally-active volcanic regions, directly contributes to atmospheric CO_2 consumption.

6.2 Introduction

Hydrothermally-active volcanic regions contribute significantly to the global flux of solutes to the ocean and consumption of atmospheric CO_2 through silicate weathering (Louvat and Allègre, 1997; Gaillardet et al, 1999; Dupré et al, 2003; Gislason and Oelkers, 2011). Silicate weathering fluxes are usually assessed by summing the total dissolved elements and silica concentrations in rivers. However, a portion of the element fluxes in these hydrothermally-active volcanic areas also derives from weathering reactions driven by protons from magmatic activity as a source of acidity, i.e., not consuming atmospheric CO_2 (Dessert et al, 2009; Hurwitz et al, 2010; Schopka et al, 2011; Gaillardet et al, 2011; Rivé et al, 2013).

Seasonal changes in riverine chemistry in volcanic regions are reported with changes in runoff (Gaillardet et al, 2011), e.g., during flood events (Lloret et al, 2011), or at snowmelt (Hurwitz et al, 2010). Runoff is paramount to weathering processes as it modifies water residence time in soils (White and Blum, 1995). The water residence time in soils dictates the proportion of water available for mineral dissolution/formation: lower water residence time favors primary minerals dissolution by leaching the elements released in solution whereas higher water residence time favors clay minerals formation (White and Blum, 1995). Runoff influences also the discharge of dissolved weathering fluxes to rivers. Changing runoff might therefore change the contribution from meteoric weathering processes to riverine weathering fluxes relative to the contribution from hydrothermally-driven weathering fluxes. However, uncertainties remain regarding the seasonal respective contributions of these major controls on riverine weathering fluxes, and this prevents accurate estimates of the atmospheric CO_2 consumption by silicate weathering from these hydrothermally-active volcanic areas. Better constraining these uncertainties requires to unravel the relative contributions of meteoric and hydrothermal sources and processes to the overall response of riverine weathering fluxes to changing runoff.

The germanium to silicon ratios (Ge/Si ratios) and the stable silicon (Si) isotopes ($\delta^{30}Si$) are particularly well-suited geochemical tracers to assess the advance of meteoric weathering processes (Cornelis et al, 2011; Opfergelt and Delmelle, 2012 and references therein). The Ge/Si ratio and $\delta^{30}Si$ can be combined to investigate overlapping influence of weathering and hydrothermal processes onto rivers draining volcanic terrains (Gaspard et al, submitted). Seasonally, the riverine Ge/Si ratio may reflect changes in weathering contribution with runoff during flood events (Ameijeiras-Mariño et al, 2018), and seasonal changes in riverine $\delta^{30}Si$ have been attributed to changing contribution from mineral weathering and biological Si uptake (e.g., Engström et al, 2010). Here, the aim is to combine the Si isotopes and the Ge/Si ratio to investigate potential seasonal changes in hydrothermal and weathering contributions to riverine element fluxes in hydrothermally-active volcanic areas, where the influence of biological uptake on Si fluxes is expected to be limited relative to the contribution from chemical weathering and hydrothermal processes.

The Yellowstone Plateau Volcanic Field (YPVF) is particularly a well-suited hydrothermally-active volcanic region to investigate changing controls on riverine chemistry with runoff given that base flow is dominated by hydrothermal discharge (Hurwitz et al, 2010; Hurwitz and Lowenstern, 2014) and that a well-defined seasonal increase in runoff at snowmelt is reported to be associated with seasonal change in riverine chemistry (Hurwitz et al, 2007). In this study, temporal variations in the Ge/Si ratio and in the Si isotopic composition of rivers of YPVF are investigated to better understand the influence of runoff variability on the controlling processes of riverine element fluxes in YPVF.

6.3 Environmental setting

The continental hotspot of the YPVF hosts Earth's largest "restless" caldera (Newhall and Dzurisin, 1988; Christiansen, 2001; Lowenstern et al, 2006), covering about 6500 km^2 at an average elevation of 2400 asl. Volcanism at Yellowstone likely started together with the Columbia River flood basalts, producing basaltic flows during the Tertiary (Liu and Stegman, 2012), and rhyolitic emissions during the Quaternary (Trettin and Bartelli, 1980; Smith and Siegel, 2000). The YPVF (44°N, 110°W) hydrothermal system has a single "parent" fluid at an estimated depth between 2 and 5 km. The fluid is rich in dissolved CO_2 and H_2S with Cl^- ~ 400 $mg.l^{-1}$ and low HCO_3^- and SO_4^{2-} concentrations with temperatures of 340 to 370 °C (Fournier, 1989).

YPVF is comprised of 9 geyser basins (among which from North to South: Norris Geyser Basin (NGB), Lower Geyser Basin (LGB), Midway Geyser Basin, Upper Geyser Basin (UGB), Shoshone Geyser Basin (SGB), and Heart Lake Geyser Basin (HLGB); **Fig. 6.1**), thermal areas (such as Mammoth Hot Springs (MHS), and Mud Volcano area (MV)), some 280 named rivers and more than 150 named lakes whose largest is the Yellowstone Lake (350 km^2). Following the classification of Giggenbach (1988), three thermal water types are found in the YPVF. Thermal springs are neutral Cl-waters in MGB, i.e., with neutral to slightly alkaline pH values and with relatively high concentrations of Cl^-, Si and siliceous sinter deposition (Hurwitz et al, 2007). Alkaline HCO_3-waters are found at MHS, i.e., rich in HCO_3^-, SO_4^{2-}, Cl^- and precipitating travertine as a result from subsurface flow through a sedimentary sequence (Pierce et al, 1991). Presence of acid SO_4-waters are reported in MV. Sublacustrine hydrothermal activity in Yellowstone Lake has been inferred for >100 year with alkaline HCO_3-waters and neutral Cl-waters water types (Hayden, 1878; Fowler et al, 2019a, 2019b).

The YPVF is covered in forest (~80 %, Kokaly et al, 2003) rooted in well-drained soils. Soils in the western side of Yellowstone Lake are mainly derived from rhyolite while soils in the southwest part of YPVF are developed on basalt (Rodman et al, 1996). The YPVF climate is temperate

with cold winters and low annual temperatures characterized by snow from October (average temperatures: -6 to 11 °C) to April (average temperatures: -6 to 8 °C), followed by snowmelt in May which induces a well-defined seasonal increase in runoff. The vast majority of YPVF precipitation is locked-in as snow during winter months (~70% of the annual precipitation as snowfall; Despain, 1987), with an annual average of 180 cm water equivalent, occurring mainly between October and April with maxima in January, and annual snowmelt occurring reliably between May and June. Precipitation is distributed evenly over the year (annual range: 33 to 58 mm), apart from during July which is the driest month with precipitation values of ~2 mm (National Park Service, 2020).

The YPVF is drained by four main rivers (Madison, Yellowstone, Snake and Falls Rivers; **Fig. 6.1**) that have a well-constrained hydrological budget (Hurwitz et al, 2007), with base flow conditions from late September-October to April followed by rapid increase in river discharge during snowmelt. Rivers in YPVF have distinct river discharges resulting from different water inputs (**Fig. 6.1**). The Yellowstone river has the largest drainage area including contribution from Yellowstone Lake, Gardner River, and springs from MV (Hurwitz et al, 2007; McCleskey et al, 2019). The Madison river integrates the discharge of Firehole river draining the LGB, MGB and UGB, and the Gibbon river receives contribution from the NGB (McCleskey et al, 2010a, 2010b). The Falls river drains the southwest of YPVF, and the Snake river drains the South of the YPVF receiving thermal inputs from HLGB and SGB but also from travertine depositing spring in the Upper Snake River (Hurwitz et al, 2007; Hurwitz et al, 2020).

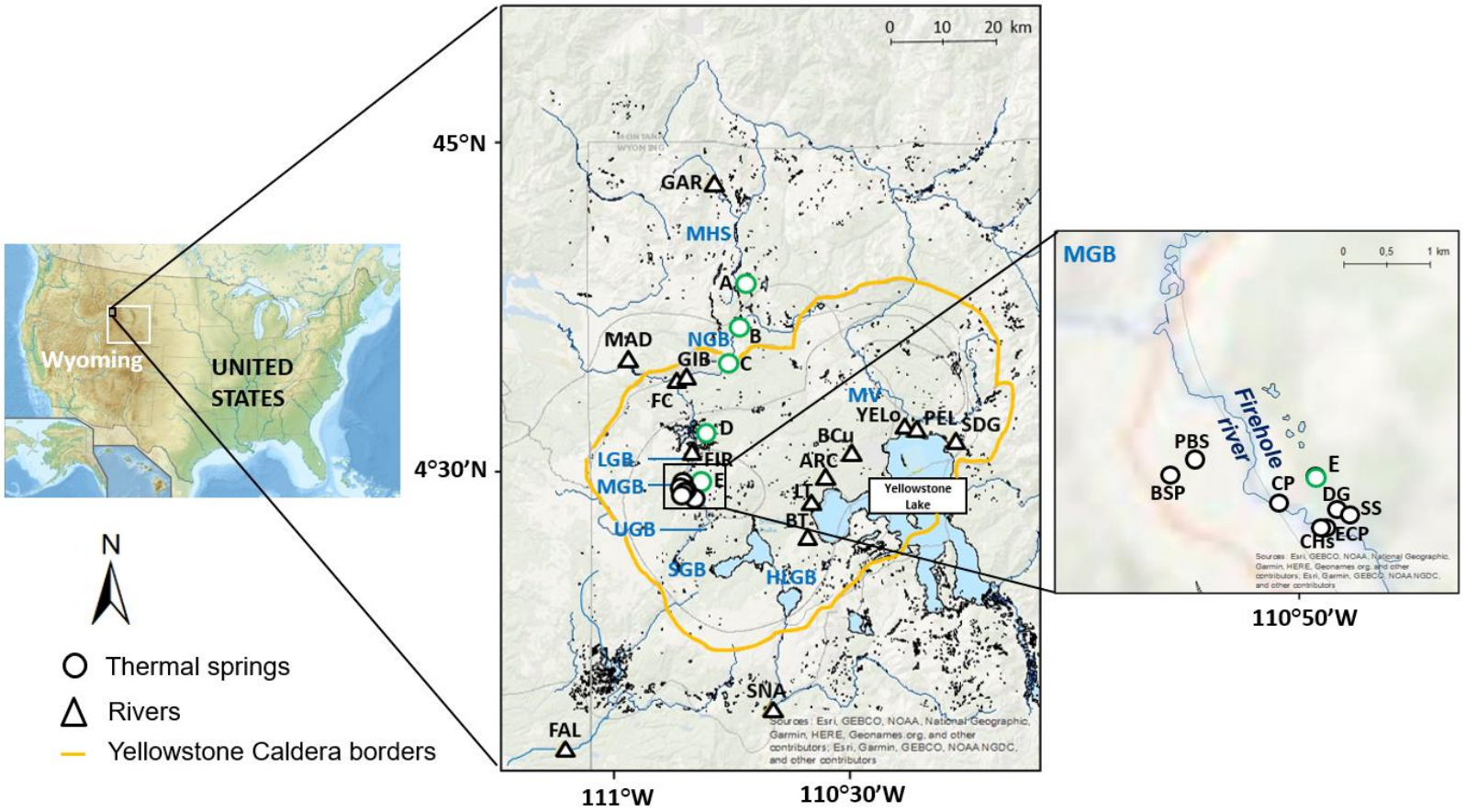
Wyoming
UNITED STATES
N
Thermal springs
Rivers
Yellowstone Caldera borders
0 10 20 km
45°N
4°30'N
111°W
110°30'W
GAR
MHS
A
B
C
D
E
MAD
NGB
GIB
FC
FIR
LGB
MGB
UGB
SGB
HLGB
MV
YELo
PEL
SDG
BCU
ARC
LT
BT
Yellowstone Lake
SNA
FAL
MGB
0 0,5 1 km
Firehole river
PBS
BSP
CP
E
DG
SS
ECP
CHS
110°50'W

Fig. 6.1: Location of thermal spring waters (circle) and river waters (triangle) studied in Yellowstone Plateau Volcanic Field (YPVF). Thermal springs from this study (black circle; from Midway Geyser Basin) are located relative to samples from literature (green circle): from Douthitt (1982) (A = Porcelaine Terrace, B = Cistern, C = Beryl, E = Ear, and Minerva spring outside the map), and from Chen et al (2020) (B = Cistern, D = Deerbone). Major geyser basins and thermal areas are located (dark blue), from North to South, respectively: MHS = Mammoth hot springs; NGB = Norris Geyser Basin; MV = Mud volcano; LGB = Lower Geyser Basin; MGB = Midway Geyser Basin; UGB = Upper Geyser Basin; SGB = Shoshone Geyser Basin; HLGB = Heart Lake Geyser Basin. The river codes are explained in **Table 6.1**.

6.4 Materials and methods

6.4.1 Sampling campaign

Sampling sites for thermal springs and river waters are shown in **Fig. 6.1**. Seven thermal springs of MGB were sampled in April 2015, at their outlet from the riverbed. Fourteen river waters flowing through YPVF were collected in September (corresponding to base flow) and in June (during snowmelt) between 2016 and 2017 (n=30), away from any visible anthropogenic contributions. River water samples were collected for three main rivers (from North to South: Madison (MAD), Snake (SNA), Falls (FAL)), and their tributaries (from North to South: Gardner (GAR), Gibbon (GIB), and Firehole at two locations, i.e., Firehole Canyon at gage (FC) and Firehole above Old Faithful (FIR)). For these rivers, temperature (°C) and pH were measured *in situ* with an Hanna HI 991300 electrod. River water samples were also collected from rivers adjacent to Yellowstone Lake (from the western to eastern side of the lake: Big Thumb creek (BT), Little Thumb creek (LT), Arnica creek (ARC), Bridge creek (BCu), Yellowstone at lake outlet (YELo), Pelican creek (PEL), Sedge creek (SDG). For these river samples, temperature and pH were not measured. All water samples were filtered at 0.45 µm through polycarbonate membranes within 24h and stored at 4 °C in the dark in pre-washed polypropylene (PP) bottles.

Most of the sampled rivers (except SNA and FC) are equipped with gaging stations and monitored by USGS (FAL, MAD, FIR, GAR, GIB, ARC,

BCu, LT, BT, SDG, PEL, YELo), and water flow and element flux data are available since 1983 (McCleskey et al, 2012). The sampling period can be considered as representative of the discharge conditions, based on a long-term trend in riverine discharge available for six rivers (YELo, SNA, GIB, GAR, FIR, FAL; National Water Information System (NWIS), 2019; **Suppl. Mat. 6.1**). Based on the USGS database (**Suppl. Mat. 6.2**), the discharge data corresponding to the day and location of sample collection in this study support an increase in riverine discharge at snowmelt relative to base flow (standardized to the catchment size) between 1.3 and 33.3. The largest increase in discharge at snowmelt is for one of the smaller draining area (SDG; **Fig. 6.2**).

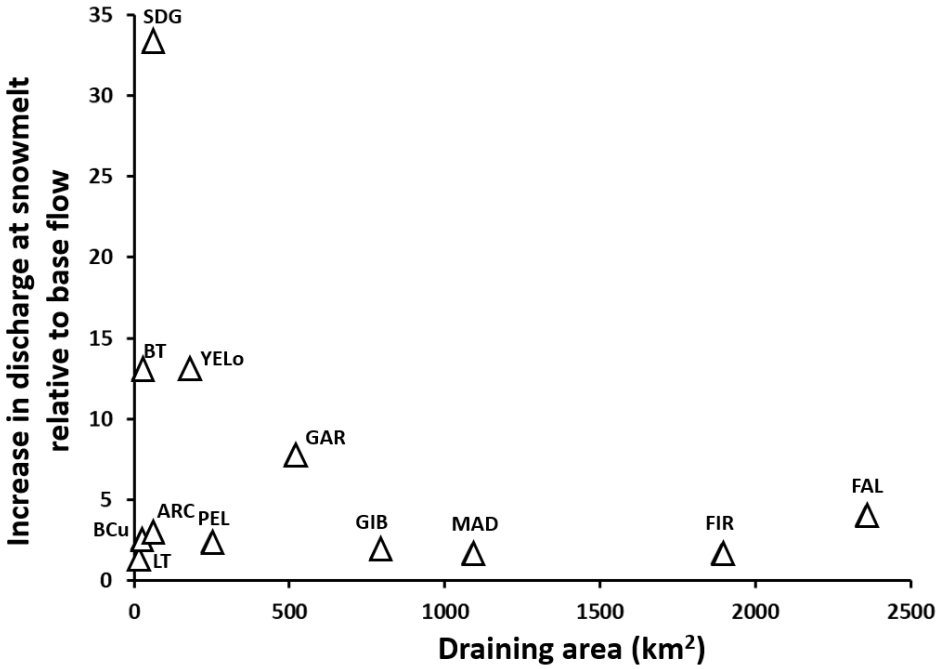

Fig. 6.2: Change in discharge (standardized to catchment size) between snowmelt (June) and base flow (September) in river waters flowing through YPVF as a function of the draining area. Discharge data and drainage area data (USGS database; NWIS, 2019) correspond with the sampling days and sampling locations in this study. The river codes are explained in **Table 6.1**.

6.4.2 Water compositions analysis

The concentrations of Ca, Na, Mg, K, Al, Fe and Si in the water samples were determined by inductively-coupled plasma-optical emission spectrometry (ICP-OES; iCAP 6500 Thermo Fisher Scientific). The accuracy on majors elements (Ca, Na, Mg, K, Al, Fe and Si) analyses was assessed using the trueness (± 3%, ± 4%, ± 1%, ± 7%, ± 4%, ± 2% and ± 4%; respectively) on the river water reference material SLRS-5 (Yeghicheyan et al, 2013) and the analytical precision (± 0.5%) for each element. The detection limit are 0.05, 0.43, 0.21, 0.26, 0.37, 0.18 and 0.36 $\mu mol.l^{-1}$ for Ca, Na, Mg, K, Al, Fe and Si, respectively. Anions (SO_4^{2-}, Cl^-) were measured by ion chromatography (Dionex ICS2000, column: AG15/AS15). The accuracy on SO_4^{2-} and Cl^- was assessed by using the trueness (± 3% and ± 4%; respectively) on river water certified reference material LGC6025 (UKAS, 2014) and the analytical precision (± 2%) for each anion. The detection limit are 1.5 and 3.1 for SO_4^{2-} and Cl^-, respectively. Total dissolved solids (TDS; $\mu mol.l^{-1}$) were obtained by summing major elements (Ca, Na, Mg, K) and SiO_2 concentrations in rivers.

6.4.3 Ge measurements and Ge/Si ratio calculation

The Ge concentration in the thermal (n=7) and river (n=30) waters was determined by ICP-mass spectrometry (ICP-MS, ICAPQ Thermo Fisher Scientific) using the ^{74}Ge isotope. Accuracy and long-term repeatability of the analysis were assessed by measuring two international riverine standards, namely SLRS-5 ([Ge] = 0.083 ± 0.014 $nmol.l^{-1}$; n=3) and SLRS-6 ([Ge] = 0.097 ± 0.0069 $nmol.l^{-1}$; n=3) (Yeghicheyan et al, 2013), and one in-house standard (i.e., the Gallion Blanc (GAB) thermal spring of La Soufrière volcano in Basse-Terre Island: [Ge] = 23.95 ± 0.096 $nmol.l^{-1}$; n=14) in each analytical session between July 2017 and June 2018. The limit of detection on Ge is 0.04 $nmol.l^{-1}$ and the analytical precision (n= 3) is ± 8% for Ge concentrations < 0.013 $nmol.l^{-1}$ and 4% for Ge concentrations > 0.013 $nmol.l^{-1}$. The precision on our Ge/Si ratio is 10% (SD).

6.4.4 Silicon isotope measurements

Purification of silicon

For thermal spring waters, the Si concentrations are above the limit of amorphous silica solubility (~1700-2300 µmol.l^{-1} at 25 °C; Fournier and Rowe, 1977). Therefore, to ensure the solubilization of potential amorphous silica precipitates formed after filtration, the water sample was dried down on a hotplate at 100 °C, followed by a leaching with 0.125M NaOH at 100 °C for four hours after sonication for 10 minutes (adapted from Ragueneau et al, 2005). Following leaching, the pH of sample solutions was adjusted using suprapure HNO_3 to reach pH 2 in a final volume at a Si concentration below the limit of amorphous silica solubility.

To prevent matrix effects from anions such as SO_4^{2-} and Cl^- during mass spectrometry, Si in thermal waters was purified using a two step column chemistry with anionic exchange resin (Biorad AG MP-1) and cationic exchange resin (Biorad AG50W-X12) following the method developed by Gaspard et al, submitted. After column chemistry, the Si recovery was > 98%, the concentrations of Na, SO_4^{2-} and Cl^- in the purified solution were < 0.43, 1.5 and 3.1 µmol.l^{-1}, respectively (i.e., the detection limit values), and the blank level was < 0.36 µmol Si.l^{-1}, i.e., the detection limit for Si by ICP-OES.

Mass spectrometry

Silicon isotope compositions were measured in thermal springs (n=6) and river waters (n=17) from YPVF. Silicon isotope compositions were analyzed by MC-ICP-MS (Neptune Plus™ High Resolution Multicollector ICP-MS, Thermo Fisher Scientific) in wet plasma mode in medium resolution (Δm/m~6000) using a PFA nebulizer of 100 µl.min^{-1} uptake rate. The instrumental mass bias was corrected for by using the standard-sample bracketing technique and an external Mg doping (Cardinal et al, 2003). The analyses were performed in 2% v/v HNO_3 matrix, with a typical sensitivity of 7 V for 2 mg.l^{-1} Si and an instrumental blank <30 mV. Silicon isotope compositions are expressed in relative deviations of $^{30}Si/^{28}Si$ ratio from the NBS-28 reference standard using the common δ-notation (‰): $\delta^{30}Si=[(^{30}Si/^{28}Si)_{sample}/(^{30}Si/^{28}Si)_{NBS\text{-}28} -1]\times1000$. One measurement comprises 30 cycles with 4.2 s integration time corrected by blank in a 2% v/v HNO_3 matrix. Each single δ-value (n) represents one sample run and two bracketing standards. $\delta^{30}Si$-values are

reported as the mean of replicate isotopic analyses ± standard deviation (SD). Quality control of mass bias was performed by ensuring that $\delta^{30}Si$ and $\delta^{29}Si$ measurements fit to a mass-dependent fractionation array, supporting the interference-free determination of all three Si isotopes via MC-ICP-MS (**Suppl. Mat. 6.3**). The long-term precision and accuracy of the MC-ICP-MS $\delta^{30}Si$ analyses were assessed on the reference materials diatomite ($\delta^{30}Si$ = 1.30 ± 0.09 ‰, SD, n=20), BHVO-2 ($\delta^{30}Si$ = -0.27 ± 0.06 ‰, SD, n=10) and quartz Merck ($\delta^{30}Si$ of 0.04 ± 0.09 ‰, SD, n=6) with values consistent with those reported earlier (Reynolds et al, 2007; Abraham et al, 2008).

6.5 Results

General parameters (temperature, pH, TDS) and chemical composition of thermal waters (of Midway Geyser Basin) and river waters in Yellowstone Plateau Volcanic Field (YPVF) are shown in **Table 6.1**. The abbreviations for thermal spring and river water samples are explained in **Table 6.1**. The ion balance of the water samples never exceeds 10%.

Table 6.1: General parameters (temperature, pH, TDS) and chemical composition of thermal and river waters in Yellowstone Plateau Volcanic Field (YPVF) collected in September (at base flow) and in June (during snowmelt). Small rivers surrounding Yellowstone Lake are reported from the western to eastern side of the lake, and larger rivers draining the YPVF are reported from North to South. Also shown is a typical volcanic rock composition for rhyolite, which is the dominant bedrock in YPVF.

	Sampling date	Sample	Label	Temperature	pH	TDS	Ca	Na	Mg	K	Al	Fe	Si	SO_4	Cl
	dd.mm.yy			°C		µmol.l^{-1}									
Thermal Springs	13.04.15	Black Sand Pool (6 m depth)	BSP	94.2	8.7	30066	8	19583	n.d	541	13	0.2	4647	183	10172
	14.04.15	Punch Bowl Spring (4.4 m depth)	PBS	93.0	7.6	30963	9	19243	n.d	482	7	n.d	5252	179	8787
	15.04.15	Crested Pool (11.33 m depth)	CP	111.4	9.2	29119	10	17501	n.d	493	13	n.d	5198	219	11040
	16.04.15	East Chinaman Pool (5 m depth)	ECP	95.2	7.6	25987	18	14326	n.d	464	6	n.d	5229	217	11955
	16.04.15	Chinese Springs (4.6 m depth)	CHS	97.2	7.8	24082	16	13921	n.d	438	6	n.d	4540	237	11454
	16.04.15	Sulphide Spring	SS	90.1	6.6	10485	70	4833	12	394	2	1	2421	319	3144
	16.04.15	Dome Geyser	DG	88.5	7.1	27474	13	14554	0.4	536	4	n.d	5786	451	11489
Rivers	18.09.16	Big thumb creek	BT	-	-	5912	235	1478	151	248	n.d	16	1778	54	-
	22.06.17	Big thumb creek	BT	-	-	609	48	29	14	14	n.d	1	236	n.d	-
	18.09.16	Little thumb creek upstream	LT	-	-	1745	153	207	91	77	n.d	6	570	16	-
	22.06.17	Little thumb creek upstream	LT	-	-	447	60	52	15	19	n.d	n.d	141	3	-
	18.09.16	Arnica creek	ARC	-	-	3310	181	739	63	81	n.d	3	1050	28	-
	22.06.17	Arnica creek	ARC	-	-	2236	173	327	42	51	n.d	n.d	769	18	-
	18.09.16	Bridge creek upstream	BCu	-	-	4490	213	565	81	128	n.d	1	1638	30	-
	22.06.17	Bridge creek upstream	BCu	-	-	1529	96	38	21	13	3	2	637	n.d	-
	21.09.16	Yellowstone river outlet	YELo	-	-	1150	154	415	104	49	n.d	n.d	200	81	-
	24.09.16	Yellowstone river outlet	YELo	-	-	1119	148	410	102	44	n.d	n.d	194	81	-
	09.10.16	Yellowstone river outlet	YELo	-	-	2150	257	747	210	95	n.d	1	393	333	-
	22.06.17	Yellowstone river outlet	YELo	-	-	1093	143	361	97	43	n.d	n.d	210	78	-
	18.09.16	Pelican creek	PEL	-	-	5931	523	2028	567	362	10	2	1147	1180	-
	22.06.17	Pelican creek	PEL	-	-	1268	85	103	59	22	3	1	467	64	-
	18.09.16	Sedge creek	SDG	-	-	2861	339	754	340	79	50	62	631	1520	-
	22.06.17	Sedge creek	SDG	-	-	1031	100	171	65	28	n.d	3	312	266	-
	06.06.17	Gardner river	GAR	14.9	8.0	1497	549	207	206	51	n.d	n.d	227	162	120
	01.12.17	Gardner river	GAR	10.0	8.0	4633	1472	1153	699	253	2	1	494	1105	879
	07.06.17	Madison River near W. Yellowstone	MAD	18.6	7.7	4180	114	1866	24	134	5	2	955	81	827
	20.09.17	Madison River near W. Yellowstone	MAD	11.0	8.1	7119	158	3667	29	214	7	2	1427	208	2817
	06.06.17	Gibbon River at gage	GIB	18.5	7.1	3394	155	1337	42	132	7	4	809	118	610
	20.09.17	Gibbon River at gage	GIB	11.3	6.9	6652	206	3214	50	276	15	4	1359	341	1711
	06.06.17	Firehole Canyon at gage	FC	18.1	8.2	3800	76	1704	15	106	5	2	888	59	799
	20.09.17	Firehole Canyon at gage	FC	14.2	8.4	7515	125	3821	19	188	5	1	1572	164	2028
	06.06.17	Firehole above Old Faithful	FIR	8.6	6.9	1095	53	199	11	40	6	2	370	16	104
	22.09.17	Firehole above Old Faithful	FIR	5.7	7.4	2322	89	575	15	81	5	2	730	38	378
	05.06.17	Snake R. above Flagg Ranch	SNA	10.3	7.8	923	251	184	67	25	2	1	185	38	64
	13.09.17	Snake R. above Flagg Ranch	SNA	17.0	8.4	3054	411	1162	121	113	n.d	n.d	583	288	443
	07.06.17	Falls river	FAL	12.5	7.5	995	77	267	29	29	n.d	n.d	278	10	-
	21.09.17	Falls river	FAL	6.7	7.9	2644	118	913	32	74	n.d	1	705	24	265

Volcanic rock	Type	Sample	Label	Reference	Ca	Na	Mg	K	Al	Fe	Si
					wt (%)						
	Rhyolite	RGM-1 USGS reference material	RHY	Bobrow et al, 1983	1.00	2.98	0.01	4.07	6.98	1.55	34.47

- = not measured

n.d = not detected.

6.5.1 Elemental composition of the thermal springs from YPVF

Thermal springs in MGB have high temperatures ranging from 88.5 to 111.4 °C and neutral to alkaline pH values (6.9-9.2). These thermal springs exhibit high dissolved elements (TDS: 10485-30963 $\mu mol.l^{-1}$) and silicon concentrations vary from 2421 to 5786 $\mu mol.l^{-1}$. Thermal springs in MGB contain high Cl^- concentrations (3144-11955 $\mu mol.l^{-1}$) followed by SO_4^{2-} (111-451 $\mu mol.l^{-1}$), and Na is the dominant cation with concentrations ranging from 4833 to 19583 $\mu mol.l^{-1}$ (**Fig. 6.3a**). These data agree with the view that MGB thermal springs are neutral to slightly alkaline waters (Hurwitz et al, 2007) and neutral Cl-waters. The MGB thermal springs differ from other thermal spring areas in YPVF such as NGB (Porcelaine Terrace, Cistern, Beryl) which has neutral chloride waters enriched in K and Cl^-, and MHS alkaline HCO_3-waters that are enriched in Ca and Mg (**Fig. 6.3a** and **6.3b**; Bargar, 1978).

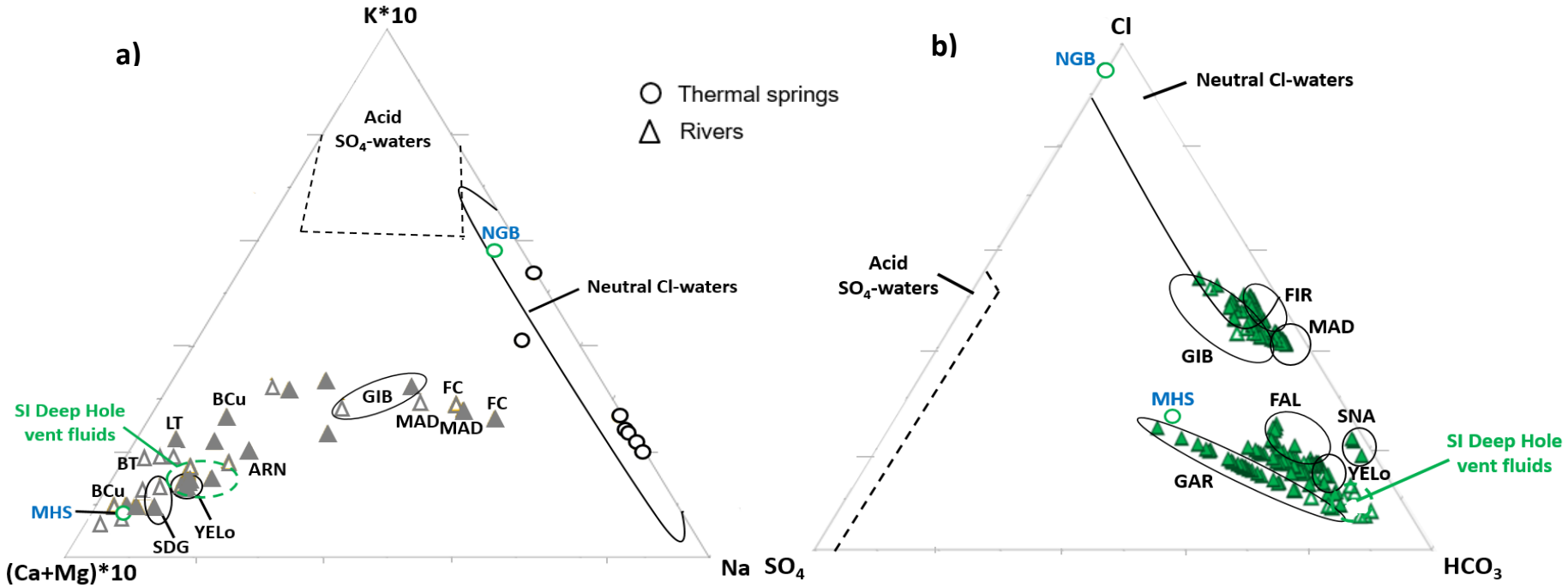

Fig. 6.3: Ternary diagrams of the major cation (a) and anion (Giggenbach, 1988) (b) composition of the thermal springs (circle) and river waters (triangle) from the YPVF. River waters at base flow (plain triangle) are compared with river waters during snowmelt (open triangle). Data from this study (dark grey) are compared with literature data (green): rivers from Gemery-Hill et al (2007), thermal springs from Norris Geyser Basin (NGB) and Mammoth Hot Springs (MHS) from Bargar (1978), and SI Deep Hole vent fluids from Fowler et al (2019b). Alkalinity is not available for our samples. The river codes are explained in **Table 6.1**.

6.5.2 Elemental composition of the river waters from YPVF

River waters in YPVF display neutral to alkaline pH values (6.9-8.4) and exhibit a large range of dissolved elements concentrations as reflected by high TDS values (TDS: 447-7515 $\mu mol.l^{-1}$). The Si concentrations in river waters range from 141 to 1778 $\mu mol.l^{-1}$. We observe spatial heterogeneity in the chemical composition of river waters in YPVF, irrespective of seasonal flow regime **(Fig. 6.3a**). River waters downstream of the MGB such as GIB, MAD and FC rivers have higher Na (1337-3821 $\mu mol.l^{-1}$) and K (106-276 $\mu mol.l^{-1}$) concentrations (**Fig. 6.3a**) compared to river waters such as BCu, SDG and YELo, with Na (38-754 $\mu mol.l^{-1}$) and Ca (96-339 $\mu mol.l^{-1}$).

We observe seasonal variations in the chemical composition of river waters between base flow and snowmelt conditions that are superimposed on these underlying spatial variations. Notably, river waters collected during snowmelt (June) show lower TDS values (447-4180 $\mu mol.l^{-1}$) than rivers sampled at base flow (September; 1150-7515 $\mu mol.l^{-1}$) highlighting that river waters are diluted at snowmelt (**Fig. 6.4**), well in agreement with previous studies (McCleskey et al, 2012, 2016; **Suppl. Mat. 6.4).** To compare element concentrations between base flow and snowmelt, dilution-corrected element concentrations were obtained by normalizing element concentrations to Na. Indeed, Na shows a strong positive correlation with TDS ($R^2 = 0.88$, **Suppl. Mat. 6.5**), indicating that riverine Na concentrations are governed by dilution and can be used here to correct elements for dilution during the snowmelt event (**Fig. 6.5**). River water compositions during snowmelt are enriched in Si relative to base flow, and more specifically in BCu ($Si/Na_{snowmelt} = 16.9$), BT ($Si/Na_{snowmelt} = 8.18$) and PEL ($Si/Na_{snowmelt} = 4.54$; **Fig. 6.5b**). Moreover, for all rivers, there is an enrichment in Mg and K at snowmelt relative to base flow, and a depletion in Cl^- at snowmelt relative to base flow (**Fig. 6.5a**, **6.5c** and **6.5d**).

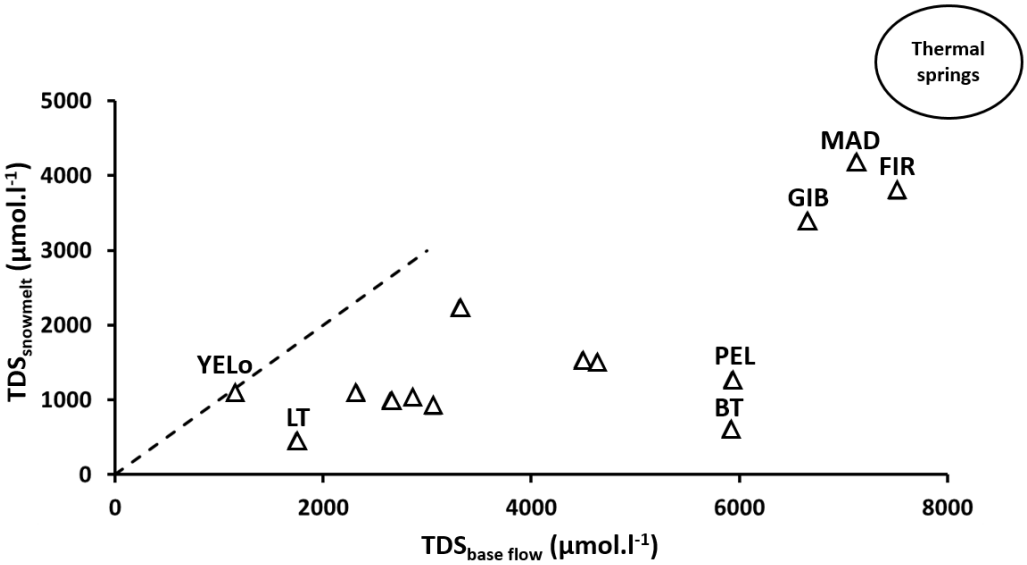

Fig. 6.4: Total dissolved solids (TDS) at snowmelt period ($TDS_{snowmelt}$; June) relative to base flow ($TDS_{base\ flow}$; September) in river waters (triangle) flowing in Yellowstone Plateau Volcanic Field (YPVF). The river codes are explained in **Table 6.1**. The end-member for $TDS_{thermal\ springs}$ is shown for comparison (circle).

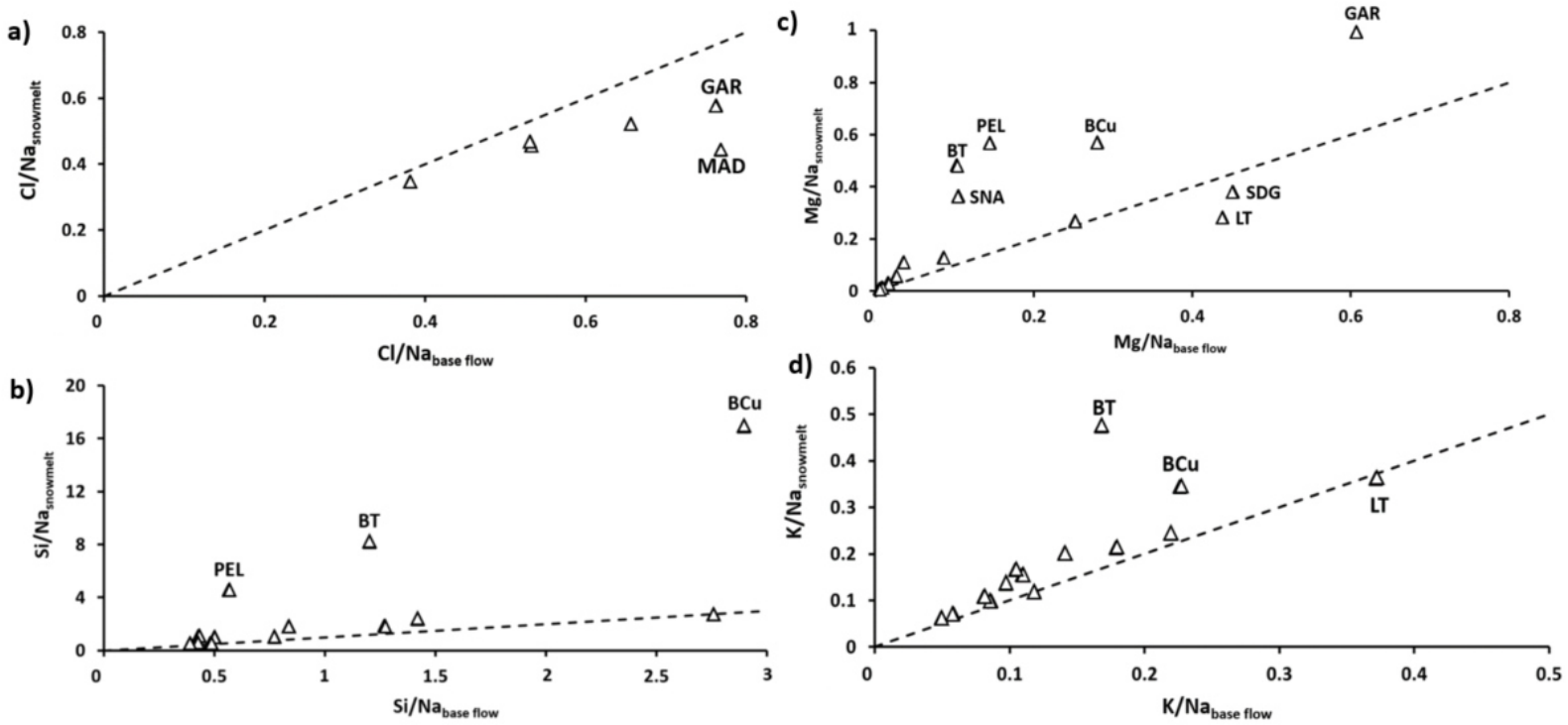

Fig. 6.5: Plots showing the Na-normalized element concentrations (molar ratio) at snowmelt (June) as a function of Na-normalized element concentrations at base flow (September) in river waters flowing through YPVF: (a) Cl, (b) Si, (c) Mg and (d) K. The river codes are explained in **Table 6.1**. The dashed line corresponds to the 1:1 ratio; element ratios above (or below) the dashed lines indicate an enrichment in this element at snowmelt (or at base flow; respectively).

6.5.3 Ge/Si ratio of the thermal springs and river waters

The Ge/Si ratio of thermal springs of Midway Geyser Basin and river waters flowing through Yellowstone Plateau Volcanic Field, collected in September (at base flow) and in June (during snowmelt), are reported in **Table 6.2** and shown in **Fig. 6.6a**.

Table 6.2: Germanium concentrations, Ge/Si ratios and silicon isotope compositions ($\delta^{29}Si$ and $\delta^{30}Si$) in thermal and river waters flowing in Yellowstone Plateau Volcanic Field (YPVF). River waters were collected in September (at base flow) and in June (during snowmelt). n = number of measurements.

Label	Sampling date	Ge	Ge/Si	$\delta^{29}Si$	SD	$\delta^{30}Si$	SD	n
	dd.mm.yy	nmol.l^{-1}	µmol.mol^{-1}	‰		‰		
Thermal springs								
BSP	13.04.15	828.74	159.71	-0.04	0.04	-0.04	0.03	2
PBS	14.04.15	775.06	143.85	-0.12	0.01	-0.13	0.07	1
CP	15.04.15	1011.84	188.92	-0.09	0.05	-0.09	0.08	2
ECP	16.04.15	991.19	182.29	-0.09	0.02	-0.14	0.03	2
CHs	16.04.15	960.90	181.70	-0.07	0.04	-0.05	0.05	2
SS	16.04.15	235.41	110.98	-	-	-	-	-
DG	16.04.15	1010.46	170.69	-0.04	0.05	-0.08	0.01	2
Rivers								
BT	18.09.16	12.48	7.05	0.61	0.06	1.19	0.03	1
BT	22.06.17	0.21	0.89	0.32	0.12	0.86	0.02	1
LT	18.09.16	0.83	1.47	0.49	0.06	0.92	0.06	1
LT	22.06.17	0.14	0.99	0.53	0.06	1.09	0.11	1
ARC	18.09.16	4.79	4.58	0.09	0.09	0.40	0.04	1
ARC	22.06.17	4.32	5.64	0.10	0.08	0.37	0.05	1
BCu	18.09.16	4.31	2.64	0.22	0.01	0.48	0.01	1
BCu	22.06.17	1.32	2.08	0.32	0.05	0.71	0.07	1
YELo	21.09.16	4.02	20.13	1.07	0.03	2.17	0.03	1
YELo	24.09.16	4.49	23.29	1.04	0.04	2.01	0.09	2
YELo	09.10.16	5.32	13.60	0.77	0.05	1.63	0.03	1
YELo	22.06.17	3.81	18.21	0.89	0.02	1.82	0.04	1
PEL	18.09.16	10.23	8.95	0.59	0.05	1.17	0.06	1
PEL	22.06.17	1.45	3.12	0.26	0.10	0.78	0.07	1
SDG	18.09.16	7.14	11.35	0.50	0.02	1.05	0.05	1
SDG	22.06.17	1.87	6.02	0.39	0.14	0.77	0.05	1
GAR	06.06.17	2.55	11.77	-	-	-	-	-
GAR	01.12.17	16.86	34.27	0.29	0.01	0.57	0.02	1
MAD	07.06.17	60.02	72.32	-	-	-	-	-
MAD	20.09.17	99.12	77.62	-	-	-	-	-
GIB	06.06.17	30.49	42.77	-	-	-	-	-
GIB	20.09.17	63.19	51.64	-	-	-	-	-
FC	06.06.17	65.80	83.95	-	-	-	-	-
FC	20.09.17	130.09	91.92	-	-	-	-	-
FIR	06.06.17	7.37	21.41	-	-	-	-	-
FIR	22.09.17	21.27	32.41	-	-	-	-	-
SNA	05.06.17	3.10	18.19	-	-	-	-	-
SNA	13.09.17	22.30	40.56	-	-	-	-	-
FAL	07.06.17	3.44	13.48	-	-	-	-	-
FAL	21.09.17	12.60	20.06	-	-	-	-	-

- = not measured.

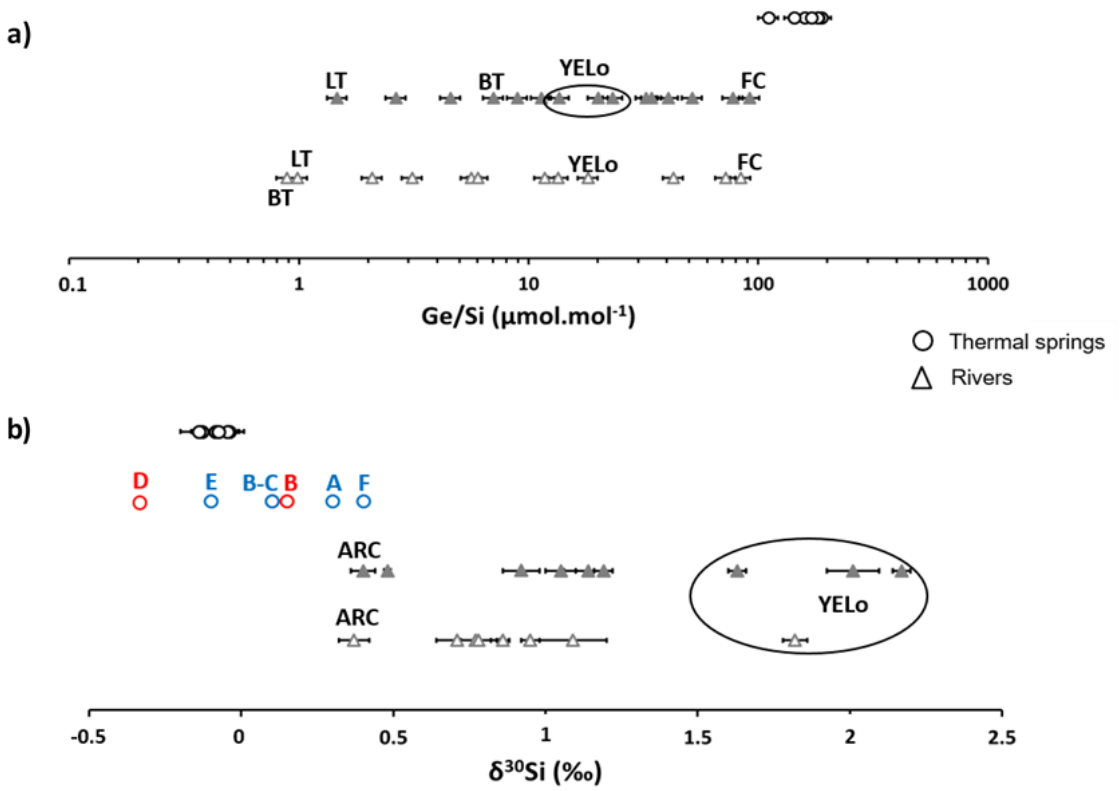

Fig. 6.6: Plots showing the Ge/Si ratio (± SD) (a) and Si isotope composition (δ^{30}Si ± SD) (b) of the thermal spring (circle) and river water (triangle) samples from the YPVF. River waters at base flow (plain dark grey triangle) are compared with river waters during snowmelt (open dark grey triangle). Si isotope data from this study (black) are compared with reported literature values from YPVF (located in **Fig. 6.1**): Douthitt (1982) (blue; A = Porcelaine Terrace, B = Cistern, C = Beryl, E = Ear, F = Minerva; white circles), Chen et al (2020) (red; B = Cistern, D = Deerbone). The river codes are explained in **Table 6.1**.

The highest Ge/Si ratios were measured for thermal springs in MGB and range from 110.98 (SS) to 188.92 (CP) μmol.mol^{-1}. River waters show lower Ge/Si ratios than thermal spring, with values ranging from 0.89 μmol.mol^{-1} (BT) to 91.92 μmol.mol^{-1} (FC).

River waters sampled during snowmelt (June) and base flow (September) display Ge/Si values within the same range (0.89-83.95 and 1.47-91.92 μmol.mol^{-1}). Considering each river separately, the Ge/Si ratio in rivers decreases during snowmelt relative to base flow (**Fig. 6.7a**). The exception to this is ARC river which has the same Ge/Si ratio during snowmelt (5.64 μmol.mol^{-1}) and base flow (4.58 μmol.mol^{-1}) taking into account precision on Ge/Si (10%, SD).

6.5.4 Si isotope composition of the thermal springs and river waters

The Si isotope composition of thermal springs in MGB and river waters draining Yellowstone Plateau Volcanic Field, collected in September (at base flow) and in June (during snowmelt), are reported in **Table 6.2** and shown in **Fig. 6.6b**.

Thermal springs are characterized by lower δ^{30}Si values (-0.14 ± 0.03 ‰ in ECP to -0.04 ± 0.03 ‰ in BSP) than those of river waters (0.37 ± 0.05 ‰ in ARC to 2.17 ± 0.03 ‰ in YELo) draining YPVF. The YELo river is enriched in ^{30}Si relative to other collected rivers (δ^{30}Si = 1.63 ‰ to 2.17 ‰).

Considering each river separately, there is no systematic seasonal trend between Si isotope compositions at base flow and during snowmelt. Some rivers show similar δ^{30}Si values at snowmelt relative to base flow (e.g., ARC, δ^{30}Si = 0.37 ± 0.05 ‰ relative to 0.40 ± 0.04 ‰), some rivers have higher δ^{30}Si values at snowmelt relative to base flow (e.g., BCu, δ^{30}Si = 0.71 ± 0.07 ‰ relative to 0.48 ± 0.01‰), and some rivers display lower δ^{30}Si values at snowmelt relative to base flow (e.g., BT, SDG, YELo, PEL) (**Fig. 6.7b**).

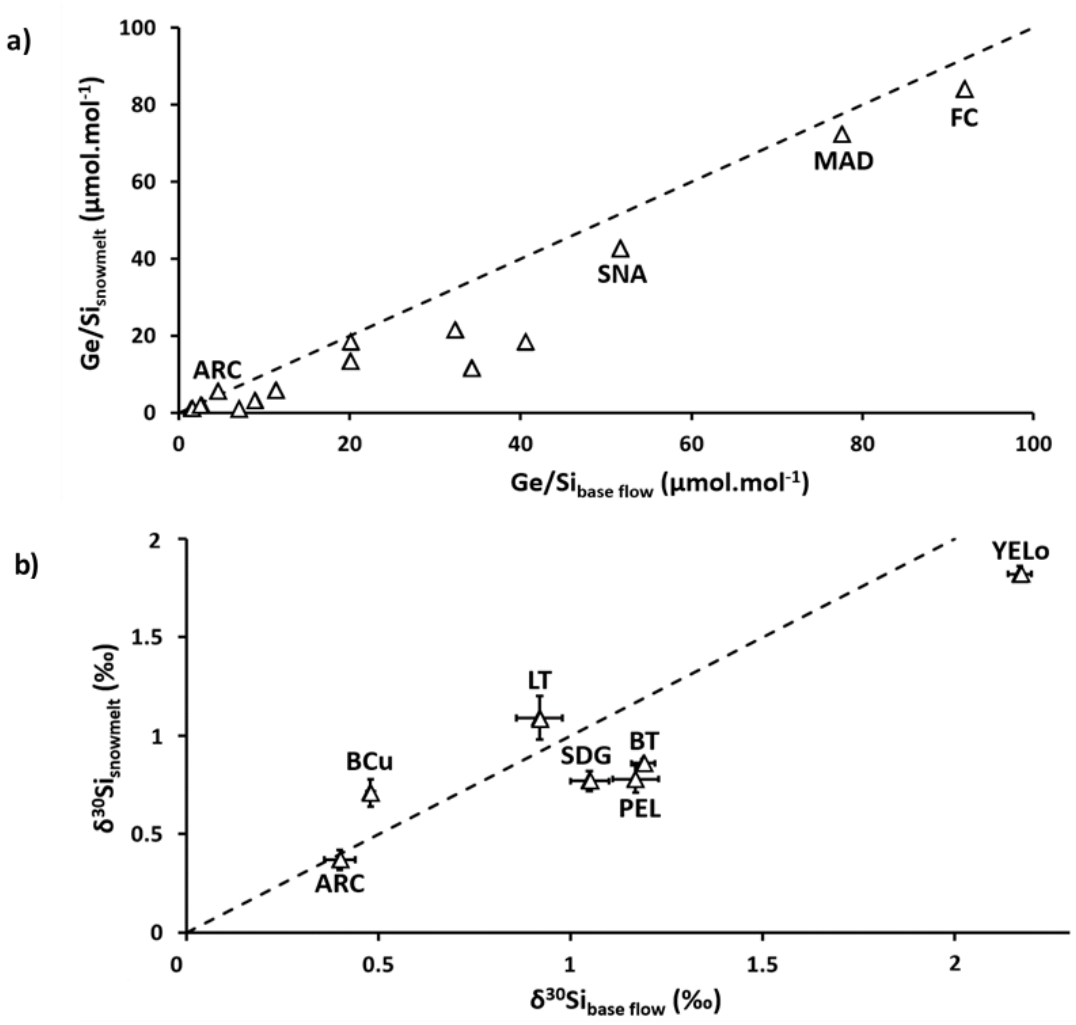

Fig. 6.7: Plots showing the variations in (a) Ge/Si ratios and (b) Si isotope compositions in river waters during snowmelt (June) as a function of the same parameters at base flow (September) in YPVF. The river codes are explained in **Table 6.1.** The dashed line corresponds to the 1:1 ratio; the Ge/Si ratios of δ^{30}Si values above (or below) the dashed lines indicate an enrichment in Ge/Si ratios or δ^{30}Si values at snowmelt (or at base flow; respectively).

6.6 Discussion

6.6.1 Variations in $\delta^{30}Si$ and Ge/Si ratio in thermal springs in YPVF

The Si isotope composition of the six neutral Cl-waters from MGB reported in this study ($\delta^{30}Si$: -0.14 ± 0.03 ‰ to -0.04 ± 0.03 ‰) are on the lower end of the $\delta^{30}Si$ values reported for thermal waters in volcanic regions ($\delta^{30}Si$ = -0.6 to 1.7 ‰; e.g., Opfergelt et al, 2011; Geilert et al, 2015; Ding et al, 2017). Our values from MGB are in agreement with one $\delta^{30}Si$ value reported in Ear spring from MGB ($\delta^{30}Si$ = -0.1‰; Douthitt, 1982; **Fig. 6.1**). But our range of values for thermal springs MGB is lower than the Si isotope composition reported for thermal springs from NGB (Porcelaine Terrace, Cistern, Beryl and Minerva; located as A, B, C on **Fig. 6.1**) where $\delta^{30}Si$ values range from 0.1 to 0.4 ‰ (Douthitt, 1982; Chen et al, 2020).

This can be explained by the chemical differences between thermal springs from MGB and NGB (located more than 22 km north of MGB). The MGB and NGB (Porcelaine Terrace, Cistern, Beryl) are neutral Cl-waters (Bargar, 1978; Hurwitz et al, 2007) (**Fig. 6.3a** and **6.3b**), but the differences in Cl^- and HCO_3^- concentrations observed in these thermal springs is attributed to varying degrees of conductive cooling, decompressional boiling and with mixing of different thermal waters (Fournier, 1989), that likely differ between MGB and NGB. Contrasting temperatures are reported for thermal springs for MGB and NGB: the average temperature of thermal springs from NGB (91 °C; Bargar, 1978) is in the lower end of range of temperature from thermal springs from MGB (88-111 °C). And their Si concentrations also differ: the Si concentration are higher in thermal springs from NGB (6990 $\mu mol.l^{-1}$; Bargar, 1978) than in those from MGB (2421-5786 $\mu mol.l^{-1}$).

As a result, thermal springs from MGB have overall higher temperatures and lower Si concentrations than thermal springs from NGB. We hypothesize that the differences in Si isotope compositions between the thermal springs from these two areas can be explained by differences in conditions for the precipitation of siliceous sinters. As shown experimentally (Geilert et al, 2014), sinters incorporate preferentially the lighter Si isotopes and enriches surrounding waters in the heavy Si isotopes. This has recently been confirmed at YPVF with silica sinters from Cistern and Deerbone springs showing light $\delta^{30}Si$ (from -4.79 to -

2.25 ‰ and from -0.81 to -0.11 ‰, for Cistern and Deerbone springs) relative to their corresponding thermal springs (from 0.15 to 0.70 ‰ and from -0.32 to -0.17 ‰, for Cistern and Deerbone springs, respectively; Chen et al, 2020). Therefore, the heavier $\delta^{30}Si$ values measured in thermal springs from NGB suggest a potentially larger influence of silica sinters precipitation in NGB than in MGB, due to Si concentrations above the limit of amorphous silica solubility at 91 °C at NGB (~5000-5800 $\mu mol.l^{-1}$; Fournier and Rowe, 1977). A similar explanation has been provided to explain the heavier $\delta^{30}Si$ on Cistern spring from NGB (0.15 ‰) than in Deerbone spring from LGB (-0.32 ‰) (Chen et al, 2020).

The Ge/Si ratios measured on thermal springs of MGB (110.98-188.92 $\mu mol.mol^{-1}$; **Table 6.2**) are high values, in agreement with values reported for other volcanic thermal springs (Iceland: 3-185 $\mu mol.mol^{-1}$; Arnòrsson, 1983, 1987; Siebert et al, 2006; Wheat and McManus, 2008; Escoube et al, 2015). High Ge/Si ratios in metamorphic springs from hydrothermally-impacted areas are generally explained by the precipitation of Ge-poor silica such as quartz (Evans and Derry, 2002) and silica sinters (Arnòrsson, 1987) with much lower values than in their associated thermal waters, therefore suggesting the role of the precipitation of silica sinters on the Ge/Si values of thermal springs from MGB, as highlighted with Si isotopes. This is confirmed by the saturation index ($SI = \log IAP/K_{sp}$ with IAP the ion activity product of the chemical species in the fluids and K_{sp} their solubility product, calculated with the PHREEQC geochemical modeling program) > 0 for quartz in all thermal springs of MGB.

6.6.2 Spatial variations in $\delta^{30}Si$ and Ge/Si ratio in rivers from YPVF

The riverine Ge/Si ratios found in GIB, MAD and FIR (42.77-51.64, 72.32-77.62 and 21.41-32.41 $\mu mol.mol^{-1}$, respectively) are higher than those from river waters located on the shores of Yellowstone Lake (Ge/Si ratios = 0.99-23.29 $\mu mol.mol^{-1}$). This could be explained by spatial differences in the hydrothermal influence to riverine chemistry, considering that contribution of atmospheric deposition-derived solutes (atmospheric input) to the river load can be considered as negligible (Miller and Drever, 1977; Zelt et al, 1998; Kharaka et al, 2002; Hurwitz et al, 2007).

The chemical composition of river waters located adjacent to Yellowstone Lake such as YELo, BCu, SDG, LT and BT highlights higher (Ca+Mg)/K ratios (ranging from 1.6 to 8.6) relative to river waters located further from the lake, such as GIB, MAD and FIR ((Ca+Mg)/K = 0.9-1.6) (**Fig. 6.3a**). The chemistry of rivers adjacent to Yellowstone Lake (YELo, BCu, SDG, LT, BT) is likely influenced by a hydrothermal contribution with a common reservoir feeding the hydrothermal vents at the bottom of the lake: this is supported by a similar anion chemistry between these rivers and the SI Deep Hole vent fluids located at the bottom of the lake in the North Eastern part of the lake (Fowler et al, 2019a, 2019b) (**Fig. 6.3b**). This is consistent with recent study of McCleskey et al (2019) showing that thermal features draining into Yellowstone Lake account for 34% of the Cl^- flux at the river YELo. In contrast, rivers within the vicinity of MGB thermal springs (GIB, MAD and FIR) are influenced by the neutral chloride springs of MGB with $HCO_3/Cl \sim 1.2$ (Hurwitz et al, 2007) reflecting the hydrothermal influence of MGB thermals springs on YPVF rivers (**Fig. 6.3b**).

Thermal springs of MGB are known to contribute to GIB, MAD and FIR rivers (McCleskey et al, 2010a, 2010b; McCleskey et al, 2012). The high Ge/Si ratio in GAR river (11.77-34.27 $\mu mol.mol^{-1}$) is also likely explained by a local contribution from thermal springs, given that GAR river is known to receive a significant contribution from the MHS area (McCleskey et al, 2019). This is also supported by a $\delta^{30}Si$ value in GAR ($\delta^{30}Si$ = 0.57 ‰) lighter than in most other rivers of YPVF, considering that the $\delta^{30}Si$ values of thermal springs in the YPVF are light, ranging between -0.32 and 0.40 ‰; this study, Doutthit, 1982, Chen et al, 2020).

Overall, river waters flowing through YPVF display a range of Ge/Si ratios (0.89-91.92 $\mu mol.mol^{-1}$; **Table 6.2**; **Fig. 6.6a**) that is larger than the range reported for rivers draining volcanic regions (Ge/Si = 0.16-20 $\mu mol.mol^{-1}$; e.g., Derry et al, 2005; Scribner et al, 2006; Baronas et al, 2018, 2020), and a range of Si isotope compositions ($\delta^{30}Si$ = 0.37-2.17‰; **Table 6.2**; **Fig. 6.6b**) within the range of values reported for rivers draining volcanic areas ($\delta^{30}Si$ = -0.1 to 3.4 ± 0.01 ‰; e.g., Opfergelt and Delmelle, 2012; Frings et al, 2016). The highest riverine $\delta^{30}Si$ values in the YPVF were measured in the YELo river collected at the outlet of Yellowstone Lake (**(**$\delta^{30}Si$ = 1.63-2.17 ‰; **Table 6.2**). This is highlighting an additional factor of spatial variations affecting the riverine chemistry within the YPVF: the influence of biological processes. Indeed, these high $\delta^{30}Si$ values likely reflect the preferential uptake of light Si isotopes by diatoms for their silica frustule (De La Rocha et al, 1997) thereby imparting a

distinctive heavy Si isotope signal to the residual lake waters contributing to YELo river. The presence of diatoms is well studied in Yellowstone Lake (Interlandi et al, 2003). Seasonal diatoms bloom in the lake may result in larger Si uptake decreasing the Si concentration in June (210 μmol.l^{-1}) or September (194-200 μmol.l^{-1}) relative to colder periods such as October (393 μmol.l^{-1}; **Table 6.1**) and thereby inducing higher δ^{30}Si value in rivers in June (1.82 ‰) or September (2.01-2.17 ‰) relative to October (1.63 ‰; **Table 6.2**). Given that amorphous silica solubility increases above pH 8 (Alexander et al, 1954), a contribution from diatom frustule dissolution could partly decrease the influence of Si uptake in YELo river (pH 8.25; McCleskey et al, 2019).

6.6.3 Seasonal variations in δ^{30}Si and Ge/Si ratio in rivers from YPVF

6.6.3.1 Possible change in contributions to rivers at snowmelt

Changes in Ge/Si ratios in rivers between snowmelt and base flow support the accepted view that the fraction of hydrothermal inputs to the river is reduced at snowmelt relative to base flow (Hurwitz et al, 2007). Indeed, rivers display lower Ge/Si ratios and Cl concentrations during snowmelt relative to base flow (**Fig. 6.7a**; **Fig. 6.5a**). Based on the high Ge/Si ratios measured in thermal springs (**section 6.6.1**), it is assumed that higher Ge/Si ratios should be associated with rivers dominated by a hydrothermal contribution relative to rivers diluted by snowmelt. The chemical composition of rivers from YPVF are dominated by hydrothermal contribution at base flow (Hurwitz et al, 2010; Hurwitz and Lowenstern, 2014). Overall, the combined evidence from Ge/Si ratios in thermal springs and river waters, TDS values (fully consistent with long-term monitoring of riverine conductivity; **Suppl. Mat. 6.4**), and chemical compositions supports that snowmelt reduces the fraction of hydrothermal contribution to rivers.

A simple dilution by water from snowmelt is not enough to explain the observed changes in riverine Ge/Si ratio, given that snow contains negligible Si and Ge concentrations.

Even if the fraction of hydrothermal inputs to the river is reduced at snowmelt relative to base flow (**Fig. 6.5a**), the dilution-corrected Si

concentrations are enriched during snowmelt relative to base flow (**Fig. 6.5b**), especially in BCu, BT and PEL rivers. This Si enrichment is associated with an enrichment in Mg and K at snowmelt relative to base flow (**Fig. 6.5c** and **6.5d**) which in combination can be explained by a contribution from surface water influenced by weathering processes resulting from surface water-rock interaction or the flushing of soil pore water (Engström et al, 2010). The lithology of surface rocks in the studied part of the YPVF is mainly crystal poor rhyolite (Trettin and Bartelli, 1980; Smith and Siegel, 2000; Christiansen, 2001), and rhyolitic rocks are mainly composed of quartz, amphibole and feldspar, i.e., with high Si and K content (34.47 and 4.07 wt %; as illustrated with one rhyolite international standard in **Table 6.1**). The congruent weathering of primary minerals originated from fresh rhyolite may explain the release of Si, K, and a contribution from an easily leached element such as Mg (Bobrow et al, 1983; Rowe et al, 1992) even if present in low amount in rhyolite. In a mixing diagram using Na-normalized molar ratio, the river waters fit close to the "silicates" reservoir (**Suppl. Mat. 6.6**). The variability in riverine Ca/Na and Mg/Na ratios is higher at snowmelt than in base flow suggesting that the change in runoff at snowmelt is likely to mobilize other sources of dissolved elements in contact with primary minerals. The dissolved riverine Ca and Na concentrations may also be affected by hydrothermal salts formed by the subsurface cooling or mixing of acid-SO_4-saturated thermal waters (e.g., gypsum) as reported in YPVF (Pierce et al, 1991).

The enrichment of Mg, Si and K in rivers draining YPVF during snowmelt is likely influenced by changes in water residence time in the catchment. The water residence time in soils dictates the proportion of water available for mineral dissolution/formation: lower water residence time favors the primary minerals dissolution and higher water residence time favors clay minerals formation (White and Blum, 1995). Rivers draining YPVF show an increase in discharge at snowmelt relative to base flow standardized to the catchment size (**Fig. 6.2**). The largest increase in discharge at snowmelt has been reported for one of the smaller draining area (SDG), thereby likely affecting to a larger extent the soil water residence time in smaller catchments. Based on this observation, it is hypothesized that the influence of the change in runoff on soil water residence time, soil weathering processes and eventually riverine discharge and riverine chemistry will partly depend on the catchment size.

Note that other possible sources of Si have been identified during the snowmelt period in Arctic rivers such as Si leaching from the forest leaves/needles (Engström et al, 2008, 2010) or Si dissolved from river suspended load (Pokrovksy et al, 2013). Regarding a contribution from Si leaching from the forest leaves/needles, this cannot ruled out given that the YPVF is covered in forest (~80 %; Kokaly et al, 2003). However, based on a study of the Si cycling in a temperate forested granitic catchment with similar tree species (Cornelis et al, 2010; with granite being the equivalent intrusive magmatic rock composition to the extrusive rhyolite), it can be considered that the dissolution of phytoliths does not control the dissolved Si concentrations of the forest floor leachates. Indeed, the biogenic Si stock can be considered as low relative to the crystalized Si stock with minerals being incorporated into organic horizons by bioturbation, and the dissolved Si concentration in forest floor leachates is essentially controlled by mineral weathering (Cornelis et al, 2010). Regarding river suspended load, we have considered the contribution from that pool as negligible given that river ice is less important in YPVF than in the Arctic rivers, leading to less erosion of the river banks by ice blocks and so less-mineral-dominated suspended load to supply Si. Moreover, the river catchments in YPVF are smaller compared to large Arctic Rivers, so there is less transport time for in-river particle attachment and/or dissolution processes to occur.

6.6.3.2 Ge/Si mass balance calculation of contributions to rivers with boundary conditions fixed by Si isotopes

Based on **Fig. 6.5b** for Si, we hypothesize that at least one external source of water containing Si and Ge is contributing to the measured Ge/Si ratio in river waters in June. According to the increase in Si, Mg, K at snowmelt (**Fig. 6.5b**, **6.5c** and **6.5d**), we consider a contribution from a surface water influenced by rhyolite weathering and potentially also by secondary mineral formation (**section 6.6.3.2**). During snowmelt, fresh event waters fill in the rock and soil surface porosity resulting in the expulsion of pre-event surface water that was previously in contact with the rock/soil, influenced by rhyolite dissolution and/or secondary mineral formation, thereby contributing to riverine chemistry at snowmelt.

Here, we performed two scenarii taking into account the catchment size, the increase in riverine discharge at snowmelt, and the expected soil water residence time. We hypothesize that the water residence time in soils is

inversely correlated with the catchment size (based on section *6.6.3.1)*. In Scenario 1, the following hypothesis is tested: at snowmelt, rivers draining higher catchment size are affected by a contribution from a surface water mainly influenced by rhyolite weathering (primary mineral dissolution) due to a lower soil water time residence relative to catchments of lower size. In Scenario 2, we assume that, at snowmelt, rivers draining lower catchment size are affected by a contribution from a surface water influenced by primary mineral dissolution and by clay mineral formation, which was favored with higher soil water residence time relative to catchments of higher size.

We have the possibility to test the contributions of both rhyolite weathering and secondary mineral formation using Ge/Si ratio and Si isotopes for five rivers for which both Ge/Si ratios and silicon isotope data are available (BT, SDG, PEL, BCu, LT).

We use the following equation:

$$Ge/Si_{SM} = Ge/Si_{BF}.x + Ge/Si_{NW}.(1-x) \qquad \text{Eq. 1}$$

with Ge/Si_{SM} as the Ge/Si river water during snowmelt, Ge/Si_{BF} as the Ge/Si ratios of river water at base flow, Ge/Si_{NW} as the Ge/Si ratios of a new water source, x as the contribution of river water at base flow and (1-x) as the contribution of the new water. The hypothesis is that the new water is a combination of snow and the surface water influenced by rhyolite dissolution and/or secondary mineral formation (**Fig. 6.8b**). To calculate (1-x), the contribution of the new water, we can use the Ge/Si_{SM} and Ge/Si_{BF} measured in June and September, respectively, and an hypothesis has to be made on the value of Ge/Si_{NW}. This is why the two scenari (Scenario 1 and 2) are tested.

With Scenario 1, we tested the contribution of surface water affected only by primary mineral dissolution. Based on the literature, it can be anticipated that surface water controlled by the dissolution of a fresh volcanic rock ($\delta^{30}Si$ of rhyolite = -0.14 ± 0.16 ‰; Savage et al, 2011) would decrease the $\delta^{30}Si$ of the river. Based on **Fig 6.7b**, this scenario 1 can explain the lower $\delta^{30}Si$ observed at snowmelt than in base flow for BT, SDG, PEL. Therefore, to solve Eq. 1 for these three rivers, we posit that Ge/Si_{NW} = 2 $\mu mol.mol^{-1}$ to reflect the congruent dissolution of rhyolite

(Bernstein, 1985). The results (**Table 6.3**) indicate that at snowmelt the contribution to the river of surface water influenced by primary mineral dissolution ranges from 57% for SDG and 84% for PEL. This scenario cannot explain the Ge/Si ratio measured in June (at snowmelt) for BT, as a contribution >100% is predicted by the mixing model. At BT, the Ge/Si value measured in June (at snowmelt) is lower than predicted by a contribution from rhyolite dissolution. One hypothesis could be an additional contribution from the dissolution of amorphous silica precipitates. Low Ge/Si values can be expected for silica sinters based on the low Ge/Si values reported for silica precipitates (0.35-1.74 μmol.mol^{-1}) relative to their corresponding springs (2 - 1000 μmol.mol^{-1}; Evans and Derry, 2002) in a metamorphic context. And the formation of amorphous silica during the winter is reported in the YPVF as cryogenic opal-A deposition (Channing and Butler, 2007). Indeed, sub-zero winter temperatures on the YPVF favor the opal-A precipitation pathway of fluid erupting from hot springs. These opal-A particles can accumulate in and below water-ice and be remobilized and solubilized at snowmelt (Channing and Butler, 2007). BT is located on the west side of the lake close to the SE West Thumb Deep Vent field with a chemistry analogous to that producing siliceous deposits in subaerial YPVF Midway Geyser Basin (Fowler et al, 2019a, 2019b), as compared to PEL and SDG located further from that hydrothermal area. A more intense hydrothermal activity in the area of BT may partly contribute to favor cryogenic opal-A deposition in the area of BT.

With Scenario 2, we tested the contribution of surface water affected not only by primary mineral dissolution but also by clay mineral formation. Based on the literature, it can be anticipated that surface water influenced by clay mineral formation would be characterized by higher δ^{30}Si values relative to water not influenced by this process, and this can be attributed to the preferential incorporation of the light Si isotopes into secondary minerals during weathering (Opfergelt and Delmelle, 2012). Based on **Fig 6.7b**, this scenario 2 can explain the higher δ^{30}Si observed at snowmelt than in base flow for BCu and LT. This hypothesis is supported by the fact that BCu and LT can be considered as small drainage basins with a smaller increase in discharge between snowmelt and base flow relative to BT, SDG and PEL (**Supp. Mat. 6.2**): this likely contributes to favor a higher soil water residence time for clay mineral formation. Therefore, to solve Eq. 1 for these two rivers, we posit that Ge/Si_{NW} = 0.7 μmol.mol^{-1}, the value reported for soil solutions influenced by granite (i.e., the intrusive equivalent of rhyolite) weathering and secondary mineral formation (Lugolobi et al, 2010). The results (**Table 6.3**) indicate that at snowmelt

the contribution to the river of surface water influenced by primary mineral dissolution and clay mineral formation ranges between 29% for BCu and 63% for LT.

Overall, this Ge/Si mass balance calculation with boundary conditions fixed using Si isotopes supports that at snowmelt, these five rivers from YPVF receive a contribution from surface water that are influenced by (i) primary mineral dissolution at SDG and PEL, (ii) by primary mineral dissolution and likely by cryogenic opal-A solubilization at BT, and (iii) by both primary mineral dissolution and clay mineral formation at BCu and LT.

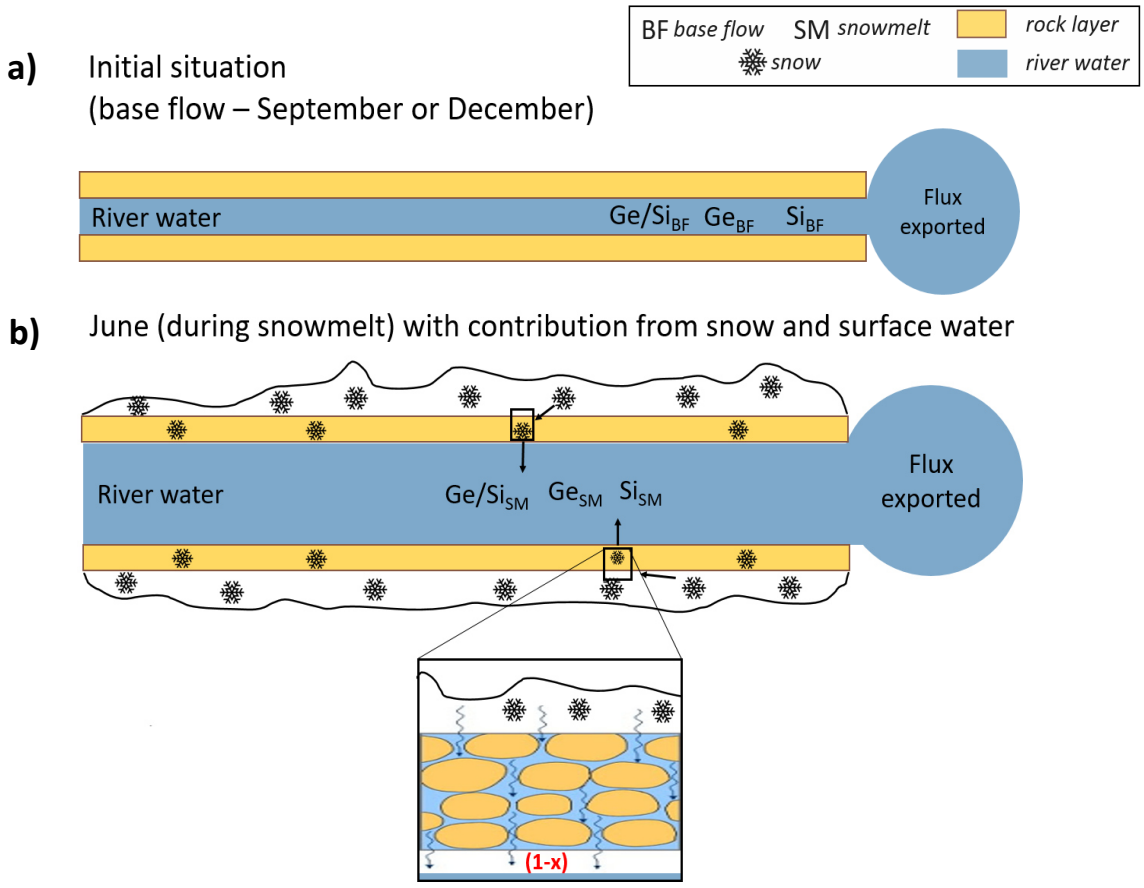

Fig. 6.8: Schematic showing a plan view of river waters and surrounding bedrock in Yellowstone Plateau Volcanic Field (YPVF) in (a) base flow conditions (BF), where river water discharge is low and $Ge/Si_{river} = Ge/Si_{BF} = Ge/Si$ measured in rivers collected in September to December, and in (b) high discharge conditions at snowmelt to depict the mixing of snowmelt waters (SM) with base flow waters (BF) with the additional contribution from surface waters (the term (1-x) corresponds to the contribution from surface waters in Eq. 1 (influenced by the dissolution of primary minerals and/or by clay mineral formation; see **section 6.6.3.2** for details).

Table 6.3: The results from the mixing model calculation using measured Ge/Si ratios, Si and Ge concentrations on 5 river waters flowing through Yellowstone Plateau Volcanic Field (YPVF) to assess the proportion of surface water contribution influenced by dissolution of primary minerals from rhyolite (Scenario 1) and influenced by clay mineral formation (Scenario 2). x = the contribution of river water at base flow and (1-x) = the contribution of the new water. The river base flow is defined in September (in blue) and provides a reference for the snowmelt period.

			Scenario 1		Scenario 2	
Label	Sampling date dd.mm.yy	Ge/Si µmol.mol^{-1}	x	(1-x)	x	(1-x)
BT	18.09.16	7.05				
	22.06.17	0.89	-0.22	1.22		
SDG	18.09.16	11.35				
	22.06.17	6.02	0.43	0.57		
PEL	18.09.16	8.95				
	22.06.17	3.12	0.16	0.84		
BCu	18.09.16	2.64				
	22.06.17	2.08			0.71	0.29
LT	18.09.16	1.47				
	22.06.17	0.99			0.37	0.63

6.6.4 Influence of runoff variation on chemical weathering fluxes from YPVF

The quantification from **section 6.6.3** demonstrates that the seasonal variability in runoff induced by snowmelt adds pulses of Si derived from meteoric weathering processes (up to 84%) to riverine Si fluxes generally dominated by hydrothermal contribution. Even if these pulses are limited in time, they directly contribute to atmospheric CO_2 consumption. Few studies have shown a positive correlation between riverine discharge and element flux from volcanic regions (Ingebritsen et al, 2001; Friedman and Norton, 2007; Hurwitz et al, 2007). But the seasonal changes in processes controlling these fluxes and the associated atmospheric CO_2 consumption are generally unaccounted for.

Here, we evaluate how changing riverine discharge affect riverine weathering fluxes, by comparing the chemical weathering rates (CWR, $t.km^{-2}.yr^{-1}$) calculated on a seasonal and on an annual basis in this hydrothermally-active volcanic region of YPVF. More precisely, we calculated the CWR in twelve river waters flowing through YPVF using SiO_2, Na, K, Mg, Ca concentrations (**Table 6.1**), the riverine discharges (**Suppl. Mat. 6.2**), and the specific draining surface area (USGS, 2007). Three scenarios were performed (**Fig. 6.9a**): (i) "base flow conditions" (BF) considering data in September, (ii) "snowmelt conditions" (SM) based on data in June, then (iii) CWR were extrapolated on an annual basis averaging "base flow conditions" (eleven $months.yr^{-1}$) and "snowmelt conditions" (one $month.yr^{-1}$) (ANN), based on the discharge database reported by NWIS (2019).

Our data show distinct CWR values between "base flow conditions" (0.9-91 $t.km^{-2}.yr^{-1}$) and "snowmelt conditions" (0.3-1106 $t.km^{-2}.yr^{-1}$) depending of riverine total dissolved species and discharges variation after seasonal snowmelt (**Fig. 6.9b**). The highest value of CWR is obtained for YELo under "snowmelt conditions" (1106 $t.km^{-2}.yr^{-1}$). Compared to the CWR values reported for four rivers from the YPVF (YELo, GAR, GIB, FIR; **Fig. 6.9b**; Hurwitz et al, 2010), the CWR value calculated here on an annual basis is higher for YELo, similar for GAR and GIB, and lower for FIR. Our hypothesis of one month for snowmelt conditions was a first order estimate, and should be refined in the future to be closer to the exact field conditions.

More specifically, our calculations highlight that during snowmelt, if the riverine dilution factor ($f = D_{SM}/D_{BF}$) is higher than the enrichment factor ("E", $E = TDS_{BF}/TDS_{SM}$), CWR values at snowmelt are between 6.9 and 1323% higher than in base flow (for ARC, SDG, YELo, FAL, GAR, GIB: values in SM = 10, 18.5, 1106, 36, 89 and 31 $t.km^{-2}.yr^{-1}$, and values in BF = 4.8, 1.3, 89, 23, 34 and 29 $t.km^{-2}.yr^{-1}$, respectively; **Fig. 6.9a**). Inversely, if $f < E$, the CWR under "base flow conditions" is higher than CWR under "snowmelt conditions" as observed in BCu, LT, BT, PEL, FIR and MAD (**Fig. 6.9b**). Even if limited in duration, pulses of increasing CWR at snowmelt directly control estimates of CWR on an annual basis (**Fig 6.9a**).

The CWR calculated here for the YPVF rivers (except for the YELo) are (i) lower than values of CWR reported for andesite volcanic islands (Martinique and Guadeloupe: 100-120 $t.km^{-2}.yr^{-1}$; Rad et al, 2006), (ii) in the same range or lower than the CWR values reported for basaltic volcanic islands (Iceland: 19-146 $t.km^{-2}.yr^{-1}$, Stefánsson and Gislason,

2001; La Réunion: 63-170 $t.km^{-2}.yr^{-1}$, Louvat and Allègre, 1997), and (iii) higher than the CWR values reported for the andesite volcanic arc of Kamchatka (21 $t.km^{-2}.yr^{-1}$; Dessert et al, 2009). However, direct comparison of CWR values must be considered with caution given that the calculated fluxes of solutes were obtained by different methods that integrate the seasonal variability at different temporal resolutions (Hurwitz et al, 2010).

We confirm that seasonal runoff variability in hydrothermally-active volcanic regions may significantly influence the CWR depending of riverine discharge and total dissolved species transported by rivers under contrasted flow regime. We raise that (i) the CWR from these regions generally assessed by extrapolation of instantaneous riverine dissolved compositions and discharges could be improved by considering the influence of f and E on CWR annual values, and (ii) the estimates of the associated atmospheric CO_2 consumption should consider that even if limited in duration, short pulses from meteoric weathering processes may contribute to riverine weathering fluxes at snowmelt, relative to annual fluxes dominated by hydrothermal contributions.

Importantly, these short pulses of changes in processes controlling weathering fluxes may be amplified in the future given that runoff variability is predicted to increasingly affect dissolved riverine chemistry based on the projected changes in precipitation with ongoing climate change (IPCC, 2013). At YPVF, a better assessment of the impact of snowmelt on future riverine discharge (duration, amplitude) would be needed to increase the accuracy of the estimates of annual chemical weathering fluxes and of the changes in the relative contribution between hydrothermal and meteoric contributions.

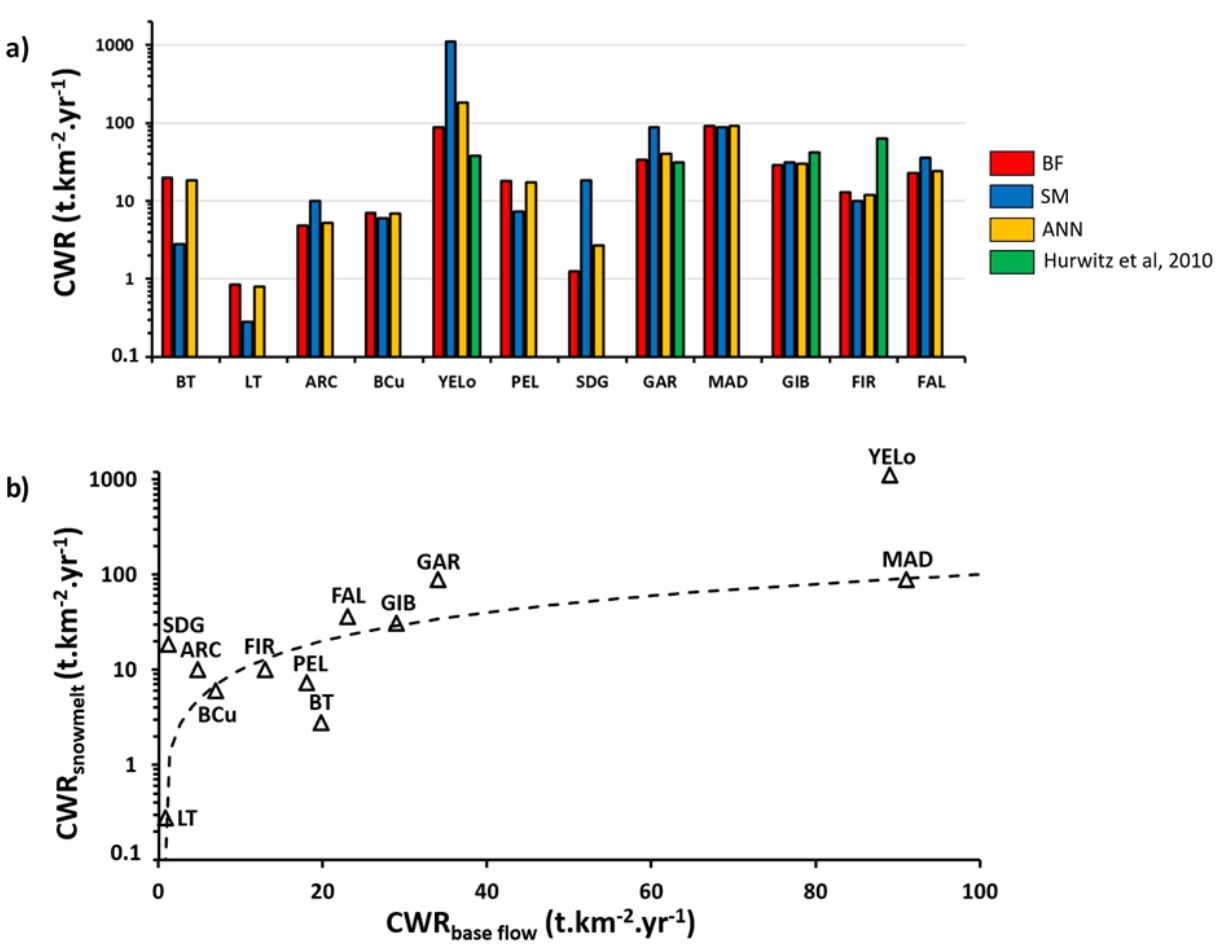

Fig. 6.9: Chemical weathering rates (CWR, $t.km^{-2}.yr^{-1}$) on river waters flowing through Yellowstone Plateau Volcanic Field (YPVF) using riverine discharge at base flow (BW), during snowmelt (SM), estimated on an annual basis (ANN) and compared with data presented by Hurwitz et al (2010) (see **section 6.6.4**). The river codes are explained in **Table 6.1**.

6.7 Conclusion

We determined the Ge/Si ratios and $\delta^{30}Si$ of 7 thermal springs and 14 rivers collected at base flow and at high discharge (during snowmelt) through the Yellowstone Plateau Volcanic Field to investigate changing controls on riverine chemistry with runoff. The main conclusions that can be drawn from this study are the following:

(i) Elevated riverine Ge/Si ratios (29 ± 3 μmol.mol^{-1}) at base flow can be explained by a dominant contribution from thermal springs (160 ± 27 μmol.mol^{-1}) to rivers.

(ii) At snowmelt, decreasing Ge/Si ratios in rivers and increasing dilution-corrected Si concentrations ($Si/Na_{snowmelt} > Si/Na_{base\ flow}$) suggest an additional Si contribution to rivers in Spring.

(iii) The riverine Si isotope data indicate that higher surface runoff at snowmelt may release surface water mainly influenced by (a) dissolution of primary minerals from rhyolite ($\delta^{30}Si_{snowmelt} < \delta^{30}Si_{base\ flow}$) in large drainage basins, or by (b) dissolution of primary minerals and clay mineral formation ($\delta^{30}Si_{snowmelt} > \delta^{30}Si_{base\ flow}$) in smaller drainage basins.

(iv) This study highlights that the relative contributions of hydrothermal and meteoric processes controlling weathering fluxes in YPVF vary as a function of runoff. The seasonal meteoric weathering signal should be accounted for in estimates of weathering fluxes from hydrothermally-active volcanic regions, as it directly contributes to atmospheric CO_2 consumption.

6.8 References

Abraham, K., Opfergelt, S., Fripiat, F., Cavagna, A-J., de Jong, J., Foley, S.F., André, L., Cardinal, D., 2008. δ^{30}Si and δ^{29}Si determinations on USGS BHVO-1 and BHVO-2 reference materials with a new configuration on a Nu Plasma Multi-Collector ICP-MS. Geostand. Geoanal. Res. 32(2), 193-202.

Alexander, G.B., Heston, W.M., Iler, R.K., 1954. The solubility of amorphous silica in water. J. Phys. Chem. 58, 453–455.

Ameijeiras-Mariño, Y., Opfergelt, S., Derry, L.A., Robinet, J., Govers, G., Minella, J.P., Delmelle, P., 2018. Ge/Si ratios point to increased contribution from deeper mineral weathering to streams after forest conversion to cropland. Appl. Geochem. 96, 24–34.

Arnòrsson, S., 1983. Chemical equilibria in Icelandic geothermal systems. Geothermics 12, 119-128.

Arnòrsson, S., 1987. Germanium in Icelandic geothermal systems. Geochim. Cosmochim. Ac. 48, 2489-2502.

Bargar, K.E., 1978. Geology and thermal history of Mammoth Hot Springs, Yellowstone National Park, Wyoming. Geological Survey Bulletin.

Baronas, J.J., Torres, M.A., West, A.J., Rouxel, O., Georg, B., Bouchez, J., Gaillardet, J., Hammond, D.E., 2018. Earth Planet. Sci. 503, 194-215.

Baronas, J.J, West, A.J., Burton, K.W., Hammond, D.E., Opfergelt, S., Pogge von Strandmann, P.A.E., James, R.H., Rouxel, O.J., 2020. Ge and Si isotopes behaviour during intense tropical weathering. Global Biogeochem. Cy. doi:10.1029/2019gb006522.

Bernstein, L.R., 1985. Germanium geochemistry and mineralogy. Geochim. Cosmochim. Ac. 49, 2409–2422.

Bobrow, D.J., Kyle, P.R., Osburn, G.R., 1983. Miocene rhyolitic volcanism in the Socorro Area of New Mexico. In C.E. Chapin (Ed.) Socorro Region II, New Mexico Geological Society 34th Annual Field Conference. 211-218.

Cardinal, D., Alleman, L.Y., De Jong, J., Ziegler, K., André, L., 2003. Isotopic composition
of silicon measured by multicollector plasma source mass spectrometry in dry plasma
mode. J. Anal. Atom. Spectrom. 18, 213–218.

Channing, A., Butler, I.B., 2007. Cryogenic opal-A deposition from Yellowstone hot springs. Earth. Planet. Sc. Lett. 257, 121-131.

Chen, X-Y., Chafetz, H.S., Lapen, T.J., 2020. Silicon isotope variations in hydrothermal systems at Yellowstone National Park, Wyoming, USA. Geochim. Cosmochim. Ac. 283, 184-200.

Christiansen, R.I., 2001. The Quaternary and Pliocene Yellowstone Plateau volcanic field of Wyoming, Idaho, and Montana. U.S. Geological Survey Professional Paper P0729-G, 1-145.

Cornelis, J.-T., Delvaux, B., Cardinal, D., André, L., Ranger, J., Opfergelt, S., 2010. Tracing mechanisms controlling the release of dissolved silicon in forest soil solutions using Si isotopes and Ge/Si ratios. Geochim. Cosmochim. Ac. 74, 3913–3924.

Cornelis, J-T., Delvaux, B., Georg, R.B., Lucas, Y., Ranger, J., Opfergelt, S., 2011. Tracing the origin of dissolved silicon transferred from various soil-plant systems towards rivers: a review. Biogeosciences 8, 89-112.

De La Rocha, C.L., Brzezinski, M.A., DeNiro, M.J., 1997. Fractionation of silicon isotopes by marine diatoms during biogenic silica formation. Geochim. Cosmochim. Ac. 61, 5051–5056.

Derry, L.A., Kurtz, A.C., Ziegler, K., Chadwick, O.A., 2005. Biological control of terrestrial silica cycling and export fluxes to watersheds. Lett. Nature 433, 728–731.

Despain, D., 1987. The climate of Yellowstone National Park. Proceedings of the Montana Academy of Science 47, 11-19.

Dessert, C., Gaillardet, J., Dupré, B., Schott, J., Pokrovsky, O.S., 2009. Fluxes of high-versus low-temperature water-rock interactions in aerial volcanic areas: Example from the Kamchatka Peninsula, Russia. Geochim. Cosmochim. Ac. 73, 148–169.

Ding, T.P., Jiang, S., Li, Y., Gao, J., Hu, B., 2017. Geochemistry of silicon isotopes.

Douthitt, C.B., 1982. The geochemistry of the stable isotopes of silicon. Geochim. Cosmochim. Ac. 46, 1449–1458.

Dupré, B., Dessert, C., Oliva, P., Goddéris, Y., Viers, J., François, L., Gaillardet, J., 2003. Rivers, chemical weathering and Earth's climate. Geoscience. 335, 1141-1160.

Engström, E., Rodushkin, I., Öhlander, B., Ingri, J., Baxter, D.C., 2008. Silicon isotopic composition of boreal forest vegetation in Northen Sweden. Chem. Geol. 257, 247-256.

Engström, E., Rodushkin, I., Ingri, J., Baxter, D.C., Ecke, F., Österlund, H., Öhlander, B., 2010. Temporal isotopic variations of dissolved silicon in a pristine boreal river. Chem. Geol. 271, 142-152.

Escoube, R., Rouxel, O.J., Edwards, K., Glazer, B., Donard, O.F.X., 2015. Coupled Ge/Si and Ge isotope ratios as geochemical tracers of seafloor hydrothermal systems: Case studies at Loihi Seamount and East Pacific Rise 9°50'N. Geochim. Cosmochim. Ac. 167, 93-112.

Evans, M.J., Derry, L.A., 2002. Quartz control of high germanium/silicon ratios in geothermal waters. Geology 30, 1019–1022.

Fournier, R.O., Rowe, J.J., 1977. The solubility of amorphous silica in water at high temperatures and high pressures. Am. Mineral. 62, 1052-1056.

Fournier, R.O., 1989. Geochemistry and dynamics of the Yellowstone National Park hydrothermal system. Annu. Rev. Earth Planet. Sci. 17, 13–53.

Fowler, A.P.G., Tan, C., Cino, C., Scheuermann, P., Volk, M.W.R., Shanks, P.S., Seyfried, W.E., 2019a. Vapor-driven sublacustrine vents in Yellowstone Lake, Wyoming, USA. Geology 47, 223-226.

Fowler, A.P.G., Chunyang, T., Luttrel, K., Tudor, A., Scheuermann, P., Shanks III, W.C.P., Seyfried Jr., W.E.S., 2019b. Geochemical heterogeneity of sublacustrine hydrothermal vents in Yellowstone Lake, Wyoming. J. Volcano. Geoth. Res. 386, 106677.

Friedman, I., Norton, D.R., 2007. Is Yellowstone losing its steam? Chloride flux out of Yellowstone National Park. In: Morgan, L.A. (Ed.), Integrated Geoscience Studies in the Greater Yellowstone Area: Volcanic, Hydrothermal and Tectonic Processes in the Yellowstone Geoecosystem: U.S. Geological Survey Professional Paper, 1717, 274-297.

Frings, P.J., Clymans, W., Fontorbe, G., De La Rocha, C.L., Conley, D.J., 2016. The continental Si cycle and its impact on the ocean Si isotope budget. Chem. Geol. 425, 12-36.

Gaillardet, J., Dupré, B., Louvat, P., Allègre, C.J., 1999. Global silicate weathering and CO_2 consumption rates deduced from the chemistry of large rivers. Chem. Geol. 159, 3-30.

Gaillardet, J., Rad, S., Rivé, K., Louvat, P., Gorge, C., Allègre, C-J., Lajeunesse, E., 2011. Orography-driven chemical denudation in the Lesser Antilles : Evidence for a new feed-back mechanism stabilizing atmospheric CO_2. Am. J. Sci. 311, 851-894.

Gaspard, F., Opfergelt, S., Dessert, C., Robert, V., Ameijeras-Marino, Y., Delmelle, P. Imprint of chemical weathering and hydrothermalism on the Ge/Si ratio and Si isotopic composition of rivers in a volcanic tropical island, Basse-Terre, Guadeloupe (French West Indies). Submitted to Chem. Geol.

Geilert, S., Vroon, P.Z., Keller, N., Gudbrandsson, S., Stefànsson, A., Van Bergen, M.J., 2014. Silicon isotope fractionation during silica precipitation from hot springs waters, Geophys. Res. Abstract EGU 2014: EGU2014-7951.

Geilert, S., Vroon, P.Z., Keller, N., Gudbrandsson, S., Stefànsson, A., Van Bergen, M.J., 2015. Silicon isotope fractionation during silica precipitation from hot-springs waters: evidence from the Geysir geothermal field, Iceland. Geoch. Cosmochim. Acta 164, 403-427.

Giggenbach, W.F., 1988. Geothermal solute equilibria. Derivation of Na-K-Mg-Ca geoindicators. Geochim. Cosmochim. Ac. 52, 2749-2765.

Gislason, S. R., Oelkers, E. H., 2011. Silicate rock weathering and the global carbon cycle, in Harmon, R. S., and Parker, A., editors, Frontiers in Geochemistry: Contribution of Geochemistry to the Study of the Earth: Chichester, United Kingdom, Wiley-Blackwell, 84–103.

Hayden, F.V., 1878. Survey of the territories—A report of progress of the exploration in Wyoming and Idaho for the year 1878, Part II: Yellowstone National Park: Geology, thermal springs,

topography: U.S. Geological and Geographical Survey Annual Report 12, 503.

Hurwitz, S., Lowenstern, J.B., Heasler, H., 2007. Spatial and temporal geochemical trends in the hydrothermal system of Yellowstone National Park: Inferences from river solute fluxes. J. Volcanol. Geoth. Res. 162, 149-171.

Hurwitz, S., Evans, W.C., Lowenstern, J.B., 2010. River solute fluxes reflecting active hydrothermal chemical weathering of the Yellowstone Plateau Volcanic Field, USA. Chem. Geol. 276, 331-343.

Hurwitz, S., Lowenstern, J.B., 2014. Dynamics of the Yellowstone hydrothermal system. Reviews of Geophysics. American Geophysical Union. AGU Publications.

Hurwitz, S., McCleskey, R.B., Bergfeld, D., Peek, S.E., Susong, D.D., Roth, D.A., Hungerford, J.D.G., White, E.B., Harrison, L.N., Hosseini, B., Vaughan, R.G., Hunt, A.G., Paces, J.B., 2020. Hydrothermal activity in the southern Yellowstone Plateau Volcanic Field. Geochemistry, Geophysics, Geosystems. 21, e2019GC008848.

Ingebritsen, S.E., Galloway, D.L., Colvard, E.M., Sorey, M.L., Mariner, R.H., 2001. Time-variation of hydrothermal discharge at selected sites in the western United States: implications for monitoring. J. Volcanol. Geotherm. Res. 111, 1-23.

Interlandi, S.J., Kilham, S.S., Theriot, E.C., 2003. Diatom-chemistry in Yellowstone Lake (Wyoming) sediments: Implications for climatic and aquatic processes research. Limnol. Oceanogr. 48, 79-92.

Kharaka, Y.K., Thordsen, J.J., White, L.D., 2002. Isotope and chemical compositions of meteoric and thermal waters and snow from the greater Yellowstone National Park Regions. U.S. Geological Survey Open-File Report 02-194, 75.

Kokaly, R.F., Despain, D.G., Clark, R.N., Livo, K.E., 2003. Mapping vegetation in Yellowstone National Park using spectral feature analysis of AVIRIS data. Remote Sens. Environ. 84, 437-456.

Liu, L., Stegman, R., 2012. Origin of Columbia River flood basalt controlled by propagating rupture of the Farallon slab. Nature, 482, 386-389.

Lloret, E., Dessert, C., Gaillardet, J., Albéric, P., Crispi, O., Chaduteau, C., Benedetti, M., 2011. Comparison of dissolved inorganic and organic carbon yields and fluxes in the watersheds of tropical volcanic islands, examples from Guadeloupe (French West Indies). Chem. Geol. 280, 65–78.

Louvat, P., Allègre, C.J., 1997. Present day denudation rates of the island of Reunion determined by river geochemistry: basalt weathering and mass budgets between chemical and mechanical erosions. Geochim. Cosmochim. Ac. 61, 3645–3669.

Lowenstern, J.B., Smith, R.B., Hill, D.P., 2006. Monitoring super-volcanoes: geophysical and geochemical signals at Yellowstone and other caldera system. Philos. T. Roy. Soc. 264, 2055-2072.

Lugolobi, F., Kurtz, A.C., Derry, L.A., 2010. Germanium–Silicon fractionation in a tropical,
granitic weathering environment. Geochim. Cosmochim. Ac. 74, 1294–1308.

McCleskey, R.B., Nordstrom, D.K., Susong, D.D., Ball, J.W., Holloway, J.M., 2010a. Source and fate of inorganic solutes in the Gibbon River, Yellowstone National Park, Wyoming, USA: I. Low-flow discharge and major solute chemistry. J. Volcanol. Geotherm. Res. 193, 189-202.

McCleskey, R.B., Nordstrom, D.K., Susong, D.D., Ball, J.W., Taylor, H.E., 2010b. Source and fate of inorganic solutes in the Gibbon River, Yellowstone National Park, Wyoming, USA. II. Trace element chemistry. J. Volcanol. Geotherm. Res. 196, 139-155.

McCleskey, R.B., Clor, L.E., Lowenstern, J.B., Evans, W.C., Nordstrom, D.K., Heasler, H., Huebner, M.A., 2012. Solute and geothermal flux monitoring using electrical conductivity in the Madison, Firehole, and Gibbon rivers, Yellowstone National park. Appl. Geochem. 27, 2370–2381.

McCleskey, R.B., Lowenstern, J.B., Schaper, J., Nordstrom, D.K., Heasler, H.P., Mahony, D., 2016. Geothermal flux monitoring and the source and fate of solutes in the Snake River, Yellowstone National Park, WY. Appl. Geochem. 73, 142-156.

McCleskey, R.B., Roth, D.A., Mahony, D., Nordstrom, D.K., Kinsey, S., 2019. Sources, fate, and flux of geothermal solutes in the Yellowstone and Gardner Rivers, Yellowstone National Park, WY. Appl. Geochem. 111. p.104458.

Miller, W.R., Drever, J.I., 1977. Chemical weathering and related controls on surface water chemistry in the Absaroka Mountains, Wyoming. Geochim. Cosmochim. Ac. 41, 1693-1702.

National Park Service, 2020. Weather. https://www.nps.gov/yell/planyourvisit/weather.htm.

Newhall, C.G., Dzurisin, D., 1988. Historical unrest at large calderas of the world. U.S. Geol. Surv. Bull. 1855 (1108 pp.).

NWIS, 2019. National Water Information System. USGS Water-Quality Data for the Nation.

Opfergelt, S., Eiriksdottir, E.S., Burton, K.W., Einarsson, A., Siebert, C., Gislason, S.R., Halliday, A.N., 2011. Quantifying the impact of freshwater diatom productivity on silicon isotopes and silicon fluxes: Lake Myvatn, Iceland. Earth. Planet. Sc. Lett. 305, 73-82.

Opfergelt, S., Delmelle, P., 2012. Silicon isotopes and continental weathering processes: Assessing controls on Si transfer to the ocean. Comptes Rendus Geosci. 344, 723–738.

Pierce, K.L., Adams, K.D., Sturchio, N.C., 1991. Geologic setting of the Corwin Springs known geothermal resources area mammoth hot springs area in and adjacent to Yellowstone National Park. In: Sorey, M.L. (Ed.), Effects of Potential Geothermal Development in the Corwin Springs Known Geothermal Resources Area, Montana, on the thermal features of Yellowstone National Park. U.S. Geol. Surv. Water Res. Invest. Rep. 91-4052, pp. C1–C37.

Pokrovsky, O.S., Reynolds, B.C., Prokushkin, A.S., Schott, J., Viers, J., 2013. Silicon isotope variations in Central Siberian rivers during basalt weathering in permafrost-dominated larch forests. Chem. Geol. 355, 103-116.

Rad, S., Louvat, P., Gorge, C., Gaillardet, J., Allègre, C.J., 2006. River dissolved and solid loads in the Lesser Antilles: new insight into basalt weathering processes. J. Geoch. Explor. 88, 308-312.

Ragueneau, O., Savoye, N., Del Amo, Y., Cotten, J., Tardiveau, B., Leynaert, A., 2005. A new method for the measurement of biogenic silica in suspended matter of coastal waters: using Si:Al ratios to correct for the mineral interference. Cont. Shelf Res. 25, 697–710.

Reynolds, B.C., Aggarwal, J., André, L., Baxter, D., Beucher, C., Brzezinski, M.A., Engström, E., Georg, B., Land, M., Leng, M.J., Opfergelt, S., Rodushkin, I., Sloane, H.J., Van den Boorn, S.H.J.M., Vroon, P.Z., Cardinal, D., 2007. An inter-laboratory comparison of Si isotope reference materials. J. Anal. Atom. Spectrom. 22, 561-568.

Rivé, K., Gaillardet, J., Agrinier, P., Rad, S., 2013. Carbon isotopes in the rivers from the Lesser Antilles: origin of the carbonic acid consumed by weathering reactions in the Lesser Antilles. Earth Surf. Proc. Land. 38, 1020–1035.

Rodman, A., Shovic, H., Thoma, D., 1996. Yellowstone Center for Resources, YNP, Wyoming, YCR-NRSR-96-2.

Rowe, G.L., Brantley, S.L., Fernandez, M., Fernandez, J.F., Borgia, A., Barquero, J., 1992. Fluid-volcano interaction in an active stratovolcano: the volcanic lake system of Poa´s Volcano, Costa Rica. J. Volcanol. Geotherm. Res. 49, 23–51.

Savage, P.S., Georg, R.B., Williams, H.M., Burton, K.W., Halliday, A.N., 2011. Silicon isotope fractionation during magma differentiation. Geochim. Cosmochim. Ac. 75, 6124-6139.

Sieber, C., Ross, A., McManus, J., 2006. Germanium isotope measurements of high-temperature geothermal fluids using double-spike hydride generation MC-ICP-MS. Geochim. Cosmochim. Acta 70, 3986-3995.

Schopka, H. H., Derry, L. A., Arcilla, C. A., 2011. Chemical weathering, river geochemistry and atmospheric carbon fluxes from volcanic and ultramafic regions on Luzon Island, the Philippines. Geochim. Cosmochim. Ac. 75, 978–1002.

Scribner, A.M., Kurtz, A.C., Chadwick, O.A., 2006. Germanium sequestration by soil: targeting the roles of secondary clays and Fe-oxyhydroxides, Earth and Plan. Sc. 243, 760-770.

Smith, B., Siegel, L.J., 2000. Windows into the Earth - The Geologic Story of Yellowstone and Grand Teton National Parks, 242.

Stefánsson, A., Gislason, S.R., 2001. Chemical weathering of basalts, southwest Iceland: effect of rock crystallinity and secondary minerals on chemical fluxes to ocean. J. Am. Sci. 301, 513-556.Trettin, C.C., Bartelli, L.J., 1980. Characterization of Soils in Yellowstone National Park. Annual Reports of Wyoming University. 4,22.

United Kingdom Accreditation Body (UKAS)., 2014. Certificate of measurement, river water-anion, certified reference material LGC6025. 4005.

USGS, 2007. Integrated Geoscience Studies in the Greater Yellowstone Area – Volcanic, Tectonic, and Hydrothermal Processes in the Yellowstone Geoecosystem. Professional Paper 1717.

Wheat, C., McManus, J., 2008. Germanium in mid-ocean ridge flank hydrothermal fluids. Geochem. 9: Q03025.

White, A.F., Blum, A.E., 1995. Effects of climate on chemical weathering in watersheds. Geochim. Cosmochim. Ac. 59, 1729-1747.

Yeghicheyan, D., Bossy, C., Bouhnik Le Coz, M., Douchet, C., Granier, G., Heimburger, A., Lacan, F., Lanzanova, A., Rousseau, T.C.C., Seidel, J-L., Tharaud, M., Candaudap, F., Chmeleff, J., Cloquet, C., Delpoux, S., Labatut, M., Losno, R., Pradoux, C., Sivry, Y., Sonke, J.E., 2013. A Compilation of Silicon, Rare Earth Element and Twenty-One other Trace Element Concentrations in the Natural River Water Reference Material SLRS-5 (NRC-CNRC). Geostand. Geoanal. Res. 37(4), 449-467.

Young, E.D., Galy, A., Nagahara, H., 2002. Kinetic and equilibrium mass-dependent isotope fractionation laws in nature and their geochemical and cosmochemical significance. Geochim. Cosmochim. Ac. 66, 1095-1104.

Zelt, R.B., Boughton, G., Miller, K.A., Mason, J.P., Gianakos, L.M., 1998. Environmental settings of the Yellowstone River Basin, Montana, North Dakota, and Wyowing, U.S. Geological Survey Water Resources Investigation Report 98-4269.

6.9 Supplementary Materials

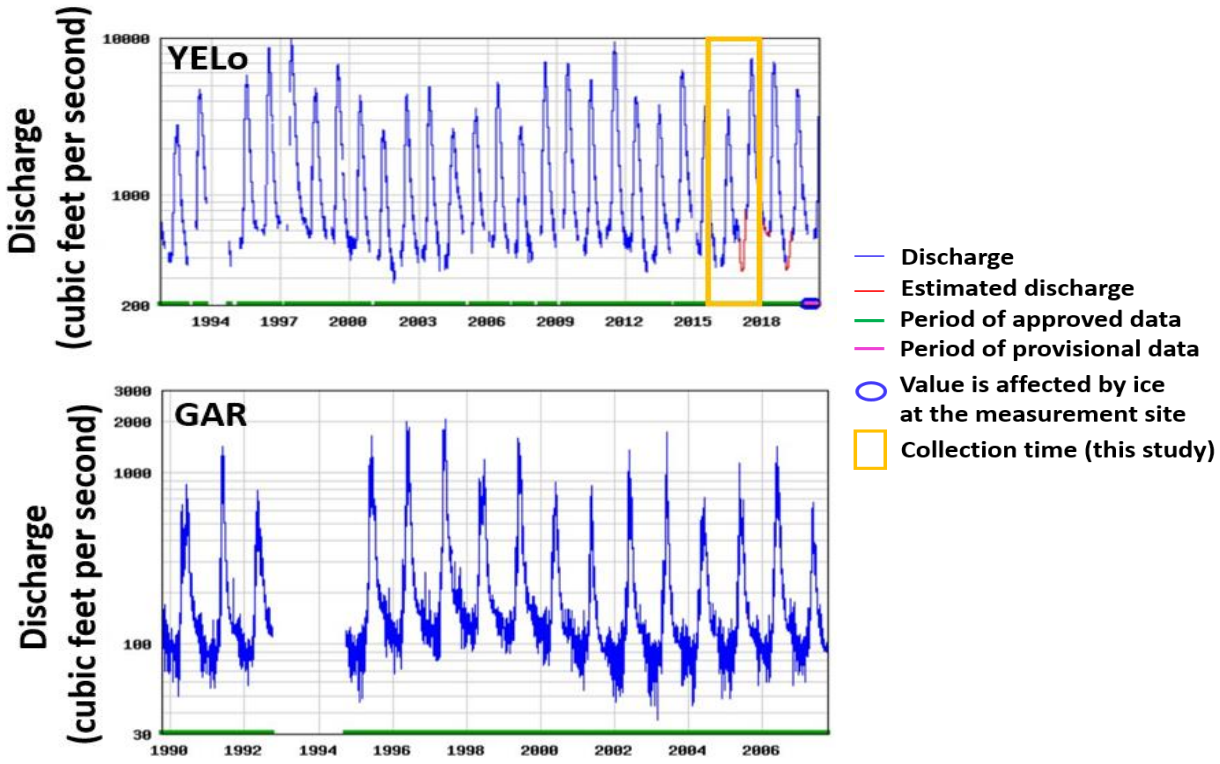

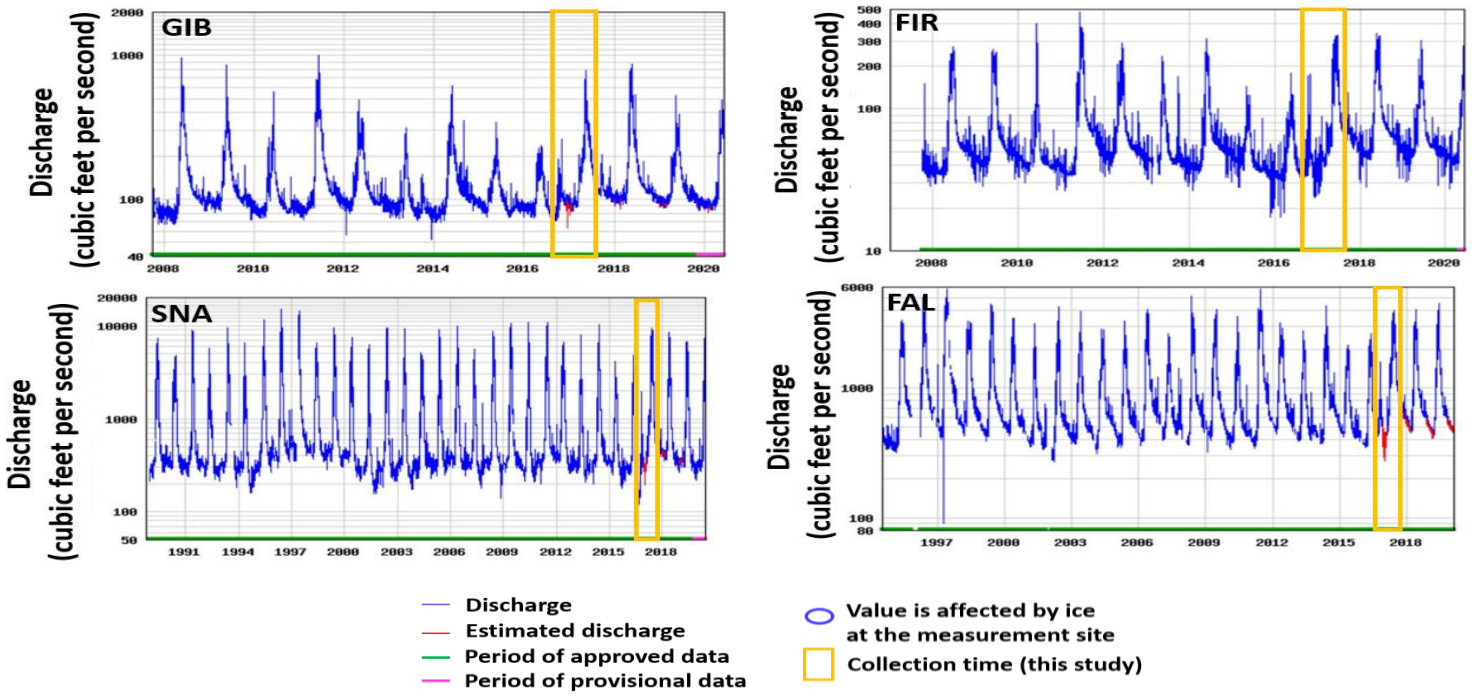

Suppl. Mat. 6.1: Discharge (cubic feet per second) of six river waters flowing through YPVF (YELo, GAR, GIB, FIR, SNA, FAL) monitored by USGS on long term period (~30 years). Data are from the USGS database (NWIS, 2019). The sampling period of these rivers in this study is indicated (yellow square), except for GAR for which the sampling period is outside the recording period.

Suppl. Mat. 6.2: Discharge ($m^3.s^{-1}$) during snowmelt (June) as a function of discharge at base flow (September) in river waters flowing through YPVF, and draining area of each river catchment for which discharge data are available. The data are from the USGS database (NWIS, 2019) on the sampling day at the sampling point of collection. BF = base flow; SM = snowmelt.

River	draining area	Discharge BF	Discharge SM	Increase in discharge*
	km^2	$m^3.s^{-1}$	$m^3.s^{-1}$	
BT	26	0.01	0.1	13.0
LT	15	0.01	0.0	1.3
ARC	60	0.10	0.3	3.0
BCu	23	0.04	0.1	2.5
YELo	179	15.60	204.4	13.1
PEL	250	1.30	3.0	2.3
SDG	60	0.03	1.0	33.3
GAR	520	4.00	31.1	7.8
MAD	1088	16.90	27.4	1.6
GIB	793	4.20	8.4	1.9
FIR	1891	11.90	18.6	1.6
FAL	2354	24.10	96.1	4.0

*Increase in discharge at snowmelt standardized to catchment size

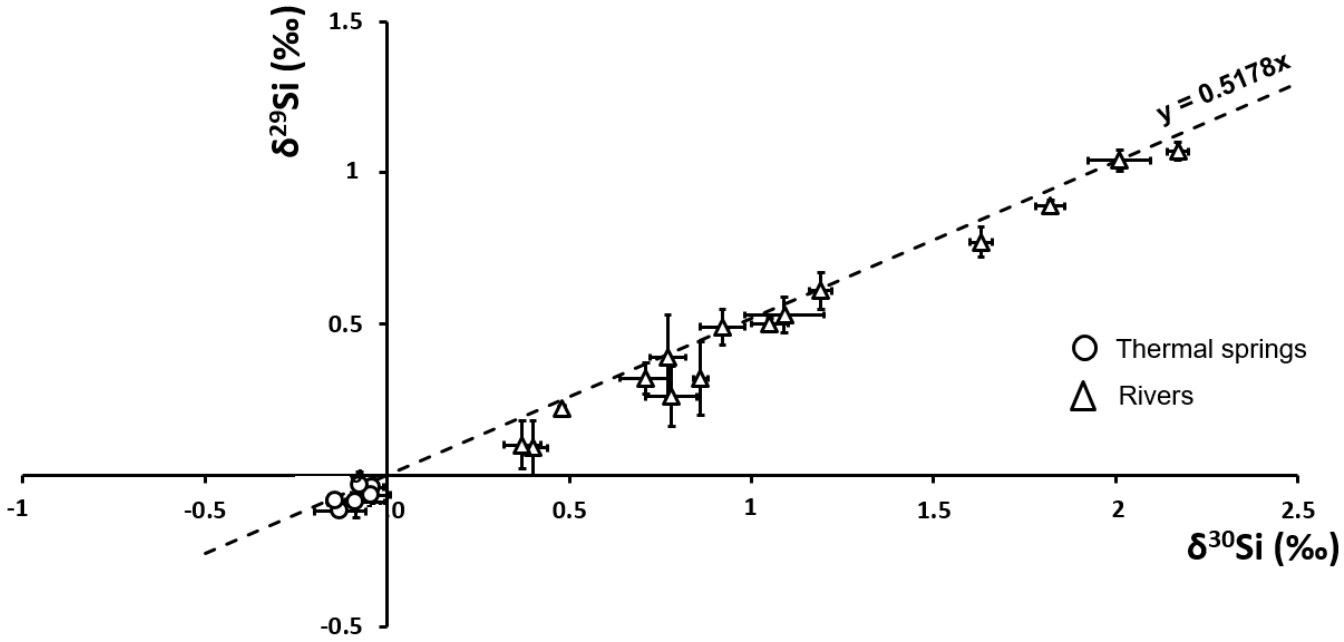

Suppl. Mat 6.3: Silicon isotope measurements of all samples fit onto a mass-dependent fractionation array $\delta^{30}Si$ and $\delta^{29}Si$ (theorical 0.5178 slope for equilibrium mass-dependent fractionation; Young et al, 2002).

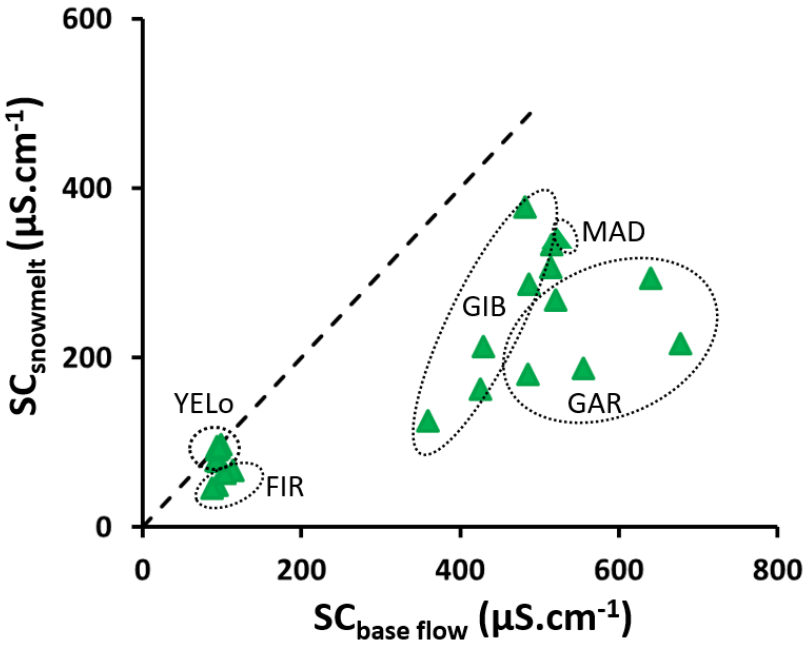

Suppl. Mat. 6.4: Plot of the specific conductivity (SC) in high discharge as a function of the SC in base flow based on long term-monitoring on five rivers from the YPVF: FIR from 2009 to 2013, GAR from 2009 to 2012, GIB from 2008 to 2013, MAD for 2012, YELo from 2009 to 2012. Sample names as in **Table 6.1**. Data from McCleskey et al, 2010a, 2010b, 2012, and 2016.

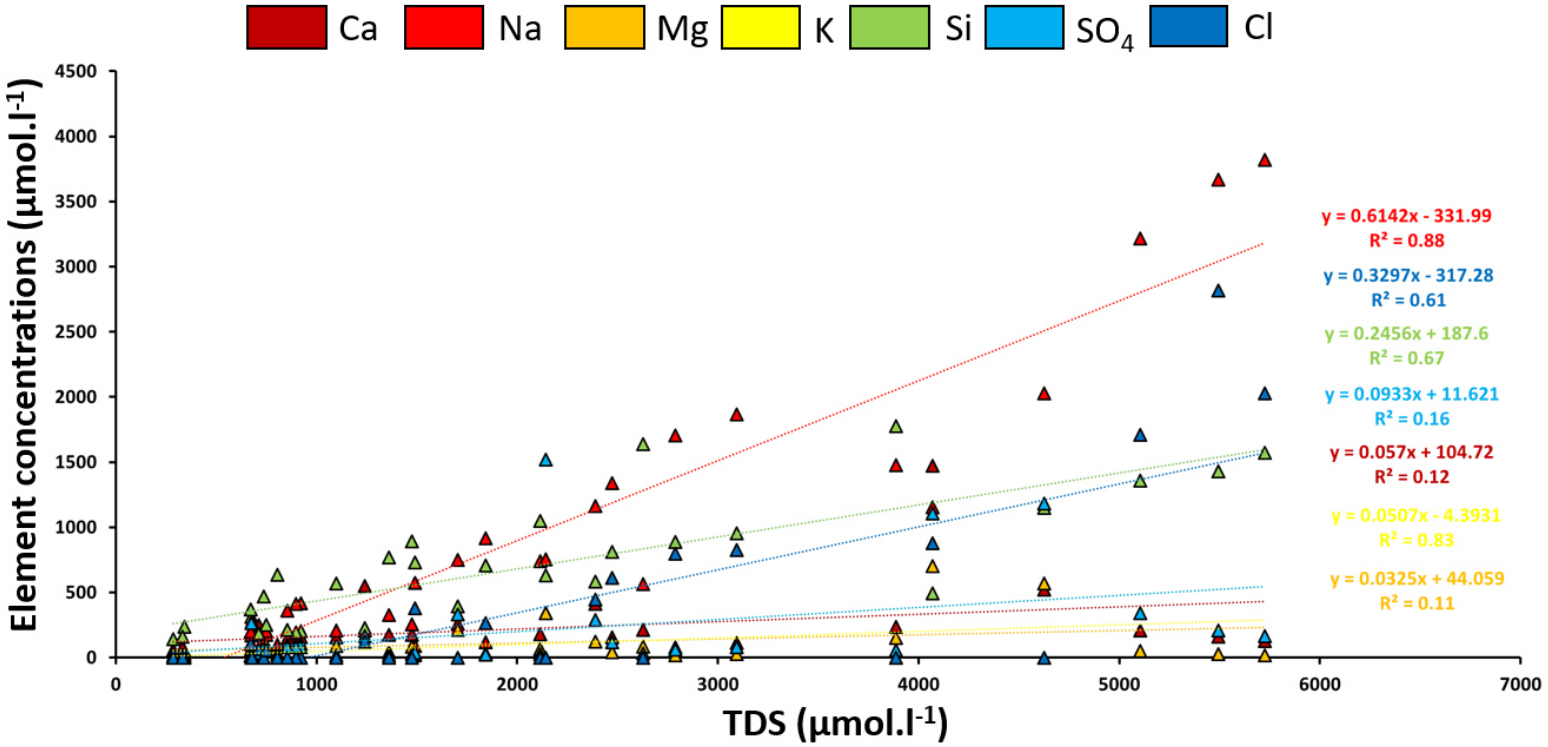

Suppl. Mat. 6.5: Major elements (Ca, Na, Mg, K), Si, SO_4 and Cl as a function of total dissolved solids (TDS) in river waters flowing through YPVF.

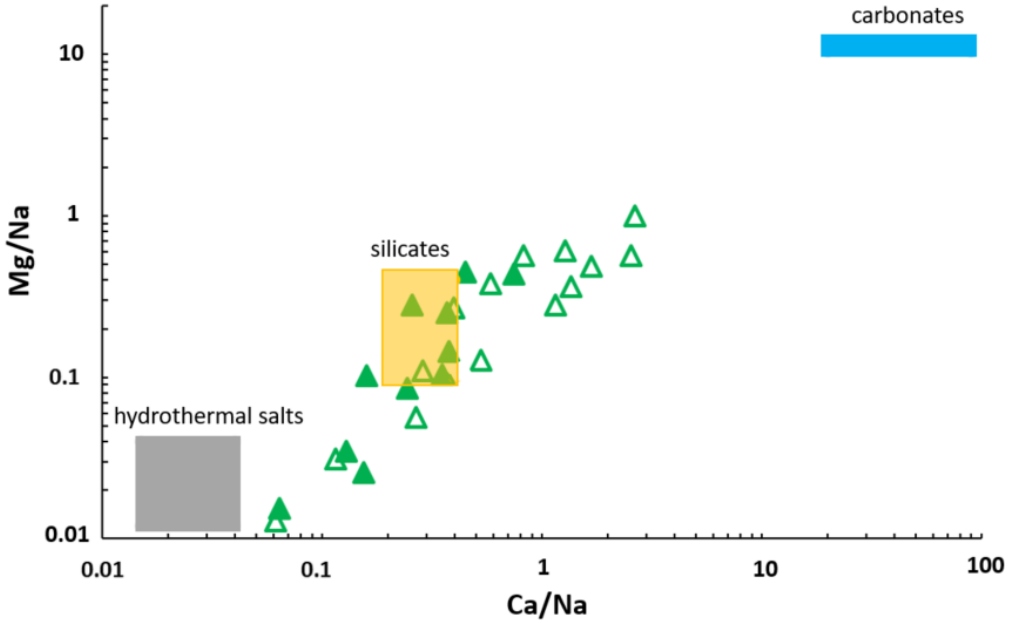

Suppl. Mat. 6.6: Mixing diagram using Na-normalized molar ratio in the dissolved phase of the rivers from YPVF at snowmelt (open triangle) and in base flow (plain triangle). Data from end-members reservoirs are from Gaillardet et al (1999). In this hydrothermal context, "hydrothermal salts" are present and represented here with the values from the evaporites from Gaillardet et al (1999).

Chapter 5:

Tracing changing seasonal contribution to river waters from the Aso caldera, Japan, with Ge/Si ratio and Si isotopes

7.1 Abstract

Rivers draining hydrothermally-active volcanic regions are dominated by a hydrothermal contribution affecting the estimations of weathering fluxes and the associated consumption of atmospheric CO_2. However, seasonal change in runoff may influence the relative contribution from thermal springs, groundwater and surface runoff to rivers draining these volcanic regions. These changes are generally overlooked in the estimation of weathering fluxes from these regions. Here, we use the germanium to silicon ratio (Ge/Si ratio) and the stable silicon isotopes ($\delta^{30}Si$) to trace changing sources (thermal springs, groundwaters, surface runoff) and processes affecting the relative contribution to rivers draining the Aso caldera (Kyūshū Island, Japan) between base flow (fall, spring) and high discharge (summer). Based on Ge/Si and Cl/B ratios, the data demonstrate that in rivers draining the Aso caldera, the fraction of hydrothermal input to riverine chemistry in base flow is seasonally reduced relative to groundwater and surface runoff contribution. A contribution from mineral dissolution at high discharge is supported by Si isotopes ($\delta^{30}Si_{high\ discharge} < \delta^{30}Si_{base\ flow}$). Importantly, the changes observed within the caldera on smaller river catchments are not detected at larger spatial scale at the outlet of the caldera. This highlights the importance of small catchment scale studies to nail down the sources and processes contributing to river weathering fluxes in hydrothermally-active volcanic regions, given the implications for global estimates of the associated atmospheric CO_2 consumption.

7.2 Introduction

Hydrothermally-active volcanic regions, including volcanic islands, contribute significantly to the global flux of solutes to the ocean and consumption of atmospheric CO_2 through silicate chemical weathering (Louvat and Allègre, 1997; Gaillardet et al, 1999; Dupré et al, 2003; Dessert et al, 2003; Gislason and Oelkers, 2011). In these regions, hydrothermal fluids act as an additionnal source of acids – beside atmospheric CO_2 – for weathering reactions and hydrothermal contribution largely controls riverine weathering fluxes (Louvat and Allègre, 1997; Dessert et al, 2009; Hurwitz et al, 2010; Schopka et al, 2011; Gaillardet et al, 2011; Rivé et al, 2013).

In volcanic islands, the runoff can change drastically as a function of orography and infiltration but also seasonally (Gaillardet et al, 2011). The seasonal runoff variability in volcanic islands is paramount to weathering processes as it modifies water residence time in soils (White and Blum, 1995), dictates the amount of water available for mineral dissolution as well as the discharge of dissolved weathering fluxes to rivers (Dessert et al, 2015). Only few studies have shown a considerable positive correlation between riverine discharge and mass flux (Ingebritsen et al, 2001; Friedman and Norton, 2007; Hurwitz et al, 2007). Importantly, runoff variability is predicted to increase based on the projected changes in precipitations with ongoing climate change (IPCC, 2013). However, the influence of change in runoff on the relative contribution from thermal springs, groundwater and surface runoff to rivers draining the hydrothermally-active volcanic regions are generally overlooked leading to inacuraccies in the estimation of weathering fluxes and the associated atmospheric CO_2 consumption from these regions.

Geochemical tracers such as the germanium to silicon ratio (Ge/Si ratio) and the stable silicon isotopes ($\delta^{30}Si$) have been combined in volcanic islands to trace weathering processes (Derry et al, 2005; Ziegler et al, 2005; Opfergelt et al, 2010; 2013; Baronas et al, 2018; 2020). According to the few studies using theses tracers in rivers draining regions affected by thermal input, either volcanic thermal input (Gaspard et al, submitted) or

metamorphic thermal input (Han et al, 2015; Wang et al, 2019), their combination provides a way to identify changes in contribution from thermal springs relative to rock and soil weathering processes.

The Aso caldera (Kyūshū Island, Japan) is ideal to evaluate the relative contributions from thermal springs, groundwater and surface runoff to rivers with changing runoff given that (i) the presence of thermal discharge in the Aso caldera is well described (Nagai et al, 1986; Shimano, 1997, 1999; Yamada et al, 2011; Hosono et al, 2018), (ii) a net change in runoff is expected with the summer rainy season in Japan (June-September) characterized by precipitations 5.5 times higher than the average annual precipitations, (iii) groundwater location and their water residence time are available (Hase et al, 2005; Kagabu et al, 2011; Yadama et al, 2011; Terada et al, 2012).

In this study, the seasonal variation in chemistry, Ge/Si ratios and Si isotope compositions of all contributors to rivers (thermal springs, groundwaters and surface runoff) and rivers from the Aso caldera are determined to evaluate the influence of changing runoff on the relative contributions and changing controls on river element fluxes in this hydrothermally-active volcanic region.

7.3 Environmental setting

Formed in the context of the subduction of the Philippine Sea plate beneath the Eurasian plate, the Aso caldera (located in Kyūshū Island) is one of the largest caldera in the world (376 km^2, 24 km NS by 18 km EW; Nakada, 2003). The caldera's current shape is the result of four major explosive eruptions which produce voluminous pyroclastic flows (~300 km^3; Nakada, 2003) covering much of central Kyūshū: Aso-1 (270 ky), Aso-2 (140 ky), Aso-3 (120 ky) and Aso-4 (90 ky) (Ono et al, 1977). The overall population in the Aso caldera reaches to 500 000. The Aso caldera is highly cultivated (41% of the total caldera surface with ~15500 ha) and is dominated by rice paddy fields (25% of the total caldera surface with ~9600 ha; estimated using Digital Elevation Model on QGIS software by Meunier (2019)).

The Aso stratovolcano (32°N, 131°E), situated within the caldera (at 1592m asl), is a cluster of central volcanoes consisting of different craters (Nekodake, Takadake, Nakadake, Eboshidake and Kishimadake) of various types of rocks ranging from basalt to rhyolite reflecting different magmatic activities (Ono and Watanabe, 1985). The soil of Aso volcano is classified as Andosol (Huang et al, 1995). Continuous observations of the Aso volcano have been carried out by Volcanological Laboratory (attached to Kyoto University) since 1928 including observations of terrestrial magnetism and geodetic surveys including levelling, ranging, gravity, electric resistance, heat, gas and thermal springs (Nakada, 2003). The crater of Nakadake, is one of the most active volcanoes in Japan in terms of the persistent release of volatiles and thermal energy and contains a hot (surface temperature = 60-70 °C) hyper acid lac water (pH<1) showing variations in water level and temperatures (Saito et al, 2008; Terada et al, 2012). Other surface hydrothermal manifestations of Aso volcano observed on the central cones are fumarolic gas discharges originated from hydrothermal systems at Yuno-tani and Tarutama areas on the western slope of Mont Eboshidake (Yamada et al, 2011) and natural thermal springs around this area are recognized as steam-heated thermal springs. The formation processes of the thermal springs, including their

relation to magmatic emanation, have not been investigated at Aso volcano (Yamada et al, 2011). Recently, Hosono et al (2018) presented a deep fluid discharge model showing that thermal springs located in the northwestern plain derive from highly-concentrated hydrothermal fluids sources. Since 1991, the surface unrest at Nakadake has been mild for most of the period, except for some mud eruptions, which occurred in 1992, 1994 and 1995 (Hase et al, 2005).

The caldera floor is separated into north (Aso Valley) and south (Nango Valley) part respectively discharged by Shirakawa river and Kurokawa river (main rivers), each aggregating the signal of the northern and southern part of the caldera, respectively (**Fig. 7.1**). The two main rivers receive also inputs from rivers tributaries on both side of the Aso caldera. The Aso valley is covered with lake sediments (Tanaka, 2000) and the Nango Valley landform implies a simple stratified structure of the groundwater flow system at the Aso Valley area. Those rivers, which meet within the caldera, flow out from the caldera at the western rim of the caldera (S33; **Fig. 7.1**).

The humid continental climate in Aso caldera consists of four distinct seasons: winter (from November to March), spring (from March to May), summer (from June to September) and fall (from September to October). The mean annual temperature reported by the Japan Meteorological Agency (JMA) is 13.2 °C (JMA, 2019). Precipitations are high throughout the year (min 500 mm of rainfall/month) but the summer rainy season (June-September) is characterized by highest precipitations compared to mean annual precipitations (~5.5 time higher in wet season; JMA, 2019).

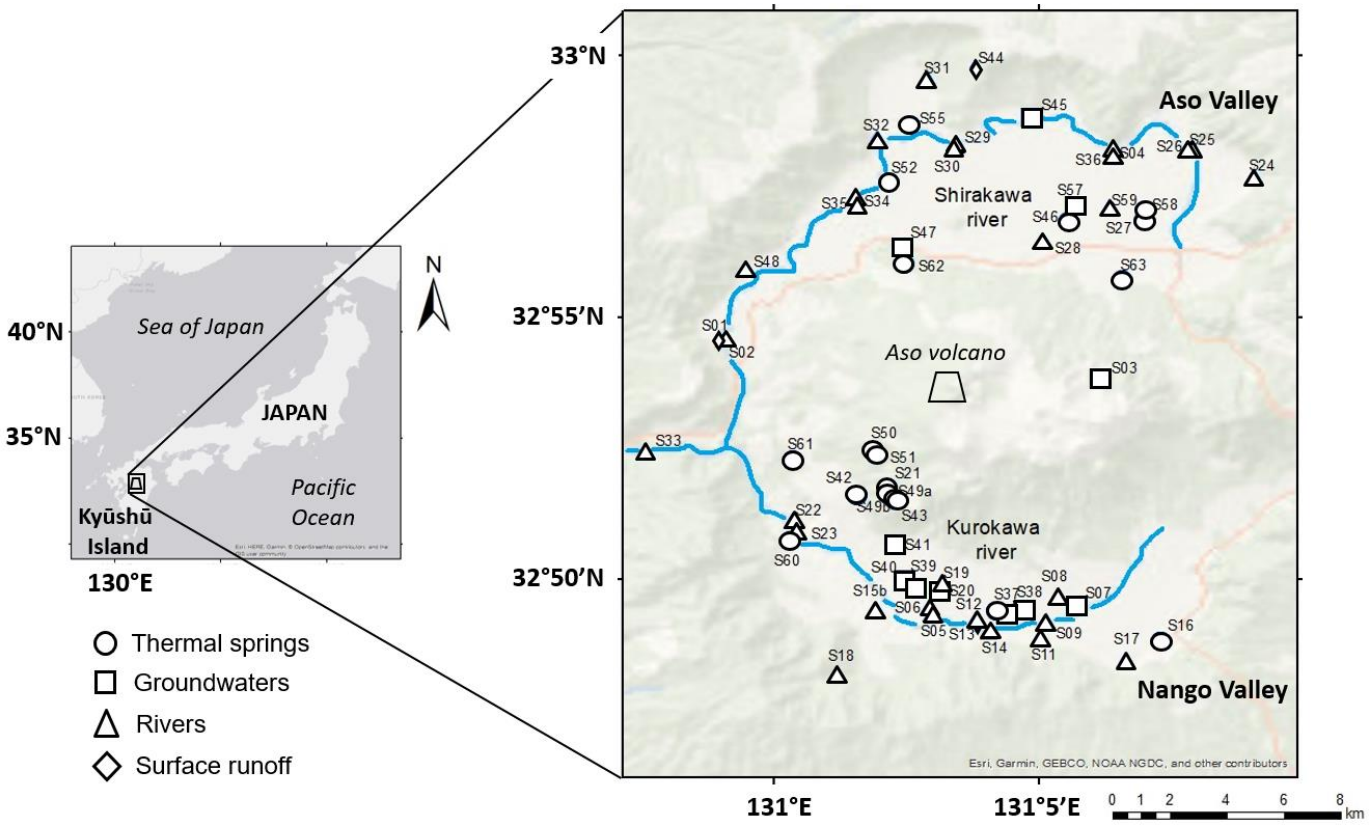
40°N
35°N
130°E
Sea of Japan
JAPAN
Pacific Ocean
Kyūshū Island
N
33°N
32°55'N
32°50'N
131°E
131°5'E
Aso Valley
Nango Valley
Shirakawa river
Kurokawa river
Aso volcano
Thermal springs
Groundwaters
Rivers
Surface runoff
Esri, Garmin, GEBCO, NOAA NGDC, and other contributors
0 1 2 4 6 8
km

Fig. 7.1: Location of thermal springs, groundwaters, river waters and surface runoff flowing into the Aso caldera, Kyūshū Island, Japan. The numbers refer to **Table 7.1**.

7.4 Materials and methods

7.4.1 Sampling campaign

All sampling sites are represented at **Fig. 7.1**. Seventeen thermal springs (n=21), eleven groundwaters (n=28), thirty river waters (n=46) and three surface runoff (water flowing on the ground sampled just after rainfall) (n=4) were collected manually on both side of the Aso caldera between 2014 and 2016 in five distinct seasons: fall 2014, spring 2015, summer 2015 (sum 15), summer 2016 (sum 16) and fall 2016. More precisely, in the northern part of the Aso caldera, Shirakawa river was collected at 9 distinct locations (n=17) and 8 tributaries (secondary rivers flowing into Shirakawa river) were sampled. In the southern part of the Aso caldera, Kurokawa river was collected at 4 distinct locations (n=5) and 8 tributaries (secondary rivers flowing into Kurokawa river) (n=10) were sampled. The confluence at the outlet of the caldera (S33) was collected twice in spring and sum 15, respectively. Based on precipitations (mm) and discharges ($m^3.s^{-1}$) measured from a gauging station at the site S33 located at the outlet of the Aso caldera between 2014 and 2015 (**Fig. 7.2**), we consider the summer seasons (sum 15 and sum 16) as "high discharge" conditions and the other seasons (fall 2014, spring 2015 and fall 2016) as "base flow" conditions (with discharge at "high discharge" being ~1.4 times higher than at "base flow"). Thermal spring waters were sampled at their outlets from the riverbed and sampling of the rivers took place away from any visible anthropogenic contributions.

Temperature (°C) and pH were measured *in situ* with handheld sensors. Water samples were filtered within 24h at 0.45 µm through polycarbonate membranes, acidified at 0.5% suprapure HNO_3 and stored at 4 °C in the dark in acid-washed polypropylene (PP) bottles. Alkalinity was determined on the sampling day using an automatic acid-base titration stand (Metrohm 916 Ti-Touch titrator).

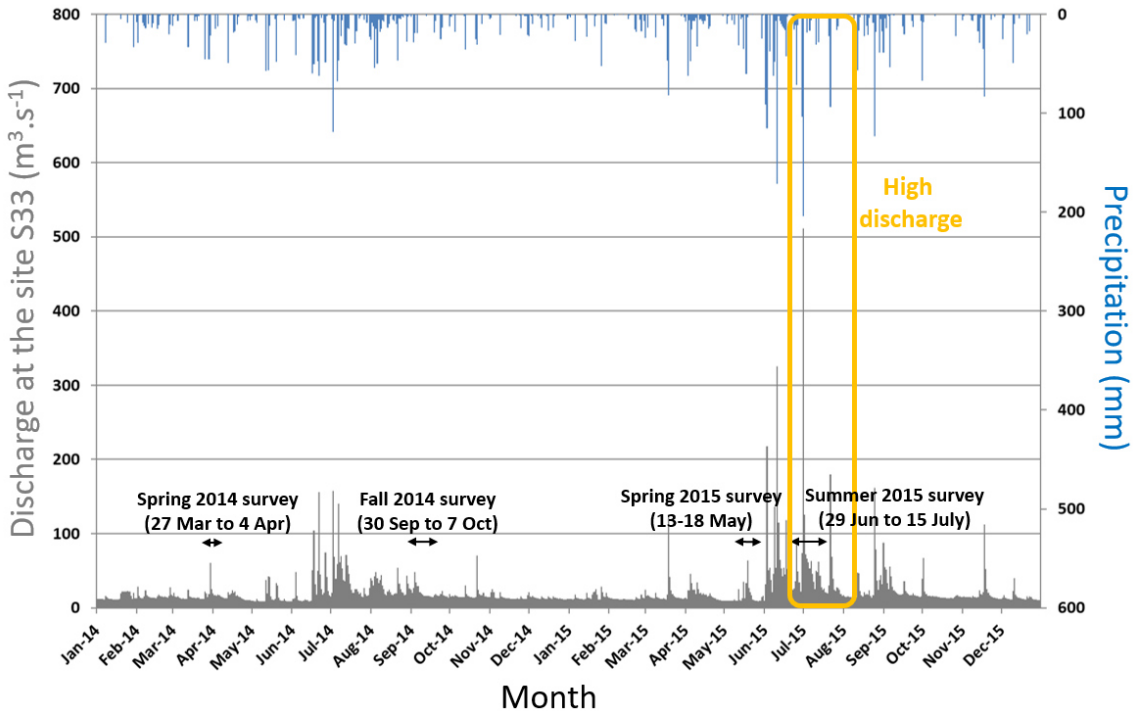

Fig. 7.2: Discharge ($m^3.s^{-1}$) as a function of precipitation (mm) at the outlet the Aso caldera between 2014 and 2015 (S33 in **Table 7.1**). Summer (sum) is considered as "high discharge" conditions and the other seasons are considered as "base flow" conditions. For our sampling seasons: high discharge conditions (sum 2015 and sum 2016) and "base flow" conditions (fall 2014, spring 2015 and fall 2016).

7.4.2 Water compositions analysis

Major element concentrations (Ca, Na, Mg, K), Al, Fe and Si were determined on all types of water by inductively coupled plasma-optical emission spectrometry (ICP-OES; iCAP 6500 Thermo Fisher Scientific) at the Earth & Life Institute, UCLouvain, Belgium. The accuracy on majors elements (Ca, Na, Mg, K, Al, Fe and Si) analyses was assessed using the trueness (± 3%, ± 4%, ± 1%, ± 7%, ± 4%, ± 2% and ± 4%; respectively) on the river water reference material SLRS-5 (Yeghicheyan et al, 2013) and the analytical precision (± 0.5%) for each element. The detection limit are 0.05, 0.43, 0.21, 0.26, 0.37,

0.18 and 0.36 µmol.l^{-1} for Ca, Na, Mg, K, Al, Fe and Si, respectively. Anions (SO_4^{2-}, Cl^-) were measured by ion chromatography (Dionex ICS2000, column: AG15/AS15). The accuracy on SO_4^{2-} and Cl^- was assessed by using the trueness (± 3% and ± 4%; respectively) on river water certified reference material LGC6025 (UKAS, 2014) and the analytical precision (± 2%) for each anion. The detection limit are 1.5 and 3.1 for SO_4^{2-} and Cl^-, respectively. Total dissolved solids (TDS; µmol.l^{-1}) were obtained by summing major elements (Ca, Na, Mg, K) and SiO_2 concentrations in rivers. The B concentrations were measured by HR-ICP-MS at IPGP, Paris (collaboration with P. Louvat). The ion balance of the water samples never exceeds 10%.

7.4.3 Ge measurements and Ge/Si ratio calculation

The Ge concentration in the thermal springs (n=21), groundwaters (n=28), river waters (n=46) and surface runoff just after rainfall (n=4) was determined by ICP-mass spectrometry (ICP-MS, ICAPQ Thermo Fisher Scientific, Earth & Life Institute, UCLouvain, Belgium) and using the ^{74}Ge isotope. Accuracy and long-term repeatability of the analysis were assessed by measuring two international riverine standards, namely SLRS-5 ([Ge] = 0.083 ± 0.014 nmol.l^{-1}; n=3) and SLRS-6 ([Ge] = 0.097 ± 0.0069 nmol.l^{-1}; n=3) (Yeghicheyan et al, 2013), and one in-house standard (i.e., the Gallion Blanc (GAB) thermal spring of La Soufrière volcano in Basse-Terre Island: [Ge] = 23.95 ± 0.096 nmol.l^{-1}; n=14) in each analytical session between July 2017 and June 2018. The analytical precision (n= 3) is ± 8% for Ge concentrations < 0.001 µg.l^{-1} and 4% for Ge concentrations > 0.001 µg.l^{-1}. The limit of detection for Ge is 0.04 nmol.l^{-1}. Ge/Si ratios (expressed in µmol.mol^{-1}) were calculated using Si concentrations measured by ICP-OES (**Table 7.1**), and Ge concentrations measured by ICP-MS. The precision on the Ge/Si ratio is 10% (SD).

7.4.4 Silicon isotope measurements

Purification of silica- and anion-rich samples

For thermal spring waters, the Si concentration is beyond the limit of amorphous silica solubility (~1700-2300 µmol.l^{-1} at 25 °C; Fournier and Rowe, 1977). Therefore, to ensure the solubilization of potential amorphous silica precipitates formed after filtration, the water samples were dried down on a hotplate at 100 °C, followed by a leaching with

0.125M NaOH at 100 °C for four hours after sonication for 10 minutes (adapted from Ragueneau et al, 2005), then by the neutralization of the reaction with suprapure HNO_3 to reach pH 2 in a final volume at a Si concentration below the limit of amorphous silica solubility.

To prevent from matrix effects in mass spectrometry with anions such as SO_4 and Cl, Si in thermal waters has been purified by performing a two-step column chemistry: anion-exchange resin (Biorad AG MP-1) and cation-exchange resin (Biorad AG50W-X12) following the method developed by Gaspard et al, submitted. After column chemistry, the Si recovery was always > 98%, the concentrations of Na, SO_4 and Cl in the purified solution were < 0.43, 1.5 and 3.1 $\mu mol.l^{-1}$, respectively (i.e., below the detection limit), and the blank level was < 0.36 $\mu mol\ Si.l^{-1}$, i.e., below the detection limit for Si by ICP-OES.

Mass spectrometry

Silicon isotope compositions were measured in 9 thermal springs (n=11), 3 groundwaters (n=5), 14 river waters (n=23) and 2 surface runoff just after rainfall (n=2) of the Aso caldera. Silicon isotope compositions were analyzed by MC-ICP-MS (Neptune Plus™ High Resolution Multicollector ICP-MS, Thermo Fisher Scientific, Earth & Life Institute, UCLouvain, Belgium) in wet plasma mode in medium resolution ($\Delta m/m \sim 6000$) using a PFA nebulizer of 100 $\mu l.min^{-1}$ uptake rate. The instrumental mass bias was corrected using the standard-sample bracketing technique and an external Mg doping (Cardinal et al, 2003). The analyses were performed in 2% HNO_3 matrix, with a typical sensitivity of 7V for 2 $mg.l^{-1}$ Si and an instrumental blank <30 mV. Silicon isotope compositions are expressed in relative deviations of $^{30}Si/^{28}Si$ ratio from the NBS-28 reference standard using the common δ-notation (‰) as follow: $\delta^{30}Si=[(^{30}Si/^{28}Si)_{sample}/(^{30}Si/^{28}Si)_{NBS-28} -1]\times 1000$. One measurement comprises 30 cycles with 4.2s integration time corrected by blank in a 2% HNO_3 matrix. Each single δ-value (n) represents one sample run and two bracketing standards. $\delta^{30}Si$-values are reported as the mean of replicate isotopic analyses ± standard deviation (SD). Quality control of mass bias was performed by ensuring that $\delta^{30}Si$ and $\delta^{29}Si$ measurements fit onto a mass-dependent fractionation array, supporting the interference-free determination of all three Si isotopes via MC-ICP-MS (**Suppl. Mat. 7.1**). The long-term precision and accuracy of the MC-ICP-MS $\delta^{30}Si$ analyses were assessed on the reference materials diatomite ($\delta^{30}Si$ =

1.30 ± 0.09 ‰, SD, n=20), BHVO-2 (δ^{30}Si = -0.27 ± 0.06 ‰, SD, n=10) and quartz Merck (δ^{30}Si of 0.04 ± 0.09 ‰, SD, n=6) with values consistent with those reported earlier (Reynolds et al, 2007; Abraham et al, 2008).

7.5. Results

7.5.1 Elemental composition of thermal springs from the Aso caldera

The temperature, pH and chemical composition of thermal springs is presented in **Table 7.1**.

Table 7.1: Temperature, pH and chemical composition of thermal springs, groundwaters, river waters and surface runoff of water samples from the Aso caldera, Kyūshū Island, Japan. River water samples were collected between fall 2014 and 2016 (sum = summer). north = northern part of the Aso caldera. south = southern part of the Aso caldera. - : not measured; n.d : not detected.

	Sampling season	Type	Label	Temperature	pH	TDS	Ca	Na	Mg	K	Al	Fe	Si	SO_4	Cl	HCO_3	B
				°C		µmol.l^{-1}											
Thermal springs	spring 15	cold springs south	S16	15.6	8.0	3134	331	298	231	89	0.20	0.13	1022	58	86	1265	0.5
	fall 16	cold springs south	S16	16.2	7.8	2906	334	257	222	81	0.05	0.01	940	47	65	1286	0.7
	spring 15	hot springs south	S21	42.3	2.1	7171	897	784	492	269	-	-	2211	9499	145	0	51.7
	fall 14	hot springs south	S42	46.0	6.0	11236	2387	2642	1263	404	0.48	13.91	2122	1779	162	4459	152.8
	spring 15	hot springs south	S42	46.0	6.1	11788	2340	2494	1216	505	0.04	0.95	2446	1688	152	6717	145.0
	spring 15	hot springs south	S43	66.2	2.4	6152	659	439	453	176	1411.05	204.26	2069	8014	78	0	1.3
	spring 15	hot springs south	S49a	41.0	3.4	7932	662	927	491	284	259.12	24.40	2603	2590	149	0	113.1
	spring 15	hot springs south	S49b	45.9	5.8	8674	916	1268	805	436	0.06	0.05	2453	1302	191	0	75.8
	fall 16	hot springs south	S50	39.8	6.5	8231	2019	446	931	158	n.d	0.05	2186	570	69	5800	2.3
	fall 16	hot springs south	S51	25.7	7.6	5512	461	738	362	272	0.12	0.01	1720	1149	75	803	4.6
	fall 16	hot springs north	S52	23.5	6.7	19052	4148	6037	3477	538	n.d	0.80	2268	5853	3225	722	59.6
	sum 16	hot springs north	S55	42.9	7.1	12859	793	6372	1052	575	0.15	2.24	1901	2972	1267	2988	74.5
	fall 16	hot springs north	S55	40.8	7.2	12081	723	5823	953	523	0.07	2.60	1898	2606	1187	2738	78.8
	fall 16	hot springs north	S56	16.2	6.0	4827	844	577	411	108	0.34	0.02	1349	1119	243	510	4.0
	fall 16	hot springs north	S57	15.7	6.8	4900	874	897	651	147	0.05	0.02	1090	1265	610	846	6.7
	fall 16	hot springs north	S58	15.9	7.0	3975	631	497	376	125	0.02	0.01	1097	552	253	1192	3.1
	fall 16	hot springs north	S59	15.7	6.9	4254	737	590	442	155	0.01	0.01	1090	646	306	1224	2.4
	fall 16	hot springs south	S60	26.5	7.0	7318	570	2670	719	304	0.03	0.02	1428	494	229	3976	108.9
	fall 16	hot springs south	S61	43.4	7.3	15065	672	8387	949	959	0.13	6.13	1916	1836	906	7329	144.2
	fall 16	hot springs north	S62	52.6	6.9	13345	623	7133	824	819	n.d	0.11	1844	1606	762	5586	224.5
	fall 16	hot springs north	S63	19.8	7.2	7886	932	2824	1195	224	0	0.03	1268	2060	846	1878	17.6
Groundwaters	spring 15	crater	S03	20.3	4.3	5272	1869	731	437	117	521.16	2.74	990	2500	1686	0	5.6
	sum 15	crater	S03	23.3	5.2	3134	663	335	185	71	88.65	0.03	879	940	599	0	1.7
	spring 15	groundwater (cone, south)	S07	14.2	7.1	3640	548	428	277	118	0.03	0	1061	540	164	881	1.3
	sum 15	groundwater (cone, south)	S07	16.5	7.0	2533	164	36	35	13	0.00	n.d	1068	85	15	244	0.5
	sum 16	groundwater (cone, south)	S07	16.7	7.0	3725	546	419	270	114	0.06	n.d	1111	420	152	910	1.7
	fall 16	groundwater (cone, south)	S07	14.5	6.9	3542	509	398	257	101	0.05	0.01	1065	475	156	889	1.5
	spring 15	groundwater (cone, south)	S19	16.1	6.9	3967	418	452	225	122	0.02	0.02	1285	504	155	622	1.8
	sum 15	groundwater (cone, south)	S19	17.2	6.5	3913	405	433	221	120	n.d	n.d	1278	427	142	678	0.8
	fall 16	groundwater (cone, south)	S19	15.2	6.5	3499	374	387	204	105	0.04	0.01	1136	428	137	611	2.1
	spring 15	groundwater (cone, south)	S37	14.7	6.3	4528	778	556	387	125	0.19	0.001	1253	1096	251	542	2.8
	sum 16	groundwater (cone, south)	S37	17.2	6.5	4039	640	493	329	109	0.06	n.d	1154	681	205	576	-
	fall 16	groundwater (cone, south)	S37	14.8	6.2	4098	702	472	331	103	0.15	0.02	1164	857	211	565	2.5
	fall 14	groundwater (cone, south)	S38	15.7	6.6	4175	774	505	394	127	0.90	0.04	1111	748	234	646	1.8
	spring 15	groundwater (cone, south)	S38	15.2	6.6	4008	643	464	324	124	0.13	0.03	1146	743	207	694	2.1
	fall 16	groundwater (cone, south)	S38	15.4	6.4	3789	572	408	294	115	0.25	0.12	1122	614	182	791	2.0
	spring 15	groundwater (cone, south)	S39	15.7	6.5	4152	470	501	259	157	0.02	0.001	1292	482	165	876	2.3
	fall 16	groundwater (cone, south)	S39	16.3	6.4	3952	426	450	237	135	0.02	0.01	1264	350	144	975	2.1
	spring 15	groundwater (cone, south)	S40	16.1	6.5	4105	460	528	269	167	0.02	0.05	1253	499	185	902	2.6
	fall 16	groundwater (cone, south)	S40	16.7	6.4	4000	424	471	256	146	0.03	0.01	1264	393	157	954	2.3
	spring 15	groundwater (cone, south)	S41	16.0	6.9	4251	450	799	334	139	0.09	0.001	1182	667	234	918	5.2
	spring 15	groundwater (rim, north)	S45	17.6	7.2	2865	207	300	153	103	0.04	0.07	983	45	83	844	1.0
	fall 16	groundwater (rim, north)	S45	17.5	6.8	2699	287	273	158	84	0.05	0.01	887	41	81	828	0.9
	spring 15	groundwater (old, north)	S46	15.6	7.2	4170	677	642	406	131	0.03	0.003	1082	837	360	821	3.5
	sum 15	groundwater (old, north)	S46	16.3	8.3	2825	221	128	90	27	0.02	0.02	1103	196	56	268	1.8
	sum 16	groundwater (old, north)	S46	15.4	7.1	4168	653	634	411	125	0.42	n.d	1096	719	342	831	3.7
	fall 16	groundwater (old, north)	S46	14.2	7.1	3850	604	572	372	109	0.01	0.01	1025	753	330	804	3.2
	spring 15	groundwater (old, north)	S47	15.1	7.1	2165	250	344	153	85	0.02	0.004	623	189	179	528	2.2
	fall 16	groundwater (old, north)	S47	14.7	7.0	2077	236	268	128	66	0.07	0.01	644	113	138	631	1.8

	Sampling season	Type	Label	Temperature	pH	TDS	Ca	Na	Mg	K	Al	Fe	Si	SO_4	Cl	HCO_3	B
				°C		µmol.l^{-1}											
River waters	spring 15	tributary (north-west rim)	S48	14.7	7.1	2356	217	238	151	67	0.14	0.03	787	25	54	892	0.8
	fall 16	tributary (north-west rim)	S48	14.7	6.7	2366	199	222	147	54	0.07	0.01	815	19	46	905	0.7
	spring 15	main river north	S01	16.2	7.3	4109	791	937	616	165	0.86	0.92	748	1311	547	812	6.9
	sum 15	main river north	S01	23.3	7.6	3365	508	609	394	132	0.02	0.001	805	652	287	870	3.6
	sum 16	main river north	S01	21.6	7.2	3563	570	797	493	151	0.09	0.03	726	844	377	835	6.9
	spring 15	main river north	S04	21.0	8.4	2831	542	452	358	139	0.54	0.17	627	457	260	1192	1.9
	sum 15	main river north	S04	21.6	7.9	2092	194	60	53	18	0.01	0.02	826	49	21	434	0.7
	spring 15	tributary south	S05	18.1	7.3	4598	785	782	384	148	0.19	0.08	1168	874	263	833	9.3
	spring 15	main river south	S06	18.8	7.9	3712	576	523	311	123	-	-	1018	651	217	872	4.7
	spring 15	tributary south	S08	20.1	4.5	5239	n.d	846	737	229	178.83	2.24	1602	4934	496	0	13.4
	fall 16	tributary south	S08	20.9	4.0	6807	2332	643	591	194	152.98	0.73	1424	2896	381	0	13
	spring 15	tributary south	S09	18.6	7.0	4337	736	1012	305	136	-	-	1004	797	858	728	1.9
	spring 15	main river south	S10	21.5	7.6	3796	625	462	300	132	0.07	0.02	1065	556	191	1077	1.2
	spring 15	tributary south	S11	19.0	7.9	2664	277	269	255	96	0.18	0.03	826	97	90	920	0.6
	spring 15	tributary south	S12	17.7	6.6	4399	799	614	422	119	0.39	0.04	1143	1150	274	569	2.3
	spring 15	main river south	S14	20.0	8.0	3531	489	402	262	117	0.07	0.02	1057	408	170	935	1.1
	spring 15	tributary south	S15b	18.1	7.8	2531	326	287	171	79	0.03	0.004	780	162	121	848	0.9
	spring 15	tributary north	S17	16.8	8.0	2727	326	274	222	92	0.35	0.05	847	60	83	1202	0.5
	spring 15	tributary north	S18	14.4	7.7	1066	127	112	42	22	0.24	0.02	356	24	45	366	0.2
	spring 15	tributary south	S20	16.0	7.7	3564	400	503	215	139	-	-	1079	350	154	865	1.9
	spring 15	spring 15	S22	17.5	7.5	2784	380	378	218	132	0.26	0.09	783	330	142	831	3.0
	sum 15	tributary south	S22	22.4	8.7	3184	351	374	195	125	0.53	0.07	1001	362	120	666	1.5
	spring 15	main river south	S23	18.3	8.0	3526	410	680	292	133	0.18	0.07	940	378	186	1237	8.4
	sum 15	main river south	S23	20.7	8.9	2262	152	69	36	17	0.05	0.05	929	49	14	326	3.7
	spring 15	tributary (north-east rim)	S24	18.3	8.0	2595	268	277	181	94	0.05	0.13	830	52	91	1016	0.8
	spring 15	main river north	S25	19.3	7.6	3311	483	561	399	260	0.45	0.02	751	254	314	1549	1.8
	spring 15	main river north	S26	18.6	7.6	3284	323	440	251	166	0.23	0.09	790	389	198	1163	1.9
	spring 15	tributary north	S27	27.0	7.7	3323	664	510	452	211	0.94	0.08	705	1631	330	1304	2.4
	sum 15	tributary north	S27	27.3	8.4	3401	614	488	423	221	0.02	0.07	769	1228	273	0	1.1
	spring 15	tributary north	S28	22.7	7.4	7356	2174	1469	1348	330	0.07	1.24	951	2675	894	2243	10.6
	sum 15	tributary north	S28	30.3	6.3	3545	810	312	303	86	0.01	0.01	951	915	219	600	4.3
	sum 16	tributary north	S28	23.0	7.0	3760	922	699	554	165	0.02	0.07	664	992	519	738	4.3
	spring 15	main river north	S29	22.5	7.5	5840	1412	1384	1088	280	0.93	0.21	783	2193	895	822	8.9
	sum 15	main river north	S29	19.7	8.4	4912	1109	937	861	222	0.03	0.01	833	1560	724	1276	4.4
	spring 15	main river north	S30	20.2	7.7	3126	483	469	356	189	0.28	0.06	815	1146	272	1112	2.1
	sum 15	main river north	S30	17.6	8.5	3108	418	417	305	140	0.05	0.03	855	233	169	1241	0.8
	spring 15	tributary north	S31	15.5	7.7	2226	173	205	98	58	0.50	0.02	790	24	89	629	0.6
	spring 15	tributary north	S32	22.2	7.3	2507	287	501	188	114	0.42	0.25	662	205	231	837	22.3
	spring 15	river confluence	S33	18.1	8.0	3566	506	687	372	175	n.d	n.d	853	1634	146	1121	6.9
	sum 15	river confluence	S33	21.3	8.5	3932	555	702	392	178	n.d	n.d	983	1734	52	394	2.9
	spring 15	main river north	S34	19.0	7.4	5160	1014	1765	651	222	0.23	0.04	705	1206	584	955	11.6
	sum 15	main river north	S34	24.1	7.7	2739	334	674	226	118	0.03	n.d	648	440	304	655	2.7
	spring 15	main river north	S35	17.9	7.4	4230	789	950	618	175	0.43	0.04	794	1169	550	966	9.2
	sum 15	main river north	S35	21.7	7.7	3451	559	655	427	147	0.07	0.03	777	694	316	981	3.6
	spring 15	main river north	S36	16.2	7.6	3099	293	360	215	144	0.27	0.45	976	90	138	1066	1.9
	sum 15	main river north	S36	20.9	8.0	2988	305	326	220	125	0.03	0.11	940	80	115	1166	0.6
Surface runoff	spring 15	drainage	S02	17.1	7.6	2225	199	264	133	67	0.21	0.64	730	96	88	687	-
	spring 15	drainage	S13	19.6	7.5	3584	608	514	333	140	0.45	0.06	929	685	289	785	1.4
	spring 15	rain cold springs	S44	13.9	7.6	1850	209	166	87	32	0.44	0.005	634	20	44	564	0.4
	fall 16	rain cold springs	S44	15.4	7.1	1587	156	159	74	32	0.32	0.01	545	17	36	586	0.3

The thermal springs display a large range in surface temperatures (from 15.6 °C to 66.2 °C) similar or warmer than groundwaters (14.2-23.3 °C), river waters (14.4-30.3 °C) and surface runoff (13.9-19.6 °C). Thermal springs also present the highest TDS values (2906-19052 µmol.l^{-1}), the highest Si concentrations (940-2603 µmol.l^{-1}) and the lowest pH relative to rivers (TDS = 1066-5272 µmol.l^{-1}; Si = 356-1292 µmol.l^{-1}), groundwaters and surface runoff (**Fig. 7.3**). The most acidic values of pH are reported in the southern part of the Aso caldera for the thermal springs S21 (pH = 2.1), S43 (pH = 2.4), S49a (pH = 3.4) and S49b (pH = 5.8), and for the crater groundwater S03 (pH = 4.3-5.2) and the river water tributary S08 (pH = 4.0-4.5).

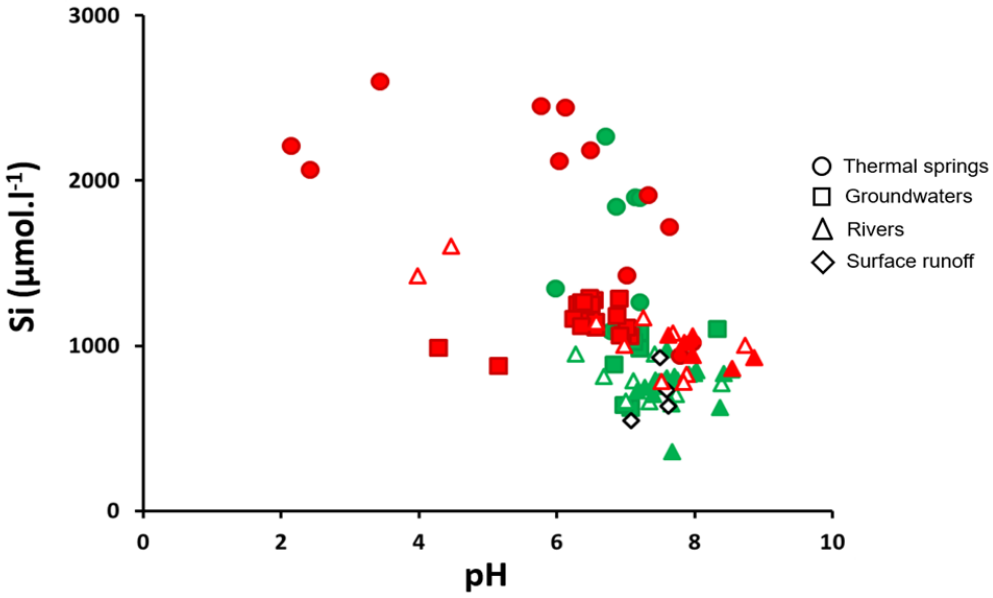

Fig. 7.3: Plot of the Si concentration as a function of pH for the water samples from the northern (green) and southern (red) part of the Aso caldera: thermal springs (circle), groundwaters (square), river waters (triangle; with main river (plain triangle) and tributaries (open triangle)), and surface runoff (diamond).

Thermal springs are characterized by a large range of HCO_3 (0-7329 $\mu mol.l^{-1}$) followed by SO_4 (47-9499 $\mu mol.l^{-1}$) and Cl (65-3225 $\mu mol.l^{-1}$). More specifically, the highest HCO_3 concentrations are found in the northern thermal springs (510-5587 $\mu mol.l^{-1}$) relative to the southern thermal springs (0-975 $\mu mol.l^{-1}$; **Table 7.1**). On the opposite, the highest SO_4 concentrations are measured in the southern thermal springs (47-9499 $\mu mol.l^{-1}$) relative to the northern thermal springs (552-5853 $\mu mol.l^{-1}$; **Table 7.1**; **Fig. 7.4**). The most acidic thermal springs (S43 and S49a located in the southern part of the caldera with pH 2.4-3.4) are generally enriched in dissolved Fe and Al (24-204 and 259-1411 $\mu mol.l^{-1}$, respectively) compared to the other thermal springs (0-14 and 0-0.5 $\mu mol.l^{-1}$, respectively) given that Fe and Al are soluble at these pH values (Michard, 1980). In thermal springs, the dominant cation is Na (257-8387 $\mu mol.l^{-1}$), followed by Ca (331-4148 $\mu mol.l^{-1}$), Mg (222-3477 $\mu mol.l^{-1}$) and then K (81-819 $\mu mol.l^{-1}$) (**Fig. 7.4a**). The highest B concentrations (144-224 $\mu mol.l^{-1}$ for S42, S61, S61) are reported for the most SO_4, HCO_3 and Cl concentrated thermal springs (**Table 7.1**; **Fig. 7.4**).

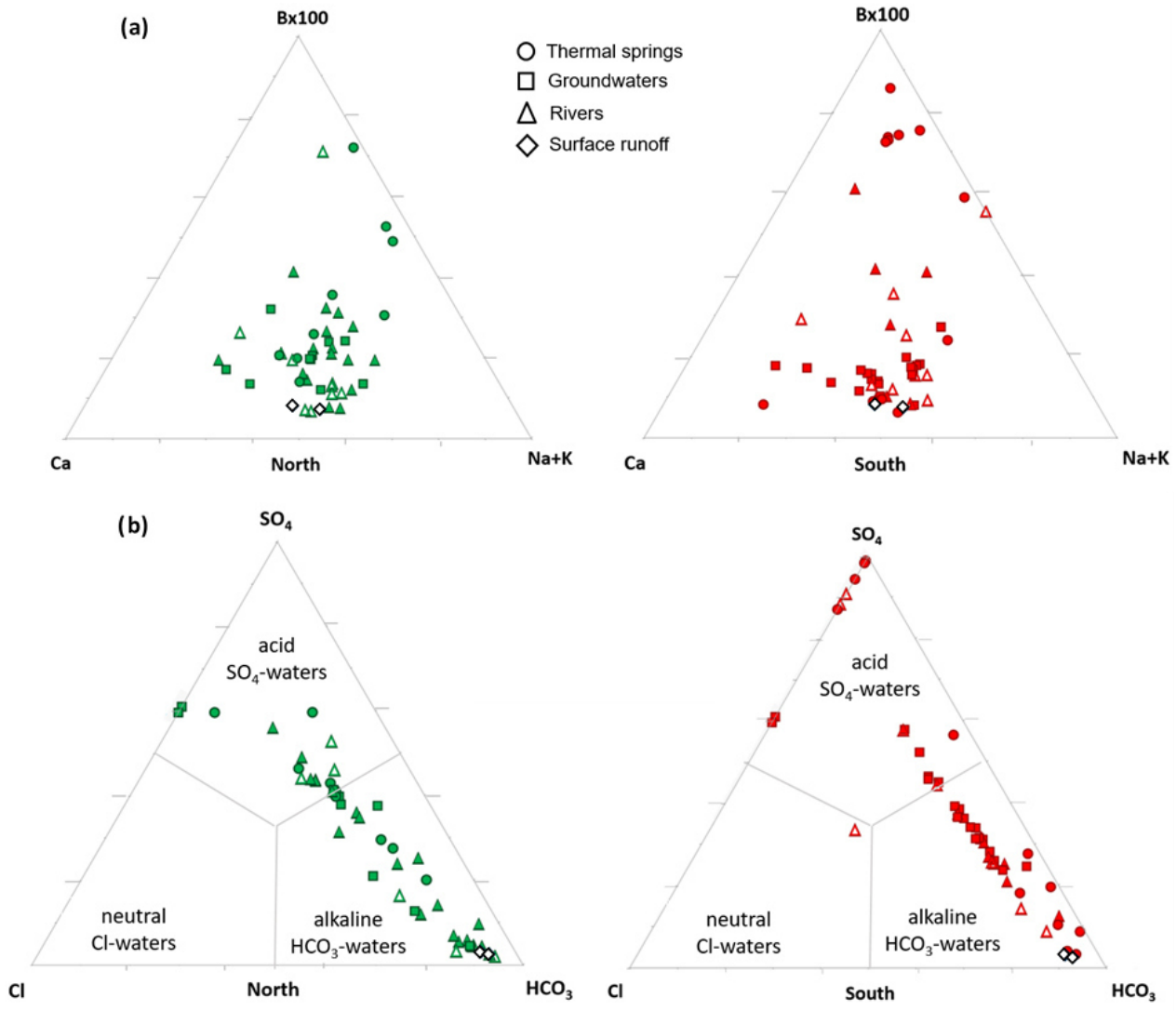

Fig. 7.4: Ternary diagrams of the (a) cationic composition and (b) anionic composition of the water samples from the northern (green) and southern (red) part of the Aso caldera: thermal springs (circle), groundwaters (square), river waters (triangle; with main river (plain triangle) and tributaries (open triangle)), and surface runoff (diamond). The HCO_3 concentration is calculated based on the charge balance.

Overall, the thermal springs can be classified as acid SO_4-waters (S21, S43, S49a, S49b, S52, S56, S57) and alkaline HCO_3-waters (S16, S42, S50, S55, S58, S59, S60, S61, S62) (**Fig. 7.4b**; *Ch1*; Giggenbach, 1988), and both types are present in the northern and in the southern part of the Aso caldera (**Fig. 7.4b**). Some thermal springs represent mixed thermal waters, i.e., "mixed neutral HCO_3-SO_4 waters" (S51, S63). This classification agrees with the available geochemical of the springs from the Aso caldera (Nagai et al, 1986; Shimano, 1997, 1999; Yamada et al, 2011; Hosono et al, 2018). The chemical composition of the thermal springs from the Aso caldera has been considered as stable according to the survey available since 1968 (Nagai et al, 1986; Shimano, 1997, 1999).

7.5.2 Elemental composition of river waters, groundwaters and surface runoff from the Aso caldera

The chemical composition of groundwaters, river waters and surface runoff is shown in **Table 7.1**. Groundwater, river waters, surface runoff display neutral to alkaline values of pH (6.0-8.9) (**Fig. 7.3).** The major cations are, respectively, Ca in most of groundwaters (164-1869 $\mu mol.l^{-1}$) and Na in most of river waters (60-1765 $\mu mol.l^{-1}$) (**Fig. 7.4a**). Major cation in surface runoff is Ca (156-608 $\mu mol.l^{-1}$) followed by Na (159-514 $\mu mol.l^{-1}$), Mg (74-333 $\mu mol.l^{-1}$) and K (32-140 $\mu mol.l^{-1}$) (**Fig. 7.4a**). Bicarbonate is the dominant anion in most of the groundwaters, river waters and surface runoff from the Aso caldera (**Fig. 7.4b**). The surface runoff exhibits anions dominated by HCO_3 (564-785 $\mu mol.l^{-1}$) followed by SO_4 (17-685 $\mu mol.l^{-1}$) and Cl (36-289 $\mu mol.l^{-1}$) (**Fig. 7.4b**). Boron (B) shows concentrations <6 $\mu mol.l^{-1}$ in groundwaters and <1 $\mu mol.l^{-1}$ in surface runoff (**Table 7.1**). River waters present generally low B concentrations (<20 $\mu mol.l^{-1}$) relative to thermal springs except in the northern S32 tributary (22.3 $\mu mol.l^{-1}$) (**Table 7.1**; **Fig. 7.4**).

The TDS values in river waters (1066-7356 $\mu mol.l^{-1}$) are in between the range of TDS values reported for thermal springs (2906-19052 $\mu mol.l^{-1}$), groundwaters (2077-5272 $\mu mol.l^{-1}$) and surface runoff (1587-3584 $\mu mol.l^{-1}$). Accordingly, river waters display Si concentration (356-1602 $\mu mol.l^{-1}$) generally lower than in thermal springs (940-2603 $\mu mol.l^{-1}$), and close to groundwaters (623-1292 $\mu mol.l^{-1}$) and surface runoff (545-929 $\mu mol.l^{-1}$) (**Fig. 7.3**). The anion concentrations support that the chemical composition of rivers from the northern part of the caldera (SO_4 and Cl= 18-2675 and 21-896 $\mu mol.l^{-1}$, respectively) and from the

southern part of the caldera (SO_4 and Cl = 49-4933 and 14-859 µmol.l^{-1}, respectively) is very similar (**Fig. 7.4**).

Seasonally in river waters, lower TDS are generally observed at high discharge than in base flow conditions in groundwaters and river waters except for the S33 confluence (**Fig. 7.5**). Dilution-corrected element concentrations between high discharge and base flow were obtained by normalizing element concentrations to Mg, i.e., the element the most sensitive to dilution (as supported by the highest correlation with TDS, R^2 = 0.78; **Suppl. Mat. 7.2**). The results show that, at high discharge relative to base flow conditions, riverine compositions are characterized by similar or lower dilution-corrected Cl concentrations ($Cl/Mg_{high\ discharge}$ = or < $Cl/Mg_{base\ flow}$; **Fig. 7.6a**), similar or higher dilution-corrected Si and Ca ($Si/Mg_{high\ discharge}$ = or > $Si/Mg_{base\ flow}$; **Fig. 7.6b** and $Ca/Mg_{high\ discharge}$ = or > $Ca/Mg_{base\ flow}$; **Fig. 7.6e**). Both higher and lower riverine dilution-corrected K, Na and B concentrations are measured at high discharge relative to base flow conditions (**Fig. 7.6c, 7.6d** and **7.6f**).

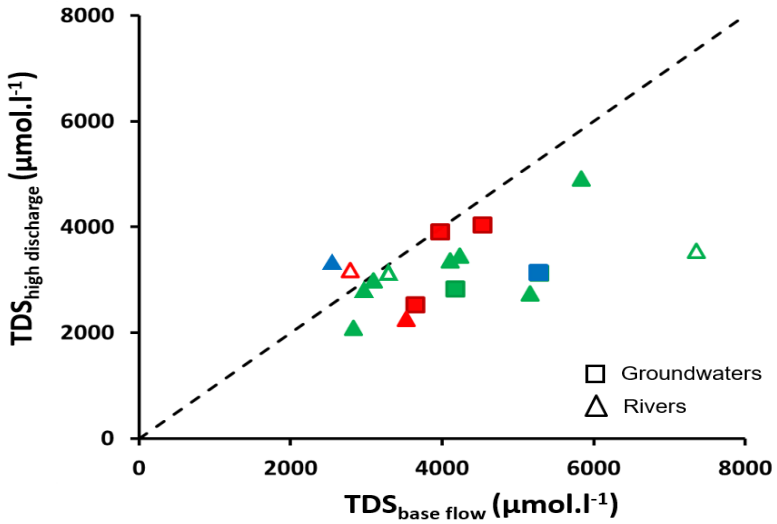

Fig. 7.5: Plot of the Total Dissolved Solid (TDS) at high discharge as a function of the TDS in base flow in the water samples from the northern (green) and southern (red) part of the Aso caldera: groundwaters (square), and river waters (triangle; with main river (plain triangle) and tributaries (open triangle)). The confluence S33 (in **Table 7.1**; plain blue triangle) and the crater groundwater S03 (plain blue square) are highlighted.

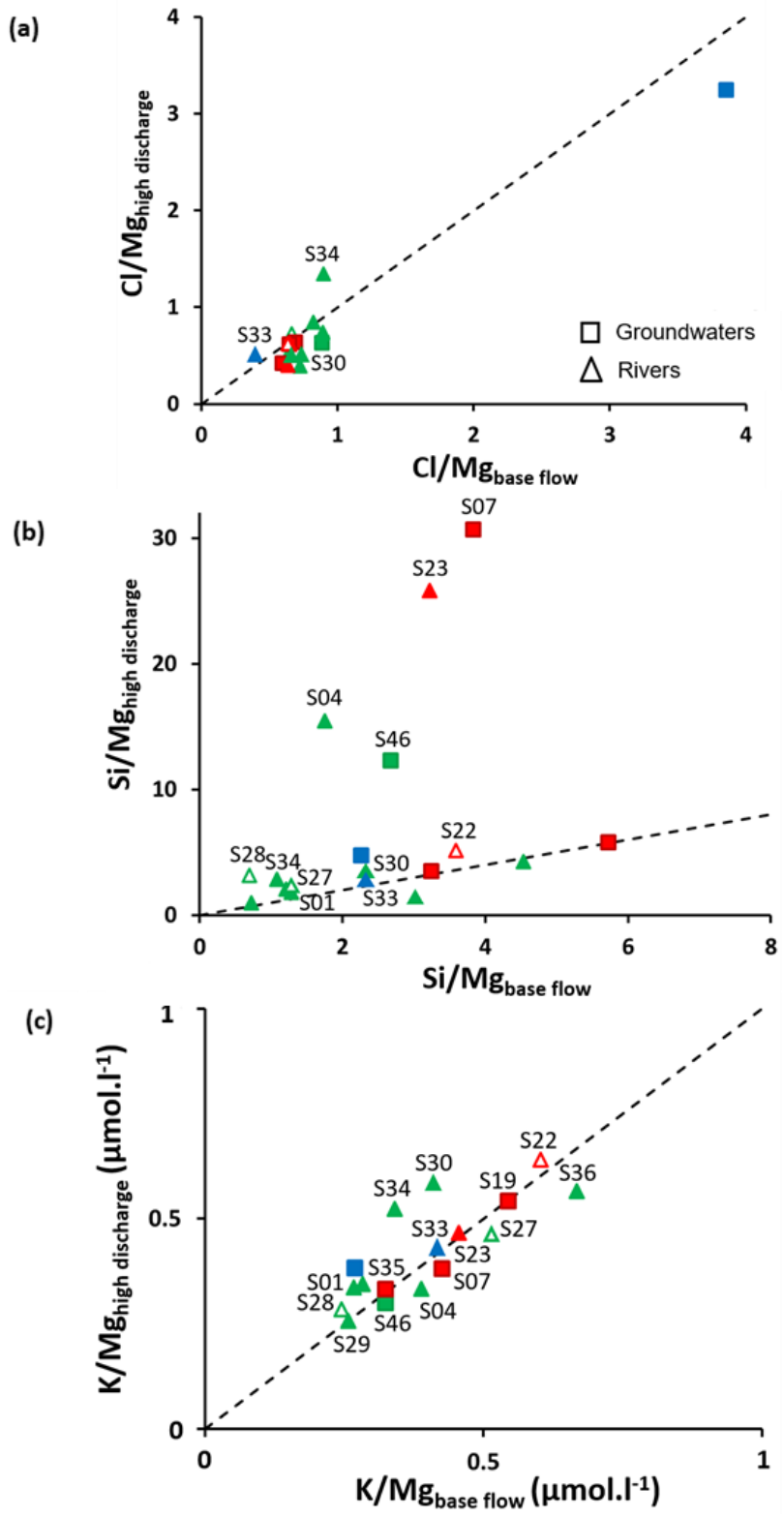
(a)
Cl/Mg high discharge
Cl/Mg base flow
S34
S33
S30
Groundwaters
Rivers
(b)
Si/Mg high discharge
Si/Mg base flow
S07
S23
S04
S46
S22
S28
S34
S27
S01
S30
S33
(c)
K/Mg high discharge (µmol.l-1)
K/Mg base flow (µmol.l-1)
S22
S30
S34
S19
S36
S33
S27
S23
S35
S01
S07
S28
S04
S46
S29

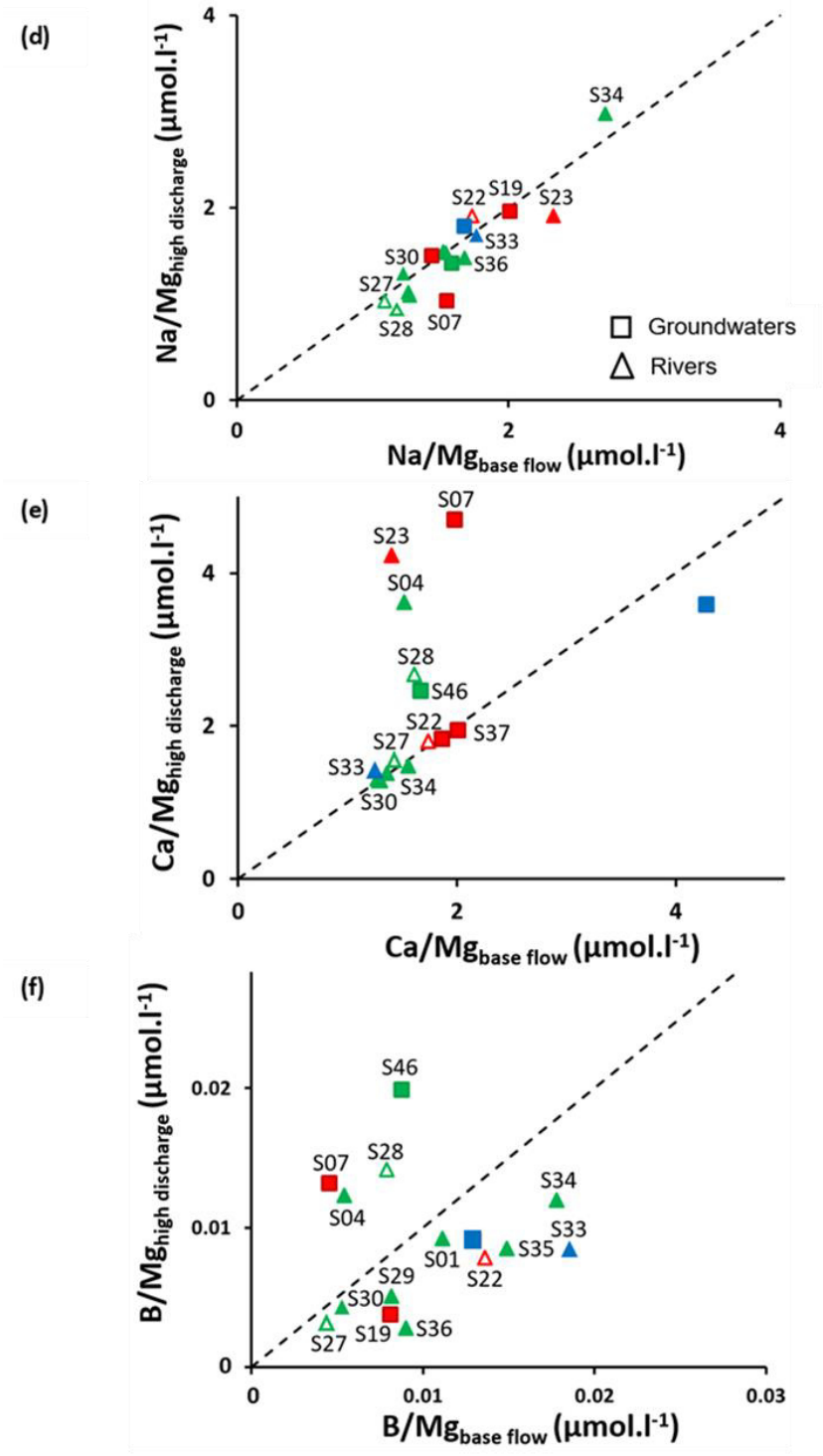
(d)
Na/Mg high discharge (µmol.l-1)
Na/Mg base flow (µmol.l-1)
S34
S22
S19
S23
S33
S30
S36
S27
S28
S07
Groundwaters
Rivers
(e)
Ca/Mg high discharge (µmol.l-1)
Ca/Mg base flow (µmol.l-1)
S07
S23
S04
S28
S46
S22
S37
S27
S33
S34
S30
(f)
B/Mg high discharge (µmol.l-1)
B/Mg base flow (µmol.l-1)
S46
S07
S28
S34
S04
S33
S01
S35
S22
S29
S30
S27
S19
S36

Fig. 7.6: Plot of the dilution-corrected element concentration at high discharge versus at base flow for (a) Cl, (b) Si, (c) K, (d) Na, (e) Ca and (f) B in the water samples from the northern (green) and southern (red) part of the Aso caldera: thermal springs (circle), groundwaters (square), river waters (triangle; with main river (plain triangle) and tributaries (open triangle)), and surface runoff (diamond). The confluence S33 (in **Table 7.1**; plain blue triangle) and the crater groundwater S03 (plain blue square) are highlighted.

7.5.3 Ge/Si ratios of waters from the Aso caldera

The Ge/Si ratios of all water samples (thermal springs, groundwaters, river waters and surface runoff just after rainfall) are reported in **Table 7.2**. Across the Aso caldera, the thermal springs display a large range of Ge/Si ratios values (0.20-19.47 $\mu mol.mol^{-1}$) generally higher than those reported for river waters (0.13-2.74 $\mu mol.mol^{-1}$ except one value at 25.46 $\mu mol.mol^{-1}$ for S32), and than those for groundwaters (0.11-1.12 $\mu mol.mol^{-1}$) and surface runoff (0.15-0.30 $\mu mol.mol^{-1}$) (**Fig. 7.7a**). For the thermal springs, the highest Ge/Si ratios are measured in the southern springs (0.3-19.5 $\mu mol.mol^{-1}$) relative to the northern springs (0.2-3.8 $\mu mol.mol^{-1}$; **Fig. 7.7a**). Whereas for the rivers, the highest Ge/Si value is found in a northern river water (S32 = 25.5 $\mu mol.mol^{-1}$), but overall rivers from the northern part of the caldera are characterized by similar Ge/Si ratios (0.2-2.74 $\mu mol.mol^{-1}$) than in rivers from the southern part of the caldera (0.1-1.2 $\mu mol.mol^{-1}$).

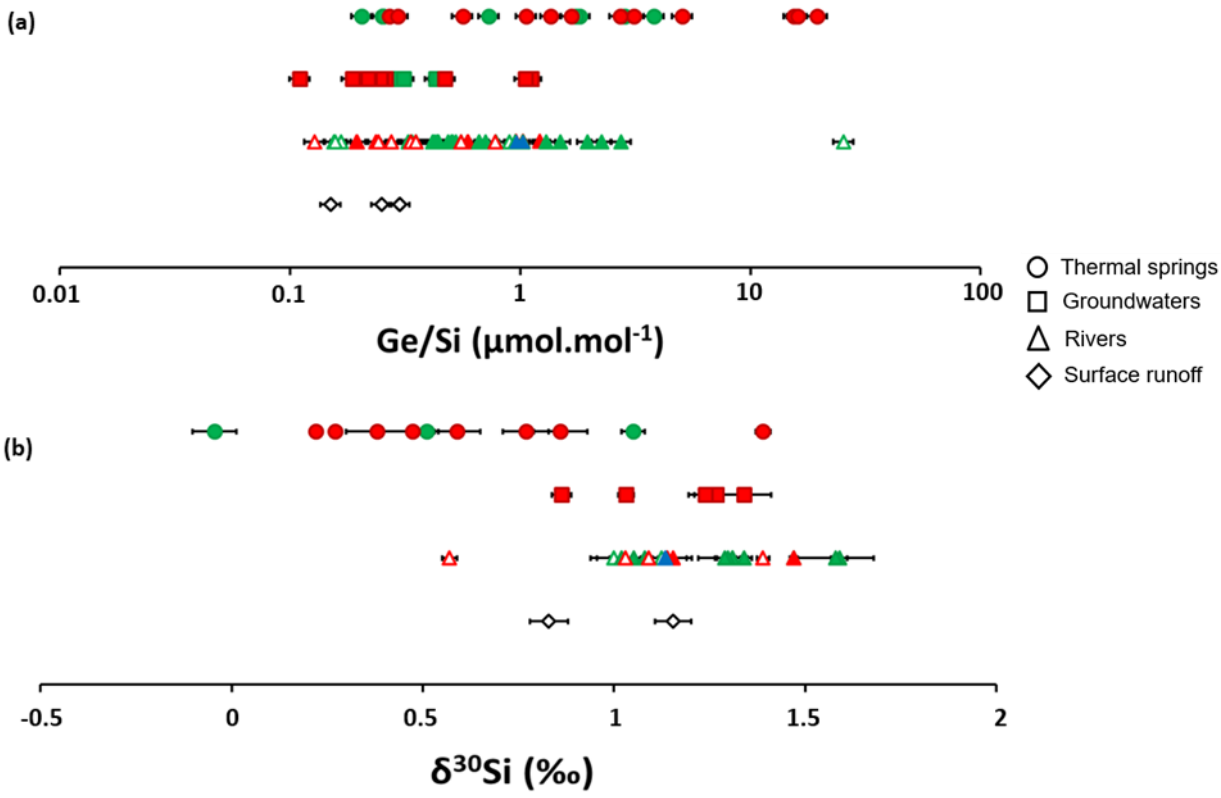

Fig. 7.7: Plot of the (a) Ge/Si ratios (± SD) and (b) Si isotope compositions (δ^{30}Si ± SD) in the water samples from the northern (green) and southern (red) part of the Aso caldera: thermal springs (circle), groundwaters (square), river waters (triangle; with main river (plain triangle) and tributaries (open triangle)), and surface runoff (diamond). The confluence S33 (in **Table 7.1**) is highlighted (plain blue triangle).

Seasonally, groundwaters display generally the same Ge/Si values at different seasons except for the crater groundwater S03 showing lower Ge/Si ratio at high discharge (0.47 µmol.mol^{-1}) compared to base flow (1.12 µmol.mol^{-1}) (**Fig. 7.8a**). In rivers, Ge/Si ratios are similar (± 10%, SD) or lower at high discharge relative to base flow (**Fig. 7.8a**), except for S22. And the river water collected at the outlet of the Aso caldera (S33) shows a similar value of Ge/Si at base flow (1.03 µmol.mol^{-1}) and at high discharge (0.96 µmol.mol^{-1}) considering precision on Ge/Si ratio (10%; SD) (**Fig. 7.8a**).

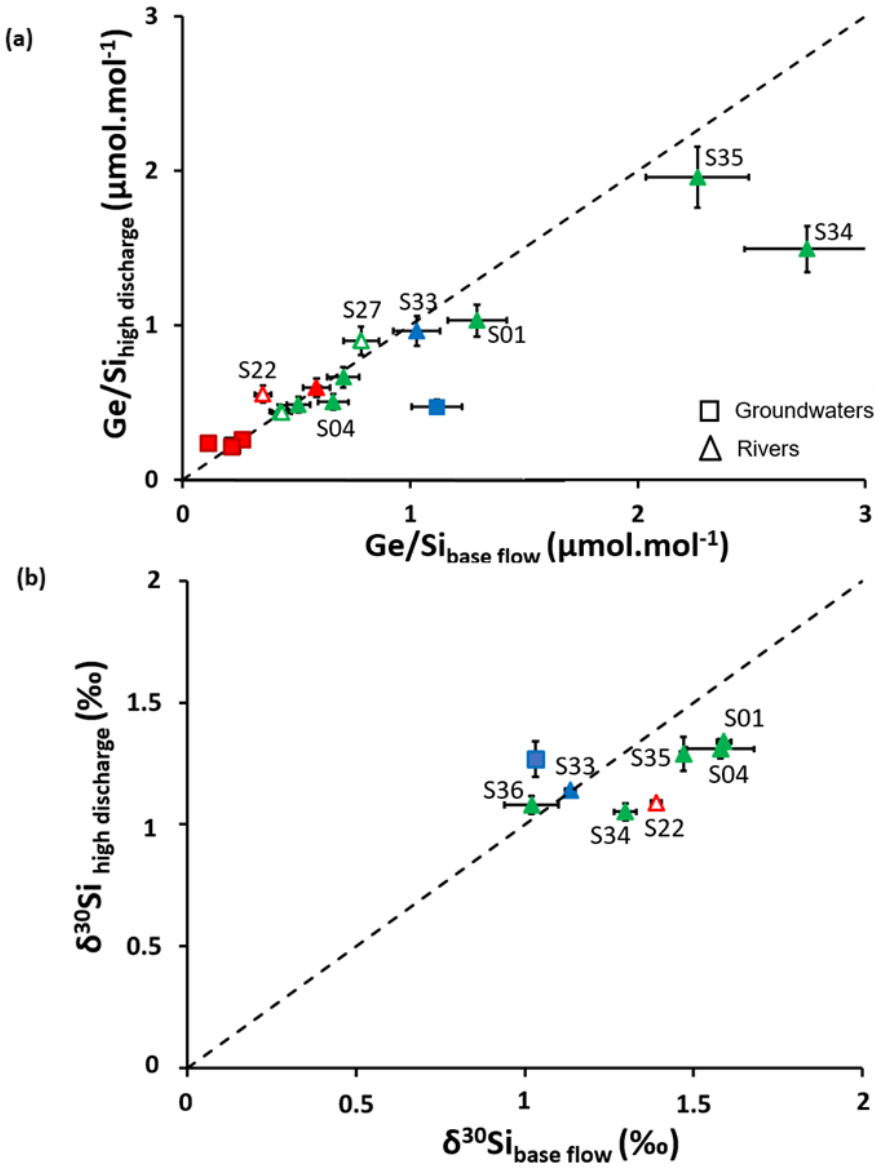

Fig. 7.8: Plot of the (a) Ge/Si ratio (± SD) at high discharge as a function of the Ge/Si ratio at base flow and (b) the Si isotope composition (δ^{30}Si ± SD) at high discharge as a function of the δ^{30}Si at base flow in the water samples from the northern (green) and southern (red) part of the Aso caldera: groundwaters (square), and river waters (triangle; with main river (plain triangle) and tributaries (open triangle)). The confluence S33 (in **Table 7.1**; plain blue triangle) and the crater groundwater S03 (plain blue square) are highlighted.

7.5.4 Si isotope compositions of waters from the Aso caldera

The Si isotope compositions measured on thermal springs, groundwaters, river waters and surface runoff just after rainfall are reported in **Table 7.2**. Thermal springs are generally characterized by lower δ^{30}Si values (from -0.05 ± 0.06 ‰ to 1.05 ± 0.03 ‰, except one higher value at 1.39 ± 0.02 ‰ for S51) than in river waters from the Aso caldera (from 1.00 ± 0.04 ‰ to 1.59 ± 0.02 ‰, except one lower value at 0.57 ± 0.02 ‰ for S05; **Fig. 7.7b**). Groundwaters and surface runoff display Si isotope compositions ranging from 0.86 to 1.34 ‰ and from 0.83 to 1.15 ‰, respectively (**Fig. 7.7b**). Overall, the riverine Si isotope composition is similar in the northern and southern part of the Aso caldera (δ^{30}Si = from 1.00 to 1.59 ‰ and from 0.57 to 1.47 ‰, respectively; **Table 7.2**). And a similar observation can be made for the δ^{30}Si in groundwaters (from 1.03 to 1.27 ‰ in the north and from 0.86 to 1.34 ‰ in the south of the Aso caldera; **Table 7.2**; **Fig. 7.7b**), and for δ^{30}Si in thermal springs (from -0.05 to 1.05 ‰ in the north and from 0.22 to 1.39 ‰ in the south of the Aso caldera; **Table 7.2**; **Fig. 7.7b**).

Based on the available seasonal Si isotopes data, it can be observed that the crater groundwater S03 is enriched in ^{30}Si (δ^{30}Si = 1.27 ± 0.07 ‰) at high discharge relative to base flow (δ^{30}Si = 1.03 ± 0.02 ‰) (**Fig. 7.8b**). In river waters, Si isotope compositions are either lower at high discharge relative to base flow (S01, S04, S22, S34, S35) or similar (S36) (**Fig. 7.8b**). Specifically, and as already highlighted for the Ge/Si ratio, the river water collected at the outlet of the Aso caldera (S33) shows a similar value of δ^{30}Si at base flow (1.14 ± 0.02 ‰) than at high discharge (1.14 ± 0.00 ‰) (**Fig. 7.8b**).

Table 7.2: Germanium concentrations, Ge/Si ratios and silicon isotope compositions (δ^{29}Si and δ^{30}Si) in thermal springs, groundwaters, river waters and surface runoff of water samples from the Aso caldera, Kyūshū Island, Japan. n = number of measurements. sum = summer.

	Label	Sampling season	Ge	Ge/Si	$\delta^{29}Si$	SD	$\delta^{30}Si$	SD	n
			$nmol.l^{-1}$	$\mu mol.mol^{-1}$	‰		‰		
Thermal springs	S16	spring 15	0.28	0.27	0.43	0.02	0.86	0.07	1
	S16	fall 16	0.28	0.29	0.43	0.07	0.77	0.06	1
	S21	spring 15	6.88	3.12	0.24	0.07	0.47	0.01	2
	S42	fall 14	41.16	19.47	0.20	0.06	0.38	0.08	1
	S42	spring 15	37.72	15.48	0.10	0.01	0.22	0.01	1
	S43	spring 15	3.44	1.67	-	-	-	-	-
	S49a	spring 15	2.75	1.06	-	-	-	-	-
	S49b	spring 15	12.39	5.07	0.14	0.03	0.27	0.01	1
	S50	fall 16	5.92	2.72	-	-	-	-	-
	S51	fall 16	0.96	0.56	0.72	0.06	1.39	0.02	1
	S52	fall 16	1.65	0.73	-	-	-	-	-
	S55	sum 16	3.44	1.82	-	-	-	-	-
	S55	fall 16	3.3	1.75	0.27	0.01	0.51	0.03	1
	S56	fall 16	0.28	0.2	-	-	-	-	-
	S57	fall 16	0.28	0.25	-	-	-	-	-
	S58	fall 16	0.28	0.25	0.59	0.01	1.05	0.03	1
	S59	fall 16	0.28	0.25	-	-	-	-	-
	S60	fall 16	1.93	1.36	0.30	0.01	0.59	0.06	1
	S61	fall 16	30.56	16.02	-	-	-	-	-
	S62	fall 16	5.23	2.85	0.03	0.01	-0.05	0.06	2
	S63	fall 16	4.82	3.82	-	-	-	-	-
Groundwaters	S03	spring 15	1.10	1.12	0.56	0.01	1.03	0.02	1
	S03	sum 15	0.41	0.47	0.68	0.06	1.27	0.07	1
	S07	spring 15	0.28	0.26	-	-	-	-	-
	S07	sum 15	0.28	0.26	-	-	-	-	-
	S07	sum 16	0.21	0.19	-	-	-	-	-
	S07	fall 16	0.28	0.26	-	-	-	-	-
	S19	spring 15	0.28	0.22	-	-	-	-	-
	S19	sum 15	0.28	0.22	-	-	-	-	-
	S19	fall 16	0.28	0.24	-	-	-	-	-
	S37	spring 15	0.14	0.11	-	-	-	-	-
	S37	sum 16	0.28	0.24	-	-	-	-	-
	S37	fall 16	0.28	0.24	-	-	-	-	-
	S38	fall 14	0.28	0.25	0.70	0.03	1.34	0.07	1
	S38	spring 15	0.28	0.24	0.66	0.02	1.24	0.03	1
	S38	fall 16	0.28	0.25	-	-	-	-	-
	S39	spring 15	0.28	0.21	-	-	-	-	-
	S39	fall 16	0.28	0.22	-	-	-	-	-
	S40	spring 15	0.28	0.22	-	-	-	-	-
	S40	fall 16	0.28	0.22	-	-	-	-	-
	S41	spring 15	1.24	1.05	0.46	0.03	0.86	0.03	3
	S45	spring 15	0.23	0.24	-	-	-	-	-
	S45	fall 16	0.28	0.31	-	-	-	-	-
	S46	spring 15	0.23	0.22	-	-	-	-	-
	S46	sum 15	0.25	0.23	-	-	-	-	-
	S46	sum 16	0.25	0.23	-	-	-	-	-
	S46	fall 16	0.28	0.27	-	-	-	-	-
	S47	spring 15	0.28	0.44	-	-	-	-	-
	S47	fall 16	0.28	0.43	-	-	-	-	-

- : not measured.

	Label	Sampling season	Ge	Ge/Si	$\delta^{29}Si$	SD	$\delta^{30}Si$	SD	n
			nmol.l^{-1}	µmol.mol^{-1}	‰		‰		
River waters	S48	spring 15	0.28	0.35	-	-	-	-	-
	S48	fall 16	0.28	0.34	-	-	-	-	-
	S01	spring 15	0.96	1.29	0.82	0.03	1.59	0.02	2
	S01	sum 15	0.83	1.03	0.68	0.01	1.34	0.01	1
	S01	sum 16	0.69	0.95	0.68	0.01	1.31	0.01	1
	S04	spring 15	0.41	0.66	0.81	0.01	1.58	0.10	1
	S04	sum 15	0.41	0.50	0.70	0.04	1.31	0.04	1
	S05	spring 15	0.28	0.24	0.29	0.01	0.57	0.02	1
	S06	spring 15	1.24	1.22	0.76	0.07	1.47	0.01	1
	S08	spring 15	1.24	0.78	0.53	0.02	1.03	0.04	1
	S08	fall 16	1.10	0.78	0.59	0.01	1.08	0.06	1
	S09	spring 15	0.28	0.28	-	-	-	-	-
	S10	spring 15	0.21	0.19	-	-	-	-	-
	S11	spring 15	0.28	0.33	-	-	-	-	-
	S12	spring 15	0.28	0.24	-	-	-	-	-
	S14	spring 15	0.21	0.20	0.57	0.06	1.16	0.04	2
	S15b	spring 15	0.30	0.39	-	-	-	-	-
	S17	spring 15	0.28	0.33	0.48	0.09	1.00	0.04	2
	S18	spring 15	0.06	0.16	-	-	-	-	-
	S20	spring 15	0.14	0.13	-	-	-	-	-
	S22	spring 15	0.28	0.35	0.74	0.01	1.39	0.02	2
	S22	sum 15	0.55	0.55	0.58	0.03	1.09	0.01	1
	S23	spring 15	0.55	0.59	-	-	-	-	-
	S23	sum 15	0.55	0.59	-	-	-	-	-
	S24	spring 15	0.14	0.17	0.55	0.07	1.18	0.01	2
	S25	spring 15	0.41	0.55	-	-	-	-	-
	S26	spring 15	0.41	0.52	-	-	-	-	-
	S27	spring 15	0.55	0.78	-	-	-	-	-
	S27	sum 15	0.69	0.90	-	-	-	-	-
	S28	spring 15	0.41	0.44	-	-	-	-	-
	S28	sum 15	0.41	0.44	-	-	-	-	-
	S28	sum 16	0.28	0.42	-	-	-	-	-
	S29	spring 15	0.55	0.71	-	-	-	-	-
	S29	sum 15	0.55	0.66	-	-	-	-	-
	S30	spring 15	0.41	0.51	-	-	-	-	-
	S30	sum 15	0.41	0.49	-	-	-	-	-
	S31	spring 15	0.12	0.16	-	-	-	-	-
	S32	spring 15	16.8	25.46	0.56	0.02	1.12	0.08	1
	S33	spring 15	0.96	1.03	0.58	0.01	1.14	0.02	2
	S33	sum 15	0.83	0.96	0.56	0.03	1.14	0.01	1
	S34	spring 15	1.93	2.74	0.65	0.04	1.30	0.03	1
	S34	sum 15	0.96	1.49	0.54	0.02	1.05	0.04	1
	S35	spring 15	1.79	2.26	0.77	0.01	1.47	0.01	1
	S35	sum 15	1.51	1.96	0.60	0.01	1.29	0.07	1
	S36	spring 15	0.41	0.42	0.46	0.12	1.02	0.08	2
	S36	sum 15	0.41	0.44	0.51	0.04	1.08	0.04	2
Surface runoff	S02	spring 15	0.22	0.30	0.44	0.01	0.83	0.05	1
	S13	spring 15	0.28	0.30	-	-	-	-	-
	S44	spring 15	0.10	0.15	0.55	0.01	1.15	0.05	1
	S44	fall 16	0.14	0.25	-	-	-	-	-

- : not measured.

7.6. Discussion

7.6.1 Tracing the hydrothermal input to rivers from the Aso caldera using the Ge/Si and Cl/B ratios

It is recognized that both acid SO_4-waters and alkaline HCO_3-waters are present in the northern and in the southern part of the Aso caldera (Nagai et al, 1986; Shimano, 1997, 1999; Yamada et al, 2011; Hosono et al, 2018), and the presence of these thermal springs is confirmed by our data (**section 7.5.1**; **Fig. 7.4**). Both types of thermal waters are likely to contribute to the sampled river waters. It is indeed reported that about 3.2 to 4.1% of the water flux at the caldera outlet (corresponding to the sampling site S33) derives from the thermal deep fluid from hydrothermal system of the Aso volcano (Hosono et al, 2008).

The hydrothermal contribution to river waters from the Aso caldera can be suspected based on their Ge/Si ratios (0.13-2.74 $\mu mol.mol^{-1}$ except one value at 25.46 $\mu mol.mol^{-1}$ for S32) with values higher than other riverine contributors such as groundwater (0.11-1.12 $\mu mol.mol^{-1}$) and surface runoff (0.15-0.30 $\mu mol.mol^{-1}$), with thermal springs being the only contributor with higher Ge/Si ratios (0.20-19.47 $\mu mol.mol^{-1}$) (**Fig. 7.7a**). According to *Ch1*, the Ge/Si ratio in acid SO_4-waters and alkaline HCO_3-waters result from water-rock interaction and varies depending on silica precipitation. With this type of thermal contribution, the formal identification of a hydrothermal input based on Ge/Si ratio is best confirmed by a combination with element ratios classicaly used in hydrothermal context, such as for example the SO_4/Cl ratio and SO_4 concentration used in Basse-Terre Island (*Ch3*), or the Cl/B or B/SO_4 ratio (Louvat et al, 2011). The advantage of using a ratio involving B is the sensitivity of B to high temperature providing a recognized indicator for hydrothermalism (Louvat et al, 2011).

Boron enrichment is typical in thermal springs due to high volatility of B at high temperature (Louvat et al, 2011). The B source in thermal springs derives from magma intrusion and high temperature water-rock interaction with B-bearing volcanic rocks (Arnórsson and Andrésdóttir, 1995). Rivers influenced by hydrothermal input in volcanic terrains display high concentrations of B (3-52 $\mu mol.l^{-1}$ in rivers from Basse-Terre Island, Guadeloupe; Louvat et al, 2011). The range in B concentrations in the thermal springs of Aso volcano is higher than those reported in thermal springs of La Soufrière volcano

in Guadeloupe (3-89 µmol.l^{-1}; Louvat et al, 2011) and in the thermal springs of Iceland (5-93 µmol.l^{-1}; Arnórsson and Andrésdóttir, 1995).

The hydrothermal contribution to river waters from the Aso caldera is supported by their generally higher Ge/Si ratio and lower Cl/B ratio relative to other riverine contributors such as groundwater and surface runoff (**Fig. 7.9**). Indeed, the highest value of riverine Ge/Si ratio in S32 (25.46 µmol.mol^{-1}) is associated with highest riverine B concentration (22.3 µmol.l^{-1}) and the lowest Cl/B ratio (9.5; **Fig. 7.9**). These ratios in river waters reflect the contribution from thermal springs characterized by high Ge/Si values and low Cl/B ratios relative to other riverine contributors (**Fig. 7.9**).

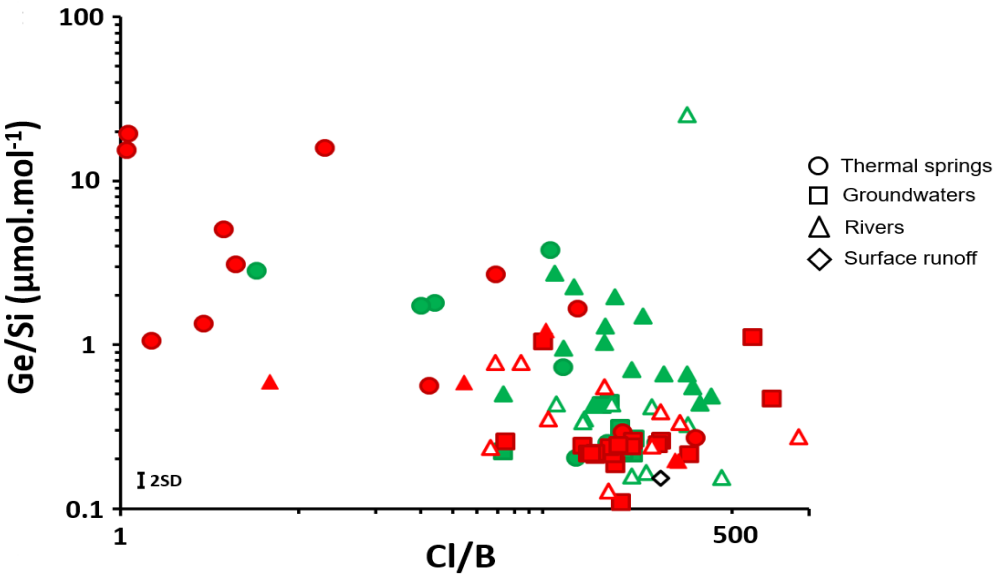

Fig. 7.9: Plot of the Ge/Si ratio as a function of the Cl/B ratio in the water samples from the northern (green) and southern (red) part of the Aso caldera: thermal springs (circle), groundwaters (square), river waters (triangle; with main river (plain triangle) and tributaries (open triangle)), and surface runoff (diamond).

7.6.2 Seasonal change in riverine Ge/Si and $\delta^{30}Si$ values with discharge as indicators of changes in the relative contribution from thermal springs, groundwater and surface runoff within the Aso caldera

7.6.2.1 The fraction of hydrothermal contribution to rivers is reduced in wet season

The concentrations of major cations, Si and anions (SO_4, Cl and HCO_3) in river waters flowing in the Aso caldera display seasonal variations (**Table 7.1**) that are primarily due to rainwater dilution effect during the summer seasons (highest precipitations and riverine discharge; **Fig. 7.2**). Precipitation rates are reported as the dominant hydrological forcing in this area (JMA, 2019). However, not all elements are diluted in a similar way (according to their different correlations with TDS; **Suppl. Mat. 7.2**). This supports the view that variations in concentrations in rivers are not only caused by rain water dilution but result from the mixing of distinct contributors (thermal springs, groundwaters and surface runoff).

Decreasing the Ge/Si ratio in main rivers (S01, S04, S34, S35) at high discharge supports a lower relative contribution of hydrothermal input to rivers at high discharge (**Fig. 7.8a**). This hypothesis is strongly supported by lower Cl concentrations ($Cl/Mg_{high\ discharge} < Cl/Mg_{base\ flow}$, except for S34; **Fig. 7.6a),** lower TDS values (**Fig. 7.5**), and lower B concentration ($B/Mg_{high\ discharge} < B/Mg_{base\ flow}$; except S28 and S04; **Fig. 7.6f**) in river waters at high discharge relative to base flow conditions.

One exception is the higher B dilution-corrected concentration observed in river water S28 at high discharge. This could reflect the increasing relative contribution of groundwater at high discharge, as suggested by the higher B dilution-corrected concentration of the nearby groundwater S46 at high discharge relative to low discharge (**Fig. 7.6f**; both located in the northern part of the caldera; **Fig. 7.1**).

7.6.2.2 The processes controlling groundwater contribution to rivers change seasonally

The contribution of groundwaters to riverine chemistry of the Aso caldera is supported by the existing understanding of the groundwater flow system in the Aso volcanic edifice (Hase et al, 2005; Hosono et al, 2008; Yamada et al, 2011; Terada et al, 2012). The morphology and topography of the Aso caldera watershed are characterized by symmetrical features between the northern and southern catchments, from higher altitude close to the Aso volcano to lower altitude on the border of the Aso caldera, except for a slightly larger catchment area in the north, partly associated with the relatively flat plain, favoring the contribution of groundwaters to northern rivers (Hosono et al, 2008).

Most groundwater samples are from low altitudes (except S03, the crater groundwater). At high discharge, the hydrothermal contribution to groundwater can either increase or decrease according the lower or higher B concentration in high discharge relative to base flow (**Fig. 7.6f**). This may depend on the groundwater depth as it is reported that at lower altitudes in the Aso caldera, deeper groundwaters are mainly influenced by a significant contribution of magmatic CO_2 due to proximity with the magma at the bottom of the Aso volcano (Yamada et al, 2011). Groundwaters also display similar (S19, S37) or higher (S46, S07) dilution-corrected Si and Ca concentrations at high discharge relative to base flow (**Fig. 7.6b**). This could be dictated by the amount of water available for mineral dissolution and modifying water-rock interaction in favor of primary mineral dissolution. The river waters were plotted in a mixing diagram using Na-normalized molar ratio and are shown to fit close to the "silicates" reservoir (**Suppl. Mat. 7.3**). The range in riverine Ca/Na and Mg/Na ratios from the Aso caldera is larger at high discharge than at base flow suggesting that the change in runoff during the rain season is likely to mobilize other sources of dissolved elements in contact with primary minerals.
In contrast, the groundwater sample from the crater (S03) provides insights on the functioning of a higher altitude groundwater at Aso. The lower Ge/Si ratio in S03 at high discharge (0.47 $\mu mol.mol^{-1}$; **Fig. 7.8a**) relative to base flow (1.12 $\mu mol.mol^{-1}$) suggests a seasonal dilution of the fraction of hydrothermal input in groundwater due to water recharge with rainfall. This agrees with the reported mixing of magmatic CO_2 into groundwater beneath the Aso volcano (Yamada et al, 2011). Moreover, the S03 crater groundwater displays a higher $\delta^{30}Si$ value at high discharge (1.27 ‰) than at base flow (1.03 ‰) (**Fig.**

7.8b). Heavier Si isotope compositions may result from clay mineral formation, a process preferentially taking up the light Si isotopes leading to a residual water enriched in the heavy Si isotopes (e.g., Opfergelt and Delmelle, 2012). At Aso, groundwaters located at higher altitudes have higher residence time (~30-35 years) relative to groundwater located at lower altitudes (~20 years) (Yamada et al, 2011). It can therefore be hypothesized that a longer water residence time in rock fractures would favor clay formation in groundwater located at higher altitude, and that the influence of this process is only transferred to groundwater upon rainfall recharge (increasing pH from 4.3 to 5.2 between base flow and high discharge conditions in S03; **Table 7.1**).

7.6.2.3 Higher contribution from mineral weathering to rivers at high discharge

For some rivers, the Si isotope compositions are lower at high discharge than at base flow (S01, S04, S22, S34, S35; **Fig. 7.8b**). The δ^{30}Si values and the Si concentration in groundwater and surface runoff are in the same range than in the river waters (**Fig. 7.10a**). Therefore, lower riverine δ^{30}Si values at high discharge relative to base flow support the contribution from waters controlled by distinct Si sources or involving Si isotope fractionation processes. More precisely, the riverine δ^{30}Si values are either lower at high discharge relative to base flow (S01, S04, S22, S34, S35) or similar (S33, S36; **Fig. 7.8b**). Among those rivers, the dilution-corrected element concentrations show that some of these rivers are enriched in Si (S01, S04, S22, S34; **Fig. 7.6b**), in K (S01, S22, S34, S35; **Fig 7.6c)** and in Ca (S04, S22; **Fig. 7.6e**) at high discharge relative to base flow, whereas no change in dilution-corrected Na concentrations were observed for these rivers (**Fig. 7.6d**).

These element concentration data suggest that a lighter Si isotope composition might originate from the contribution of primary mineral dissolution of volcanic rocks releasing Si and K (**Fig. 7.10**). This is supported for the northern rivers by a correlation between the δ^{30}Si and the Ca/K ratio (**Fig. 7.10b**). At Aso, the lithology ranges from basalt to rhyolite (Nakada et al, 2003). A contribution from rhyolite and basalt dissolution may contribute to release Si and K (rhyolite) and Si and Ca (basalt) (**section 7.6.2.2**). A contribution from rhyolite and basalt dissolution (δ^{30}Si of rhyolite = -0.14 ± 0.16 ‰; δ^{30}Si of basalt =

-0.29 ± 0.11 ‰; Savage et al, 2011) following flow paths that storm flow can take to the river (Kirchner et al, 2000) can explain the lower $\delta^{30}Si$ in rivers at high discharge relative to base flow. This is also supported by the lower Ge/Si ratios at high discharge relative to base flow for 4 of the 5 rivers characterized by lower $\delta^{30}Si$ at high discharge (S01, S04, S34, S35). Indeed, a contribution from rhyolite and basalt dissolution (Ge/Si of rhyolite = 2-3 $\mu mol.mol^{-1}$; Ge/Si of basalt = 2.6 $\mu mol.mol^{-1}$; Rouxel et al, 2003) can also explain the lower Ge/Si ratio in rivers at high discharge relative to base flow.

A lighter Si isotope composition in rivers at high discharge relative to low discharge could also partly be attributed to the redissolution of clay minerals or amorphous silica (e.g., biogenic silica from diatoms or phytoliths), both being generally characterized by light Si isotope compositions (Opfergelt and Delmelle, 2012). However, secondary mineral redissolution is rather unlikely under these pH conditions (6.0-8.9 for 43 on 46 river samples) decreasing the solubility of Fe- and Al-bearing minerals. In the same way, the pH conditions for amorphous silica redissolution are not met (41 on 46 river samples have pH < 8.25), considering that amorphous silica solubility increases above pH 8 (Alexander et al, 1954) such as reported for diatom frustule dissolution in the Yellowstone river at pH> 8.25 (McCleskey et al, 2019).

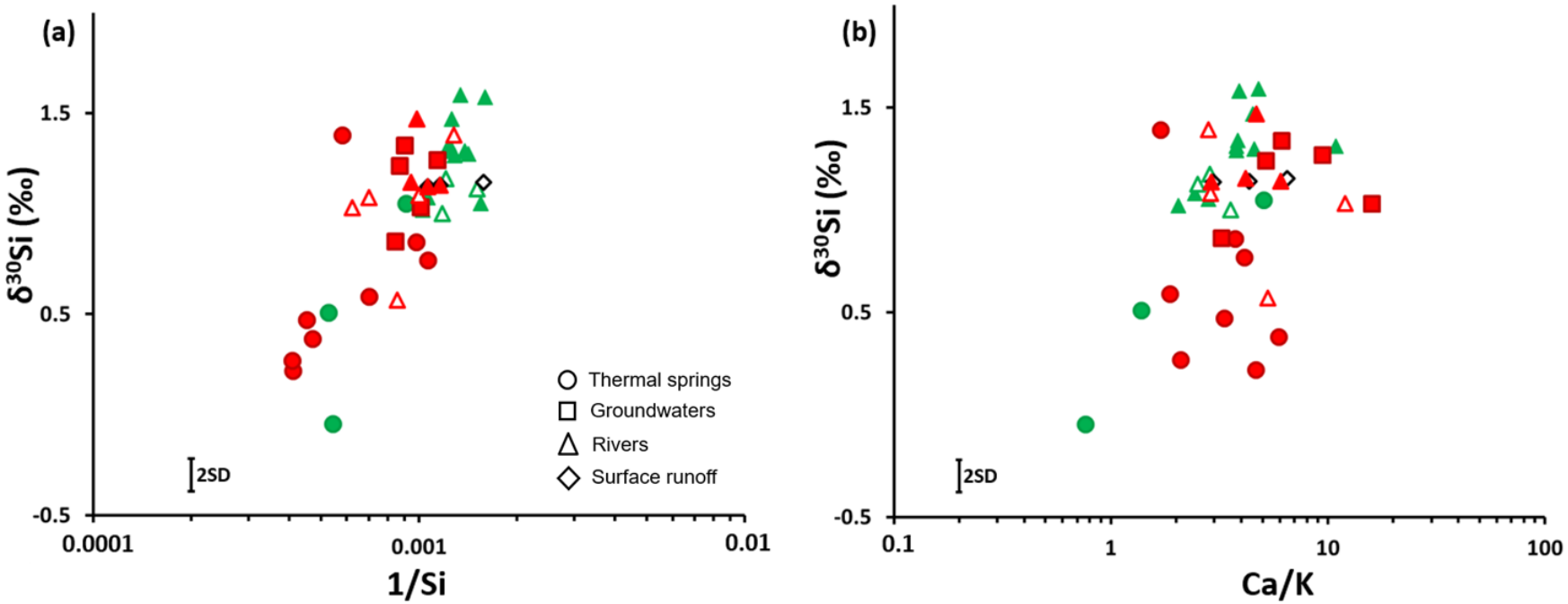

Fig. 7.10: Plot of the Si isotope composition ($\delta^{30}Si \pm SD$) as a function of (a) the Si concentration and (b) the Ca/K ratio in the water samples from the northern (green) and southern (red) part of the Aso caldera: thermal springs (circle), groundwaters (square), river waters (triangle; with main river (plain triangle) and tributaries (open triangle)), and surface runoff (diamond).

Even if surface runoff is promoted by high precipitations throughout the year (minimum 500 mm of rainfall/month), a higher contribution from surface runoff to rivers can be expected in the summer given that precipition are more than five times higher in the summer than in the Spring in the area (annual average of 2373 mm and 437 mm, respectively; JMA, 2019). In the Aso caldera, it is well known that water provided by rainfall on the central cones flows down the volcanic edifice along the topography (Yamada et al, 2011). This is likely to modifie water residence time in rock fractures and soils (White and Blum, 1995). The observed changes in Si and K concentrations, in $\delta^{30}Si$ and in Ge/Si ratios values in rivers at high discharge relative to base flow in rivers support the hypothesis that rainfall water fill in the rock and soil surface porosity resulting in the expulsion to rivers of a pre-rainfall surface water that was previously in contact with the rock/soil, and influenced by primary mineral dissolution and/or secondary mineral formation (**Fig. 7.11**).

This observation is consistent with the contribution from mineral weathering at snowmelt highlighted in the rivers draining the Yellowstone Plateau Volcanic Field (*Ch4*), and highlights that geochemical tracers such as Ge/Si ratio and Si isotopes provide a way to identify seasonal changes in riverine chemistry that may be a short-term pulse of element but has implications for the assessment of weathering fluxes and the associated atmospheric CO_2 consumption, a major stake in hydrothermally active volcanic regions where a portion of the source of CO_2 is magmatic.

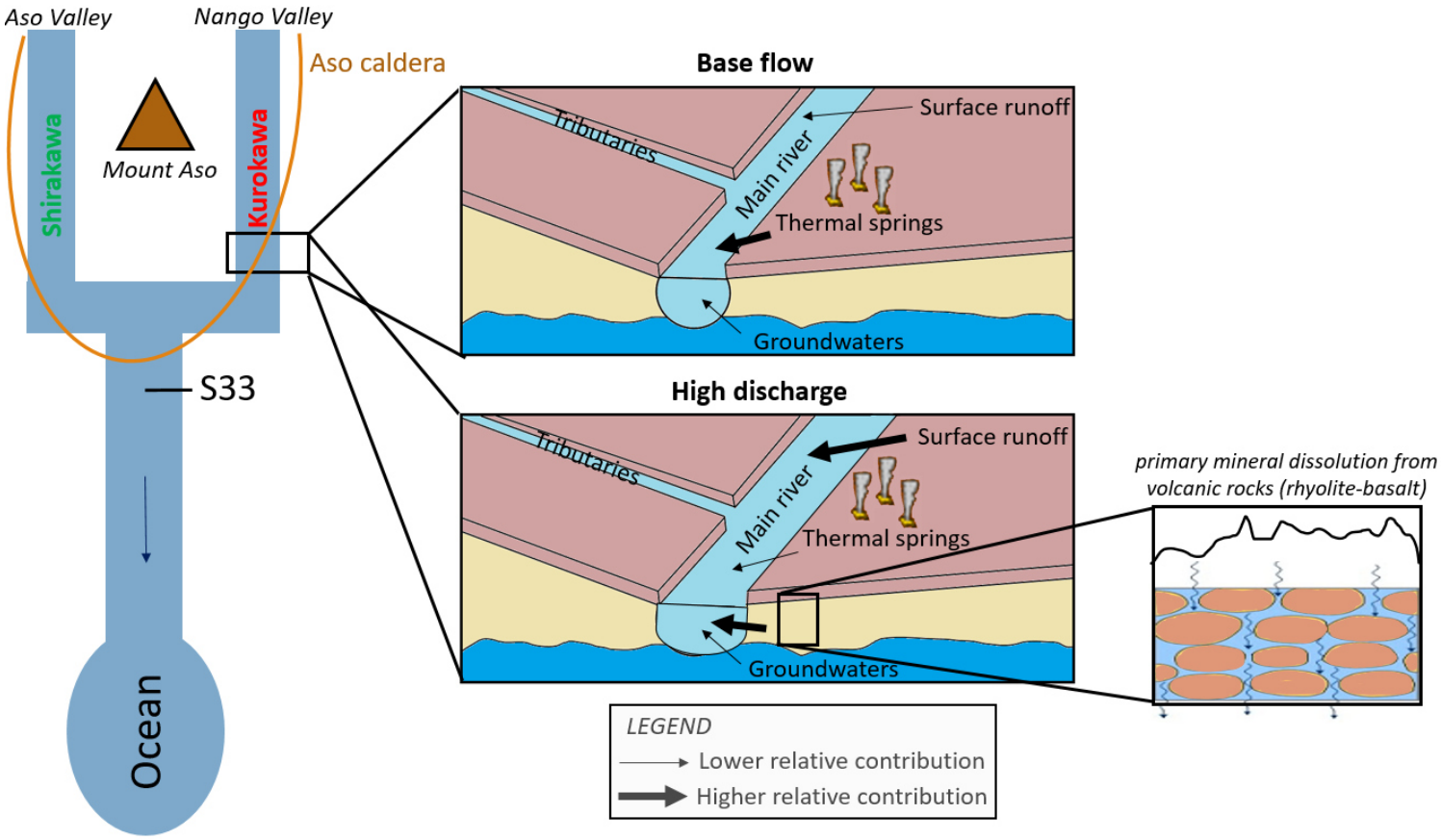
Aso Valley
Nango Valley
Aso caldera
Shirakawa
Kurokawa
Mount Aso
S33
Ocean
Base flow
Tributaries
Main river
Surface runoff
Thermal springs
Groundwaters
High discharge
Tributaries
Main river
Surface runoff
Thermal springs
Groundwaters
primary mineral dissolution from volcanic rocks (rhyolite-basalt)
LEGEND
Lower relative contribution
Higher relative contribution

Fig. 7.11: Schematic of the influence of the flow regime (base flow and high discharge) on the different contributors to river waters in the Aso caldera (northern river in green, southern river in red). The main contributors are thermal springs, groundwater and surface runoff. The width of the arrow is proportional to the relative input from the contributors. At high discharge, the fraction of hydrothermal input is reduced relative to other contributions, i.e., groundwater, surface runoff, and a contribution from subsurface water influenced by primary mineral dissolution.

7.6.3 Implications for seasonal changes at the outlet of the Aso caldera

Despite the seasonal variations in riverine chemistry observed for rivers from the Aso caldera, the river water collected at the outlet of the Aso caldera (S33) displays similar value of dilution-corrected Cl/Mg, Si/Mg, K/Mg, Na/Mg and Ca/Mg at high discharge relative to base flow (**Fig. 7.6a, b, c, d, e**). Only lower dilution-corrected B/Mg is observed at high discharge relative to base flow (**Fig. 7.6f**). Moreover, a similar value of Ge/Si ratios and $\delta^{30}Si$ at base flow (1.03 $\mu mol.mol^{-1}$ and 1.14 ± 0.02 ‰, respectively) and high discharge (0.96 $\mu mol.mol^{-1}$ and 1.14 ± 0.00 ‰, respectively) (**Fig. 7.8a, b**) suggests no major changes in contributions and controlling processes to the S33 river water. This observation shows that despite local seasonal variations in riverine chemistry within the caldera, these effects cannot be detected at larger scale in the riverine chemistry at the outlet of the caldera (S33). This highlights that a comprehensive understanding of the sources and processes contributing to riverine chemistry, and the seasonal influence on these sources and processes, can only be obtained from a local scale investigation (**Fig. 7.11**). At larger spatial scale such as S33 integrating the scale of the caldera and mainly controlled by hydrothermal contribution, it seems that the potential seasonal influence from meteoric weathering observed within the caldera is masked here by the large spatial variability.

Even if changes in controlling processes cannot be directly identified on the river water from S33, this sampling location provides the unique opportunity to compare the chemical weathering rates (CWR, $t.km^{-2}.yr^{-1}$) at the scale of the Aso caldera for different discharge regime. The CWR was calculated at base flow (spring 15) and at high discharge (sum 15) using riverine SiO_2, Na, K, Mg and Ca concentrations, with a catchment surface estimated at 376 km^2 and discharge measured at

the S33 gauging station, and then extrapolated on an annual basis considering a rainy season of two months/year and using the average total discharge of spring 2014-2015 for base flow conditions and the average total discharge of summer 2014-2015 for high discharge conditions. The CWR obtained at high discharge (80 $t.km^{-2}.yr^{-1}$) is 1.5 times higher than CWR at base flow (52 $t.km^{-2}.yr^{-1}$), and the annual CWR of the Aso caldera is estimated at 59 $t.km^{-2}.yr^{-1}$. The difference between CWR at high and low discharge is similar to the difference in CWR between wet and dry season for Banyu Pahit/Banyu Putit, i.e., 1.6 times higher in wet season (*Ch2*), and consistent with the range of difference in CWR between high discharge (at snowmelt) and base flow obtained for rivers from the Yellowstone Plateau Volcanic Field, i.e., 1.1 and 2.6 higher in high discharge (with two exceptions above 12 times higher; *Ch4*). This underlines the importance to carefully consider seasonal changes in element fluxes when assessing the contribution from volcanic regions to global weathering estimates.

7.7 Conclusion

In this study, we investigated the Ge/Si ratio and the Si isotope compositions of the main rivers draining the Aso caldera, and their contributors (thermal springs, tributaries, groundwater, surface runoff). The influence of seasonal change in discharge on the processes involved and the relative contribution from these reservoirs to rivers (**Fig. 7.11**) has been peformed based on a seasonal sampling at base flow and at high discharge. The following main conclusions can be drawn from this study:

(i) Thermal discharge in the Aso caldera are acid SO_4-waters and alkaline HCO_3-waters, and also involved mixed neutral HCO_3-SO_4 waters. The data confirms that these types of thermal waters are present in the northern and southern part of the caldera. The Ge/Si ratio combined with the Cl/B ratio support a direct hydrothermal contribution to rivers draining the Aso caldera.

(ii) The chemical composition and the Ge/Si ratio of the rivers support that seasonally, the fraction of hydrothermal contribution relative other contributors (groundwaters, surface runoff) to rivers is reduced during the rainy season, i.e., when the rivers are at high discharge.

(iii) Processes controlling groundwater chemical composition i.e., clay mineral formation or hydrothermal contribution, can be modified seasonally at high discharge. Hydrothermal contribution to groundwater is influenced by the depth of the groundwater with deeper groundwaters being influenced by a significant contribution of magmatic CO_2 due to proximity with the magma. And clay mineral formation, typically influenced by water residence time in groundwater, likely affects more high altitude groundwater known for their longer water residence time in the Aso caldera than lower altitude groundwater.

(iv) A short-term pulse of contribution from mineral dissolution is observed in river waters at high discharge based on the element concentrations, the Ge/Si ratios, and the δ^{30}Si values. This seasonal weathering signal, previously unaccounted for in hydrothermally-active volcanic regions, directly contributes to chemical weathering fluxes and associated atmospheric CO_2 consumption.

(v) At the scale of the Aso caldera, the change in relative contribution from thermal springs, groundwaters and surface runoff with discharge

can not be detected at the outlet of the caldera, likely erased by the variability at larger spatial scale. This supports that a comprehensive understanding of the sources and processes involved seasonally in the control of riverine chemistry from a hydrothermal active volcanic region can only be obtained at a smaller catchment scale, i.e., inside the caldera.

7.8 References

Abraham, K., Opfergelt, S., Fripiat, F., Cavagna, A-J., de Jong, J., Foley, S.F., André, L., Cardinal, D., 2008. $\delta^{30}Si$ and $\delta^{29}Si$ determinations on USGS BHVO-1 and BHVO-2 reference materials with a new configuration on a Nu Plasma Multi-Collector ICP-MS. Geostand. Geoanal. Res. 32(2), 193-202.

Alexander, G.B., Heston, W.M., Iler, R.K., 1954. The solubility of amorphous silica in water. J. Phys. Chem. 58, 453–455.

Arnórsson, S., Andrésdóttir, A., 1995. Processes controlling the distribution of boron and chlorine in natural waters in Iceland. Geochim. Cosmochim. Acta 59, 4125–4146.

Baronas, J.J., Torres, M.A., West, A.J., Rouxel, O., Georg, B., Bouchez, J., Gaillardet, J., Hammond, D.E., 2018. Earth Planet. Sci. 503, 194-215.

Baronas, J.J, West, A.J., Burton, K.W., Hammond, D.E., Opfergelt, S., Pogge von Strandmann, P.A.E., James, R.H., Rouxel, O.J., 2020. Ge and Si isotopes behaviour during intense tropical weathering. Global Biogeochem. Cy. doi:10.1029/2019gb006522.

Cardinal, D., Alleman, L.Y., De Jong, J., Ziegler, K., André, L., 2003. Isotopic composition of silicon measured by multicollector plasma source mass spectrometry in dry plasma mode. J. Anal. Atom. Spectrom. 18, 213–218.

Derry, L.A., Kurtz, A.C., Ziegler, K., Chadwick, O.A., 2005. Biological control of terrestrial silica cycling and export fluxes to watersheds. Lett. Nature 433, 728–731.

Dessert, C., Dupré, B., Gaillardet, J., Francois, L.M., Allegre, C.J., 2003. Basalt weathering laws and the impact of basalt weathering on the global carbon cycle. Chem. Geol. 202, 257-273.

Dessert, C., Lajeunesse, E., Lloret, E., Clergue, C., Crispi, O., Gorge, C., Quidelleur, X., 2015. Controls on chemical weathering on a mountainous volcanic tropical island: Guadeloupe (French West Indies). Geochim. Cosmochim. Ac. 171, 216–237.

Dupré, B., Dessert, C., Oliva, P., Goddéris, Y., Viers, J., François, L., Gaillardet, J., 2003. Rivers, chemical weathering and Earth's climate. Geoscience. 335, 1141-1160.

Fournier, R.O., Rowe, J.J., 1977. The solubility of amorphous silica in water at high temperatures and high pressures. Am. Mineral. 62, 1052-1056.

Friedman, I., Norton, D.R., 2007. Is Yellowstone losing its steam? Chloride flux out of Yellowstone National Park. In: Morgan, L.A. (Ed.), Integrated Geoscience Studies in the Greater Yellowstone Area: Volcanic, Hydrothermal and Tectonic

Processes in the Yellowstone Geoecosystem: U.S. Geological Survey Professional Paper, 1717, 274-297.

Gaillardet, J., Dupré, B., Louvat, P., Allègre, C.J., 1999. Global silicate weathering and CO_2 consumption rates deduced from the chemistry of large rivers. Chem. Geol. 159, 3-30.

Gaillardet, J., Rad, S., Rivé, K., Louvat, P., Gorge, C., Allègre, C-J., Lajeunesse, E., 2011. Orography-driven chemical denudation in the Lesser Antilles: Evidence for a new feed-back mechanism stabilizing atmospheric CO_2. Am. J. Sci. 311, 851-894.

Gaspard, F., Opfergelt, S., Dessert, C., Robert, V., Ameijeras-Marino, Y., Delmelle, P. Imprint of chemical weathering and hydrothermalism on the Ge/Si ratio and Si isotopic composition of rivers in a volcanic tropical island, Basse-Terre, Guadeloupe (French West Indies). Submitted to Chem. Geol.

Giggenbach, W.F., 1988. Geothermal solute equilibria. Derivation of Na-K-Mg-Ca geoindicators. Geochim. Cosmochim. Ac. 52, 2749-2765.

Gislason, S. R., Oelkers, E. H., 2011. Silicate rock weathering and the global carbon cycle, in Harmon, R. S., and Parker, A., editors, Frontiers in Geochemistry: Contribution of Geochemistry to the Study of the Earth: Chichester, United Kingdom, Wiley-Blackwell, 84–103.

Han, Y., Huh, Y., Derry, L., 2015. Ge/Si ratios indicating hydrothermal and sulphide weathering input to rivers of the Eastern Tibetan Plateau and Mt. Baekdu. Chem. Geol. 410, 40-52.

Hase, H., Hashimoto, T., Sakanaka, S., Kanda, W., Tanaka, Y., 2005. Hydrothermal system beneath Aso volcano as inferred from self-potential mapping and resistivity structure. J. Volcan. Geoth. Res. 143, 259-277.

Hosono, T., Hartmann, J., Louvat, P., Amann, T., Washington, K.E., West, A.J., Okamura, K., Böttcher, M.E., Gaillardet, J., 2018. Earthquake-induced structural deformations enhance long-term solute fluxes from active volcanic systems. Scientific reports.

Huang, P.M., Berthelin, J., Bollag, J.M., McGill, W.B., 1995. Environmental impacts of soil component interactions: land quality, natural and anthropogenic organics. CRC Press.

Hurwitz, S., Lowenstern, J.B., Heasler, H., 2007. Spatial and temporal geochemical trends in the hydrothermal system of Yellowstone National Park: Inferences from river solute fluxes. J. Volcanol. Geoth. Res. 162, 149-171.

Hurwitz, S., Evans, W.C., Lowenstern, J.B., 2010. River solute fluxes reflecting active hydrothermal chemical weathering of the Yellowstone Plateau Volcanic Field, USA. Chem. Geol. 276, 331-343.

Ingebritsen, S.E., Galloway, D.L., Colvard, E.M., Sorey, M.L., Mariner, R.H., 2001. Time-variation of hydrothermal discharge at selected sites in the western United States: implications for monitoring. J. Volcanol. Geotherm. Res. 111, 1-23.

IPCC, 2013. Fifth Assess. Rep.IPCC (eds T.F. Stocker et al.) Cambridge University Press.

Japan Meteorological Agency (JMA), 2019. Climate of Northern Kyūshū district.

Kagabu, M., Shimada, J., Shimano, Y., Higuchi, S., Noda, S., 2011. Groundwater flow system in Aso caldera. Journal of Japanese Association of Hydrological Sciences 41, 1, 17.

Kirchner, J. W., Feng, X., Neal C., 2000. Fractal stream chemistry and its implications for contaminant transport in catchments. Nature 403, 524–527.

Louvat, P., Allègre, C.J., 1997. Present denudation rates on the Island of Réunion determined by river chemistry, Geochim. Cosmochim. Ac. 61, 3645–3669.

Louvat, P., Gaillardet, J., Paris, G., Dessert, C., 2011. Boron isotope ratios of surface waters in Guadeloupe, Lesser Antilles. Appl. Geochem. 26, S76–S79.

McCleskey, R.B., Roth, D.A., Mahony, D., Nordstrom, D.K., Kinsey, S., 2019. Sources, fate, and flux of geothermal solutes in the Yellowstone and Gardner Rivers, Yellowstone National Park, WY. Appl. Geochem. 111. p.104458.

Meunier, J., 2019. Export du silicium par les cultures de riz par rapport aux flux de Si exportés par les rivières dans les arcs insulaires volcaniques. Student master thesis, UCLouvain.

Michard, G., 1980. Contrôle de la concentration des éléments dissous dans les eaux thermales et géothermales. J. Fr. Hydrologie 11, 7-16.

Nagai, S., Taguchi, Y., Shimano, Y. & Tanaka, N., 1986. Hydrochemistry of the groundwater and river water within the Aso caldera watershed. J. Indust. Water 337, 10–21.

Nakada, S., 2003. IUGG 2003 Field trip guide, A3:1–A3:38.

Ono, K., Matsumoto, Y., Miyahisa, M., Teraoka, Y., Kambe, N., 1977. Geology of the Taketa district. Geological Survey of Japan 145.

Ono, K., Watanabe, K., 1985. Geological map of Aso volcano, 1:50 000. Geological Map of Volcanoes 4. Geological Survey of Japan.

Opfergelt, S., Cardinal, D., André, L., Delvigne, C., Bremond, L., Delvaux, B., 2010. Variations of d^{30}Si and Ge/Si with weathering and biogenic input in tropical basaltic ash soils under monoculture. Geochim. Cosmochim. Acta 74, 225–240.

Opfergelt, S., Delmelle, P., 2012. Silicon isotopes and continental weathering processes: Assessing controls on Si transfer to the ocean. Comptes Rendus Geosci. 344, 723–738.

Opfergelt, S., Burton, K.W., Pogge von Strandmann, P.A.E., Gislason, S.R., Halliday, A.N., 2013. Riverine silicon isotope variations in glaciated basaltic terrains: implications for the Si delivery to the ocean over glacial-interglacial intervals. Earth. Planet. Sc. Lett. 369-370, 211-219.

Ragueneau, O., Savoye, N., Del Amo, Y., Cotten, J., Tardiveau, B., Leynaert, A., 2005. A new method for the measurement of biogenic silica in suspended matter of coastal waters: using Si:Al ratios to correct for the mineral interference. Cont. Shelf Res. 25, 697–710.

Reynolds, B.C., Aggarwal, J., André, L., Baxter, D., Beucher, C., Brzezinski, M.A., Engström, E., Georg, B., Land, M., Leng, M.J., Opfergelt, S., Rodushkin, I., Sloane, H.J., Van den Boorn, S.H.J.M., Vroon, P.Z., Cardinal, D., 2007. An inter-laboratory comparison of Si isotope reference materials. J. Anal. Atom. Spectrom. 22, 561-568.

Rivé, K., Gaillardet, J., Agrinier, P., Rad, S., 2013. Carbon isotopes in the rivers from the Lesser Antilles: origin of the carbonic acid consumed by weathering reactions in the Lesser Antilles. Earth Surf. Proc. Land. 38, 1020–1035.

Rouxel, O., Galy, A., Elderfield, H., 2003. Germanium isotopic variations in the igneous rocks and marine sediments. Geochim. Cosmochim. Acta 70, 3387-3400.

Saito, T., Ohsawa, S., Hashimoto, T., Terada, A., Yoshikawa, S., Ohkura, T., 2008. Water, heat and chloride balances of the crater lake at Aso volcano, Japan. J. Geotherm Res. Soc. Jpn. 30, 107–120 (in Japanese).

Savage, P.S., Georg, R.B., Williams, H.M., Burton, K.W., Halliday, A.N., 2011. Silicon isotope fractionation during magma differentiation. Geochim. Cosmochim. Ac. 75, 6124-6139.

Schopka, H. H., Derry, L. A., Arcilla, C. A., 2011. Chemical weathering, river geochemistry and atmospheric carbon fluxes from volcanic and ultramafic regions on Luzon Island, the Philippines. Geochim. Cosmochim. Acta 75, 978–1002.

Shimano, Y., 1997. Hydrochemistry of the spring water within the Aso caldera watershed. Ann. Rep. Bunsei Univ. 8, 43–67.

Shimano, Y., 1999. Hydrochemistry of the river water within the Aso caldera watershed. Ann. Rep. Bunsei Univ. 10, 3–30.

Tanaka, N., 2000. The history of Ichinomiya-cho, Mt. Aso and Water. Ichinomiya-cyo, Kumamoto Japan. (in Japanese).

Terada, A., Hashimoto, T., Kagiyama, T., 2012. A water flow model of the active crater lake at Aso volcano, Japan: fluctuations of magmatic gas and groundwaters fluxes from the underlying hydrothermal system. Bull. Volcanol. 74, 641-655.

United Kingdom Accreditation Body (UKAS)., 2014. Certificate of measurement, river water-anion, certified reference material LGC6025. 4005.

Wang, W., Wei, H-Z., Jiang S-Y., Tan, H-B., Eastoe C.J., Williams-Jones, A.E., Hohl, S.V., Wu, H-P., 2019. The origin of rare alkali metals in geothermal fluids of southern Tibet, China: a silicon isotope perspective. Sci. Rep. 9, 7918.

White, A.F., Blum, A.E., 1995. Effects of climate on chemical weathering in watersheds. Geochim. Cosmochim. Ac. 59, 1729-1747.

Yamada, M., Ohsawa, S., Kazahaya, K., Yasuhara, M., Takahashi, H., Amita, K., Mawatari, H., Yoshikawa S., 2011. Mixing of magmatic CO_2 into volcano groundwater flow at Aso volcano assessed combining carbon and water stable isotopes. J. Geochem. Explor. 108, 81-87.

Yeghicheyan, D., Bossy, C., Bouhnik Le Coz, M., Douchet, C., Granier, G., Heimburger, A., Lacan, F., Lanzanova, A., Rousseau, T.C.C., Seidel, J-L., Tharaud, M., Candaudap, F., Chmeleff, J., Cloquet, C., Delpoux, S., Labatut, M., Losno, R., Pradoux, C., Sivry, Y., Sonke, J.E., 2013. A Compilation of Silicon, Rare Earth Element and Twenty-One other Trace Element Concentrations in the Natural River Water Reference Material SLRS-5 (NRC-CNRC). Geostand. Geoanal. Res. 37(4), 449-467.

Young, E.D., Galy, A., Nagahara, H., 2002. Kinetic and equilibrium mass-dependent isotope fractionation laws in nature and their geochemical and cosmochemical significance. Geochim. Cosmochim. Ac. 66, 1095-1104.

Ziegler, K., Chadwick, O.A., Brzezinski, M.A., Kelly, E.F., 2005. Natural variations of $d^{30}Si$ ratios during progressive basalt weathering, Hawaiian Islands. Geochim. Cosmochim. Acta 69, 4597–4610.

7.9 Supplementary Materials

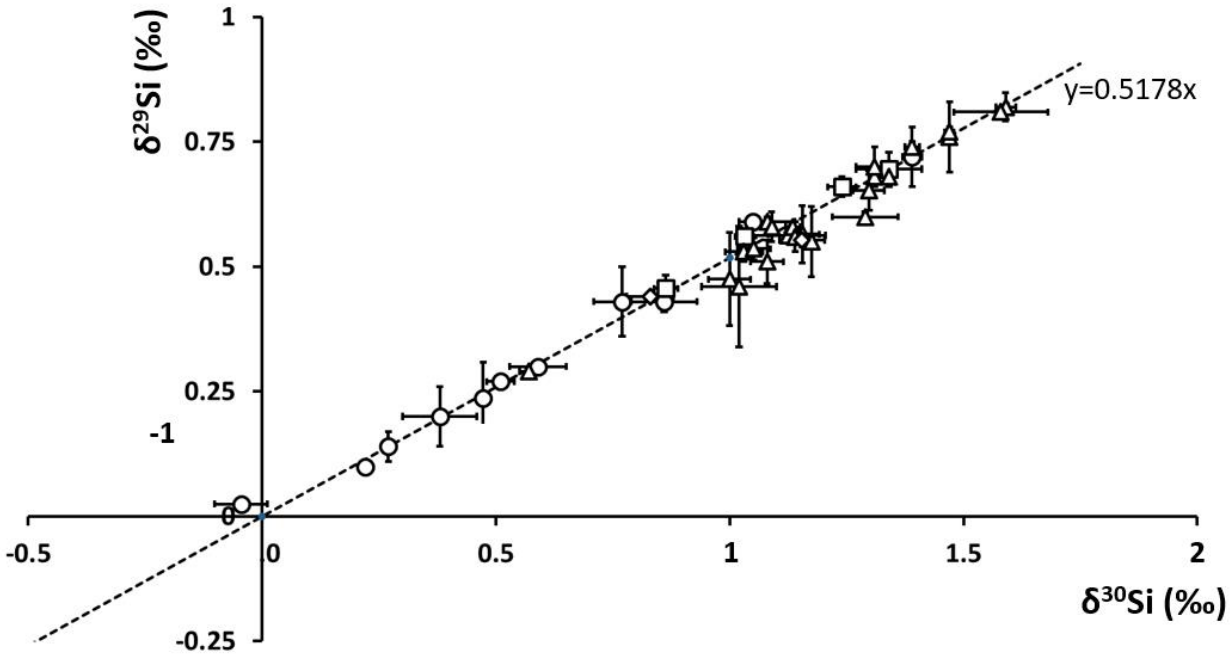

Suppl. Mat. 7.1: Plot of the silicon isotopes measurements of all water samples from the Aso caldera (thermal springs, groundwaters, river waters and surface runoff) onto a mass-dependent fractionation array $\delta^{30}Si$ and $\delta^{29}Si$ (theorical 0.5178 slope for equilibrium mass-dependent fractionation; Young et al, 2002).

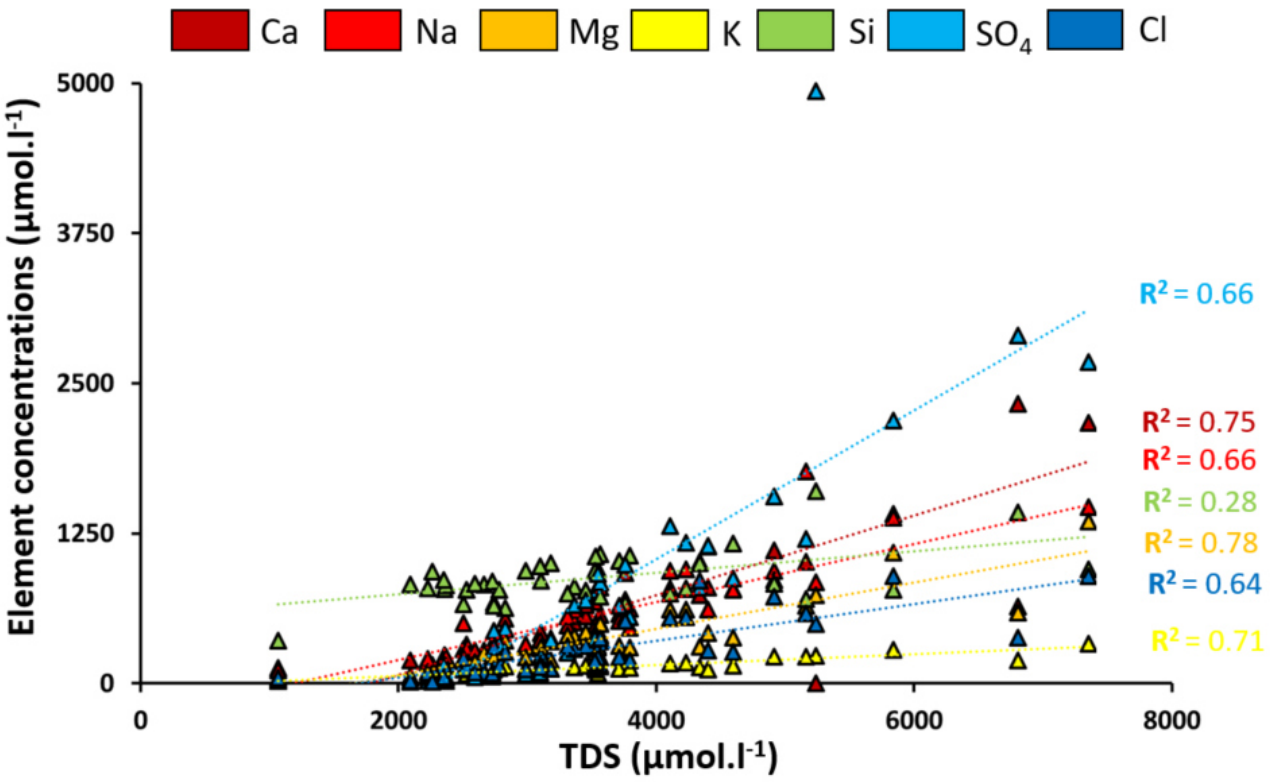

Suppl. Mat. 7.2: Major element (Ca, Na, Mg, K), Si, SO_4 and Cl concentrations as a function of total dissolved solids (TDS) in river waters flowing into the Aso caldera, Kyūshū Island, Japan.

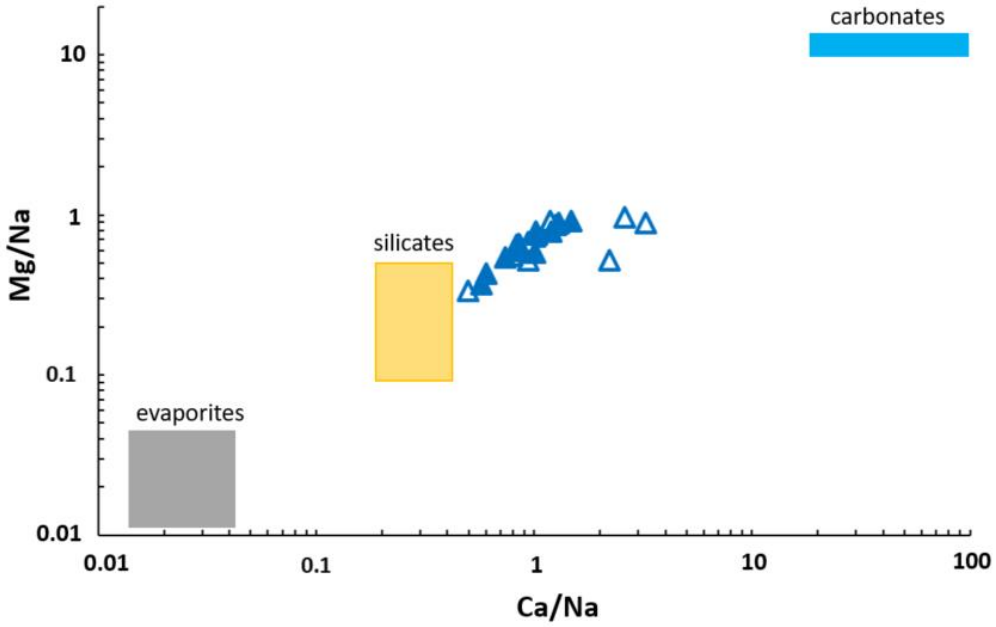

Suppl. Mat. 7.3: Mixing diagram using Na-normalized molar ratio in the dissolved phase of the rivers from the Aso caldera at high discharge (open triangle) and in base flow (plain triangle). Data from end-members reservoirs are from Gaillardet et al (1999).

Part IV

CONTRIBUTION OF THE STUDY

Contribution of the study

8.1 Contribution of the study to the estimation of chemical weathering rates from volcanic regions and the associated atmospheric CO_2 consumption

In the PhD thesis, we obtained chemical weathering rates (CWR) for three volcanic regions: the Banyu Pahit/Banyu Putih river, Java island (*Ch2*), the rivers from the YPVF (*Ch4*) and the river draining the Aso caldera, Kyūshū island (*Ch5*). The quantification of CWR ($t.km^{-2}.yr^{-1}$) is obtained via the following equation:

CWR ($t.km^{-2}.yr^{-1}$) = $(Na+K+Mg+Ca+SiO_2)$.(riverine discharge).(draining basin surface area)$^{-1}$

with the element concentration in $mg.l^{-1}$, the riverine discharge in $l.yr^{-1}$ and the draining basin surface area in km^2.

The CWR values from Kawah Ijen volcano in Java Island (*Ch2*), i.e., andesitic-basaltic, are in the range of values reported for basaltic or andesitic volcanic islands, and higher than the one reported for more silicic magmatic rocks, i.e., dacitic volcanic islands (**Fig. 8.1**). The CWR values from Aso volcano in Kyūshū island (*Ch5*) are also within that range, despite including magmatic rocks from basaltic to rhyolitic compositions. The CWR values from YPVF (*Ch4*) i.e., mainly rhyolitic, present the highest reported CWR values at high river flow regime (high discharge), up to 6.5 times higher than the highest literature value.

However, direct comparison of CWR values between studies remain to be considered with caution given that the calculated fluxes of solutes were obtained by different methods integrating seasonal variability (Hurwitz et al, 2010). This may have large impact on the calculated as

illustrated by the up to 12 times higher CWR value obtained for rivers draining the YPVF in high discharge relative to the CWR value for the same rivers in base flow.

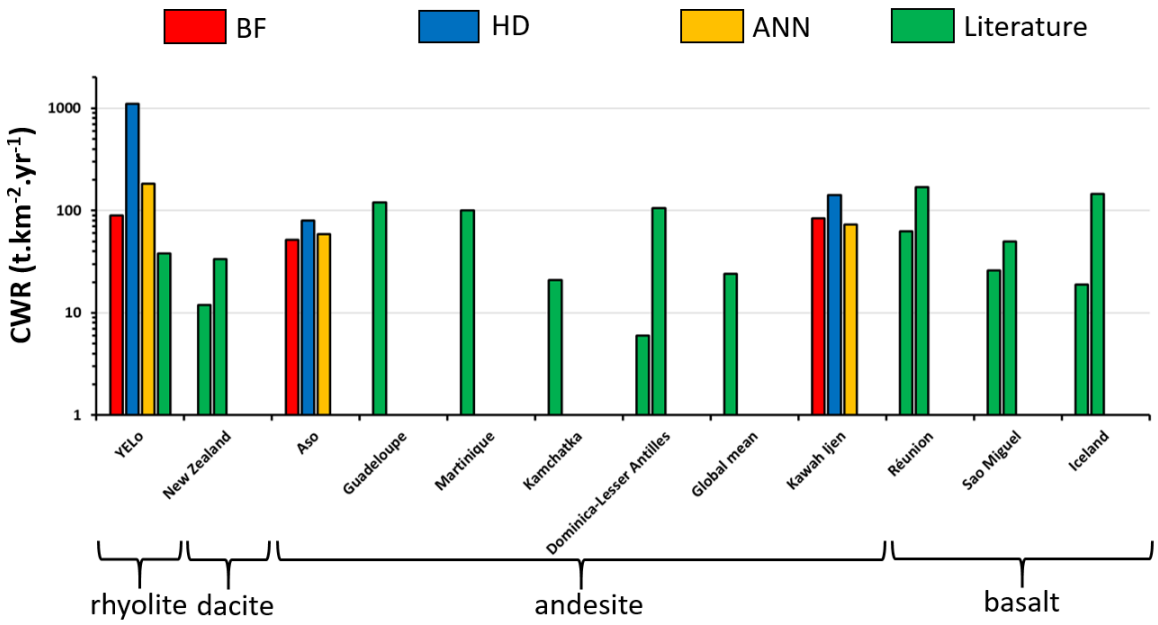

Fig. 8.1: Comparison between the chemical weathering rates (CWR; $t.km^{-2}.yr^{-1}$) calculated in the PhD thesis (YPVF: *Ch4*; Aso: *Ch5*; Kawah Ijen: *Ch2*) and the literature, presented from the more silicic magmatic rocks (left) to the less silicic magmatic rocks (right). BF = base flow, HD = high discharge initiated by snowmelt (YPVF) or rain season (Aso, Kawah Ijen), ANN = annual basis. YELo, the main river of YPVF is generally used to assess CWR from YPVF (Hurwitz et al, 2010). Data from La Réunion: Louvat and Allègre, 1997; Sao Miguel: Louvat and Allègre, 1997; Iceland: Stefánsson and Gislason, 2001; Martinique and Guadeloupe: Rad et al, 2006; Kamchatka: Dessert et al, 2009; Dominica: Goldsmith et al, 2010; New Zealand: Goldsmith et al, 2008.

Comparing the Si concentration in river waters from this PhD thesis with the reported Si concentrations in rivers draining volcanic regions confirms a general correlation of the Si concentration with the Total Dissolved Solids (TDS; **Fig. 8.2**). The data from Java Island (*Ch2*) display the highest Si concentrations and the highest TDS values relative to the reported values, reflecting the **hyper-acid weathering conditions** from the Kawah Ijen volcano. The limited range in Si concentrations and TDS values in the river draining the Aso caldera (*Ch5*) relative to other rivers likely reflect a **more homogeneous weathering degree** within the catchment than in other sites, such as for example for the rivers draining Basse-Terre Island, Guadeloupe (*Ch3*). Multiple catchments studies (*Ch3, Ch4*) display more variable riverine Si concentrations and TDS values likely reflecting the variability in soil weathering degree, thermal input, runoff (etc.) between catchments. The Si concentrations and TDS values from Basse-Terre Island (*Ch3*) agree with data reported in the Lesser Antilles (Basse-Terre Island, Martinique/Dominique), La Réunion, Kamchatka and New Zealand. All of these studies involve catchments with distinct soil weathering degree, except river waters from La Réunion showing a lower range of Si concentrations. Note that additional parameters should also be further considered to compare the variations in Si concentrations and TDS values between these studies, such as the **climate** (e.g., the tropical climate in volcanic islands, with high precipitations and temperature, enhances chemical weathering), the **lithology**, and the **hydrological connectivity** within the catchments (connection to groundwater, number of tributaries, etc.).

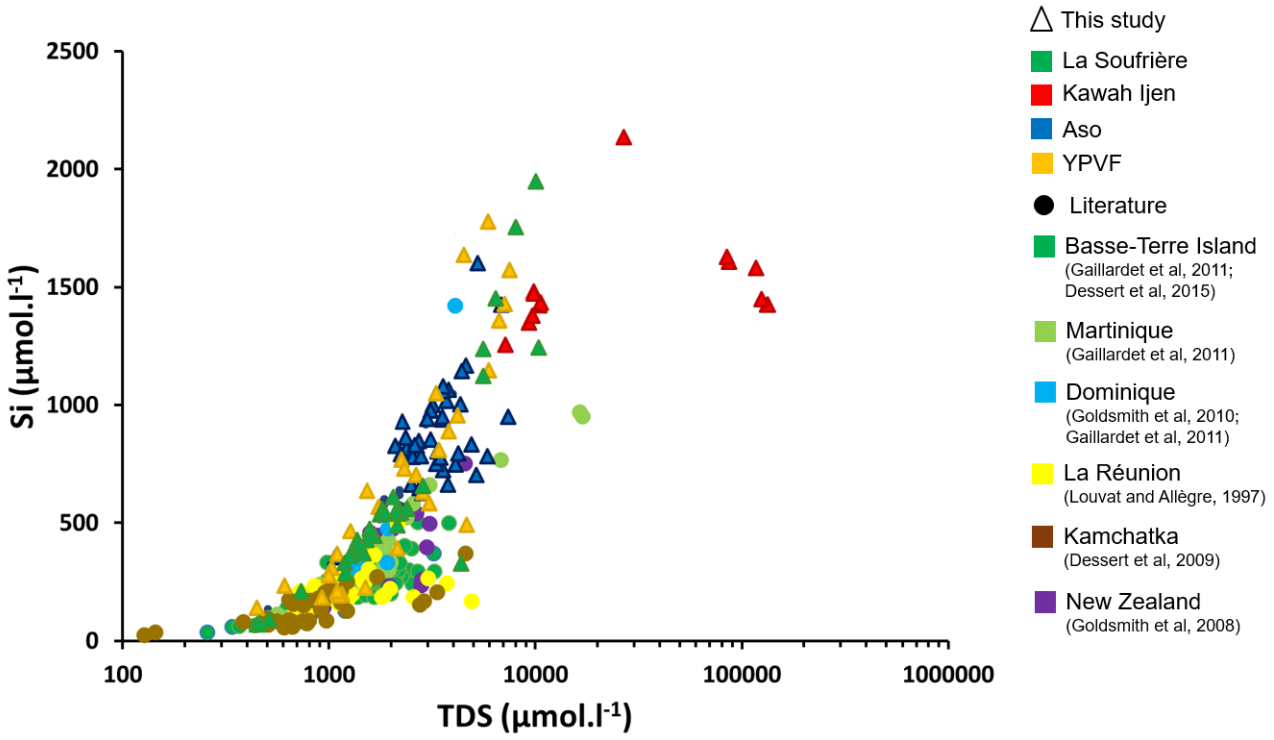

Fig. 8.2: Plot of the Si concentration as a function of the Total Dissolved solid (TDS) in river waters from this study (triangle; Basse-Terre Island, Java Island, Kyūshū Island, YPVF) and from the literature (circle). The water samples from this PhD thesis were filtered at 0.45 µm whereas filtration at 0.22 µm was used in the studies from the literature, i.e., potentially leading to differences in colloidal Si.

This thesis contributes to improve the estimates on the hydrothermal contribution to CWR hydrothermally active volcanic regions by demonstrating that (**Fig. 8.3**) (i) **river sampling location**, i.e., depending on the distance to the magmatic gases source, largely control the hydrothermal contribution of magmatic CO_2 (between 54 % close to the volcanic crater to 2 % 40 km downstream at Kawah Ijen volcano, *Ch2*), and that (ii) short **pulse of meteoric weathering** contributing at high river discharge (at snowmelt or during the rain season) should be considered for atmospheric CO_2 consumption (*Ch4, Ch5*).

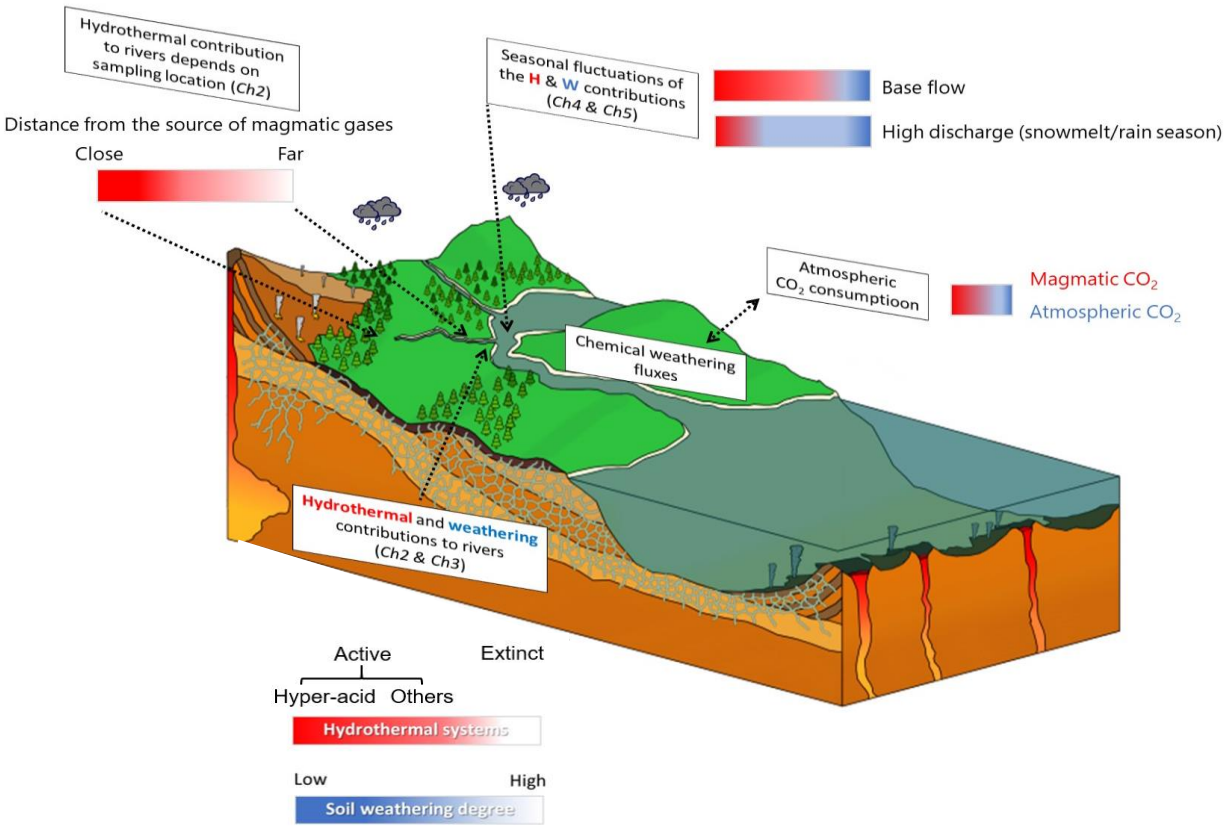

Fig. 8.3: Conceptual scheme on the hydrothermal (red) and weathering (blue) contributions to Chemical Weathering Rates (CWR) in rivers draining volcanic terranes featuring hydrothermal manifestations. The associated consumption of atmospheric CO_2 depends on the contribution from magmatic CO_2. The intensity of the color (red or blue) is proportional to the contribution (hydrothermal or weathering, respectively) to CWR in rivers, and hence to magmatic or atmospheric CO_2 consumption.

8.2 Contribution of the study to the range of variations in Ge/Si ratios and Si isotopes in terrestrial reservoirs

This PhD thesis provides a total of 245 original data of Ge/Si ratios and 132 original data of Si isotope compositions across different terrestrial reservoirs (thermal springs, river waters, groundwaters, soil solutions, surface runoff and hydrothermally-altered rock; **Table 8.1**).

Table 8.1: Numbers of Ge/Si ratios and Si isotope compositions measured in each study sites. n=total number of samples (some locations were sampled multiple times for seasonal comparison).

	Samples	La Soufrière	Kawah Ijen	YPVF	Aso	Kanlaon	Mutnovsky
		Basse-Terre Island	Java Island	Continental hot spot	Kyūshū Island	Negros Island	Kamchatka
Ge/Si	Thermal springs	15 (n=26)	13 (n=13)	8 (n=8)	17 (n=21)	1 (n=2)	2 (n=2)
	River waters	22 (n=36)	4 (n=14)	15 (n=33)	30 (n=46)	-	-
	Soil solutions	7 (n=7)	4 (n=4)	-	-	-	-
	Groundwaters	-	-	-	11 (n=28)	-	-
	Surface runoff	-	-	-	3 (n=4)	-	-
	Hydrothermally-altered rock	1 (n=1)	-	-	-	-	-
δ^{30}Si	Thermal springs	9 (n=12)	13 (n=13)	7 (n=7)	9 (n=11)	1 (n=2)	2 (n=2)
	River waters	15 (n=17)	4 (n=11)	8 (n=17)	14 (n=23)	-	-
	Soil solutions	7 (n=7)	2 (n=2)	-	-	-	-
	Groundwaters	-	-	-	3 (n=5)	-	-
	Surface runoff	-	-	-	2 (n=2)	-	-
	Hydrothermally-altered rock	1 (n=1)	-	-	-	-	-

Across the different chapters, we contributed to expand the knowledge on the variations of the Ge/Si ratio in volcanic context (**Fig. 8.4**). More specifically, we expanded the range of reported Ge/Si ratios: (i) in **volcanic thermal springs** (literature: 0.72-185.23 µmol.mol^{-1}) towards lower values (with the lowest at 0.05 µmol.mol^{-1} from La Soufrière volcano) and towards higher values (with the highest at 188.92 µmol.mol^{-1} in YPVF); (ii) largely in **rivers** draining volcanic areas (literature: 0.16-

20 µmol.mol^{-1}) towards lower values (with the lowest at 0.13 µmol.mol^{-1} from Aso volcano) and towards higher values (with the highest at 513.9 µmol.mol^{-1} in YPVF); and (iii) in **groundwaters** (literature: 0.24-0.74 µmol.mol^{-1}) towards lower and higher values with groundwaters from Aso volcano (0.11-1.12 µmol.mol^{-1}); and we remained within the range reported in **soil solutions** (literature: 0.7-14 µmol.mol^{-1}).

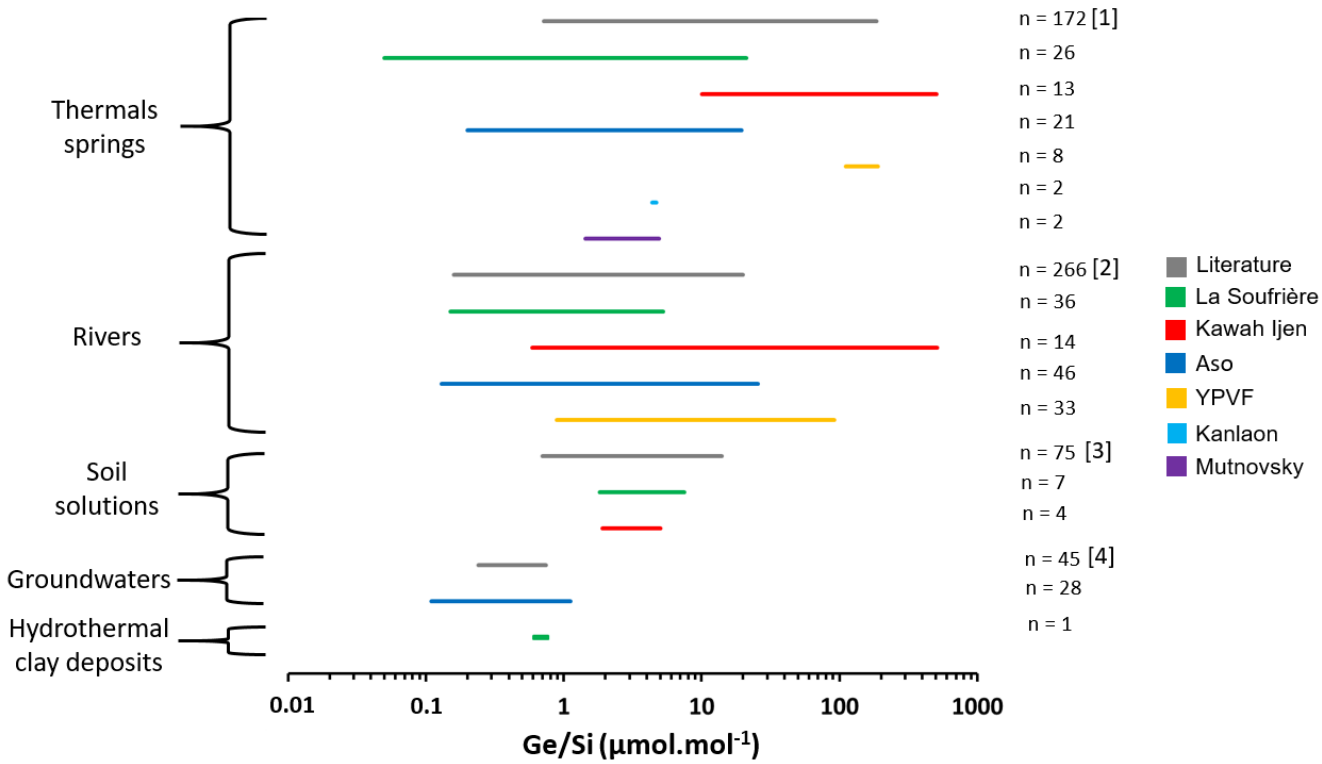

Fig. 8.4: Contribution of the PhD thesis to the knowledge on the variations of the Ge/Si at the surface of the Earth. [1] Arnòrsson, 1983, 1987; Siebert et al, 2006; Wheat and McManus, 2008; Escoube et al, 2015 [2] Mortlock and Froelich, 1987; Froelich et al, 1992; Kurtz et al, 2002; Kurtz and Derry, 2004; Derry et al, 2005; Scribner et al, 2006; Opfergelt et al, 2010; Han et al, 2015; Baronas et al, 2018, 2020 [3] Derry et al, 2005 [4] Derry et al, 2005 [5] Lugolobi et al, 2010; Kurtz et al, 2011; Ameijeras-Mariño et al, 2018. n = total number of data.

We also contributed to expand the knowledge on the δ^{30}Si variations in terrestrial reservoirs (**Fig. 8.5**). More specifically, we remained within the range of reported δ^{30}Si values: (i) in **volcanic thermal springs** (literature: -0.7 to 1.7‰); and (ii) in **rivers** (literature: -0.1 and 3.4 ‰). And we expanded the range of reported δ^{30}Si values: (i) in **soil solutions** (literature: -1.85 to 1.25‰) towards heavier values (with the heaviest at 1.56‰, Kawah Ijen volcano); (ii) in **groundwaters** (literature: -1.43 to 0.43‰) towards heavier values (with the heaviest at 1.34‰, Aso volcano; and (iii) in **hydrothermal clay deposits** (literature: -0.1 to 0.1‰) towards a lighter value (-0.35 ‰, La Soufrière volcano).

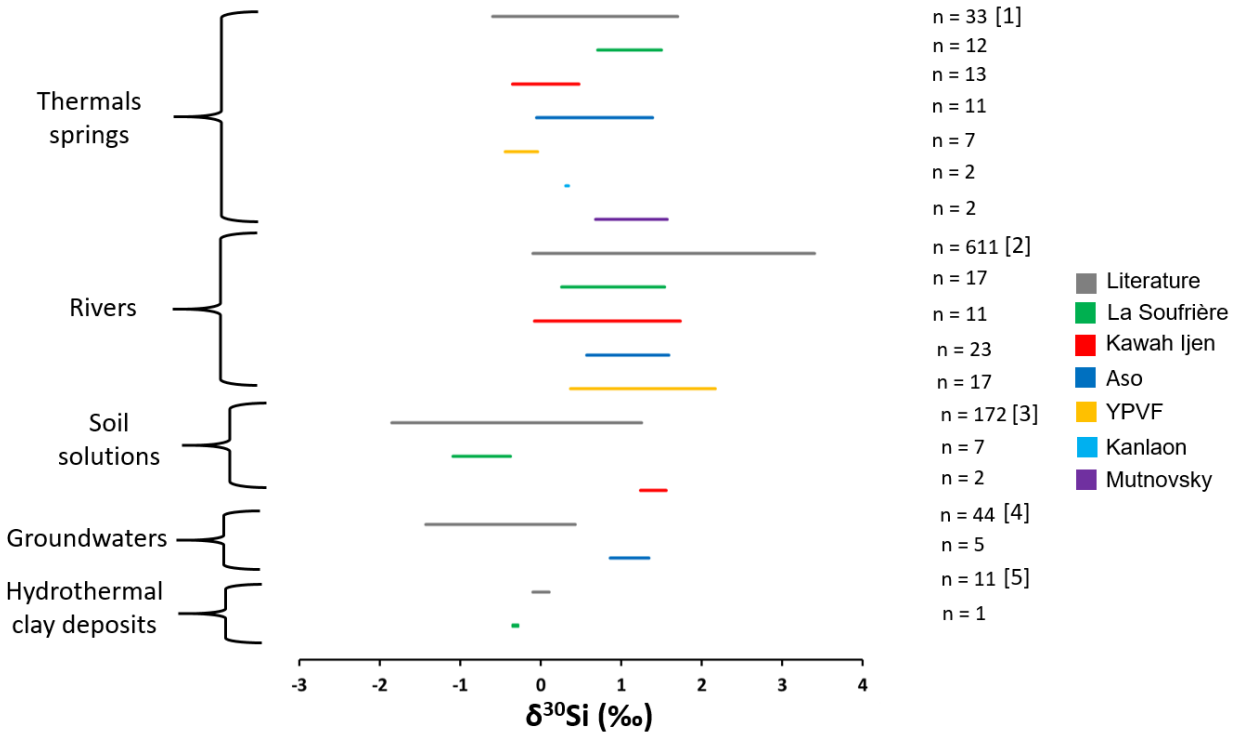

Fig. 8.5: Contribution of the PhD thesis to the knowledge on Si isotope variations at the surface of the Earth. [1] Douthitt, 1982; Ding et al, 1996, 2017; Opfergelt et al, 2011, 2013; Geilert, 2014; Wang et al, 2019; Chen et al, 2020 [2] De La Rocha et al, 2000; Ding et al, 2004, 2016, 2017; Allemand et al, 2005; Georg et al, 2006, 2007; Cardinal et al, 2010; Engström et al, 2010; Hughes et al, 2011, 2013; Opfergelt and Delmelle, 2012; Pokrovsky et al, 2013; Fring et al, 2016 ; Baronas et al, 2020 [3] Ziegler et al, 2005 [4] Georg et al, 2005, 2007, 2009 [5] Ding et al, 1996. n = total number of data.

8.3 Implications for the interpretation of $\delta^{30}Si$ and Ge/Si in rivers draining volcanic regions

Overall, the comparison between the $\delta^{30}Si$ values and the Ge/Si ratios measured in all thermal spring, river and soil solution water samples from this PhD thesis (across all chapters; **Fig. 8.6**) shows that: (i) soil solutions display the lowest $\delta^{30}Si$ values (end-member for highly weathered soils; Basse-Terre Island, *Ch3*) whereas the highest $\delta^{30}Si$ values are found in river waters (end-member for rivers influenced by biological fractionation by lake diatoms; Yellowstone river draining the Yellowstone lake, *Ch4*), and (ii) the highest Ge/Si ratios are found in thermal springs (end-member for hyper-acid thermal water; Kawah Ijen volcano, *Ch2*) whereas the lowest Ge/Si values are measured in river waters. The Ge/Si ratio is not enough to distinguish rivers impacted by hydrothermal input from the non-impacted rivers (element ratios such as Cl/SO_4 should be used, *Ch3*), but among the rivers impacted by hydrothermal input, rivers draining extinct hydrothermal systems are characterized by the lowest Ge/Si values, except for three low Ge/Si values measured in rivers draining the Aso caldera (S05, S14, S24 from *Ch5*; the lowest Ge/Si values among the yellow triangles in **Fig. 8.6**) in which the occurrence of extinct hydrothermal manifestations has not been investigated, thereby potentially leading to a mis-attribution of these three river water samples to rivers only impacted by active hydrothermal input.

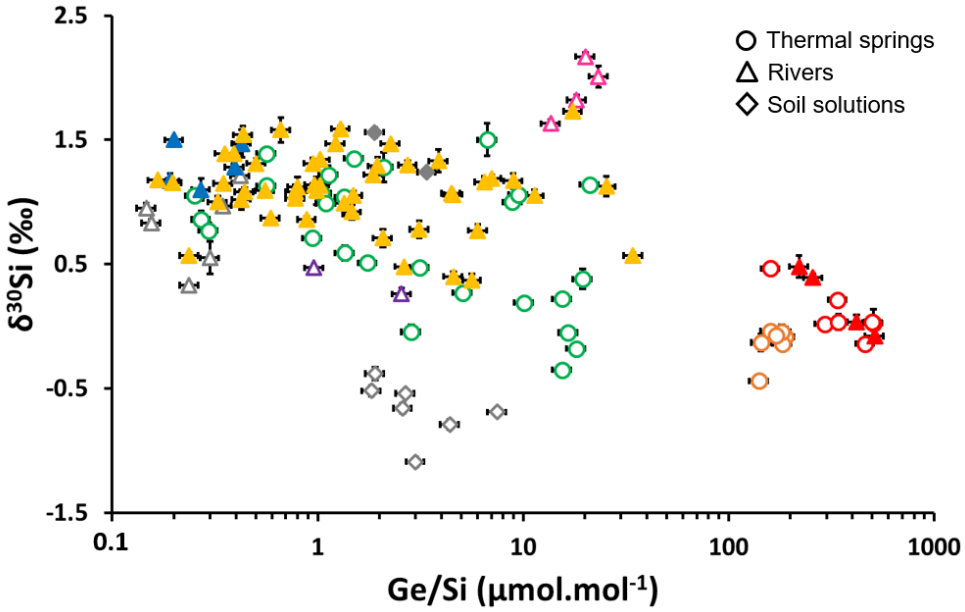

Fig. 8.6: Plot of the Si isotope composition as a function of the Ge/Si ratio in water samples from this PhD thesis: thermal springs (circle; hyper-acid SO_4-Cl waters (open red circle), acid-SO_4, alkaline HCO_3, immature neutral-Cl, mixed acid SO_4-Cl and mixed neutral HCO_3-SO_4 waters (open green circle), mature neutral Cl waters (open orange circle)), rivers waters (triangle; draining hyper-acid thermal discharges (plain red triangle), receiving fluctuating input from active hydrothermal systems (plain yellow triangle), draining extinct hydrothermal systems (plain blue triangle), not impacted by hydrothermal input and draining catchments with low to moderate soil weathering degree (open grey triangle), not impacted by hydrothermal input and draining highly weathered catchments (open purple triangle), influenced by biological fractionation by lake diatoms (open pink triangle)), and soil pore waters (lower soil weathering degree (plain grey diamond), higher soil weathering degree (open grey diamond)).

As a summary, the identified controls on Ge/Si ratio and δ^{30}Si values in thermal springs and river waters are summarized in **Fig. 8.7.**

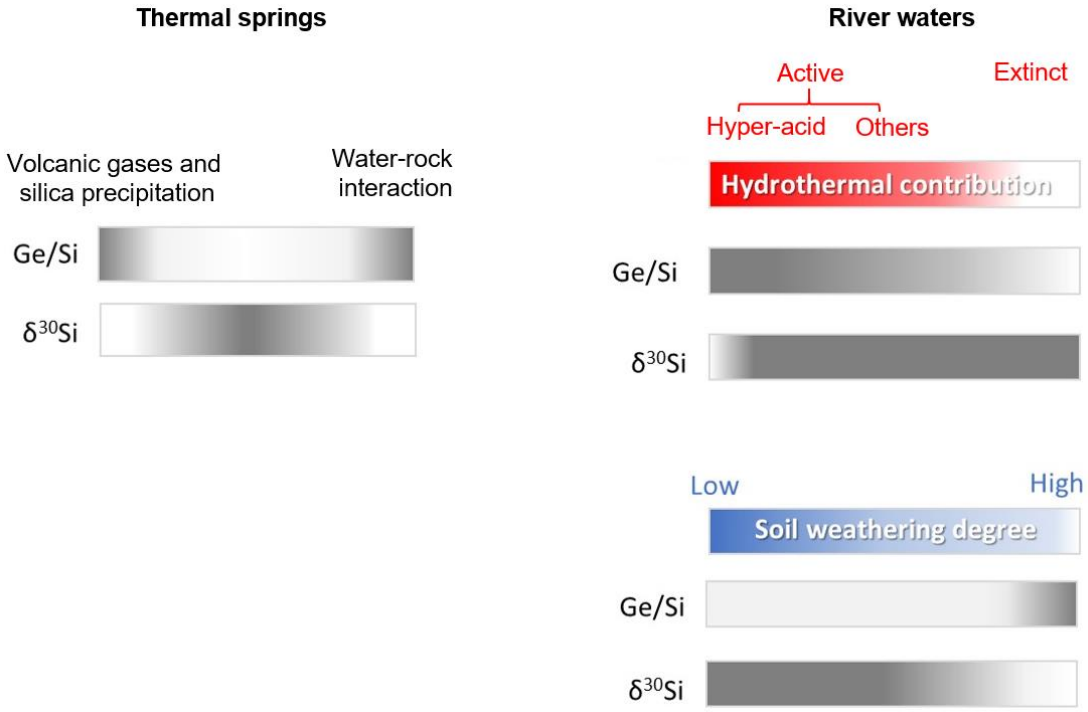

Fig. 8.7: Conceptual schema of the evolution of the Ge/Si ratio and the δ^{30}Si value in thermal springs (left) and river waters (right) as a function of the identified controls (see text for details). The intensity of the grey color decreases with decreasing value of the riverine Ge/Si or δ^{30}Si.

A value of Ge/Si ratio or δ^{30}Si in a river draining a volcanic region can therefore be considered to be driven by three main factors (**Fig. 8.8**): a **hydrothermal** input (from a hyper-acid endmember to a extinct end-member depending on location), a **weathering driver** (with a magmatic or atmospheric *source of acidity* depending on the hydrothermal

contribution, and with the *soil weathering degree* of the catchment depending on location), **seasonal** fluctuations (induced by snowmelt or by the rain season) of the relative contribution from hydrothermal discharges relative to meteoric weathering contributions. What is particularly relevant to improve the estimates of chemical weathering rates in volcanic regions and the associated atmospheric CO_2 consumption is that combining Ge/Si ratio and $\delta^{30}Si$ values allows the identification of (i) rivers consuming magmatic CO_2 for weathering, i.e., receiving input from hyper-acid endmember (*Ch1, Ch2*) to other types of thermal waters (*Ch1-5*) to extinct hydrothermal endmember (*Ch3*), and (ii) rivers dominated by hydrothermal input but receiving seasonal contributions (pulse) from meteoric weathering processes consuming atmospheric CO_2 (by comparing seasonal Ge/Si ratio and the $\delta^{30}Si$ value; *Ch4, Ch5*) (**Fig. 8.8**).

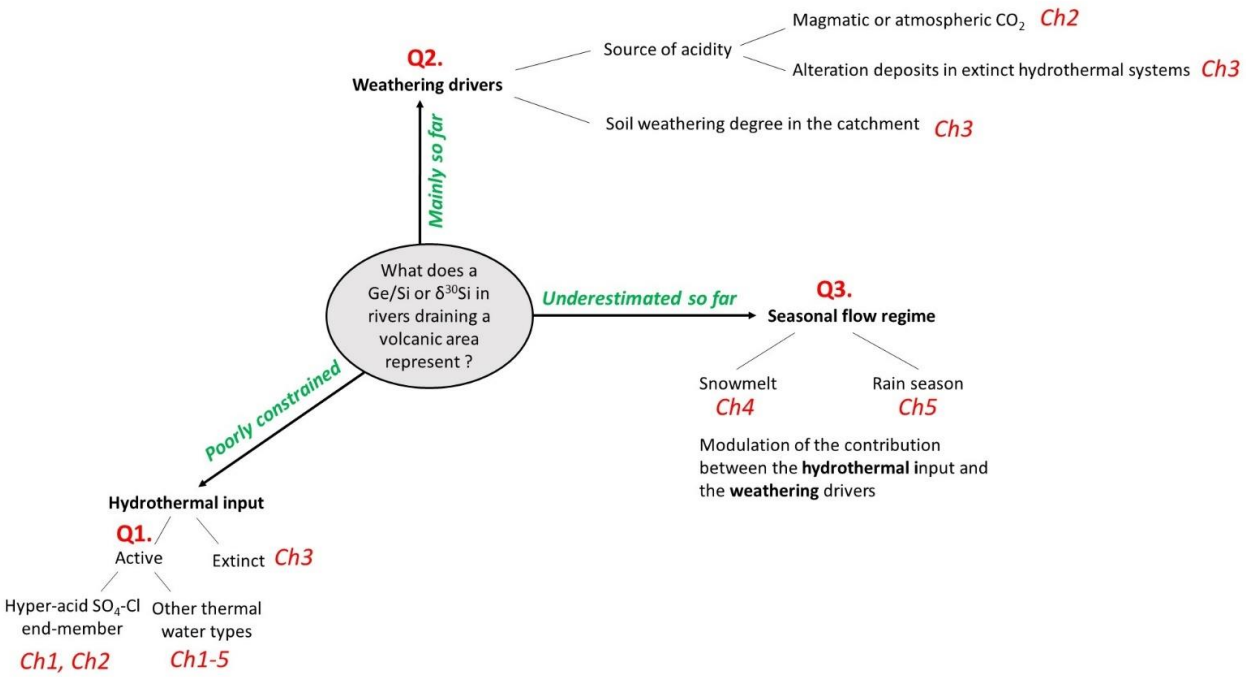

Fig. 8.8: Schematic view of factors influencing Ge/Si ratios and Si isotope compositions of river waters draining hydrothermally-active volcanic regions. These factors were discussed separately via the three research questions (**Q1, Q2, Q3**) in the relevant data chapters (*Ch1,2,3,4,5*) of the thesis (in red). The consideration for the factors in the existing literature is mentioned in green. The biological effect on Si (by plants or intra-rivers) is not represented here but often investigated in the literature.

8.4 General conclusions

The overarching aim of the PhD thesis was to better understand the factors controlling weathering fluxes in rivers draining hydrothermally-active volcanic regions. We used a multi-proxy approach combining riverine element concentrations and geochemical compositions (Ge/Si ratio and Si isotopes).

In order to address this goal, we successfully developed a method allowing the reliable determination of Si isotopes in anion (SO_4^{2-} and Cl^-)-rich aqueous solutions. The new method, which involves a two-step purification of the sample using ion exchange resins, expands our capacity to characterize the Si isotope composition of natural waters, such as thermal springs, rivers affected by hydrothermal discharges, river plume waters and seawater, which were hitherto difficult to measure. The protocole involves: (i) sulfates purification by addition of suprapure $Ba(NO_3)_2$ for water samples with SO_4^{2-} concentration > 210 000 µmol.l^{-1} (*Ch2*), (ii) drying down, dissolution by NaOH leaching, and dilution to ensure the solubilization of potential amorphous silica precipitates for samples with Si concentration beyond the saturation for amorphous silica (*Ch4*), (iii) a two-step purification using anion- and cation-exchange resin (Part II; Gaspard et al, submitted). We also tested and validated a methodology to measure Ge concentrations in water samples by ICP-MS (Part II).

Based on these analytical developments, this PhD thesis addresses the following conclusions to the three specific research questions.

Q1. What controls the variability of Ge/Si ratio and δ^{30}Si in thermal springs from the main generic types of thermal waters?

We provide for the first time analyses of the Ge/Si ratios and δ^{30}Si values of a range of thermal waters representative of the main generic types of thermal springs (*Ch1*). Some key processes that likely control their Ge/Si ratios and δ^{30}Si have been explored: **volcanic gases, silica**

precipitation and **water-rock interaction** (**Fig. 8.7**). In immature hyper acid SO_4-Cl waters ("magmatic end-member"), the high Ge/Si ratios likely result from Ge enrichment in thermal waters due to Ge volatility and transport by volcanic gases (via GeF_4, $GeCl_4$ and GeS) and by silica precipitation. The large range of values of Ge/Si ratios and $\delta^{30}Si$ values measured in acid SO_4 -, alkaline HCO_3- and neutral Cl-thermal waters can be explained by an increasing intensity of water-rock interaction involving silica precipitation. Extensive water-rock interaction erases the imprint of intermediate levels of water-rock interaction on the Ge/Si ratios and $\delta^{30}Si$ values in thermal waters and leads to similar values than in waters from the original magmatic end-member.

Q2. Can Ge/Si ratio and $\delta^{30}Si$ in rivers be used as good indicators of weathering processes in volcanic terranes featuring hydrothermal manifestations?

We highlight that the riverine Ge/Si and $\delta^{30}Si$ values can be useful to identify the **source of acidity** for weathering (magmatic or atmospheric CO_2, or alteration deposits from extinct hydrothermal systems) (*Ch2 & Ch3*; **Fig. 8.8**). We used the Ge/Si ratio to provide the first **quantitative assessment of the hydrothermal contribution** in a river draining a hyper-acid hydrothermal system (*Ch2*) and we highlight the importance to account for river sampling location, i.e., the distance from the source of magmatic gases, to estimate the hydrothermal contribution to river weathering fluxes, and hence the proportion of magmatic CO_2 in the estimates of atmospheric CO_2 consumption by volcanic rock weathering (**Fig. 8.3**).

We show that the Ge/Si ratio and $\delta^{30}Si$ of rivers free from hydrothermal additions record different **degrees of soil weathering**. The Ge/Si ratio imparted to rivers due to weathering is concealed when thermal spring discharges mix with river waters (*Ch3*). Only rivers draining extinct hydrothermal systems display distinctively low Ge/Si ratios (**Fig. 8.6**).

Q3. What is the influence of seasonal change in runoff on the relative hydrothermal and weathering contributions to rivers draining hydrothermally-active volcanic regions?

We demonstrate that the **seasonal** change in Ge/Si and $\delta^{30}Si$ values between base flow and high discharge periods in rivers draining hydrothermally-active volcanic regions (high discharge being at snowmelt (*Ch4*) or in the rain season (*Ch5)*) reflects changes in the **relative contribution of hydrothermal and meteoric processes** to chemical weathering fluxes in those rivers as a function of runoff (**Fig. 8.8**). The seasonal meteoric weathering signal at high discharge (involving the dissolution of primary minerals) should be accounted for estimates of weathering fluxes, as it directly contributes to atmospheric CO_2 consumption (**Fig. 8.3**). In volcanic areas, the average intensity of tropical cyclones, the proportion of category 4 and 5 tropical cyclones and the associated average precipitation rates are projected to increase for a 2 °C global temperature rise above pre-industrial level (IPCC, 2014). Recent detection of trends in extreme precipitation and discharge in some catchments implies greater risks of flooding at regional scale (IPCC, 2014). This underlines the importance to carefully consider seasonal changes in the factors controlling riverine element fluxes when assessing the contribution from volcanic regions to global weathering estimates and associated atmospheric CO_2 consumption.

8.5 Perspectives

This PhD thesis contributes to a better understanding of controls on weathering fluxes from hydrothermally-active volcanic regions. These findings are not exhaustive and many questions remain still open. Further investigations concerning the following aspects would be interesting perspectives:

- Exploit the newly developed method to purify Si from anion (SO_4^{2-} and Cl^-)-rich aqueous solutions to other thermal springs, other locations with rivers affected by hydrothermal discharges, but also river plume waters and seawater.

- Coupling the multi-proxy approach of Ge/Si ratios and Si isotopes with **other isotopic systems** such as, Ge isotopes to better understand the Ge behavior in different terrestrial reservoirs, S isotopes to better understand magmatic processes influencing chemistry of the thermal springs, B isotopes to better understand hydrothermal input to rivers.

- In the *Appendix*, our preliminary study suggests that the **influence of Si-accumulating crops harvest** on dissolved Si fluxes exported to the ocean should be considered in volcanic islands. To better quantify this effect in volcanic context, we suggest to: (i) build a database by volcanic island listing Si-accumulating crops species, cultivated area surface and associated particular agricultural practices; (ii) compare data obtained *in situ* (via fresh/dry and total/per parts weights) with data of Si-accumulating crops yield reported by FAO and using specific Harvest Index (HI) listed by species in the literature; (iii) consider the roots impact of plants releasing cations and which can potentially contribute to weathering; (iv) carry out simulations adjusting different parameters (Si-accumulating species, number of crops harvest by year, agricultural practices) and estimate the parameters sensitivity on the assessment of fluxes exported by Si-

accumulating crops; (v) improve the assessment of Si fluxes in rivers taking into account punctual events (floods, droughts) and data measured during wet and dry season varying with runoff and rainfalls; (vi) evaluate the soil impact and its potential contribution to rivers in hydrothermally-active volcanic areas; (viii) extrapolate at the global scale the impact of Si export by crops on the main volcanic islands on Si fluxes exported to the ocean and on the assessment of the atmospheric CO_2 consumption by silicate weathering based on riverine Si concentrations.

8.6 List of publications

Journal Article

Submitted

Gaspard, F., Opfergelt, S., Dessert, C., Robert, V., Ameijeiras-Marino, Y., Delmelle, P., 2020. Imprint of chemical weathering and hydrothermalism on the Ge/Si ratio and Si isotope composition of rivers in a volcanic tropical island, Basse-Terre, Guadeloupe (French West Indies). Submitted in Chemical Geology.

2020

Hirst, C., Opfergelt, S., **Gaspard, F.**, Hendry, K.R., Hatton, J.E., Welch, S., McKnight, D.M., Lyons, W.B., 2020. Silicon isotopes reveal a non-glacial source of silicon to Crescent Stream, McMurdo Dry Valleys, Antarctica. Frontiers Earth Scicence, doi: 10.3389/feart.2020.00229.

Conference paper

2020

Gaspard, F., Opfergelt, S., Zahajská, P., Hirst, C., Delmelle, P., 2020. Snowmelt initiates an additional source of silicon to streams in Yellowstone National Park, USA. Goldschmidt 2020 (Hawaï, du 21/06/2020 au 26/06/2020). Accepted abstract and included into the online archive, conference attendance cancelled due to the covid-19 crisis).

Opfergelt, S., **Gaspard, F.**, Hirst, C., 2020. Waters in hydrothermal and polar environments: further developments for Si isotope measurements. Goldschmidt 2020 (Hawaii, du 21/06/2020 au 26/06/2020). Accepted abstract and included into the online archive, conference attendance cancelled due to the covid-19 crisis).

2019

Descamps, C., **Gaspard, F.**, Delmelle, P., Jacquemart, A-L., 2019. Accompagner la dynamique de groupe dans un projet transdisciplinaire: un pari gagné avec 180 étudiants bioingénieurs.

QPES 2019. Questions de Pédagogies dans l'Enseignement Supérieur (Brest, France, du 17/06/2019 au 21/06/2019). In: Données Clés de l'Enseignement Supérieur et de la Recherche dans le Pays de Brest. p. 15.

Hirst, C., Opfergelt, S., **Gaspard, F.**, Hendry, K.R., Mc Knight, D., Welch, S., Lyons, W.B., Hatton, J.E., 2019. Tracing the contribution from weathering to a glacial stream in Antarctica. Artic Week (Paris, France, du 09/12/2019 au 13/12/2019).

Gaspard, F., 2019. Silicon isotopes and Ge/Si ratios as weathering proxy in streams of Guadeloupe (FWI): methodological development and first results. Symposium "Non-Traditional Stable Isotopes in Glacial and Non-Glacial Environments". Oral presentation (07/01/19, UCLouvain, Louvain-la-Neuve, Belgium).

2018

Gaspard, F., Opfergelt, S., Hartmann, J., Hosono, T. , Dessert, C., Delmelle, P., 2018. Assessing the contribution of hydrothermal alteration to element fluxes from volcanic island arcs using dissolved Ge/Si ratios in rivers. IsoWorkshop (Sorèze, France, du 08/01/2018 au 11/01/2018).

Gaspard, F., Opfergelt, S., Hartmann, J., Hosono, T., Delmelle, P., 2018. Seasonal variations of dissolved Ge:Si ratios in streams from the Aso caldera, Kyùshù, Japan. Goldschmidt 2018 (Boston, USA, du 12/08/2018 au 17/08/2018).

2017

Gaspard, F., Opfergelt, S., Ameijeiras Mariño, Y., Dessert, C., Derry, L., Delmelle, P., 2017. Germanium/silicon ratio to trace weathering and hydrothermal contribution to element fluxes in river waters from Guadeloupe (FWI). Goldschmidt 2017 (Paris, France, du 13/08/2017 au 18/08/2017). In: Goldschmidt 2017 Abstract, 2017.

Gaspard, F., Opfergelt, S., Delmelle, P., 2017. Si fluxes exported from volcanic islands: a case study from Kawah Ijen volcano, Indonesia. Si Workshop (AgroBio Tech, Gembloux, Belgium, 20/11/2017).

8.7 References

Alleman, L.Y., Cardinal, D., Cocquyt, C., Plisnier, P.-D., Descy, J.P., Kimirei, I., Sinyinza, D., André, L., 2005. Silicon isotopic fractionation in Lake Tanganyika and its main tributaries. J. Great Lakes Res. 31, 509–519.

Arnórsson, S., 1983. Chemical Equilibrian in Icelandic Geothermal Systems. Geothermics 12, 119-128.

Arnòrsson, S., 1987. Germanium in Icelandic geothermal systems. Geochim. Cosmochim. Ac. 48, 2489-2502.

Baronas, J.J., Torres, M.A., West, A.J., Rouxel, O., Georg, B., Bouchez, J., Gaillardet, J., Hammond, D.E., 2018. Earth Planet. Sci. 503, 194-215.

Baronas, J.J, West, A.J., Burton, K.W., Hammond, D.E., Opfergelt, S., Pogge von Strandmann, P.A.E., James, R.H., Rouxel, O.J., 2020. Ge and Si isotopes behaviour during intense tropical weathering. Global Biogeochem. Cy. doi:10.1029/2019gb006522.

Cardinal, D., Gaillardet, J., Hugues, H., Opfergelt, S., André, L., 2010. Contrasting silicon isotope signatures in rivers from the Congo basin and the specific behaviour of organic-rich waters, Geophys. Res. Lett. 37, L12403.

Chen, X-Y., Chafetz, H.S., Lapen, T.J., 2020. Silicon isotope variations in hydrothermal systems at Yellowstone National Park, Wyoming, USA. Geochim. Cosmochim. Ac. 283, 184-200.

De La Rocha, C.L., Brzezinski, M.A., DeNiro, M.J., 2000. A first look at the distribution of the stable isotopes of silicon in natural waters. Geochim Cosmochim. Ac. 64, 2467–2477.

Derry, L.A., Kurtz, A.C., Ziegler, K., Chadwick, O.A., 2005. Biological control of terrestrial silica cycling and export fluxes to watersheds. Lett. Nature 433, 728–731.

Dessert, C., Gaillardet, J., Dupré, B., Schott, J., Pokrovsky, O.S., 2009. Fluxes of high- versus low-temperature water-rock interactions in aerial volcanic areas: Example from the Kamchatka Peninsula, Russia. Geochim. Cosmochim. Ac. 73, 148–169.

Dessert, C., Lajeunesse, E., Lloret, E., Clergue, C., Crispi, O., Gorge, C., Quidelheur, X., 2015. Controls on chemical weathering on a mountainous volcanic tropical island: Guadeloupe (French West Indies). Geochim. Cosmochim. Ac. 171, 216-237.

Ding, T. P., Jiang, S., Wan, D., Li, Y., Li, J., Song, H., Liu, Z., Yao, X., 1996. Silicon Isotope Geochemistry. Geological Publishing House edition.

Ding, T.P., 2004. Analytical methods for silicon isotope determinations. Handbook of Stable Isotope Analytical Techniques, Volume I, Elsevier B.V., 523–39.

Ding, T.P., Gao, J., Tian, S., Wang, H., Li, M., Wang, C., Luo, X., Han, D., 2016. Chemical and isotopic characteristics of the water and suspended particulate materials in the Yellow river and their geological and environmental implications. Acta Geol. Sin. (Engl. Ed.), 90(1), 285–351.

Ding, T.P., Jiang, S., Li, Y., Gao, J., Hu, B., 2017. Geochemistry of silicon isotopes. De Gruyter.

Douthitt, C.B., 1982. The geochemistry of the stable isotopes of silicon. Geochim. Cosmochim. Acta 46, 1449–1458.

Engström, E., Rodushkin, I., Ingri, J., Baxter, D., Ecke, F., Österlund, H., Öhlander, B., 2010. Temporal isotopic variations of dissolved silicon in a pristine boreal river. Chem. Geol. 271, 142–152.

Escoube, R., Rouxel, O.J., Edwards, K., Glazer, B., Donard, O.F.X., 2015. Coupled Ge/Si and Ge isotope ratios as geochemical tracers of seafloor hydrothermal systems: Case studies at Loihi Seamount and East Pacific Rise 9°50'N. Geochim. Cosmochim. Ac. 167, 93-112.

Frings, P.J., Clymans, W., Fontorbe, G., De La Rocha, C.L., Conley, D.J., 2016. The continental Si cycle and its impact on the ocean Si isotope budget. Chem. Geol. 425, 12-36.

Froelich, P.N., Blanc, V., Mortlock, R.A., Chillrud, S.N., 1992. River fluxes of dissolved silica to the ocean were higher during glacials: Ge/Si in diatoms, rivers and oceans. Paleoceanography 7, 739-767.

Gaillardet, J., Rad, S., Rivé, K., Louvat, P., Gorge, C., Allègre, C-J., Lajeunesse, E., 2011. Orography-driven chemical denudation in the Lesser Antilles: Evidence for a new feed-back mechanism stabilizing atmospheric CO_2. Am. J. Sci. 311, 851-894.

Geilert, S., Vroon, P.Z., Keller, N., Gudbrandsson, S., Stefànsson, A., Van Bergen, M.J., 2014. Silicon isotope fractionation during silica precipitation from hot springs waters, Geophys. Res. Abstract EGU 2014: EGU2014-7951.

Georg, R.B., Reynolds, B.C., Frank, M., Halliday, A.N., 2005. Mechanisms controlling the silicon isotopic compositions of river waters. Earth Planet. Sci. Lett. 249, 290–306.

Georg, R. B., Reynolds, B.C., West, A.J., Burton, K.W., Halliday, A.N., 2007. Silicon isotope variations accompanying basalt weathering in Iceland, Earth Planet. Sci. Lett. 261, 476-490.

Georg, R.B., West, A.J., Basu, A.R., Halliday, A.N., 2009. Silicon fluxes and isotope composition of direct groundwater discharge into the Bay of Bengal and the effect on the global ocean silicon isotope budget. Earth Planet. Sci. Lett. 283, 67–74.

Goldsmith, S.T., Carey, A.E., Lyons, W.B., Hicks, D.M., 2008. Geochemical fluxes and weathering of volcanic terrains on high standing islands: Taranaki and Manawatu-Wanganui regions of New Zealand. Geochim. Cosmochim. Ac. 72, 2248-2267.

Goldsmith, S.T., Carey, A.E., Johnson, B.M., Welch, S.A., Lyons, W.B., Hicks, D.M., McDowell, W.H., Pigott, J.S., 2010. Stream geochemistry, chemical weathering and CO_2 consumption potential of andesitic terrains, Dominica, Lesser Antilles. Geochim. Cosmochim. Ac 74, 85-103.

Han, Y., Huh, Y., Derry, L., 2015. Ge/Si ratios indicating hydrothermal and sulphide weathering input to rivers of the Eastern Tibetan Plateau and Mt. Baekdu. Chem. Geol. 410, 40-52.

Hughes, H., Delvigne, C., Korntheuer, M., De Jong, J., André, L., Cardinal, D., 2011. Controlling the mass bias introduced by anionic and organic matrices in silicon isotopic measurements by MC-ICP-MS, J. Anal. Spectrom. 26, 1892-1896.

Hughes, H.J., Sondag, F., Santos, R.V., André, L., Cardinal, D., 2013. The riverine silicon isotopes composition of the Amazon Basin. Geochim. Cosmochim. Acta. 121, 637-651.

Hurwitz, S., Evans, W.C., Lowenstern, J.B., 2010. River solute fluxes reflecting active hydrothermal chemical weathering of the Yellowstone Plateau Volcanic Field, USA. Chem. Geol. 276, 331-343.

IPCC, 2014. Fifth Assess. Rep. IPCC (eds T.F. Stocker et al.) Cambridge University Press.

Kurtz, A.C., Derry, L.A., Chadwick, O.A., 2002. Germanium-silicon fractionation in the weathering environment. Geochim. Cosmochim. Ac. 66, 1525–1537.

Kurtz, A. C., Derry, L. A., 2004. Tracing silicate weathering and terrestrial silica cycling with Ge/Si ratios, in: Proceedings of 11th International Symposium on Water Rock Interaction, Leiden, Netherlands. 833–836.

Kurtz, A.C., Lugolobi, F., Salvucci, G., 2011. Germanium-silicon as a flow path tracer: application to the Rio Icacos watershed. Water Resour. Res. 47.

Louvat, P., Allègre, C.J., 1997. Present denudation rates on the island of Reunion determined by river geochemistry: Basalt weathering and mass budget between chemical and mechanical erosions. Geochim. Cosmochim. Ac 61, 3645-3669.

Lugolobi, F., Kurtz, A.C., Derry, L.A., 2010. Germanium–Silicon fractionation in a tropical, granitic weathering environment. Geochim. Cosmochim. Ac. 74, 1294–1308.

Mortlock, R.A., Froelich, P.N., 1987. Continental weathering of germanium: Ge/Si in the global river discharge, Geochim. Cosmochim. Acta, 51, 2075-2082.

Opfergelt, S., Delvaux, B., André , L., Cardinal, D., 2008. Plant silicon isotopic signature might reflect soil weathering degree. Biogeochemistry 91, 163–175.

Opfergelt, S., Eiriksdottir, E.S., Burton, K.W., Einarsson, A., Siebert, C., Gislason, S.R., Halliday, A.N., 2011. Quantifying the impact of freshwater diatom productivity on silicon isotopes and silicon fluxes: Lake Myvatn, Iceland. Earth Planet. Sci. Lett. 305, 73–82.

Opfergelt, S., Delmelle, P., 2012. Silicon isotopes and continental weathering processes: Assessing controls on Si transfer to the ocean. Comptes Rendus Geosci. 344, 723–738.

Opfergelt, S., Burton, K.W., Pogge von Strandmann, P.A.E., Gislason, S.R., Halliday, A.N., 2013. Riverine silicon isotope variations in glaciated basaltic terrains: implications for the Si delivery to the ocean over glacial-interglacial intervals. Earth. Planet. Sc. Lett. 369-370, 211-219.

Pokrovsky, G.S., Schott, J., 1998. Experimental study of the complexation of silicon and germanium with aqueous organic species: implications for germanium and silicon transport and Ge/Si ratios in natural waters. Geochim. Cosmochim. Ac. 62, 3413-3428.

Pokrovsky, O. S., Reynolds, B. C., Prokushkin, A. S., Schott, J., Viers, J., 2013. Silicon isotope variations in Central Siberian rivers during

basalt weathering in permafrostdominated larch forests. Chem. Geol., 355, 103–116.

Rad, S., Louvat, P., Gorge, C., Gaillardet, J., Allègre, C.J., 2006. River dissolved and solid loads in the Lesser Antilles: new insight into basalt weathering processes. J. Geoch. Explor. 88, 308-312.

Scribner, A.M., Kurtz, A.C., Chadwick, O.A., 2006. Germanium sequestration by soil: targeting the roles of secondary clays and Fe-oxyhydroxides, Earth and Plan. Sc. 243, 760-770.

Siebert, C., Ross, A., McManus, J., 2006. Germanium isotope measurements of high-temperature geothermal fluids using double-spike hydride generation MC-ICP-MS. Geochim. Cosmochim. Acta 70, 3986-3995.

Stefánsson, A., Gislason, S.R., 2001. Chemical weathering of basalts, southwest Iceland: effect of rock crystallinity and secondary minerals on chemical fluxes to ocean. J. Am. Sci. 301, 513-556.

Wang, W., Wei, H-Z., Jiang, S-Y., Tan, H-B., Eastoa, C.J., Williams-Jones, A.E., Hohl, S.V., Wu, H-P., 2019. The origin of rare alkali metals in geothermal fluids of southern Tibet, China: A silicon isotope perspective. Scientific reports 9, 7918.

Wheat, C., McManus, J., 2008. Germanium in mid-ocean ridge flank hydrothermal fluids. Geochem. 9: Q03025.

Ziegler, K., Chadwick, O.A., Brzezinski, M.A., Kelly, E.F., 2005. Natural variations of $d^{30}Si$ ratios during progressive basalt weathering, Hawaiian Islands. Geochim. Cosmochim. Acta 69, 4597–4610.

APPENDIX

Appendix 1:

Preliminary assessment of the influence of Si-accumulating crop harvest on Si fluxes exported from volcanic islands: a case study from Asembagus Plain (Kawah Ijen, Java Island) and Aso caldera (Aso volcano, Kyūshū Island)

9.1 Introduction

Land-use is another uncertainty that may influence weathering fluxes from hydrothermally-active regions and more specifically relates to cultivation of silicon-accumulating crops which are commonly found in tropical volcanic islands. Indeed, volcanic soils, most of them being Andisols, support more than 10% of the total world population while it represent less than 1% of the total land surface, are fertile and suitable for crops cultivation (Delmelle et al, 2015). As a result, volcanic islands are the most-cultivated areas worldwide (Ramankutty et al, 2008). The most cultivated crops worldwide, i.e. sugar cane, maize, rice, and wheat (FAOSTAT, 2015), are Si-accumulating plants: Si taken up by the plant is precipitated as biogenic Si in the plant tissue (phytoliths; Jones and Handreck, 1965) leading to Si content of ~1% Si dry weight in the plant, and up to 5% in rice (Datnoff et al, 2001).

Cultivation and harvest of Si-accumulating crops, including plant biomass export, result in the loss of a non-accounted sink for Si released during weathering (e.g., Desplanques et al, 2006). We suggest that crop

harvest may also influence the flux of dissolved Si exported to the ocean because the estimated global agricultural Si export (0.22×10^{12} $kg_{Si}.yr^{-1}$; Matichenkov and Bocharnikova, 2001) is on the same order of magnitude than the riverine Si discharged into the ocean as dissolved and biogenic Si (0.20×10^{12} $kg_{Si}.yr^{-1}$; Tréguer and De La Rocha, 2013).

Considering the global increasing demand for agricultural soils (Godfray et al, 2010), the impact of crop harvest on global Si export to the ocean is likely to be emphasized in the future and needs to be better quantified given that Si is a key nutrient for diatoms, which are essential organisms for the oceanic C pump (Smetacek, 1999). The effect may be particularly pronounced in volcanic island arc regions, which contribute disproportionately to the dissolved Si delivery to the ocean (Dürr et al, 2011) mainly influenced by input of surface water (~66%, rivers and lake).

In this preliminary study, we bring first assessment of Si-accumulating crop harvest influence on Si fluxes exported from volcanic islands with a case study at small spatial scale with good constraints on Si and water fluxes (Asembagus Plain (36 km^2), Kawah Ijen volcano, Java Island) and at larger spatial scale (Aso caldera (353 km^2), Aso volcano; Kyūshū Island) to provide a knowledge base to implement the impact of crop harvest on dissolved Si fluxes to the ocean in global models.

9.2 Study sites

At small spatial scale, the site of Asembagus Plain (7°44'S, 114°12'E) located in Eastern Java is an ideal study case. The study site (Kawah Ijen volcano and Banyu Pahit/Banyu Putih catchment) is described more specifically in *Ch2*. The Banyu Putih river serves to irrigate an intensively cultivated zone, the Asembagus plain (36 km^2), before reaching the ocean (Löhr et al, 2005; van Rotterdam-Los et al, 2008), dominated by Si-accumulating crops, mainly rice (~1000 ha) and sugar cane (~2000 ha). The climate of Indonesia is separated in two seasons: the wet (October-April) and the dry (May-September) season. Flooded rice crops are cultivated in wet season (October-March) and two rice crop harvest are observed over a year.

At large spatial scale, the Aso caldera (32°55'N, 131°E) located in Kyūshū Island, one of the largest caldera volcanoes in the world (353

km^2; Nakada, 2003), is an ideal study case. The site (Aso volcano and the Aso caldera) is described more in details in *Ch5*. The north (Aso Valley) and south (Nango Valley) part of the caldera are respectively discharged by Kurokawa river and Shirakawa river. The cultivated area within the caldera is ~10 times larger than that found in the Asembagus plain and is also dominated by rice paddy fields. Japan is a large contributor to dissolved Si to the ocean (6.6 times higher than the world average; Hartmann et al, 2010). The climate of Japan is divided in four seasons (winter, spring, summer and fall) with wet season during summer between June and August. Flooded rice crops are cultivated between spring and fall and one rice crop harvest is observed over a year.

9.3 Materials and methods

9.3.1 River waters and biomass sampling

The Banyu Putih river water was collected at the Lewung damn ~40 km before irrigating the coastal Asembagus Plain before irrigating two rice (BP1R, BP2R) and sugar cane (BP1C, BP2C) plots. We also collected the alkaline Bangoran river located in the north-east part of the Java Island and irrigating rice (BAR) and sugar (BAC) plots. On each plot (BP1R, BP2R, BP1C, BP2C, BAR and BAC), five plant biomass were collected randomly. All samples were collected on field in February 2017 during wet season and locations are shown in **Fig. 9.1**.

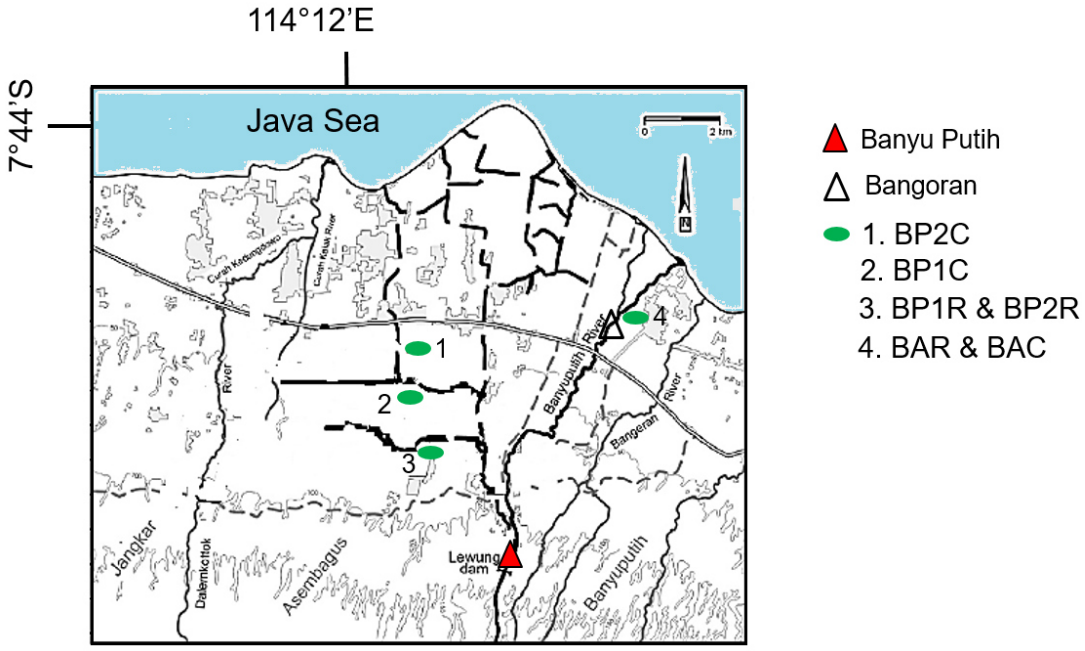

Fig. 9.1: Location of Banyu Putih (BP10) river water sampled at Lewung damn ~ 40 km of Kawah Ijen's acid lake downstream before irrigating two rice (BP1R, BP2R) and sugar cane (BP1C, BP2C) plots in the Asembagus Plain. The alkaline Bangoran (BA) river water and irrigated rice (BAR) and sugar cane (BAC) plot are also represented.

In the Aso caldera, river water samples were collected at the confluence of Kurokawa and Shirakawa at the outlet of the caldera (S33) on different seasons (spring 15, summer 15). Five rice plants were collected randomly in September 2018 on four rice plots (two in the northern part of the caldera (N1, N2) irrigated by Kurokawa and two in the southern part of the caldera (S1, S2) irrigated by Shirakawa river). Samples location is shown in **Fig. 9.2**. The plant biomass was collected at the terminal stage of growth just before harvest.

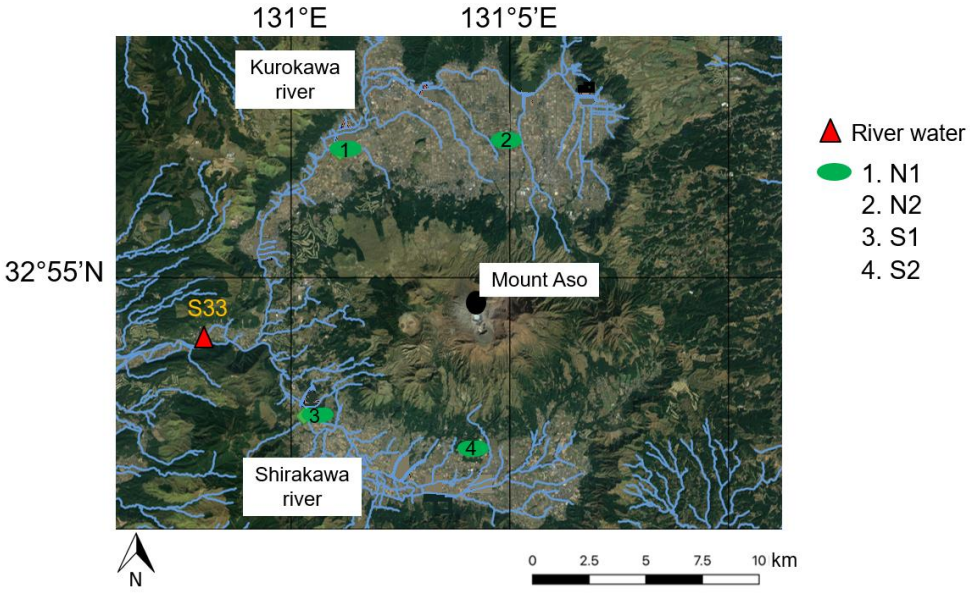

Fig. 9.2: Location of the two rice plots irrigated by Kurokawa river in the northern part (N1, N2) and by Shirakawa river in the southern part (S1, S2) of the Aso caldera. These rivers, surrounding the Aso caldera drain the Mount Aso, Kyūshū Island. S33 represents the river water resulting from mixing of Kurokawa and Shirakawa river waters at the outlet of the Aso caldera.

The waters sampling methodology was described more in details in *Ch2* for Asembagus Plain rivers and in *Ch5* for Aso caldera rivers.

9.3.2 Waters flow rate measurements

Water flow rate ($m^3.s^{-1}$) in Banyu Putih was measured *in situ* using flow meter (Flo-Mate Model FH950) based on the Faraday law of electromagnetic induction and the following equation: Flow rates ($m^3.s^{-1}$) = $\bar{U}$ ($m.s^{-1}$) × S (m^2) with $\bar{U}$ representing the average steam velocity and S the cross-sectional area (m^2). The method is more detailed in *Ch2*. We assess the water flow rate discharging out the Aso caldera (S33) by averaging total annual flow rates obtained by flow monitoring station on daily basis during two years (2014-2015).

9.3.3 Biomass: Si content analysis

Si content analysis

The total fresh weight and fresh weight per part (grains, stems and leaves for rice; stems and leavs for sugar cane) of all plant biomass were determined *in situ* using balance scale (accuracy = 0.01g). All data are represented in **Table 9.1**. Samples were then placed for one week at 50°C in oven to measure their dry weights. An alkaline fusion (1:4 lithium meta:tetraborate; Hauptkorn, 2001) at 1000°C was performed on crushed composite samples with liquid nitrogen and Si content was measured by inductively-coupled plasma-optical emission spectrometry (ICP-OES; iCAP 6500 Thermo Fisher Scientific) after dissolution of the melting sparkle with suprapure HNO_3 (detection limit of Si = 0.36 $\mu mol.l^{-1}$).

Table 9.1: Total/per parts fresh weight (g) and total/per parts dry weight of plant biomass collected on (a) three rice plots of Java Island irrigated by Banyu Putih (BP1R, BP2R) and Bangoran river (BAR), (b) three sugar cane plots of Java Island irrigated by Banyu Putih (BP1C, BP2C) and Bangoran river (BAC), (c) two rice plots of Kyūshū Island irrigated by Kurokawa river (N1, N2) and (d) two rice plots of Kyūshū Island irrigated by Shirakawa river (S1, S2). BPxRy with x = first or second rice plot irrigated by Banyu Putih and y = G (grains), L (leaves) and S (stems). R = rice and C = sugar cane. BA = Bangoran. N = northern plot and S = southern plot. N2R2S = steam part of second rice sample on second northern parcel.

a)

Sample	Sampling date dd.mm.yy	Label	Fresh weight g	Total fresh weight g	Percentage fresh weight %	Dry weight g	Total dry weight g	Percentage dry weight %
1	04.02.17	BP1R1G	2.76	41.14	6.7	1.31	11.12	11.8
		BP1R1L	11.96		29.1	3.47		31.2
		BP1R1S	26.42		64.2	6.33		57.0
2	04.02.17	BP1R2G	19.03	83.09	22.9	8.27	26.21	31.6
		BP1R2L	15.56		18.7	5.16		19.7
		BP1R2S	48.50		58.4	12.77		48.7
3	04.02.17	BP1R3G	11.76	54.13	21.7	7.22	19.45	37.1
		BP1R3L	11.71		21.6	4.87		25.0
		BP1R3S	30.66		56.6	7.36		37.9
4	04.02.17	BP1R4G	12.63	70.25	18.0	5.74	23.24	24.7
		BP1R4L	17.53		25.0	6.14		26.4
		BP1R4S	40.09		57.1	11.36		48.9
5	04.02.17	BP1R5G	14.23	101.13	14.1	6.66	34.16	19.5
		BP1R5L	25.30		25.0	11.62		34.0
		BP1R5S	61.60		60.9	15.88		46.5
Sample	Sampling date dd.mm.yy	Label	Fresh weight g	Total fresh weight g	Percentage fresh weight %	Dry weight g	Total dry weight g	Percentage dry weight %
1	04.02.17	BP2R1G	20.28	94.27	21.5	10.72	31.74	33.8
		BP2R1L	24.71		26.2	9.33		29.4
		BP2R1S	49.28		52.3	11.68		36.8
2	04.02.17	BP2R2G	15.22	90.46	16.8	7.81	29.29	26.7
		BP2R2L	27.87		30.8	11.34		38.7
		BP2R2S	47.37		52.4	10.13		34.6
3	04.02.17	BP2R3G	23.12	117.12	19.7	12.19	37.47	32.5
		BP2R3L	29.59		25.3	12.77		34.1
		BP2R3S	64.41		55.0	12.50		33.4
4	04.02.17	BP2R4G	22.82	106.22	21.5	15.42	37.44	41.2
		BP2R4L	31.36		29.5	9.33		24.9
		BP2R4S	52.04		49.0	12.69		33.9
5	04.02.17	BP2R5G	15.72	88.76	17.7	9.96	32.12	31.0
		BP2R5L	20.84		23.5	7.79		24.2
		BP2R5S	52.20		58.8	14.37		44.7
Sample	Sampling date dd.mm.yy	Label	Fresh weight g	Total fresh weight g	Percentage fresh weight %	Dry weight g	Total dry weight g	Percentage dry weight %
1	06.02.17	BAR1G	15.42	106.85	14.4	6.92	30.51	22.7
		BAR1L	30.53		28.6	8.21		26.9
		BAR1S	60.90		57.0	15.38		50.4
2	06.02.17	BAR2G	13.32	97.74	13.6	7.07	34.57	20.4
		BAR2L	31.84		32.6	14.30		41.4
		BAR2S	52.58		53.8	13.21		38.2
3	06.02.17	BAR3G	19.48	130.44	14.9	9.96	45.8	21.7
		BAR3L	38.80		29.7	10.46		22.8
		BAR3S	72.16		55.3	25.38		55.4
4	06.02.17	BAR4G	14.17	105.83	13.4	6.72	37.11	18.1
		BAR4L	38.28		36.2	14.15		38.1
		BAR4S	53.38		50.4	16.24		43.8
5	06.02.17	BA1R5G	10.28	63.02	16.3	4.72	26.76	17.6
		BA1R5L	18.46		29.3	10.99		41.1
		BA1R5S	34.28		54.4	11.06		41.3

b)

Sample	Sampling date dd.mm.yy	Label	Fresh weight g	Total fresh weight g	Percentage fresh weight %	Dry weight g	Total dry weight g	Percentage dry weight %
1	05.02.17	BP1C1S	1259.15	1402.73	89.8	289.04	339.08	85.2
		BP1C1L	143.58		10.2	50.04		14.8
2	05.02.17	BP1C2S	1274.09	1439.21	88.5	294.95	352.39	83.7
		BP1C2L	165.12		11.5	57.44		16.3
3	05.02.17	BP1C3S	1521.56	1657.20	91.8	303.95	348.78	87.1
		BP1C3L	135.64		8.2	44.83		12.9
4	05.02.17	BP1C4S	1309.92	1467.13	89.3	327.33	380.18	86.1
		BP1C4L	157.21		10.7	52.84		13.9
5	05.02.17	BP1C5S	815.13	933.12	87.4	214.25	259.22	82.7
		BP1C5L	117.99		12.6	44.97		17.3
Sample	Sampling date dd.mm.yy	Label	Fresh weight g	Total fresh weight g	Percentage fresh weight %	Dry weight g	Total dry weight g	Percentage dry weight %
1	05.02.17	BP2C1S	1204.31	1384.31	87.0	269.83	335.64	80.4
		BP2C1L	180.00		13.0	65.80		19.6
2	05.02.17	BP2C2S	1065.89	1211.85	88.0	248.68	300.82	82.7
		BP2C2L	145.96		12.0	52.14		17.3
3	05.02.17	BP2C3S	1140.45	1196.08	95.3	257.71	275.93	93.4
		BP2C3L	55.63		4.7	18.22		6.6
4	05.02.17	BP2C4S	1346.85	1522.33	88.5	386.85	436.11	88.7
		BP2C4L	175.48		11.5	49.26		11.3
5	05.02.17	BP2C5S	1219.30	1287.53	94.7	193.23	217.37	88.9
		BP2C5L	68.23		5.3	24.15		11.1
Sample	Sampling date dd.mm.yy	Label	Fresh weight g	Total fresh weight g	Percentage fresh weight %	Dry weight g	Total dry weight g	Percentage dry weight %
1	06.02.17	BAC1S	1080.54	1232.79	87.6	291.77	347.78	83.9
		BAC1L	152.25		12.4	56.00		16.1
2	06.02.17	BAC2S	2316.55	2596.89	89.2	670.77	771.41	87.0
		BAC2L	280.34		10.8	100.64		13.0
3	06.02.17	BAC3S	1625.40	1837.19	88.5	495.07	573.76	86.3
		BAC3L	211.79		11.5	78.69		13.7
4	06.02.17	BAC4S	1728.01	1901.27	90.9	465.17	531.31	87.6
		BAC4L	173.26		9.1	66.14		12.4
5	06.02.17	BAC5S	2071.01	2314.17	89.5	481.37	563.62	85.4
		BAC5L	243.16		10.5	82.25		14.6

c)

Sample	Sampling date dd.mm.yy	Label	Fresh weight g	Total fresh weight g	Percentage fresh weight %	Dry weight g	Total dry weight g	Percentage dry weight %
1	22.09.18	N1-1G	3.45	6.84	50.4	3.11	5.38	57.8
		N1-1L	1.04		15.2	0.95		17.7
		N1-1S	2.35		34.4	1.32		24.5
2	22.09.18	N1-2G	3.55	8.48	41.9	3.00	6.17	48.6
		N1-2L	2.08		24.5	1.73		28.0
		N1-2S	2.85		33.6	1.44		23.3
3	22.09.18	N1-3G	3.23	7.13	45.3	2.93	5.37	54.6
		N1-3L	1.36		19.1	1.24		23.1
		N1-3S	2.54		35.6	1.20		22.3
4	22.09.18	N1-4G	4.34	9.84	44.1	3.73	6.66	56.0
		N1-4L	1.72		17.5	1.43		21.5
		N1-4S	3.78		38.4	1.50		22.5
5	22.09.18	N1-5G	4.08	8.72	46.8	3.88	7.42	52.3
		N1-5L	1.58		18.1	1.59		21.4
		N1-5S	3.06		35.1	1.95		26.3

Sample	Sampling date dd.mm.yy	Label	Fresh weight g	Total fresh weight g	Percentage fresh weight %	Dry weight g	Total dry weight g	Percentage dry weight %
1	22.09.18	N2-1G	4.27	9.33	45.8	3.53	6.39	55.2
		N2-1L	1.62		17.4	1.28		20.0
		N2-1S	3.44		36.9	1.58		24.7
2	22.09.18	N2-2G	4.36	9.70	44.9	3.76	6.68	56.3
		N2-2L	1.72		17.7	1.38		20.7
		N2-2S	3.62		37.3	1.54		23.1
3	22.09.18	N2-3G	3.33	8.06	41.3	2.78	5.44	51.1
		N2-3L	1.45		18.0	1.17		21.5
		N2-3S	3.28		40.7	1.49		27.4
4	22.09.18	N2-4G	4.49	9.59	46.8	3.78	6.37	59.3
		N2-4L	1.43		14.9	1.12		17.6
		N2-4S	3.67		38.3	1.47		23.1
5	22.09.18	N2-5G	3.60	7.40	48.6	3.01	5.25	57.3
		N2-5L	1.17		15.8	0.97		18.5
		N2-5S	2.63		35.5	1.27		24.2

d)

Sample	Sampling date dd.mm.yy	Label	Fresh weight g	Total fresh weight g	Percentage fresh weight %	Dry weight g	Total dry weight g	Percentage dry weight %
1	22.09.18	S1-1G	3.63	8.49	42.8	2.72	5.22	52.1
		S1-1L	2.26		26.6	1.41		27.0
		S1-1S	2.60		30.6	1.09		20.9
2	22.09.18	S1-2G	3.03	7.43	40.8	2.31	4.65	49.7
		S1-2L	1.55		20.9	1.05		22.6
		S1-2S	2.85		38.4	1.29		27.7
3	22.09.18	S1-3G	3.91	8.46	46.2	2.97	4.92	60.4
		S1-3L	1.59		18.8	0.85		17.3
		S1-3S	2.96		35.0	1.10		22.4
4	22.09.18	S1-4G	3.42	9.42	36.3	2.65	6.22	42.6
		S1-4L	2.68		28.5	1.81		29.1
		S1-4S	3.32		35.2	1.76		28.3
5	22.09.18	S1-5G	3.23	8.69	37.2	2.47	5.43	45.5
		S1-5L	2.06		23.7	1.38		25.4
		S1-5S	3.40		39.1	1.58		29.1
Sample	Sampling date dd.mm.yy	Label	Fresh weight g	Total fresh weight g	Percentage fresh weight %	Dry weight g	Total dry weight g	Percentage dry weight %
1	22.09.18	S2-1G	2.57	5.58	46.1	2.01	3.41	58.9
		S2-1L	1.20		21.5	0.76		22.3
		S2-1S	1.81		32.4	0.64		18.8
2	22.09.18	S2-2G	3.41	7.29	46.8	2.62	4.60	57.0
		S2-2L	1.06		14.5	0.87		18.9
		S2-2S	2.82		38.7	1.11		24.1
3	22.09.18	S2-3G	3.08	7.32	42.1	2.34	4.53	51.7
		S2-3L	1.39		19.0	1.00		22.1
		S2-3S	2.85		38.9	1.19		26.3
4	22.09.18	S2-4G	3.09	7.02	44.0	2.53	4.52	56.0
		S2-4L	1.34		19.1	0.94		20.8
		S2-4S	2.59		36.9	1.05		23.2
5	22.09.18	S2-5G	3.63	8.27	43.9	2.79	5.21	53.6
		S2-5L	1.61		19.5	1.10		21.1
		S2-5S	3.03		36.6	1.32		25.3

9.3.4 Method to assess the influence of Si-accumulating crops on Si fluxes

The strategy for estimating Si fluxes (gSi) exported by Si-accumulating crops ($Flux_{exported}$) is based on closed system following equation: $Flux_{in}$ (Si fluxes in river water irrigating the cultivated area) = $Flux_{exported}$ + $Flux_{out}$ (Si fluxes in river water flowing out the cultivated area) and summarized in **Fig. 9.3**. Briefly, $Flux_{in}$ and $Flux_{out}$ are assessed with Si concentration (DSi; $mg.l^{-1}$) and water flow rate (D; $m^3.s^{-1}$) in river waters irrigating (e.g., BP10, Asembagus Plain) and flowing out (e.g., S33, Aso caldera) the cultivated area, respectively. $Flux_{exported}$ is obtained using the total Si fresh weight ($Si_{exported\ by\ plant}$) obtained by extrapolating the Si concentration ($gSi_{exported\ by\ parts}.g_{DW}^{-1}$) measured by ICP-OES and the dry weight (g_{DW}) measured in plant parts biomass, the fraction of different plant parts, the number of plants biomass surveyed in 1 m^2 and the cultivated area (m^2) assessed via the catchment surface area (m^2). The respective catchment surface area is estimated using Digital Elevation Model (DEM: U.S. Geological Survey, Earth Explorer) on QGIS software. To determine $Flux_{exported}$, we used $Flux_{in}$ in Asembagus Plain (via BP10) and $Flux_{out}$ in Aso caldera (via S33) (**Fig. 9.3**).

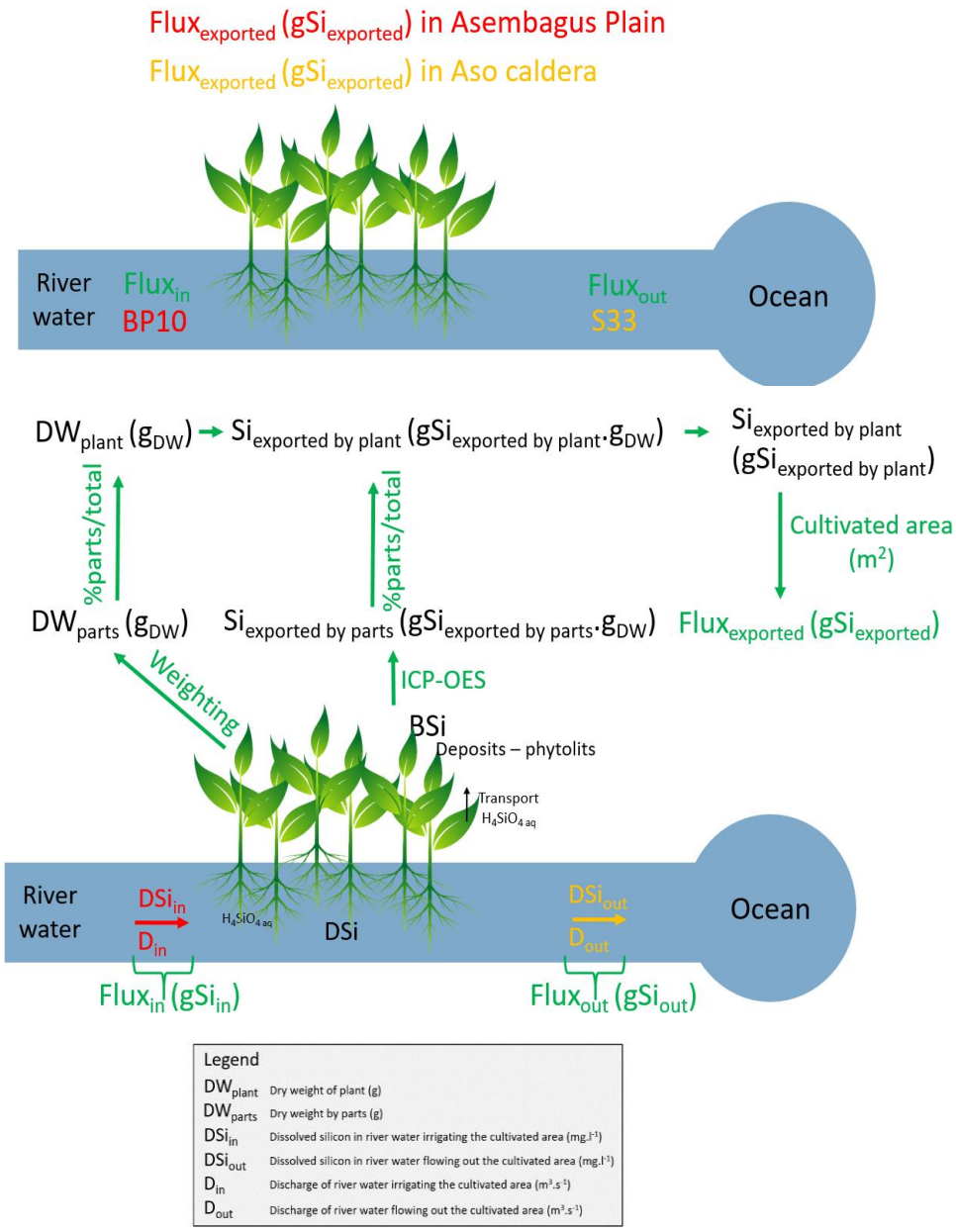

Fig. 9.3: Strategy for estimating Si fluxes (gSi) exported by Si-accumulating crops ($Flux_{exported}$) based on closed system following equation: $Flux_{in}$ (Si fluxes in river water irrigating the cultivated area) = $Flux_{exported}$ + $Flux_{out}$ (Si fluxes in river water flowing out the cultivated area). To determine $Flux_{exported}$ by Si-accumulating crops harvest, we used $Flux_{in}$ in Asembagus Plain (B10) and $Flux_{out}$ in Aso caldera (S33).

9.4 Results and discussion

General parameters (Si concentrations, pH) of streams from Java Island (BP10 and BA) and from Kyūshū Island (S33 sampled in different seasons) are presented in **Table 9.2**. The Si content ($g.kg^{-1}_{DW}$) of plant biomass are in **Table 9.3**.

Table 9.2: pH and silicon concentration ($mg.l^{-1}$) of the acidic Banyu Putih irrigating the Asembagus Plain (BP10), the alkaline Bangoran (BA) river water from Java Island and of the S33 river water from Kyūshū Island (river confluence at the outlet of the Aso caldera). Data of August 1996 in BP10 1996 are from Delmelle and Bernard (2000).

	Sampling date	Flux	Sample	pH	Si
					$mg.l^{-1}$
Kawah Ijen	Feb-17	in	BP10	3.8	41.4
River waters	Aug-96	in	BP10	4.3	45.8
	Feb-17	in	BA	8.1	38.7
Aso	spring 15	out	S33	8.0	26.4
River waters	sum 15	out	S33	8.5	24.2

Table 9.3: Si content ($g.kg^{-1}_{DW}$) of plant biomass (rice and sugar cane) collected on the Asembagus Plain (1st column) and in the Aso caldera (2nd column). BPxRy with x = 1 (first) or 2 (second) rice plot irrigated by Banyu Putih and y = G (grains), L (leaves) and S (stems). R = rice and C = sugar cane. BA = Bangoran. N = northern plot and S = southern plot. N2R2S = stem part of second rice sample on second northern parcel.

Asembagus Plain		Aso caldera	
Sample	Si $g.kg^{-1}_{DW}$	Sample	Si $g.kg^{-1}_{DW}$
BP1RG	49.14	N1R1G	21.22
BP1RL	46.49	N1R1L	99.23
BP1RS	50.62	N1R1S	58.12
BP2RG	26.16	N1R2G	14.57
BP2RL	-	N1R2L	118.95
BP2RS	58.44	N1R2S	62.08
BARG	50.74	N1R3G	26.23
BARL	49.20	N1R3L	124.57
BARS	34.16	N1R3S	66.63
BP1CL	21.87	N1R4G	23.18
BP1CS	42.71	N1R4L	110.67
BACL	22.77	N1R4S	65.51
BACS	33.49	N1R5G	22.09
		N1R5L	116.21
		N1R5S	57.49

9.4.1 Assessment at small spatial scale: the Asembagus Plain

In Java Island, the Si flux irrigating the Asembagus Plain for BP10 ($Flux_{in}$) was assessed using Si concentration and water flow rate of BP10 first (1) measured in wet season and extrapolated to a one-year scale (Si = 41.4 $mg.l^{-1}$; flow rate = 6.9 $m^3.s^{-1}$; $Flux_{in}$ = 9004.2 $tSi.yr^{-1}$; **Table 9.4**) (Scenario A) and (2) calculated by combining data of wet and dry season (Delmelle and Bernard, 2000) considering seven months of wet season and five months of dry season for averaging Si concentrations (43.2 $mg.l^{-1}$) and using mean BP10 flow rates on 20 years (1981-2000) reported by Löhr et al (2005) (5.5 $m^3.yr^{-1}$ and $Flux_{in}$ = 4768.2 $tSi.yr^{-1}$; **Table 9.4**) (Scenario B).

Table 9.4: Percentage (%) of Si fluxes exported by Si-accumulating crops involving rice and sugar cane ($F_{exported}$) relative to Si fluxes irrigating the coastal Asembagus Plain assessed for BP10 ($Flux_{in}$) river water in Java Island, Indonesia.

Farming practice			$Flux_{exported}$ /$Flux_{in}$ (%)	
Our data			*A*	B
	All plant parts exported (irrigating by acidic water)	min	20.35	38.43
	All plant parts exported (irrigating by acidic water)	mean	37.02	69.89
	All plant parts exported (irrigating by alkaline water)		52.29	98.75
FAO (2014)	All plant parts exported		26.41	49.90
	Edible parts exported, inedible parts restored		2.76	5.22
	All plant parts exported, leaves of sugar cane restored		4.72	8.91

[A]Year = data of wet season × 12; BP10 = 41.4 mg.l^{-1}; BP10 flow rate = 6.9 m^3.s^{-1}; $Flux_{in}$ = 9004.2 tSi.yr^{-1}; 1 harvest.yr^{-1}

[B]Year = (7/12 × data of wet season)+(5/12 × data of dry season); BP10 = 43.2 mg.l^{-1}; BP10 flow rate = 5.5 m^3.s^{-1}; $Flux_{in}$ = 4768.2 tSi.yr^{-1}; 1 harvest.yr^{-1}

In the two scenario A and B, and respecting agricultural practises in Indonesia (one harvest. yr^{-1}), we performed different scenarios to assess the percentage of Si fluxes exported by Si-accumulating crops (rice and sugar cane) on the Asembagus Plain. With our data of total/per parts biomass weight (**Table 9.1**), Si contents (**Table 9.3**) and the cultivated area in Asembagus Plain, we calculated $Flux_{exported}$ in Scenario A in the case of all plant part are exported (irrigating by acidic BP10 river water) and the results show values ranging from 20.35 % (using rice and sugar cane plots with lower Si concentrations exported by plant) and 37.02% (using rice and sugar cane plots with mean Si concentrations exported by all plants). These values are lower than those reported for Scenario B and in the case of irrigating by alkaline water (BA). Indeed, the alkaline Bangoran river displays Si rice yield (54.76 gSi.m^{-2}) higher than acidic B1R and B2R (40.36 and 53.38 gSi.m^{-2}, respectively) and Si sugar cane yield (160.93 gSi.m^{-2}) higher than acidic B1C and B2C (112.13 and 132.65 gSi.m^{-2}, respectively), highlighting the potential effect on crop yield in areas irrigated with acid water (van Rotterdam-Los et al, 2008). Nordstrom (1982) show that the acidified Asembagus Plain soil quality is altered because of occurrence of an aluminium hydroxysulfate that generates a cyclic seasonal pattern of retention and releases of Al and SO_4.

Finally, we compare our results with the FAO's average rice yield in 2014 for Indonesia (5.66 t.ha^{-1}; FAO, 2014) and the harvest Index (HI = $FW_{harvest\ part\ of\ crop}$.$FW_{non\text{-}harvest\ part\ of\ crop}^{-1}$) of Saccharum officinarum rice plant

and Oryza sativa sugar cane plant (HI = 0.39; Carey and Fulweiler, 2016). In the case of all plant parts are exported, generally applied in Indonesia, the results obtained by FAO data vary in the same range (26.41-49.90%) than those obtained with our data (20.35-38.43%). We also perform simulations in the case of only edible plant parts are exported (grains for rice, stem for sugar cane) and other parts are restored to the soil and $Flux_{exported}$ strongly decreases in Scenario A and B (2.76 and 5.22%, respectively).

9.4.2 Assessment at large spatial scale: the Aso caldera

In Kyūshū Island, the Si flux flowing out the Aso caldera for S33 ($Flux_{out}$) was estimated using the mean Si concentration measured in spring 2015 and summer 2015 (25.3 $mg.l^{-1}$; **Table 9.5**) and water flow rate of S33 (mean of total annual flow rates obtained by flow monitoring station on daily basis during two years (2014-2015); flow rate = 8.5 $m^3.s^{-1}$; **Table 9.5)** and display the value of 6752.2 $tSi.yr^{-1}$.

Table 9.5: Si fluxes exported by Si-accumulating rice plants ($F_{exported}$) relative to Si fluxes flowing out the Aso caldera assessed for S33 ($Flux_{out}$) river water in Kyūshū Island, Japan

Farming practice	$Flux_{exported}/Flux_{out}$		
	1 harvest	**2 harvests**	**3 harvests**
All rice parts exported	2.43	3.11	3.79
Grains and leaves exported, stems restored	1.71	2.19	2.66
All rice parts exported, leaves of sugar cane restored	0.57	0.73	0.89

[1] S33 = 25.3 $mg.l^{-1}$ (mean of spring 2015 and summer 2015); S33 flow rate = 8.5 $m^3.s^{-1}$ (mean of total flow rates during 2014-2015 obtained by summing daily flow rates) ; $Flux_{out}$ = 6752.2 $tSi.yr^{-1}$

Using total/per parts biomass weight (**Table 9.1**), Si contents (**Table 9.3**) and the cultivated area in Aso caldera, we assess the $Flux_{exported}/Flux_{out}$ for different simulation (all rice parts exported, grains and leaves exported + stems restored, all rice parts exported, leaves of sugar cane restored to the soil) ranging from 0.57 to 2.43 times the $Flux_{exported}$ (1 $harvest.yr^{-1}$), from 0.73 to 3.11 times the $Flux_{exported}$ (2 $harvests.yr^{-1}$) and from 0.89 to 3.79 times the $Flux_{exported}$ (3 $harvests.yr^{-1}$). Note that the first harvest provides 60% of the annual production.

9.4.3 Sampling bias on the estimation of Si fluxes exported by Si-accumulating crops

Our results of $Flux_{exported}$ present a large range of values. This could be induced by a sampling bias. The collection of five-plant biomass randomly on each plot may lead to inaccuracies. We need to consider potential effects of:

- Representativity: The total number of plants at the plot scale has been extrapolated from the number of plants assessed in a 1 m^2 plot. This extrapolation requires a homogeneous distance between each plant. To increase accuracy, we need to increase the number of collected plants.
- Field border effects: Plant biomass can be overestimated due to border effects (difference in growth and therefore yield between plants located on the border or inside a plot). A study of Gomez and Datta (1971) reported a yield increase ranging from 63% to 159% for rice plants located at the plot border. This could be due to more sunshine access, a better ventilation and less competition for nutrients. We need to sample plants distributed all along the plot.
- The sampling season: In order to be more representative for the Si concentration exported by biomass, we need to collect Si-accumulating crops just before harvest. Indeed, a study of Makabe-Sasaki et al (2014) shows that Si absorption in rice plant is more important at the harvest stage than in tillering stage. In Kawah Ijen, due to field conditions, we harvested plants just before the final stage of growth and this can lead to underestimates of Si export.
- The rice species: The comparison of Si concentrations exported in Indonesia and Japan is difficult because the rice species are different (*Oriza Sativa Indica* in Indonesia and *Oriza Sativa japonica* in Japan) and each species accumulate differently Si in their biomass. This should be taken into account in future studies.

9.5 Conclusion

Our preliminary results suggest that the influence of Si-accumulating crop harvest on dissolved Si fluxes exported by rivers to the ocean should be considered in hydrothermally-active volcanic regions such as volcanic islands.

Indeed, in this study, the first assessments show that, in Kawah Ijen, if all plant parts are exported, $Flux_{exported}$ ranges from 20.35 to 69.89% for acidic waters and from 52.29 to 98.75% for alkaline waters. If we consider that edible parts of plant are exported and inedible parts are restored, the $Flux_{exported}$ falls to 2.76-5.22%. The agricultural practices are crucial to provide accurate assessment. In Aso caldera, the $Flux_{exported}$ is also significant and strongly depends on the number of harvest.yr^{-1}. Further studies are needed to better assess the influence of Si-accumulating crop harvest on DSi fluxes exported to oceans in volcanic islands, contributing disproportionately to DSi delivery to ocean.

9.6 References

Carey, C.J., Fulweiler, W.R., 2016. Human appropriation of biogenic silicon – the increasing role of agriculture, Funct. Ecol. 30: 1331-1339.

Datnoff, L., Snyder, G.H., Korndöfer, G.H., 2001. Silicon in Agriculture, Studies in Plant science. 8, 393.

Delmelle, P., Bernard, A., 2000. Downstream composition changes of acidic volcanic waters discharged into the Banyupahit stream, Ijen caldera, Indonesie. J. Volcanol. Geoth. Res. 97, 55-75.

Delmelle, P., Opfergelt, S., Cornelis, J.T., Ping, C.L, 2015. Volcanic soils, The Encyclopedia of Volcanoes, 2nd Edition, Academic Press, 1253-1264.

Desplanques, V., Cary, L., Mouret, J.C., Trolard, F., Bourrie, G., Grauby, O., Meunier, J.C., 2006. Silicon transfers in a rice field in Camargue (France), J. Geochem. Explor. 88, 190-193.

Dürr, H.H., Meybeck, M., Hartmann, J., Laruelle, G.G., Roubeix, V., 2011. Global spatial distribution of natural riverine silica inputs to the coastal zone, Biogeosciences 8, 597-620.

FAO, Indonesia, 2019. Consulted on 28.05.19: https://www.fao.org/3/Y4347E/y4347e0x.html.

FAOSTAT, 2015. http://faostat3.fao.org/

Godfray, H. C. J., Beddington, J. R., Crute, I. R., Haddad, L., Lawrence, D., Muir, J.F., Pretty, J., , Robinson, S., Thomas S.M., Toulmin, C., 2010. Food security: the challenge of feeding 9 billion people. Science 327, 812.

Gomez, K. A., Datta, S. K. D., 1971. Border Effects in Rice Experimental Plots I. Unplanted Borders. Experimental Agriculture. 7, 87-92.

Hartmann, J., Moosdorf, N., Dürr, H.H., Harashima, A., Okubo, K., Kempe, S., 2010. Predicting riverine dissolved silica fluxes to coastal zones from a hyperactive region and analysis of their first-order controls. Int. J. Earth. Sci. 99: 207-230.

Hauptkorn, S., Pavel, J., Seltner, H., 2001. Determination of silicon in biological samples by ICP-OES after non-oxidative decomposition under alkaline conditions. Fresen. J. Anal. Chem. 370, 246–250.

Jones, L.H.P., Handreck, K.A., 1965. Studies of silica in the oat plant. Plant and Soil. 23, 79-96.

Löhr, A., Bogaard, T.A., Heikens, A., Hendriks, M.R., Sumarti, S., Van Bergen, M.J., van Gestel, C.A.M., van Straalen, N.M., Vroon, P.Z., Widianarko, B., 2005. Natural pollution caused by the extremely acid crater lake Kawah Ijen, East Java, Indonesia. Environ. Sci. Pollut. R. 12: 89-95.

Makabe-Sasaki, S., Kakuda, K.-I., Sasaki, Y., Ando, H., 2014. Effects of slag silicate fertilizer on silicon content of rice plants grown in

paddy fields on the Shounai Plain, Yamagata, Japan. Soil. Sci. Plant. Nutr. 60, 708-721.

Matichenkov, V.V., Bocharnikova, E.A., 2001. The relationship between silicon and soil physical and chemical properties. Studies in plant science. Elsevier. 209-219.

Nakada, S., 2003. IUGG 2003 Field trip guide, A3:1–A3:38.

Nordstrom, D.K., 1982. The effect of sulfate on aluminum concentrations in natural waters: some stability relations in the system Al2O3–SO3–H2O at 298 K. Geochim. Cosmochim. Acta 46, 681–692.

Ramankutty, N., Evan, A., Monfreda, C., Foley, J. A., 2008. Farming the planet: 1. Geographic distribution of global agricultural lands in the year 2000. Global Biogeochem. Cy. 22, 1.

Smetacek, V., 1999. Diatoms and the ocean carbon cycle. Protist, 150, 25-32.

Tréguer, P., De La Rocha, C.L., 2013. The world ocean silica cycle. Annu. Rev. Mater. Sci. 5, 477-501.

U.S. Geological Survey. EarthExplorer. Consulted on 21.03.19: https://earthexplorer.usgs.gov/

van Rotterdam-Los, A. M. D., Vriend, S. P., van Bergen, M. J., van Gaans, P. F. M., 2008. The effect of naturally acidified irrigation water on agricultural volcanic soils. The case of Asembagus, Java, Indonesia. J. Geochem. Explor. 96, 53-68.